Cyclic Variation in the Flow Field Behaviour within a Direct Injection Spark Ignition Engine: A High Speed Digital Particle Image Velocimetry Study

Timothy Justham

M.Eng (Hons)

A Doctoral Thesis submitted in partial fulfilment of the requirements for the award of Doctor of Philosophy of Loughborough University

July 2010

Certificate of Originality

This is to certify that I am responsible for the work submitted in this thesis, that the original work is my own except as specified in the acknowledgements or in footnotes, and that neither the thesis nor the original work contained therein has been submitted to this or any other institution for a higher degree.

…… (Signed)

…… (Date)

Abstract

Currently environmental concerns are driving internal combustion engine manufacturers to seek greater fuel efficiency, more refinement and lower emissions. Cyclic variation is a known obstacle to achieving the greatest potential against these goals and therefore an understanding of how to reduce these is sought. It is widely accepted that cyclic variation in in-cylinder flow motions is a key contributor to overall cyclic variation and therefore the characterisation of factors affecting these is an important step in the process of achieving a better understanding and ultimately control of cyclic variation.

This thesis reports the development of a novel optical engine research facility in which high speed digital particle image velocimetry (HSDPIV) has been applied to the study of flow field behaviour within a direct injection spark ignition (DISI) engine. This study investigates the spatial and temporal development of flow structures over and within many engine cycles. Flow field PIV measurements have been captured with a high spatial resolution and temporal frequencies up to 5 kHz from a number of measurement locations at a large range of crank angles.

The major contributions from this work have included the use of the novel measurement technique to investigate spatial and temporal flow field development in the intake runner, valve jet, in-cylinder tumble and swirl planes and the pent roof. The gathered data have been used to investigate cycle by cycle variations in both high and low frequency flow structures. Major findings of this work have included the observation of highly varying flow fields throughout the engine cycle. Frequency analysis of these flows has allowed the low frequency bulk motions and higher frequency turbulent components to be studied. The low frequency flow field components are shown to create varying flow field interactions within the cylinder that also affect the manner in which the flow develops over the course of the cycle. The intensity of the turbulence

fluctuations, u', has been calculated based upon the high frequency components within the flow and variations within this are shown to correlate with pressure related combustion parameters.

Acknowledgements

I would like to thank my supervisors, Professor Colin Garner, Professor Graham Hargrave and Dr Andrew Clark for their help and encouragement to even begin the research discussed within this thesis. The opportunity they gave me and continued support offered during the course of my studies is very much appreciated. It takes special people to never give up supporting someone. The level of encouragement and support afforded to me during the course of my research and throughout my period of 'writing up' will never be forgotten. Thank you.

I would like to extend a special thanks to Simon Jarvis, and Peter Wileman for two reasons, first and foremost their technical expertise in helping setting up, from a blank canvas, and running the research facility developed during the course of this work. Secondly for their characters, and hence the working environment created in the laboratory, helping make it a very enjoyable (yet character building) place to work.

At Jaguar, many thanks go to Steve Richardson, Stan Wallace, Dave Richardson and colleagues, whose support of this work and of me is not to be forgotten. Along with those named above the support for this work received from the EPSRC, Jaguar LandRover and Shell Global Solutions has been greatly appreciated.

Martin Hyde and TSI for their product support for the High Speed Digital PIV system. Also the opportunity they offered through the loan of the second system used within this research.

A big thank you must go to Stephen Molloy, a true friend.

Lastly but certainly not least I must make a big thank you to my wife Laura who's bottomless love and support for me was invaluable during the completion of this thesis. She may never fully understand how much this has meant to me but without it I am certain this work would not be presented here.

To Laura

Table of contents

Certificate of Originality ..... **i**

Abstract ..... **ii**

Acknowledgements ..... **iv**

Table of contents ..... **vii**

Nomenclature ..... **xi**

Chapter 1 Introduction **1**

1.1 Background 1

1.2 Research objectives 2

1.3 Contributions from this work 2

1.4 Overview of thesis 4

Chapter 2 Spark ignition engine flow fields **6**

2.1 Introduction 6

2.2 The reciprocating internal combustion engine 7

2.3 Spark ignition engine fluid motion 8

2.3.1 Intake flows 8

2.3.2 In-cylinder flow motion 17

2.4 Turbulence 21

2.4.1 Turbulent flow 22

2.4.2 Turbulent length scales 24

2.4.3 Turbulent premixed combustion in SI engines 27

2.5 Cycle by cycle variation 30
2.5.2 Flow field cycle by cycle variation 37
2.6 Flow field characterisation 39
2.7 Flow field diagnostics 43
2.7.1 Laser Doppler Velocimetry 44
2.7.2 Particle Image Velocimetry 44
2.8 Summary 45
Chapter 3 High Speed Particle Image Velocimetry 46
3.1 Introduction 46
3.2 Theory of Particle Image Velocimetry 47
3.2.1 Flow seeding 50
3.2.2 Image recording 55
3.2.3 Image Analysis 59
3.3 High Speed Digital Particle Image Velocimetry 64
3.3.1 Overview of system used 64
3.4 Errors 72
3.5 Summary 76
Chapter 4 Experimental Configuration 77
4.1 Introduction 77
4.2 Jaguar single cylinder optical engine 78
4.2.1 The engine 78
4.2.2 Optical intake runner 83
4.2.3 Tumble Flap 85
4.3 Auxiliary Equipment 85
4.3.1 Engine timing 85
4.3.2 Motoring and absorbing drive system 87

4.3.3 Data acquisition 87
4.3.4 Pressure measurement 88
4.3.5 Lambda sensor 89
4.4 PIV alignment and calibration procedure 89
4.5 Fired engine baseline tests 91
4.6 Summary 98
Chapter 5 Flow field variation around combustion 100
5.1 Introduction 100
5.2 Flame Imaging 100
5.2.1 Images through the piston crown 101
5.2.2 Imaging through the pent roof window 111
5.3 Pent roof flow 120
5.3.1 Measurement conditions 120
5.3.2 Measured velocity fields 124
5.4 Synchronised pressure and flow field measurements 143
5.4.1 Measurement conditions 143
5.4.2 Measured velocity fields and pressure data 144
5.5 Summary 147
Chapter 6 Cyclic variability of intake flows 149
6.1 Introduction 149
6.2 Intake runner flow 150
6.2.1 Measurement conditions 150
6.2.2 Measured velocity fields 153
6.3 Intake valve jet 166
6.3.1 Measurement conditions 166
6.3.2 Measured velocity fields 170

6.4 Summary 212

Chapter 7 Cyclic variability of in-cylinder flows 213

7.1 Introduction 213

7.2 Tumble plane 213

7.2.1 Bore centre line 213

7.3 Swirl plane 279

7.3.1 Measurement conditions 279

7.3.2 Measured velocity fields 282

7.4 In Cylinder u' Spatial Averaging 308

7.5 Summary 313

Chapter 8 Conclusions and further work 314

8.1 Conclusions 314

8.2 Future work 316

References 319

Appendix A Combustion calculations I

Nomenclature

A_c	Imaging array size
A_p	Pixel width
a_p	Particle radius
a_I	Imaged area size
c_r	Critical value to assess whether the imaged particle size is sufficient
$c_{\max}$	Maximum displacement of a particle image between captures
D	Pipe diameter or characteristic length
Da	Damkohler number
D_a	Lens aperture diameter
dV	Volumetric variation
d_a	Actual particle displacement
d_b	Mean bias error
d_I	Imaged particle diameter
d_i	Measured displacement
d_m	Mean particle displacement
d_p	Seed particle diameter
d_s	Airy disk diameter
F/A	Fuel air ratio
F_p	Viscous force
f	Focal length
$f^{\#}$	Lens f-number
f_u	Frequency of fluid velocity fluctuations
I_1	Interrogation region 1
I_2	Interrogation region 2
I_d	Size of interrogation region
i	Cycle number
L	Characteristic width of flow or macro-scale
L_i	Interrogation region size
ℓ_K	Kolmogorov micro scale
ℓ_o	Integral scale or turbulence macro-scale

ℓ_λ	Taylor micro-scale
l/u	Lifespan of a typical eddy: turn-over time
M_o	Image magnification
m_a	Mass of air induced into the cylinder
$\dot{m}_a$	Mass flow rate of air
m_p	Mass of the particle
N	Rotational speed of the crankshaft (rps)
N	Number of particle image pairs per interrogation region
n	Number of cycles included in the average
n_R	Number of crank revolutions for each power stroke per cylinder
P	Indicated power or Pressure
Q_{HV}	Heating value of the fuel
q	Normalised diameter for Mie scattering
R	Cross correlation field between two interrogation regions
Re	Reynolds number
Re_T	Turbulent Reynolds Number
S_L	Laminar flame speed
t	Time
U	Velocity component in the x-direction
$\bar{U}$	Mean flow velocity
$U(t)$	Instantaneous velocity at t
U_0	Amplitude of fluid velocity fluctuations
$\lvert U_o \rvert$	Velocity magnitude associated with the interrogation region
U_{LF}	Low frequency or bulk flow velocity component
U_{HF}	High frequency velocity component
$\bar{U}_{LF}$	Mean low frequency flow field components
U_{CVLF}	Low frequency cyclic variation
$\overline{\overline{U_{(\theta)}}}$	Spatial mean of the ensemble mean velocity field
$U_{rmsCVLF}$	Root-mean-square (rms) of the low frequency cyclic variation
u	Fluctuating component (can be only in the orthogonal direction x)
$u(t)$	Random velocity fluctuations
u'	Intensity of the turbulent fluctuations
$u'_{HF\ (spatial)}$	Spatial turbulence intensity
$u'_{HF\ (temporal)}$	Temporal turbulence intensity
u_{CV}	Spatial velocity variation
V	Velocity
V	Velocity component in y-direction

V_d	Displaced cylinder volume.
V_s	Swept volume
$\hat{V}$	Relative Velocity
v	Fluctuating component in the orthogonal direction y
W	Laser sheet width
w	Fluctuating component in the orthogonal direction z
x	Position in x within vector field
y	Position in y within vector field

Greek Symbols

Δt	Time separation
δ_L	Laminar flame thickness
ε_{bias}	Bias error
ε_{random}	Random error
$\varepsilon_{residual}$	Residual error
$\varepsilon_{systematic}$	Systematic error
ε_{total}	Estimation of the single displacement error
η_v	Volumetric efficiency
η_f	Fuel conversion efficiency
θ	Angle between U and M or crank angle
λ	Wavelength
λ	Lambda, ratio of actual to stoichiometric air fuel
μ	Dynamic viscosity
μ_{fluid}	Dynamic viscosity of the fluid
ν	Fluid kinematic viscosity
v_p	Particle velocity
ρ	Fluid density
ρ_p	Particle density
$\rho_{a,i}$	Inlet air density
σ	Standard deviation
σ_E	rms of the velocity variation
σ_{imep}	Standard deviation of imep
τ_T	Characteristic flow or mixing time
τ_L	Characteristic chemical reaction time
τ_p	Time constant for particle response to change in velocity
ϕ_l	Phase lag
ω	Angular velocity of the crank shaft

Abbreviations

ABDC	After Bottom Dead Centre
AFR	Air fuel ratio
ATDC	After Top Dead Centre
BDC	Bottom Dead Centre
CA	Crank Angle
CFD	Computational Fluid Dynamics
COV	Co-efficient of Variance
DISI	Direct Injection Spark Ignition
DOF	Depth of focus
ECM	Engine control and monitoring
EGR	Exhaust Gas Residuals
ETU	Engine timing unit
FFT	Fast Fourier Transform
fps	Frames per second
HSDPIV	High Speed Digital Particle Image Velocimetry
IC	Internal Combustion
imep	indicated mean effective pressure
isfc	Indicated specific fuel consumption
LDV	Laser Doppler Velocimetry
LSP	Laser Speckle Photography
LSV	Laser Speckle Velocimetry
MBT	Maximum break torque
mfb	mass fraction burned
Nd:YLF	Neodymium Yttrium Lithium Fluoride laser
NO_x	Oxides of Nitrogen
PID	Proportional Integral Derivative
PIV	Particle Image Velocimetry
POD	Proper Orthogonal Decomposition
rms	root mean squared
RPM	Revolutions per minute
RPS	Revolutions per second
SI	Spark Ignition
SNR	Signal to Noise Ratio
TDC	Top Dead Centre
TKE	Turbulent kinetic energy
TR	Tumble ratio
TTL	Transistor-Transistor-Logic

Chapter 1 Introduction

1.1 Background

The internal combustion engine has been an increasingly significant part of our lives for more than a century. Growing awareness of problems associated with engine emissions has lead to pressures being placed on manufacturers to reduce the environmental impact and increase the fuel economy of their products. Automotive engine manufactures have to invest in new technologies which will allow these demands to be met. One important aspect of fulfilling this challenge is to build a better understanding of the processes involved in the in-cylinder combustion event. Measurement of these processes is fundamental to advancing knowledge in this area.

There are many factors which are influential to in-cylinder combustion, one of which is that of the charge motion (Ozdor *et al.* (1994)). It is well documented that fluid flow motions generated within the cylinder during the intake and compression strokes have a fundamental effect on engine performance. Consequently cyclic variations in these are likely to contribute to cyclic variations in engine performance. An understanding of the development of these variations will assist engine designers to design for reduced levels of cyclic variation thereby helping drive for improved mean cycle performance.

1.2 Research objectives

The two major objectives of the research reported in this thesis were:

1. To develop an optical engine research facility and robust set of experiment tools for the routine application of temporally resolved high speed digital particle image velocimetry (HSDPIV) to study flow fields within the engine. This facility was to be able to operate in both motored and fired modes and allow the synchronised capture of HSDPIV and in-cylinder pressure data for comparative analysis.
2. Perform temporally resolved HSDPIV measurements on flows within the optical engine to investigate the behaviour of cyclic variations within these flow fields.

1.3 Contributions from this work

A major achievement from this work has been the development of a novel optical engine facility which enables the routine capture of in-cylinder flow fields using temporally resolved HSDPIV at kHz rates, under realistic fired engine conditions. This research facility allows the synchronised acquisition of flow field and cycle performance data via a data acquisition system, also built as part of this work.

This facility has allowed the flow field on a planar region to be tracked temporally as the cycle develops. This ability has generated substantial amounts of data, only a fraction of which can be presented in this thesis. One important application where these data have been applied is in the validation of CFD models used by the engine manufacturers.

Cyclic variations have been tracked both spatially and temporally throughout the engine cycle, from intake to combustion. Data have been collected in various planes within the optical engine, predominantly under motored conditions. Data collected have shown correlations between flow field characteristics and cycle pressure data.

The culmination of this work occurred when the research facility was commissioned for fired engine study and the continuation of investigations in this area has already begun, using the facility and tools developed by the author. This work has considered the link between the high frequency flow fluctuations, measured with the HSDPIV system, and the cycle performance in terms of burn rate and imep (Rimmer *et al.* (2009)).

Publications arising from this work:

1. **Justham, T.**, **Jarvis, S.**, **Clarke, A.**, **Garner, C.P.**, **Hargrave, G.K.** and Richardson, D., "Single Cylinder Motored SI IC Engine Intake Runner Flow Measurement Using Time Resolved Digital Particle Image Velocimetry, SAE Paper No 2006-01-1043", *Proceedings of the SAE 2006 World Congress & Exposition*, Detroit, Michigan, USA, April 2006.
2. **Jarvis, S.**, **Justham, T.**, **Clarke, A.**, **Garner, C.P.**, **Hargrave, G.K.** and Richardson, D., "Motored SI IC Engine In-Cylinder Flow Field Measurement Using Time Resolved Digital PIV for Characterisation of Cyclic Variation, SAE Paper No 2006-01-1044", *Proceedings of the SAE 2006 World Congress & Exposition*, Detroit, Michigan, USA, April 2006.
3. **Justham, T.**, **Jarvis, S.**, **Clarke, A.**, **Garner, C.P.**, **Hargrave, G.K.** and **Halliwell, N.A.**, "Simultaneous Study of Intake and In-Cylinder IC Engine Flow Fields to Provide an Insight into Intake Induced Cyclic Variations", *Journal of Physics: Conference Series 45*, 2006, ISSN 1742-6588.
4. **Jarvis, S.**, **Justham, T.**, **Clarke, A.**, **Garner, C.P.**, **Hargrave, G.K.** and **Halliwell, N.A.**, "Time Resolved Digital PIV Measurements of Flow Field Cyclic Variation in an Optical IC Engine", *Journal of Physics: Conference Series 45*, 2006, ISSN 1742-6588
5. **Long, E.J**., **Hargrave, G.K.**, **Jarvis, S.**, **Justham, T.** and **Halliwell, N.A.**, "Characterisation of the interaction between toroidal vortex structures and flame front propagation", *Journal of Physics: Conference Series 45*, 2006, ISSN 1742-6588

6. **Stansfield, P.**, **Wigley, G.**, **Justham, T.**, **Catto, J.** and Pitcher, G., "PIV Analysis of In-cylinder Flow Structures Over a Range of Realistic Engine Speeds", *Experiments in Fluids*, 43(1), July 2007, 135-146, ISSN 07234864.
7. **Justham, T.**, **Jarvis, S.**, **Clarke, A.**, **Garner, C.P.**, **Hargrave, G.K.** and **Halliwell, N.A.**, "Simultaneous Study of Intake and In-Cylinder IC Engine Flow Fields to Provide an Insight into Intake Induced Cyclic Variations", *Second International Conference on Optical and Laser Diagnostics*, *(ICOLAD 2005)*, London, UK, 2005 [CD-ROM].
8. **Jarvis, S.**, **Justham, T.**, **Clarke, A.**, **Garner, C.P.**, **Hargrave, G.K.** and **Halliwell, N.A.**, "Time Resolved Digital PIV Measurements of Flow Field Cyclic Variation in an Optical IC Engine", *Proceedings of the Second International Conference on Optical and Laser Diagnostics (ICOLAD 2005)*, London, UK, 2005 [CD-ROM].
9. **Long, E.J., Hargrave, G.K.**, **Jarvis, S.**, **Justham, T.** and **Halliwell, N.A.**, "Characterisation of the interaction between toroidal vortex structures and flame front propagation", *Proceedings of the Second International Conference on Optical and Laser Diagnostics (ICOLAD 2005)*, London, UK, 2005 [CD-ROM]

1.4 Overview of thesis

This thesis has been divided into seven further chapters. Chapter 2 presents a review of SI engine operation and select previous literature (from the vast amount published on this subject) to provide an outline of previous findings within this field. The chapter begins with an introduction to the reciprocating IC engine and introduces previous work on fluid motions which occur within the SI engine. A review of turbulence and its characterisation is then given leading to a discussion on engine cyclic variations and the importance of improving our understanding of flow field cyclic variation. Methods of flow field characterisation are then discussed along with a brief introduction to flow field measurements.

Chapter 3 introduces the cutting edge HSDPIV measurements system used within this study, along with important considerations which should be made when setting up PIV measurements in order to maximise the accuracy of the results.

Chapter 4 introduces the optical engine and auxiliary equipment used within the novel research facility developed during this work. This chapter also introduces cycle pressure data to demonstrate the baseline level of cyclic variation experienced by the engine under investigation.

Chapter 5 describes the development of the flame kernel through high speed chemiluminescence imaging to investigate cyclic variations visible within the flame structure. This leads on to a study of the spatial and temporal nature of the flow fields around the spark plug at the time of ignition. This chapter finishes by comparing, on a cycle by cycle nature, the high frequency turbulence characteristics of the flow fields within this region to burn rate and cycle performance parameters.

Chapter 6 builds upon the understanding obtained within Chapter 5 and returns to the beginning of the engine cycle (i.e. Induction) to begin the journey of tracing how cyclic variations in the flow field behaviour at the time of combustion are instigated. HSDPIV studies of the flow field within both the intake runner and valve jet flow are presented. This has investigated both cyclic variations in the bulk motion characteristics and within the superimposed higher frequency turbulent fluctuations.

Chapter 7 presents HSDPIV data in both tumble and swirl planes of the engine. In these regions the cyclic variation in bulk flow motions are investigated, studying how the variations shown in Chapter 6 develop throughout the remainder of the cycle therefore providing the flow field characteristics previously shown in Chapter 5.

Chapter 8 summarises the contributions from this thesis, and discusses possible further work and improvement to aid the understanding of the affect of flow field cyclic variations on the overall cycle performance.

Chapter 2 Spark ignition engine flow fields

2.1 Introduction

This chapter introduces the internal combustion (IC) engine, concentrating on gasoline spark ignition (SI) engines operating on a four stroke cycle. This is followed by a review of the importance of air flow motion generated by the induction process and its basic behaviour as the engine cycle progresses. A discussion on turbulent flow is presented and its fundamental effect on the turbulent premixed combustion processes and particularly flame propagation.

The main aim of this research has been to investigate cyclic variation in air flow motion within a Direct Injection Spark Ignition (DISI) engine. Section 2.5 therefore introduces the main indicators and sources of cyclic variation in an SI engine. Details of previous work into flow cyclic variations are introduced. This is followed, in Section 2.6, by a discussion of standard flow field characterisation techniques which can be used for studying flow behaviour within an IC engine.

Finally, Section 2.7 introduces common flow diagnostic techniques commonly used in the study of IC engine flow behaviour. The relative merits of each are discussed with respect to the work presented within this thesis giving the motivation for selecting High Speed Digital Particle Image Velocimetry (HSDPIV) for the measurement of intake and in-cylinder flow.

2.2 The reciprocating internal combustion engine

Ferguson (2001) defines an internal combustion engine as "*an engine in which the chemical energy of the fuel is released inside the engine and used directly for mechanical work*". The basic operating principles of the IC engine are described in introductory texts such as Heywood (1988) and Stone (1999). A brief description of the fundamentals of IC engine operation is included here. This description is limited to gasoline SI engines operating on a four stroke cycle since this is the focus of this Thesis.

The four stroke operating cycle can be divided into its individual strokes as described by Stone (1999):

Induction: The inlet valve is open, and the piston travels down the cylinder drawing in fresh charge;

Compression: Both valves are closed and the piston travels up the cylinder. As the piston approaches top dead centre (TDC) ignition occurs;

Expansion: The power or working stroke. Combustion propagates throughout the charge raising the temperature and pressure and forcing the piston down. As the power phase comes to an end, the exhaust valve opens and an irreversible expansion of the exhaust gases (termed 'blow-down') occurs;

Exhaust: With the exhaust valve kept open, the piston travels up the cylinder and much of the remaining gases are expelled. At the end of the exhaust stroke, when the exhaust valve closes some exhaust gas residuals will be left; these will dilute the charge of the next cycle.

It is well understood that in-cylinder flow motion within a spark ignition engine is a major factor that affects the combustion process; both the bulk flow convective motion and turbulence are important. The in-cylinder flow structures, which are defined initially by the intake process, may then be substantially modified by the piston motion

during compression. The jet like character of the intake flow and the way in which it interacts with the cylinder walls and moving piston creates large scale rotating flow structures within the cylinder. These flows are largely dependant on the inlet port, valve, cylinder and piston geometries. In general, re-circulating flows of this nature are sensitive to small variations within the flow and, therefore, substantial cyclic variations can occur within the in-cylinder flow (Heywood (1988)). The primary tasks of the engine induction and fuel systems are to prepare, from ambient air and fuel, an air-fuel mixture that satisfies the requirements of the engine over its entire operating range. Both the turbulence characteristics and the bulk flow motion in the cylinder are strongly affected by the inlet port and valve design. Nadarajah *et al.* (1998) comments that it has long been recognised that the turbulent flow field in an engine cylinder at the end of the compression stroke has a profound effect on the combustion process, influencing the fuel consumption, performance and exhaust emissions. Therefore, the variations which may occur due to small variations in the recirculating flow can influence the breakdown in to turbulent motions and hence, the turbulent flow field present at the end of the compression stroke.

2.3 Spark ignition engine fluid motion

2.3.1 Intake flows

Although engine intake system design is primarily optimised for good engine performance, in practice, the intake manifold design, for example, is often compromised by factors such as cost, ease of manufacture and assembly, and package space at the expense of optimised flow (Stone (1999)). The purpose of the intake process is to allow the fresh charge for the next combustion event to enter the engine cylinder. Heywood (1988) shows that the mass of air induced into the cylinder (m_a) is proportional to the indicated power (P) as given by the following expression

$$P = \frac{\eta_f m_a N Q_{HV} \left(F/A\right)}{n_R}, \qquad \text{Equation 2.1}$$

where η_f is the fuel conversion efficiency, N is the rotational speed of the crankshaft (revolutions per second), Q_{HV} is the heating value of the fuel, F/A is the fuel air ratio and n_R is the number of crank revolutions for each power stroke per cylinder. Pressure losses occur as the air or air-fuel mixture passes through each component in the induction system. The volumetric efficiency (η_v), an overall measure of the effectiveness of a four stroke engine's intake and exhaust system as an air pumping device, is defined as follows

$$\eta_v = \frac{2\dot{m}_a}{\rho_{a,i} V_d N}, \qquad \text{Equation 2.2}$$

where $\dot{m}_a$ is the mass flow rate of air, $\rho_{a,i}$ is the inlet air density and V_d is the displaced cylinder volume. The pressure drop experienced in the intake system depends on the engine speed, the flow resistance imposed by the elements within the system, the cross sectional area through which the fresh charge moves and the charge density.

It is usual to take advantage of the inertia of the gasses during the intake and the exhaust processes through control of valve timing and phasing, and in the case of naturally aspirated engines the passage of pressure waves within the intake (Stone (1999); Winterbone and Pearson (1999)). As engine speed increases, the inertia of the air in the intake system increases the pressure in the intake port and continues the charging process as the piston reaches bottom dead centre (BDC) and starts the compression stroke. This 'ram' effect increases as engine speed is increased. Since intake valve timing is designed to take full advantage of the ram effect at high engine speeds the intake valve is often closed well into the compression stroke. However, at low engine speeds when the inertia in the intake charge flow is lower, backflow or reverse flow into the intake system from the cylinder can occur as the cylinder pressure rises due to the upward piston motion. Limitations are imposed through fixed cam geometries controlling both valve lift and timing. Therefore, optimisation is not available for all engine operating conditions. Variable valve timing strategies such as cam phasing,

switchable tappets or cams offer some level of optimisation of valve timing and variable valve lift. However, the advantages offered by these solutions are limited to a fixed number of switchable hardware configurations. Fully variable valve actuation systems offer substantial improvements in optimisation for engine speed and load conditions; however; their power requirements and the package size and weight mean that they are currently the reserve of research engines to give added flexibility.

The intake system geometry, especially the inlet ports and valves, is understood to be of great importance in the control of the flow motion generated within the cylinder. The effect of the intake system on the in-cylinder flow is therefore of significant importance when designing an engine and optimising its performance. The remainder of this section focuses on the flow motions within the manifold, port and valves.

2.3.1.1 Flow in intake manifolds

The requirements of an intake manifold are to provide the engine's cylinder with the required air or air-fuel charge and to do this in a way which best enhances the operation of the engine. To maximise the volumetric efficiency (Equation 2.2) the intake manifold must provide the most efficient flow possible, minimising the pressure drop created within the intake system and allowing the maximum trapped mass within the cylinder. During throttled operation an intentional pressure drop is imposed to limit the trapped charge, and hence reduce the engine's power.

The intake process can be broken down into three distinct flow phases. The first phase, often referred to as the overlap backflow, which occurs as the intake valve is opening if the cylinder pressure is greater than the pressure in the intake manifold. This phase is more obvious at part throttle conditions and is dependant on the valve timing strategy. The second phase, which is the main intake flow phase, occurs as the piston draws charge into the cylinder through the intake port. The third and final phase, backflow, occurs at low and intermediate engine speeds when the inertia of the charge is low and the intake valve closes too late to prevent charge from flowing back into the intake port

due to the rising piston and in-cylinder pressure. This phase is commonly referred to as displacement backflow as charge which has been successfully introduced into the cylinder is lost back into the intake system.

Air flow in a manifold occurs as series of pulses, going to each cylinder in turn, and is dependant on the number of cylinders served by the manifold, the cam timing and the firing order of the engine. There is a fluctuating flow at the throttle which is a direct consequence of the pulsating nature of the flow created by the periodic filling of the engine cylinders. Heywood (1988) describes the pulsations to occur in two stages. The first stage occurs when the outflow from the manifold into the cylinder undergoing its intake stroke is larger than the flow entering past the throttle; at this point the cylinder also draws from the rest of the intake manifold. The second stage occurs when the flow into the cylinder is lower than the flow past the throttle; at this point flow will enter the rest of the manifold.

Engines using port or direct fuel injection systems only require the intake manifold to manage the air flow since there is not the need to transport fuel throughout the entire manifold as with, for example, carburettor systems. This allows designers to take advantage of the greater freedom within the packaging constraints, optimising for the inertia and wave effects of the flow.

The air flows to each cylinder of a multi-cylinder engine are not identical, even under steady engine operating conditions. The geometrical differences and the relationship of the intake branches can lead to significant variations in the mass flow rate and flow behaviours experienced by each cylinder. Heywood (1988) comments that variations in average air mass flow rate to each individual cylinder of up to ± 5% are quite common. Larger peak-to-peak variations (± 15%) have been measured. The extent of the variation is affected by engine speed and load changes. As a result, each cylinder may perform in a different way at a given engine speed and load condition. Careful consideration is required in the design of the intake manifold geometry to provide similar flows to each cylinder. If exhaust gas residuals (EGR) are introduced into the manifold the

distribution between cylinders needs to be carefully studied to ensure that each cylinder receives the correct amount of EGR for, for example, NO_x emissions control.

The time-varying inlet flow into the cylinder causes expansion waves to propagate back into the intake manifold. The expansion waves travel at the local speed of sound relative to the moving gas. When they reach the open end of the manifold at the plenum a positive pressure wave is reflected towards the cylinder. The arrival of these positive pressure waves at the intake valve causes the local pressure to be raised above the previous intake pressure, forcing more mass into the cylinder and increasing the overall inducted air mass. It is therefore common to tune the intake system to take advantage of the wave action. However, as with cams, a fixed manifold length means that optimisation for all engine speed and load conditions is not possible. Variable or multi-stage manifolds allow the engine to be tuned for a greater range of speeds (Winterbone and Pearson (1999).

Many publications discuss the unsteady gas motion within intake manifolds. These include experimental investigations and numerical simulation methods (Winterbone and Pearson (1999)). Very few studies have investigated the detailed fluid flow structures within the intake manifold. One study of note is that of Gindele *et al.* (1997) where a motored single cylinder engine with an optical access spacer was fitted in the intake runner just preceding the port. This allowed the flow field within the manifold to be investigated with the use of particle image velocimetry (PIV). Two two-dimensional planes within the manifold were studied. The first was a vertical plane on the manifold centre line which showed the flow velocity into the cylinder, the second was a plane cutting through the cross section of the manifold. This study showed that the velocity components acting on the cross sectional plane was less than ten percent of the flow velocity into the cylinder. At low engine speeds no overall bulk motion of the gas core during the valve closed period was detected in the vertical plane due to wave motion. However, at higher engine speeds the pressure waves were strong enough to move the gas core with velocities up to 10 $m.s^{-1}$. Periods of backflow were observed at both valve opening and valve closing, with the backflow at valve closure not being visible above an engine speed of 4800 rpm for the valve timing strategy and intake system geometry

used. Gindele *et al.* (1997) used this study to validate velocity estimations based on pressure data recorded within the runner. These estimations were then used to develop an estimation of mass flow.

2.3.1.2 Flow in the intake port

The function of the intake port is to establish a desired flow pattern around the intake valves which, in turn, affects the way the flow enters the cylinder. Due to the difficulty imposed by the complex geometry of the intake ports, studies of these flows in real engines are generally limited to investigating the effect of changes to port geometry on the in-cylinder flow structure. Steady flow experiments have been more commonly used to investigate flow fields within the intake port allowing simplified physical models to be produced without water or oil galleries and the need for a cam shaft. Further to this the refractive index matching techniques have been employed to minimise the problems caused by imaging through the complex curves within the port (Yianneskis *et al.* (1993)). This required optically clear models to be manufactured from a material such as acrylic and to be used with a working fluid selected to have a similar refractive index to the surrounding material. Yianneskis *et al.* (1993) performed steady flow experiments using this technique and employed PIV to generate planar velocity field data within a detailed geometry. The work investigated flow instabilities and their effect on the performance of the port with a fixed valve lift of 10 mm. By comparing the instantaneous flow fields with the ensemble average flow field, strong variations were noted in the flow preceding the valve.

Omori *et al.* (1991) used windows machined into the port to perform their study. Laser Doppler Velocimetry (LDV) was employed to investigate the flow in two different ports; conventional and tumble, under steady flow conditions. The conventional port was seen to turn the flow to a greater extent creating an even flow heading towards the valve. The tumble port has less effect on steering the flow, presenting the valve with a flow that has a greater bias towards one area of the valve. They noted that the turbulence intensity at combustion had already been determined by the middle of the

intake stroke. This was governed by the tumble motion generated through the intake port and valve geometry. Omori *et al.* (1991) concluded that to enhance the engine's tumble ratio it is essential to increase the air flow in the upper valve curtain section allowing increased air flow across the head towards the exhaust valve side of the engine.

2.3.1.3 Flow through the Inlet Valves

This discussion is limited to considering the poppet valve as it is the most commonly used inlet valve. The poppet valve has the advantage of being inexpensive, with good sealing characteristics and is easy to lubricate. The in-cylinder flow fields are strongly influenced by the characteristics of the flow entering the cylinder through the inlet valve curtain. Three basic flow regimes have been highlighted by Annand and Roe (1974) and are shown in Figure 2.1 for steady flow through a valve. These flow regimes occur during the valve opening and closing event due to changes in the maximum effective flow area.

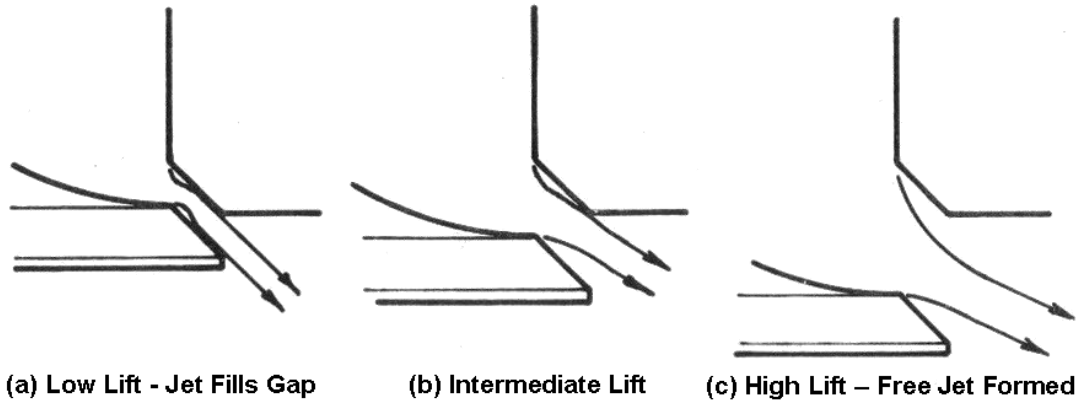

Figure 2.1 - Flow regimes through an inlet valve (Annand and Roe (1974))

At very low lifts the jet fills the valve curtain area and the flow remains attached to the valve head and seat as displayed in Figure 2.1 (a). This gives the flow a high discharge coefficient. As the valve lift increases, the flow separates from the valve head and the

inner edge of the valve seat as presented in Figure 2.1 (b). A sudden decrease in the discharge coefficient is experienced at this point. At high valve lift the flow separates further from the inner edge of the valve seat as shown in Figure 2.1 (c). Heywood (1988) comments that the dynamic flow behaviour of the valve may cause the 'change points' between the different flow regimes to occur at a slightly different valve lifts when compared to the steady flow behaviour. The valve curtain area is an annulus and the flow exiting this can be affected by proximity to cylinder walls or another valve. A basic illustrative schematic of the valve jet flow for an engine with two intake valves and symmetric intake ports is presented in Figure 2.2.

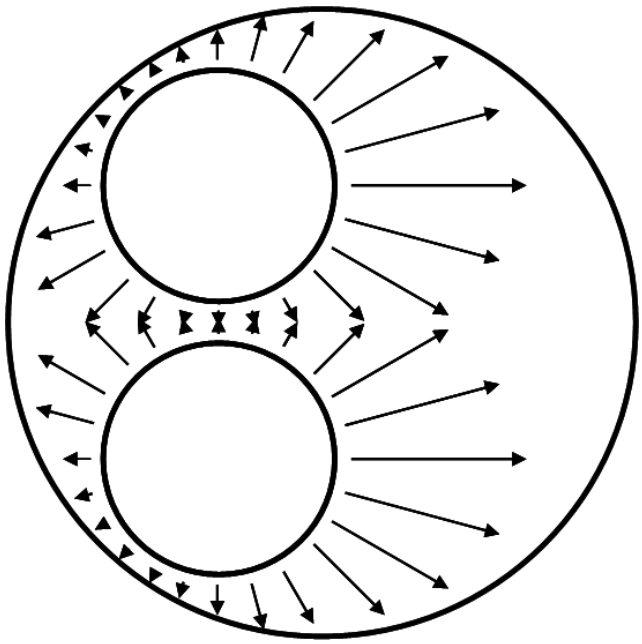

Figure 2.2 - Schematic to illustrate the basic valve jet flow into the cylinder for a cylinder head with two intake valves and symmetric ports

The performance and flow behaviour of the inlet valve assembly is affected by many design details. Influential factors include the valve seat angle, valve seat width, rounding of seat corners, valve head diameter, valve separation, and design of the intake port providing the flow to the valves (Heywood (1988); Stone (1999)).

When the intake jet enters into the cylinder through the intake valve, it experiences a sudden expansion and exhibits complex fluid motions. Lee and Farrell (1993) studied the intake jet as it entered the cylinder. Their study used a cylinder head mounted on to an optical cylinder and connected to a steady flow bench. The valves were actuated by an electric motor providing the required cam rotation. Investigations were performed under static and dynamic valve lift conditions. The basic overall shape of the valve jet flow was repeatable, but exhibited noticeable cyclic variations in its detailed flow pattern. As expected, at the exit of the intake valve a high velocity jet profile was seen. As the jet left the valve curtain area it was seen to entrain the in-cylinder air as a result of the shear layer created, this caused vortices to form. When valve lift was large, flow separation from the valve seat was observed as described by Annand and Roe (1974).

At high cam speeds, Lee and Farrell (1993) observed that the shear flow between the intake jet and the ambient air became thinner. Large scale interactions between the jet flow and in-cylinder air were experienced during valve opening, but overall flow structures remained similar. Comparisons between static and dynamic studies showed more active entrainment of the ambient air in the static flow cases, with higher jet velocities being reached for the same pressure drop across the valve. The cyclic variations in the intake valve flow were exhibited as changes in the in-cylinder air flow, flow at the jet boundary and the jet breakdown pattern.

Most of the turbulence generated during induction arises from eddies generated by the valve jet flow. Heywood (1988) states that the eddies responsible for most of the turbulence production during the intake are the large eddies in the conical inlet jet flow. These eddies are approximately equal in size to the local intake jet thickness. Stone (1999) comments that the radial and axial velocity components within the jet are an order of magnitude greater than the piston velocity. Shear between the jet and the cylinder content lead to the formation of eddies. These eddies are unstable and break down into a cascade of smaller eddies. It is clear that this flow and variations in it can have a large knock on effect on the rest of the cycle.

2.3.2 In-cylinder flow motion

The in-cylinder charge motion within an IC engine has a significant effect on the engine power output, fuel efficiency and exhaust emissions by affecting mixture preparation and the flame development. The fluid motions created during the induction process and the development of these flows through the compression process determine the flow conditions in which the combustion process occurs. As a result of this the flow during the induction process must be controlled to generate conditions which are beneficial for the combustion event. Variations within the flow during the induction process can alter the flow field characteristics at the time of the combustion event.

Arcoumanis *et al.* (1990) comment on the performance gains offered by four valve per cylinder SI engines over their two valve counterparts with regard to engine power and exhaust emissions. These gains are due, in part, to the associated turbulence enhancement resulting from the breakdown of bulk tumble motion generated during the induction stroke. This enhanced turbulent flow field acts to promote rapid burn rates, fast flame propagation and lowers cyclic variation. It is important to note that excessive bulk flow motions can have an adverse affect on the initiation of the flame kernel and therefore early flame growth. This can be due to stretching the arc discharge from the spark plug, or by convection of the early flame kernel towards quenching zones (Reeves *et al.* (1996)).

2.3.2.1 Tumble flow

Tumbling fluid motion is generated during the induction process. This is a large scale rotational motion about an axis perpendicular to the axis of the cylinder. Tumble characteristics are initiated by the induction process when the majority of the flow entering the cylinder is directed across it towards the exhaust valves and is steered downwards, by the confines of the cylinder, towards the piston. As the flow reaches the piston it is steered back towards the intake valve side of the engine. This creates a net rotational motion. The shape and features of the inlet port governs the flow distribution

around the valve curtain and therefore the relative amounts of flow contributing to the bulk tumble motion. The rotational flow motion is deformed as the piston rises during the compression stroke, causing the large scale motion to break down into smaller scales. A tumble ratio is defined as the ratio of the angular velocity of the large scale flow to the engine speed and it is often used to define the tumble characteristics produced by an engine. It can be calculated in many ways depending on the measurement technique but this definition always holds.

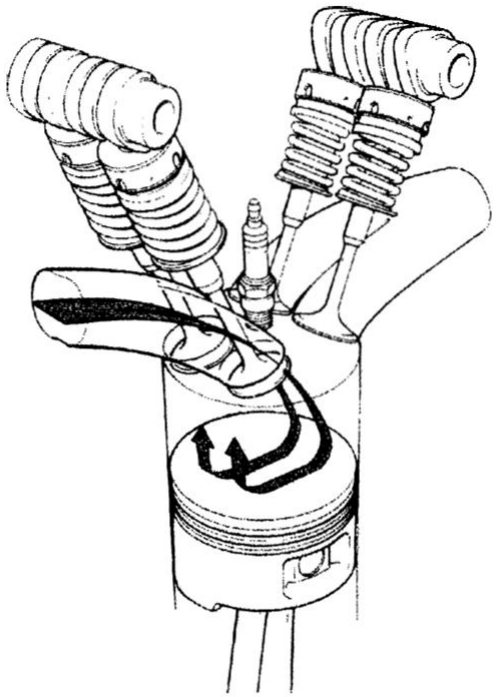

Figure 2.3 - Schematic to illustrate the basic tumble flow behaviour (Wilson *et al.* (1993))

Tumble flow has been the topic of many studies. Kiyota *et al.* (1992), for example, used two different intake geometries and generated different levels of tumble to study flow field motion in an optical engine. The intake which generated the strongest tumble also generated the greatest in-cylinder turbulence. By injecting fuel into only one port, stratification of the charge was maintained throughout the compression stroke. Hu *et al.* (1992) also studied tumble using two cylinder heads with different port geometries producing tumble ratios of 0.4 and 1.7. This study also concluded that stronger tumble produced greater turbulence levels during the compression stroke. A reduction in

specific fuel consumption and an increase in the burn rate was noticed for the higher tumble ratio geometry. Also a reduction in the cyclic variation of in-cylinder pressure and a corresponding extension to the lean operating limit, thought to be due to the increased burn rate, was recorded.

Reeves *et al.* (1999) studied the tumble motion in a four valve pent roof production engine using PIV. Planes of measurement were aligned parallel to the cylinder axis, one containing an inlet and exhaust valve axis and another in parallel containing the bore centre line. Using a blockage in the intake port the flow was restricted in certain areas thus enhancing the tumble. Tumble was observed to last late into the compression stroke for both cases; however, the enhanced tumble case showed strong tumble features later into the engine cycle.

Combustion stability, especially under lean mixture conditions, can be improved through the enhancement of flow characteristics. This was confirmed by a number of studies including Le Coz *et al.* (1990); Hadded and Denbratt (1992). Church and Farrell (1998) studied the effects of three intake port angles (5°, 10° and 20° from the horizontal) on the in-cylinder flow structure. For all angles the flow exhibited large scale tumble motions that persisted beyond 270 degrees after top dead centre (ATDC) gas exchange but had largely disappeared by top dead centre (TDC) combustion. The shallowest port angle, 5°, had the most organised flows and a notably higher tumble ratio at BDC after the intake stroke. The 10° port displayed a significant decrease in tumble between BDC and 270° ATDC gas exchange. The largest port angle, 20°, exhibited significantly lower tumble ratio and less structured flow at BDC. Jeon *et al.* (1998) investigated the effect of tumble on lean burn combustion stability. It was noted that by increasing the tumble ratio from 1.05 to 2.40 gave a 14% decrease in combustion duration for 0 to 90% of the mass fraction to burn, along with a 40% reduction in the cyclic variation of maximum pressure.

2.3.2.2 Swirl flow

Swirl is usually defined as an organised rotation of the charge about the cylinder axis (Heywood (1988)). Swirl is generated initially by giving the intake flow angular momentum, generally through the use of helical or directed inlet ports. Some decay in swirl occurs due to friction; however, the deformation imposed by the rising piston is less than that experienced by tumble. A lower deformation rate means that less kinetic energy is dissipated which allows the swirl motion to persist longer into the cycle. Heywood comments that this motion can be seen to continue through the combustion and expansion process. Swirl is commonly designed into diesel engine combustion systems to promote rapid mixing of the injected fuel with the in-cylinder air and helping to increase burn rates. In the past swirl has been used in SI engines to help increase burn rates by increasing the convective flow to enhance flame propagation (Heywood (1988)). However, modern SI combustion systems usually seek turbulence enhancement through the breakdown of the tumble motion to achieve rapid combustion of the charge.

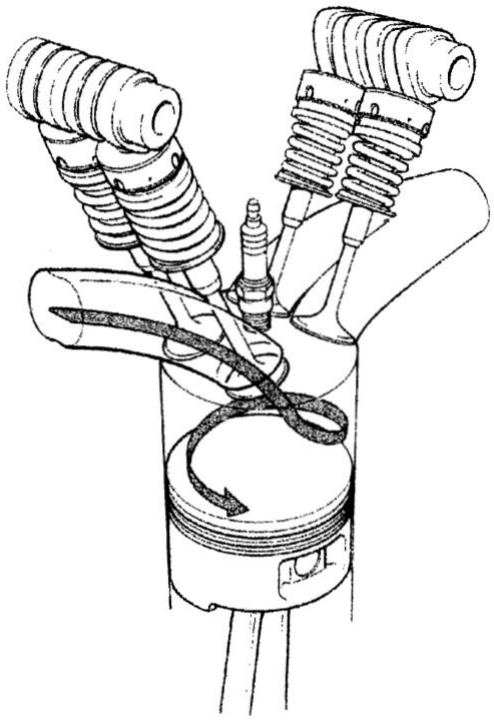

Figure 2.4 - Schematic to illustrate the basic tumble flow behaviour (Wilson *et al.* (1993))

SI engines using two intake valves with symmetrical ports designed to generate a tumble motion will not exhibit classical bulk swirl motion. It is more usual to observe 'wing vortices' (Kuwahara *et al.* (1994)) where the intake jets from each valve interact with each other along the central axis of the cylinder creating two counter rotating vortices, one on each side of the cylinder.

2.4 Turbulence

Modelling turbulent flows has challenged scientists and engineers for many years since the mathematical description of a turbulent flow and solving the resulting governing conservation equations is difficult and is not a trivial problem. Therefore, analytical and numerical solutions to turbulent flows are approximations even for the most simple of geometries and can be subject to significant errors. When studying flow within practical devices such as an IC engine it is important to have an understanding of turbulence and its effects. Turbulence is inherent within an IC engine and exhibits complex three-dimensional motions influenced by combinations of turbulent shear layers, re-circulating regions (eddies) and boundary layers. These features are stretched, twisted and translated as the flow field develops and are influenced by the local vorticity distribution (Davidson (2004). The turbulent flow within the cylinder is unsteady and may experience substantial random variation. The following Section is aimed at providing an introduction to common analysis methods used to extract quantitative turbulence data from a series of flow fields. The discussion is restricted to turbulent, non-reacting, incompressible flows to highlight essential features of interest and provide knowledge required for interpreting the data presented later in this Thesis. Many texts, for example Piquet (1999); Pope (2000); Bernard and Wallace (2002); Davidson (2004) cover the topic of turbulence and turbulent flows in more detail. Following this discussion the impact of turbulence on premixed combustion is discussed.

2.4.1 Turbulent flow

Turbulence is stochastic in nature with in-cylinder flows exhibiting a large range of both spatial and temporal frequencies which have a fundamental effect on the combustion process. Therefore, the turbulent nature of the in-cylinder flow field has been the subject of many studies, for example Arcoumanis *et al.* (1990); St. Hill *et al.* (2000); Song *et al.* (2001); Lee and Lee (2003). Managing the effects of turbulence on combustion systems is an important area in improving and optimising their design to generate improvements in engine power, exhaust emissions and refinement.

Fluid motion may be classified as either laminar or turbulent in nature. In order to distinguish between the two classifications of flow, Osborne Reynolds (1842-1912), demonstrated a dimensionless parameter that differentiated laminar and turbulent flow. The Reynolds number (Re) is the ratio of the inertia force to the viscous force acting on an element in the fluid and is given as follows

$$\mathrm{Re} = \frac{\rho V D}{\mu}. \qquad \text{Equation 2.3}$$

It relates fluid density (ρ), velocity (V), pipe diameter or characteristic length (D) and dynamic viscosity (μ), as a dimensionless number. The Reynolds number for which laminar or turbulent pipe flows are experienced is not precisely given. It is widely accepted, however, that the flow in a round pipe is laminar if the $\mathrm{Re} < 2100$. Similarly flow in a round pipe is turbulent if the $\mathrm{Re} \gtrsim 4000$. For Reynolds numbers between these limits the flow may switch between laminar and turbulent in an apparently random fashion, this characteristic has been named transitional flow (Munson *et al.* (1998)). Due to this transitional flow, the actual transition from laminar to turbulent flow depends on system characteristics and is not easy to define. An important point to note is that fluid motion is almost always inherently unstable and these instabilities are suppressed only if the viscous dissipation is high enough

(Davidson (2004)). Pope (2000) gives two factors which cause turbulent flow to be random and unpredictable, these are:

i. In any flow there are unavoidable perturbations in initial conditions, boundary conditions and material properties.

ii. Turbulent flow fields display an acute sensitivity to such perturbations.

The random unsteadiness associated with various flow properties is the signature of a turbulent flow. A basic theory for turbulent flow fields can be considered as random motions (or fluctuations) in three dimensions with vortices of varying size superimposed on the uniform (mean) motion of the fluid. Viscous shear stresses dissipate the vortices and in doing so generate smaller vortices with an overall loss in turbulent energy. As energy is required to generate turbulence, if no further energy is supplied to the flow then the turbulent flow will decay.

If the time average of a turbulent flow can be assumed to be steady then the flow in general can be decomposed into a mean motion plus a random fluctuating component. The mean quantities can be defined by taking the time average of any flow property (e.g. velocity, pressure, temperature) over a sufficiently large time interval (Turns (2000)). Ideally this time interval tends to infinity; however, the mean is likely to converge to an approximate solution well before this. The calculation of the mean flow velocity ($\bar{U}$) for a turbulent flow is

$$\bar{U} = \frac{1}{\Delta t}\int_{t_1}^{t_2} U(t) \qquad \text{Equation 2.4}$$

where $\Delta t = t_2 - t_1$ and represents the time over which the average is calculated and $U(t)$ is the instantaneous velocity at time t. The random velocity fluctuations ($u(t)$) are defined as the difference between the instantaneous velocity and the mean flow

velocity. The instantaneous velocity can, therefore, be expressed as the sum of the mean flow velocity and the velocity fluctuation at that same instance,

$$U(t) = \bar{U} + u(t). \qquad \text{Equation 2.5}$$

The decomposition into the mean and fluctuating (turbulent) component is referred to as the Reynolds decomposition. It is common to describe the intensity of the turbulent fluctuations u' in terms of a root-mean-square (*rms*) such that

$$u' = \sqrt{\overline{u^2}}. \qquad \text{Equation 2.6}$$

By normalising the turbulence intensity by the mean flow velocity the relative turbulence intensity is calculated as

$$\frac{u'}{\bar{U}} \qquad \text{Equation 2.7}$$

and is often expressed as a percentage.

2.4.2 Turbulent length scales

In turbulence literature it is clear that u consists of a random collection of eddies with a broad spectrum of scales. Over time many length scales have been defined however, there are four scales which are of general relevance and are frequently cited. Turns (2000) lists these four scales as

L	Characteristic width of flow or macro-scale
ℓ_o	Integral scale or turbulence macro-scale

ℓ_λ Taylor micro-scale

ℓ_K Kolmogorov micro-scale

The characteristic width of flow (L) is the largest possible scale in the system and is the upper limit for the largest possible eddies. For example in a jet flow, L is the local width of the jet at any axial location.

The integral scale (ℓ_o) represents the mean size of the large scale structures in a turbulent flow, namely those eddies with low frequency and large wavelength. ℓ_o is always smaller than L but is of the same order of magnitude. Measurements of velocity made at two points separated by a distance x which is considerably less than ℓ_o will correlate with each other. ℓ_o can be measured by integrating the correlation coefficient for fluctuating velocities obtained as a function of the distance between two points. This is defined as

$$\ell_o = \int_0^\infty R_x(r).dr \qquad \text{Equation 2.8}$$

where

$$R_x(r) = \frac{\overline{u'_x(0)u'_x(r)}}{u'_{x,rms}(0)u'_{x,rms}(r)}. \qquad \text{Equation 2.9}$$

The Taylor micro-scale (ℓ_λ) is an intermediate length scale lying somewhere between ℓ_o and ℓ_K. Bernard and Wallace (2002) comment that this scale is a measure of the scales of motion at which turbulent energy dissipation takes place. It is defined by the relationship of the fluctuating strain rate of the turbulent flow field to the turbulence intensity and can be defined as follows

$$\ell_{\lambda} = \frac{u'_{x,rms}}{\left[\overline{\left(\frac{\partial u_x}{\partial x}\right)^2}\right]^{1/2}}. \qquad \text{Equation 2.10}$$

The Kolmogorov micro-scale (ℓ_K) is the smallest length scale associated with turbulent flows. It is the representative dimension at which dissipation of turbulent kinetic energy to fluid internal energy occurs. Therefore, ℓ_K is the scale at which molecular effects become significant (Turns (2000)).

It is important to understand how these turbulence measures relate to the turbulence confined within the cylinder. The cylinder boundaries limit the largest eddies experienced, with molecular diffusion limiting the smallest. Stone (1999) comments that the "jet like" flow that emerges from the inlet valve produces eddies which are responsible for producing most of the turbulence during induction. The shear between the jet and the cylinder contents leads to the formation of eddies which are unstable and break down into a cascade of smaller eddies. The turbulent energy cascade theory states that kinetic energy enters a fluid's turbulent flow at the largest scales of motion. Inertial instabilities in the larger scales cause them to 'break up' or develop into smaller vortices transferring energy into the smaller scales. The smaller eddies created are themselves unstable and in turn energy is transferred to smaller and smaller scales. The life span of a typical eddy is in the order of its turn-over time (l/u). Viscous stresses can be assumed to be negligible during this cascade with the whole process being driven by inertial forces. However, the cascade comes to a halt when the eddy size becomes so small that the Reynolds number based on the size of the smallest eddies is in the order of unity. At this point the viscous forces become significant and the energy is dissipated by them. This energy cascade is particularly pronounced in regions where instantaneous gradient in velocity, and hence the shear stress is large.

2.4.3 Turbulent premixed combustion in SI engines

The combustion process in a spark ignition engine takes place in turbulent flow with a premixed fuel-air mixture. The flow field created during the intake stroke is modified during compression and results in the turbulent conditions which are present during the combustion event. The fuel-air mixture is designed to mix thoroughly before it is ignited by an electrical discharge between two electrodes. The duration of the subsequent combustion event, controlled by the turbulent flame speed, is important since it affects the engine's thermal efficiency, its lean operating limit, its tolerance to exhaust gas recirculation and the production of emissions. Unlike a laminar flame, which has a propagation velocity dependant upon the thermal and chemical properties of the mixture, the turbulent flame speed is fundamentally affected by the turbulent characteristics of the flow during the combustion event. Many published resources on combustion are available, detailing previous work and theories in this area. See, for example, a good introduction provided by Turns (2000) with a spark ignition engine specific summary provided by Heywood (1988).

Combustion reactions in a premixed gas can be assumed to occur in a thin reaction zone which only affect the adjacent section of the mixture, propagating to form a combustion 'wave' or flame front (Barnard and Bradley (1985)). The heat required for the combustion reaction to propagate into the unburned mixture is provided by diffusion from the current thin reaction zone. Premixed laminar flames can be characterised by the laminar flame speed S_L and laminar flame thickness δ_L. These parameters are important not only in laminar flames but are also an integral part in understanding and modelling turbulent flames (Williams (1985)).

The interaction between the flame front and the flow characteristics of the fuel-air mixture is very complex. The intricate interaction between the physical and chemical properties of both the flame and the mixture has been the basis of studies by many experimental and theoretical researchers, for example Reuss *et al.* (1989); Bray (1996); Wassenberg and Adomeit (1996); Patel and Ibrahim (2002); Jarvis (2003). When the

flame enters a turbulent flow field the flame front is wrinkled by the turbulent flow structures which increases its surface area (Williams (1985)). This increase in the flame's surface area results in an overall increase in burning rate, however, locally the flame is still assumed to propagate at the laminar burning velocity Bray (1985).

There are several dimensionless parameters used to characterise turbulent premixed flames. The Damköhler number Da is defined as the ratio of the characteristic flow or mixing time τ_T to the characteristic chemical reaction time τ_L and is an inverse measure of the influence the turbulent flow has on the chemical processes occurring within the flame. For the case of premixed turbulent flames τ_T is defined as the characteristic eddy turnover time such that

$$\tau_T = \frac{\ell_o}{u'}. \qquad \text{Equation 2.11}$$

where ℓ_o is the integral length scale and u' is the turbulence intensity. The characteristic chemical reaction time is the residence time in a laminar flame, with respect to the flame thickness and laminar flame speed, such that

$$\tau_L = \frac{\delta_L}{S_L}. \qquad \text{Equation 2.12}$$

Therefore, the Damköhler number Da can be written as

$$Da = \frac{\tau_T}{\tau_L} = \frac{\ell_o}{\delta_L}\frac{S_L}{u'}. \qquad \text{Equation 2.13}$$

The turbulent Reynolds number Re_T relates the inertia of the turbulence defined by the turbulence intensity and characteristic integral length scale to the dissipative effect of the fluid kinematic viscosity ν as

$$\mathrm{Re}_T = \frac{u'\ell_o}{\nu}. \qquad \text{Equation 2.14}$$

By comparing the Damköhler number to the turbulent Reynolds number different regimes of turbulent flame can be identified as shown on Figure 2.5. For the combustion observed in SI engines (the cross hatched region in Figure 2.5) the Damköhler number and turbulent Reynolds number lie predominantly in the reaction sheet flame regime. The structure of the flame would therefore be expected to be that of a thin reaction sheet which is wrinkled by the turbulent flow. The schlieren photography presented by Namazian *et al.* (1980); and Witze (1982) supports the observation that SI engines operate in this regime as highly wrinkled thin regions signifying where the flame front is observed.

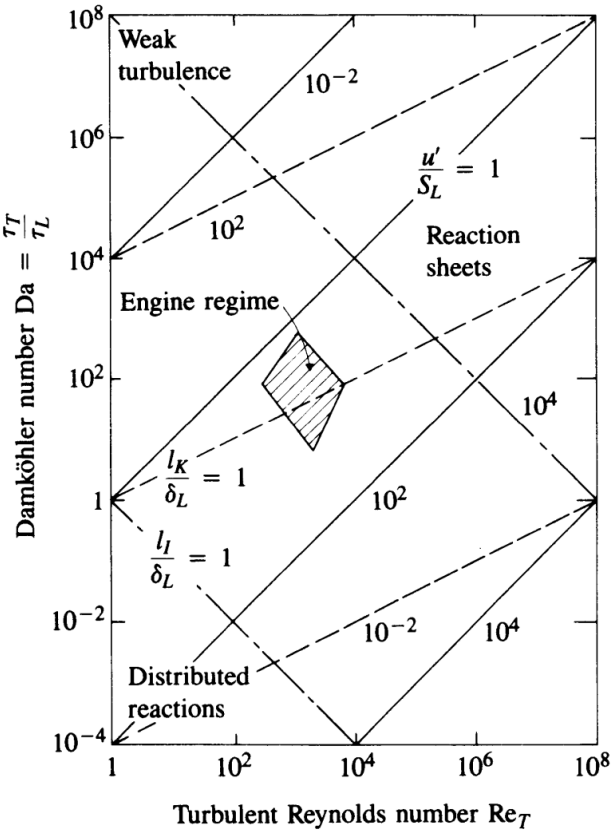

Figure 2.5 - Turbulent flame regimes shown on a plot of Damköhler number versus turbulent Reynolds number (Heywood (1988))

Different scales of motion relative to the flame can have a variety of effects on combustion process. Convection of the flame can occur when the flow scale is much larger than the flame size. In this case the flame is carried in the flow as a whole. For smaller flow scales, down to approximately the flame thickness, the flow influences the flame geometry and therefore the flame front wrinkling. For flow scales smaller than the flame front thickness the fluid motion has negligible effect on the flame geometry. For a turbulent flow which can be assumed to be steady on average the degree of flame wrinkling is strongly linked to u', Bradley and Sheppard (1988); Bradley (1992).

Not only does the flame wrinkling affect flame propagation, so too does the local strain rate. The strain field local to the flame front affects the flame growth through the processes of surface production and flame quenching. Mueller *et al.* (1996) used PIV to investigate the effects of stretch on a highly repeatable axisymmetric propagating flame interacting with a torroidal vortex. The study revealed differences between the effects of positive and negative stretch.

It is clear that the flame is heavily affected by the flow motion surrounding it. The design of combustion systems attempt to take advantage of the positive effects that turbulence can have on flame speed. The development of gasoline direct injection (DI) and stratified charge lean burn engines is aimed at meeting the lower emissions levels and improved fuel economy requirements outlined by ever tightening legislation. These combustion systems require large scale tumble motions which decay to produce enhanced turbulence before ignition. These tumble motions can also be used to stratify regions of mixture for example with different stoichiometry. For further details on these combustion systems please refer to some of the many published sources on this subject, for example, Kim *et al.* (1999).

2.5 Cycle by cycle variation

SI engines superficially operating under steady-state conditions do not maintain perfectly stable operation i.e. a comparison between one cycle and another reveals

random variations in, for example, the in-cylinder peak and indicated mean pressures (Ozdor *et al.* (1994)). Very early in the combustion event taking place within the cylinder, cyclic variation in peak cylinder pressure, the rate of pressure rise and the work done by the gas are observed. Ozdor *et al.* (1994) comment that despite many years of experimentation and research a full understanding of cyclic variation is still lacking. They also mention previous studies which have shown that it may be possible to achieve a 10% increase in power for the same fuel consumption if cyclic variations could be eliminated. However, the elimination of cyclic variation may not be truly desirable even if it were possible. For example Stone *et al.* (1992) highlight that total elimination of cyclic variation is not desirable for engine management systems that retard the ignition when incipient knock is detected. If there were no cyclic variation there would be no foresight for the engine management system to detect when the onset of knock will occur.

Extensive research has led to operating conditions being identified which aim to reduce cyclic variation in the combustion process. Reductions in cyclic variation enable the engine's operating conditions to be further optimised with a view to reductions in both fuel consumption and pollutant emissions for the same power output as well as improvements in engine refinement. Additional work in this area is still required to further the fundamental understanding of the origins of cyclic variation within the combustion event and to create strategies which optimise engine operating conditions and geometries to reduce cyclic variation.

Two terms are often used when discussing cyclic variations; these are "cycle by cycle variation" and "cyclic variation". The former is used when discussing differences between cycle n and cycle n+1 where as the latter is used when referring to differences over a range of cycles.

2.5.1.1 Indicators of cyclic variation

Many parameters are used as indicators of the amount of cyclic variation experienced by an engine. The most commonly used parameters are:

i. Indicated mean effective pressure (imep);

ii. In-cylinder pressure (maximum pressure and crank angle at which maximum pressure occurs);

iii. The rate of cylinder pressure change;

iv. Combustion duration and mass fraction burned (mfb).

Many previous studies have used cyclic variation in indicated mean effective pressure (imep) as a measure of the level of variation experienced by an engine. The imep for a 4-stroke engine is found from

$$imep = \frac{\textit{indicated work output (by the gas on the piston) per cylinder per mecanical cycle}}{\textit{swept volume per cylinder}}, \quad \text{Equation 2.15}$$

where the indicated work output term is linked to the in-cylinder pressure history. This therefore can be expressed as

$$imep = \frac{1}{V_s} \oint P.dV, \quad \text{Equation 2.16}$$

where V_s is the swept volume, P is the pressure in the space, and dV denotes the volumetric variation (Tsuchiya and Nagashima (2003))

The use of pressure related parameters are a natural choice to describe the cyclic variations occurring within the cylinder and can be measured simply. When studying cyclic variation Heywood (1988) comments that a coefficient of variance (COV) of imep greater than 10% is noticeable to a driver as a deterioration in vehicle drivability. COV of imep is defined as the standard deviation in imep divided by the mean imep and is usually expressed as a percentage,

$$COV_{imep} = \frac{\sigma_{imep}}{\overline{imep}} \times 100. \qquad \text{Equation 2.17}$$

Stone *et al.* (1992) found that the COV of imep is a minimum when the ignition timing is set to maximum advance for maximum break torque (MBT) timing. They also warn against the use of variation in the maximum cylinder pressure since it is sensitive to factors which could lead to misleading results. A study by Brown *et al.* (1996) made similar conclusions that COV of imep and peak pressure showed no correlation with variation in ignition timing.

Ozdor *et al.* (1994) lists indicators of cyclic variation in four main areas;

i. Pressure;

ii. Combustion;

iii. Flame front;

iv. Exhaust gas related parameters.

Figure 2.6 shows the main indicators used to portray cyclic variation.

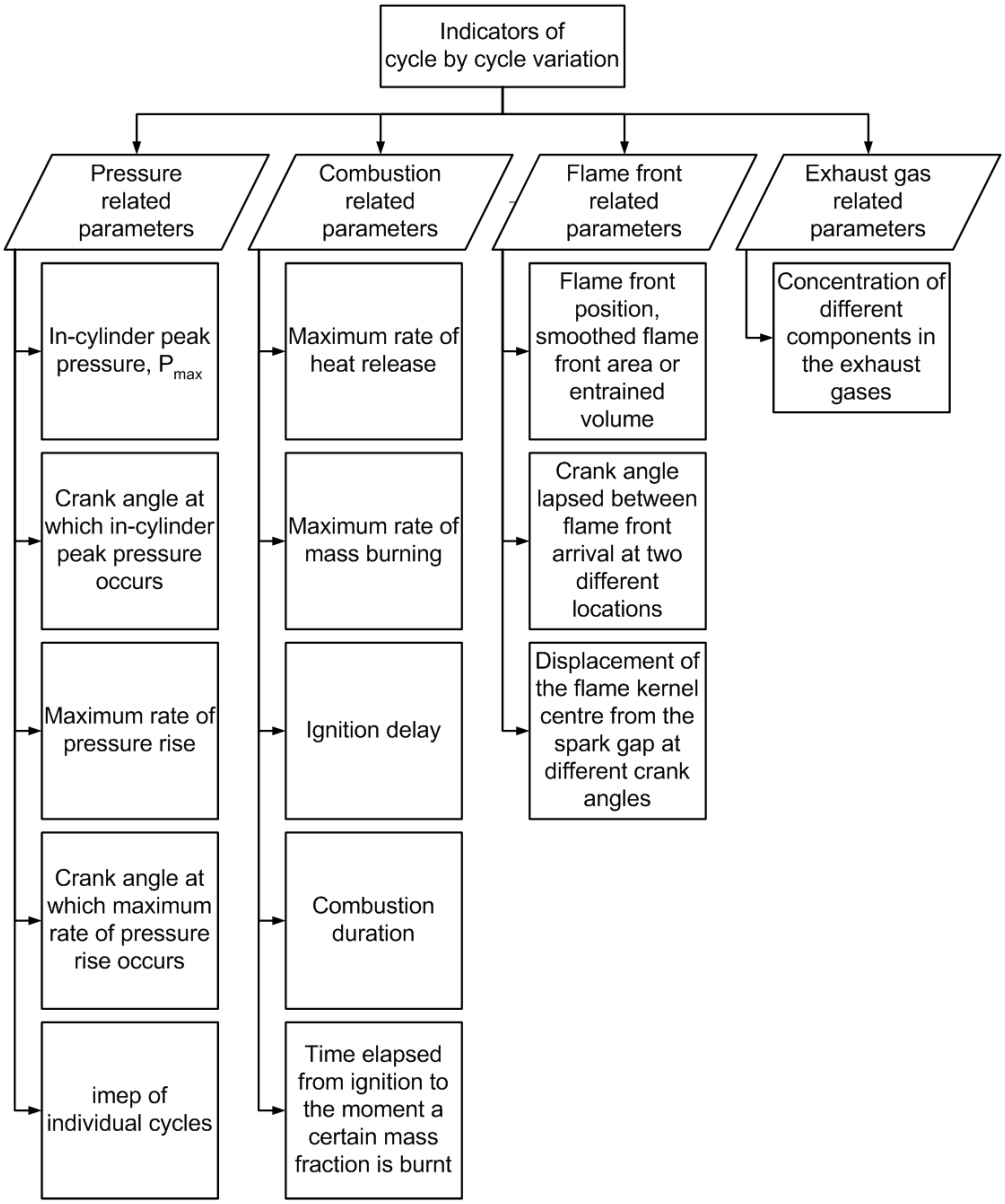

Figure 2.6 - Indicators of cycle by cycle variation, adapted from Ozdor *et al.* (1994)

2.5.1.2 Sources of cyclic variation

The main sources of cyclic variation, shown in Figure 2.7, can be divided into four areas;

i. Mixture composition;

ii. Spark and spark plug;

iii. In-cylinder mixture motion;

iv. Cyclic cylinder charging related issues.

Note that some factors such as the type of fuel and the spark plug design may affect the level of cyclic variation experienced but they themselves do not vary from one cycle to the next. Other factors such as intake generated structures are in part controlled by engine design but will also suffer from stochastic variations from one cycle to the next.

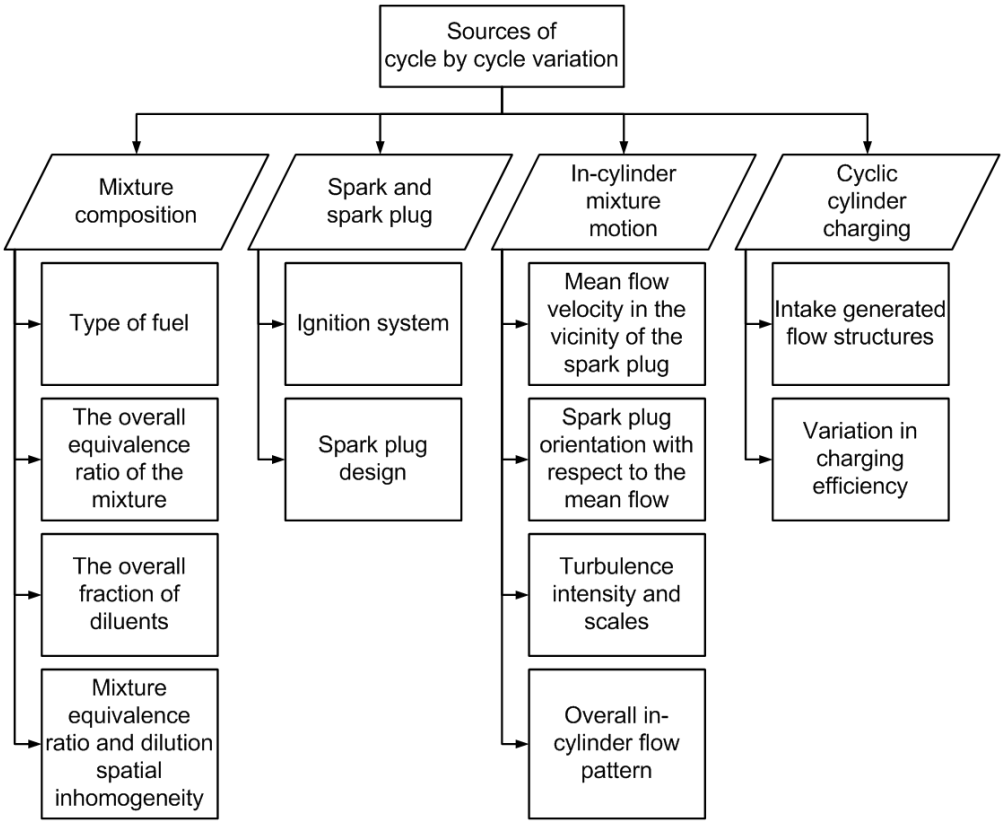

Figure 2.7 - Sources of cycle by cycle variation, adapted from Ozdor *et al.* (1994)

Researchers consider mixture motion related factors as the most influential with respect to cyclic variation in engine performance (Reuss (2000)). Since turbulence is an inevitable feature of in-cylinder motion, cyclic variation in engine performance cannot be eliminated. However, it can be minimised or controlled by judicious use of charge flow control and flow geometry. The turbulent nature of the flow has a double effect; firstly it accelerates combustion by increasing the flame front area and enhancing the heat and mass transport between the burned and unburned charge. Secondly, the random flow patterns cause fluctuations in the magnitude and direction of the charge velocity in the spark gap vicinity. Both of these effects are related to other factors such as combustion chamber geometry and spark plug location. The optimal in-cylinder flow pattern is dependant on engine geometry; however, an understanding cyclic variation should be common between engines operating similar combustion systems. The two main areas of interest for this thesis are the cyclic variations of in-cylinder motion and cyclic cylinder charging. Therefore, the following discussion concentrates on factors included in these areas. Low frequency velocity fluctuations are generally attributed to variation in the mean or bulk flow between individual cycles, whereas high frequency fluctuations are often defined as turbulence.

The major factor contributing to combustion variation is the cyclic variation in the in-cylinder flow fields (Reuss (2000)). Flow variation in the development of the intake and in-cylinder flow structures may be affected by: turbulence dissipation, residual gas momentum, flow separation in the intake port, variation in the arrival of pressure waves in the intake and exhaust ports and fuel injection. Some of these factors can only have an effect up to the closure of the inlet valve, after this point, when the cylinder is essentially sealed from further external influence, only in-cylinder phenomena can affect the flow structures.

Increasing the fraction of excess air or exhaust gas residuals (EGR) slows down the combustion process and increases its cyclic variation (Heywood (1988)). Deterioration in combustion stability limits the amount of charge dilution an engine can tolerate. In practice engine induction systems into which EGR is introduced see variations in EGR

distribution entering individual cylinders and therefore not only suffer from cyclic variation in EGR fraction but from cylinder to cylinder variation.

2.5.2 Flow field cycle by cycle variation

Calendini *et al.* (2000) studied an engine with a four valve pent roof cylinder-head. Using PIV in the symmetrical plane of the combustion chamber they studied the stability of the flow fields during the course of the engine cycle. During the intake stroke they noted that the cycle by cycle variations were lower than those experienced during the compression stroke where large unstable eddies were observed. By capturing stereoscopic PIV measurements during the compression stroke, the flow was recognised to exhibit three-dimensional unstable behaviour with high cyclic variation.

Li *et al.* (2001) studied the development of swirl motion based on two-dimensional ensemble averaged velocity fields. They questioned the applicability of the ensemble averaged mean flow as a basis for each individual cycle because if cyclic variation of the bulk flow is too significant then the mean velocity field cannot represent each individual instantaneous velocity field's bulk flow motion. In their study they noted that in each individual flow field similar large-scale vortex structures were clearly identifiable whereas, the swirl vortex centres were positioned differently. Li *et al.* (2001) proposed that since the large-scale swirl vortex structures were a fundamental feature of the instantaneous velocity fields it may be better to describe the cyclic variation of the swirl ratio and the swirl centres.

In addition Li *et al.* (2001) studied tumble within the same research engine. They found that cyclic variations of the flow in the tumble plane were significant which highlighted the problem of using the ensemble averaged mean flow to represent each individual cycle's basis velocity field. They comment that the large cyclic variation in this plane may be enhanced by the moderate tumble ratio exhibited by the engine they were investigating. Li, Zhao, Peng *et al.* (2002) found that the average turbulence intensity and fluctuating kinetic energy are seen to drop rapidly during the development of the

intake process but remain almost constant during the compression process. The two-dimensional distribution of turbulence intensity and kinetic energy are inhomogeneous throughout both the intake and compression process with areas of high fluctuating kinetic energy appearing within regions of higher mean velocity.

Joo *et al.* (2004) investigated the behaviour of large and small scale variations within the in-cylinder flow during the intake and compression stroke of a motored four valve SI engine. They noted similar results to those recorded by Li, Zhao, Peng *et al.* (2002), commenting that the turbulence intensity is observed to decrease substantially during the intake process but remains almost constant during compression.

St. Hill *et al.* (2000) observed that turbulence levels are higher within the intake valve jet region than within the cylinder during the intake process. They reported that the cyclic variation levels are substantial in both locations, but they are more significant near the centre of the cylinder. During the compression process the turbulence intensity and the cyclic variation levels decrease. By performing steady flow tests St. Hill *et al.* (2000) highlighted the need to understand the origins of cyclic variations in order to identify control techniques to reduce variation and therefore allow improved engine performance. They suggested inlet valve jet flapping and the associated flow instabilities as one possible area of investigation. These authors also highlighted the complexity of the three-dimensional turbulent motions within the engine which make the identification of the origins of the flow variation a most challenging task.

The flow motion through the spark gap is known to have several important effects. During the spark event the flow can stretch the discharge channel and affect the electrical energy deposited to initiate the flame kernel. The flow surrounding the spark plug can also convect the flame kernel during its development. This may be away from the electrode and other quench zones therefore reducing heat loss to them. Alternatively the flow may convect the kernel towards the quench zones and if this occurs, heat will be lost from the flame kernel which leads to slowing of the kernel growth or in the worst case its extinction. It is well known that early kernel growth has a large effect on the rate of mass burn and the overall combustion event; therefore, favourable conditions

for the flame kernel should be sought. Pischinger and Heywood (1990) performed calculations for the flame propagation based on experimental results giving flame centre motion and electrode energy per cycle. The results showed that two thirds of the experimentally observed cyclic variation in flame growth was due to cyclic variation in the vector describing the flame kernel centre motion. Arcoumanis and Bae (1993) studied how combustion in a cylindrical chamber reacted to different values of bulk velocity and turbulence intensity. The results showed that when mean flow velocity and turbulence intensity were high the combustion duration was shorter.

Abdi Aghdam *et al.* (2007) investigated the effects of perturbing parameters within a thermodynamic engine model. This model was then compared against experimental results for both a single cylinder research engine and a multi-cylinder direct injection engine. They found that the effects of turbulence variation proved dominant, with variations in mixture strength a secondary factor to this. Only a marginal contribution to cyclic variation was provided by variations in the concentration of prior-cycle residuals (EGR).

These findings highlight that the flow velocity and turbulence characteristics in the vicinity of the spark plug have an influence on the flame kernel growth and the overall combustion process. Studying the level of flow variation which occurs close to the spark plug and how this is influenced by flow field behaviour earlier in the engine cycle is therefore a required area of research if combustion is to be optimised.

2.6 Flow field characterisation

In-cylinder flow motion is often thought to contain two components; bulk motion and turbulence. There is no specific divide between these two components therefore; extracting the bulk flow and fluctuating or turbulent components from the raw (unrefined) flow is not always obvious.

Typical analysis of turbulent flows uses Reynolds decomposition (Equation 2.5) to decompose the flow into a mean flow and fluctuating or turbulent component. This is adequate for steady state systems, but when considering the flows in a cyclic device such as a reciprocating IC engine the decomposition may be based on the same point in the cycle over many cycles, this is termed the ensemble mean and is defined as

$$\bar{U}_{(\theta,x,y)} = \frac{1}{n}\sum_{i=1}^{n} U_{(\theta,i,x,y)}. \qquad \text{Equation 2.18}$$

This ensemble mean is a special case of Equation 2.4. This introduces a complication since for in-cylinder flow the large scale bulk motion experiences variation from one cycle to the next. Studies on engine flow fields have been the topic of many investigations. Reuss (2000), for example, demonstrated that a small cycle-sample size can result in extreme statistical bias in the ensemble mean when studying an unsteady parameter. Therefore it is important to consider the sample size to obtain high levels of statistical significance. Extending the Reynolds decomposition to include variations around the ensemble mean using low frequency filters has been investigated, notably Li, Zhao and Ladommatos (2002) and Joo *et al.* (2004), for example, used high and low frequency cut-off filters to separate the high frequency small scale flow fluctuations from the low frequency large scale bulk motion variations. The choice of cut-off frequency is not obvious since there is no clear distinction.

A further calculation based on the fluctuating component (introduced in section 2.4) is the turbulent kinetic energy (TKE) which is calculated as follows

$$TKE = \frac{u^2 + v^2 + w^2}{2} \qquad \text{Equation 2.19}$$

where u, v and w are the fluctuating components in the orthogonal directions x, y and z. Often flow field measurement techniques only provide two-dimensional measurements. An accepted method used by Pitcher *et al.* (2003) on their study is to

take the mean fluctuating component of the two known components and assume this is representative of the third missing component. A further approach also applied is to ignore the third component term and define the TKE in the two known components only.

The use of high speed digital particle image velocimetry (HSDPIV) allows an alternative decomposition technique to be applied which uses the temporal nature of the data captured as used in analysis of LDV data. The analysis of temporally resolved measurements allows the flow for each individual cycle to be decomposed into high and low frequency components as used by Fansler and French (1988). Therefore, for each individual engine cycle i the captured velocity field data can be decomposed as follows

$$U_{(\theta,i,x,y)} = U_{LF(\theta,i,x,y)} + U_{HF(\theta,i,x,y)} \qquad \text{Equation 2.20}$$

where $U_{LF(\theta,i,x,y)}$ is the low frequency or bulk flow component for cycle i at θ crank angle degrees and location x, y. Likewise $U_{HF(\theta,i,x,y)}$ is the high frequency component of the flow. Figure 2.8 illustrates the decomposition of Equation 2.20.

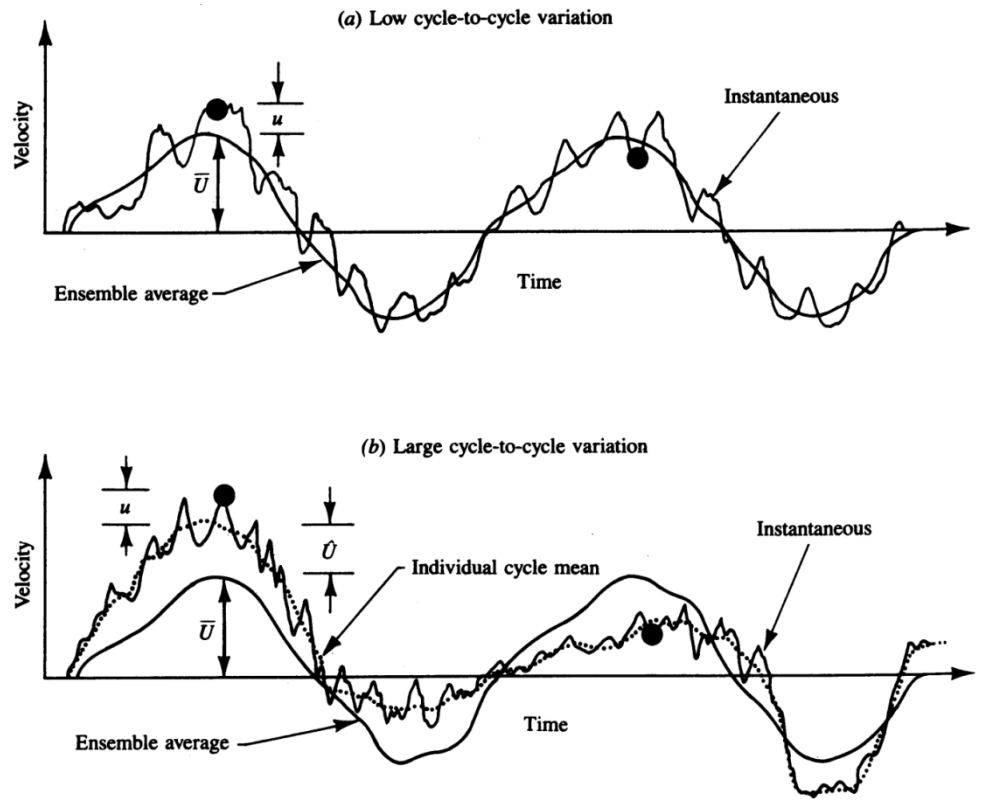

Figure 2.8 - Decomposition of flow time history into low and high frequency components (Heywood (1988))

The decomposition of flow fields into their high and low frequency components was completed by transferring each velocity component (U component in the x direction and the V component in the y direction) at each location x, y for each cycle i into the frequency domain using a fast Fourier transform (FFT). Once in the frequency domain a high and low pass filter could be applied to separate the two spectral components. The selection of cut-off frequency to apply is not trivial because there is no discrete transition between the low frequency bulk flow motion and high frequency superimposed fluctuations.

Quantifying cyclic variation in the bulk flow motion has been the focus of many research studies in the past (such as Sullivan *et al.* (1999); Reuss (2000); St. Hill *et al.* (2000); and Towers and Towers (2001); Fischer *et al.* (2004); Joo *et al.* (2004)). Individual cycle bulk flow variation can be calculated by quantifying the difference

between an individual cycle bulk flow and an average bulk flow. Sullivan *et al.* (1999) proposed that the use of the standard ensemble average as a measure of the mean bulk flow field within an SI IC engine may be inappropriate due to the inclusion of all scales of turbulent motion within the ensemble average. Therefore, to determine low frequency flow variation in this study the individual cycle low frequency motions are compared to an average cycle of the low frequency flow. A definition of low frequency cyclic variation becomes

$$U_{CVLF(\theta,i,x,y)} = U_{LF(\theta,i,x,y)} - \overline{U_{LF(\theta,x,y)}} \qquad \text{Equation 2.21}$$

where $\overline{U_{LF(\theta,x,y)}}$ represents the mean cycle of the low frequency flow field components calculated as follows

$$\overline{U_{LF(\theta,x,y)}} = \frac{1}{n}\sum_{i=1}^{n} U_{LF(\theta,i,x,y)} \qquad \text{Equation 2.22}$$

where n is the number of cycles included in the average. The remaining high frequency components have a greater chance of being independent of the geometry.

2.7 Flow field diagnostics

The measurement of fluid flow velocity is important in many areas of engineering, ranging from fluid transport in pipes through to complex flows within IC engines and aerodynamics of aircraft and automobiles. An understanding of flow field behaviour aids the design and development process for systems and their components. This Section introduces the basic characteristics of two measurement systems laser Doppler velocimetry (LDV) and particle image velocimetry (PIV). These two measurement systems are commonly used in the investigation of flow behaviour in many areas of engineering; however, they have substantially different features.

2.7.1 Laser Doppler Velocimetry

Laser Doppler velocimetry is a point-measuring technique which measures the velocity of flow tracer particles when they pass though the measurement volume in the crossing of two laser beams (Durst *et al.* (1981)). The data rate available from the LDV measurement system is high allowing single cycle analysis of the velocity development at one point in the engine cylinder with a temporal resolution below 1 degree crank angle. Due to this high temporal resolution LDV measurements are well suited to the study of flow velocity development at selected locations. However, the lack of spatial information means that statistical samples have to be compiled by scanning across the area under investigation. For the investigation performed within this thesis, LDV is not the ideal solution when compared to the alternative measurement systems available. The main drawback is the limitation of being a point measurement technique and therefore its lack of synchronised spatial and temporal data capture.

2.7.2 Particle Image Velocimetry

Particle image velocimetry (PIV) is a technique which is used to measure spatial velocity, typically over a two-dimensional plane. Standard PIV systems operating at *circa* 15 Hz do not have the temporal resolution to study flow field development during a single engine cycle as with the LDV measurement technique. The use of PIV to study engine flows has typically been limited to studying 'snapshots' of the flow at one point in time during the engine cycle. Only by capturing individual flow fields at different times through the engine cycle can average cycle flow field developments be studied. Therefore, the major disadvantage to this standard technique is the low temporal resolution offered. However, recent developments in PIV hardware have seen the advent of high speed digital particle image velocimetry (HSDPIV) allowing two-dimensional flow field capture at kHz rates. The key to these developments has been the increase in the spatial resolution of high frame rate cameras. This allows the development of the flow during the course of an engine cycle at real engine speeds to be investigated whilst also capturing spatial detail within this flow field. It is this technique

which has been employed within this study to characterise flow field development within a DISI engine as the spatial and temporal flow characteristics of individual engine cycles are able to be captured and investigated. Studies presented by Ghandhi *et al.* (2005), investigated the use of high frequency PIV measurements for in-cylinder flow field characterisation.

2.8 Summary

This chapter has presented a discussion about air flow behaviour within SI engines and how turbulence can impact the combustion event by affecting burning velocity. This has led onto a discussion about the cyclic variation experienced by the flow field and indications of how this flow field variation can impact engine performance in terms of power, emissions and refinement. The next chapter discusses the PIV measurement technique and its use in capturing flow fields within an SI engine. It also introduces the HSDPIV system used to capture the data presented later within this thesis.

Chapter 3 High Speed Particle Image Velocimetry

3.1 Introduction

Accurate measurement of fluid flow is an important aspect of many areas of engineering. This chapter discusses in more detail particle image velocimetry (PIV) and more specifically high speed digital particle image velocimetry (HSDPIV). The primary motivation for the use of PIV within the research presented in this thesis was its ability to capture high spatial resolution measurements of fluid velocity over a planar region. In addition, since it is a non-intrusive measurement technique, PIV is well matched to the measurement of fluid motion within an IC engine. The measurements obtained can be used to investigate large scale flow structures such as bulk swirl and tumble motions together with smaller scale turbulent structures within specific areas of interest. Furthermore, continual developments and technology advancements have lead to the ability to capture flow fields at kHz rates, which allows the flow field development on a measurement plane during one engine cycle to be investigated at a high temporal resolution.

Engine designers require improved understanding and control over processes which ultimately determine engine performance, emissions and level of engine refinement. The velocity field measurements which result from PIV experimentation can be used to assist the engine design process. Although performing experimental investigations is a costly approach, PIV data can be used to validate computational fluid dynamic (CFD) models to provide more confidence in their predictions and therefore allowing its use to evaluate new and altered designs. It is important to note however, that classical turbulence models within CFD codes do not account for cyclic variation in the flow

fields and will therefore only predict an ensemble average flow field and turbulence intensity. Therefore, to investigate cyclic variations, experimental investigations are essential.

The suitability of the PIV technique to the present study of flow field cyclic variation and the measurement methods applied have been presented in detail in this chapter. In addition the novel measurement system which was used throughout the experimental investigations presented in this thesis is introduced.

3.2 Theory of Particle Image Velocimetry

The key points in the development of PIV have been introduced within this Section to aid understanding of the technique and hence knowledge of its strengths and weaknesses. A comprehensive early history of PIV is given by Raffel *et al.* (1998).

The precursors to PIV lie in a solid surface measurement technique, speckle metrology, used to derive displacements in solid surfaces. First introduced by Burch and Taokarski (1968) the laser speckle metrology technique, termed Laser Speckle Photography (LSP), involved the illumination of a rough surface with a coherent laser light source. The light scattered from the surface resulted in the formation of speckle interference patterns and any movement of the surface also caused the interference pattern to move. The scattered light was recorded with a double exposure film, the first exposure preceding and the second exposure following the surface movement. These two speckle patterns were assumed to be identical but laterally shifted with respect to one another. A spatial correlation between the patterns produced a diffraction pattern consisting of Young's fringes superimposed on a speckle background. Through the use of optical processing the spacing and orientation of these fringes allowed the displacement of the surface to be derived.

Dudderar and Simpkins (1977) adapted the LSP technique and demonstrated that quantitative velocity data could be obtained from a fluid flow seeded with small

particles to act as flow tracers. This technique was termed Laser Speckle Velocimetry (LSV). In their study the flow was illuminated by a continuously pulsing laser and the resulting speckle patterns were recorded onto a high resolution film. The Young's fringes allowed the displacement of the flow to be derived. Dudderar and Simpkins reported close agreement between their experimental measurements and theoretical calculations for a fully developed laminar flow.

Lourenco and Krothapalli (1986) showed that LSV was not suited to the measurement of velocity in turbulent or unsteady flow. This was due to the recorded speckle patterns becoming de-correlated due to seed particles moving rapidly through the light sheet out of plane i.e. in the third component. As a result the Young's fringes produced had a poor signal to noise ratio (SNR).

The diffraction limited image that is produced when using LSV within a fluid did not become a speckle pattern until the seed density was high enough to create numerous overlapping diffraction limited particle images. The term particle image velocimetry was introduced by Pickering and Halliwell (1984) and Adrian (1984) to describe the measurement technique where individual particle images are recorded. This technique allows the study of turbulent and unsteady flows since the flow velocity is directly represented by the displacement of the seed particles being imaged. Since their inception, the development of PIV systems has continued and the technique is now established as a valuable tool for capturing instantaneous velocity field measurements over a planar region. The continual advancement of digital cameras, computer processors and software capabilities has resulted in the development of digital PIV (DPIV) which allows the mapping of complex flow fields in real time. More recently the advent of high speed DPIV systems has allowed for the improvement in the measurement of a flows temporal nature whilst maintaining the ability to study its spatial characteristics as this provides flow field maps at kHz rates. The continued advancement of PIV is well documented in a number of review papers. Adrian (1991) presented a review of the development of low and high particle density PIV and Grant (1997) presented a review on the PIV measurement technique. High speed PIV is

discussed in papers such as Towers and Towers (2001), Jarvis *et al.* (2006) and Justham *et al.* (2006).

Figure 3.1 shows a schematic of a typical PIV experimental arrangement. In its simplest form PIV measures two-dimensional velocity vectors on a two-dimensional plane. The technique requires seed particles to be introduced into the flow which are capable of following the flow's fluctuations. The particles which fall into the measurement plane, which is illuminated by a light sheet, scatter light towards the camera. This scattered light allows the position of the seed particles to be recorded. Capturing two images on the same measurement plane, separated by a known time interval Δt, allows the movement of the particles to be measured and thus a velocity to be derived.

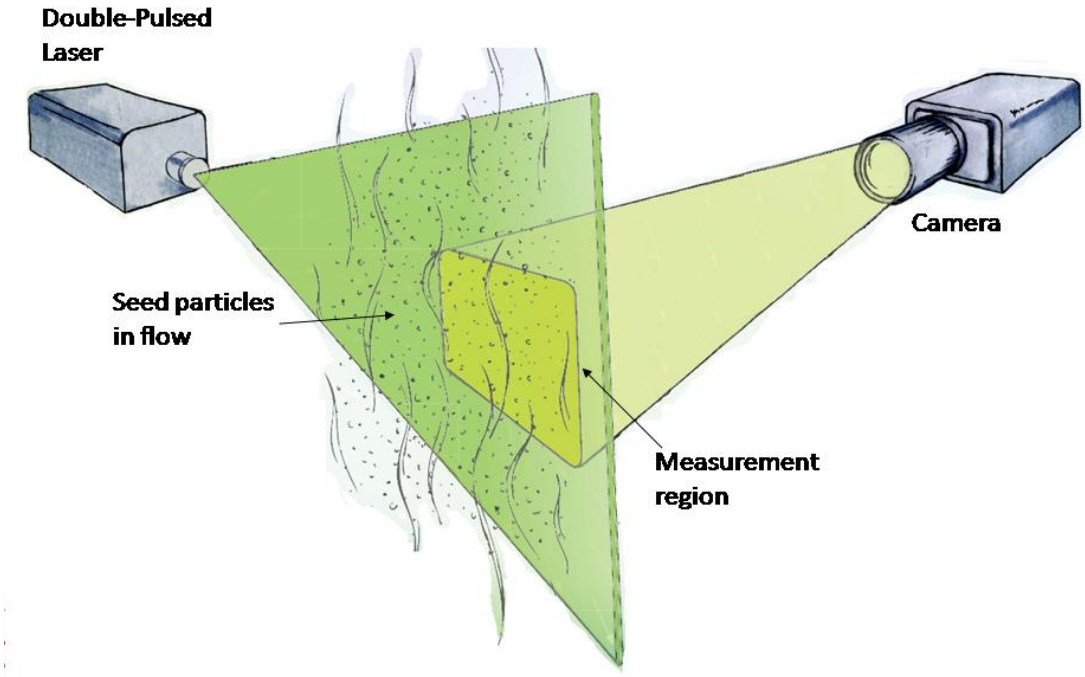

Figure 3.1 - Schematic of a typical PIV measurement system (adapted from www.tsi.com)

There are many factors which can affect the accuracy of the PIV velocity field. The selection of seeding material to provide adequate flow following accuracy along with suitable light scattering properties is discussed in the following Section. The process of recording the positions of the seed particles are discussed later in Section 3.2.2. Once

the particle images have been recorded the analysis of the images to derive the particle displacement and hence velocity is required. The analysis method used during this process is discussed in Section 3.2.3, which highlights the important considerations to reduce errors in the resulting velocity vectors.

3.2.1 Flow seeding

The PIV measurement technique requires the use of flow tracer seed particles. The selection of the type of seed particles is important in controlling the quality and accuracy of PIV measurements since the fluid velocity is inferred from the particle motion. It is therefore essential that the particles' motion is representative of the fluid motion in which they are suspended. This important criterion for selecting an adequate seed material is discussed further in Section 3.2.1.1. A second key requirement is the light scattering properties of the seed material. The magnitude and directional distribution of light scattered by a particle depends on its dimensions and material. This topic is further discussed in Section 3.2.1.2. Finally the number density of the particles introduced into the flow must be appropriate for the analysis method without overloading the fluid on a mass or volume basis and therefore significantly changing its properties.

In applications where abrasion is unfavourable, for instance when piston rings are moving over an optical engine's cylinder wall, greater weight is placed on the use of liquid droplets as a seed material in preference to that of solid particles. Liquid droplets are non-abrasive and can act to aid lubrication. However, for applications where abrasion is unimportant or where components can be replaced at little cost solid particles are often preferred as they tend to scatter light more effectively (Raffel *et al.* (1998)).

3.2.1.1 Flow following

The PIV measurement technique is based on recording the displacement of seed particles within the fluid flow over a known time period. Since it is the fluid flow velocity that is of interest, the seed particles must follow the flow with sufficient fidelity to track accurately the size of turbulent structures and fluctuations being studied. To define the flow following ability of a particle the fluid dynamics governing the particles motion must be considered. Drain (1980) presented a mathematical analysis of seed particles used in LDV; this is also relevant to considerations for PIV seeding.

Stokes' drag law can be used to define the viscous force (F_p) exerted on a particle by the viscous drag from the surrounding fluid as follows

$$F_p = m_p \frac{dv_p}{dt} = 6\pi\mu_{fluid} a_p (U - v_p), \qquad \text{Equation 3.1}$$

where m_p is the mass of the particle, v_p is the particle velocity, μ_{fluid} is the dynamic viscosity of the fluid, a_p is the particle radius and U is the fluid velocity surrounding the particle. The magnitude of this force is a controlling factor in the response of the particle to velocity fluctuations within the flow and can be solved for a constant fluid velocity to give the particle velocity at time t thus

$$v_p(t) = U + \left(v_p(0) - U\right)e^{-t/\tau_p}. \qquad \text{Equation 3.2}$$

From this a time constant (τ_p) which describes the particle's response time to a change in fluid velocity can be defined as

$$\tau_p = \frac{m_p}{6\pi\mu_{fluid} a_p} = \frac{2\rho_p {a_p}^2}{9\mu_{fluid}}, \qquad \text{Equation 3.3}$$

where ρ_p is the particle density.

To define this in terms of the particle's frequency response relative to fluid velocity fluctuations, sinusoidal fluid velocity fluctuations with an amplitude (U_0) and frequency (f_u) are considered. The equation of motion becomes

$$\frac{dv_p}{dt} = \frac{\left(\bar{U} + U_0 \cos\left(2\pi f_u t\right) - v_p\right)}{\tau_p}, \qquad \text{Equation 3.4}$$

where $\bar{U}$ is the mean velocity of the fluid. The steady-state solution of Equation 3.4 is given as

$$v_p(t) = \bar{U} + \frac{U_0 \cos\left(2\pi f_u t - \phi_l\right)}{\left(1 + 4\pi^2 \tau_p^2 f_u^2\right)^{1/2}}, \qquad \text{Equation 3.5}$$

where ϕ_l is the phase lag given by $\phi_l = 2\pi f_u \tau_p$. It is acceptable, for most purposes, to require the particle velocity to differ from the local fluid velocity by less than 1% at the maximum fluctuation frequency. The particle size to allow this can be derived from Equation 3.3 and Equation 3.5 and is given as

$$a_p^2 < 0.1 \frac{\mu_{fluid}}{f_u \rho_p}. \qquad \text{Equation 3.6}$$

As an example of the above criterion, olive oil particles of density ρ_p = 920 kg.m^{-3} suspended in a flow of air require a diameter of less than 2.8 μm to follow flow velocity fluctuations up to a frequency of 1 kHz and be within 1 % of the fluid velocity. If this fluctuation frequency were to increase to 10 kHz, the required particle diameter would have to be reduced to 0.88 μm. The choice of seed material and particle size is therefore dependent on the length and time scales of the turbulence within the system being

studied. Melling (1997) provides a summary outlining particle response for common seed materials in turbulent air flows.

Stokes' drag law is considered to apply when the particle Reynolds number (Re_p) is smaller than about unity (Melling (1997)), i.e.

$$\mathrm{Re}_p = \frac{\rho_f \hat{V} d_p}{\mu} = \frac{\hat{V} d_p}{\nu}. \qquad \text{Equation 3.7}$$

This condition is true for small particles and small relative velocities ($\hat{V}$). The drag law gives a conservative estimate of the tracking ability of particles, since the actual drag tends to be higher (Dring (1982)).

Although Stokes' drag law suffices for most flows, there are cases where additional body forces are present which introduce additional effects on the relative behaviour of the particle and the fluid. An example of this is in a swirling flow such as a vortex. The centrifugal force accelerates the particles radially out of the vortex core (Durst *et al.* (1981)), resulting in additional radial motion of the particle.

3.2.1.2 Light scattering

Each particle of the chosen seeding material must have the ability to scatter sufficient light towards the camera to allow its position to be recorded. The scattered light produced by a particle is dependant on the power of the light source and the properties of the seed particle. Low scattering efficiency requires higher powers from the light source to allow scattering to occur. However, this can have negative effects on the image quality since flare from nearby surfaces may affect the recorded image. Also due to the associated financial cost of increasing the power of the light source it is often more economical and effective to carefully choose the seed particles based on their scattering properties (Raffel *et al.* (1998)).

To define the amount of light scattered by a particle one has to consider the ratio of the refractive index of the particle to that of the surrounding medium, the particle size, shape, orientation, polarisation and the observation angle (Raffel *et al.* (1998)). For particles (which are assumed to be spherical) in air with diameters greater than the wavelength of the incident light, Mie's scattering theory can be applied. Figure 3.2 shows the polar distribution of scattered light for a 1 μm spherical oil particle at a wavelength λ = 532 nm according to Mie's theory. The intensity scales are shown logarithmically and are plotted so that neighbouring circles differ by a factor of 100.

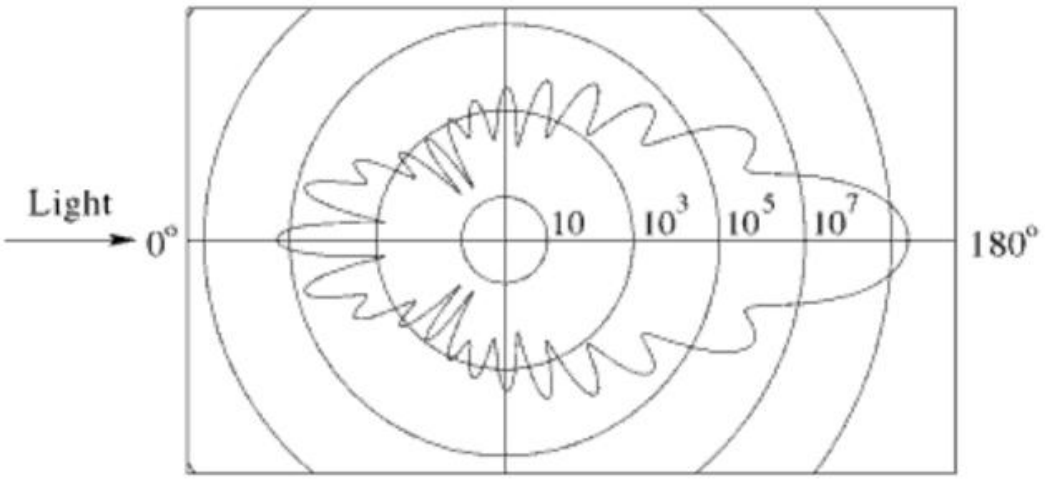

Figure 3.2 - Light Scattering of 1μm oil particle in air illuminated by 532 nm laser light (Raffel *et al.* (1998))

The Mie scattering can be characterised by the normalised diameter (q) defined as

$$q = \frac{\pi d_p}{\lambda}. \qquad \text{Equation 3.8}$$

In the angular distribution range of observation angles from 0° to 180° approximately q local maxima appear if q is larger than unity. As q increases the ratio of forward to backward scatter intensity increases rapidly and since the greatest intensity is obtained at a 180° observation angle, it would be advantageous to record in this position which is

termed ‘forward scatter’. However, due to limiting the depth of field, images for PIV are most often recorded at 90° observation angle. It can be seen from Figure 3.2 that light is scattered in all directions from the particle therefore, if a large number of particles appear inside the light sheet substantial multi-scattering occurs. The imaged light is therefore not only a result of direct illumination but is also due to fractions of light scattered by more than one particle. For the case of heavily seeded flows, multi-scattering increases the intensity of light scattered by individual particles. However, it is important to note that increasing particle density increases the background noise on the recording medium.

Particle size also strongly affects the light scattering effectiveness. By increasing the particle diameter, the required illumination power can be significantly reduced which is not only less demanding on laser power but also reduces flare caused by light scattering off nearby surfaces. It is important, therefore, to balance adequate flow following properties with acceptable light scattering behaviour to produce high quality PIV measurements.

3.2.2 Image recording

Once the flow being investigated has been adequately seeded, the displacement of the particles on the plane of interest, over a known time separation, has to be recorded. This involves providing adequate illumination to cause the seed particles to scatter light towards the imaging camera and controlling the image capture to record the relative positions of the seed particles at two time steps separated by a known time difference Δt. The light source and imaging camera are discussed in the following sections.

3.2.2.1 Laser light source

Lasers are a common choice for an illumination source in PIV measurements due to their ability to emit monochromatic light with high energy density. Common types of

laser used in the capture of PIV measurements include Nd:YAG, Copper Vapour, Ruby and more recently Nd:YLF. A good beam profile is essential for PIV. The beam intensity should be a good fit to a Gaussian distribution and provide hole-free intensity distribution without hot-spots. The resulting laser output can be manipulated by the use of a cylindrical and a spherical lens to form a thin sheet of light with satisfactory low intensity variation across it. This allows the illumination of a two-dimensional plane of interest with negligible thickness. A schematic of the sheet formation is shown in Figure 3.3.

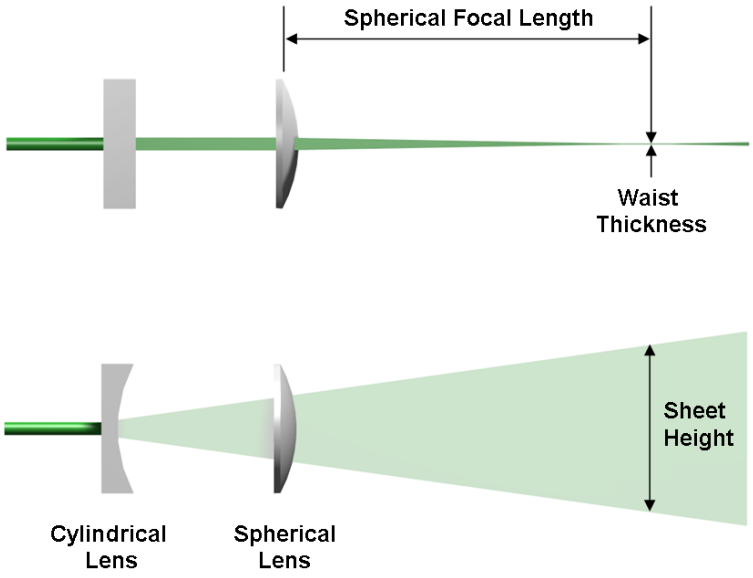

Figure 3.3 - Schematic to show the formation of a thin sheet of laser light

The area illuminated by the light sheet is determined by the focal length of the cylindrical lens. The negative focal length of the cylindrical lens causes the beam to diverge in one plane, with shorter negative focal lengths causing a more rapid divergence in the beam. The spherical lens focuses the beam to an appropriate thickness creating a waist in the laser sheet.

The short light pulses which can be generated by the laser source is also of significant advantage in the capture of PIV images as this pulse duration controls the length of image exposure onto the recording media

3.2.2.2 Imaging system

The recorded particle diameter is not solely dependant on the size of the tracer particles. The image of a distant point source such as a small scattering particle inside the light sheet, when imaged through an aperture, does not appear as a point source in the image plane but forms a diffraction pattern. Figure 3.4 shows an example diffraction pattern also known as an Airy pattern. This pattern has a bright central region known as the Airy disk. The diameter of the disk (d_s) is related to the wavelength of the illuminating light and the size of the circular aperture and represents the smallest particle image that can be obtained for a given imaging configuration.

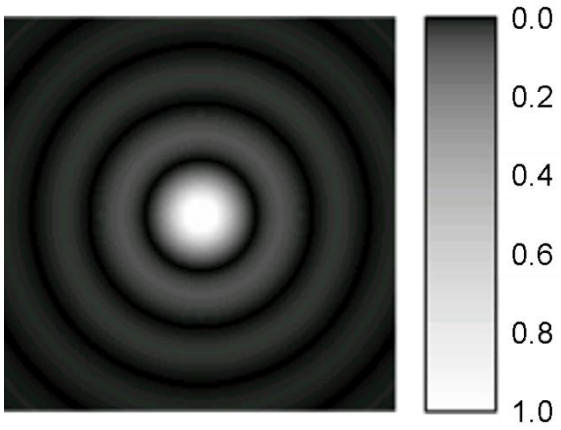

Figure 3.4 - Airy pattern or diffraction pattern caused by imaging through an aperture (The scale is indicative of light saturation onto the imaging media)

The diffraction-limited minimum particle image diameter (Adrian (1991)) can be calculated as follows:

$$d_s = 2.44\left(1+M_o\right) f^{\#}\lambda \qquad \text{Equation 3.9}$$

Where $f^{\#}$ is the f-number of the lens (ratio of focal length (f) to the aperture diameter (D_a)), λ is the wavelength of the light scattered by the particle and M_o is the image magnification which is defined by the ratio of the imaging array size (A_c) and the imaged area size (a_I) such that

$$M_o = \frac{A_c}{a_I}. \qquad \text{Equation 3.10}$$

The imaged particle diameter (d_I) can therefore be calculated from the image magnification, the seed particle diameter (d_p) and the diffraction limited spot size as follows;

$$d_I = \sqrt{\left(M_o d_p\right)^2 + \left(d_s\right)^2}. \qquad \text{Equation 3.11}$$

Adrian (1997) commented on the importance of ensuring that particle images are not under-sampled when digitised onto a pixel array as this would lead to both mean bias errors in locating the particle and a random error (these errors are discussed further in Section 3.4). However, over-sampling does little to reduce measurement error once the ratio of imaged particle diameter (d_I) to pixel width (A_p) exceeds a critical value (c_r) such that

$$c_r < \frac{d_I}{A_p}. \qquad \text{Equation 3.12}$$

The critical value is usually taken to be 2 for DPIV measurements. Satisfying Equation 3.12 ensures that a particle image is captured on at least 3 pixels of the digital image. For a given imaging array size and required imaged area the most sensitive factor in controlling the imaged particle size is the $f^{\#}$. Limiting the minimum $f^{\#}$ to

give an imaged particle size that satisfies Equation 3.12 will help reduce the mean bias error in locating the particle.

The imaged particle size calculations lead to an ideal imaged particle size, although in reality this will be increased by the particle being out of focus or aberrations occurring due to the imaging system. The depth of focus (DOF) defines the thickness of the region containing in-focus particles, outside of this range the image is blurred by an amount exceeding 20% of the focused particle diameter (Adrian (1991)). The DOF is given by

$$DOF = 4\left(1+M_o^{-1}\right)^2 f^{\#2}\lambda. \qquad \text{Equation 3.13}$$

It is clear that as the $f^{\#}$ decreases the DOF also decreases. Therefore, to keep sharp images the $f^{\#}$ has to be kept large keeping the DOF higher than the width of the light sheet. However, since the $f^{\#}$ is the ratio of the focal length to aperture diameter, a larger $f^{\#}$ means a smaller aperture reducing the light able to reach the pixel array therefore, requiring higher laser power.

3.2.3 Image Analysis

As previously mentioned, the PIV technique involves capturing the relative positions of seed particles within the flow field of interest. Through capturing two images of relative seed particle positions within the same measurement space but separated by a known time interval Δt the velocity of the particles can be derived by suitable image analysis. The accurate recording of the relative displacement of seed particles over a known time is therefore fundamental to the PIV measurement system. Its accuracy is affected by the finite uncertainty involved in identifying the centre of each particle image.

Advancements in electronic imaging have replaced traditional and cumbersome photographic film with digital imaging cameras as the preferred recording media allowing two frame cross-correlation. Therefore, the following discussion is limited to this digital analysis method only. During the development of PIV, auto-correlation and single frame cross-correlation was used for the analysis of single frame multi exposure images, for further information on these techniques please refer to review texts such as Raffel *et al.* (1998). The two frame cross-correlation technique is considered superior due to having the best signal-to-noise ratio, no directional ambiguity and its ability to measure zero velocity.

Analysis of a PIV image pair is performed by subdividing the image into smaller regions termed ‘interrogation regions’. For each of these regions a local displacement vector is determined by calculating an average displacement of the particle images between the two exposures of the same region, see Figure 3.5. This means that the velocity measurements are averaged over that region. Adrian (1997) defines this averaging operation as a volume average over the interrogation region and the thickness of the laser light sheet.

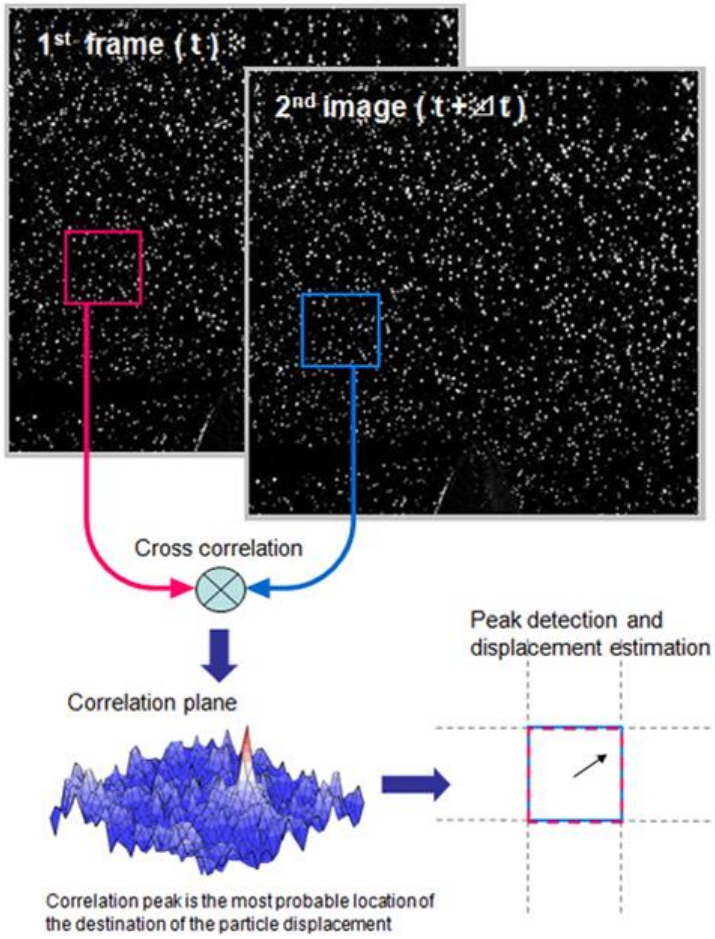

Figure 3.5 – Explanation of two frame cross correlation technique to determine mean displacement of particles within an interrogation region

The average displacement of the particle images is estimated by cross correlation analysis. A cross-correlation routine is used to compute the correlation field ($R(m,n)$) between the first interrogation area ($I_1(i,j)$) at time t and the second interrogation area ($I_2(i,j)$) at time $t+\Delta t$. The definition of $R(m,n)$ is given as

$$R(m,n)=\sum_{i=0}^{K}\sum_{j=0}^{L}I_1(i,j)I_2(i-m,j-n), \qquad \text{Equation 3.14}$$

for an in interrogation region size with length, K and width, L. Keane and Adrian (1992) highlighted the reduction in computation time that can be gained by using a Fast Fourier Transform (FFT) to perform the correlation when compared to a computation in the spatial domain. The use of FFT cross-correlation is now commonplace in commercial PIV software packages. This routine is based on the cross-correlation of two functions being equivalent to a complex conjugate multiplication of each functions Fourier transforms. Therefore,

$$R = I_1(i,j) \otimes I_2(i,j) \Leftrightarrow \hat{I}_1(\xi,\eta)\hat{I}_2^{*}(\xi,\eta) \qquad \text{Equation 3.15}$$

where $\hat{I}_1(\xi,\eta)$ represents the Fourier transform of $I_1(i,j)$ and $\hat{I}_2^{*}(\xi,\eta)$ represents the complex conjugate of the Fourier transform of $I_2(i,j)$.

A significant velocity variation is found in many flows of practical importance and therefore, an important characteristic to understand is the dynamic velocity range. This can be defined as the maximum velocity range that can be measured with a fixed set of instrument parameters divided by the minimum resolvable velocity measurement Adrian (1997). In general, the dynamic velocity range is controlled by the interrogation region size on both the first and second image and by the time separation between the laser pulses and hence the image exposures (Δt). It is important to ensure a large fraction of the particle pairs remain within an interrogation region to improve the accuracy of the cross-correlation. Adrian (1986) suggested one should control the image exposures so that the maximum displacement of a particle image ($c_{\max}$) between captures is less than one quarter of the size of the fixed interrogation region (I_d) such that

$$c_{\max} \leq \frac{I_d}{4}. \qquad \text{Equation 3.16}$$

This can be controlled by both the interrogation region size and Δt. However, the interrogation region size is often determined by the spatial resolution required for the measurements being taken. The most effective method is by setting Δt to allow an adequate particle displacement. It is important to note, however, that small displacements under 1 pixel suffer from larger proportional errors. Modern processing algorithms allow the second interrogation region to be larger than the first therefore allowing the correlation to search further whilst still correlating the whole interrogation region reducing the problems caused by particles moving out of the regions. Employing this technique improves the dynamic range when compared to two equally sized interrogation regions whilst maintaining the spatial resolution of the derived velocity vectors.

The seed particle density within the flow must be controlled in order to maximise the probability of generating valid correlations once the particle images are analysed. Too little seeding per interrogation region causes a high signal to noise ratio, increasing the likelihood of the highest correlation peak not being indicative of the particle displacement. A generally accepted rule for two frame cross-correlation PIV analysis is for there to be around 10 particle image pairs per interrogation region (TSI Incorporated (2000)). It is shown in Figure 3.6 that when particle density within the interrogation region is low (less than 8 particles) the chance of obtaining a valid particle displacement is low. As the number of particles increases the probability of achieving valid correlations in particle displacement levels out, however, overloading the interrogation region with particles will eventually cause further errors to appear as the signal-to-noise ratio reduces.

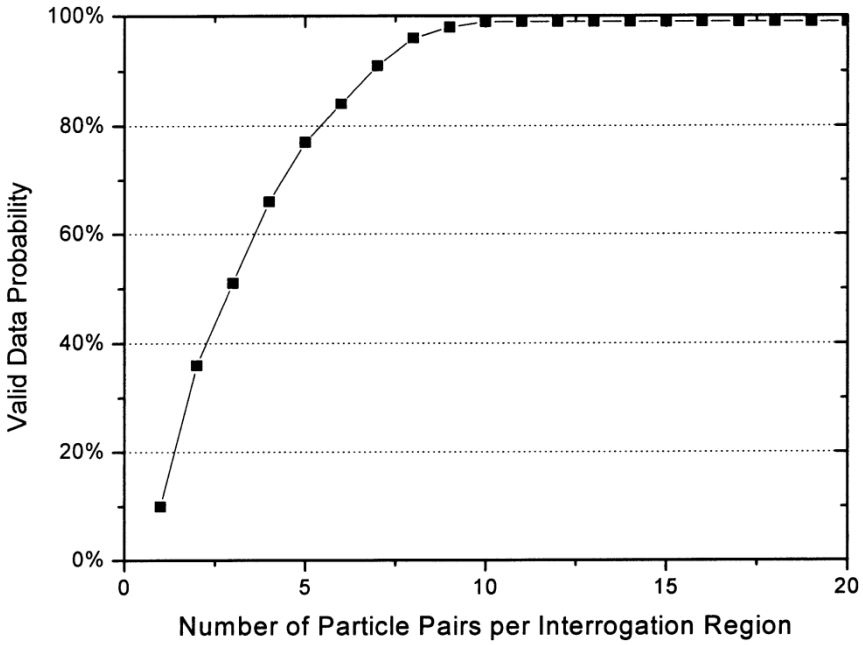

Figure 3.6 – Valid data probability with number of particle image pairs in interrogation region (TSI Incorporated (2000))

3.3 High Speed Digital Particle Image Velocimetry

3.3.1 Overview of system used

The PIV technique offers experimentalists the ability to capture the instantaneous spatial nature of a flow field. The temporal resolution of PIV measurements has typically been governed by camera frame rates with acceptable pixel resolutions to provide reasonable spatial flow field data. The development of high frame rate mega-pixel cameras has allowed PIV measurements to be captured at kHz rates. The high speed digital particle image velocimetry (HSDPIV) system used for this study was based on a commercially available PIV system. The system can be considered as a number of individual components including

i. laser light source;

ii. imaging system;

iii. synchronisation system;

iv. seeder;

v. image analysis software.

These components are described in the following sections. Details of the system set-up, including values used for control parameters, will be given in the relevant Chapter preceding the presentation of those data captured.

3.3.1.1 Laser

The laser used as part of the HSDPIV system was a New Wave Research Pegasus-PIV laser which is a dual-head, high repetition rate, diode pumped neodymium: yttrium lithium fluoride (Nd:YLF) laser system. The two heads, each with an output wavelength λ = 1053 nm, were mounted on a single base plate. The beams generated by these laser heads were combined and entered an intra-cavity, second harmonic generator to produce laser pulses with λ = 527 nm. Each of its two heads was able to operate from 1 to 10,000 pulses per second and the energy output per cavity at 1 kHz was 10 mJ as shown in Figure 3.7. The laser pulse width at 1 kHz was less than 180 ns which is adequate to control the exposure of the particle image onto the imaging medium. The raw beam diameter was 1.5 mm with a divergence of less than 3 mrad.

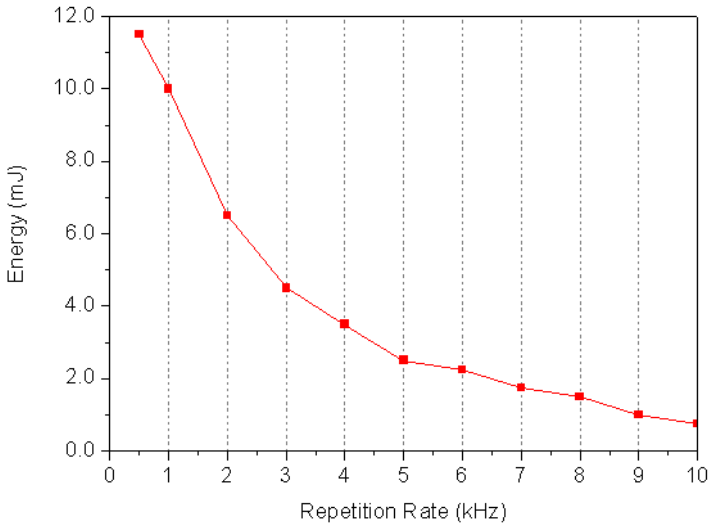

Figure 3.7 - Single cavity laser energy per pulse (adapted from NewWave Research (2004))

The light sheet was formed by passing the laser output through a cylindrical and a spherical lens as described in Figure 3.3. The cylindrical lenses used were plano-concave type with negative focal lengths of -15, -25, -50 mm. The spherical lenses were bi-convex type with a focal length of 1000 mm, which focused the beam to form the thin sheet. The 1000 mm focal length was enough to allow only a small change in sheet thickness over the maximum 60 by 60 mm image.

3.3.1.2 Imaging system

The camera used to record particle images was a Photron ultima APX-RS packaged by TSI Incorporated as a POWERVIEW HS-3000. The camera used a 1024 by 1024 pixel 10 bit monochrome CMOS (complementary metal-oxide-semiconductor) sensor. The full 1024 by 1024 pixel resolution was available at up to 3000 frames per second. Higher frame rates were available by reducing the active pixel area in steps of 128 pixels in width and 16 pixels in height. With an active resolution of 512 by 512 pixels the camera was capable of up to 10000 frames per second. Due to the high frame rate of the camera, images were stored to on-board memory during the capture sequence. *Circa* 2100 images or 1050 image pairs could be stored in the available memory before downloading to the control computer. The area of interest for each individual

experimental configuration dictated the lens requirements and either 105 mm or 60 mm Micro Nikkor lenses were employed.

The pixel size was 17 by 17 µm resulting in a sensor array size of 17.4 by 17.4 mm. This relatively large pixel size is beneficial for sensitivity. However, when compared to *circa* 9 µm pixels, which is common for lower capture rate CCD PIV cameras, this larger pixel size has an impact on the imaged particle size requirements as discussed in Section 3.2.2.2 to ensure Equation 3.12 is satisfied.

3.3.1.3 Synchronisation

The synchronisation of the HSDPIV system was controlled by the Insight 3G™ software which programs system triggers on a LASERPULSE™ synchroniser (model 610035) via a serial interface. The synchroniser acted as the master controller, distributing timing triggers to the Laser and Camera with a 1 ns resolution. The camera frame rate, required camera frames, laser pulse delay time and time between pulses were managed to allow two frame (or frame straddled) PIV image capture. A timing diagram showing the synchronisation required between the laser pulses and camera frames to allow the capture of two-frame PIV image pairs is shown in Figure 3.8.

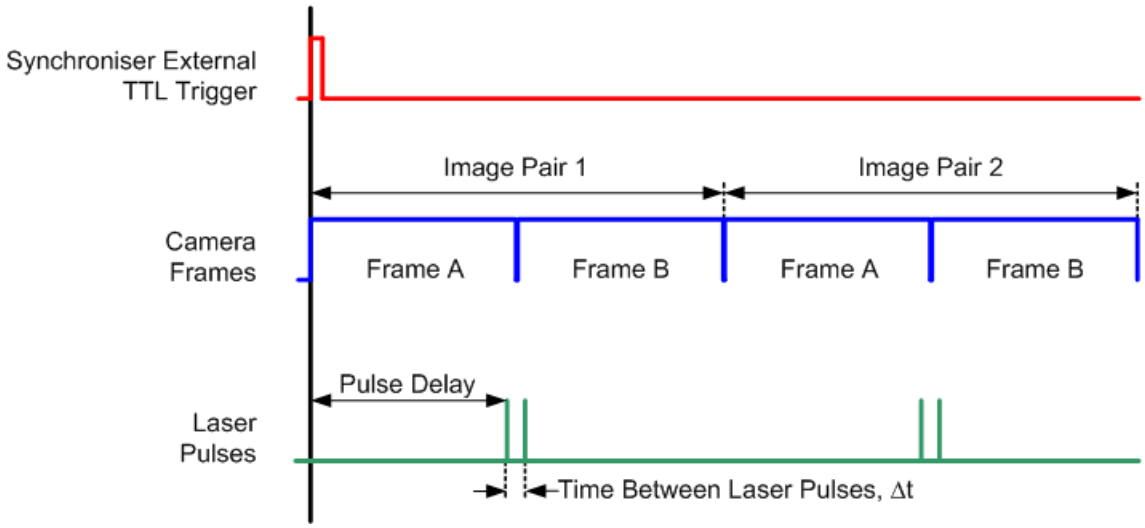

Figure 3.8 - High speed digital particle image velocimetry timing diagram

The synchroniser accepted an external TTL (transistor-transistor logic where the low voltage level is 0 to 0.8 Volts and the high voltage level is 2 to 5 Volts) trigger signal to start a capture sequence. The synchroniser was programmable to capture a predetermined number of PIV image pairs per external TTL trigger, and a total number of PIV image pairs at a predetermined capture frequency. Therefore, for engine studies HSDPIV data was able to be captured for a known crank angle range for multiple successive engine cycles until the memory limitation of the camera had been reached. An example timing diagram of the synchronisation of multi cycle HSDPIV captures is shown in Figure 3.9.

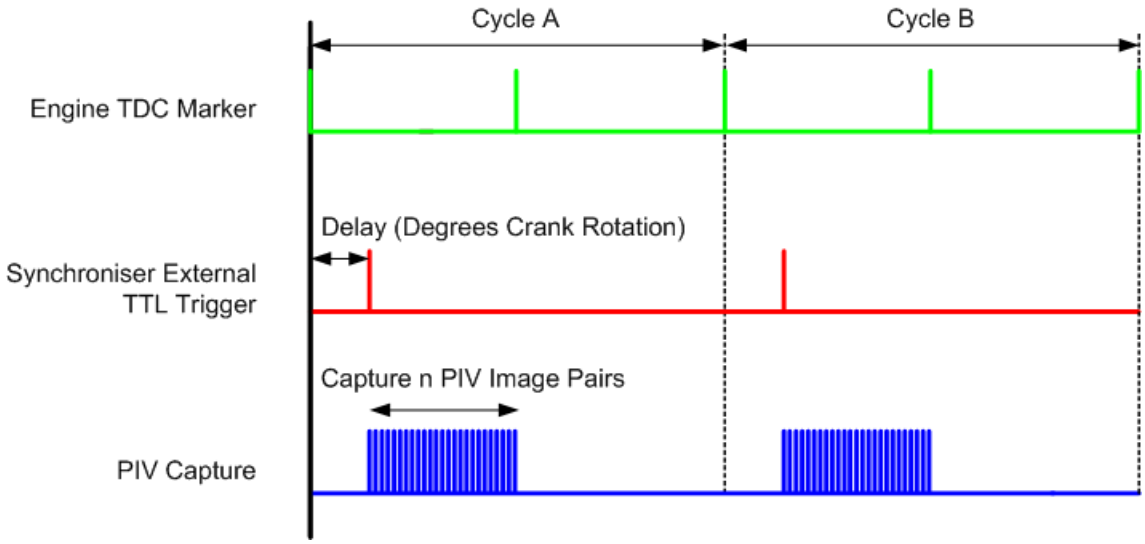

Figure 3.9 – Example multi cycle HSDPIV timing diagram

3.3.1.4 Seeder

A TSI six jet atomizer (model 9306) was employed to produce flow tracing seed particles at the required size, particle concentration and total particle output (TSI Incorporated (1992)). The atomiser was specifically designed and manufactured to produce tracer particles from virtually any liquid. The operating principle of the atomiser has been illustrated in Figure 3.10. Pressurised air is forced through an orifice with a 0.381 mm diameter and the pressure drop associated with the resulting high velocity jet draws liquid from the reservoir up the narrow tube. The liquid is then

broken up by the air jet as it reaches the top of the tube and is then entrained into the flow. Larger droplets which do not sufficiently follow the flow are unable to steer past the spherical impactor, whereas the smaller droplets avoid it and are able to exit the seeder forming an aerosol. Dilution air can be added to the aerosol around the seeder outlet pipe to reduce the seed number density.

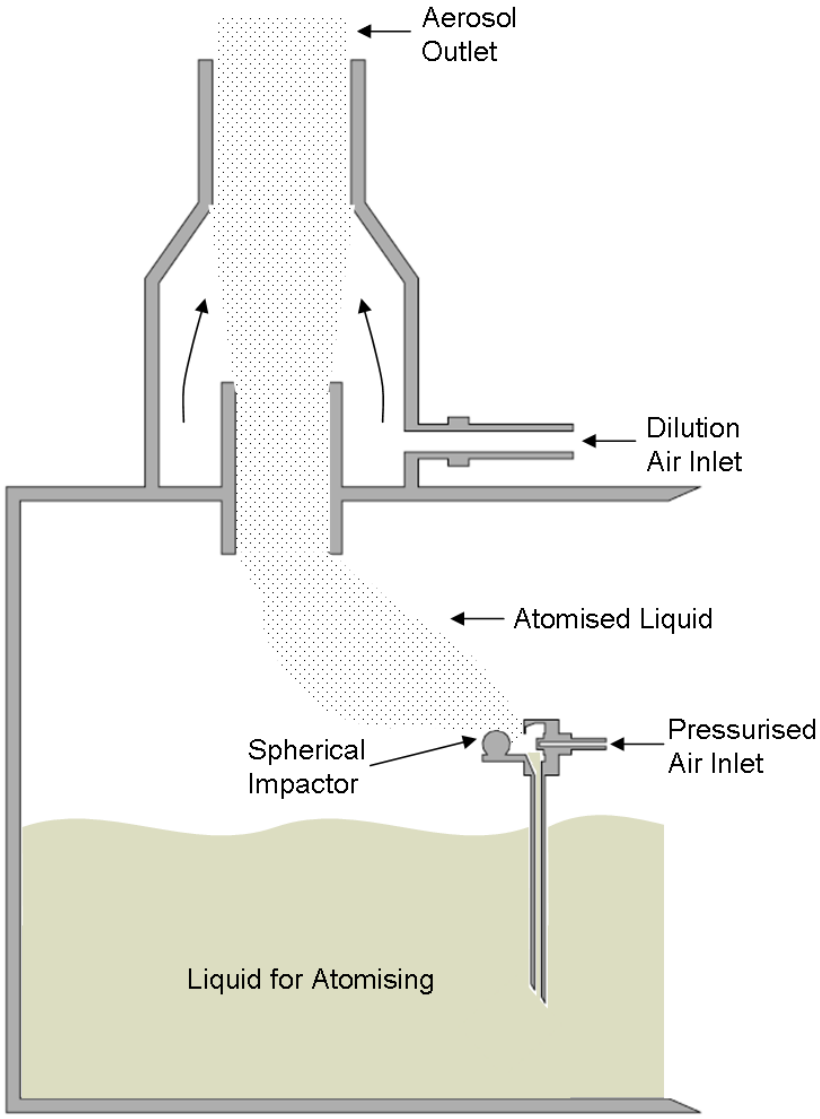

Figure 3.10 - Schematic to show the operating principle of the TSI six jet atomiser (model 9306), only one jet is shown for simplicity

The particle output number was dependant on the number of atomiser jets used and the input air pressure. Therefore, the seeder's operating parameters had to be tuned for each experiment to ensure the needs of the image analysis were satisfied. Since the HSDPIV allows multiple PIV images to be captured during the course of one engine cycle, compromises in the seeding requirements were required during parts of the cycle due to the changing pressure and volume of the gasses contained within the engine cylinder affecting the seed particle number density.

The particle size distribution when using olive oil as a seed material in the six jet atomiser was in the range 1 to 2 μm (Melling (1997)). The chosen atomiser was able to produce particles with a diameter that will trace flows with fluctuation frequencies up to 10 kHz (see Section 3.2.1.1). This is deemed adequate for the flows under investigation within the optical engine presented within this thesis.

When studying the flow during the latter stages of the compression stroke, the olive oil particles were unable to withstand the rising cylinder pressure. As a result it was unable to act as an adequate flow tracer. For this reason, Dow Corning 200 was used when studying flow fields in this portion of the cycle as it benefits from a low vapour pressure and higher dissociation temperature.

3.3.1.5 Image analysis

Image analysis of the captured HSDPIV image pairs to generate velocity vector fields was performed using the TSI Insight 3G™ software package. This allowed the recorded particle displacements to be calibrated in order to derive spatial displacement and hence velocity. Also, control over the spacing of interrogation regions was available, in all cases presented within this thesis the data was analysed with a first interrogation region of 32 by 32 pixels and a second interrogation region of 64 by 64 pixels, with an overlap of 50% on the first interrogation region. The larger second interrogation region allows the correlation to be sought over a larger region and hence allows greater movement before particles (moving on the measurement plane) are lost from the interrogation

region. The analysis options also allowed for the removal of spurious vectors and replacement vectors to be generated by interpolation of the surrounding vectors. The option to remove spurious vectors was used at edge regions of the images, when close to surfaces such as the cylinder head or valves were affected by scattered light. However, due to the subject of this work, particularly that of turbulent fluctuations, replacement values were not calculated as these would only act to skew the results obtained.

The Insight 3G software saved one data file per image pair which contained the x, y, U and V information to describe the velocity field. These data files, which possess the extension '.vec', are written so that the data is placed in four columns with the headers x, y, U and V (where U is the x component and V is the y component of the velocity vector at position x, y). These .vec files could then be loaded into Tecplot 10 via the TSI Tecplot add-on 'TSI PIV V3.00.13', or imported into alternative analysis tools such as those generated in Matlab™ for the post processing of these velocity fields.

An example processed raw velocity field is shown in Figure 3.11. This was captured with HSDPIV at 1.5 kHz, and is shown for the case of 220° CAD ATDC in the tumble plane on the bore centreline. This Figure shows each calculated vector at a vector spacing typical of that used to process the data throughout this Thesis. However, for clarity of image when presenting time sequences later in this Thesis, the data has been sub-sampled to plot every other vector.

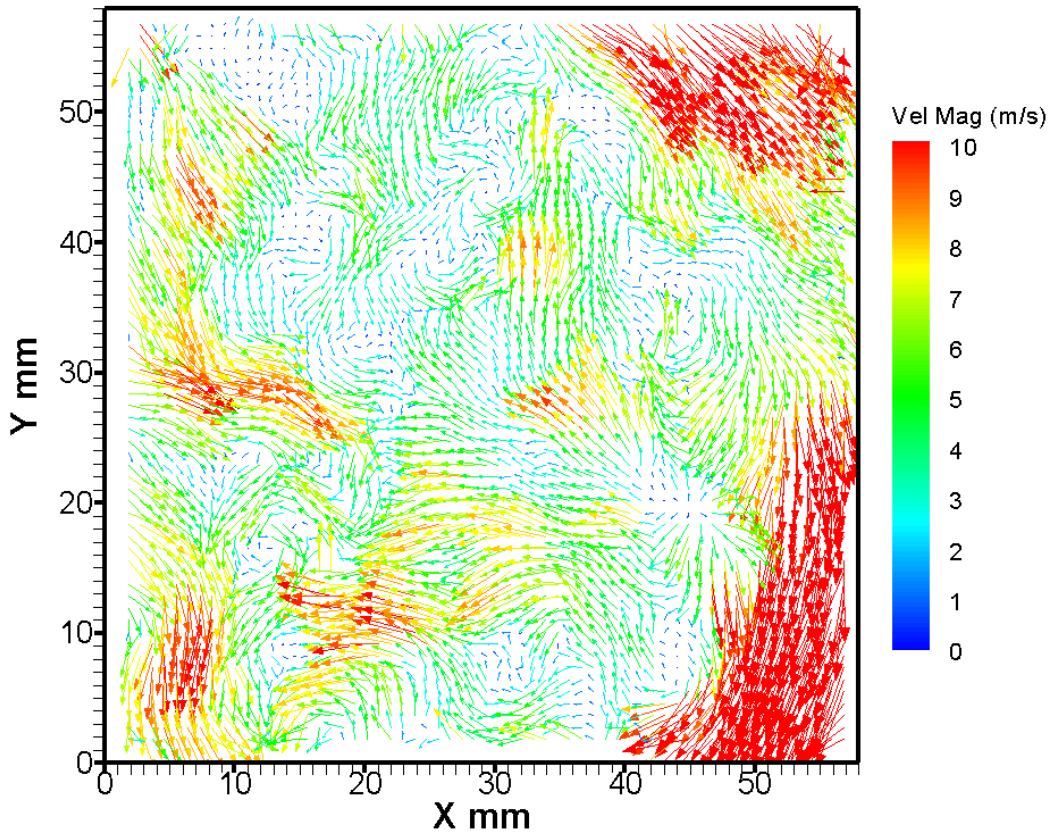

Figure 3.11 – Large scale image to show a typical raw vector field in the tumble plane on the bore centre line at 220° CA ATDC captured with HSDPIV at a rate of 1.5 kHz showing each vector generated

3.4 Errors

The overall accuracy of the PIV measurement technique is affected by a combination of aspects relating to the system components, image capture and evaluation process (Raffel *et al.* (1998)). The absolute measurement error involved in the estimation of a single

displacement vector (ε_{total}) can be defined as the sum of the systematic errors ($\varepsilon_{systematic}$) and the residual errors ($\varepsilon_{residual}$) such that

$$\varepsilon_{total} = \varepsilon_{systematic} + \varepsilon_{residual}. \qquad \text{Equation 3.17}$$

In terms of PIV the systematic errors arise from inadequacy within the statistical methods of the cross correlation. This inadequacy includes errors due to velocity gradients within an interrogation region weakening the strength of the correlation and effecting its location. In addition the inaccuracies of estimating the sub pixel peak location of the resulting correlation peak add to this systematic error.

The residual errors define the uncertainty in the measurement of the particle displacements (Raffel *et al.* (1998)) and whether these tracer particles are adequately following the flow. In reality, the seed particle displacements have infinite resolution; error exists in accurately defining the sub pixel displacements.

In practical systems the separation of systematic errors from residual errors is not trivial. Therefore, the total error of a PIV system is commonly expressed as the sum of the bias error (ε_{bias}) and the random error (ε_{random}) such that

$$\varepsilon_{total} = \varepsilon_{bias} + \varepsilon_{random} \qquad \text{Equation 3.18}$$

The bias error, generally expressed as the mean bias error, (d_b) can be defined as

$$d_b = d_m - d_a \qquad \text{Equation 3.19}$$

where d_m is the mean particle displacement and d_a is the actual particle displacement (Huang *et al.* (1997)). Random errors within the PIV measurements occur due to the random positioning of particle images within interrogation regions. This can be

quantified as the *rms* of the velocity variation (σ_E) due to particle image position such that

$$\sigma_E = \sqrt{\frac{1}{n}\sum\left(d_i - d_m\right)^2} \qquad \text{Equation 3.20}$$

where d_i is the measured displacement. Previous studies have shown that the ε_{random} is increased when velocity gradients exist across the interrogation region (Adrian (1997)). To calculate these errors for a specific measurement or processing system it is necessary to generate artificial particle images with known characteristics: diameter, shape, dynamic range and spatial density among others (Raffel *et al.* (1998)).

Random error caused by velocity gradients in the flow field is by far the most significant error within a well configured PIV system. Lawson (1995) presented a relationship between velocity gradients and random error such that

$$\sigma_E = \frac{1}{|U_o|\sqrt{12N}}\sqrt{L_i^2\left(\left(\frac{\partial U}{\partial x}\right)^2 + \left(\frac{\partial U}{\partial y}\right)^2 + \left(\frac{\partial V}{\partial x}\right)^2 + \left(\frac{\partial V}{\partial y}\right)^2\right) + W^2\left(\left(\frac{\partial U}{\partial z}\right)^2 + \left(\frac{\partial V}{\partial z}\right)^2\right)} \qquad \text{Equation 3.21}$$

where $|U_o|$ is the velocity magnitude associated with the interrogation region, N is the number of particle image pairs per interrogation region, L_i is the interrogation region size in meters and W is the laser sheet width in meters. This analysis shows, as a percentage of the measured velocity, that the random error is simply dependant on the number of particle pairs in the interrogation volume and the magnitude of the velocity gradient components for a given set of interrogation region dimensions.

An important consideration when studying two-dimensional PIV velocity fields is the impact of accurately defining the mean particle displacement. This is affected substantially by lost particles from the image region, either by movement on the measurement plane across the interrogation region boundary or due to motion in the third unmeasured spatial dimension (the third velocity component). When considering particles moving within the measurement plane, Raffel *et al.* (1998) shows that smaller interrogation regions can tolerate higher displacement gradients due to the wider spread of the correlation peak, but comments that particle density should be sufficiently high to accommodate smaller regions. Also the capabilities of modern computing allows cross correlation to be performed with a larger interrogation region size on the second frame therefore to allow the correlation to search further and avoid particles moving across the interrogation region boundary, therefore, allowing greater particle movement whilst maintaining particles within the interrogation region, and moving away from the ¼ rule defined by Adrian (1986), allowing dynamic range to be increased for the same sub pixel measurement error.

The successful recording of a PIV image suitable for interrogation requires the close control of a number of experimental parameters, even in simple steady flow conditions. The application of PIV to flows within the cylinder of an optical engine requires additional care. Seed densities vary throughout the engine cycle therefore causing additional compromise when applying HSDPIV over a wide range of crank angles. High frequency fluctuations expected within the flow require the use of micron sized seed particles which lead to high laser pulse energies being required. However, due to high repetition rates, the laser energy is often not sufficient to achieve images with high enough contrast and a small enough lens aperture to force the diffraction limited particle image to be > 2 pixels and hence reduce sub pixel location errors. This therefore requires a careful balance of system settings along with careful control of imaging optics. Failure to control the particle image size would lead to a tendency for displacements to be biased toward integer values of pixel displacements as ‘Pixel Locking’ or ‘Peak Locking’ occurs. The occurrence of this was avoided by careful system set up and data was monitored by plotting a particle displacement histogram.

Other considerations which should be made when capturing PIV images within an optical engine are that of avoiding flare from, for example, close combustion chamber walls and moving intake valves.

3.5 Summary

This chapter has investigated the theory of the PIV measurement technique, identifying that HSDPIV would allow both the spatial and temporal nature of the flow fields under investigation to be studied. The HSDPIV system used within this work was then introduced which, at the time this work was undertaken, was a cutting edge technology. The application of this measurement technique was therefore novel to the investigation of flow fields within a DISI engine. The following chapter will introduce the optical research engine and its auxiliary equipment which was developed into a world class test facility during the work presented in this thesis.

Chapter 4 Experimental Configuration

4.1 Introduction

The work presented in this thesis had two primary aims. The first was to develop an optical engine facility with a robust set of experimental tools for the routine application of high speed digital particle image velocimetry (HSDPIV) to in-cylinder flow measurements within a DISI optical engine. The second was to perform HSDPIV measurements under motored and fired engine conditions to investigate the behaviour of cyclic variations within the flows which develop within the aforementioned DISI engine.

The previous chapter introduced PIV, and outlined the HSDPIV optical diagnostic technique and its ability to measure both spatial and temporal flow field development. This chapter describes the single cylinder optical research engine experimental facility developed and used to generate those data presented within this thesis. This facility can be considered as a combination of individual systems, which include the optical engine, the motoring and absorbing drive system, the synchronisation and timing system and the data acquisition system.

4.2 Jaguar single cylinder optical engine

4.2.1 The engine

The single cylinder optical research engine used for the work presented in this thesis was provided by Jaguar LandRover Advanced Powertrain Engineering Group. The engine geometry was based on a spray guided direct injection spark ignition (DISI) concept. The engine was built on a single cylinder crank case designed and built by the Ford Research Laboratories, Dearborn, Michigan, USA. This crank case incorporated secondary balance weights to reduce vibrations inherent in single cylinder engines. Onto this crank case sat the engine block within which the primary piston ran. This primary piston provided a base for the mounting of the extended Bowditch type piston supports and the optical piston crown. The Bowditch arrangement allowed a 45 degree stationary mirror to be placed under the optical piston giving optical access through the fused silica window of the optical piston and into the cylinder. The optical piston was threaded onto the Bowditch support to allow it to be both adequately secured yet easily removed for cleaning. The cylinder head was mounted on solid supports from the engine block. A pneumatic ram under the cylinder liner was used to force it against the cylinder head. This ram system, coupled with the detachable optical piston, allowed the cylinder liner to be extracted without the need for the removal of the cylinder head. This helped achieve fast 'turn around' times when cleaning the optical components and ensured that the engine timing remained unaffected. The basic layout of the optical engine including the Bowditch piston and cylinder liner ram system is presented in Figure 4.1. The viewing area which was available by imaging through the piston crown window is presented in Figure 4.3.

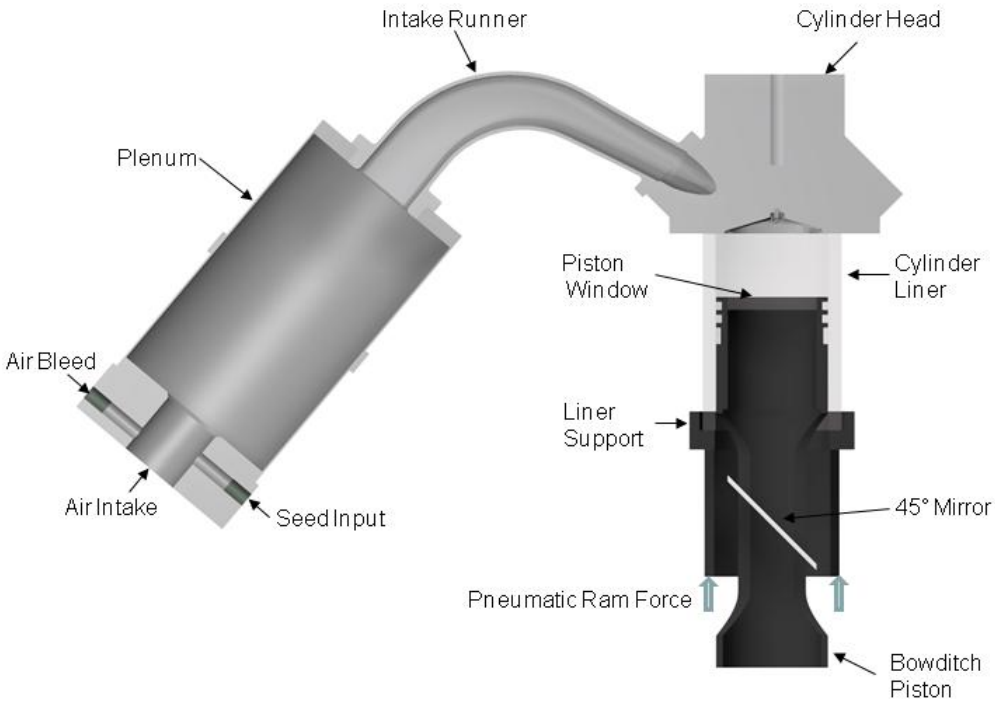

Figure 4.1 - Optical engine schematic (sectioned along intake centreline)

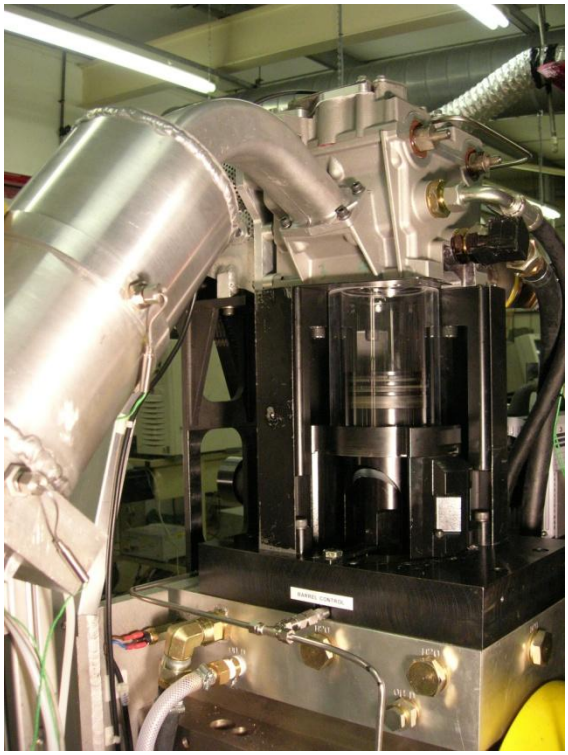

Figure 4.2 – The optical engine

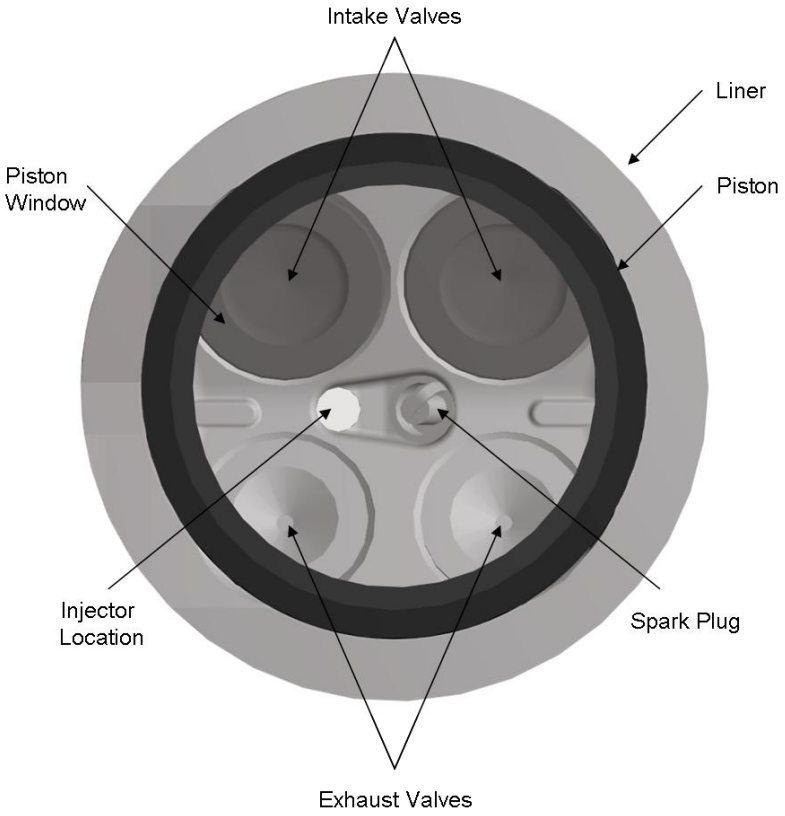

Figure 4.3 - View looking through the piston window into the combustion chamber

The engine has a pent roof combustion chamber. Optical access into the pent roof was available via a fused silica window mounted into the cylinder head, acting as a gable end to the pent roof as presented in Figure 4.4.

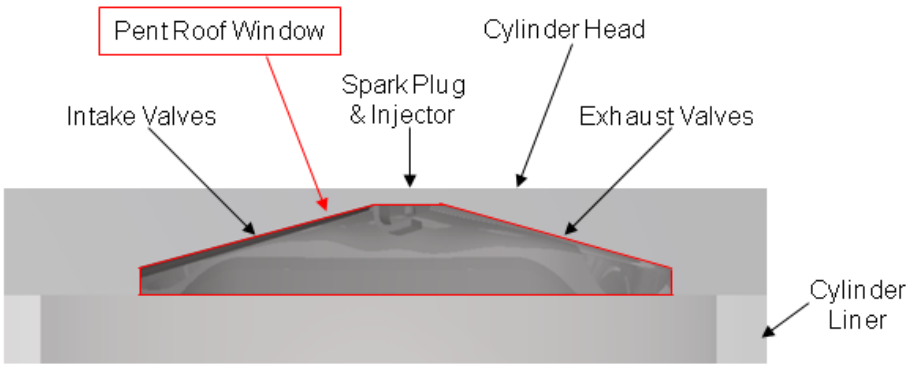

Figure 4.4 - View looking through the pent roof window

Two liner configurations were used within this study. A full length fused silica optical liner which provided optical access to the complete piston stroke, and a full length steel liner incorporating a water jacket allowing cooling or heating of the liner. This was specifically for use during fired engine work if optical access into the cylinder was not required.

The piston rings for the optical piston were manufactured from Torlon™ (a trade mark of Solvay Advanced Polymers) which is a brand name for Polyamide-imide. These were selected for their wear resistance properties at high temperature which is made possible by the graphite additive used during the material's manufacture. This offered reasonable wear performance without external lubrication, which is a fundamental requirement for an optical engine, and effective sealing at engine speeds up to 2500 rpm, but did not cause significant damage to the surface of the optical cylinder.

The important engine details are summarised in Table 4.1

Geometry

Bore	89.00 mm
Stroke	90.30 mm
Compression Ratio	10.5:1
Connecting Rod Length	148.95 mm

Valve Diameters

Intake	34.9 mm
Exhaust	29.0 mm

Valve Lift

Intake	10.53 mm
Exhaust	9.36 mm

Valve Timing

Intake Valve Opening	24° ATDC	Exhaust Valve Opening	244° BTDC
Intake Valve Max Opening	149° ATDC		
Intake Valve Closure	274° ATDC	Exhaust Valve Closure	6° BTDC

Table 4.1 - Basic engine details

The inducted air initially passed through a standard air filter to prevent the ingress of large particles. It then passed through the manually controlled throttle which provided coarse control of the static plenum pressure. Fine control of this pressure was gained by a combination of an additional air bleed, via a needle valve, and the input from the particle seeder, both of which entered the system downstream of the throttle plate. The particle seeding was added to the intake air at the entrance to the plenum to ensure that

adequate opportunity was provided for it to become homogeneously mixed. The static plenum pressure was monitored on a Digitron 2025P absolute pressure meter, which had a measurement rage of 0 to 2 bar, to ensure that the correct average operating pressure was achieved within the plenum.

The engine operated a spray-guided, gasoline direct injection (GDI) system. The spray guided concept is characterised by the close arrangement of the injector and spark plug and allows for many injection strategies to be realised. Early injection can provide a homogeneous charge whereas moving to split injection or late injection, charge stratification can be achieved. Baumgarten (2006) comments that the spray guided approach is complicated to realise and for this reason has only been investigated and tested in research engines so far. The multi-hole fuel injector required a fuel line pressure of 150 bar that was provided by a Nitrogen pressure accumulator. A schematic of the fuel delivery system is provided in Figure 4.5.

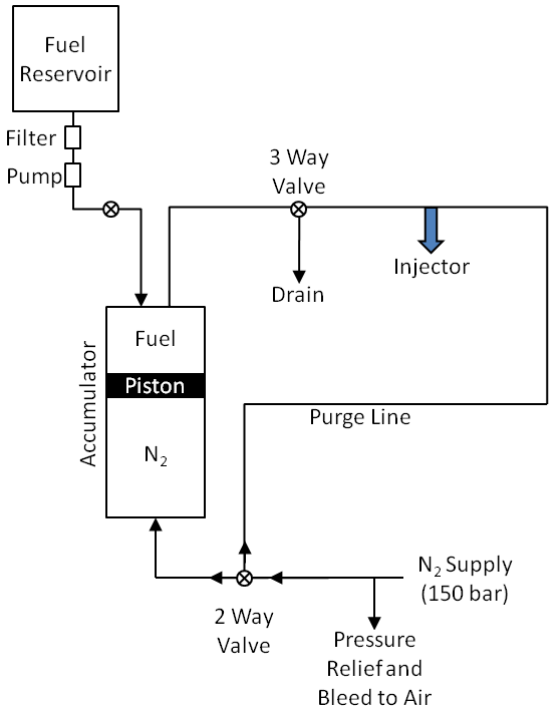

Figure 4.5 - Schematic of the fuel delivery system

The engine was operated with a dry sump and therefore required a scavenge pump to draw oil from a remote oil tank and supply this to the crank case operating at a controlled pressure. An oil feed supplied the cams with their oil requirement which was returned via an open drain to the crank case. The scavenge pump returned the oil collecting in the oil pan to the remote tank. The remote tank incorporated a heater to allow it to be preheated to a desired temperature prior to operation.

The cylinder head temperature was controlled by circulating heated water from a remote heated reservoir. This heated water allowed the cylinder head temperature to be raised to a condition close to realistic operation. When required the heated water could also be used to preheat the steel liner by passing this water through the liner's water jacket. Additionally a separate water flow could be swapped into use to provide cooling to the liner during fired engine operation. This cooling flow once required was pumped though a standard automotive water to air heat exchanger (radiator) to remove heat energy from the cooling fluid.

The optical engine, motor and services were mounted on a common base plate, which stood on four vibration dampers. The optical and control components were mounted on a stiff table rigidly fixed to the laboratory floor. This prevented vibrations due to the engine operation disturbing or damaging optical components. Reeves (1995) performed accelerometer measurements on a similar arrangement and concluded that the effects of velocity measurement error due to relative motion between the camera and the engine were negligible compared to the in-cylinder gas velocities at typical operating speeds.

4.2.2 Optical intake runner

An optical intake runner was manufactured to allow the intake runner flow entering the intake port to be characterised. This optical intake runner was manufactured by a rapid prototyping method in which a clear resin was laser sintered to create a solid geometry. Polishing of the rapid prototype parts, with diamond slurries down to 1 μm, was performed to produce an optically acceptable finish. This resulting optically accessible

intake runner matched the complex three-dimensional shape of the standard, cast intake geometry and was generated at a fraction of the cost of manufacturing a machined Perspex model. A schematic of the optical intake design is shown in Figure 4.6. This identifies the way in which the intake runner was split to allow the internal surfaces to be polished. A photograph of the finished optical intake runner is shown in Figure 4.7.

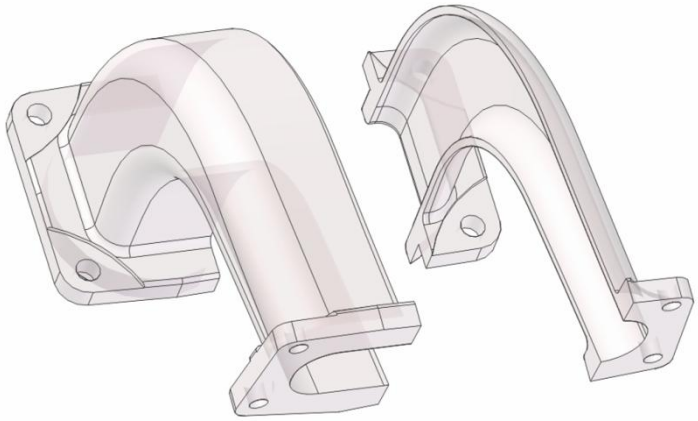

Figure 4.6 - Schematic of the optical intake

Figure 4.7 - The optical intake runner

4.2.3 Tumble Flap

A modification to the standard flow profile entering the intake ports was achieved with the use of a flow directing device which is to be referred to as a tumble flap. A schematic of the tumble flap is shown in Figure 4.8. This device comprised of a flange which was mounted between the intake runner and cylinder head, a movable flow directing flap and a static flow splitter which extended into the port. The design was such that the flow distribution passing through the valve curtain areas could be modified by directing a greater proportion of the flow over the upper or lower Section of the inlet port. The aim of this system was to provide a simple method of modifying the flow structure within the combustion chamber.

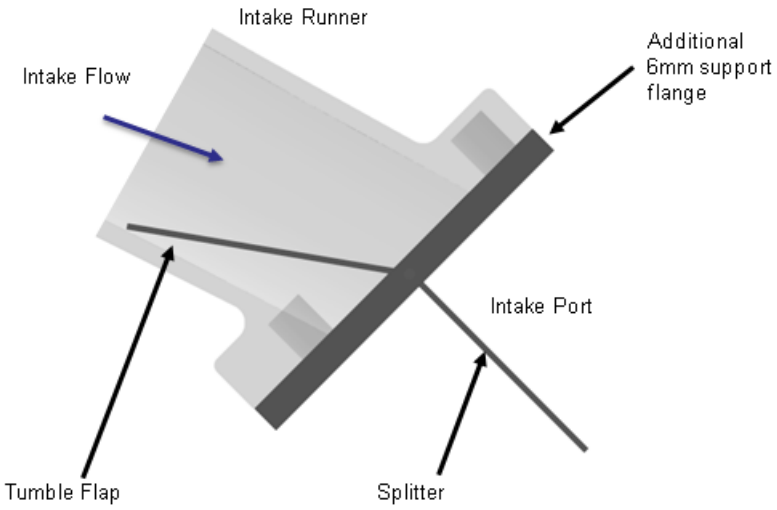

Figure 4.8 - Schematic of the tumble flap arrangement

4.3 Auxiliary Equipment

4.3.1 Engine timing

The timing of triggers synchronised to the engine's angular rotation was achieved through the use of a Leine & Linde 3600 pulse per revolution (0.1 degree resolution) incremental encoder attached to the crank shaft. This encoder also provided a once per

revolution trigger which was dynamically synchronised to correspond to the piston being at its TDC location. This synchronisation was performed by running the engine at 1500 rpm and triggering a strobe light with the once per revolution pulse. The encoder rotation was set to send a pulse as the 0° mark on the fly wheel passed the position marker. The two encoder signals were provided to an AVL 427 programmable Engine Timing Unit (ETU) which is a microprocessor controlled instrument designed to produce both crank angle and time based control and trigger signals. The ETU has eight independently programmable TTL output trigger channels with adjustable start times and pulse durations. These pulses can either be triggered individually or cyclically repeated. The first four of the available channels had the ability to produce a variable 0.1 to 10 volt programmable trigger synchronised to the standard TTL trigger along with the facility to generate two independent pulses per cycle. Given that one working cycle of the four stoke engine takes two revolutions and the encoder sends a once per revolution trigger to identify the TDC location, it is impossible to determine the cycle start. However the ETU offers a curve fitting function to identify compression TDC from the cylinder pressure signal therefore automatically identifying location within the engine cycle. The ETU was used to control timing triggers to the PIV system, the data acquisition system, the spark coil and the fuel injector driver.

It is important to ensure the engine was allowed to settle into a stable operating mode prior to data acquisition especially under fired engine operation. To do this the once per revolution signal from the encoder was split into an ‘in-house’ programmable counter unit which provided a TTL level high voltage signal as soon as a predetermined number of cycles was complete. The TTL high voltage signal was used to open an ‘in-house’ trigger gate which, until this point, was blocking the capture based output triggers from the ETU. The gating unit allowed the simultaneous gating of up to 8 independent trigger signals. When the gate was opened synchronised triggered capture of data from data acquisition and PIV systems resulted which, for example, allowed fired engine studies of flow where pressure data corresponding to PIV captures was available, see Figure 4.9.

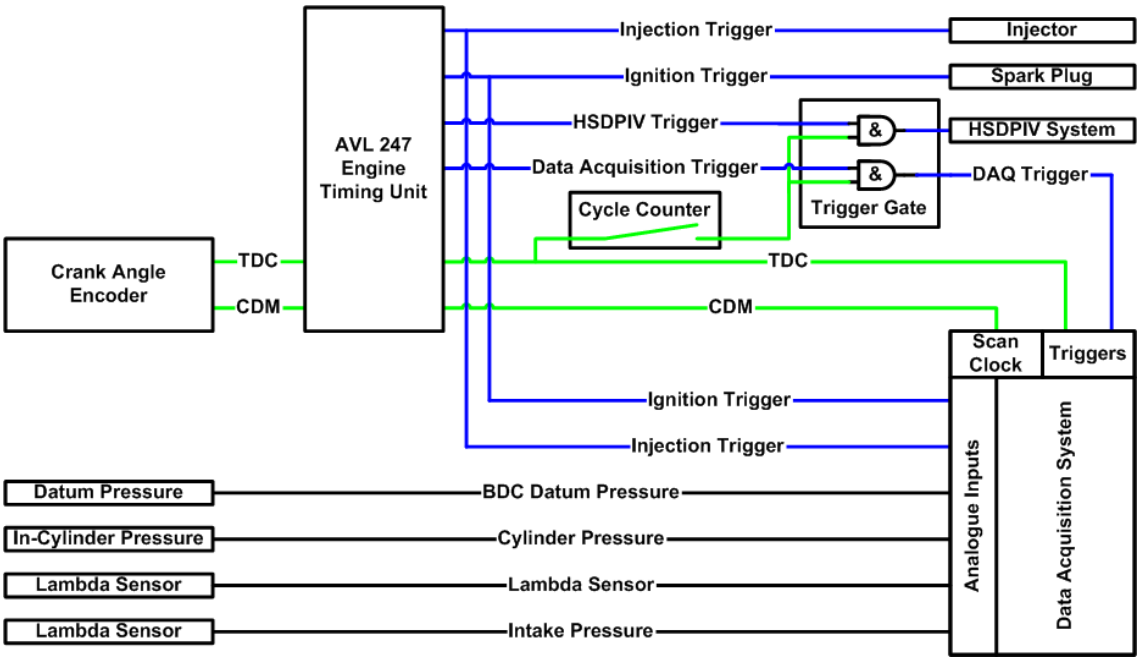

Figure 4.9 - Synchronisation of HSDPIV system and data acquisition system

4.3.2 Motoring and absorbing drive system

Engine speed control was provided by a motoring and absorbing drive system provided by Control Techniques. The regenerative shunt wound electric motor drive system had the ability to absorb the power created due to firing the engine by providing a resistive load. The motoring or absorbing load was controlled by a PID controller which acted to maintain the desired engine speed. The engine speed was controlled to within ± 2 rpm during both motored and fired operation (up to a maximum speed of 2000 rpm, the rated speed of the motor).

4.3.3 Data acquisition

A high speed data logging facility was developed during this work using a National Instruments PCI-MIO-16E-1 acquisition card connected to a BNC-2090 shielded BNC

adapter board for ease of signal connection. The analogue to digital converter on the acquisition card provided 1.25 million samples per second with 12-bit resolution and could be multiplexed across 16 single ended analogue input channels (or 8 differential analogue input channels). The acquisition card also provided 2 analogue output channels, 8 digital input/output channels and two digital 24-bit 20MHz counter/timers.

A LabView™ data acquisition and control programme was developed to record analogue signals and provide a real time display for system monitoring purposes. The engine encoder outputs were used to provide a revolution start trigger and a 0.1° crank angle resolution scan clock. At this scan rate the data acquisition system was capable of recording up to 13 analogue input channels for the engine speed of 1500 rpm (25 rps). This system, therefore, allowed the recording of cylinder pressure, intake runner pressure, lambda sensor and system timing triggers. Using one of the available counter timers, the engine speed was derived by counting the time between encoder pulses. This engine speed was provided to the engine operator via the real time display allowing the operator to drive the engine to the required speed. An external trigger provided by the ETU, via the trigger gate, allowed the data acquisition of recorded channels to be synchronised with other data acquisition sources such as the PIV system.

4.3.4 Pressure measurement

In-cylinder pressure history was measured with a Kistler piezo-capacitive pressure transducer (model 6041A) mounted within the pent roof of the cylinder head. Since this transducer measured a dynamic relative pressure change, a reference pressure was required. This reference pressure was provided by a Kistler piezo-resistive pressure transducer (model 4045A), which provided an absolute pressure measurement. This transducer was mounted in the wall of the steel liner and only became exposed to the in-cylinder pressure close to BDC. It was therefore protected from the pressure of combustion but was still able to provide a pressure reading close to BDC. The absolute pressure recorded at BDC following the intake stroke was used as a reference for the pressure history recorded via the transducer mounted in the cylinder head over the next

360° of crank revolution. This method, however, was unavailable when using the optical liner. Therefore, by obtaining an average pressure at BDC following the intake stroke over a sample of cycles for the current operating conditions using the steel liner, an average reference pressure at BDC was generated which could be applied to the in-cylinder pressure recorded for that day's measurements at that operating condition. A further Kistler piezo-resistive pressure transducer (model 4045A) was mounted in the intake runner to monitor pressure during the course of the cycle.

4.3.5 Lambda sensor

The air/fuel ratio for fired engine operation was monitored with a Lambda Pro™ 1200 sensor manufactured by Engine Control and Monitoring (ECM). The lambda sensor provided both a visual display of either lambda or AFR (gasoline) and a linear analogue 0 to 5 volt output which allowed a range of lambda values from 0.55 to 1.75 to be logged by the data acquisition system. For information, lambda λ is defined as

$$\lambda = \frac{AFR}{AFR_{Stoichiometric}}. \qquad \text{Equation 4.1}$$

4.4 PIV alignment and calibration procedure

It is important when setting up a PIV measurement system to accurately align the laser sheets to the desired measurement plane. Once this has been achieved it is important to calibrate the size of the imaged region on this same measurement plane. To aid this process within the engine cylinder, two 'mock' pistons were designed, one to assist the setup of measurements in the tumble plane and the other in the swirl plane. These are shown in Figure 4.10 (a) and (b) respectively.

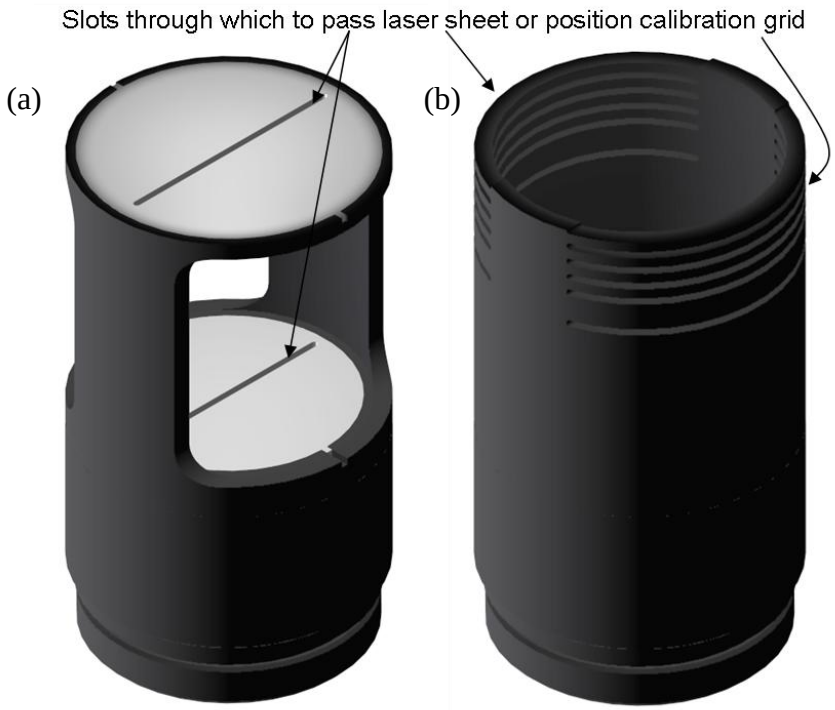

Figure 4.10 - Alignment piston (a) tumble plane measurements (b) swirl plane measurements

The slots in the pistons were manufactured to correspond to desired measurement planes. Therefore, by passing the laser sheet through vertically (tumble) or horizontally (swirl) aligned pairs of slots it was ensured that the laser sheet was on and running parallel to the required measurement plane. The slotted inserts which fit into the tumble plane alignment piston could be replaced to allow alignment onto any desired measurement plane. Alternatively, for swirl plane measurements, the alignment slots could be repositioned by setting the rotation of the crank and hence controlling the piston position.

As well as providing assistance in the alignment of the laser sheet the slots were also used to accurately position an image calibration grid. This allowed both the accurate alignment between the calibration image and the laser sheet as well as allowing the camera to be focused on the grid (and hence measurement plane) with a wide open aperture and hence minimum depth of field. Through performing this step, any

substantial miss alignment between the plane of the laser sheet and the focal plane could be removed.

Also the calibration of the PIV system, ensuring that the two laser sheets required for the two frame cross correlation were illuminating the same plane was regularly checked. This was achieved by placing a silicone block with suspended solid seed particles into the area illuminated by the laser sheets. By capturing PIV measurements on this stationary field of particles, the resulting analysed velocity vectors should reflect this lack of movement as the strongest correlation peak should occur at zero displacement. This calibration was done with the PIV system in a setup to capture in-cylinder measurements in either the tumble or swirl planes.

4.5 Fired engine baseline tests

As discussed in Chapter 2, pressure related comparisons are often used to demonstrate and evaluate the level of cyclic variation experienced by an engine. In Figure 4.11 pressure data is presented for the single cylinder optical research engine which is the basis of the studies within this thesis. These data demonstrate the level of combustion variation experienced over 100 successive engine cycles. The engine was operated at a speed of 1500 rpm with a plenum pressure of 525 mbar and fuel injection at 60° ATDC gas exchange to create a stoichiometric charge at λ=1. The ignition trigger was sent to the coil at 35° BTDC combustion. The mean Indicated Mean Effective Pressure (imep) for the 100 cycles was 2.6 bar with a coefficient of variance of 2.1 %.

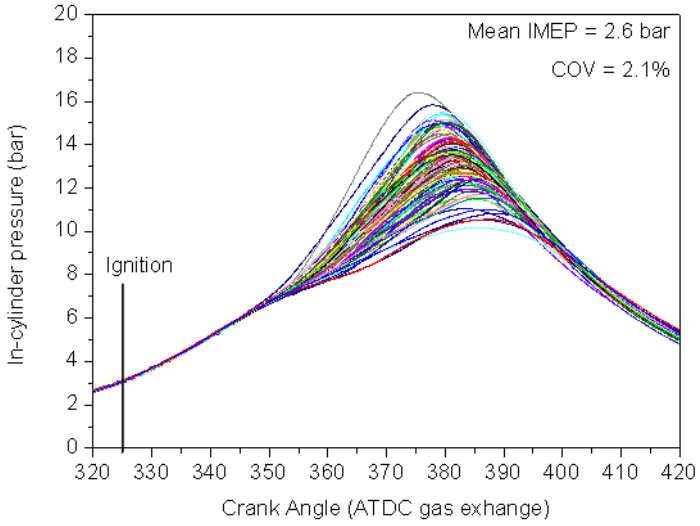

Figure 4.11 – The in-cylinder pressure history with respect to crank angle for 100 successive cycles, demonstrating the cyclic variation experienced

It is clear from Figure 4.11 that there is cyclic variation in the peak pressure and the crank angle at which this peak pressure occurs. These data are presented in Figure 4.12, where the peak pressure for a cycle is displayed against the crank angle at which it occurs. A linear trend due to the expanding volume of the cylinder can be seen. However, scatter in peak pressure corresponding to any given crank angle is also shown. The scatter reflects cyclic variations in rate of pressure rise due to variations in parameters such as flow, AFR, ignition energy and exhaust residuals.

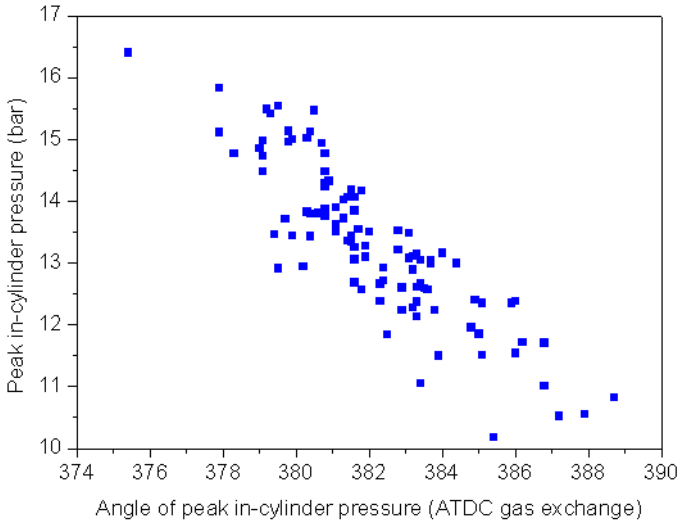

Figure 4.12 – The relationship between peak in-cylinder pressure and the angle at which peak in-cylinder pressure occurs

An alternative visualisation of Figure 4.11 is presented in Figure 4.13 by means of a pressure against volume (P-V) diagram for the 100 consecutive cycles. The area bound by the curve for one cycle demonstrates the work done during the engine cycle. Two distinct loops are shown, one representing the pumping work during the exhaust and intake strokes and the other representing the gross work output during the compression and expansion stroke. As the area contained by the curve varies so too does the work output from the cycle.

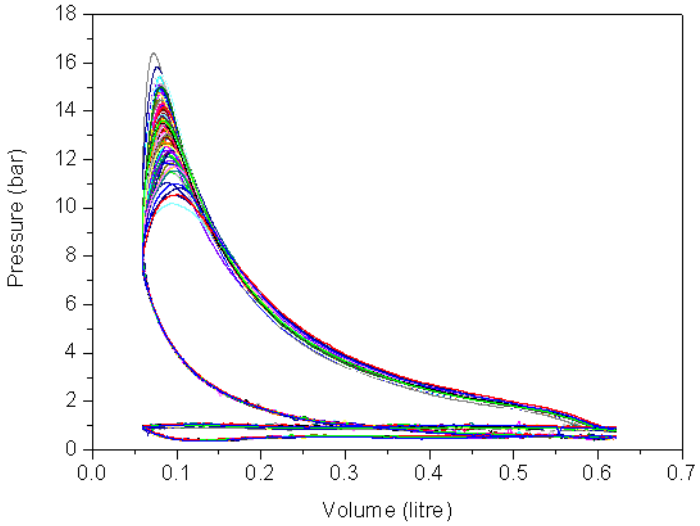

Figure 4.13 – The in-cylinder pressure with respect to volume within the cylinder for the same 100 successive cycles as presented in Figure 4.11

The work output of a cycle is often represented by the imep term. The calculation of imep from the experimental pressure data was performed using pressure and burn rate analysis code, written in Matlab™, and is discussed in Appendix A. Data are presented in Figure 4.14 which shows the scatter in the net imep for the 100 consecutive cycles discussed previously. The black line denotes the mean imep produced over the presented cycles.

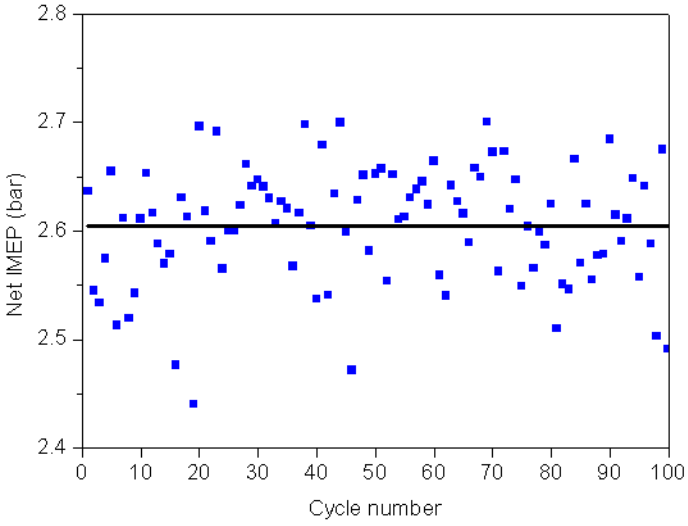

Figure 4.14 - Plot to demonstrate the scatter experienced in net imep for 100 successive engine cycles with the solid black line denoting the mean

In Figure 4.15 data are presented which show the calculated profile of mass fraction burned for the 100 successive cycles. A calculation for the rate at which fuel mass is burned within the cylinder, based on the measured in-cylinder pressure trace and method first developed by G. M. Rassweiler and L. Withrow in 1938 (Rassweiler and Withrow (1980)), has been discussed in Appendix A. These data show variations in both the mass fraction burned at a specific crank angle and also the gradient at which mass fraction is burning. These are indicative in variations of burn rate. A significant contributor to these variations are the flow field characteristics which affect the flame kernel development and the subsequent flame growth, as discussed in Chapter 2. These include variations in large scale convective effects as well as local turbulence characteristics. In Figure 4.16 the crank angle location at which 10% and 80% fuel mass fraction has burned is presented. This further highlights the variation that is apparent at one fixed operating condition over the 100 engine cycles.

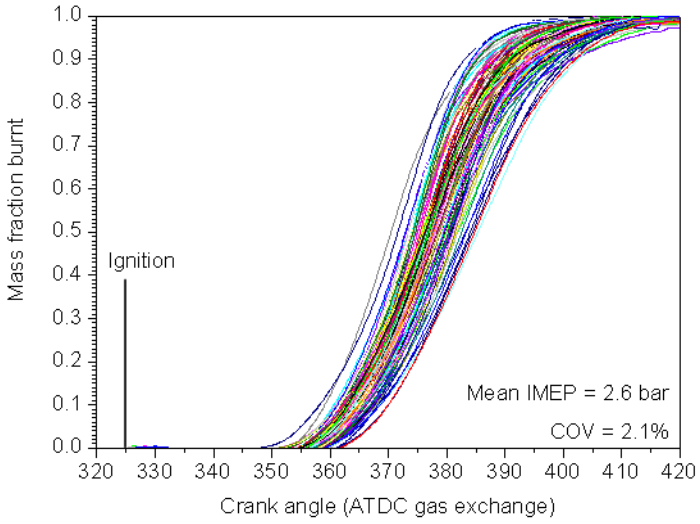

Figure 4.15 - The variation in the rate of mass fraction burn for 100 successive cycles

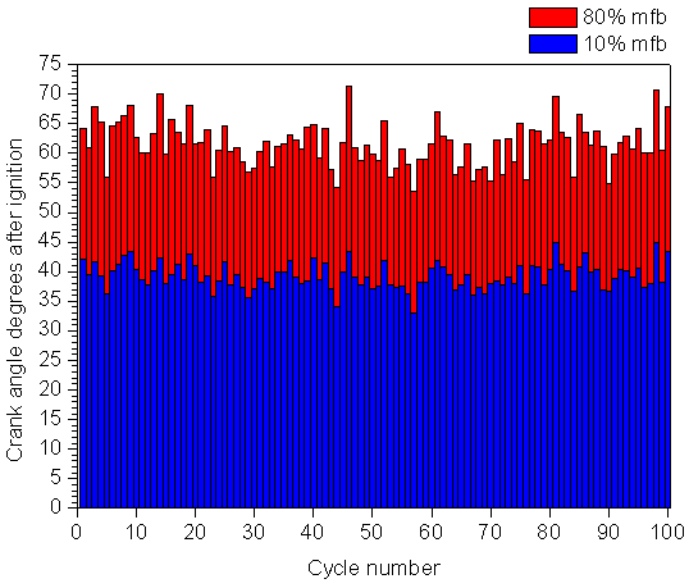

Figure 4.16 - The scatter in 0 to 10% and 0 to 80% mass fraction burn times for 100 successive engine cycles

Figure 4.17 presents mean in-cylinder pressure against volume, calculated over 100 engine cycles. For these data the engine was operated with a plenum pressure of 525 mbar, fuel injection at 60° ATDC gas exchange to create a stoichiometric charge at λ=1, however, spark timing was varied. It is shown that peak imep output is reached for a spark timing around 35° BTDC (which is the same as that used in the previous data presented). However, the COV of imep has not reached a minimum and is shown to reduce by advancing the spark timing further. Figure 4.18 presents mean in-cylinder pressure against volume, also calculated over 100 engine cycles. For these data the engine was operated with a plenum pressure of 525 mbar, injection at 60° ATDC gas exchange and ignition was at 32.5° BTDC. The stoichiometry of the air/fuel mixture was varied from λ=0.9 to λ=1.2. As expected, both the IMEP and the COV of imep reach a respective maxima and minima when the charge is slightly fuel rich (λ<1).

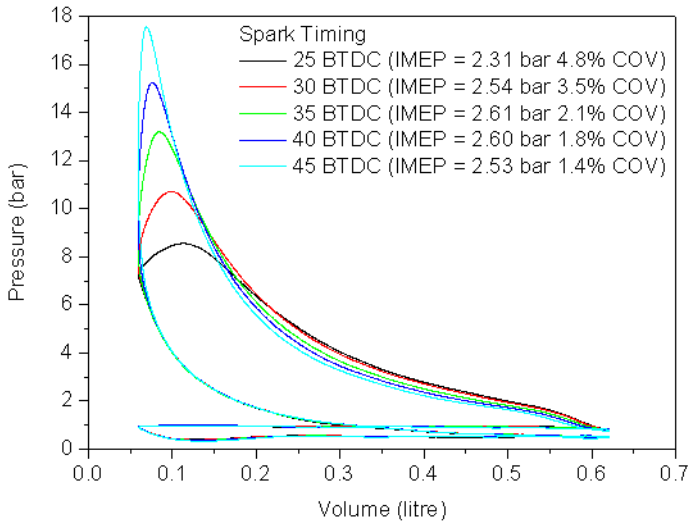

Figure 4.17 - Graph to show how mean in-cylinder pressure varies with changes in spark timing

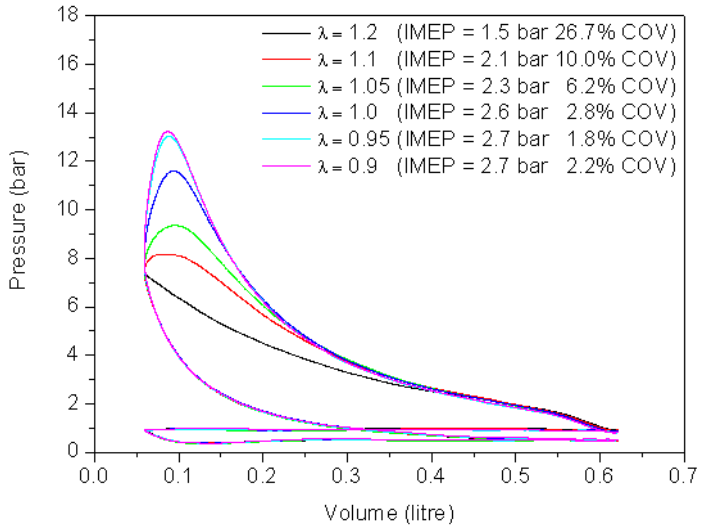

Figure 4.18 - Variation in mean in-cylinder pressure with changes in air fuel ratio

These data demonstrate the inherent cyclic variation which is commonly experienced by a single cylinder engine. It is clear that both the imep and the COV of imep can be affected by altering both the spark timing and the AFR. Slight variations in overall stoichiometry and spatial in-homogeneities in AFR from one cycle are likely to impact parameters such as flame growth. This ultimately affects both the cycle's imep as well as resulting exhaust emissions.

4.6 Summary

A description of the engine facility which was developed within this work and its auxiliary systems has been given in this chapter. The resulting single cylinder DISI optical engine research facility developed during the course of this work allows routine acquisition of synchronised optical and analogue data from both motored and fired engine operation.

In-cylinder pressure data has been presented which demonstrates the level of cyclic variation in pressure related parameters experienced by this engine. A significant

contributor to this combustion variation is the in-cylinder flow conditions around the time of ignition. An investigation of the flow field behaviour within the pent roof of the single cylinder optical research engine at the time of ignition and early flame growth is discussed in Chapter 5.

Chapter 5 Flow field variation around combustion

5.1 Introduction

The experimental configuration of the engine has been discussed in Chapter 4, which includes operating pressure data to describe the basic level of cyclic variation experienced by the single cylinder research engine used in this study. In this Chapter data is presented which shows, via chemiluminescence imaging, how the flame propagates through the combustion chamber over a number of cycles. These data are presented to demonstrate the cyclic variations which are apparent in the flame growth at a fixed operating condition. Following on from this, flow fields captured with the HSDPIV system within the pent roof of the engine around the time of the ignition event have been presented. These data show the nature of the flow and highlight the cyclic variation which is thought to significantly contribute to the combustion variations experienced.

5.2 Flame Imaging

Natural light or chemiluminescence imaging of the flame was performed to provide an indication of the cyclic variation in the flame growth. Data presented in Chapter 4 showed combustion variations that are experienced by the single cylinder research engine by means of presenting in-cylinder pressure histories. Here, the flame image data is presented to illustrate cycle to cycle variation in the flame.

The chemiluminescence images were captured with the Photron ultima APX-RS high speed digital camera used within the HSDPIV system. The camera was controlled

through the Photron PFV software interface which allows control over frame rate, active pixel array size, shutter speed and triggering of the image capture. A 105 mm Micro Nikkor lens was used to image the desired area. The light emitted from the premixed combustion flame required a wide open aperture and therefore the $f^{\#}$ was set to 2.8 which was the minimum available with the lens used. This allowed as much light through to the imaging sensor as possible. The camera shutter could be activated, if required, to shorten the time over which the imaging sensor was active to reduce blurring of the image as the flame grows. The flame images were captured with the engine operated at a speed of 1500 rpm, with a manifold pressure of 525 mbar, a stoichiometric air fuel ratio with injection at 60° CA ATDC and spark event at 35° CA BTDC.

5.2.1 Images through the piston crown

5.2.1.1 Measurement conditions

A schematic of the configuration used to capture the chemiluminescence images through the optical piston crown is presented in Figure 5.1, and the imaged area is shown in Figure 5.2. This arrangement was used for the capture of the images presented in Figure 5.3 to Figure 5.7. In these images the location of the spark plug is marked by a red cross, the intake valves are located at the top of the image and the exhaust valves are therefore at the bottom. It should be noted that the black outer circle in the images signifies the edge of the window through the piston and therefore should not be mistaken for the cylinder bore.

The camera was operated at 4500 frames per second corresponding to one image every 2° crank angle (CA) revolution and an active pixel array of 768 × 880 pixels. The camera shutter was controlled to give an exposure time of 100 μs. The camera memory was partitioned to allow 50 images to be captured at the preset frame rate per TTL trigger signal received. Therefore, by sending a trigger signal 2° CA after the ignition trigger, images were captured from 2° to 102° CA after ignition. The 2 Gb on-board memory available allowed *circa* 3100 images and hence 62 consecutive cycles to be

captured. The images were captured on a line of sight basis and therefore only the projection of the flame in this plane was captured. Please refer to Section 5.2.2 for flame images captured in an orthogonal plane through the pent roof window of this optical engine.

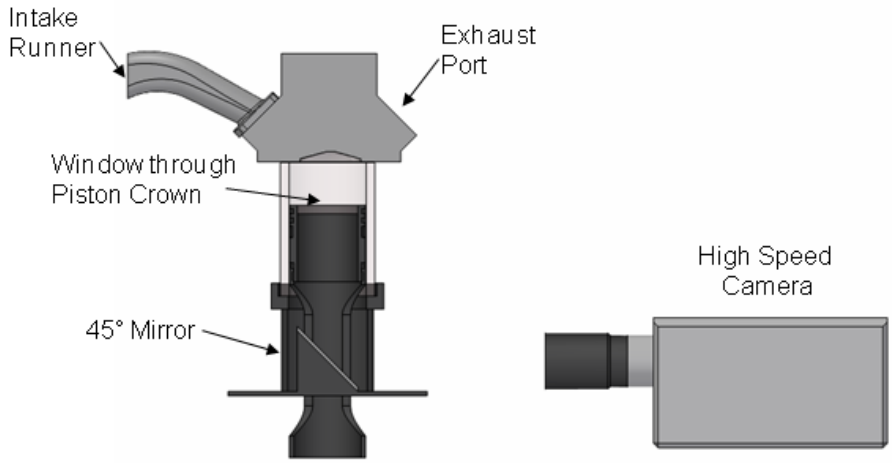

Figure 5.1 - Schematic to show the system configuration for imaging flame growth through the piston crown via the 45° mirror

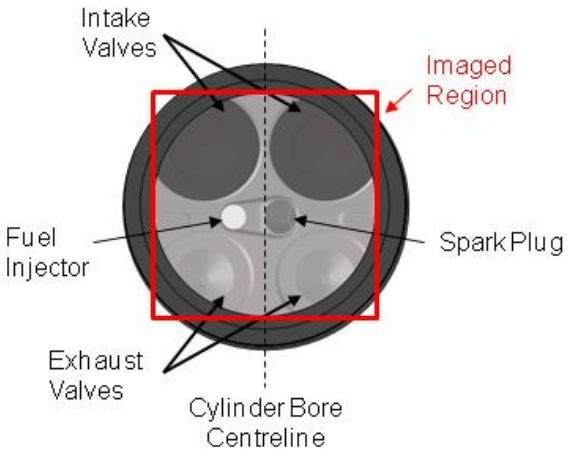

Figure 5.2 – Schematic to show the imaged area for imaging flame growth through the piston crown via the 45° mirror

5.2.1.2 Flame images

The raw chemiluminescence images were saved into an 8-bit grey scale movie file. Each individual frame was post processed to set any pixels which were not exposed to light (hence recorded as '0', and appearing black) to a value of '255' to appear as saturated white. This was performed to aid the visualisation of the chemiluminescence, which caused exposure to pixels on the imaging array and therefore raised their value from the unexposed '0' state.

The chemiluminescence images presented in Figure 5.3 show the flame for twelve individual arbitrarily selected cycles, 22° CA after ignition which corresponds to 2.44 ms after ignition. This timing is relative to the TTL pulse being sent to the ignition coil and includes any delay which may be inherent within this ignition system. It is shown in the figure that cyclic variations exist in the early stages of the flame kernel development and initial flame growth. This is displayed in the variations in size and shape of the flame images for the twelve cycles presented. In all cases however, the flame is initially drawn towards the exhaust valves as large flow scales relative to the flame act to convect it. This convection follows the dominant bulk flow motion at the top of the cylinder at this stage of the cycle, which is from the intake valve side to the exhaust valve side of the engine, as shown in Section 5.3. It is suggested in the figure that these large scales in the flow can act to shape the flame. Cycles I, J and K exhibit a flame shape which appears to be drawn in a line away from the spark plug but with varying angle.

Factors which can affect flame development speed include spark energy, air fuel ratio variations and flow variations. The flow variations are thought to be a significant factor in the combustion variation and as such, the focus of substantial past and present research has been the influence of turbulence on the combustion event Pope (1987); Arcoumanis and Bae (1993); Gillespie *et al.* (2000); Bradley *et al.* (2007) It is shown that the flame image corresponding to cycles B and L of Figure 5.3 covers a larger area in this projected plane than shown by the other cycles. It is reasonable to assume that

this correlates to a more rapid flame growth over the 22° CA (2.44 ms) since ignition. These variations in flame development are ever more apparent when comparing to cycles such as C and D where the flame appears relatively small and fragmented. Turbulent variations which, in respect to the flame, are small in scale and therefore can locally wrinkle and strain the flame front can affect the flame speed. Comparing the presented flame images it is shown that the flame behaviour at this early point in the flame development already displays significant cyclic variations.

Flame images at 26° CA (2.89 ms) after ignition for the twelve selected cycles are presented in Figure 5.4. It is shown that the early characteristics of the flame shown in Figure 5.3 are still apparent within this figure. Cycles I, J and K still display a long narrow flame consistent with being drawn out by large scale flow structures. Cycles B and L still appear to cover a larger area in this plane than that of the other presented cycles. Also, cycles C and D still exhibit the fragmented nature previously discussed.

Flame images presented in Figure 5.5 are for the same twelve selected cycles 30° CA (3.33 ms) after ignition. The flames display many of their early characteristics. However, the narrow drawn flames of cycles I, J and K appear to be broadening. This is likely to be due to the flame flow interactions. For example, as the flame grows relative to the characteristic length of local flow structures the impact of those flow structures on the flame changes. Also, as the burnt gas expands, the flow ahead of the flame is influenced by the combustion event.

A further time step for the flame images, corresponding to 40° CA (4.44 ms) after ignition, is presented in Figure 5.6. At this point the flame has started to reach the extremities of the visible area. In some cases, such as cycles J and L, the flame has a portion now hidden out of view of the piston crown window. Cycle K still exhibits the characteristic shape visible in the earlier time steps. Comparing all the flame images within this figure, cyclic variations in flame shape are still apparent. Tracing around the edge of a flame it is possible to imagine flame flow interactions occurring which causes the concave and convex regions around the flame front.

The aim of these flame images is to provide an indication of how the combustion event may be influenced by flow field variations. It is clear that the flame, in its initial stages, suffers from cyclic variations. The development of the flame over the course of the combustion event, up to 32° CA (3.56 ms) after ignition, for four of the previously presented cycles is shown in Figure 5.7. This Figure shows the flame edge plotted at 2° CA (0.22 ms) intervals throughout the initial part of the combustion event. The flame edge was established using the edge detection function within the Matlab™ image processing toolbox. Firstly the grey scale image was processed into a binary image by applying a threshold to set every pixel which was above a value of '1' in the 8-bit grey scale image to a value of '1'. The image processing toolbox function 'edge' was applied with the 'Canny' edge-finding method. The resulting edges were plotted with incrementing colour though the rainbow from blue to red to signify the progression in engine rotation. These flame edges plots show how the flame structure develops over time. Features visible within the flame edge (such as concave or convex sections) appear to influence the next step within the flame development. Local variations in separation of the plotted edges, over each 2° time step, can be observed and these signifying differences in local flame speed.

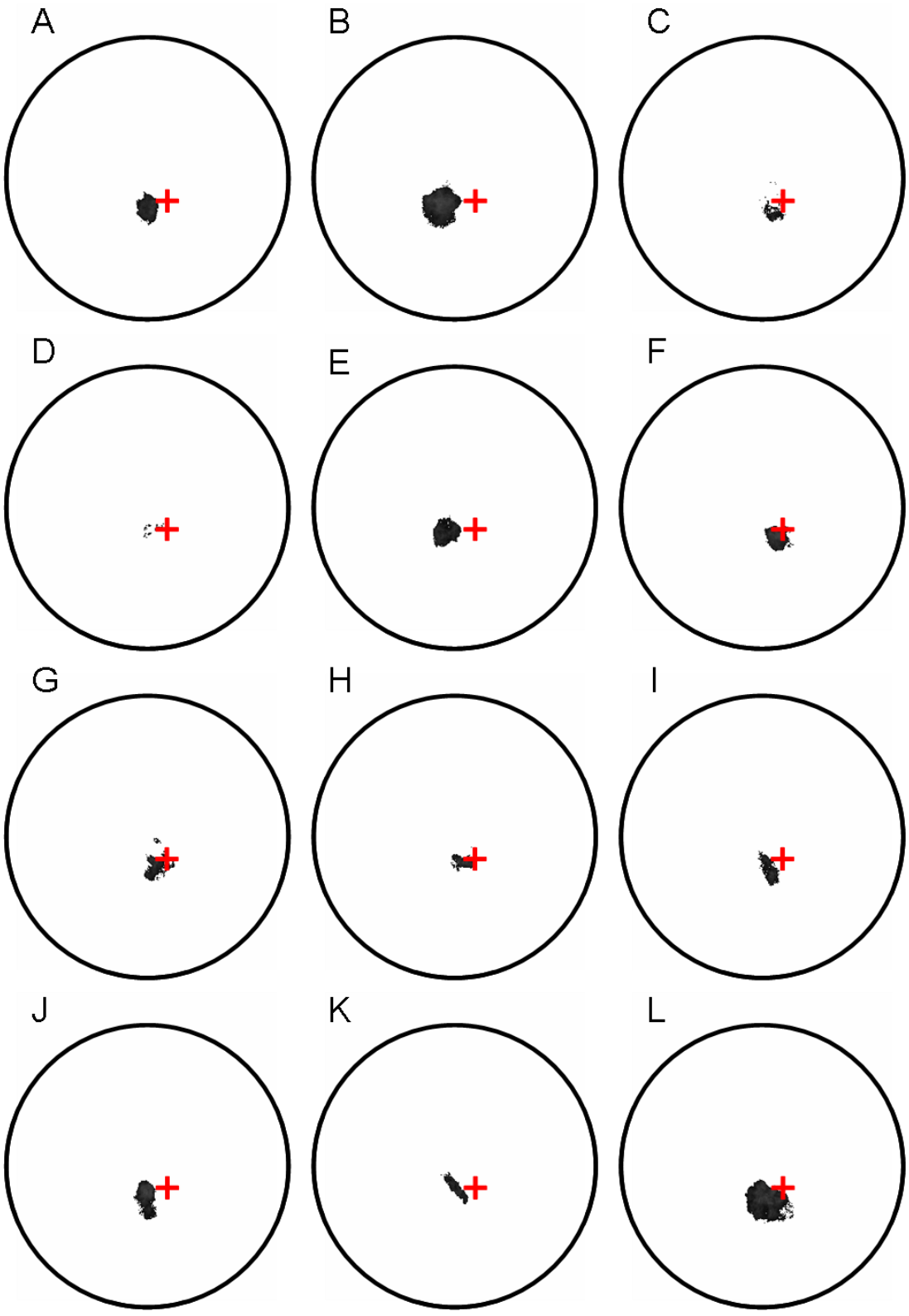

Figure 5.3 – Chemiluminescence images of the combustion flame 22° CA (2.44 ms) after ignition for the engine operating at 1500 rpm at λ≃1

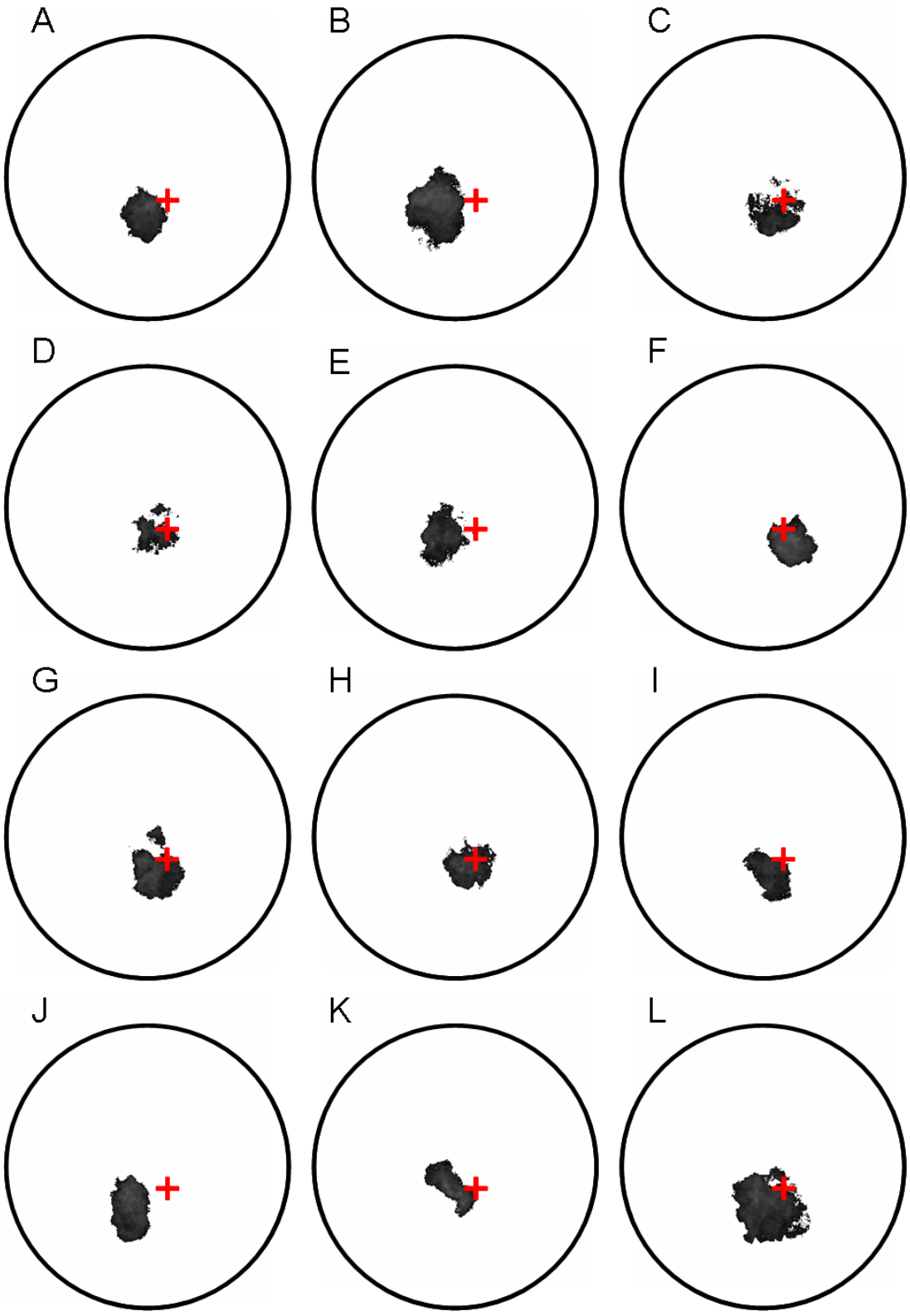

Figure 5.4 - Chemiluminescence images of the combustion flame 26° CA (2.89 ms) after ignition for the engine operating at 1500 rpm at λ≃1

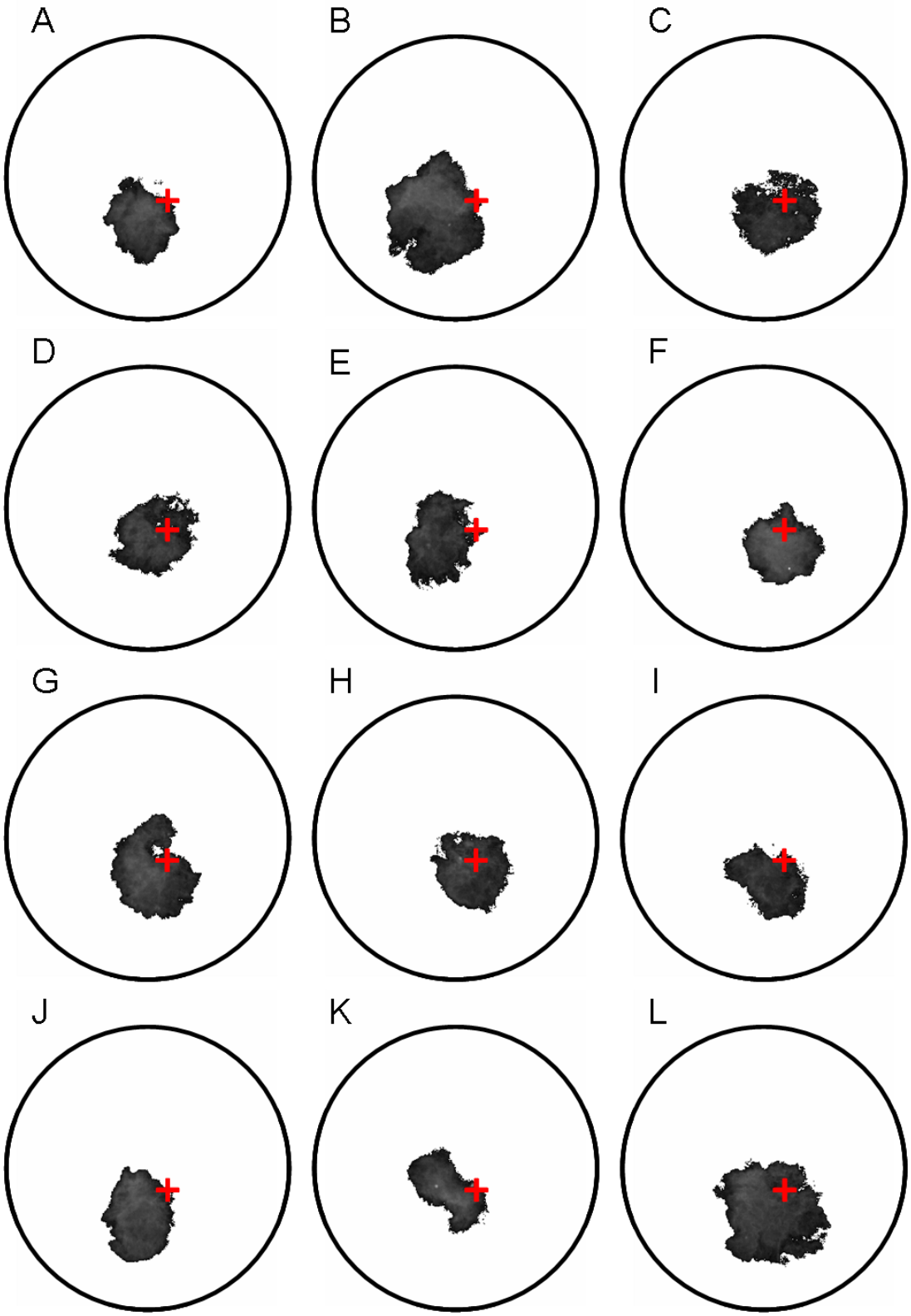

Figure 5.5 - Chemiluminescence images of the combustion flame 30° CA (3.33 ms) after ignition for the engine operating at 1500 rpm at λ≃1

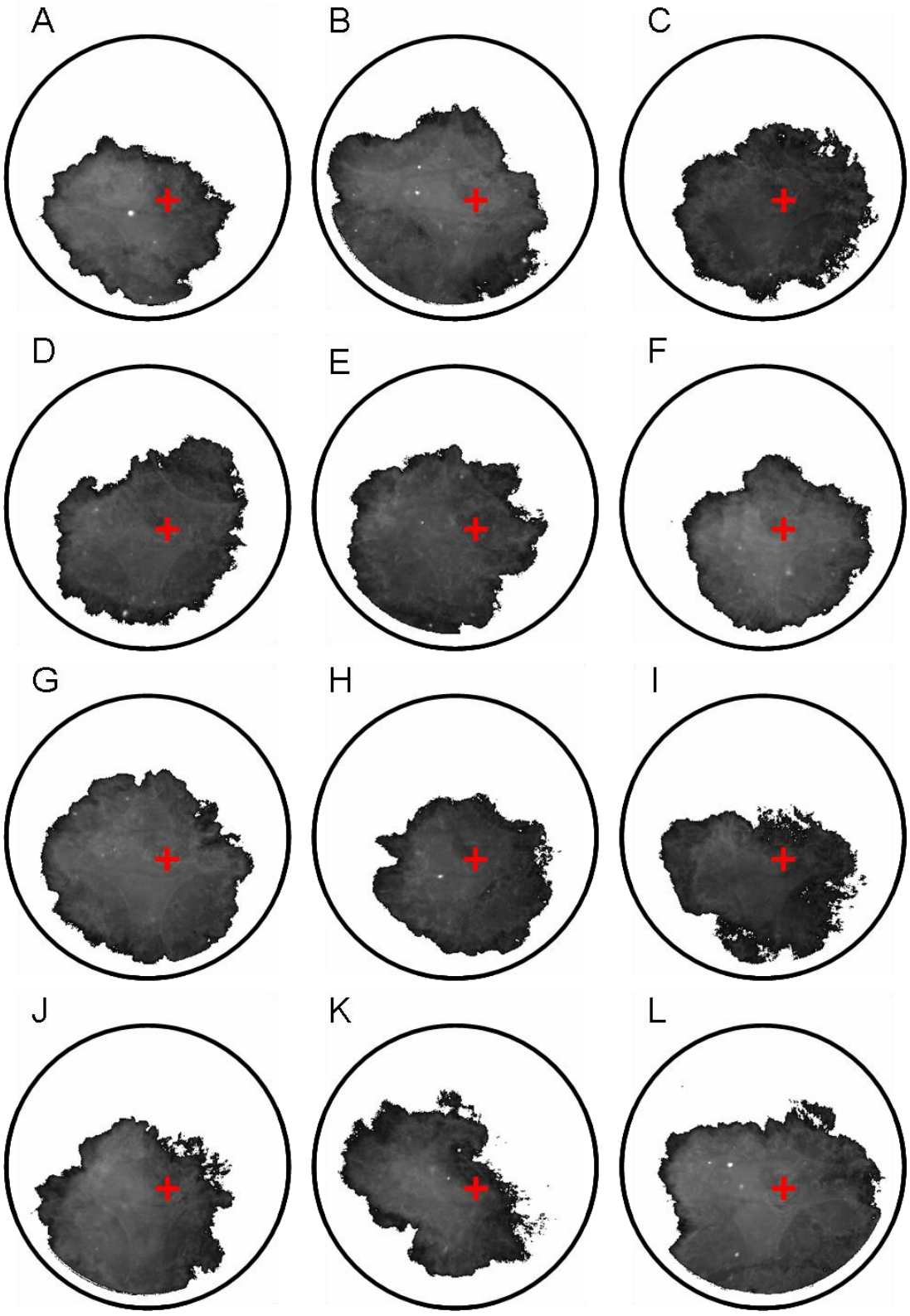

Figure 5.6 - Chemiluminescence images of the combustion flame 40° CA (4.44 ms) after ignition for the engine operating at 1500 rpm at λ≃1

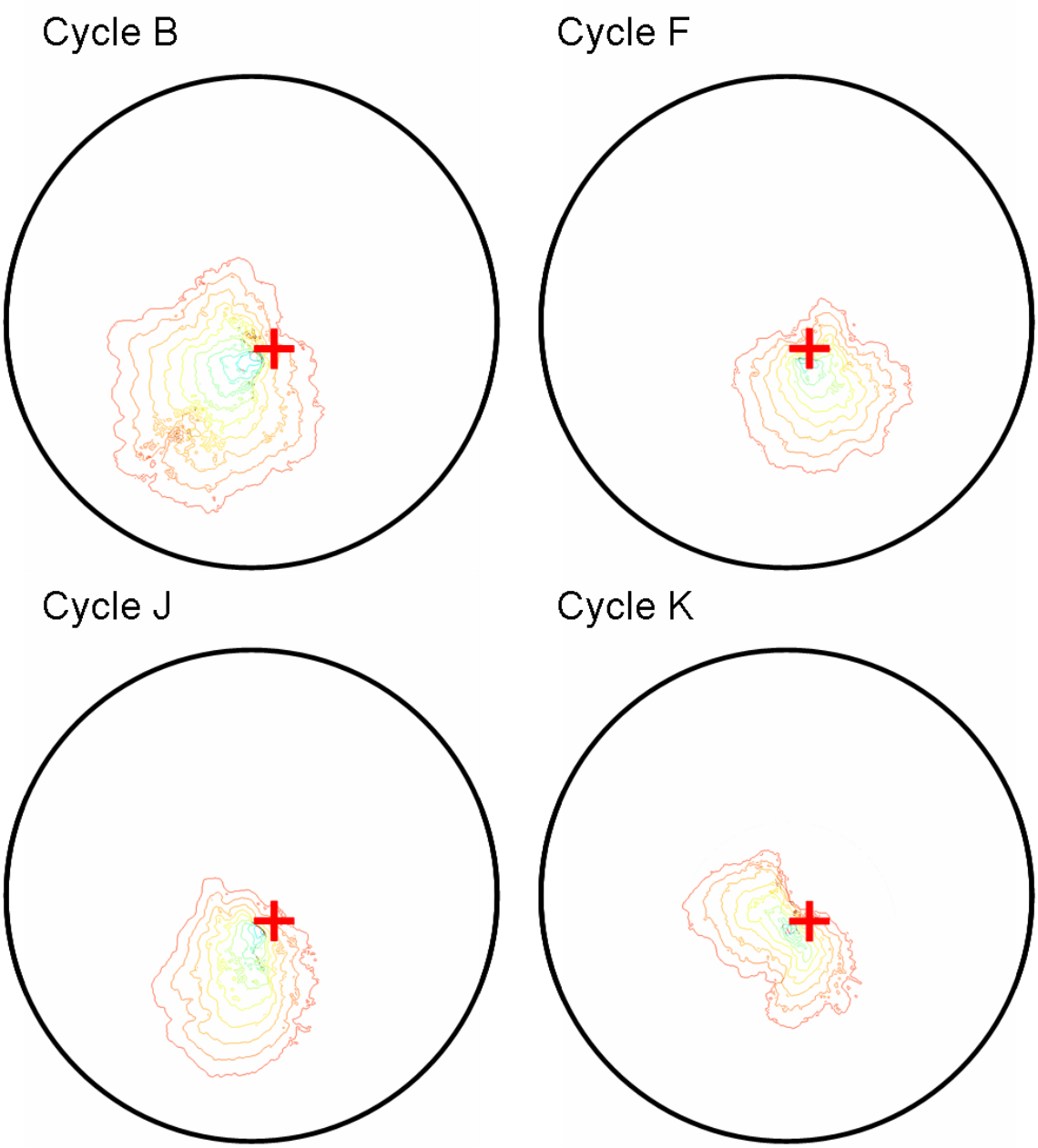

Figure 5.7 - Flame edge identified to show growth for the period to 32° CA (3.56 ms) after ignition for four cycles illustrative displayed in Figure 5.3 to Figure 5.6

5.2.2 Imaging through the pent roof window

5.2.2.1 Measurement conditions

A schematic of the configuration used to capture the chemiluminescence images through the pent roof window is shown in Figure 5.8, and the imaged area is shown in Figure 5.2. This arrangement was used for the capture of the images presented in Figure 5.10 to Figure 5.14. In these images a black 'mask' has been added to cover flare from the spark electrodes. The intake valves are on the left and the exhaust valves are on the right of the spark plug. The camera was operated at 9000 frames per second corresponding to one image every degree of crank revolution and had an active pixel array of 768 × 432 pixels. As for the imaging of the flame through the piston crown, the camera shutter was controlled to give an exposure time of 100 μs. The camera memory was partitioned to allow 50 images to be captured at the preset frame rate per TTL trigger signal received. Therefore by sending a trigger signal 2° CA after the ignition trigger, images were captured from 2° to 52° CA after ignition. The 2 Gb on-board memory available allowed *circa* 6300 images and hence 126 consecutive cycles to be captured.

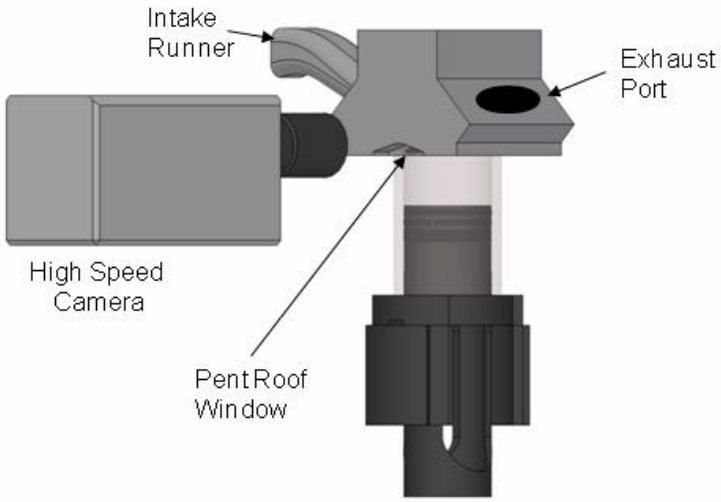

Figure 5.8 - Schematic to show the system configuration for imaging flame growth through the pent roof window

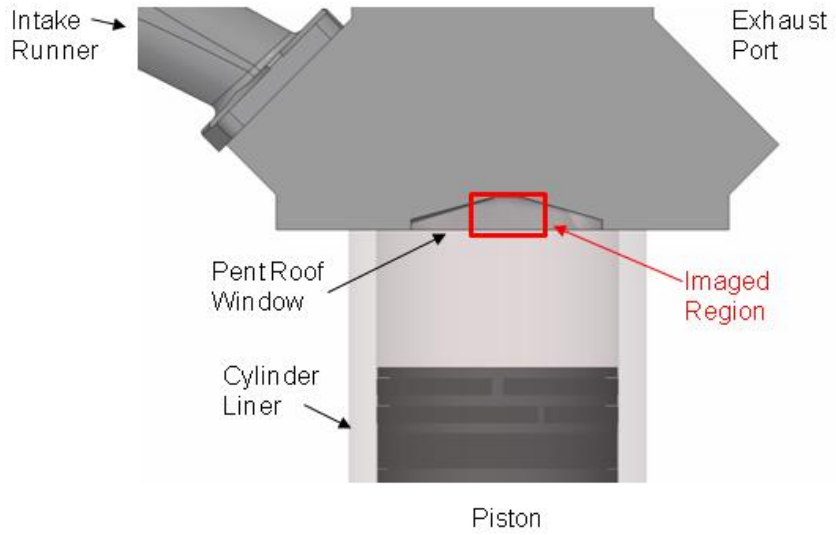

Figure 5.9 - Schematic to show the imaged area for imaging flame growth through the pent roof window

The images were obtained on a line of sight basis and therefore only the projection of the flame in this plane is captured. Refer to the previous Section (5.2.1) for flame images captured in the orthogonal plane through the piston crown window of the optical engine.

5.2.2.2 Flame images

The chemiluminescence images were processed as described in Section 5.2.1.2. This post processing was performed to aid the visualisation of the chemiluminescence created by the combustion event. Images of the flame at 14° CA (1.56 ms) after ignition are presented in Figure 5.10 for twelve individual, arbitrarily selected cycles. At this point the very early kernel is visible following the ark of the spark plug discharge and variations in the convective flow effect on the flame kernel can be seen. Comparing cycle D with E, flow effects on the kernel are observed. In cycle D the kernel is seen to have been stretched, whereas, in cycle E the kernel does not display these characteristics and appears much smaller remaining between the spark electrodes.

Flame images at 22° CA (2.44 ms) after ignition for the twelve selected cycles are presented in Figure 5.11. As shown previously the initial flame growth is towards the exhaust valve side of the engine. This corresponds to the bulk flow motion which flows from left to right of these images (see Section 5.3). The differences between cycles D and E are also apparent in this figure. Cycle D exhibits a larger flame area than cycle E. As with the images through the piston crown window presented in Section 5.2.1 it is reasonable to relate this larger flame area to a faster flame speed, likely to be due to differences in the flow field. For example, if the early flame of cycle D experienced a larger amount of strain its flame speed is likely to have been increased. Cyclic variations between the flames presented are very apparent with visible differences in flame shape and size.

The flame images presented in Figure 5.12 are for the same twelve engine cycles at 26° CA (2.89 ms) after ignition. The flames at this point have grown beyond the imaged area towards the exhaust valves, but by comparing to Figure 5.11 are also seen to have grown back (against the bulk flow) towards the intake valves. Comparing the development of the cycles in Figure 5.10 and Figure 5.11, their initial characteristics are apparent. The cycles which displayed small flame area in comparison to the others still remain small. Flame images at 30° CA (3.33 ms) after ignition are shown in Figure 5.13. The 'slow burning' cycles at this stage, show a flame with significantly smaller area and therefore presumed volume of burnt mass than those which initially appeared larger. Further progression of the flame towards the intake valves is also shown.

These flame images provide an indication of the way the combustion event may be influenced by flow field variations. It is clear that even in the initial stages of the flame, cyclic variations are exhibited. The development of the flame over the course of the combustion event, up to 34° CA (3.77 ms) after ignition, for four of the previously presented cycles are shown in Figure 5.14. This figure displays the flame edge plotted at 2° CA (0.22 ms) intervals throughout the initial part of the combustion event. The flame edge was established using the edge detection function within the Matlab™ image processing toolbox as previously discussed in Section 5.2.1.2. The resulting edges are

plotted with incrementing colour though the rainbow from blue to red to signify the progression in engine rotation.

The flame edges shown in Figure 5.14 show how the flame structure develops. Features visible within the flame edge (such as concave or convex sections) are seen to influence the next step within the flame development. As seen in Figure 5.10 to Figure 5.13 the flame image of cycle A shows a rapid development of the combustion event, covering a larger area when compared to the other selected cycles. Cycles E, F and I are relatively slow burning in comparison.

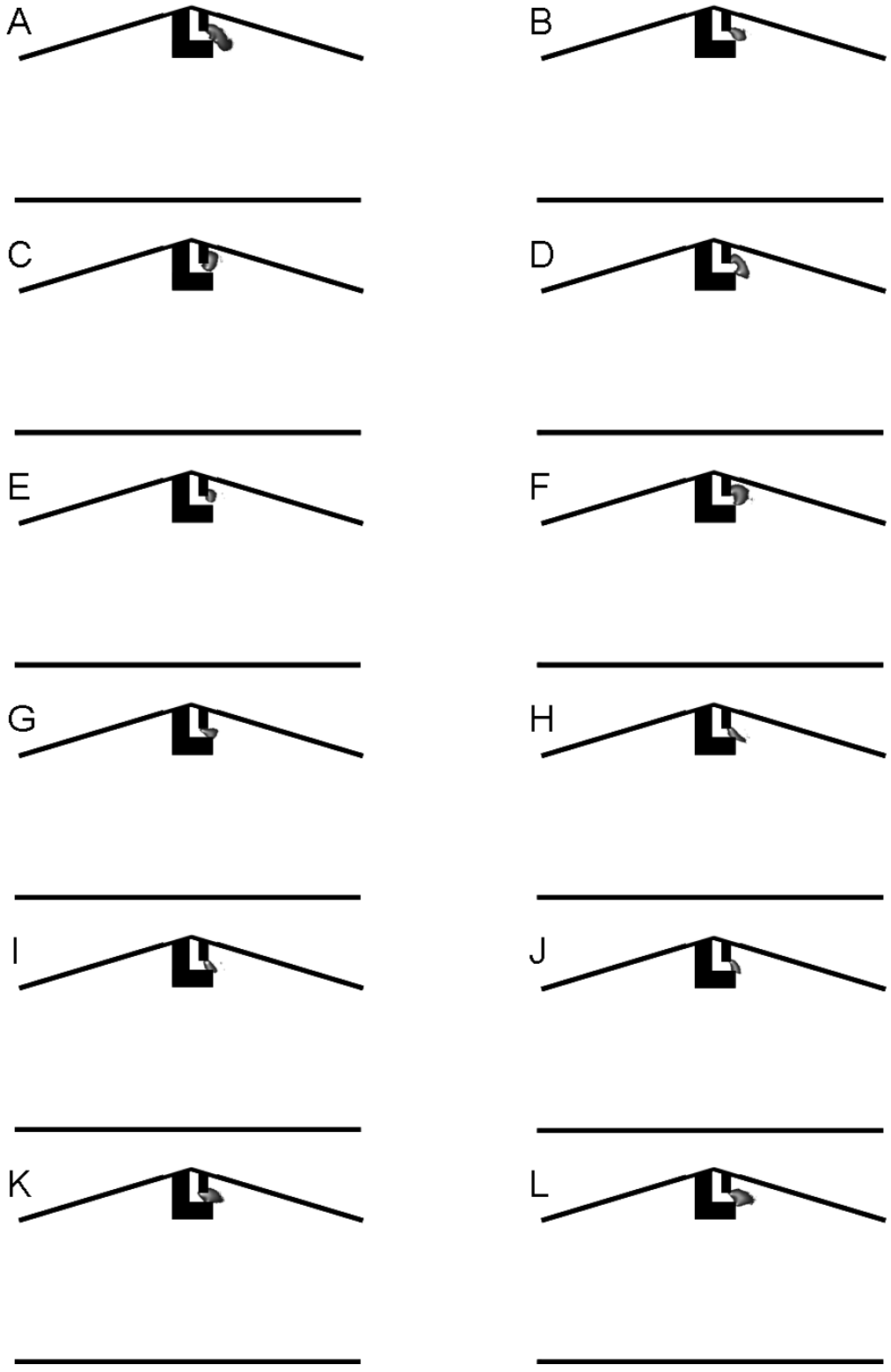

Figure 5.10 - Chemiluminescence images of the early kernel and Spark 14° CA (1.56 ms) after ignition for the engine operating at 1500 rpm at λ≃1

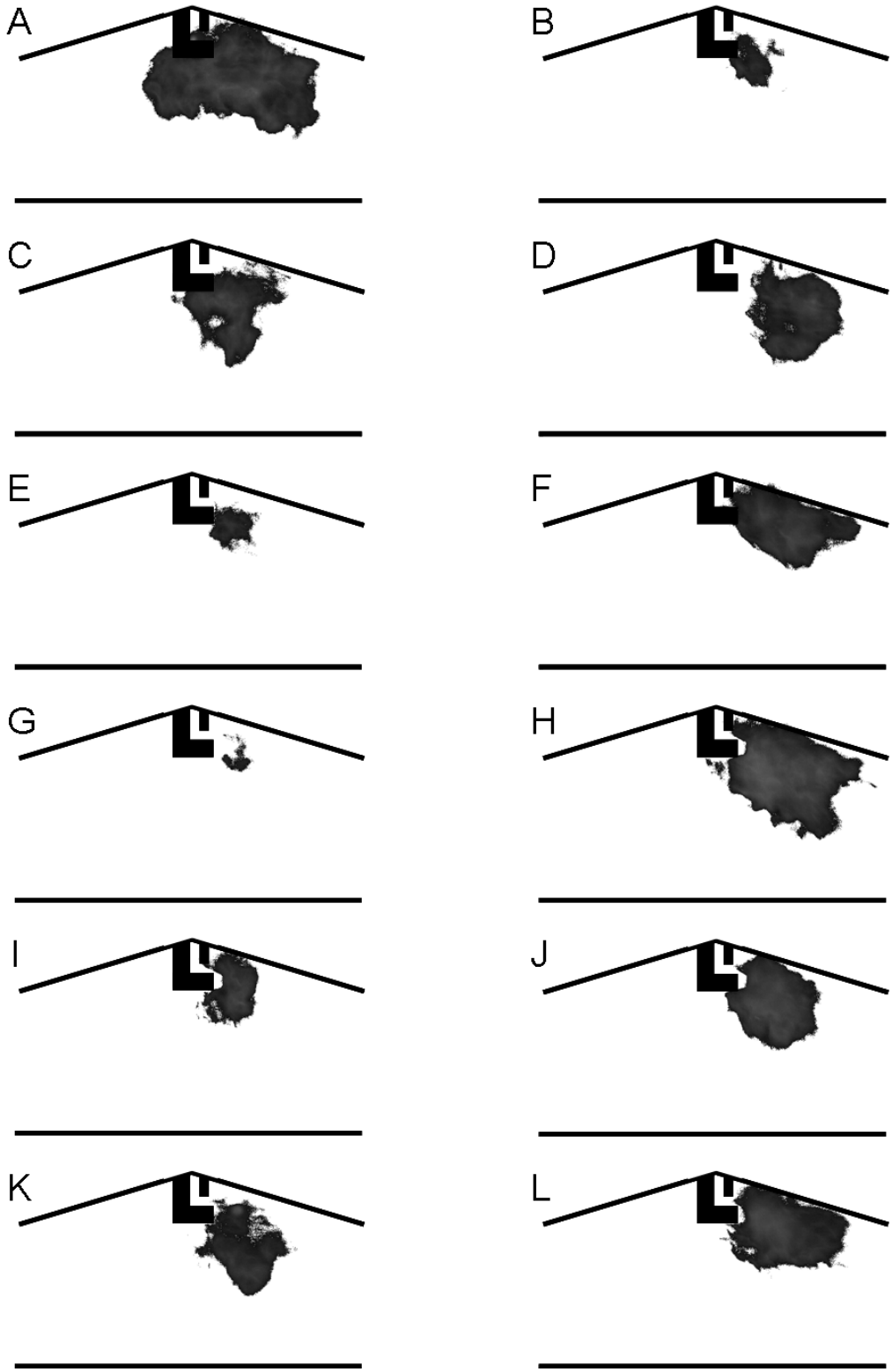

Figure 5.11 - Chemiluminescence images of the combustion flame 22° CA (2.44 ms) after ignition for the engine operating at 1500 rpm at λ≃1

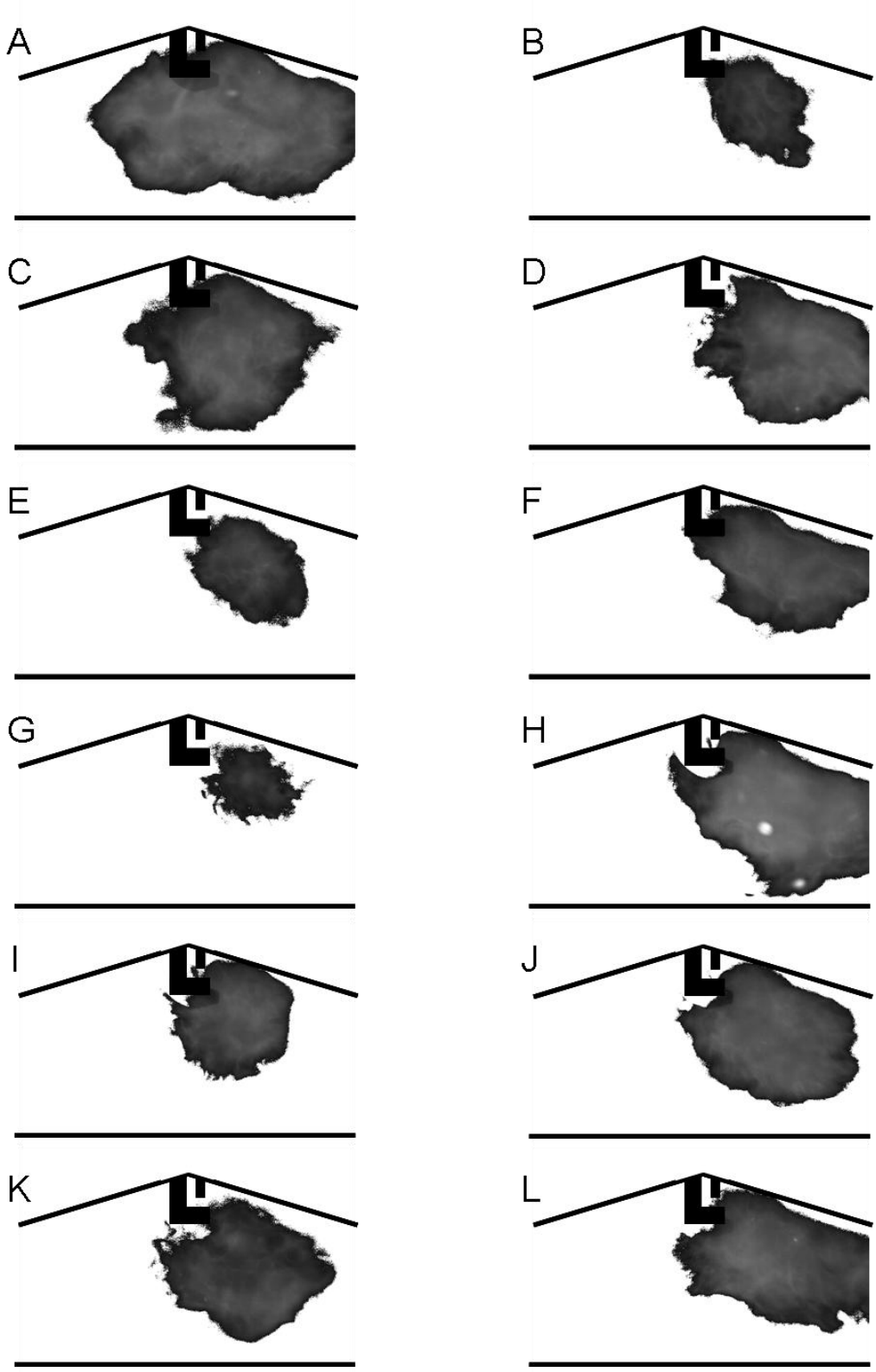

Figure 5.12 - Chemiluminescence images of the combustion flame 26° CA (2.89 ms) after ignition for the engine operating at 1500 rpm at λ≃1

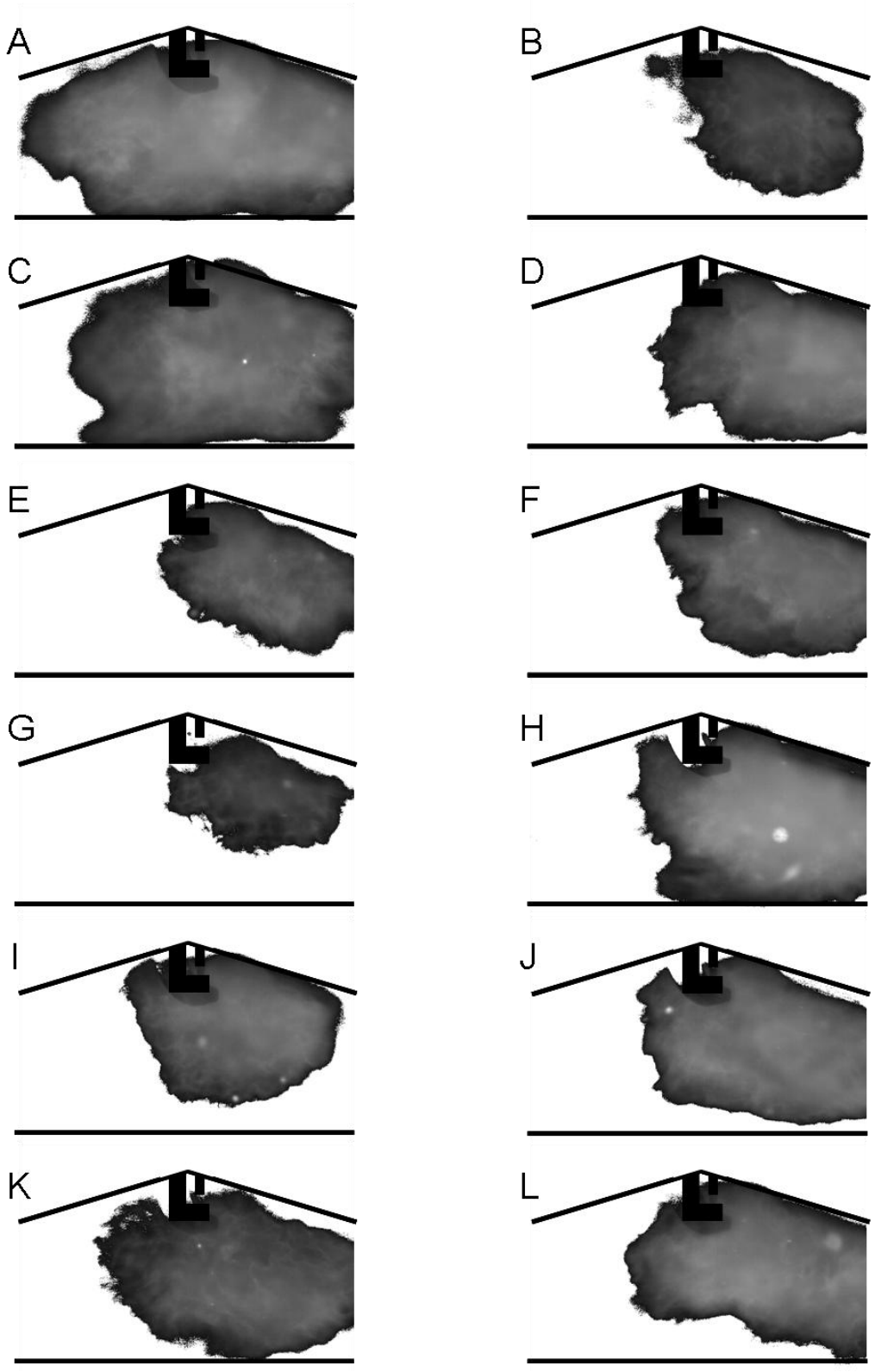

Figure 5.13 – Chemiluminescence images of the combustion flame 30° CA (3.33 ms) after ignition for the engine operating at 1500 rpm at λ≃1

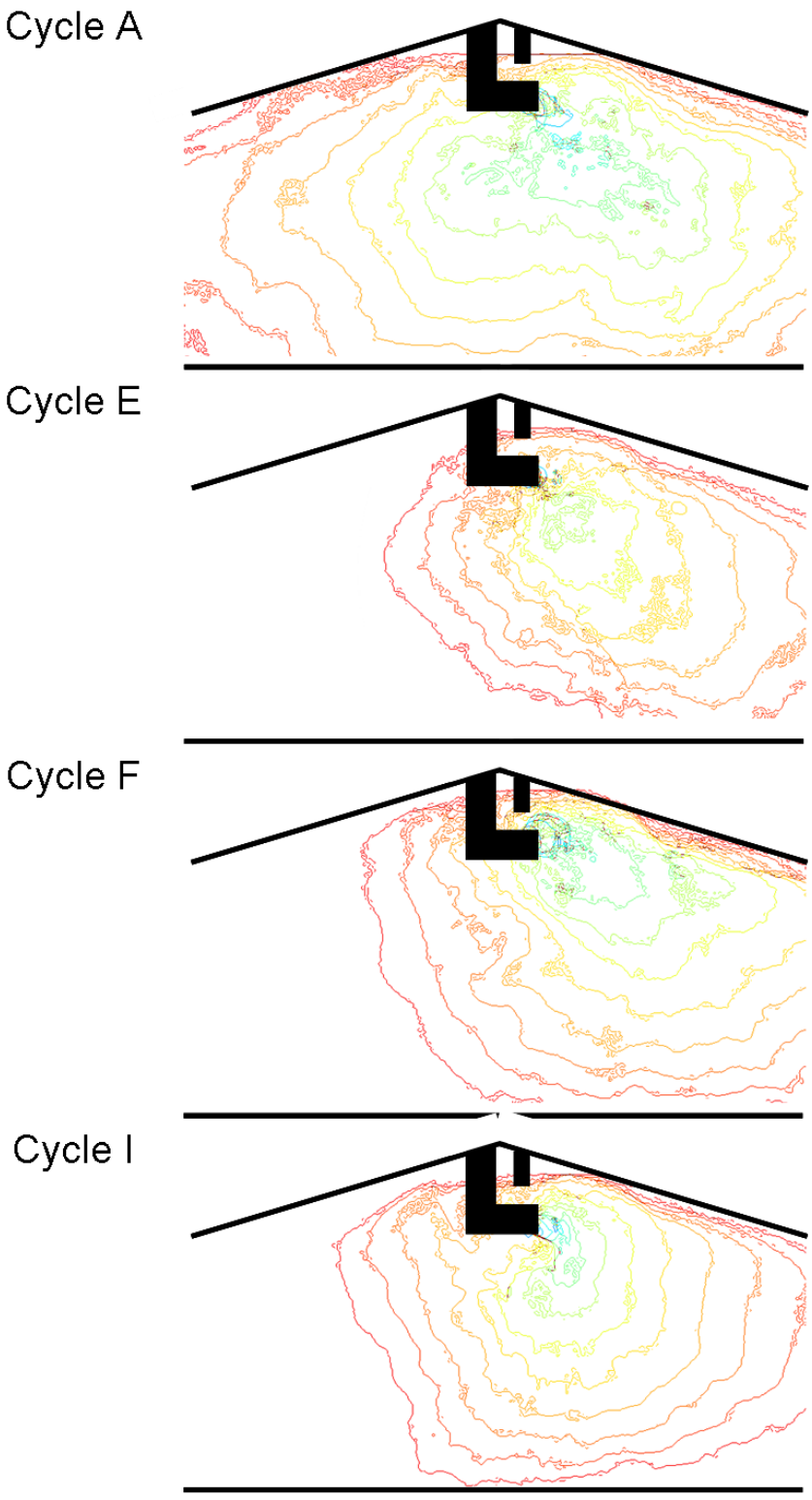

Figure 5.14 - Flame edge identified to show growth for the period to 34° CA (3.77 ms) after ignition for four cycles displayed in Figure 5.10 to Figure 5.13

5.3 Pent roof flow

The focus of the data presented in this Section investigates the characteristics of the flow field within the pent roof of the combustion chamber, during the compression stroke, as the cycle approaches the point of ignition. The flow field during the combustion event is known to influence the flame growth (Chapter 2). Thus, investigating flow field cyclic variation at this stage of the engine cycle is of great importance.

5.3.1 Measurement conditions

Those data presented within this Section were obtained on the cylinder bore centreline and in the tumble plane. The measurement area was located within the pent roof of the combustion chamber. The imaged area and measurement plane are presented in the schematics of Figure 5.15 and Figure 5.16. The engine was motored at 1500 rpm with a plenum pressure of 525 mbar.

The configuration of the HSDPIV system to capture these measurements is shown in Figure 5.17. The output from the Nd:YLF laser was formed into a thin vertical sheet and introduced into the combustion chamber via the 45° mirror under the piston and the flat topped optical piston crown. To achieve the correct laser sheet height and width in the image region, a -50 mm cylindrical lens was used in conjunction with a 1000 mm spherical lens to allow the laser to be positioned in a suitable location.

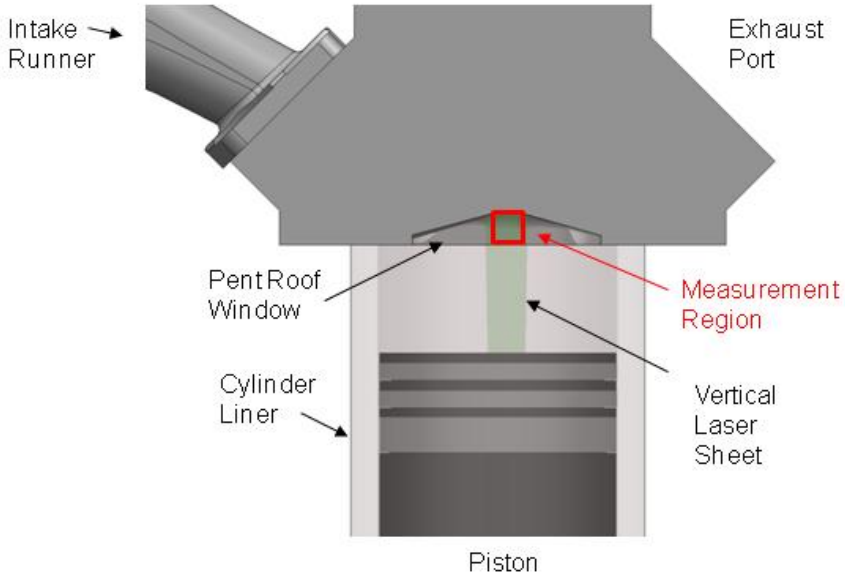

Figure 5.15 - Schematic to show the measurement location used to investigate flow around the spark plug as the cycle aproaches the point of ignition

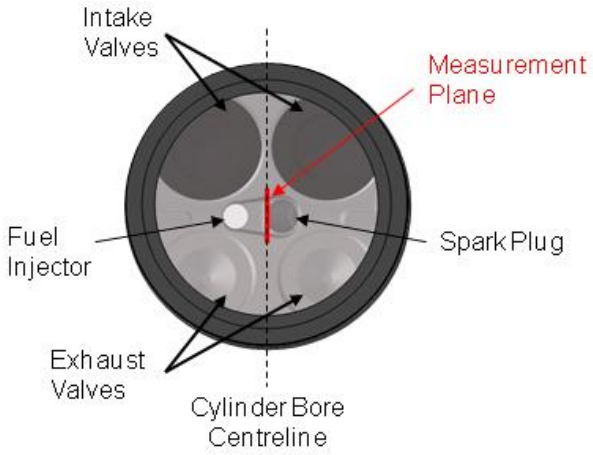

Figure 5.16 – Schematic to show the measurement plane created by the laser sheet for studying the flow around the spark plug as the cycle approaches the point of ignition (as viewed via the 45° mirror under the piston)

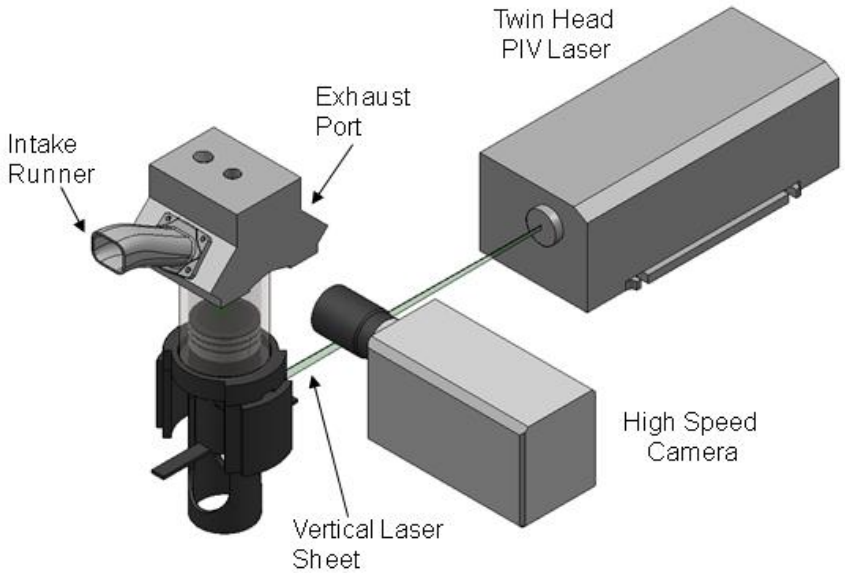

Figure 5.17 - Schematic to show the configuration of the HSDPIV system to achieve measurements to investigate flow around the spark plug as the cycle aproaches the point of ignition

At this measurement location both the larger scale bulk flow motion and the high spatial and temporal frequency smaller scale turbulent motions are of joint interest. The size of the camera's active pixel array was reduced to 512 by 512 pixels to allow the camera to operate at a frame rate of 10 kHz and therefore capture image pairs suitable for two frame cross correlation analysis at 5 kHz. The 1500 rpm motoring speed resulted in a temporal resolution of these measurements being 1.8° CA (0.2 ms) between captured flow fields. The 5 KHz velocity field sampling frequency allows analysis of turbulent frequencies up to 2.5 kHz according to the Nyquist criteria (Kang and Baek (1998)). In reality the critical frequency, if analysing the absolute structure of the turbulent motions and therefore wishing to avoid aliases, is less than 2.5 kHz.

A 105 mm AF Micro Nikkor lens was used to image a region 12 mm by 12 mm onto the active array of 512 by 512 pixels. Analysis of the captured PIV image pairs was performed with the TSI Insight 3G software. Velocity vectors were evaluated from the image pairs on a Nyquist grid with 32 by 32 pixel interrogation regions, equating to an area approximately 0.75 mm by 0.75 mm within the flow. The interrogation regions were positioned to overlap neighbouring regions by 50% leading to a vector spacing in the resulting velocity vector field of 0.375 mm. Obviously, both the spatial and

temporal resolution in the flow is not small enough to describe the finer turbulent structures, however, it is small enough to describe fluctuations below the integral length scale and therefore those which are involved in turbulent energy dissipation.

The intake air was seeded with 1 to 2 μm oil droplets. To control the imaged diffraction limited spot size the laser was operated at full power and the largest $f^{\#}$ to give adequate contrast in the particle images. Ideally the $f^{\#}$ for the measurements presented within this Section would be 16 to give a calculated diffraction limited spot size greater than 2 pixels in diameter. The system, limited by laser power and camera sensitivity, required that the $f^{\#} = 8$. This gives a calculated diffraction limited spot size of 1.1 pixels (therefore more susceptible to sub pixel displacement errors, see Section 3.2). However, the calculated spot size is for an ideal system. Aberrations and quality of focus will act to enlarge the imaged particle size. Therefore, by taking the image slightly out of focus the actual measured imaged particle size on the camera array could be controlled to be greater than 2 pixels.

The time separation (Δt) between the two laser pulses which control the exposure of the image pair was set to 20 μs. This Δt allows a flow velocity up to *circa* 18.5 $m.s^{-1}$ before the particles move more than 16 pixels (half of the interrogation region) between the two images of a pair. For the flow field under investigation this Δt was chosen as it gave an adequate velocity measurement limit whilst minimising out of plane flow motion and allowing enough movement of the particles in the slower velocity regions to control errors in sub pixel displacements. A one pixel displacement corresponds to a velocity measurement of 1.2 $m.s^{-1}$

The HSDPIV system was triggered at 300° CA ATDC gas exchange. From this external trigger the PIV system was programmed to capture 34 images at 5kHz, therefore, at 1.8° CA increments until 359.4° CA ATDC gas exchange was reached. The captured flow fields provide spatial and temporal flow information both before the time of ignition (325° CA ATDC gas exchange, 35° CA BTDC) and after, where the flame kernel is known to be sensitive to flow field variations. The 2 Gb on-board memory

available on the camera coupled with the Insight 3G control software (which saved a full 1024 by 1024 pixel frame regardless of capture rate) allowed *circa* 2100 images to be recorded. This meant that up to 30 cycles of image pairs could be recorded during one capture sequence. Following this, the images had to be downloaded from the camera to the PIV control computer. The required time for the download of the images gave a requirement to stop the engine and therefore, allowed the windows providing optical access to be cleaned, removing any seed build up which had gathered during the course of the engine operation. Performing four capture sequences gave over 100 cycles of flow field data which was considered sufficient to calculate a statistically significant mean flow.

5.3.2 Measured velocity fields

Raw velocity fields over the range 312.6° to 319.8° CA ATDC are presented for three individual cycles in Figure 5.18. These data were captured at the conditions described in Section 5.3.1. The background colour denotes velocity magnitude, and the vectors represent flow direction. Each presented cycle shows distinctly different bulk flow field behaviour in the measurement plane. Cycle A displays bulk flow velocity indicating a dominant left to right motion, cycle B also shows a bulk left to right flow however, in comparison to cycle A, a significant upward motion is also apparent. The flow presented for cycle C does not show any definite left to right bulk motion, but does show downward flow from top to bottom of the images. These HSDPIV data presented within the flow fields display both spatial and temporal development of the flow in the two-dimensional plane. Note that area of blue (low velocity) at the top of the images is due to flare from the laser light reflecting from the surface of the engine head causing high signal to noise ratio and therefore leading to erroneous velocity measurement. This scatter is difficult to avoid when measuring in this region of the combustion chamber.

The progression of these cycles are shown in Figure 5.19 where the raw flow fields for 334.2° to 341.4° CA ATDC are presented. By comparing Figure 5.18 to Figure 5.19 the development of the flow fields over this time period can be seen. Cycle A displays a

region of increased velocity, possibly influenced by an out of plane flow structure, which traverses from the left to the right during the time sequence presented. The bulk flow motion does, however, remain similar with the general trend of the flow moving from the left to the right of the image. Conversely cycle B exhibits a decrease in bulk flow velocity. Figure 5.18 showed this cycle to display regions with velocity magnitude of around 10 $m.s^{-1}$. These regions were seen to move with the bulk flow, therefore, progressing up the image. Figure 5.19 exhibits smaller regions of high velocity for this cycle, especially in the final images of the sequence (339.6° and 341.4° CA ATDC gas exchange). The flow fields presented for cycle C show significant changes in the bulk flow motion between the two sequences presented. The velocity magnitude of the flow is seen to reduce over the presented CA range. At 314.4° CA, presented in Figure 5.18, regions with velocity magnitude of around 10 $m.s^{-1}$ are apparent with a significant bulk motion from the top of the image towards the bottom left. The flow fields presented for cycle C in Figure 5.19 display a lower bulk velocity, *circa* 6 $m.s^{-1}$ at 336.0° CA ATDC gas exchange, with a clockwise bulk flow rotation entering the imaged region from the left hand side.

Comparing the three cycles presented in Figure 5.18 and Figure 5.19 it is clear that the flow field into which the combustion event is initiated varies both spatially and temporally from cycle to cycle. These raw flow fields exhibit large scale bulk flow motions and smaller scale fluctuations about this. As discussed in Chapter 2, it is common to discuss flow fields in terms of mean motion and fluctuations about that mean (see Equation 2.5). However, this method assumes that the ensemble mean motion for one crank angle position, over a statistically significant number of cycles, is representative of the large scale bulk flow motion present. The difference between the actual and the mean flow is described as the fluctuating element of the flow and is assumed to be representative of the level of turbulence.

This concept however does not account for variation in bulk flow from one cycle to the next. From the flow fields presented in both Figure 5.18 and Figure 5.19, it has been shown that significant cyclic variations in the bulk flow motion occur. To create a better understanding of the flow field cyclic variations it is important to consider both the

large scale bulk motion variations and the smaller scale flow motions which act as fluctuations to this. Therefore, it is more appropriate decompose the raw flow field into low frequency bulk flow and high frequency turbulent motions (as described by Equation 2.20). In reality there is no divide between those flow elements discussed here as low frequency bulk motion and high frequency fluctuations, therefore, this decomposition is not well defined.

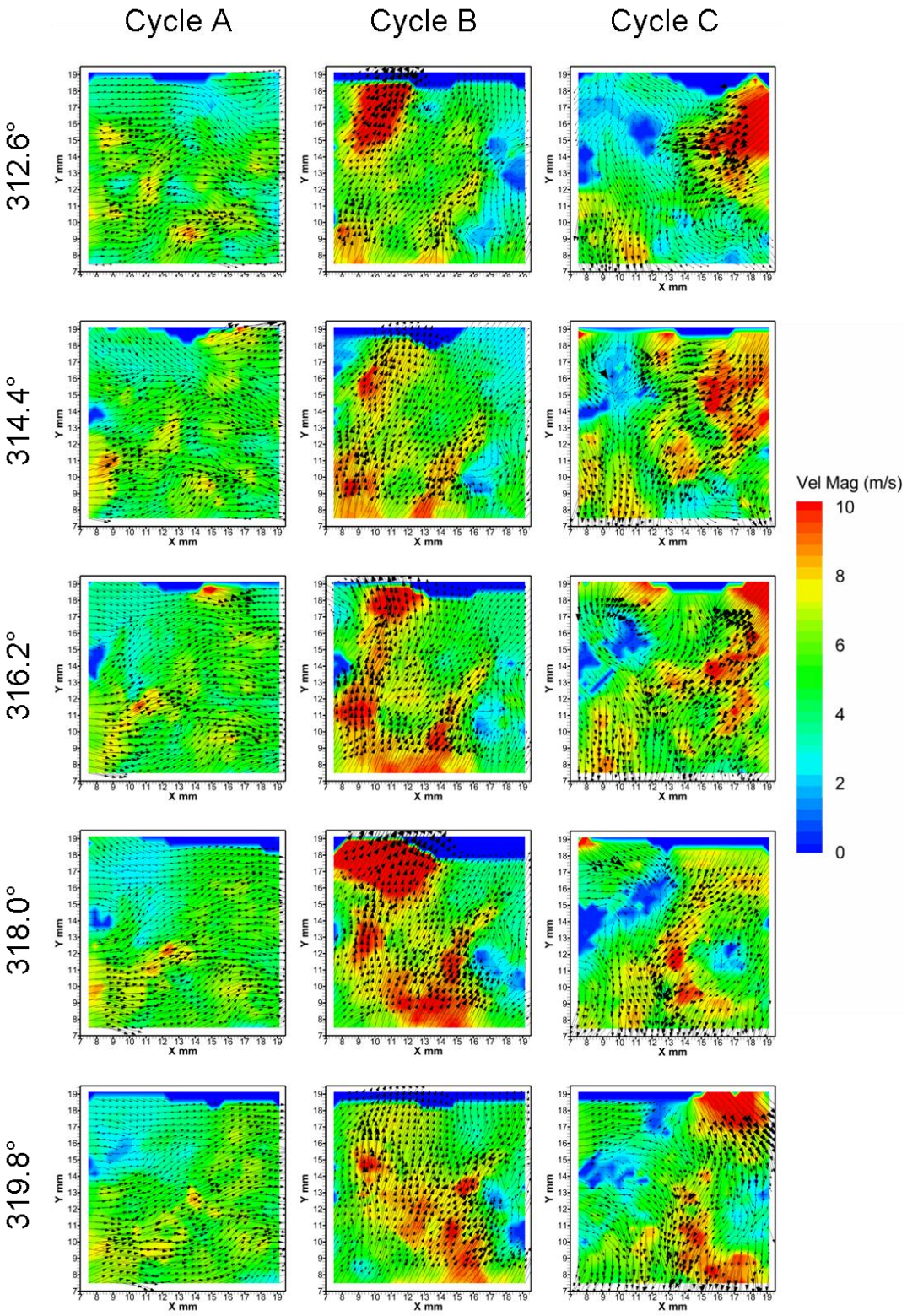

Figure 5.18 – Raw flow fields within the pent roof on the tumble plane for three individual cycles from 312.6° to 319.8° CA ATDC captured with HSDPIV at a rate of 5 kHz

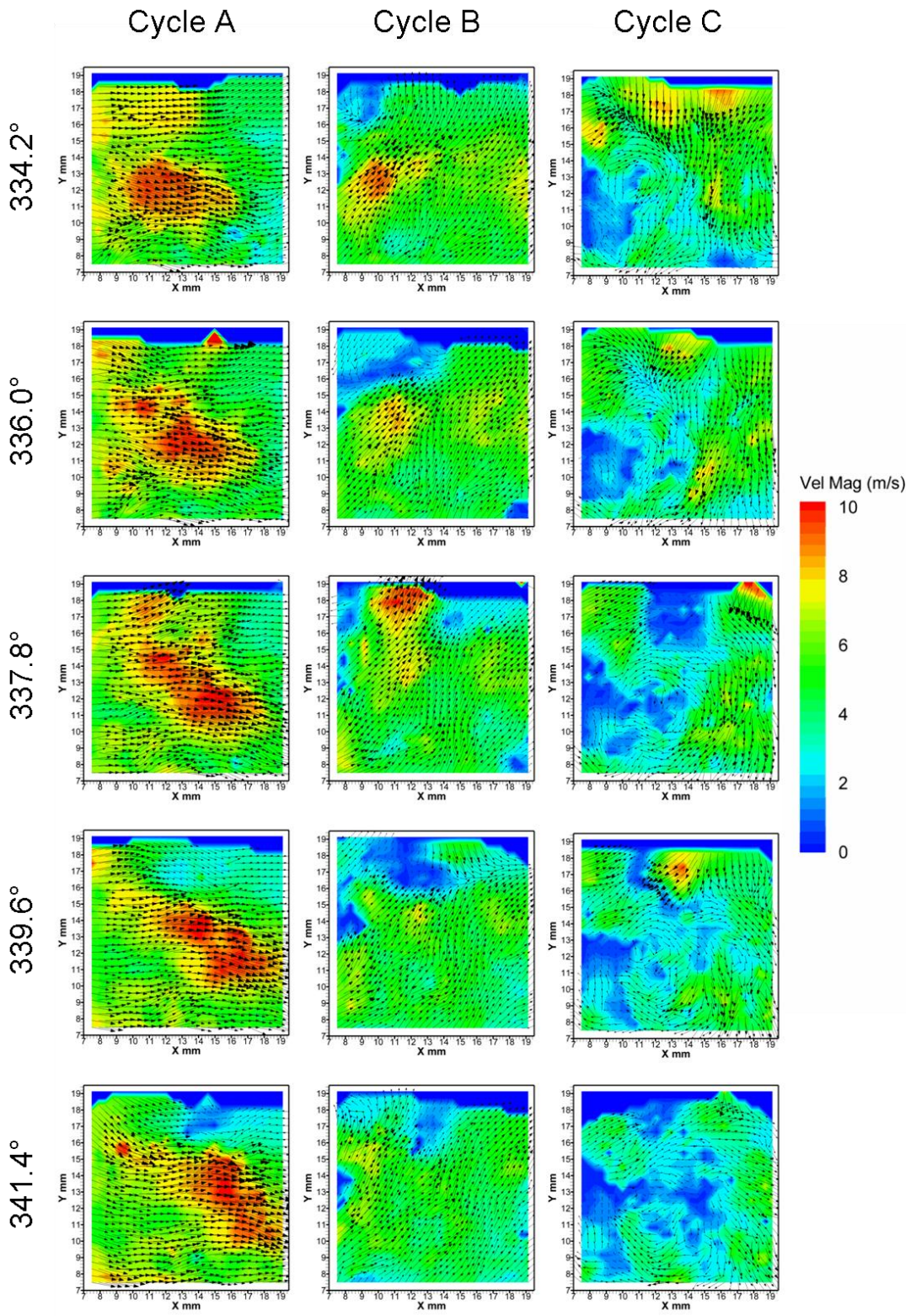

Figure 5.19 - Raw flow fields within the pent roof on the tumble plane for three individual cycles from 334.2° to 341.4° CA ATDC captured with HSDPIV at a rate of 5 kHz

The HSDPIV captures both spatial and temporal flow field measurements. This allows either the spatial or temporal domain to be selected for the decomposition of the flow into its high and low frequency components. By performing the frequency filtering in the temporal domain a 1-dimensional fast Fourier transform (FFT) was applied to both velocity components in turn, at each vector location within the flow field, across all available time steps within a cycle. Once in the frequency domain, a low pass cut-off filter was applied to remove the high frequency changes. Following this filtering of the signal, the inverse FFT was applied to return only the remaining low frequency velocity to the temporal domain. The difference between the measured 'raw' velocity data and the low frequency velocities are therefore, for the purpose of this thesis, considered to be the high frequency flow components.

The processing was performed within Matlab™ using the inbuilt signal processing toolbox. This toolbox provided the required functions to perform both the FFT, and its inverse. For the work presented, a cut-off frequency of 280 Hz was selected. This was based on the size of recirculation structures expected to occur within the low frequency 'bulk' flow motion. The validity of these expectations was confirmed by other works on IC engine bulk motion structures (Fraser and Bracco (1989); St. Hill *et al.* (2000); Li *et al.* (2001)).

Decomposing the raw flow field, as discussed in Equation 2.20, into low frequency and high frequency components allows both the bulk motion and superimposed turbulent motions to be investigated. This decomposition is shown for three cycles (A, B and C) in Figure 5.20 at a single vector location within the imaged area. Both the U and V velocity components are plotted for the raw measured (red) and calculated low frequency (blue) values over the range 310° to 350° CA ATDC gas exchange. Comparing the three selected cycles, cyclic variations in the low frequency bulk flow motion are highlighted. The cyan curve presented on each plot represents the mean of the low frequency curves calculated over a sample set of 100 cycles. This shows how the individual cycle's characteristics differ from the mean cycle.

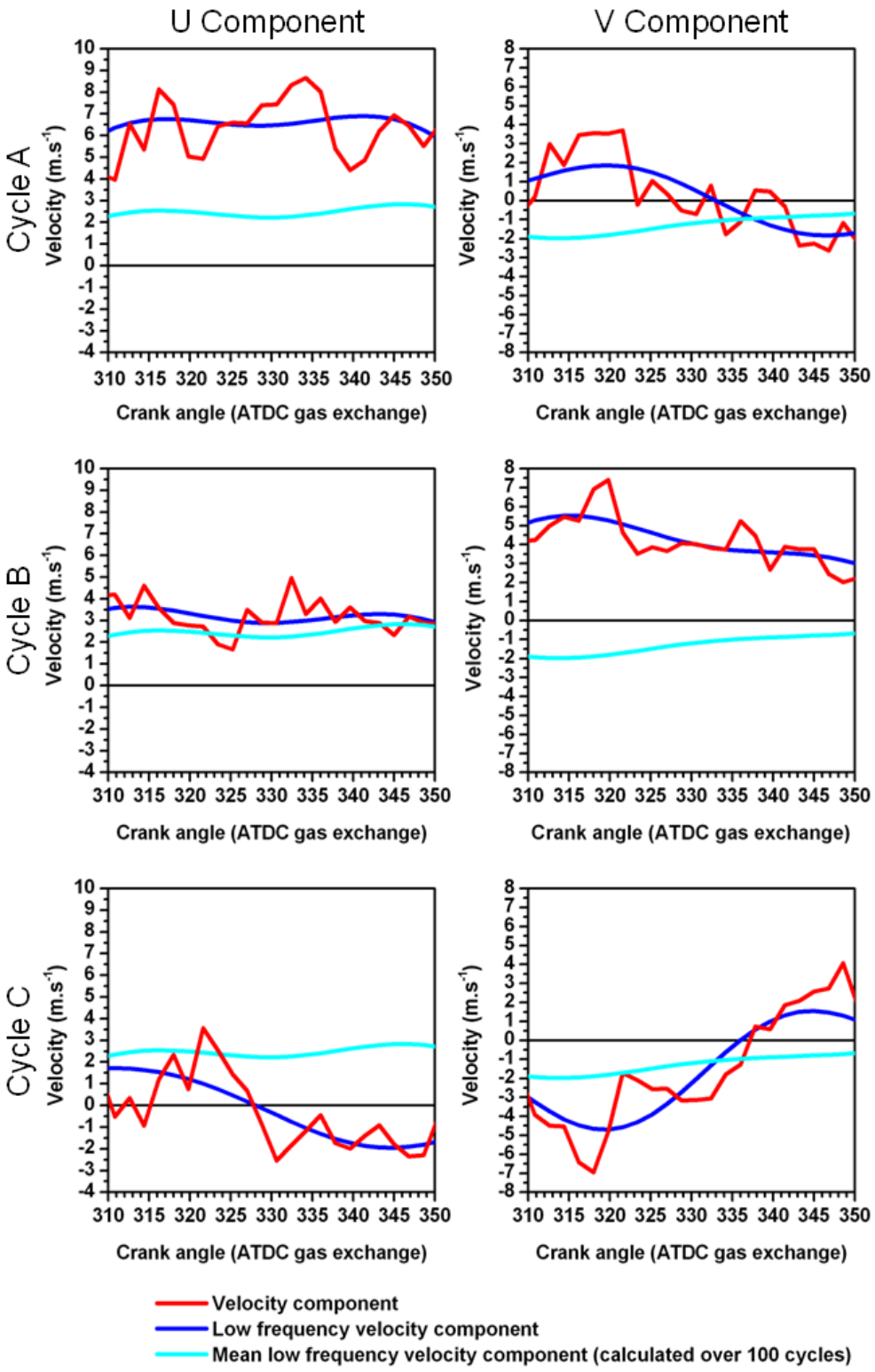

Figure 5.20 – An example raw velocity, low frequency and mean low frequency for both U and V velocity components at one location within a vector field

Low frequency flow fields for cycles A, B and C are presented in Figure 5.21 and Figure 5.22; these data are presented for the same crank angle ranges as previously presented in Figure 5.18 and Figure 5.19 respectively. Comparing the low frequency to the previously presented raw flow fields it is clear that the larger scale motions have been highlighted. The flows shown in these images, however, display a smoother flow spatially as well as temporally. Importantly, cycle C, which underwent the most obvious change in bulk flow between the two time sequences presented, displays the same trend in the low frequency flow fields. The images of cycle C in Figure 5.21, show indications of a rotating structure, seen in the same cycle in Figure 5.22, entering from the left of the image. The bulk flow within the other two cycles show a greater consistency with less obvious structural variation over the CA range presented. These features suggest that the cut-off frequency of 280 Hz, selected to decompose the flow fields into their high and low frequency components, is high enough to examine the significant bulk flows taking place.

The presented low frequency fields are the large scale flow features which act to convect and stretch the flame during its initial development. The variations seen in the cycles presented are likely to have differing affects on this flame development period. For example, it can be imagined that the early flame in cycle A would be convected towards the exhaust valves, whereas, in cycle B the flame would be more likely convected towards the cylinder head and, therefore, towards a quench zone. This highlights the importance of investigating variations in bulk flow motion.

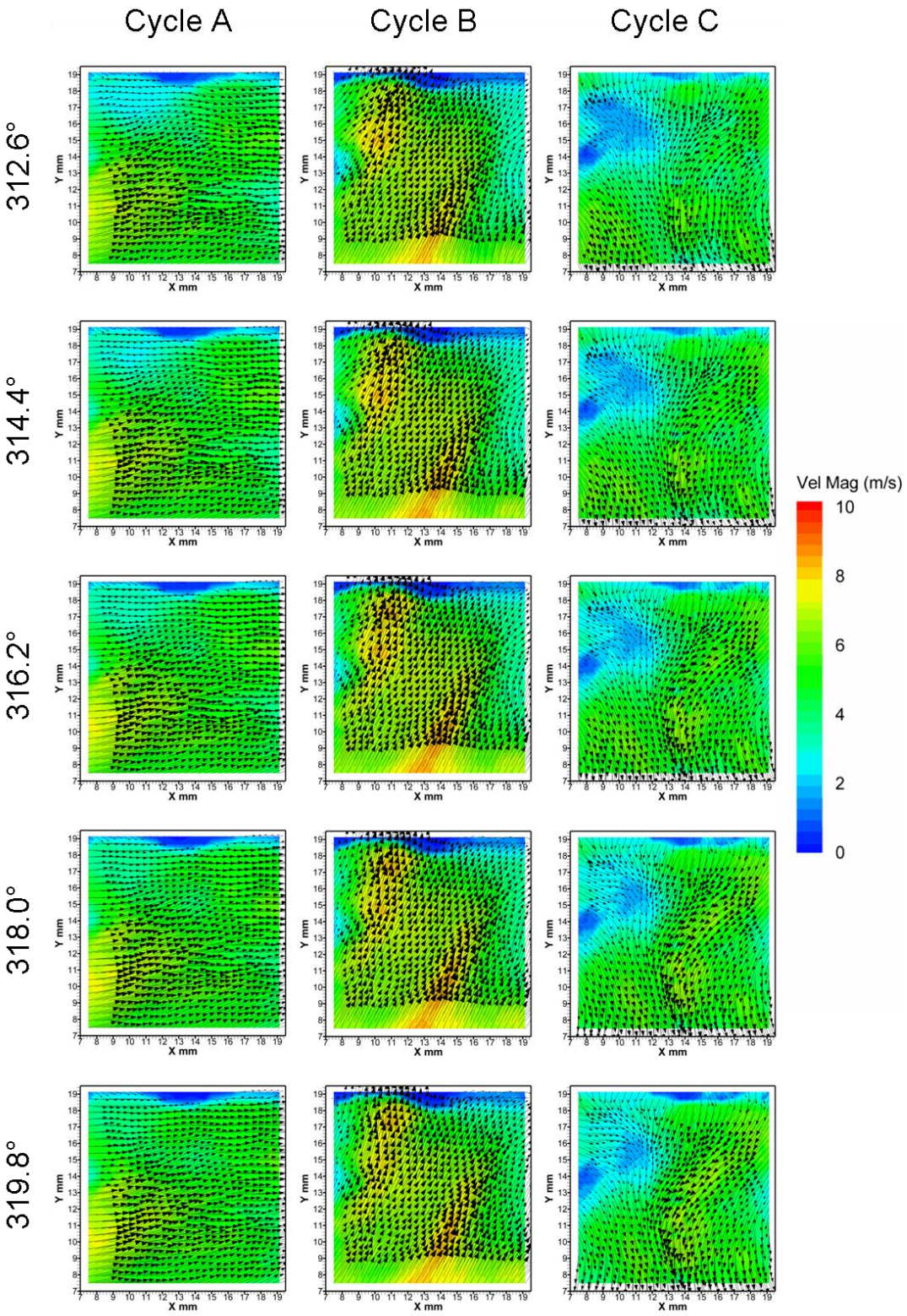

Figure 5.21 - Low frequency flow fields within the pent roof on the tumble plane for three individual cycles from 312.6° to 319.8° CA ATDC

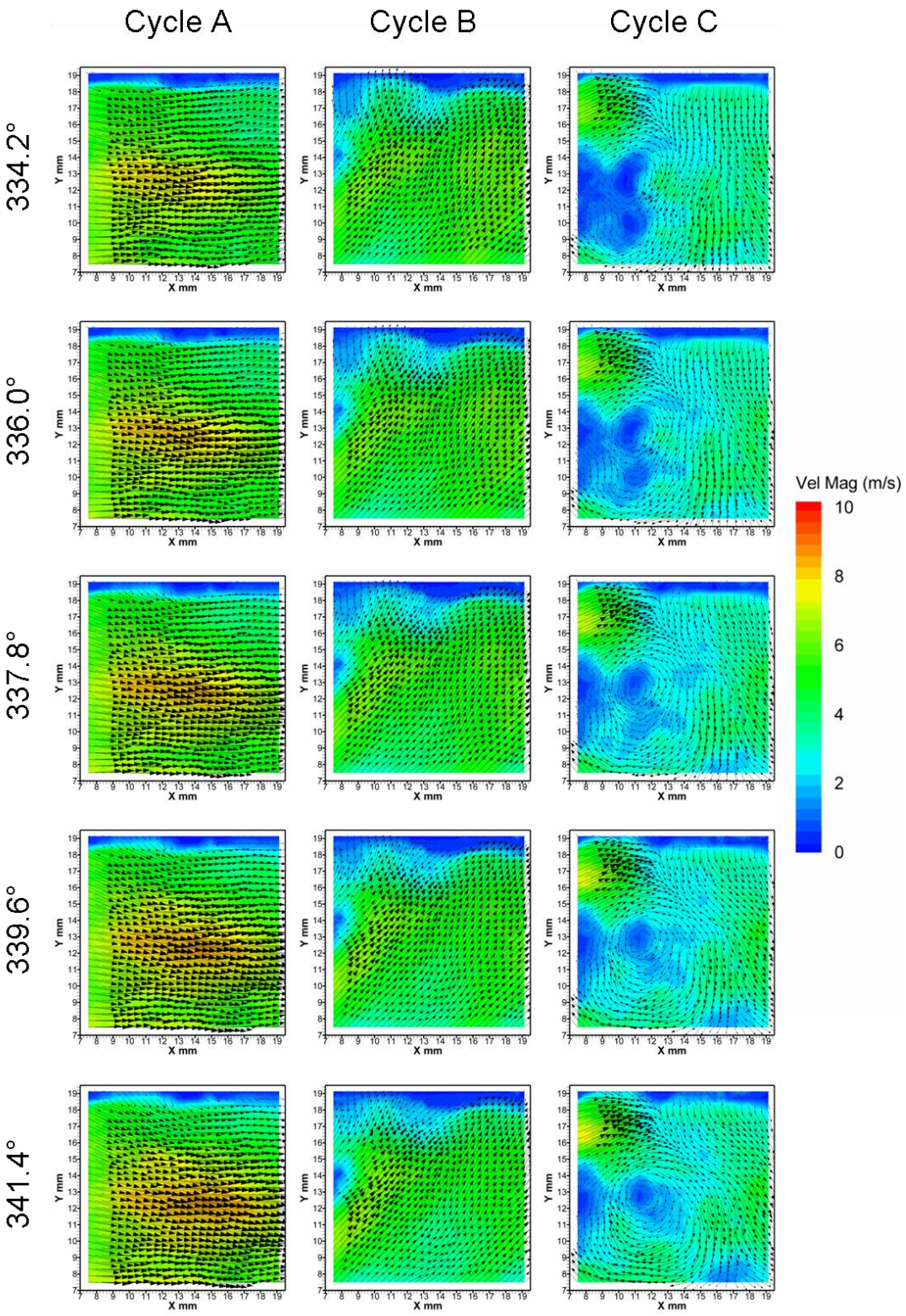

Figure 5.22 - Low Frequency flow fields within the pent roof on the tumble plane for three individual cycles from 334.2° to 341.4° CA ATDC

In Figure 5.23 a time sequence for the mean low frequency flow is presented. The sequence corresponds to the 5 kHz capture rate and hence every 1.8° CA revolution at a 1500 rpm motoring speed for the range 312.6° to 337.8° CA ATDC gas exchange. The presented mean low frequency flow fields have little in common with the bulk flow features of the flow fields previously presented. Cycle A showed the closest match from the three cycles whereas, cycles B and C were not represented by this mean motion. The difference between the mean low frequency and the individual cycle low frequency flow fields can be used to demonstrate where bulk flow cyclic variations exist.

The high frequency components of the presented raw flow fields are shown in Figure 5.24 and Figure 5.25 for the ranges 312.6° to 319.8° and 334.2° to 341.4° CA ATDC gas exchange respectively. These data present the high frequency fluctuations which are superimposed on the low frequency bulk motion and can therefore, be considered as the small scale turbulent fluctuations. These small scale motions are of the scale which will wrinkle and interact with the early flame front and have an effect on the flame growth.

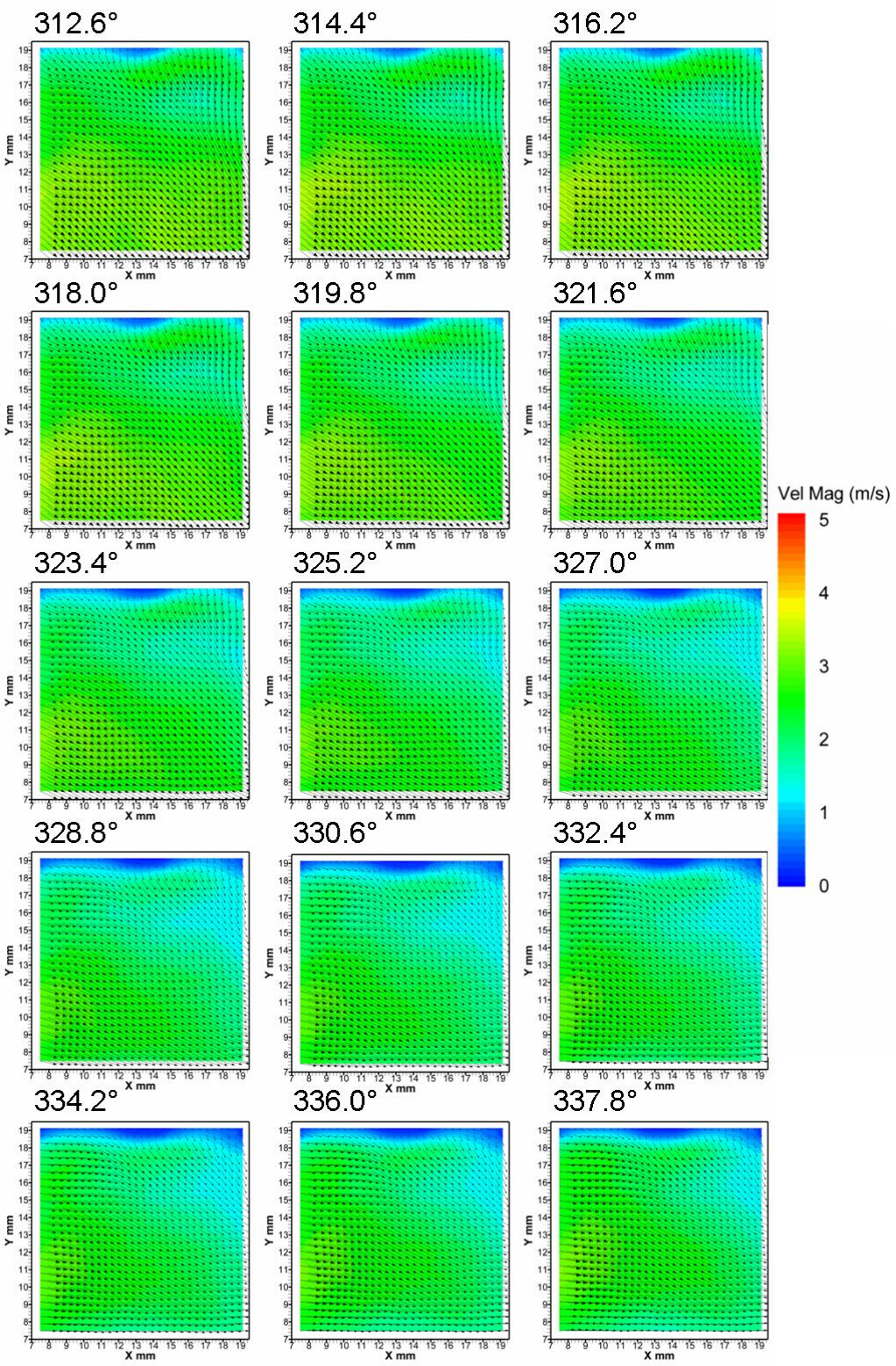

Figure 5.23 - Mean Low Frequency flow fields within the pent roof on the tumble plane for three individual cycles from 312.6° to 337.8° CA ATDC

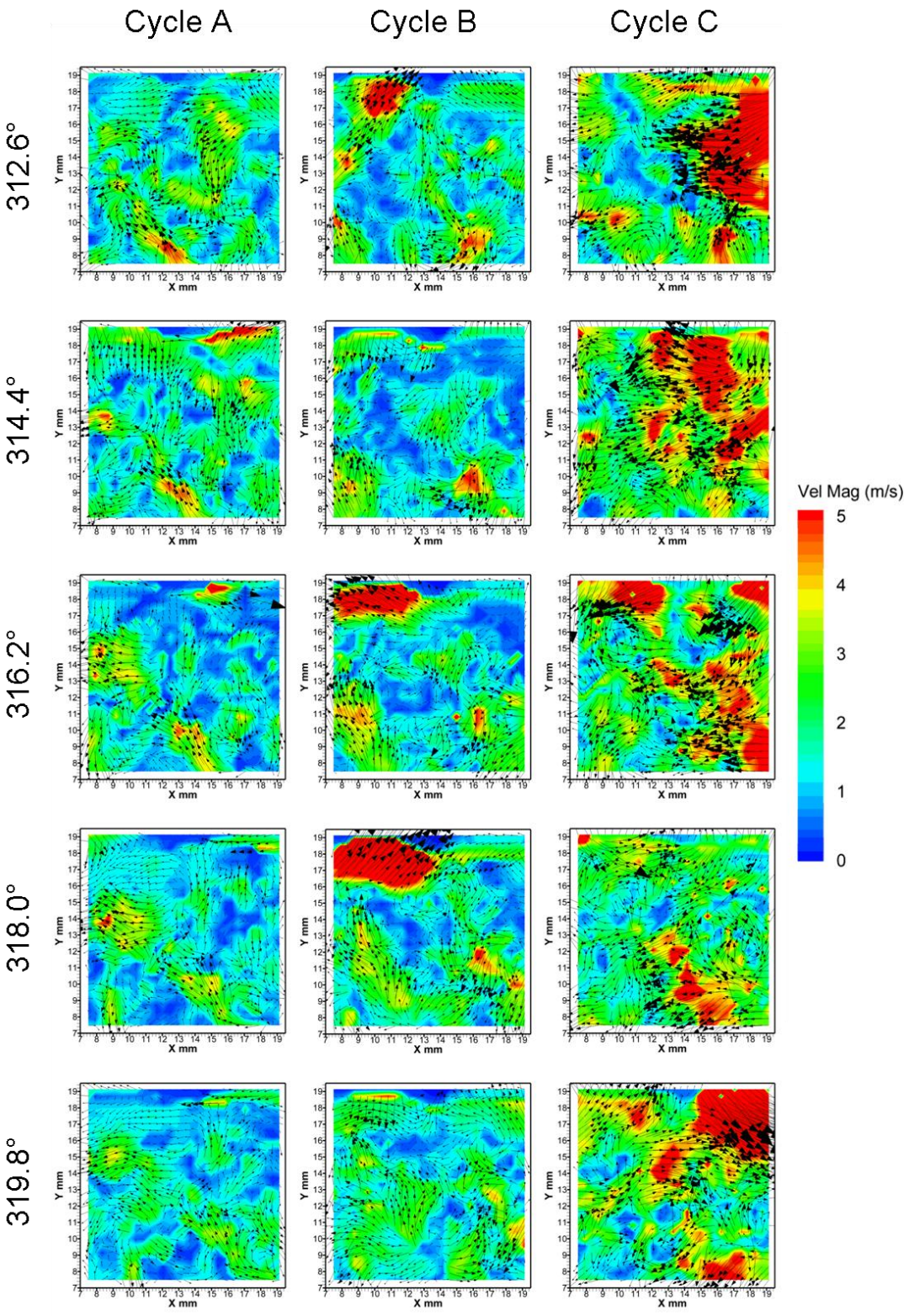

Figure 5.24 - High frequency flow fields within the pent roof on the tumble plane for three individual cycles from 312.6° to 319.8° CA ATDC

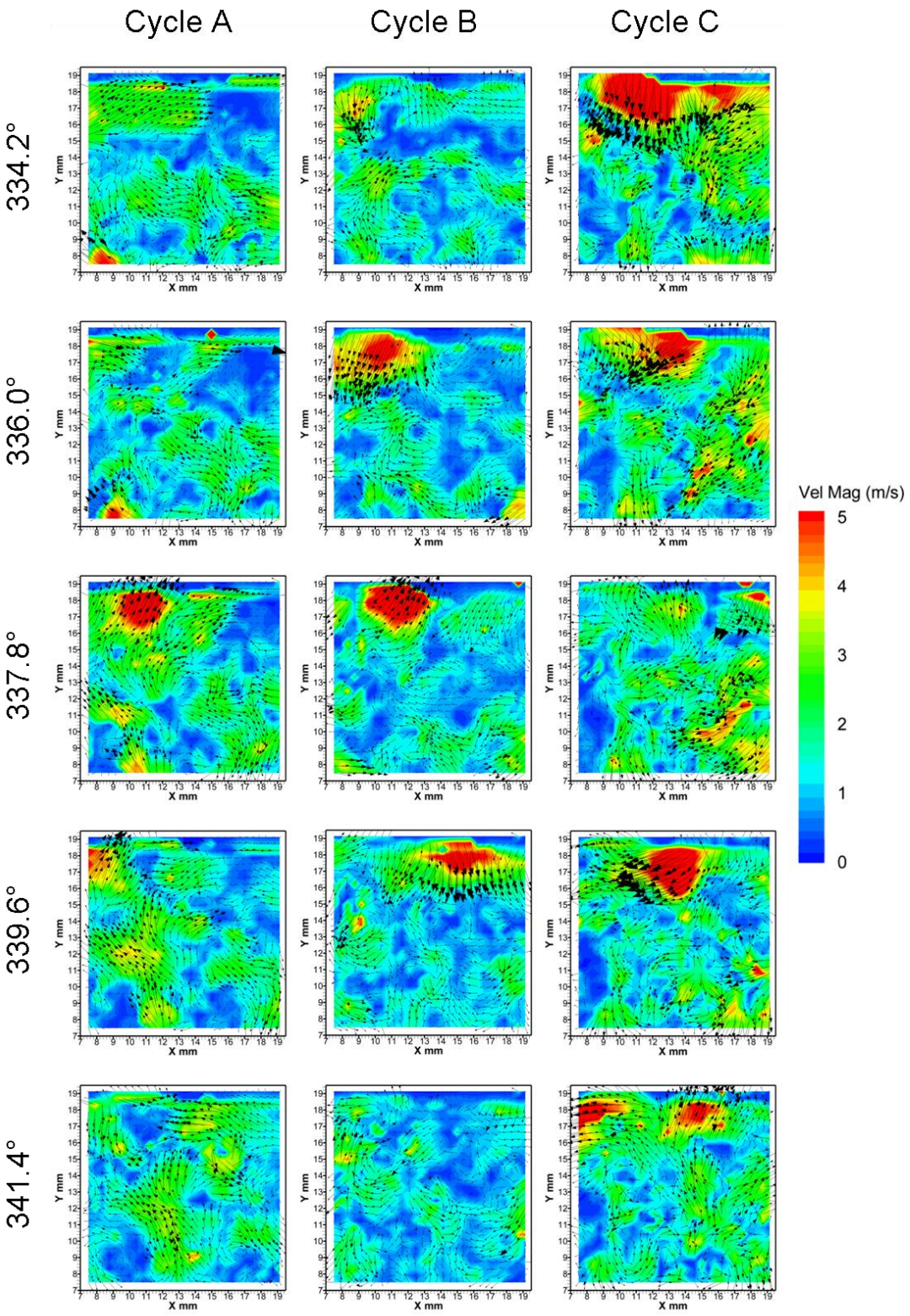

Figure 5.25 - High frequency flow fields within the pent roof on the tumble plane for three individual cycles from 334.2° to 341.4° CA ATDC

Classically, the turbulence intensity (u') has been described as the *rms* of the fluctuating components about the ensemble average (Equation 2.6). This is used to characterise the intensity of the flow variations around the ensemble average including variations in both low frequency bulk flow and high frequency turbulence. When considering the behaviour of a flame during one individual cycle, analysing the flow fluctuations about the ensemble average is inappropriate since the flame knows nothing of this average flow and hence, variations to it, but only local fluctuations from the bulk flow. Therefore, to investigate cyclic variations in high frequency turbulent fluctuations, a measure similar to u' is desired but has the need of being specific to a certain engine cycle. This can be performed by taking the *rms* of the high frequency components over a spatial (Equation 5.1) or temporal window (Equation 5.2). This gives an indication of the level of variation in the high frequency components over that spatial or temporal window giving a measure comparable to the local turbulence intensity (u').

$$u'_{HF\ (spatial)} = \sqrt{\frac{1}{m^2}\sum_{x=1}^{m}\sum_{y=1}^{m}\left(U_{HF(\theta,i,X,y)}{}^{2}\right)} \qquad \text{Equation 5.1}$$

$$u'_{HF\ (temporal)} = \sqrt{\frac{1}{n}\sum_{i=1}^{n}\left(U_{HF(\theta,i,X,y)}{}^{2}\right)} \qquad \text{Equation 5.2}$$

Using those high frequency data presented in Figure 5.24 and Figure 5.25 a temporal window corresponding to *circa* 720 Hz (7 image captures or 1.39 ms), the temporal u' was calculated. These data are presented in Figure 5.26 and Figure 5.27, for the three cycles and two time sequences previously discussed. In these figures the colour contour displays u' and the vectors display the raw velocity field. The three cycles show spatial differences in u', with cycles B and C displaying decay between the two figures.

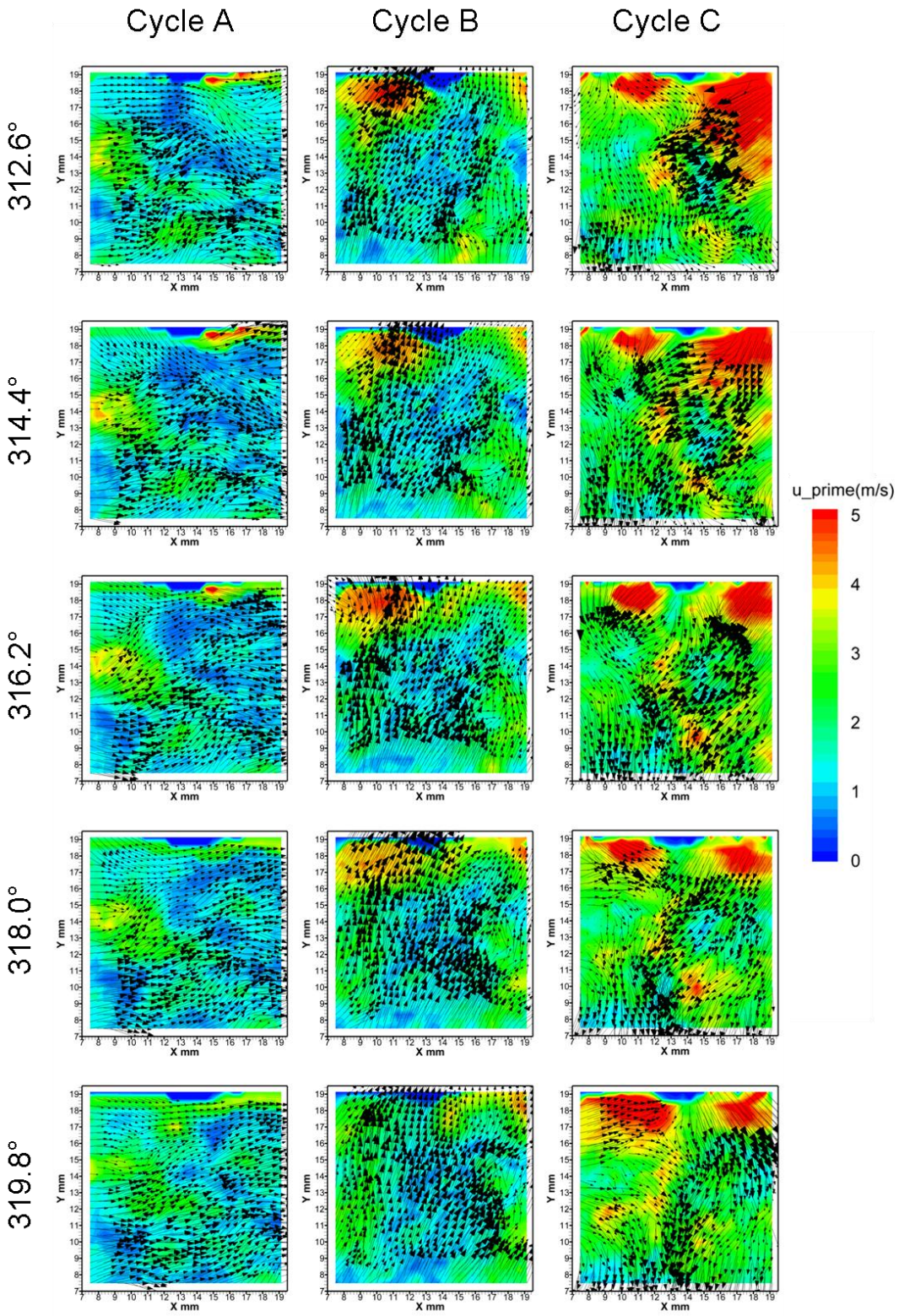

Figure 5.26 – Colour plot of u' calculated on a temporal moving average within the pent roof on the tumble plane for three individual cycles from 312.6° to 319.8° CA ATDC (vectors are raw velocity)

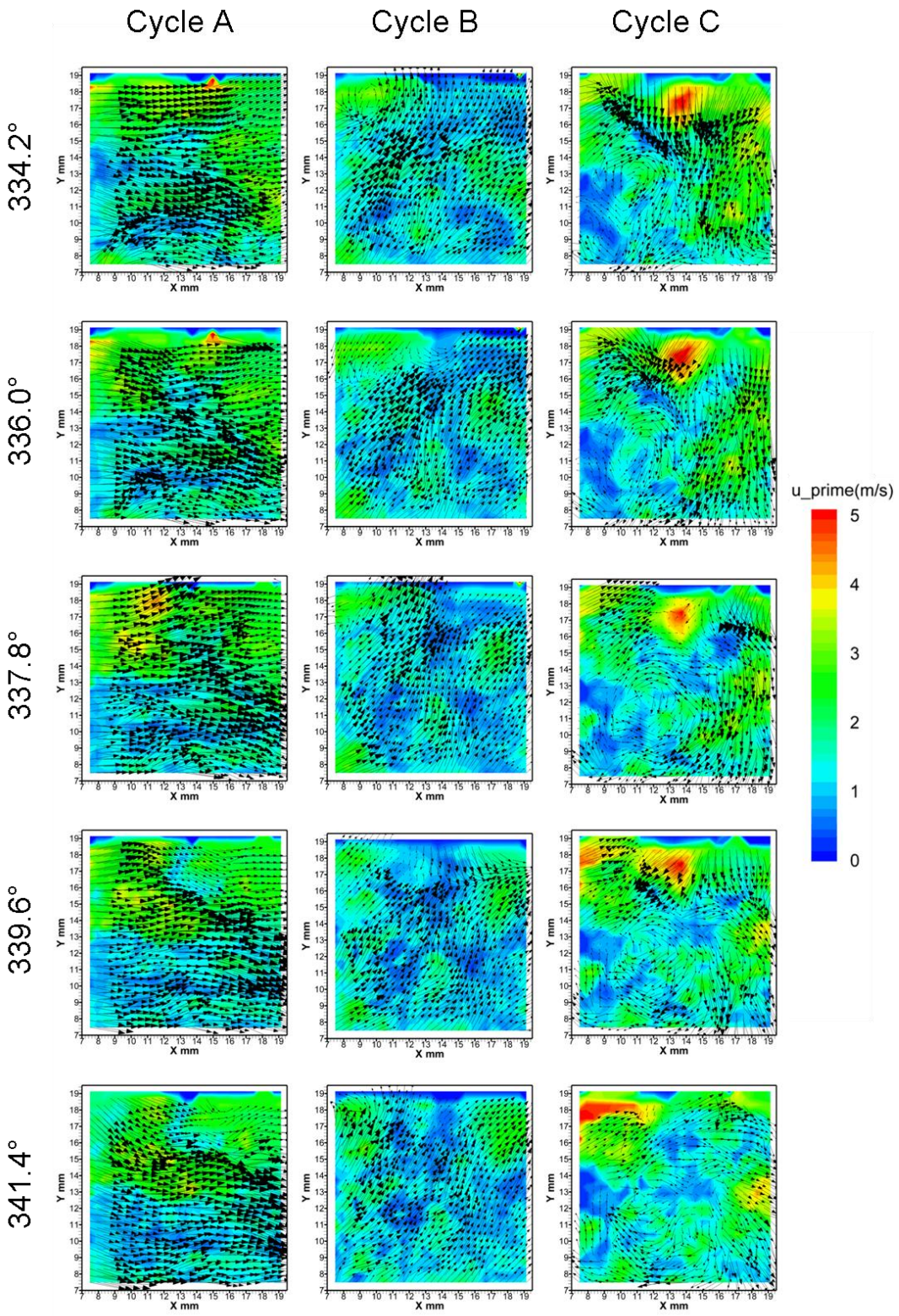

Figure 5.27 - Colour plot of u' calculated on a temporal moving average within the pent roof on the tumble plane for three individual cycles from 334.2° to 341.4° CA ATDC (vectors are raw velocity)

By calculating the mean u' within a single flow field an indication of the mean turbulence intensity experienced within that field is given. This has been completed for all time steps within a set of 100 cycles. The results are presented in Figure 5.28 (a). It is shown that a substantial cyclic variation in the mean u' is experienced; with values ranging from 1 to 3.5 $m.s^{-1}$. Turbulence variations of this order are known to affect burn rate and therefore will impact the maximum pressure and location of maximum pressure within the engine cycle. This is turn is likely to affect the engine performance in terms of imep, isfc (indicated specific fuel consumption) and emissions. Six arbitrary cycles from the 100 have been re-plotted in Figure 5.28 (b), and have been selected to show a range of u' characteristics. The most significant change in u' is displayed by cycle 6, probably corresponding to third component motions moving a structure into or out of the imaging plane.

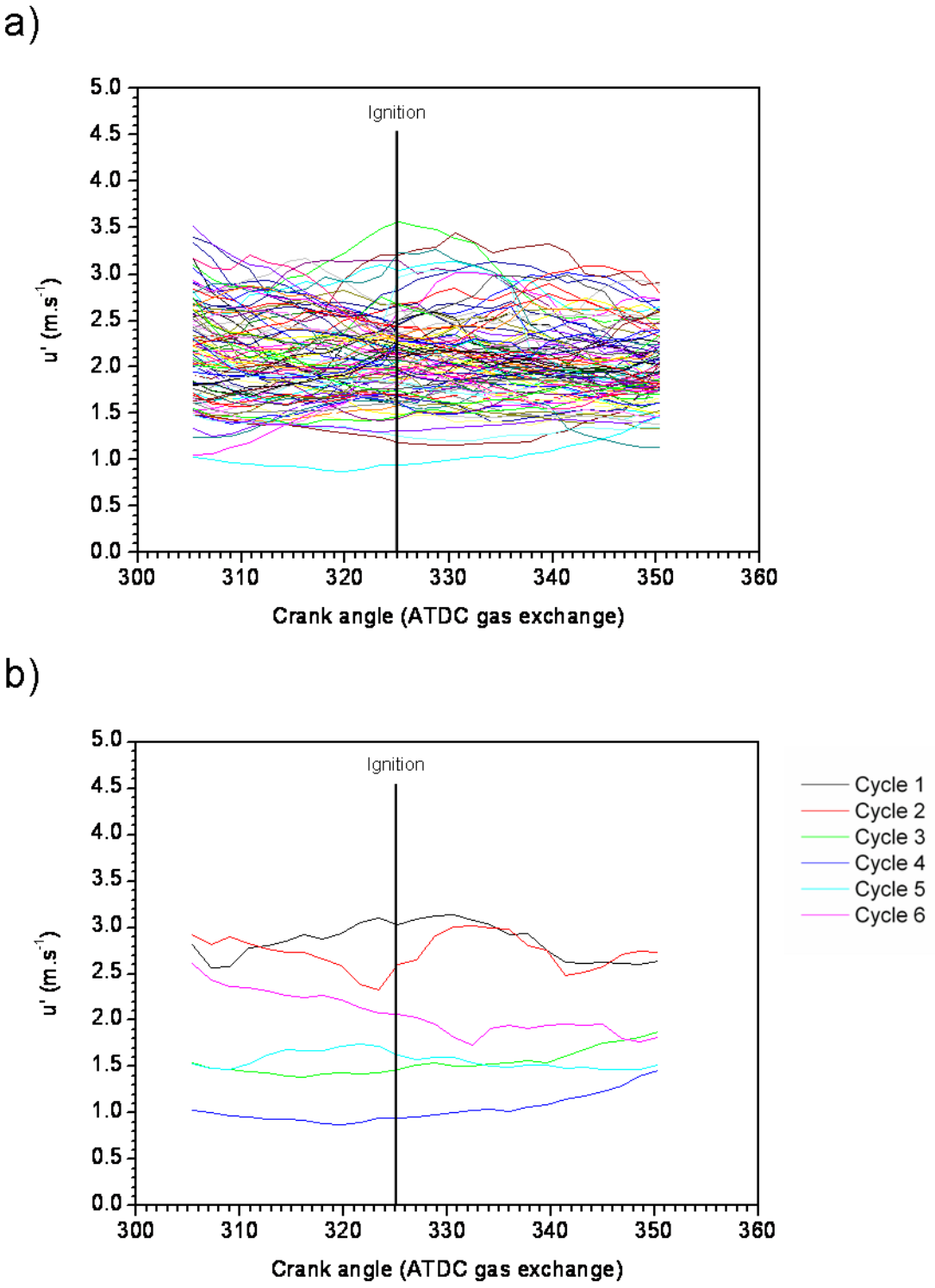

Figure 5.28 – Mean temporal u' calculated over 12.6° CA (7 PIV fields) for data captured within the pent roof on the tumble plane a) 100 cycles, b) 6 arbitrary cycles across u' range.

5.4 Synchronised pressure and flow field measurements

The in-cylinder pressure data presented in Chapter 4 showed cyclic variations in the in-cylinder pressure trace. These variations in pressure are indicative of variations in the combustion event and hence cycle performance. This chapter has introduced flame images which show variations in the behaviour of the flame during the combustion event. Features were identified which appeared to be driven by the local flow field behaviour. These local flow behaviours have been further studied through the use of spatio-temporal HSDPIV to evaluate the flow field behaviours in terms of convective flow and turbulent fluctuations. In this section simultaneously recorded HSDPIV (within the pent roof) and in-cylinder pressure data are presented. The aim of this investigation was to highlight the link between the flow field and cycle performance by correlating the flow field behaviours with in-cylinder pressure data.

5.4.1 Measurement conditions

The HSDPIV flow field measurements presented in this Section were obtained on the spark plug centreline, in the tumble plane of the engine using the same experimental set-up as previously discussed in Section 5.3 and as shown in Figure 5.17. The measurement area was located within the pent roof of the combustion chamber as per the imaged area and measurement plane are presented in the schematics of Figure 5.15 and Figure 5.16.

To ensure that the data acquisition and the HSDPIV system captured synchronized cycles a trigger gate was used which, once it received a TLL high trigger, simultaneously opened up to 8 independent channels. This allowed each channel to receive trigger signals at required crank angle locations following the gate being opened. This has been illustrated in Figure 4.9.

5.4.2 Measured velocity fields and pressure data

The synchronised capture of in-cylinder pressure and HSDPIV flow fields within the pent roof and has allowed links between high frequency turbulent fluctuations and global combustion characteristics to be investigated. The HSDPIV flow fields for this study were captured close to the end of the compression stroke to provide flow field data, which could be analysed as described within Section 5.3, to give temporal u' characteristics. The calculated u' values at a point around ignition are likely to provide reasonable indication of the global high frequency fluctuations which will affect the early flame growth characteristics.

Figure 5.29 shows a positive correlation between the calculated u' and the peak in-cylinder pressure. This is as expected since a higher u' indicates larger high frequency fluctuations which act to wrinkle the flame front promoting faster growth. The correlation coefficient (R) for the linear fit is equal to 0.52 (calculated by Origin 6.1, OriginLab Corporation). The interpretation of correlation coefficients is not straight forward, and depends on the context in which it is being used. In the case of the data presented within this section, the calculation of u' is made in 2-dimensions but is trying to represent a 3-dimensional flow. Therefore, the 3-dimensional flow field encountered by the 3-dimensional flame front is only approximated by a u' calculated on a single 2-dimensional region, this approximation of u' will act to reduce the strength of the correlation. In spite of these features, the clear correlation which can still be seen signifies a link between these two characteristics. In addition to the positive correlation between the calculated u' and the peak in-cylinder pressure, it follows that a correlation between the calculated u' and the location of peak pressure should also exist. Figure 5.30 shows this relationship and supports the observations of a higher u' promoting a faster flame growth. This is expected since it facilitates a higher pressure to be reached while the cylinder volume is small. The two outliers which can be seen in the data reduce the gradient of the linear fit and also the correlation coefficient, as described by the dashed red line in the figure. Discounting these from the linear correlation gives a correlation coefficient (R) = -0.57. This plot shows that when the high frequency fluctuations within the flow are low, the duration to reach peak pressure is longer.

Figure 5.31 shows the correlation between u' and the time taken for 10% of the mass fraction to burn. The results observed suggest a similar correlation, (R) = -0.56, providing further confirmation of the applicability of studying variations in u' from cycle to cycle being representative of variations in global cycle analysis. Finally, the correlation between u' and net imep is presented in Figure 5.32. The imep gives a measure of the indicated work output for the mechanical cycle. Therefore, this is affected by the whole combustion event and any correlation to u' at the point of ignition is likely to be reduced. However, a correlation with the calculated u' can be seen, albeit at a lower correlation coefficient.

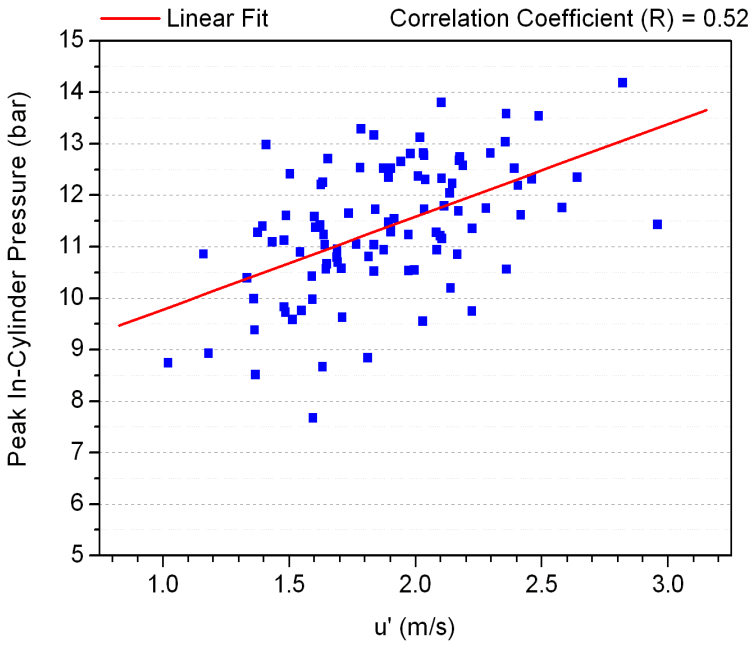

Figure 5.29 - Plot to show the correlation between u' calculated from the high frequency components of the HSDPIV flow field measurements over 12.6° CA (7 PIV fields) and the peak in-cylinder pressure

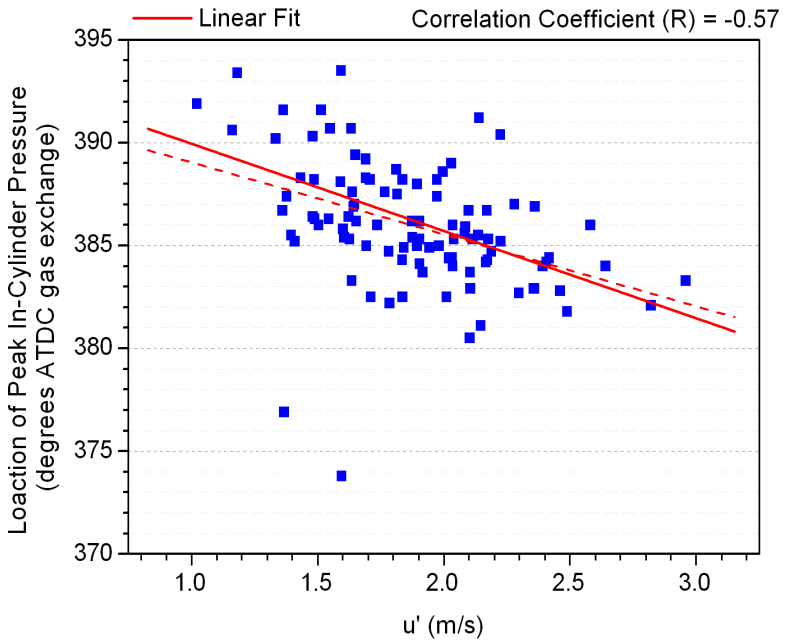

Figure 5.30 - Plot to show the correlation between u' calculated from the high frequency components of the HSDPIV flow field measurements over 12.6° CA (7 PIV fields) and the location of peak in-cylinder pressure

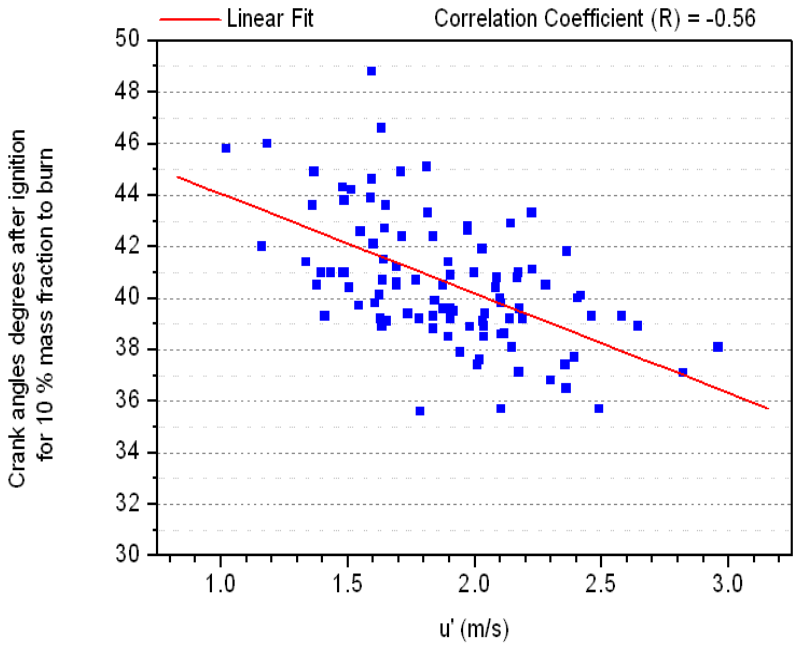

Figure 5.31 - Plot to show the correlation between u' calculated from the high frequency components of the HSDPIV flow field measurements over 12.6° CA (7 PIV fields) and the calculated number of crank angles (degrees) from ignition for 10% of the mass fraction to burn.

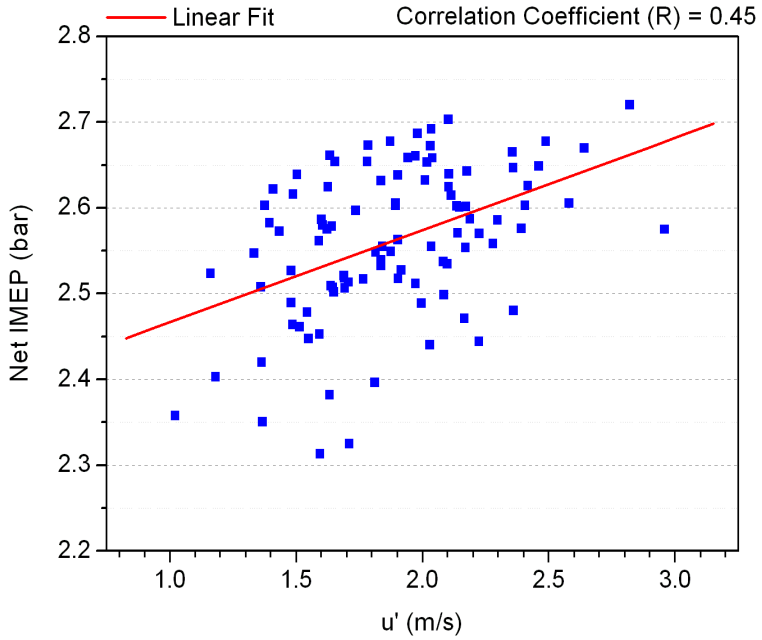

Figure 5.32 - Plot to show the correlation between u' calculated from the high frequency components of the HSDPIV flow field measurements over 12.6° CA (7 PIV fields) and the net imep.

5.5 Summary

This Chapter has demonstrated the cyclic variations which are experienced by the flame. These variations are apparent from early in the flame development, with slow burning flames generally remaining slow and fast burning flames remaining fast. It is known that large flow field velocity features relative to the flame, act to convect it in the direction of the flow. This may strain and stretch the flame due to velocity gradients within the flow field. Smaller flow scales are known to wrinkle the flame, as a portion of the flame front can be locally affected with little effect to the global flame structure. The level of wrinkling and strain experienced by a flame is known to increase its flame speed. As a result the turbulence intensity of the environment into which the flame is developing is a major factor in the burn rate. It was therefore necessary to study the flow field in the pent roof around the point of ignition to investigate the cyclic variation

which exists within this flow both in terms of convective effect on the flame and turbulence levels.

Through applying HSDPIV on a plane on the bore centreline within the pent roof of the engine both spatial and temporal flow field data was captured for the crank angle range 300° to 360° CA ATDC gas exchange at a rate of 5 kHz (1.8° CA between flow fields). These data displayed both the spatial and temporal development of the flow field on the plane of study. Comparing different engine cycles, the raw flow fields were seen to exhibit cyclic variation in the flow motion. The flow fields were decomposed into low frequency bulk motion and high frequency fluctuations. The bulk motions were seen to differ from the mean bulk motion and therefore care should be taken when using the ensemble average to describe bulk fluid motion in a cyclic device such as a reciprocating engine. Comparing the low frequency flows to the ensemble average of the low frequency flows, however, gives an indication of the level of cyclic variation experienced in this bulk flow component.

The generated u' values from the high frequency components give an indication of the turbulent fluctuations the flame may encounter. The calculation of u' on a spatial or temporal windowed average basis allows a cycle by cycle comparison to be made. This has been done by averaging the resulting u' at each time step. Comparing the average u' with cycle pressure data has shown correlation between the high frequency turbulence and cycle performance.

This fundamental link between cycle performance and flow field characteristics therefore, leads to the requirement to investigate the nature in which the flow develops leading up to the point of ignition and early flame growth. This includes how bulk flow behaviours are established as well as how the turbulent energy cascade leads to the high frequency flow characteristics present at this time. The use of HSDPIV to investigate the nature of these flows is the focus of the remainder of this thesis. Chapter 6 specifically focuses on the intake flow behaviour both within the intake runner and valve jet.

Chapter 6 Cyclic variability of intake flows

6.1 Introduction

Chemiluminescence images of the flame development during the early stages of the combustion event were presented in Chapter 5. Those images suggest that the characteristics of the flame are sensitive to the local flow behaviour. Therefore, HSDPIV was employed to further investigate the flow field behaviours which exist around the spark plug leading up to and around the time of ignition. The aim of this investigation was to identify cyclic variation within both the bulk flow motion and the high spatial and temporal frequency fluctuations. This was followed by a simultaneous HSDPIV and in-cylinder pressure investigation. This showed that the high frequency fluctuations experienced within the flow field affects the peak in-cylinder pressures and the crank angle location at which they occur. Therefore, cyclic variations in the behaviour of the flow field are shown to have a global effect on the desired output of each cycle. To understand the origins of these variations it is important to investigate flow field behaviour as the engine cycle develops.

In this chapter the flow behaviours within the intake runner and as it exits the intake valves are discussed. The flow in the intake runner has been investigated to identify whether significant cyclic spatial and temporal variations exist in this location. If significant flow variations exist, they will enter the intake port and will be drawn through the valve annulus, therefore, affecting the establishing in-cylinder flow structure. Following this, an investigation of flow exiting an intake valve is presented. This is to show development of cyclic spatial and temporal variations within the jet flow

and therefore, identifying their likely impact on cyclic variations within the in-cylinder flow fields.

6.2 Intake runner flow

6.2.1 Measurement conditions

Those data presented within this section were obtained on the intake runner centreline close to the intake ports, as depicted in the schematic of Figure 6.1 which shows the location of the measurement region. The engine was motored at 1500 rpm with a plenum pressure of 525 mbar to achieve the desired operating point.

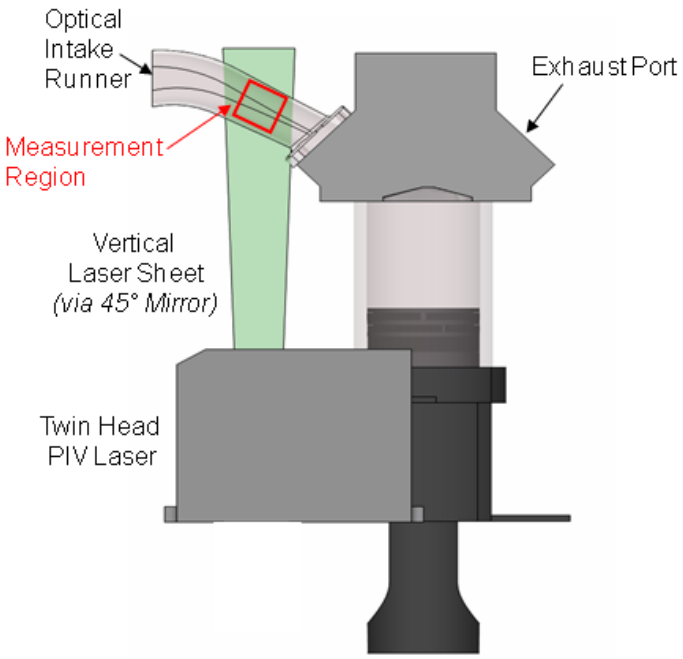

Figure 6.1 - Schematic to show the measurement location used to investigate flow in a vertical plane within the intake runner close to the intake port entry

The configuration of the HSDPIV system to capture these measurements is shown in Figure 6.2. The output from the Nd:YLF laser was formed into a thin horizontal sheet and was introduced to the intake runner via a 45° mirror to create a vertical sheet passing through the intake runner as shown. To achieve the correct laser sheet height and focus a -50 mm cylindrical lens was used in conjunction with a 1000 mm spherical lens.

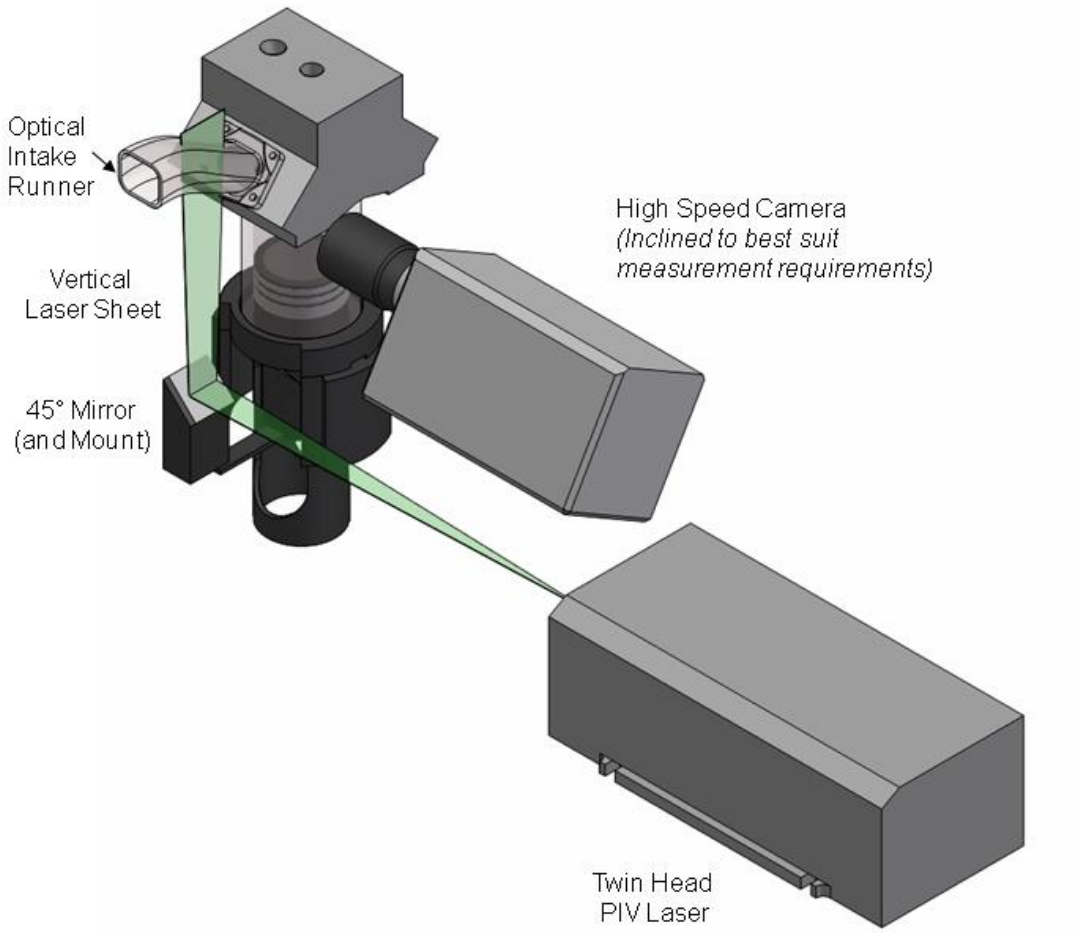

Figure 6.2 - Schematic to show the configuration of the HSDPIV system to achieve measurements in a vertical plane within the intake runner close to the intake port entry

At this measurement location the larger scale bulk flow motion and its spatial and temporal variations are of interest. The flow within the intake runner has a large velocity range over the course of the engine cycle therefore the PIV system has to be carefully configured to allow the capture of this velocity range and understand the error within the measurements.

The size of the camera's active pixel array was reduced to 512 by 1024 pixels to allow the camera to operate at a frame rate of 6 kHz and therefore, capture image pairs suitable for two frame cross-correlation analysis at 3 kHz. The engine was motored at 1500 rpm meaning that the temporal resolution of the HSDPIV system for these measurements equated to 3° CA (0.33 ms) between captured flow fields. A 105 mm AF Micro Nikkor lens was used to image a region 10 mm by 20 mm onto the active array. Analysis of the captured PIV image pairs was performed with the TSI Insight 3G software. Velocity vectors were evaluated from the image pairs on a Nyquist grid with 32 by 32 pixel interrogation regions, equating to an area approximately 0.62 mm by 0.62 mm within the flow. The interrogation regions were positioned to overlap neighbouring regions by 50% leading to a vector spacing in the resulting velocity vector field of 0.31 mm. The intake air was seeded with 1 to 2 μm oil droplets. To control the imaged diffraction limited spot size the laser was operated at full power and the largest $f^{\#}$ which gave adequate contrast in the particle images was used. Ideally the $f^{\#}$ for the measurements presented within this section would be 16 to give a calculated diffraction limited spot size greater than 2 pixels in diameter. The HSDPIV system, limited by laser power and camera sensitivity, required an $f^{\#} = 11$. This gives a calculated diffraction limited spot size of 1.6 pixels (hence more susceptible to sub-pixel displacement errors, Adrian (1997)). However, the calculated spot size is for an ideally focussed system, therefore by taking the image slightly out of focus the actual measured imaged particle size on the camera array could be controlled to be > 2 pixels.

The time separation (Δt) between the two laser pulses which control the exposure of the image pair was set to 10 μs. This Δt allowed the flow to travel with a velocity up to *circa* 31 ms^{-1} before the particles moved beyond 16 pixels (half of the interrogation

region). For the flow field under investigation this Δt was considered to be adequate to give an acceptable velocity measurement limit whilst minimising out of plane flow motion and allowing enough movement in the particles to control errors in sub pixel displacements. A one pixel displacement corresponds to a velocity measurement of 1.95 $m.s^{-1}$

The HSDPIV system was triggered at 64° CA ATDC gas exchange. From this external trigger the PIV system was programmed to capture 50 image pairs at 3 kHz, therefore at 3° CA increments until 211° CA ATDC gas exchange was reached. The flow fields captured, therefore, provided spatial and temporal flow information leading up to and beyond max valve lift, continuing well into the compression stroke and intake valve closure. With the 2 Gb onboard memory available on the camera, allowing *circa* 2100 images to be recorded, 20 cycles of image pairs could be recorded during one capture sequence. Following this the images had to be downloaded from the camera to the PIV control computer. Performing 5 capture sequences provided 100 cycles of flow field data, enough to calculate a statistically significant mean flow.

6.2.2 Measured velocity fields

Raw velocity fields for the range 85° to 100° CA ATDC are presented for three individual cycles in Figure 6.3. These data were captured with the conditions described in Section 6.2.1. The contour plot denotes the velocity magnitude and the vectors represent flow direction. The flow is shown to accelerate from *circa* 20 $m.s^{-1}$ at 85° CA ATDC to *circa* 30 $m.s^{-1}$ at 100° CA ATDC. Across the three cycles presented, the flow velocity at each crank angle appears similar in magnitude. The vectors show a strong dominant flow from left to right (i.e. U component velocity in the x-direction) as the fresh intake air flows towards the intake ports. Spatially there appears to be little variation across the flow fields; this is investigated later in this section. The V component velocity is relatively small with a mean spatial velocity, for each of the 100 cycles available, of about 2% of the U component velocity for the presented time sequence.

The progression of theses cycles are shown in Figure 6.4 for the crank angle range 136° to 151° CA ATDC. These raw velocity fields show a slower flow velocity than the previous figure. Deceleration of the flow is shown due to the reduction in velocity from 136° to 142° CA ATDC. The initial velocity at 136° CA is *circa* 10 $m.s^{-1}$, which reduces to *circa* 7 $m.s^{-1}$ at 151° CA. The U component still dominates the flow; however, due to the reduced velocity the spatial mean V component velocity is now *circa* 14% of the U component for the presented time sequence. There is still little spatial variation across the flow fields in terms of flow velocity and structure. Cycles A and C show a slight positive V component with cycle B displaying a slight negative V component.

Further progression of these cycles are shown in Figure 6.5 for the range 175° to 190° CA ATDC. At this point within the cycle spatial and temporal variations of the flow within the intake runner are displayed. At 175° CA perturbations within the flow are displayed for cycles A and C where significant V component motions are visible, cycle B does not display this perturbation. Stagnation of the flow fields are shown as 181° CA is approached, with the general trends of the flow fields developing as previously discussed. At 184° CA cycle A and B have stagnated, however, cycle C displays back flow away from the inlet ports. As the cycle further progresses cycle A begins to display back flow and finally at 190° CA cycle B also displays this condition, discussed in Section 2.3.1.

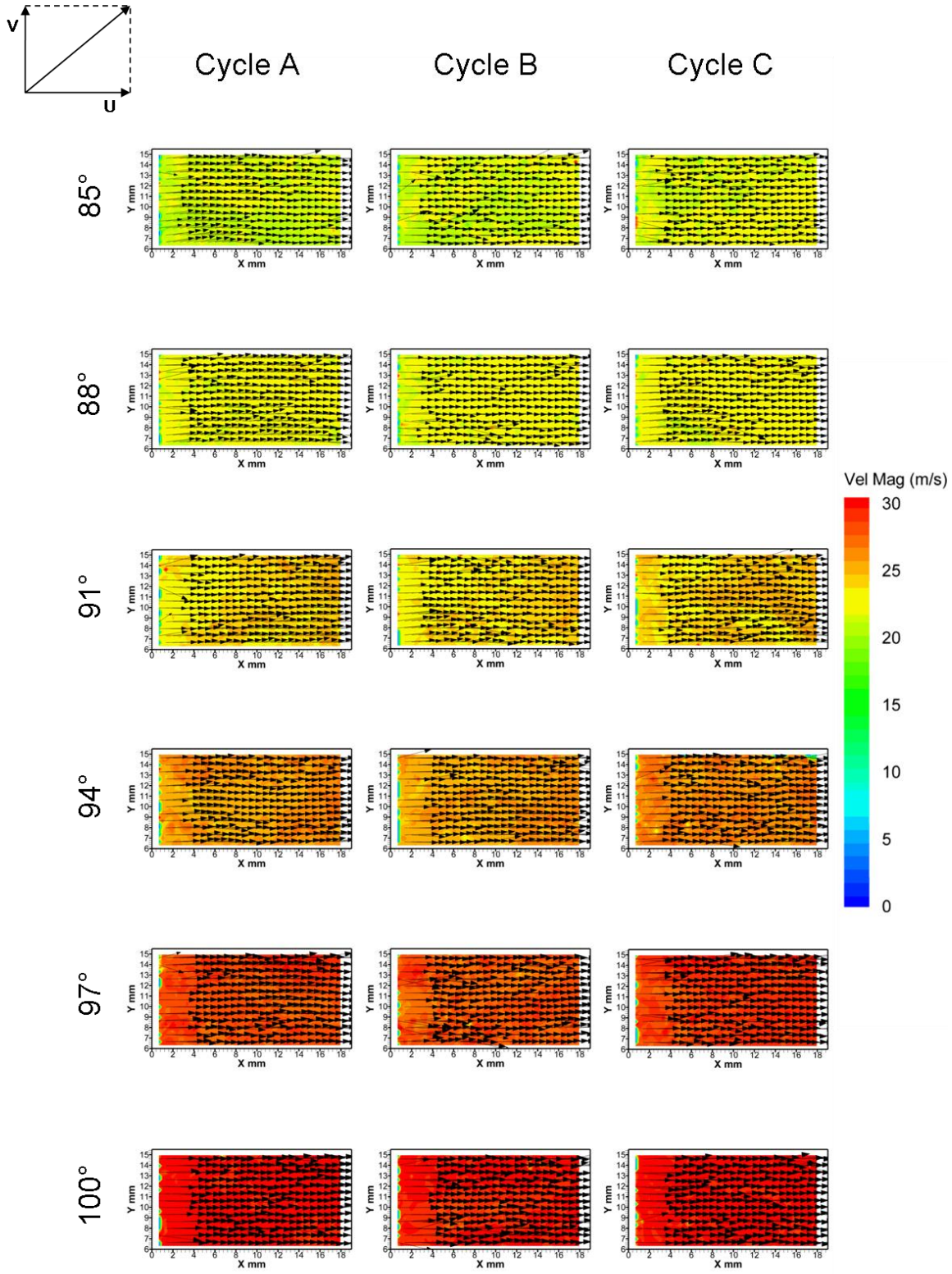

Figure 6.3 - Raw flow fields within the intake runner for three individual cycles from 85° to 100° CA ATDC captured with HSDPIV at a rate of 3 kHz

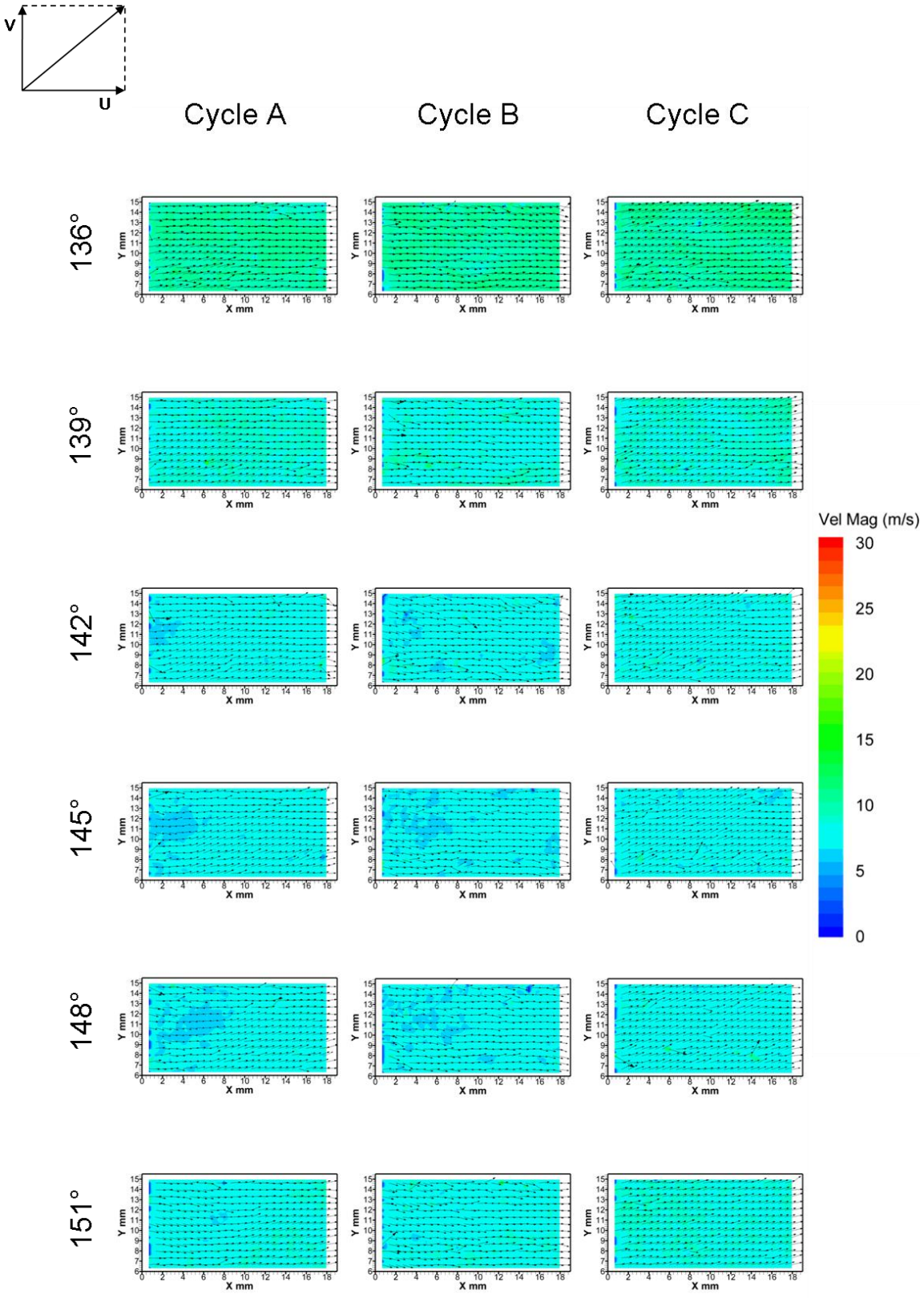

Figure 6.4 - Raw flow fields within the intake runner for three individual cycles from 136° to 151° CA ATDC captured with HSDPIV at a rate of 3 kHz

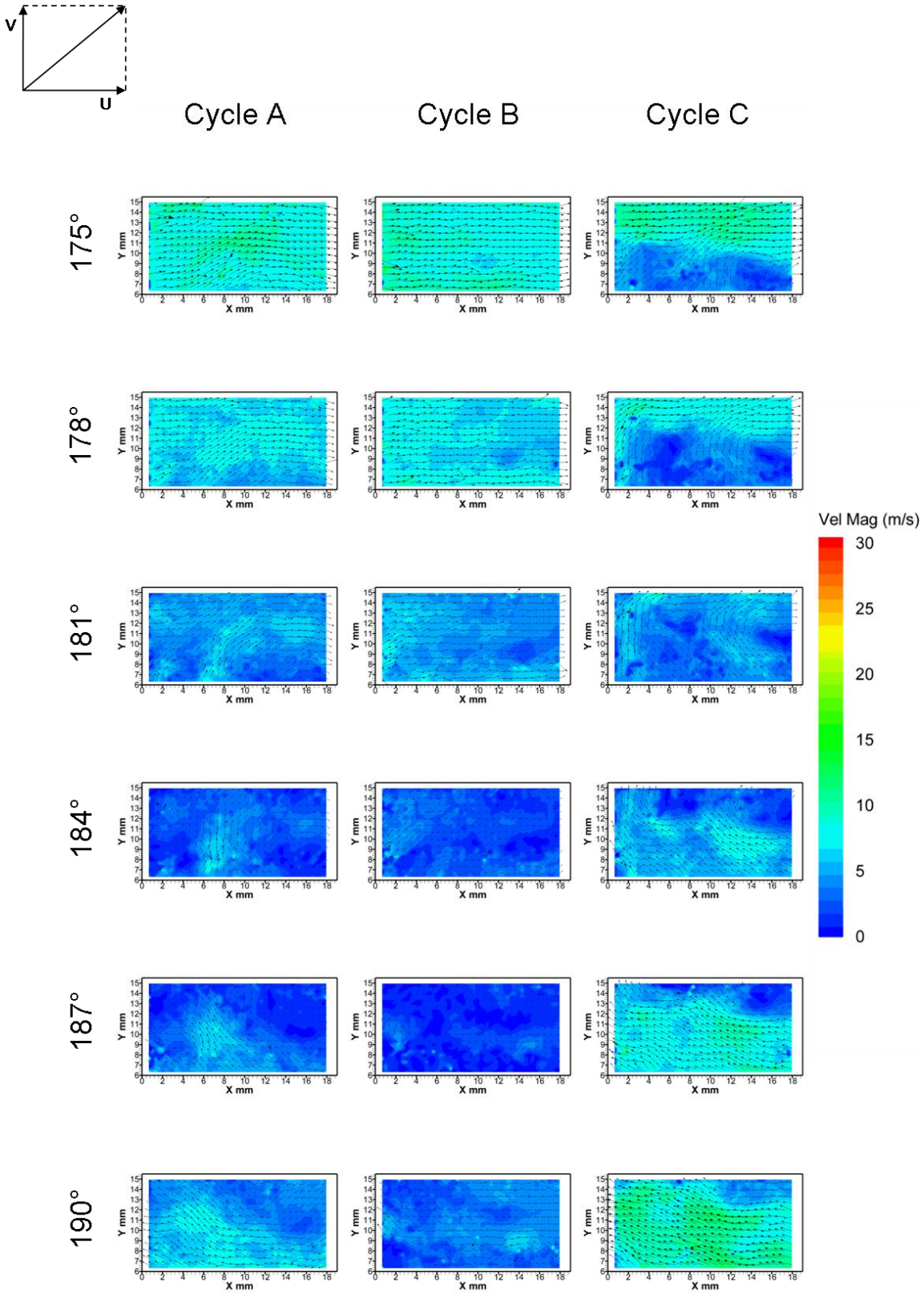

Figure 6.5 - Raw flow fields within the intake runner for three individual cycles from 175° to 190° CA ATDC captured with HSDPIV at a rate of 3 kHz

To provide an indication of the temporal variations in U component velocity which exist within the intake flow fields, the mean U component velocity for each velocity field was calculated. This is shown in Figure 6.6 for 25 consecutive cycles captured for an extended range of 12° to 282° CA ATDC. For these data the Δt between laser pulses was set to 7 μs to allow the flow to travel with a velocity up to *circa* 44.6 m.s^{-1} before the particles have moved beyond 16 pixels (half of the interrogation region). This decrease in Δt does however increase the sub pixel error, with one pixel displacement corresponding to a velocity measurement of 2.79 m.s^{-1}. This compromise had to be made to capture the peak velocity experienced during the early part of the cycle. The cyclic variation shown in Figure 6.6 is small during the early part of the cycle. However, as the flow slows and reaches its second trough (at *circa* 140° CA ATDC) greater variation in mean velocity can be seen. This level of variation is seen to exist as back flow from the cylinder enters the intake runner.

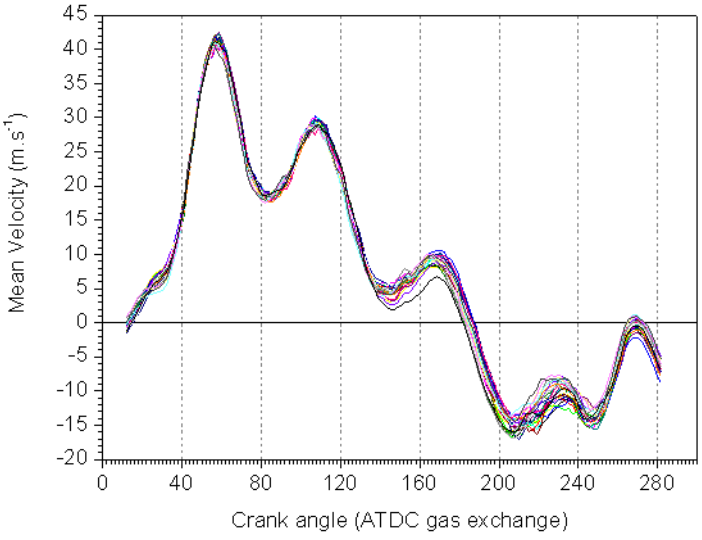

Figure 6.6 – Mean U component velocity for flow within the intake runner presented for 25 individual cycles from 12° to 282° CA ATDC gas exchange

The mean U components for the 100 cycles captured to provide the data presented in Figure 6.3 to Figure 6.5 are shown in shown in Figure 6.7. This Figure also displays a growth in the spread of mean velocity following the trough at *circa* 140° CA ATDC.

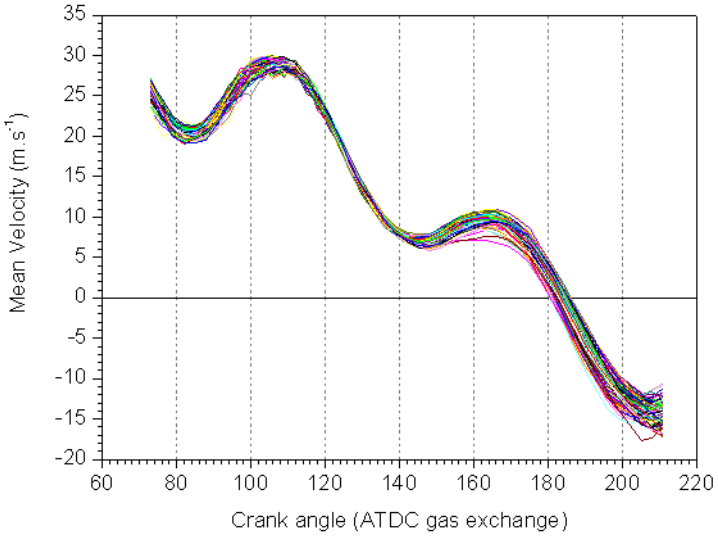

Figure 6.7 - Mean U component velocity for flow within the intake runner presented for 100 individual cycles from 73° to 211° CA ATDC gas exchange

The intake runner velocity changes significantly over the course of the cycle as shown in Figure 6.6 and Figure 6.7. Cyclic variations within flow fields are often highlighted by calculating fluctuating components about a mean flow. In the case of the intake runner flow a single mean velocity for each crank angle can be used to extract spatial variations more accurately. This velocity is found by calculating the spatial mean of the ensemble mean velocity field (over the n by m vector field) such that

$$\overline{\overline{U_{(\theta)}}} = \frac{1}{n_x \times m_y} \sum_{x=1}^{n_x} \sum_{y=1}^{m_y} \overline{U_{(\theta,x,y)}}. \qquad \text{Equation 6.1}$$

By subtracting $\overline{\overline{U_{(\theta)}}}$ from the raw velocity fields, cyclic and spatial variations within the intake runner flow is given by

$$u_{CV(\theta,i,x,y)} = U_{(\theta,i,x,y)} - \overline{\overline{U_{(\theta)}}}. \qquad \text{Equation 6.2}$$

The resulting fluctuating velocity fields of $u_{CV(\theta,i,x,y)}$ are shown in Figure 6.8 to Figure 6.10 for the three cycles previously presented in their raw velocity form. It is shown in Figure 6.8 (for the range 85° to 100° CA ATDC) that cyclic and spatial variations in the flow fields exist. At 85° CA ATDC, flow in the positive y direction is shown in cycle A, with a magnitude *circa* 2.5 $m.s^{-1}$. This structure is seen to progress with the bulk flow (see Figure 6.3) towards the intake ports and at 94° CA ATDC it is leaving the image. Cycles B and C also show the movement of spatial structures with similar velocity magnitudes (up to *circa* 2.5 $m.s^{-1}$) and hence demonstrate the existence of cyclic variation in spatial structures with low relative velocity magnitude about the mean bulk flow velocity.

The three cycles are presented for the crank angle range 136° to 151° CA ATDC in Figure 6.9, this shows similar behaviour with the fluctuating velocity displaying structures close to 2.5 $m.s^{-1}$. The velocity magnitudes of these variations are relatively higher when compared to the lower bulk flow velocities at this point within the cycle. The further progression from 175° to 190° CA ATDC is presented in Figure 6.10, for the same three cycles. At this point, the flow is beginning to enter into the back flow period. The magnitude of the fluctuating velocity has increased with structures again visible within these flow fields. The fluctuating flows shown for cycles A and B display a dominant left to right flow for all crank angles presented. This indicates the flow towards the cylinder had a velocity magnitude greater than the mean. Once the mean flow undergoes the transition into backflow, positive fluctuating flow towards the cylinder remains, indicating the initial back flow velocity is smaller and the transition to this phase occurs later. The flow fields presented for cycle C, however, show the flow in the lower half of the runner to be slower than the mean. The presence of vortices, carried within the bulk flow, is shown for this cycle. As the flow progresses the area of back flow spreads into the upper portion of the runner. This cycle, therefore, appears to enter the back flow stage earlier than the mean and exhibits a greater velocity away from the ports.

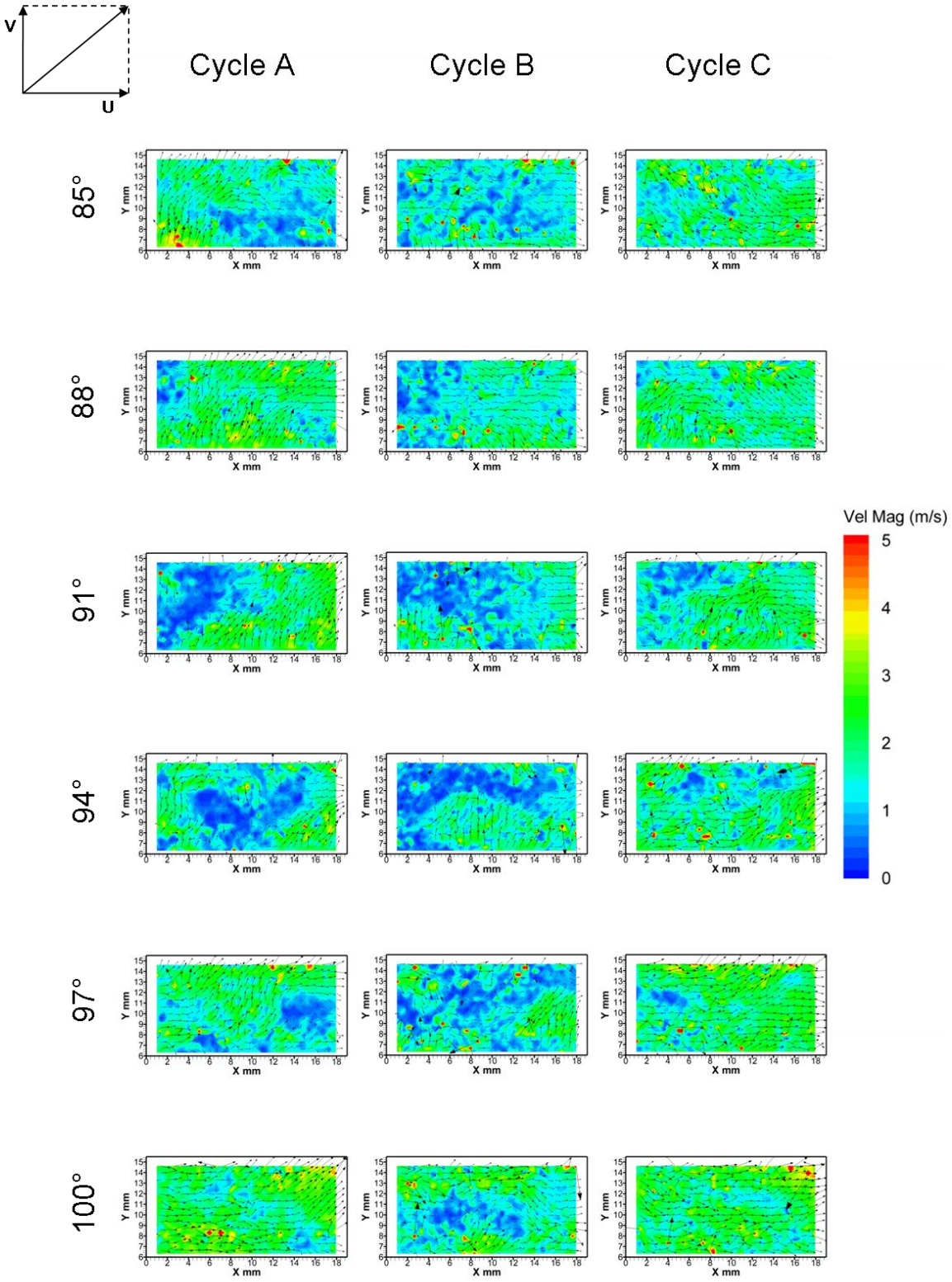

Figure 6.8 – Raw flow minus mean spatial mean flow fields within the intake runner for three individual cycles from 85° to 100° CA ATDC captured with HSDPIV at a rate of 3 kHz

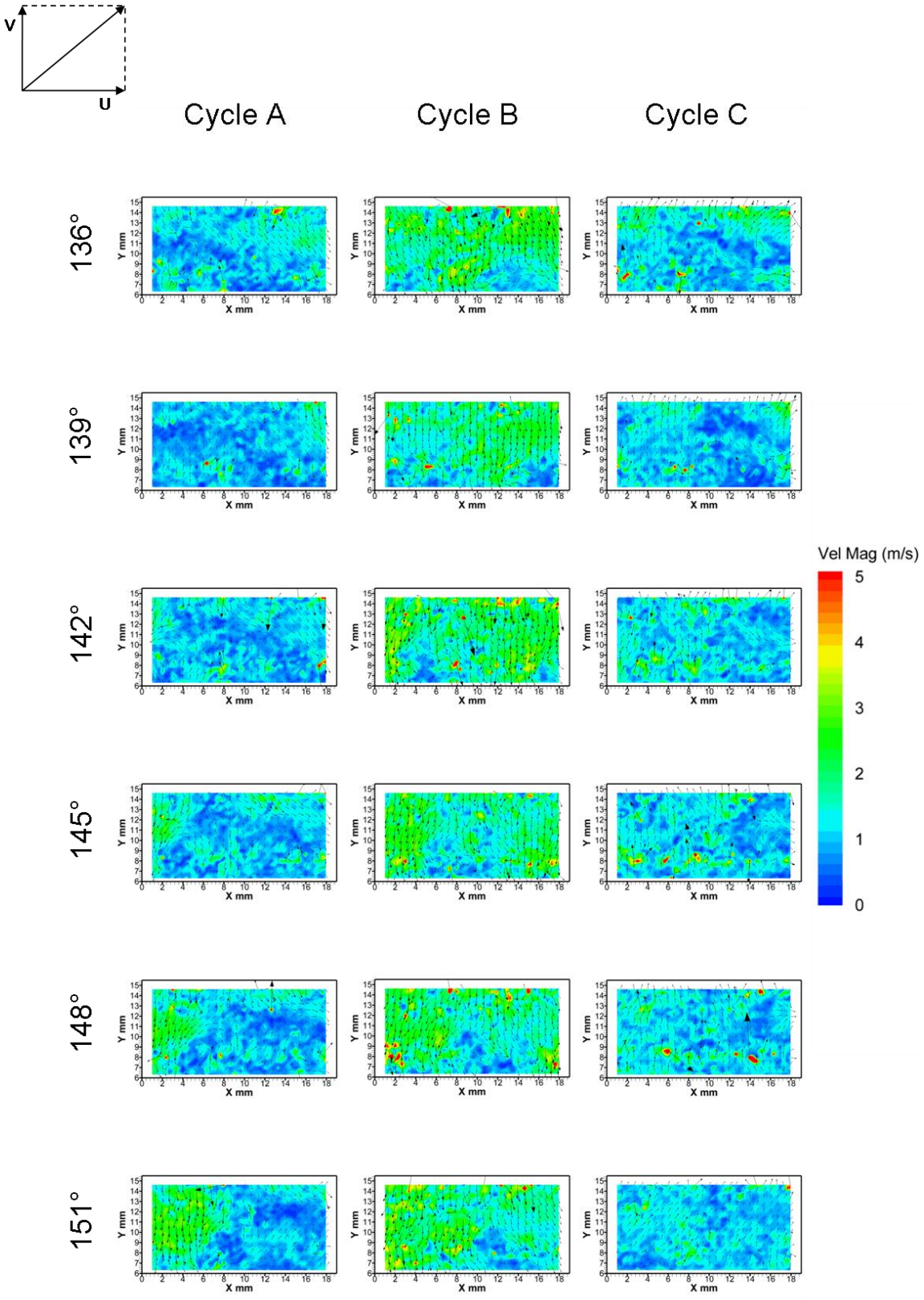

Figure 6.9 - Raw flow minus mean spatial mean flow fields within the intake runner for three individual cycles from 136° to 151° CA ATDC captured with HSDPIV at a rate of 3 kHz

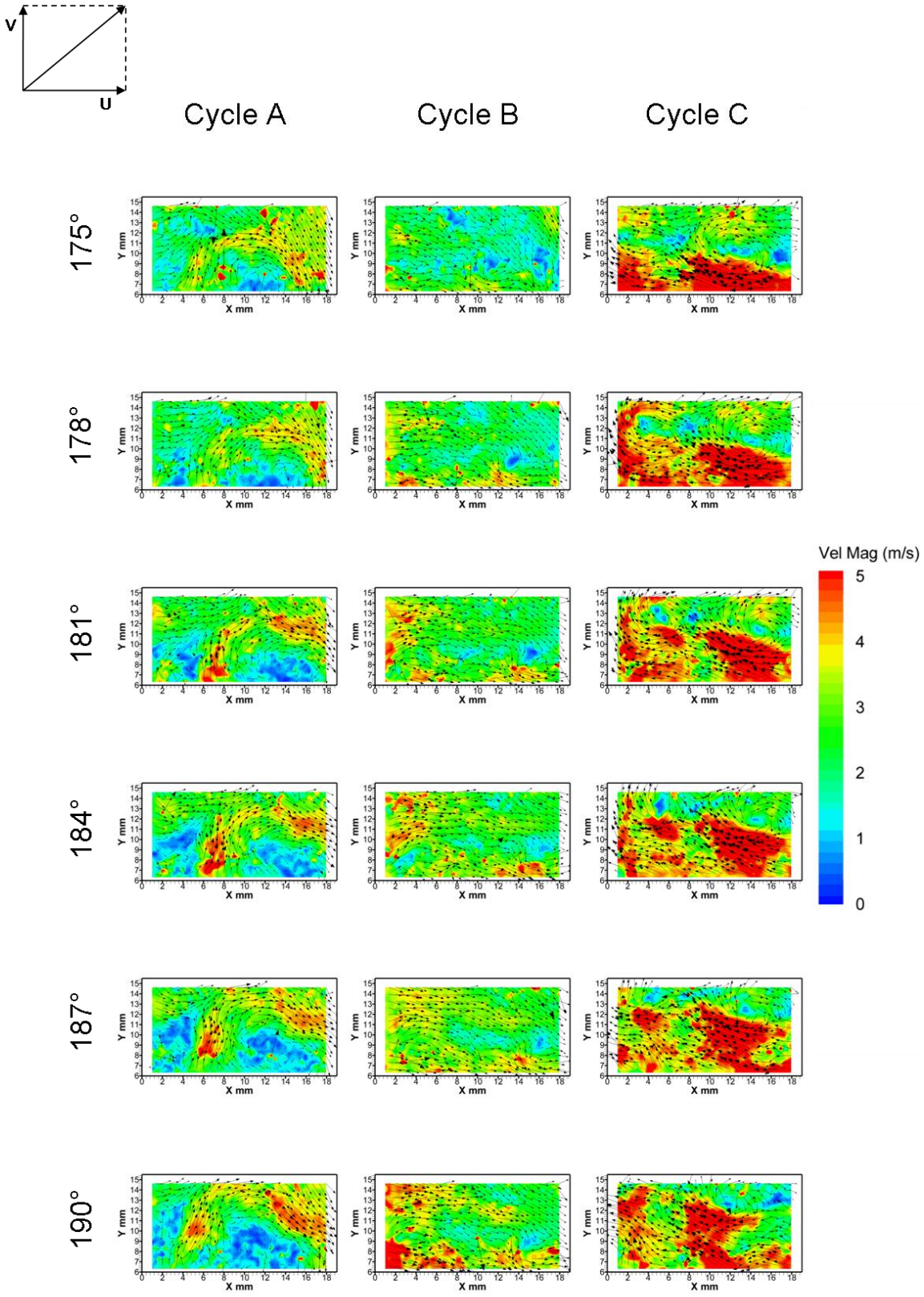

Figure 6.10 – Raw flow minus mean spatial mean flow fields within the intake runner for three individual cycles from 175° to 190° CA ATDC captured with HSDPIV at a rate of 3 kHz

Cyclic variations have been shown to exist in the flow within the intake runner. During the early stages of the intake stroke these variations are small in comparison to the bulk flow velocity. However, as the cycle progresses these variations become more significant relative to this bulk flow. Cyclic variations in flow velocity and flow profile across the intake runner during the initial part of the cycle are likely to have more influence on the in-cylinder flow fields than the variations which are apparent later on as the flow velocity is reduced or is negative and the in-cylinder flows are already well established.

The profiles of the mean U component velocity with respect to the Y-axis, within the intake runner, are presented in Figure 6.11 for 100 cycles at five different crank angles (85°, 100°, 145°, 166° and 200° ATDC). This figure shows the increase in velocity from 85° to 100° CA ATDC and, at each, an approximate spread of 3 $m.s^{-1}$. As the cycle progresses to at 145° CA ATDC, the flow is shown to have slowed and displays a slightly smaller spread of *circa* 2 $m.s^{-1}$. At 166° CA ATDC there is a slight increase in velocity observed, which correlates to the small peak shown in Figure 6.7. Initially the U component velocity is shown to be almost flat, however, at 166° CA, in some cases, instabilities can be seen to slow the flow where $Y < 10$ mm. This trend is shown in cycle C of the previously presented figures where the lower portion of the runner slows earlier than the upper portion. The profiles presented at 200° CA ATDC occur during the backflow period and have negative U velocity. The variation in velocity at this point has increased to *circa* 5 $m.s^{-1}$, but the flat U velocity profile has returned.

To highlight the characteristics of individual cycles, the 100 cycles shown in Figure 6.11 have been sub-sampled to plot only 5 arbitrarily selected cycles in Figure 6.12.

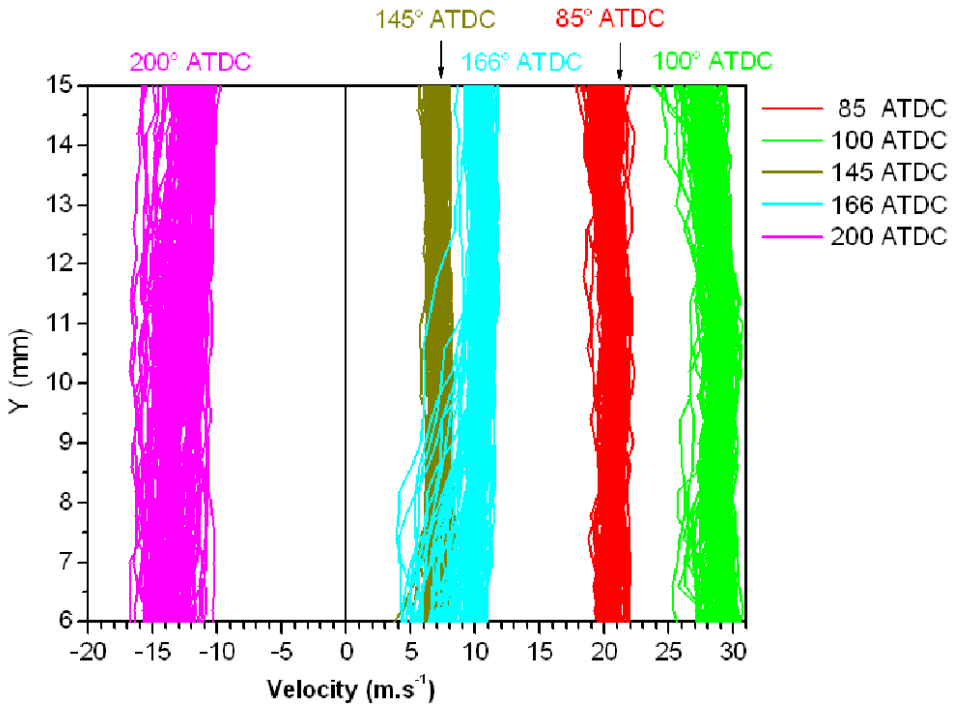

Figure 6.11 - Velocity profiles at five selected crank angle positions throughout the cycle

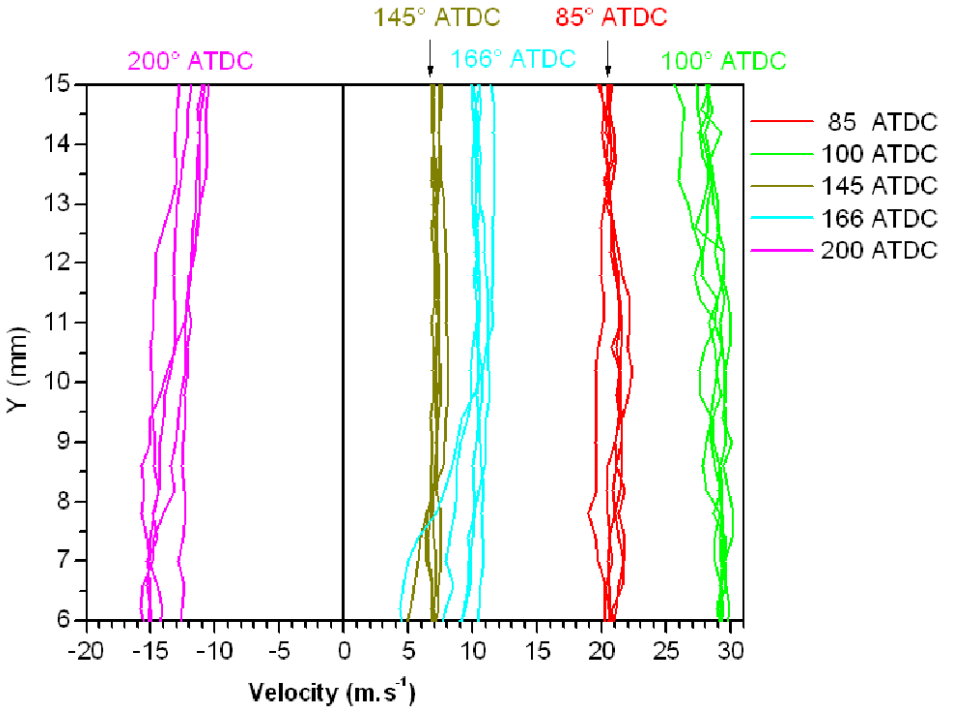

Figure 6.12 - Velocity profiles for five arbitrary cycles at the six crank angle positions previously presented in Figure 6.11

6.3 Intake valve jet

6.3.1 Measurement conditions

The data presented in the previous section showed the characteristics of the flow and its spatial and temporal variations within the intake runner. The logical progression, given the difficulties associated with capturing flow field data within the intake port, is to study the flow as it exits the intake valve annulus into the cylinder. To capture this highly transient flow, experienced within the intake valve jet, the HSDPIV system was operated to give flow fields with a temporal resolution of 5 kHz. This resulted in an active pixel area of 512 by 512 pixels. The engine was motored at 1500 rpm with an inlet plenum pressure of 525 mbar.

A schematic is presented in Figure 6.13 which shows the measurement location of the data presented. These data were obtained on the intake valve centreline in the tumble plane of the engine, for the valve closest to the pent roof window. The images were obtained through this window to capture the valve jet exiting the valve curtain and flowing towards the exhaust valve side of the engine. A schematic showing the location of the measurement plane is given in Figure 6.14.

The configuration of the HSDPIV system to capture these measurements is shown in Figure 6.15. The output from the Nd:YLF laser was formed into a thin vertical sheet and was introduced to the cylinder via the 45° mirror under the optical piston. To achieve the correct laser sheet height a -50 mm cylindrical lens was used in conjunction with a 1000 mm spherical lens.

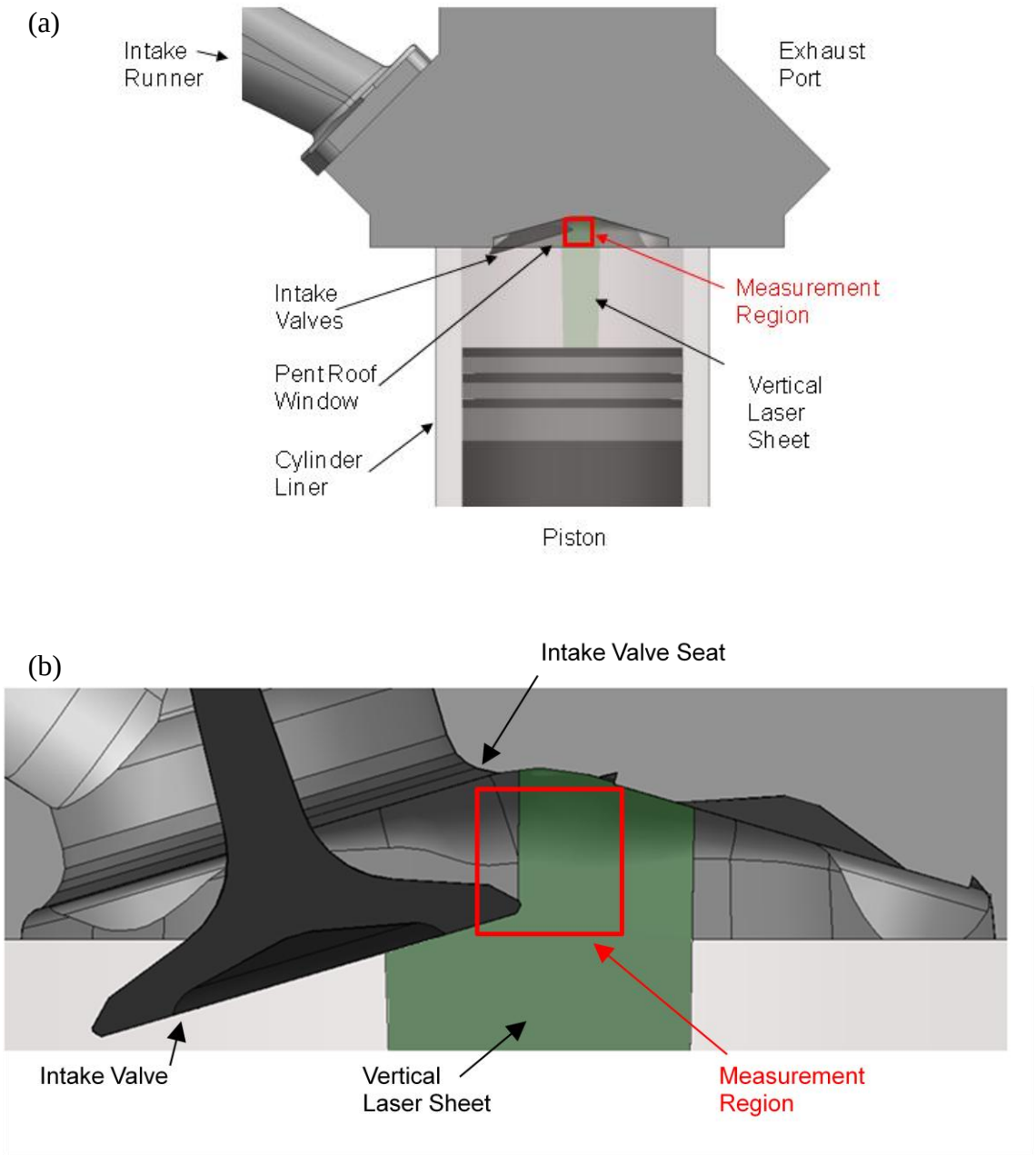

Figure 6.13 - Schematic to show the measurement location used to investigate flow exiting the intake valves (a) general view, (b) detailed view at max intake valve opening 'cut-away' upto the plane defined by the measurement plane to show the valve, valve seat and measurement region.

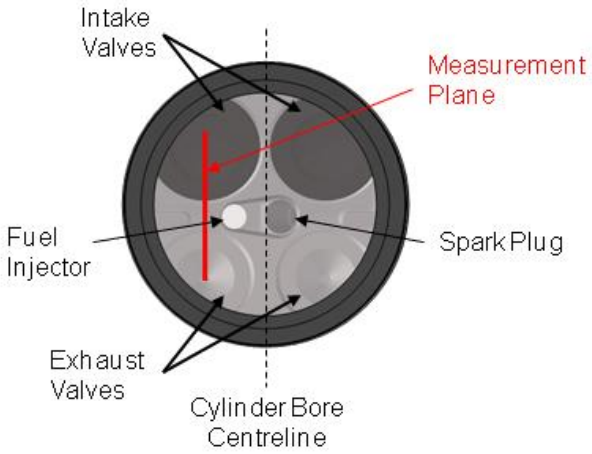

Figure 6.14 - Schematic to show the measurement plane created by the laser sheet for studying the flow exiting the intake valve closest to the pent roof window (as viewed via the 45° mirror under the piston)

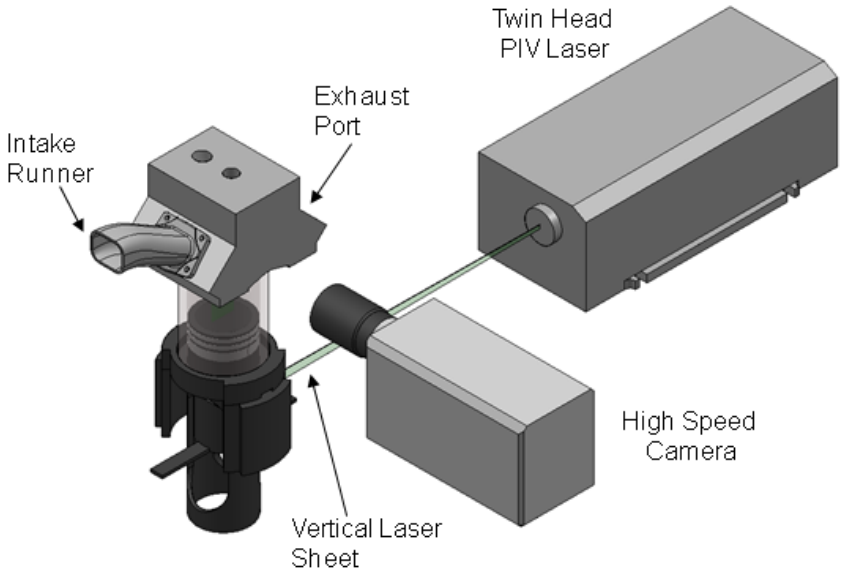

Figure 6.15 - Schematic to show the configuration of the HSDPIV system to achieve measurements to investigate flow exiting the intake valve closest to the pent roof window

At this measurement location, both the bulk flow motion and its higher frequency fluctuations that exit the valve curtain area are of interest. The interaction of this jet with the slower in-cylinder fluid creates a shear layer, and a highly changeable environment. The flow within the valve jet has a large velocity range over the course of the engine cycle along with a high peak velocity, this leads to compromises having to be made in the HSDPIV system set-up to capture these temporal flow characteristics.

The size of the camera's active pixel array was reduced to 512 by 512 pixels to allow the camera to operate at a frame rate of 10 kHz and, therefore, capture image pairs suitable for two frame cross-correlation analysis at 5 kHz. The engine was motored at 1500 rpm and as such the temporal resolution of the HSDPIV system for these measurements equated to 1.8° CA (0.2 ms) between captured flow fields.

A 105 mm AF Micro Nikkor lens was used to image a region 10 mm by 10 mm onto the active pixel array. Analysis of the captured PIV image pairs was performed with the TSI Insight 3G software. Velocity vectors were evaluated from the image pairs on a Nyquist grid with 32 by 32 pixel interrogation regions, equating to an approximate area of 0.62 mm by 0.62 mm within the flow. The interrogation regions were positioned to overlap neighbouring regions by 50% leading to a vector spacing in the resulting velocity vector field of 0.31 mm. The intake air was seeded with 1 to 2 μm oil droplets. To control the imaged diffraction limited spot size the laser was operated at full power and the largest $f^{\#}$ which gave adequate contrast in the particle images was used. Ideally the $f^{\#}$ for the measurements presented within this section would be 16 to give a calculated diffraction limited spot size greater than 2 pixels in diameter. The system, limited by laser power and camera sensitivity, required an $f^{\#} = 8$. This gives a calculated diffraction limited spot size of 1.2 pixels (therefore more susceptible to sub-pixel displacement errors). However, the calculated spot size is for an ideally focussed system, therefore by taking the image slightly out of focus the actual measured imaged particle size on the camera array could be controlled to be > 2 pixels.

The time separation (Δt) between the two laser pulses which control the exposure of the image pair was set to 6 μs. This Δt allows the flow to travel with a velocity up to *circa* 52 ms^{-1} before the particles will move beyond 16 pixels (half of the interrogation region). For the flow field under investigation this Δt was considered to be adequate to give an acceptable velocity measurement limit to allow the crank angle range required to be captured. This Δt must also minimise the out of plane flow motion and allow enough movement in the particles to control errors in sub pixel displacements. A one pixel displacement corresponds to a velocity measurement of 3.25 $m.s^{-1}$. These flows exhibit large velocity gradients as a result of the shear layer created between the jet flow and the slower speed in-cylinder fluid, which provides an added challenge to the capture of the HSDPIV data.

The HSDPIV system was triggered at 70° CA ATDC gas exchange. From this external trigger, the PIV system was programmed to capture 95 image pairs at 5 kHz, therefore, at 1.8° CA increments until 239.2° CA ATDC gas exchange was reached. The 2 Gb onboard memory available on the camera allowed *circa* 2100 images to be recorded, and 11 cycles of image pairs could be gathered during one capture sequence. Following this the images had to be downloaded from the camera to the PIV control computer. The time required for this process allowed the windows providing optical access into the engine to be cleaned, removing any seed build up which had gathered during the course of the engine run. Performing 10 capture sequences resulted in over 100 cycles of flow field data to be available, which is considered enough to calculate a statistically significant mean flow.

6.3.2 Measured velocity fields

6.3.2.1 Standard intake geometry

Raw velocity fields for 91.6° CA ATDC gas exchange are presented for three individual cycles in Figure 6.16. These data were captured with the conditions described in Section 6.3.1. The contour plot denotes velocity magnitude and the vectors represent flow direction. Note; a schematic of the intake valve has been overlaid into the images for

information. The three cycles presented display significant flow field variation in both velocity magnitude and flow structure. For example, the flow fields presented for cycles A and B show velocities within the jet to be over 40 $m.s^{-1}$, however cycle C appears to be slower with jet velocities closer to 30 $m.s^{-1}$. The flow structures for the three cycles are also notably different with cycles A and C displaying broader jets than shown for cycle B. The angles of the jet are also seen to vary across the three cycles. The jet displayed for cycle A exits in the upper half of the frame, the flow underneath the jet is shown to be moving upwards towards the jet and being entrained in the shear layer. Cycle B however, displays a jet which exits the frame with an angle close to 45°. The same upward motion is visible in the flow underneath the jet up to X = 10 mm, at which point a recirculation is shown due to entrained motion. The breath of the jet shown in cycle C makes determining jet angle difficult, however, the jet leaves the frame close to the bottom right corner at Y = 6 mm. A recirculation is visible underneath the jet as flow is entrained due to the shear layer.

The flow fields presented in Figure 6.16 for the three chosen cycles at 91.6 CA ATDC are plotted along with flow fields for twelve other cycles in Figure 6.17. These data show an indication of the fluctuations which can occur from one cycle to the next. Although, by design of the annulus, the characteristics of the flow exiting it are similar, variation can be seen in the breadth, angle and velocity of the jets once they emerge into the cylinder. Additionally, the in-cylinder flow surrounding the jet is shown to differ in structure. Entrainment of flow into the jet is shown in all cases, both above and below the jet, however, the structure of this differs from cycle to cycle. This is likely to be due to residual flow in the cylinder surrounding the jet coupled with the subtle changes in jet breadth, angle and velocity.

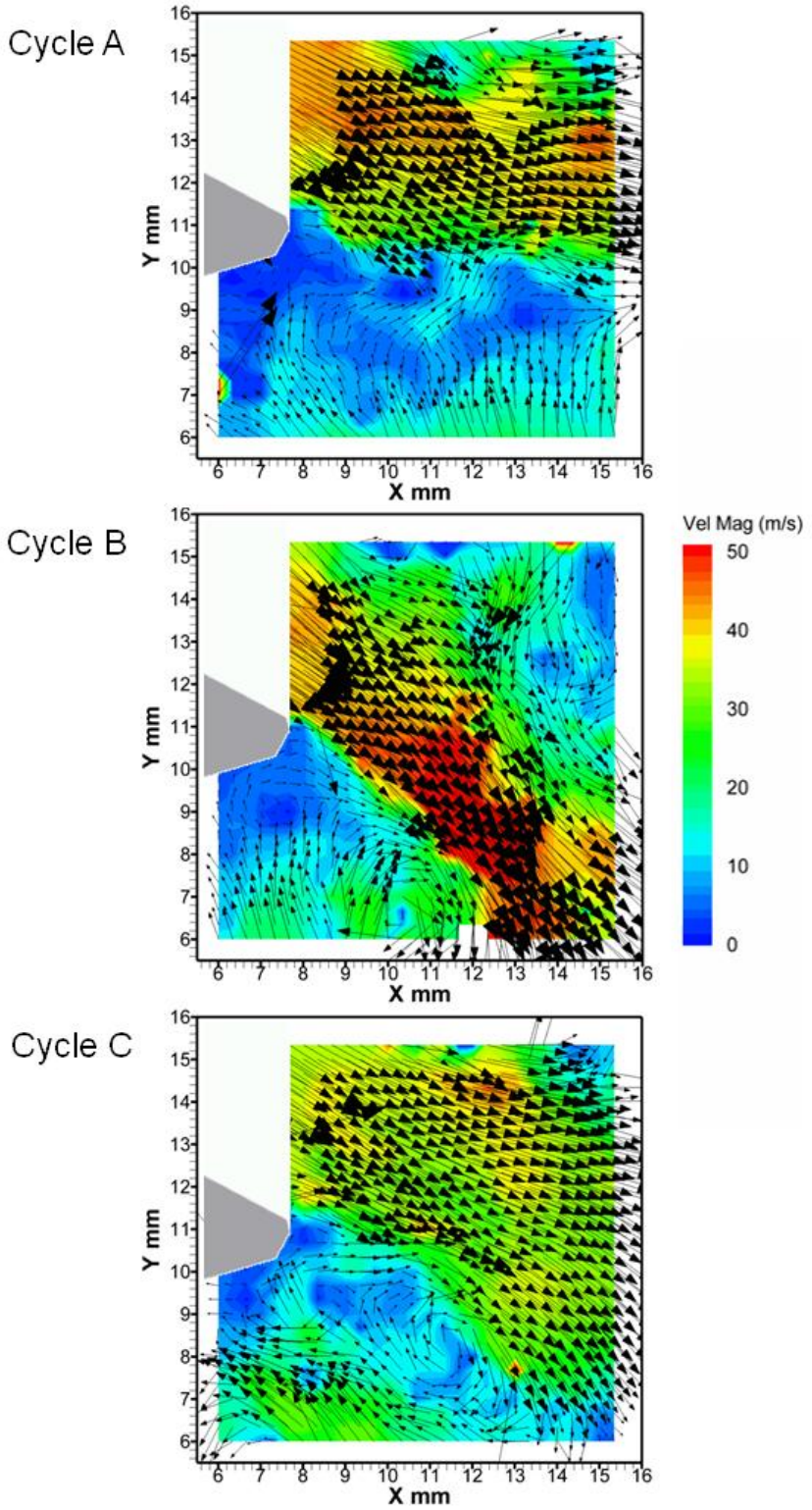

Figure 6.16 - Raw flow fields of a plane through the intake valve jet for three individual cycles at 91.6° CA ATDC captured with HSDPIV at a rate of 5 kHz

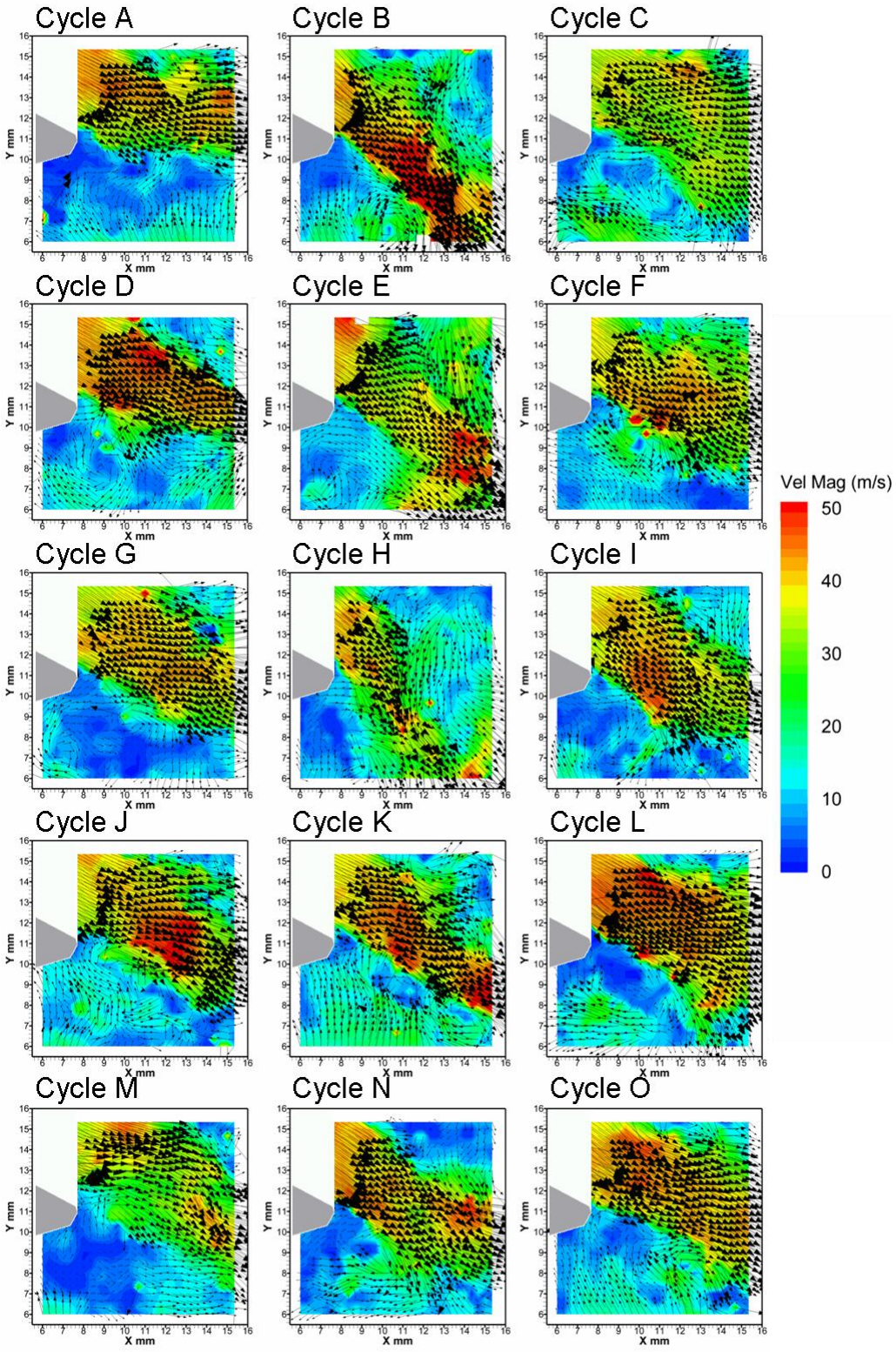

Figure 6.17 - Raw flow fields on a plane through the intake valve jet for fifteen individual cycles at 91.6° CA ATDC captured with HSDPIV at a rate of 5 kHz

Raw velocity fields for the range 91.6° to 98.8° CA ATDC gas exchange are presented in Figure 6.18 for the three individual cycles presented in Figure 6.16. This provides the temporal development of the flow within this plane of the valve jet. An increase in jet velocity is shown in the time sequence presented for cycle A. This corresponds to the increase in velocity seen within the intake runner flow shown in Figure 6.3. The flow field structure is also seen to change during this period. Initially the valve jet is observed to exit high in the frame; however, a 'kink' in the jet is evident. This 'kink' is shown to move out of the frame, and as a result the height at which the jet exits the frame drops. The shear layer is seen to entrain the charge on the outskirts of the jet, where, at 97.0° CA ATDC a vortex is seen to be forming underneath the jet due to an area with opposite flow direction. This vortex is shown to travel with the valve jet and as a result has partly moved out of the frame at 98.8° CA ATDC. The vortex does, however, appear to have lifted the point at which the jet leaves the frame when comparing this crank angle to the previous one. Cycle B has already been shown to have different characteristics at 91.6° CA ATDC, the development of this cycle also differs over the crank angle rage presented. At 91.6° CA ATDC a vortex underneath the jet was shown, this remains in a similar position until 95.2° CA ATDC. At 97.0° CA ATDC the vortex is shown to have dropped out of the frame with traces of the entrainment of flow into the shear layer still visible. At this point, the jet is shown to have broadened substantially from the previous flow fields presented for this cycle. At 91.6° CA ATDC, cycle C showed a large vortex forming underneath a broad valve jet. By 93.4° CA ATDC this vortex is shown to drop into the bottom right hand corner of the frame. In doing so, the point at which the underside of the jet leaves the image has been forced to rise causing the jet to become narrower. The vortex remains in a similar position until 97.0° CA ATDC but at 98.8° CA ATDC it is seen to have progressed with the jet moving mostly out of the frame. The flow underneath the valve in the bottom left hand quadrant of the flow fields is also seen to vary across the cycles shown. Cycles A and C display upward flows moving from right to left; at 98.8° CA ATDC in cycle A this characteristic has developed into a counter-clockwise rotation. Cycle B displays comparatively low flow velocities underneath the intake valve, especially later in the time sequence.

The same three cycles are presented for the crank angle range 142.0° to 149.2° CA ATDC in Figure 6.19. The flow fields displayed have changed significantly during the 43.2° CA since those data presented in Figure 6.18. The velocity magnitude of the flow has reduced to *circa* 20 $m.s^{-1}$, therefore reducing the magnitude of the shear between the jet flow and the in cylinder flow. The valve has opened further giving an increased annulus area available for the flow to pass into the cylinder. This acts to reduce the flow velocity for a fixed flow feeding the ports; however, in this case the main cause of this velocity magnitude reduction is the drop in velocity within the intake runner as shown in Figure 6.7. There are still visible cyclic variations between the three cycles presented. At 142.0° CA ATDC, cycles A and C show both narrower and lower velocity flow than cycle B. The angle of the flows also vary between these three cycles, the jet shown for cycle A exits lower than either cycle B or C. In all cases the flow underneath the jet is seen to move from left to right as it is entrained in to the shear layer. Due to cycles A and C displaying a narrower jet, flow entrainment in the region above can also be seen in the image. As the cycles progress from 142.0° to 149.2° CA ATDC temporal variations are shown to occur. At 143.8° CA ATDC, cycle A shows an region with flow magnitude greater than 15 $m.s^{-1}$ leaving the valve, indicating a velocity pulse in the jet flow. This velocity pulse is further highlighted at 145.6° CA ATDC by a slight trough in velocity which follows, visible in the valve jet at approximately X = 11 mm. This characteristic is shown to travel with the jet and can be seen at *circa* X = 14 mm for 147.4° CA ATDC. In the final image of the sequence the low velocity region is leaving the frame. Over the course of the cycle the jet is shown to become broader. Cycles B and C show similar trends as the velocity leaving the valve decreases and the high velocity region can be seen to progress out of the image frames with time.

The valve jet flows are slowing at his point in the cycle as the piston is slowing and the driving inertia within the intake runner is at a low due to the timing of the pressure pulses. As the cycle has progressed, the reduction of jet velocity and increase in in-cylinder velocity means that the jet flow is less dominant. The establishing in-cylinder flow structures can have a greater influence on the jet flow behaviours and *vice versa*. This leads to greater flow instabilities as the variations in the flow on either side of the boundary interact with one another. This is shown clearly in cycle C, between 143.8°

and 147.4° CA ATDC. At 143.8° CA, the flow underneath the valve is seen to be approaching normal to the jet. The shear caused by the jet flow steers this flow but since the velocities and hence inertia are close the jet is effected by the in-cylinder flow and can be seen to have been deflected.

A further time sequence from 179.8° to 187.0° CA ATDC for these three cycles is shown in Figure 6.20. The piston has reached BDC and is therefore not drawing fresh air into the cylinder. Any flow into the cylinder is due to inertia and pressure pulses. At 179.8° CA ATDC, all three cycles show a jet flow leaving the valve. Cycle A displays the edge of a recirculation within the cylinder, this appears to entrain an increasingly weak jet flow. The flow field presented for cycle B at 179.8° CA ATDC shows a very slow flow underneath the valve jet, however, a significant flow approaching from above, and normal to, the jet is visible. At 181.6° CA ATDC this flow structure has acted to deflect the valve jet. At 179.8° CA, cycle C shows a broader jet with a higher velocity than the other two cycles. By 187.0° CA ATDC even though the valve jet is shown to have stopped for both cycles A and B it is still visible in cycle C.

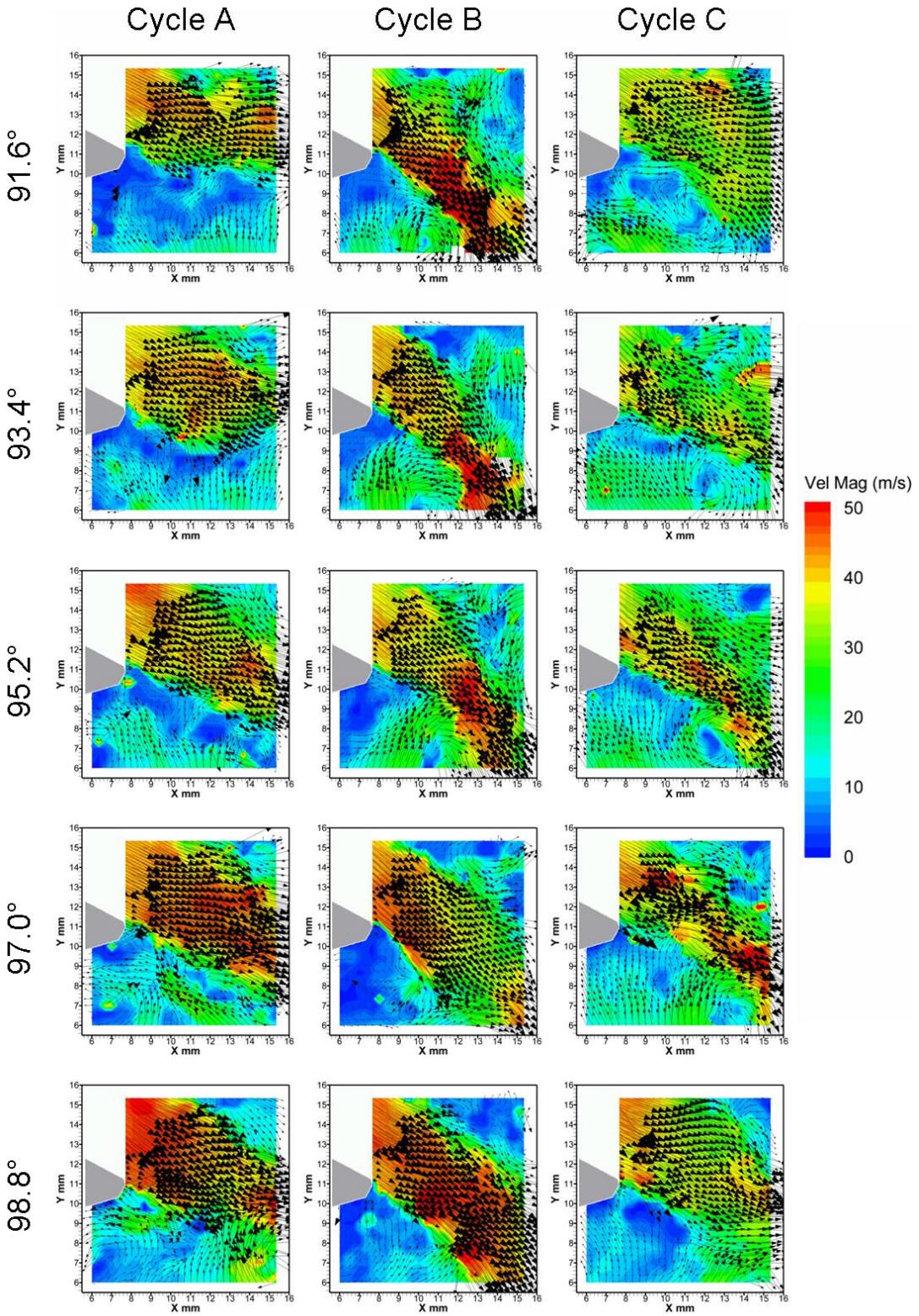

Figure 6.18 - Raw flow fields of a plane through the intake valve jet for three individual cycles from 91.6° to 98.8° CA ATDC captured with HSDPIV at a rate of 5 kHz

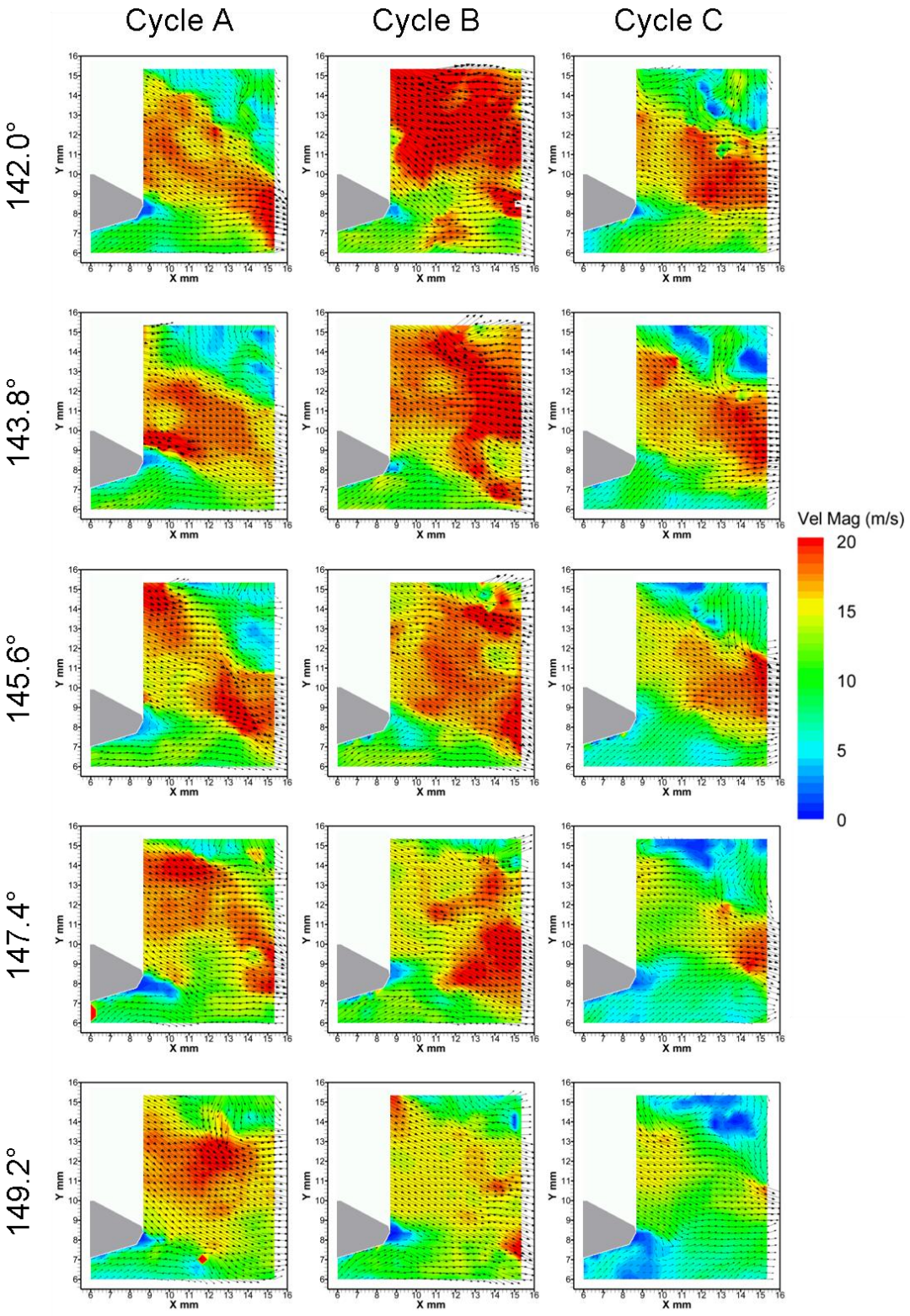

Figure 6.19 - Raw flow fields of a plane through the intake valve jet for three individual cycles from 142.0° to 149.2° CA ATDC captured with HSDPIV at a rate of 5 kHz

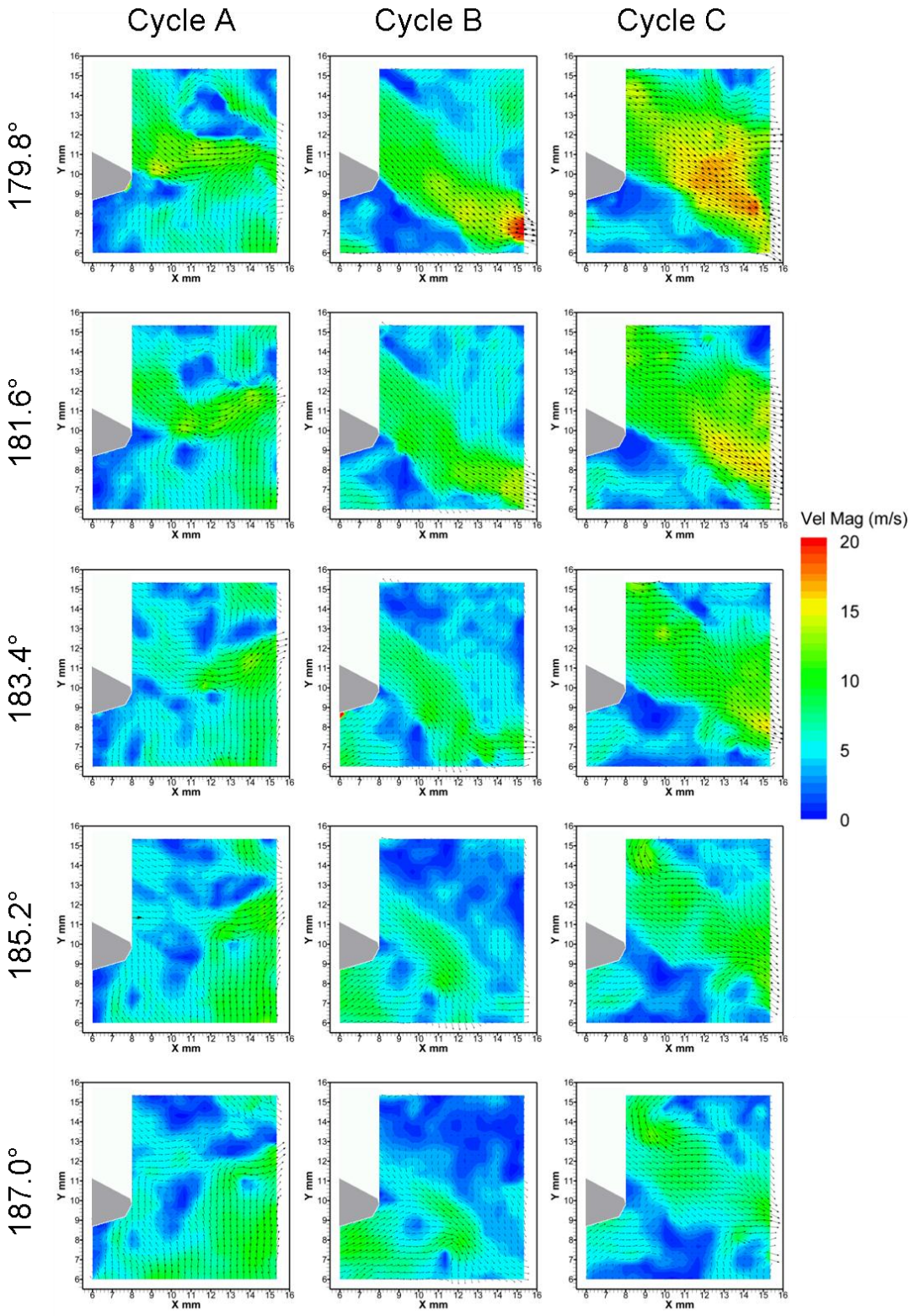

Figure 6.20 - Raw flow fields of a plane through the intake valve jet for three individual cycles from 179.8° to 187.0° CA ATDC captured with HSDPIV at a rate of 5 kHz

The valve jet has been shown to be highly turbulent with substantial high frequency spatial and temporal variations. When the momentum within the valve jet is high compared to the in-cylinder motions, the jet's characteristics affect the surrounding in-cylinder flow field. Therefore, to study large scale low frequency cyclic variations in the jet, such as angle, width and velocity, and their likely impact on in-cylinder flow motion it is important understand the way that this intake valve jet behaves in a low frequency manner. During this period of high jet momentum, there is also a high level of shear between the jet flow and motions within the cylinder. This shear in the flow is significant in generating the high level of spatial and temporal fluctuations experienced; these can be further investigated by studying the high frequency components of the flow fields.

Errors in PIV measurements were discussed in Chapter 3. A major source of error was identified to be shear within the flow fields, a measure of the resulting random error caused by shear within the flow was given in Equation 3.21. The calculated random errors for the intake valve jet flow presented in Figure 6.18 to Figure 6.20 are displayed in Figure 6.21 to Figure 6.23. The region inside the main body of the valve jet flow, where there is little shear and the PIV has been optimised to capture these flow velocities, is shown in Figure 6.21 to have a random error below 5%. Whereas, the region outside of this jet, specifically in the shear layer, is shown to have relatively much larger random errors.

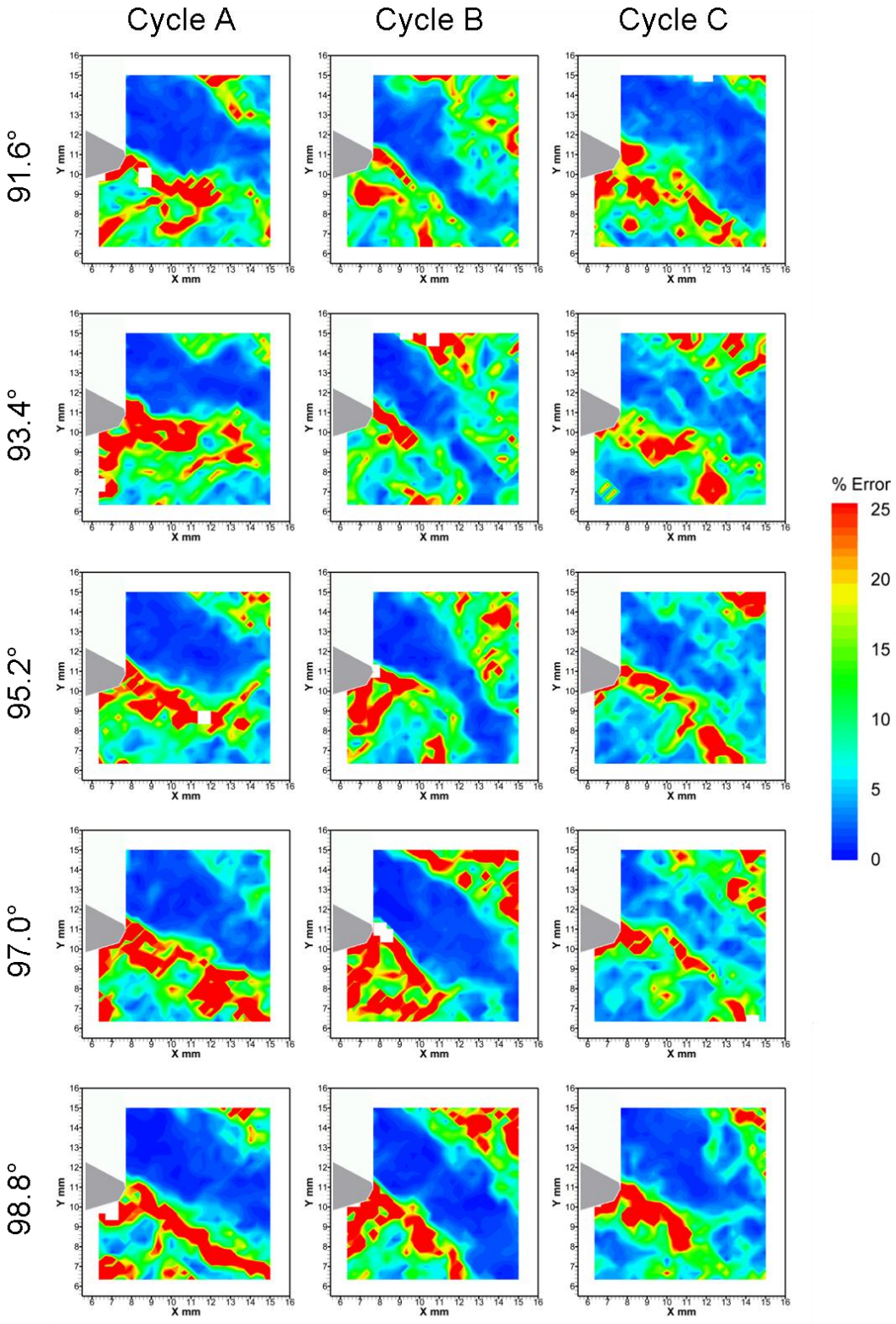

Figure 6.21 – Random error calculation (Equation 3.21) on a plane through the intake valve jet for three individual cycles from 91.6° to 98.8° CA ATDC captured with HSDPIV at a rate of 5 kHz

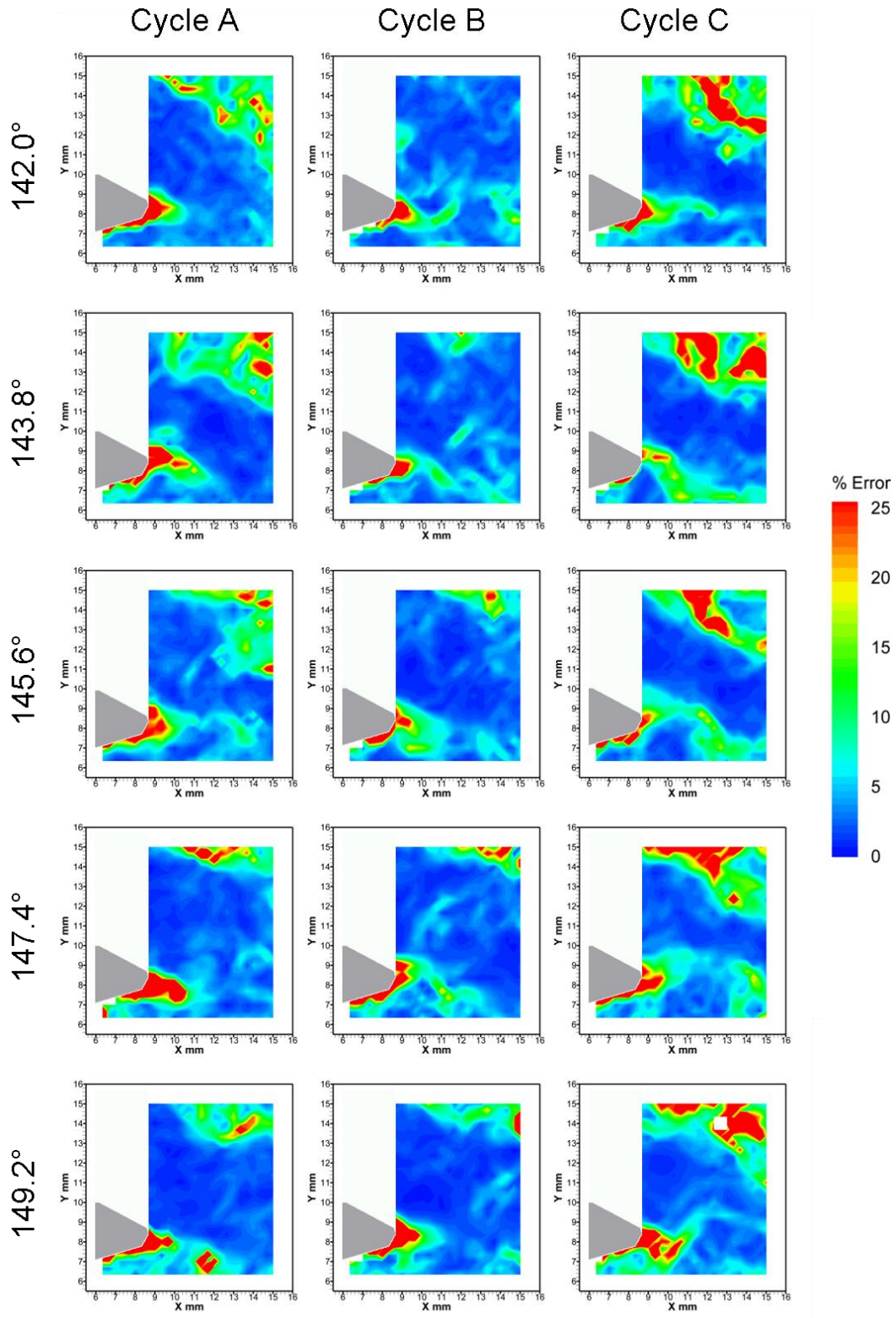

Figure 6.22 - Random error calculation (Equation 3.21) on a plane through the intake valve jet for three individual cycles from 142.0° to 149.2° CA ATDC captured with HSDPIV at a rate of 5 kHz

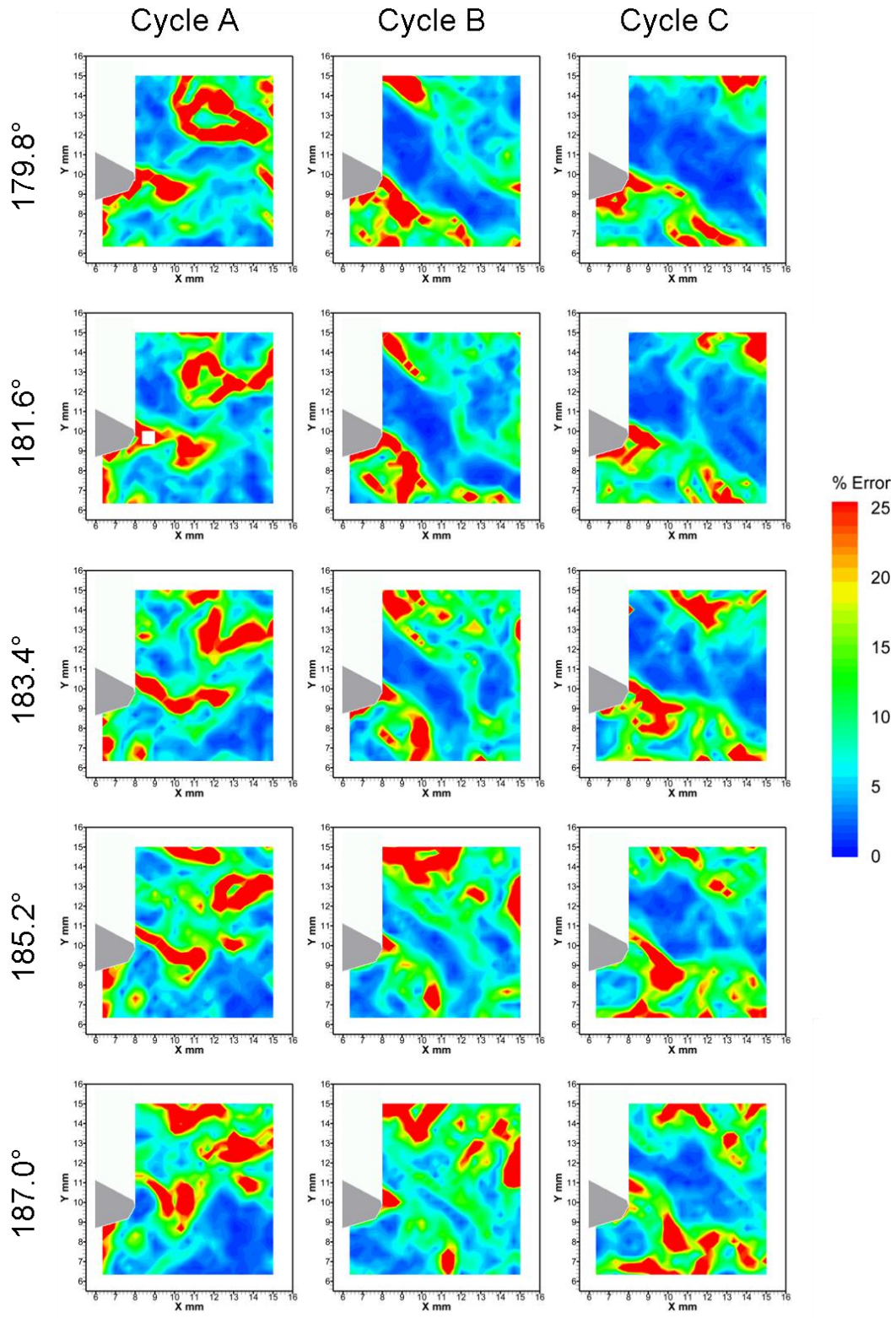

Figure 6.23 - Random error calculation (Equation 3.21) on a plane through the intake valve jet for three individual cycles from 179.8° to 187.0° CA ATDC captured with HSDPIV at a rate of 5 kHz

Using the technique presented in Chapter 5, the valve jet flow fields were filtered into their high and low frequency components using a cut-off frequency of 280 Hz. The resulting low frequency flow fields are presented in Figure 6.24 for the range 91.6° to 98.8° CA ATDC for the three cycles presented previously. At 91.6° CA ATDC, the characteristics visible in the bulk flow of the raw velocity fields, previously presented in Figure 6.18, can be identified. Cycle A shows a jet which exits the frame higher than the other two cycles shown, it also has no visible recirculation underneath it. Cycle B, in contrast shows the jet exiting low in the frame, with a clear recirculation underneath. The flow field presented for cycle C also shows a recirculation underneath the jet; however, the angle of the jet differs. The cut-off frequency selected highlights the trend in bulk flow and as a result shown less temporal variation over the crank angle range presented when compared to the raw data. A drop in the height at which the jet exits the frame can be seen in Cycle A. In both cycles B and C, the recirculation is shown to move away from the valve; however, in theses cycles there is less change in the direction of the valve jet.

The low frequency flow fields for the same three cycles are presented in Figure 6.25 for the range 142.0° to 149.2° CA ATDC. Due to the highly fluctuating nature of the valve jet flow and the choice of cut-off frequency used to decompose the flow field, the shear layer and therefore boundary of the jet is blurred. These images show subtle variations in the velocity direction within the jet. At 142.0°CA the upper boundary of the jet flow is identifiable in both cycle A and C, since a boundary region is discernable, this is less so in cycle B. However, by comparing this figure with the corresponding raw data presented in Figure 6.19 the characteristics of the low frequency flow fields can be identified as would be expected. Figure 6.25 also highlights variations in the velocity distribution within the jets; however, all three cycles show a bias for higher velocities towards the top of the jet. Variation in the flow, external to the valve jet, is also shown giving the low frequency characteristic of the entrainment into the shear layer.

Figure 6.26 shows the low frequency flow fields for the range 179.8° to 187.0° CA ATDC for these three cycles. At 179.8° CA the increasingly weak valve jet is significantly affected by the in-cylinder flows, whilst still having an influence upon

them. Cycle A shows significant upward flow underneath the jet which has deflected the right hand side of it. Deflection is also shown in cycle B where the flow above the jet approaches normal to it, with a resulting downward deflection and narrowing at this point and onwards downstream. The bulk motion characteristics of these fields correlate well with the bulk motion trends identified in Figure 6.20. The choice of cut-off frequency is significant in determining the temporal detail and therefore the influence of characteristics on the low frequency fields. It has been shown that the cut-off frequency selected for this analysis provides a bulk flow which outlines key areas of low frequency variation. This bulk flow field is extracted from the raw data without including substantial amounts of the temporal and spatial fluctuations caused by the high turbulence levels within the valve jet.

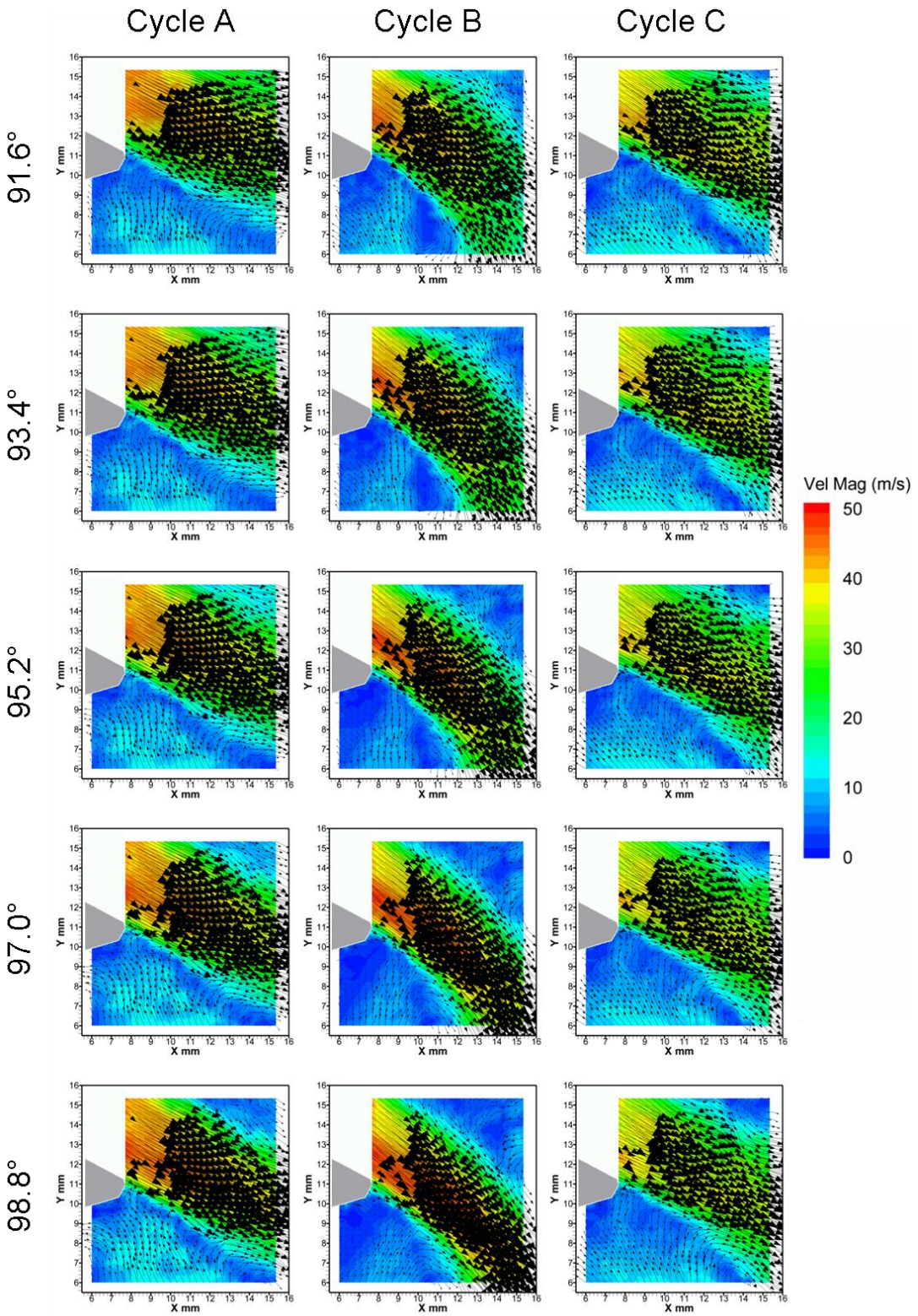

Figure 6.24 – Low frequency flow fields of a plane through the intake valve jet for three individual cycles from 91.6° to 98.8° CA ATDC captured with HSDPIV at a rate of 5 kHz

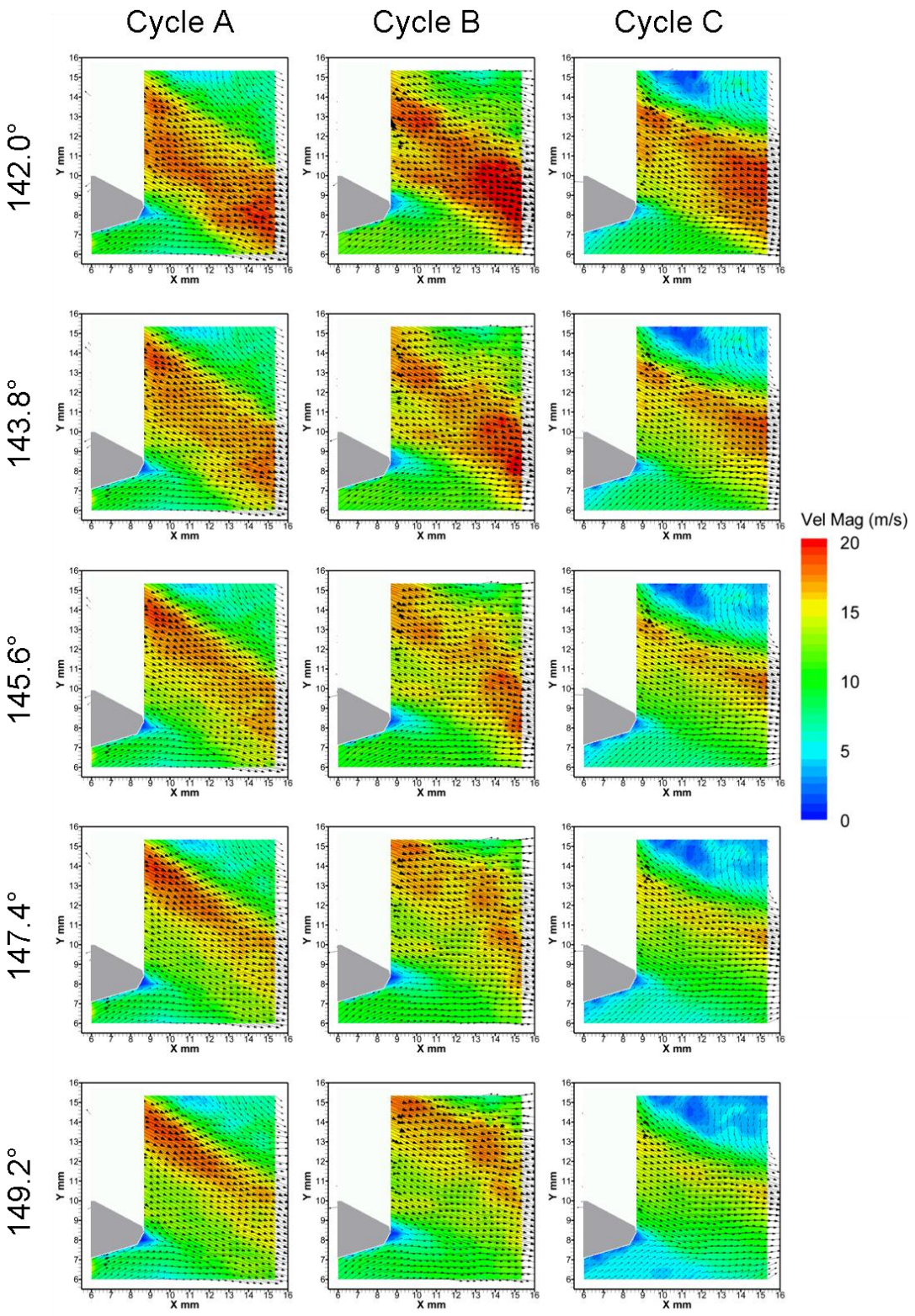

Figure 6.25 – Low frequency flow fields of a plane through the intake valve jet for three individual cycles from 142° to 149.2° CA ATDC captured with HSDPIV at a rate of 5 kHz

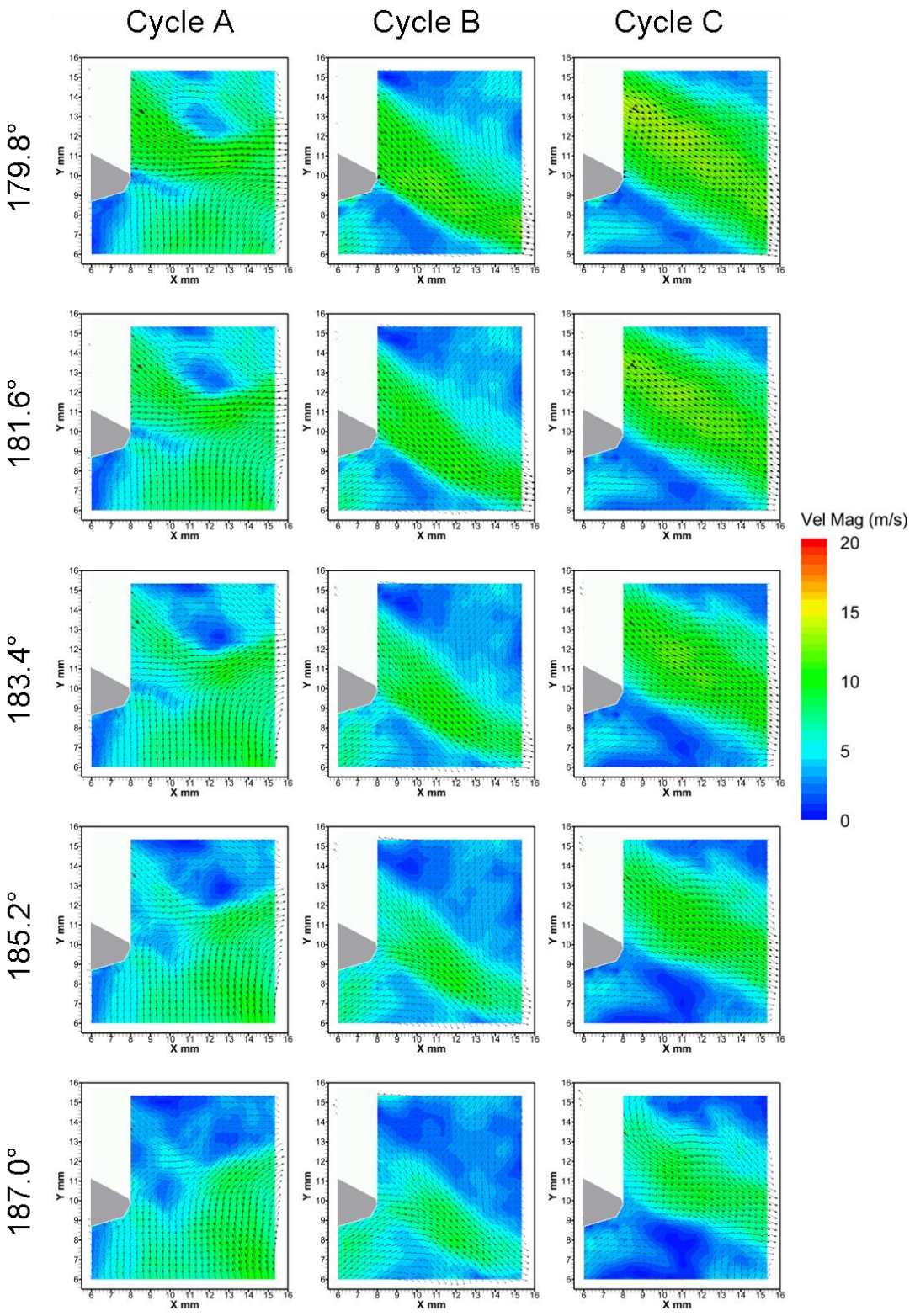

Figure 6.26 - Low frequency flow fields of a plane through the intake valve jet for three individual cycles from 179.8° to 187.0° CA ATDC captured with HSDPIV at a rate of 5 kHz

The calculation of a mean low frequency flow allows the subsequent calculation of a low frequency cyclic variation term as described in Equation 2.21. This calculation provides a fluctuation component which describes how the bulk flow characteristics of a cycle differ from the mean low frequency flow field. The mean low frequency flow fields for the three crank angle ranges previously presented are shown in Figure 6.27 to Figure 6.29. The fields presented in Figure 6.27 cover the crank angle range 91.6° to 100.6° CA ATDC intake. The presented images indicate insignificant variation during this time period. A high velocity jet flow is shown with a peak velocity over 40 $m.s^{-1}$. This is seen to decay substantially with increased distance from the central core of the jet. Also, as the jet penetrates further into the cylinder the velocity is shown to decay. Underneath the intake valve there is an area of low velocity visible which shows some entrainment into the jet due to the shear layer created. Considering that the piston speed is around its peak and is almost constant during this period, the stable high energy mean flow entering the cylinder is expected.

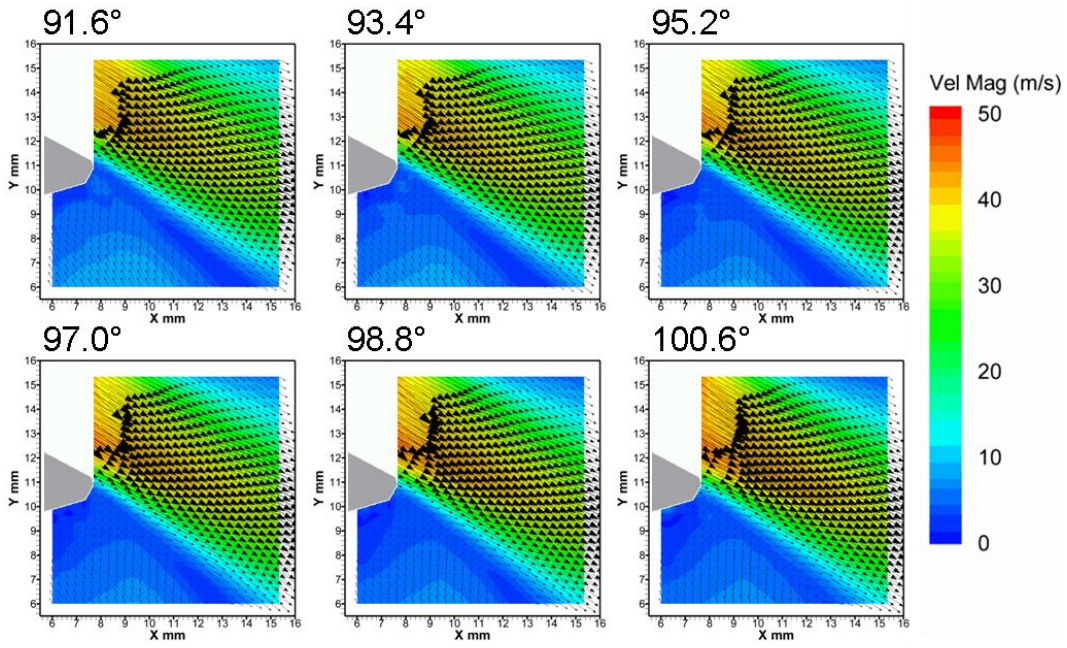

Figure 6.27 – Mean low frequency flow fields of a plane through the intake valve jet from 91.6° to 100.6° CA ATDC captured with HSDPIV at a rate of 5 kHz

Figure 6.28 presents the mean low frequency flow fields, over the range 142.0° to 151.0° CA ATDC intake. This crank angle range covers the period of maximum intake valve opening. However, since the piston speed is slowing as it reaches the bottom of its stroke and the annulus area available for the charge air to enter the cylinder is at its maximum, the jet velocity is substantially lower than shown during the previous period presented in Figure 6.27. Over the duration of the period presented the jet velocity is shown to further reduce; however, its shape is not seen to vary substantially. The low frequency flow fields for a similar crank angle range are shown in Figure 6.25, these display little resemblance to the mean low frequency flows shown here. Therefore, this indicates that there are significant cycle to cycle variations in the bulk flow entering the cylinder through the intake valves at this point in the cycle.

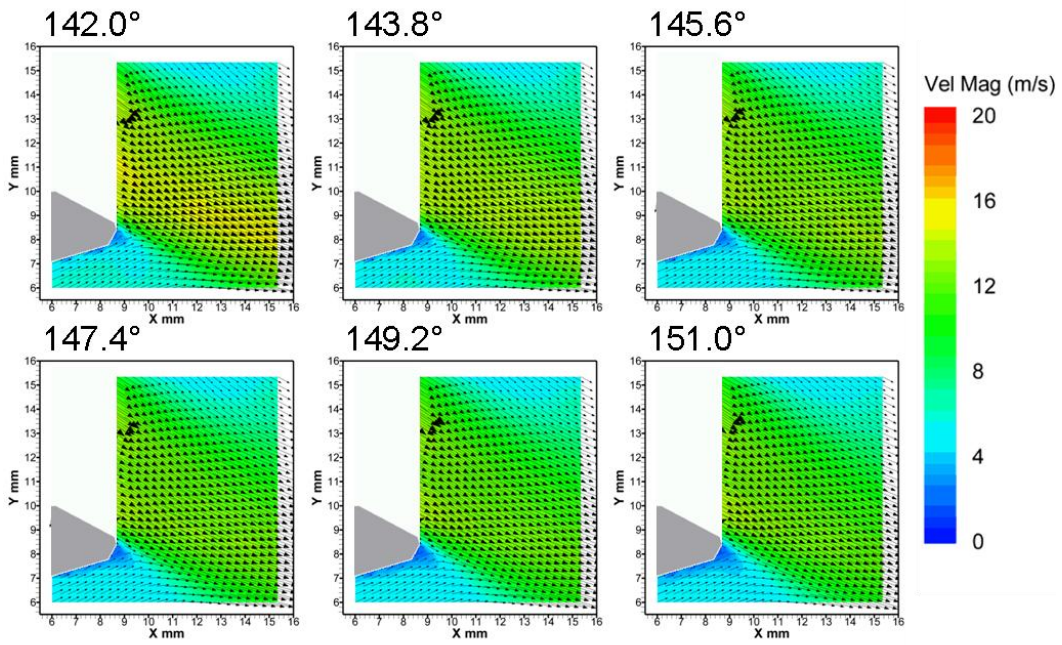

Figure 6.28 – Mean low frequency flow fields of a plane through the intake valve jet from 142.0° to 151.0° CA ATDC captured with HSDPIV at a rate of 5 kHz

The mean low frequency flow fields for the range 179.8° to 188.8° CA ATDC intake are presented in Figure 6.29. This crank angle period shows the valve jet stagnating since BDC is passed, the piston has come to rest and is slowly starting its return up the cylinder for the compression stroke. It is evident that the inertia within the intake flow

continues to drive flow through the intake valve until *circa* 7° CA ABDC. However, the flow velocity rapidly decays with the established clockwise recirculating in-cylinder flow motion becoming dominant within the field of view.

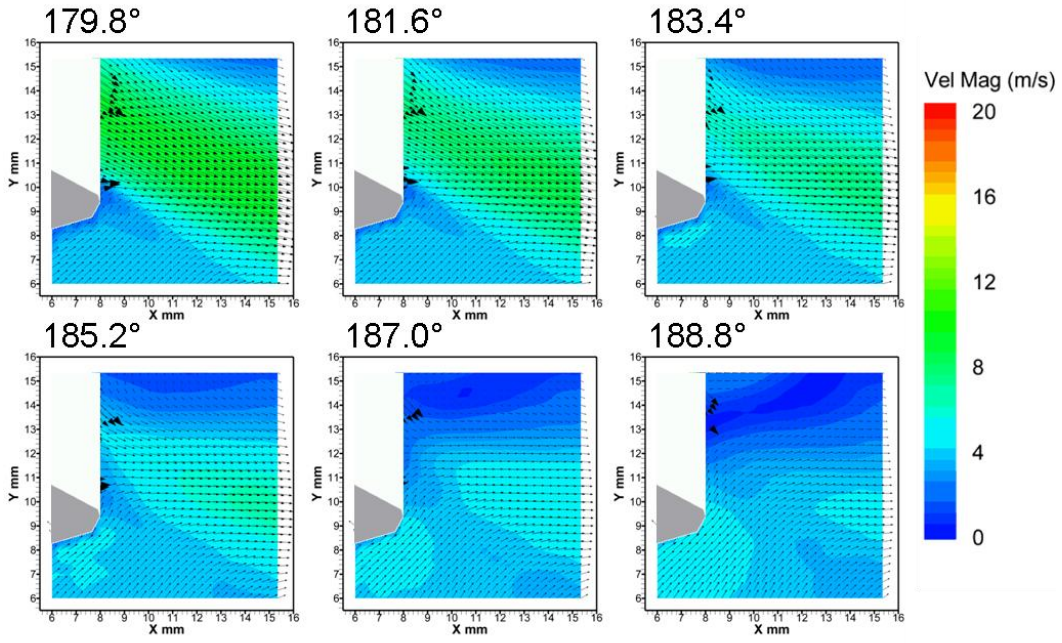

Figure 6.29 – Mean low frequency flow fields of a plane through the intake valve jet from 179.8° to 188.8° CA ATDC captured with HSDPIV at a rate of 5 kHz

Figure 6.30 to Figure 6.32 show velocity magnitude contours of low frequency cyclic variation (Equation 2.21) for the three cycles A, B and C, previously discussed within this section. These images show the velocity magnitude of the difference between the low frequency flow field for a specific engine cycle and the mean low frequency flow field. The images have been plotted with the low frequency velocity vectors overlaid so they highlight areas of high variation and show the structure of the cycle's bulk flow at this point. The range 91.6° to 98.8° CA ATDC is displayed in Figure 6.30. This shows the low frequency flows for the three cycles to vary significantly relative to the mean low frequency flow field generated by the 100 captured cycles. The cycles show relatively low variation in the core of the jet as it exits the valve annulus; however, as highlighted more prominently in cycle B, this increases towards the edge of the jet. Cycle A initially shows a high variation above the jet but as the cycle progresses to

98.8° CA, this decays, and regions of high variation appear underneath the jet. Figure 6.31 shows low frequency cyclic variation for the range 142.0° to 149.2° CA ATDC. Cycle A shows the upper portion of the jet differs from the mean in the order of 5 $m.s^{-1}$; a similar trend is shown in cycle C. In all cases, across the crank angle ranges presented (Figure 6.30 to Figure 6.32), regions of high variation, greater than 5 $m.s^{-1}$, are observed. As the magnitude of the variation rather than the variation vector has been plotted, it allows structures leading to this variation to be visible and highlights that none of these cycles' low frequency bulk flow behaviours are close to being explained using the mean low frequency cycle.

Figure 6.33 to Figure 6.35 show the *rms* low frequency cyclic variation from the valve jet over the range 91.6° to 188.8° CA ATDC. The range 91.6° to 100.6° CA ATDC is considered in Figure 6.33. In these images the variable zone in the jet shear layer clearly seen as a region of high velocity variation. The core of the jet initially shows lower variation; however this is still *circa* 3 to 4 $m.s^{-1}$, which is approximately 10% of the mean flow field. As the jet diffuses the variable zone expands, although over the sequence of images displayed, its area decreases. As the cycle progresses, into the range 142.0° to 151.0° CA ATDC shown in Figure 6.34, the mean velocity of the jet has decayed (see Figure 6.28) and with it a region of high variation relative to the shear zone beneath the jet can be seen. In Figure 6.35, as the compression stroke begins and the intake flow subsides, the *rms* of variation diminishes into a more regular flow throughout the imaged region.

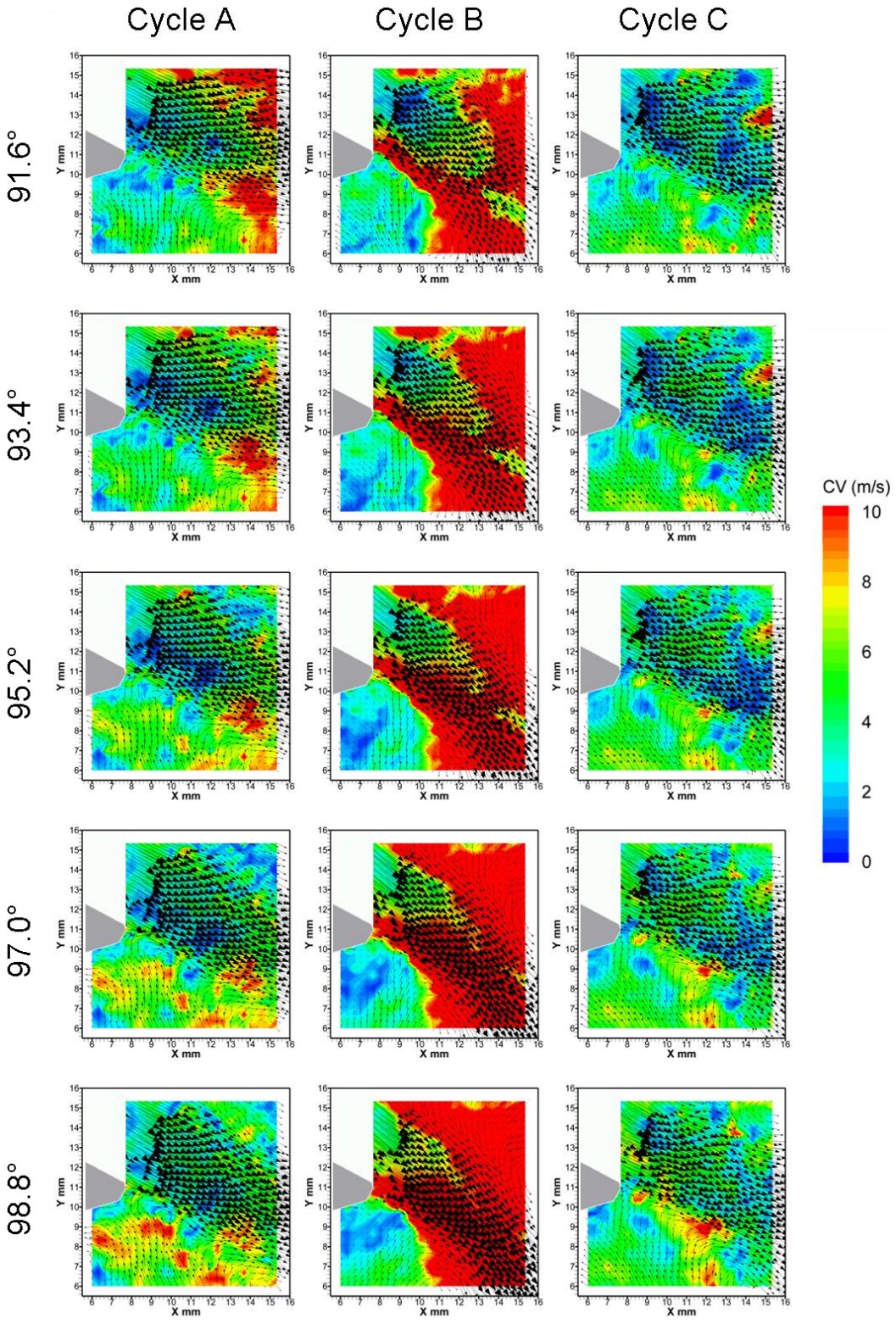

Figure 6.30 – Low frequency cyclic variation of the intake valve jet from 91.6° to 98.8° CA ATDC captured with HSDPIV at a rate of 5 kHz (overlaid are low frequency flow vectors)

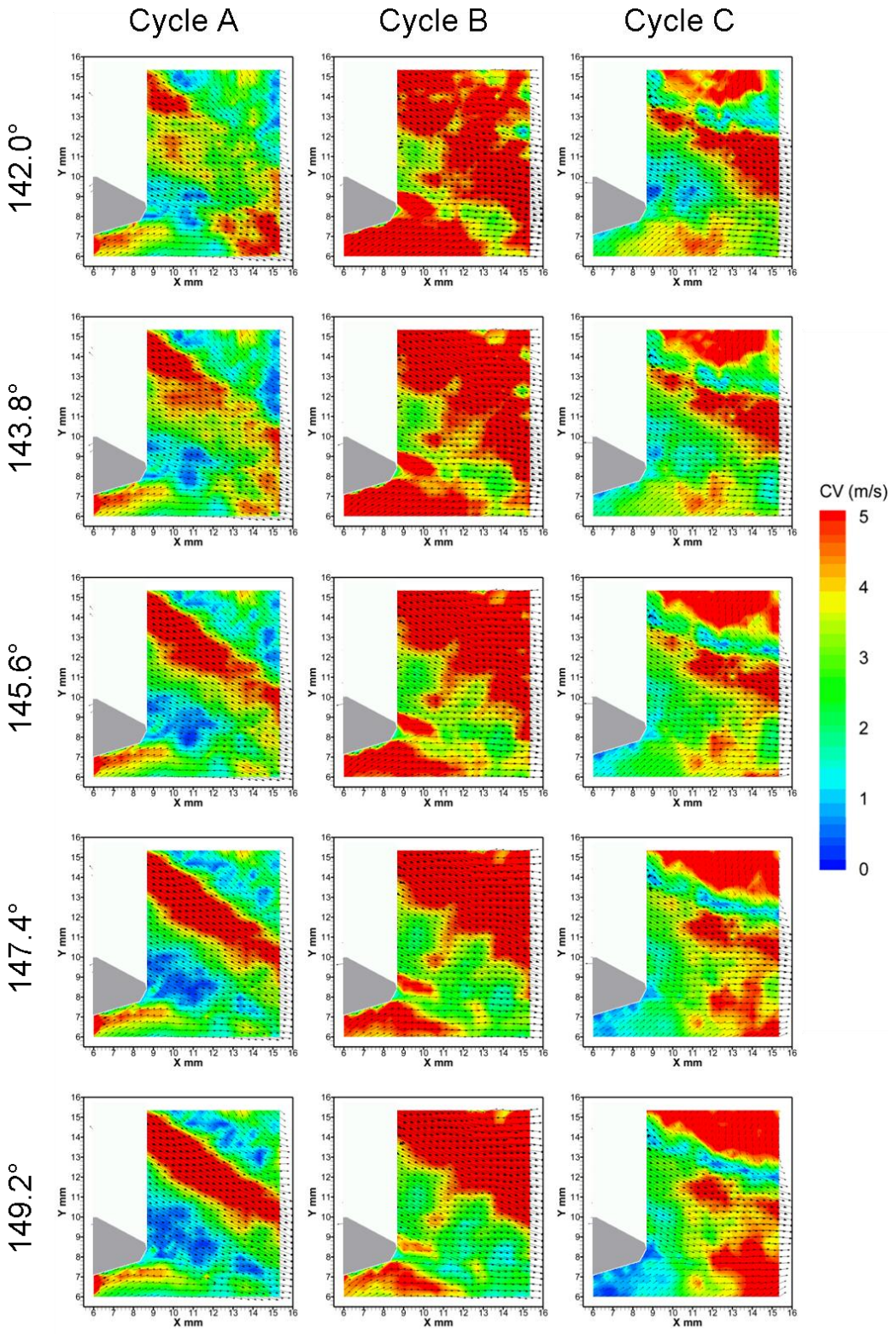

Figure 6.31 – Low frequency cyclic variation of the intake valve jet from 142° to 149.2° CA ATDC captured with HSDPIV at a rate of 5 kHz

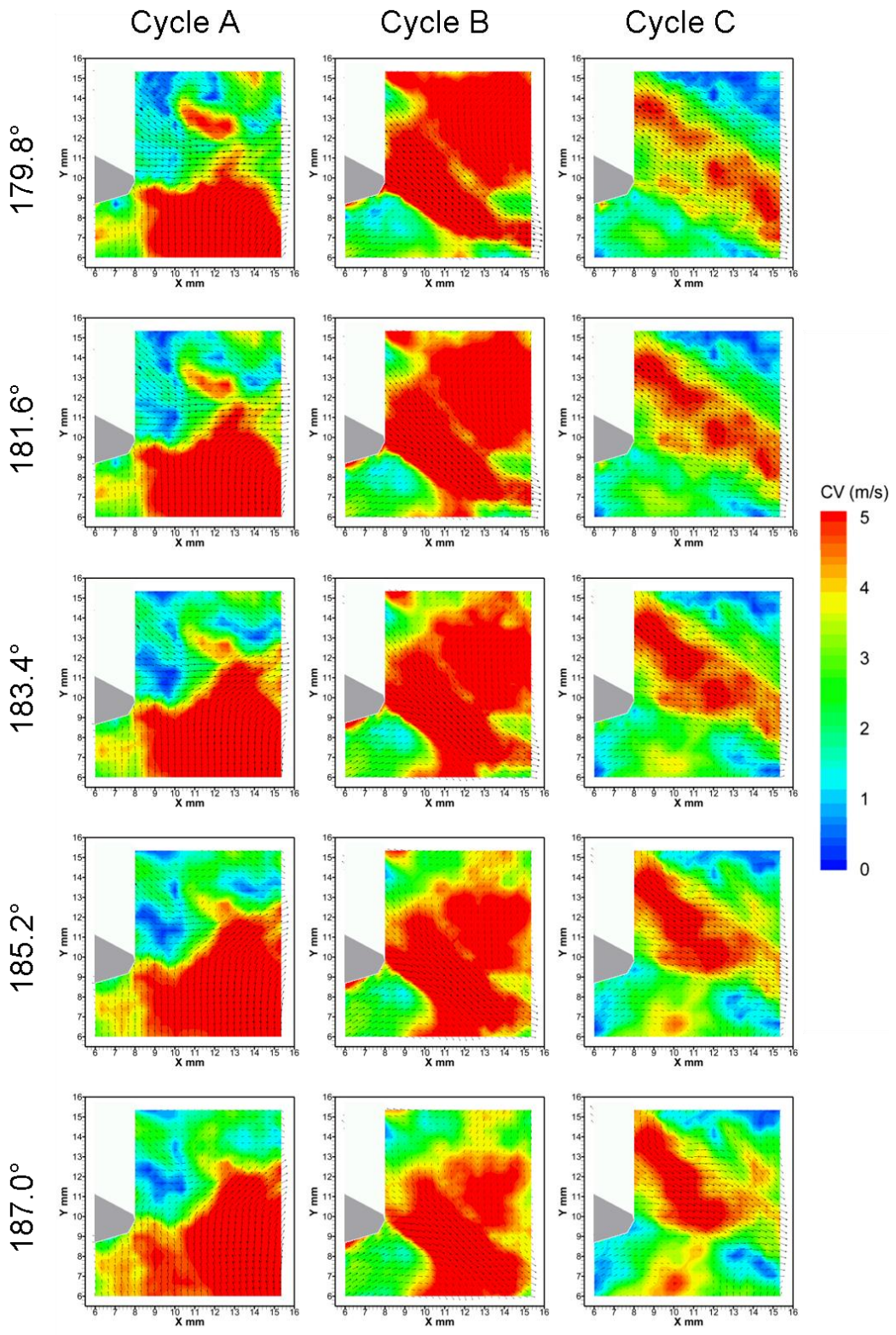

Figure 6.32 – Low frequency cyclic variation of the intake valve jet from 179.8° to 187.0° CA ATDC captured with HSDPIV at a rate of 5 kHz

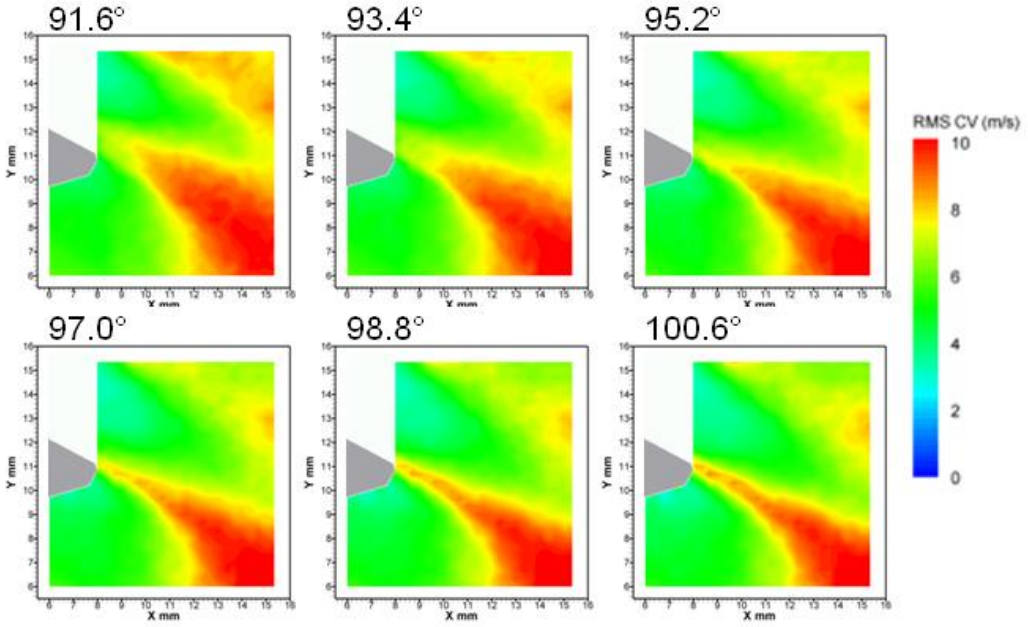

Figure 6.33 - *rms* of 100 low frequency cyclic variation flow fields of the intake valve jet from 91.6° to 100.6° CA ATDC captured with HSDPIV at a rate of 5 kHz

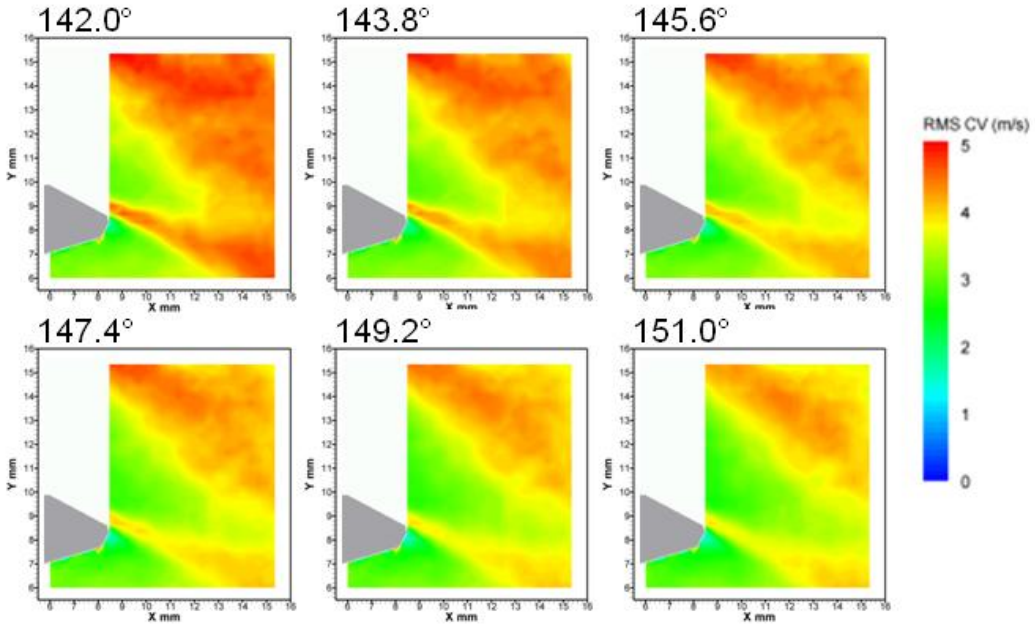

Figure 6.34 - *rms* of 100 low frequency cyclic variation flow fields of the intake valve jet from 142.0° to 151.0° CA ATDC captured with HSDPIV at a rate of 5 kHz

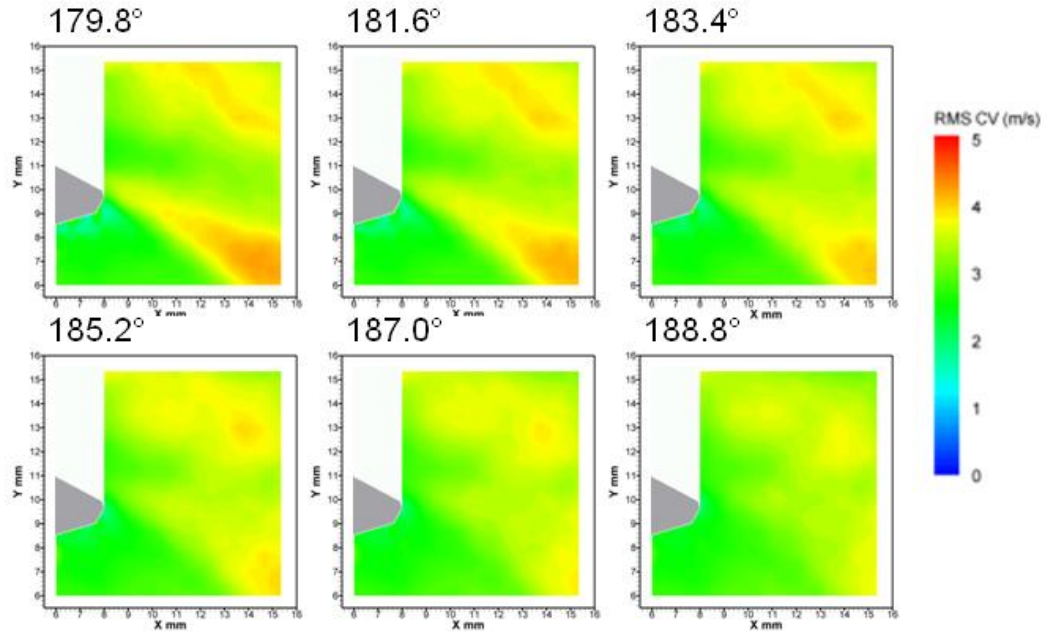

Figure 6.35 - *rms* of 100 low frequency cyclic variation flow fields of the intake valve jet from 179.8° to 188.8° CA ATDC captured with HSDPIV at a rate of 5 kHz

The low frequency characteristics of the plane through the intake valve jet have been discussed within the previous figures. The intake valve jet is, however, highly turbulent and experiences high frequency spatial and temporal variations. Therefore, it is also necessary to discuss the remaining high frequency component of the intake valve jet as described in Equation 2.20. The high frequency components for the three cycles previously presented are shown in Figure 6.36 to Figure 6.38. The high frequency components for the range 91.6° to 98.8° CA ATDC are displayed in Figure 6.36. An area of low temporal variation is shown to occur in the core of the jet close to the valve exit area. At this location the flow velocity is at its highest within the imaged region, generally greater than 40 $m.s^{-1}$. Identifiable structures exist within these high frequency flow fields, with both cycles B and C displaying vortices underneath the valve jet. In the ranges 142.0° to 149.2° CA and 179.8° to 187.0° CA ATDC the magnitude of the high frequency flow is shown to decay and become more homogeneous across the imaged field, with identifiable eddies still present. Notably, at 143.8° CA cycle C is displaying a vortex just forming around the intake valve lip. This is then seen in the following two frames travelling in the direction of the valve jet.

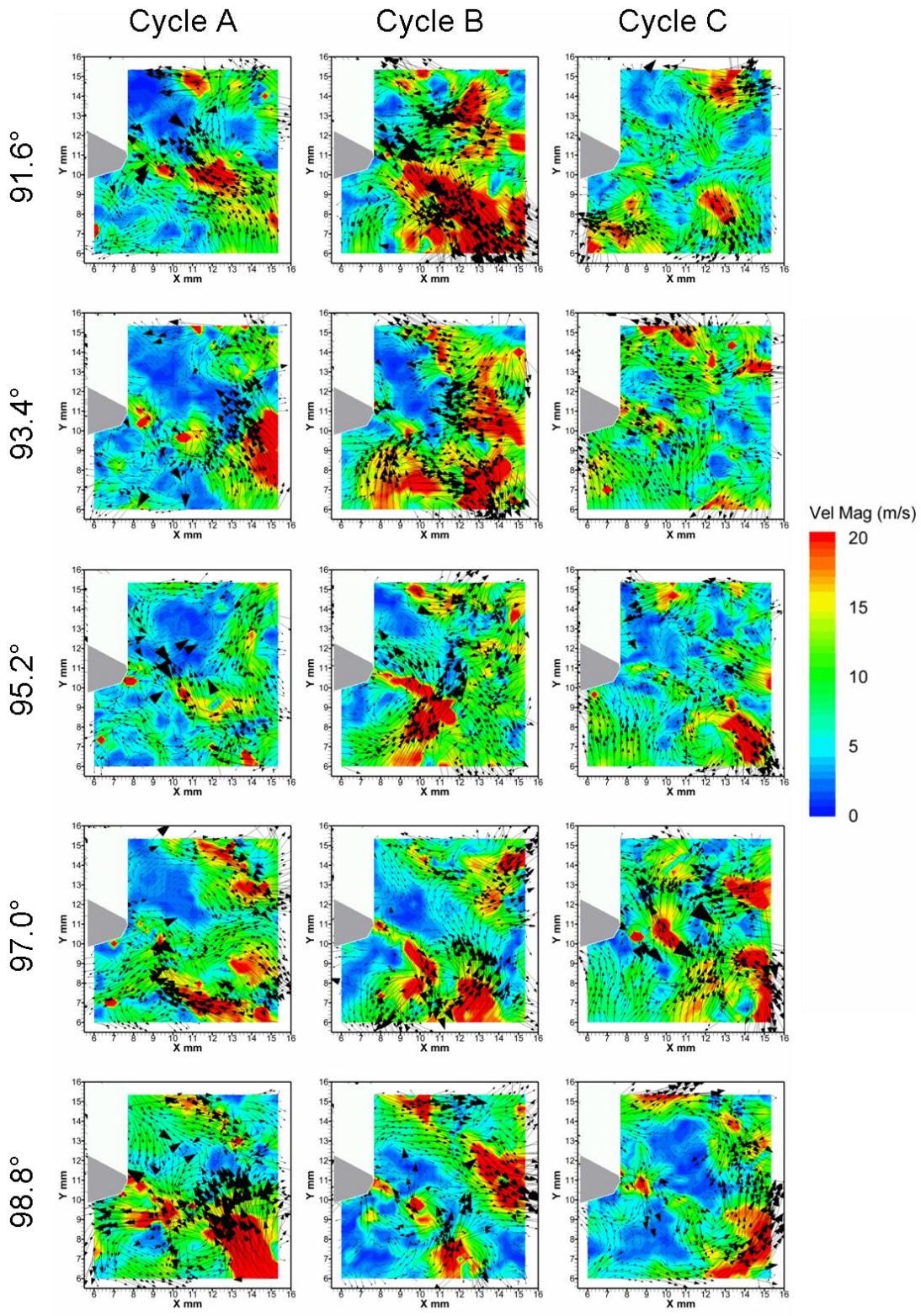

Figure 6.36 – High frequency flow fields of a plane through the intake valve jet for three individual cycles from 91.6° to 98.8° CA ATDC captured with HSDPIV at a rate of 5 kHz

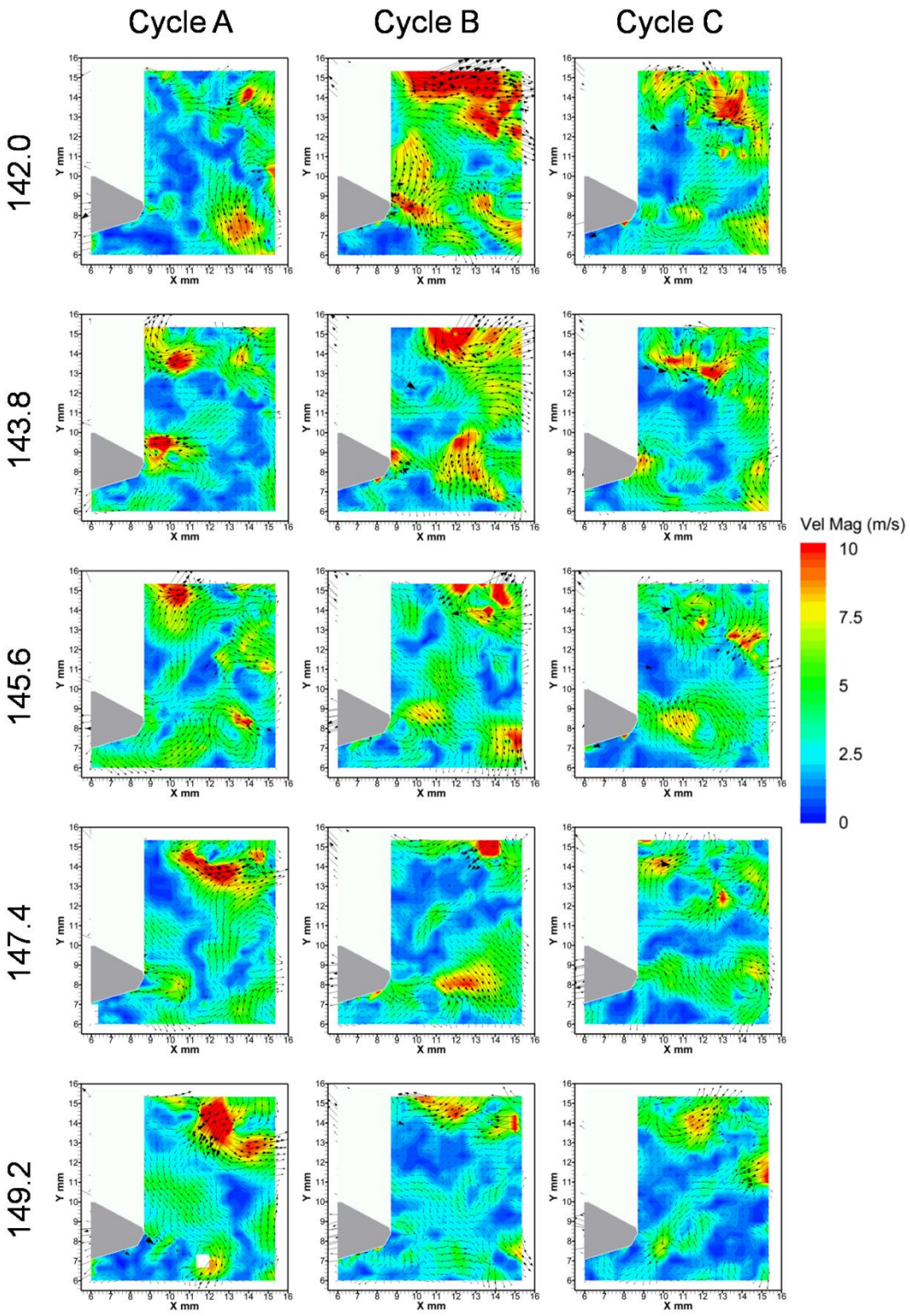

Figure 6.37 – High frequency flow fields of a plane through the intake valve jet for three individual cycles from 142° to 149.2° CA ATDC captured with HSDPIV at a rate of 5 kHz

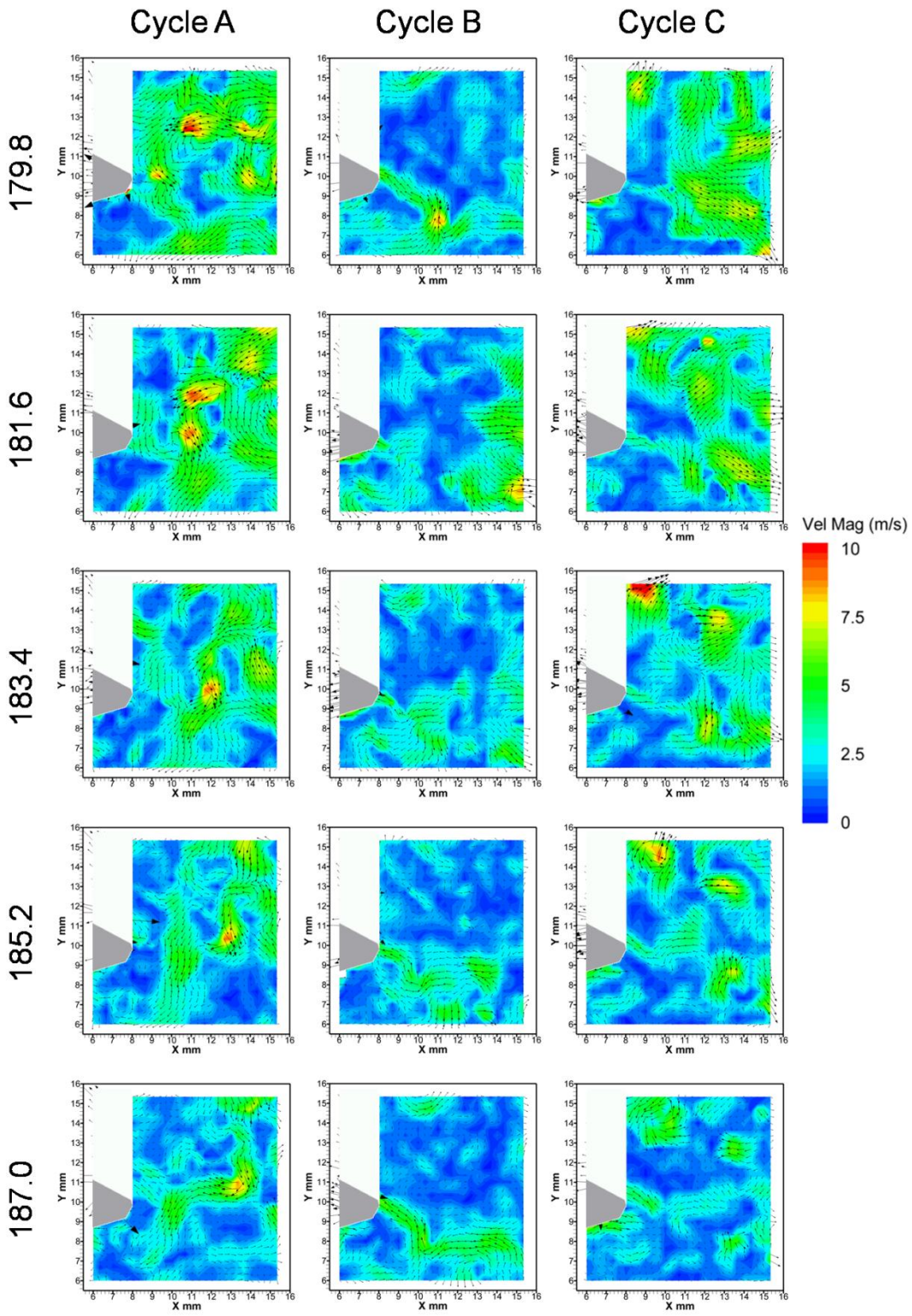

Figure 6.38 - High frequency flow fields of a plane through the intake valve jet for three individual cycles from 179.8° to 187° CA ATDC captured with HSDPIV at a rate of 5 kHz

As discussed in Chapter 5, to investigate cyclic variations in the level of turbulent fluctuations, a measure similar to u' is desired. This is provided by calculating the *rms* of the high frequency components over a spatial or temporal window. Using those high frequency data presented in Figure 6.36 to Figure 6.38 and a temporal window corresponding to the 280 Hz used to filter the raw data into its low and high frequency components, the temporal u' was calculated. In a high velocity jet flow, it is reasonable to expect a u' of *circa* 30% of the flow velocity, this expectation agrees with the calculated u' shown which is close to 20 $m.s^{-1}$.

Figure 6.39 shows u' over the range 91.6° to 98.8° CA ATDC. This highlights that the shear layer between the valve jet and in-cylinder flow is a cause of high turbulence generation since by 98.8° CA, in all three cases, there is a line of high u' both above and below the jet. However, the sizes of these high u' regions differ. Figure 6.40 shows u' over the range 142.0° to 149.2° CA ATDC. The reducing jet velocity has resulted in an overall reduction in u', and across the three cycles this is most prominent underneath the valve jet. This is likely to be due to the emerging relative dominance of the entrained flow and the established bulk flow motion underneath the jet. As the valve jet flow further slows, this decay in u' continues as shown in Figure 6.41.

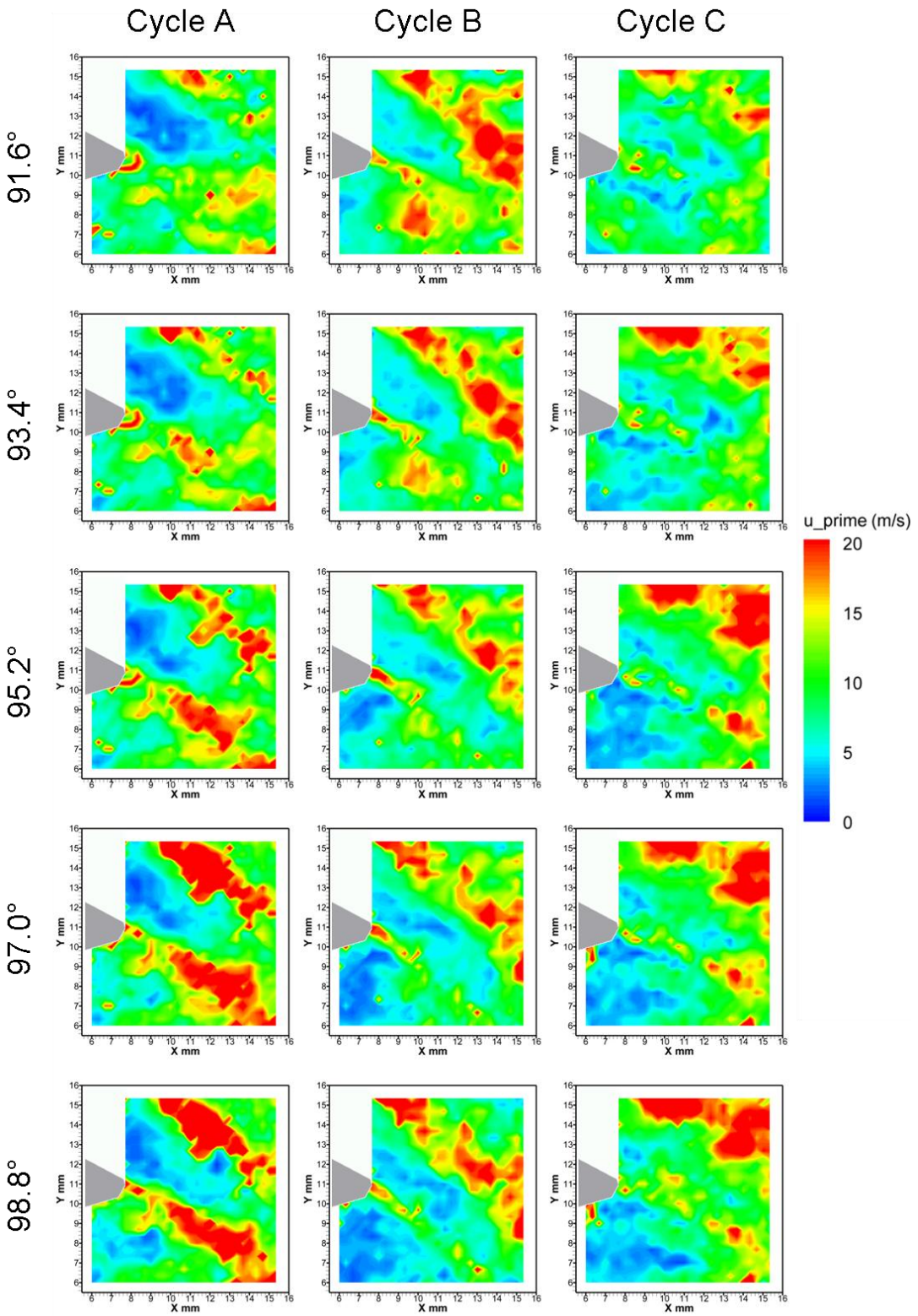

Figure 6.39 – Contour plot of u' on a plane through the intake valve jet for three individual cycles from 91.6° to 98.8° CA ATDC captured with HSDPIV at a rate of 5 kHz

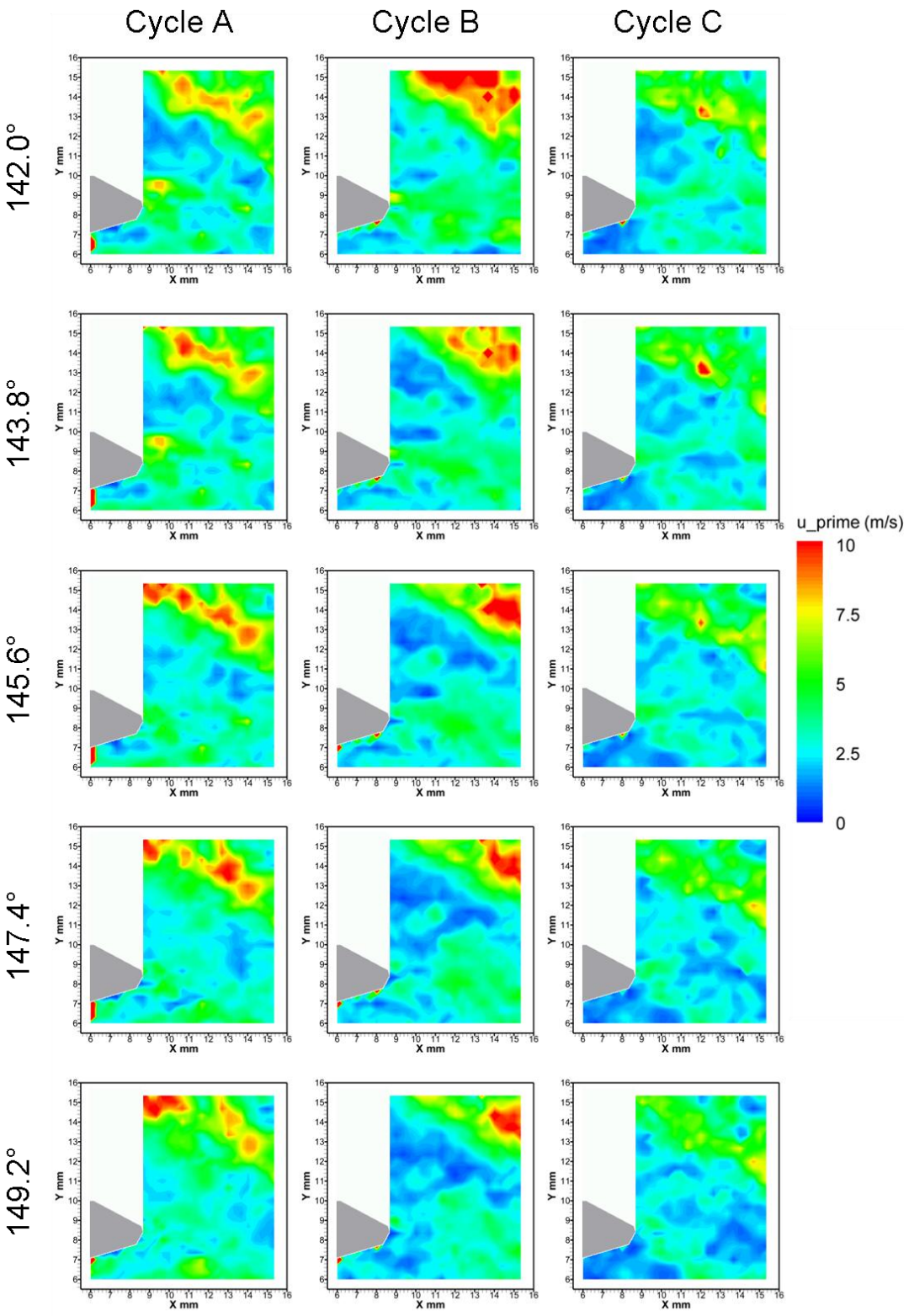

Figure 6.40 – Contour plot of u' on a plane through the intake valve jet for three individual cycles from 142° to 149.2° CA ATDC captured with HSDPIV at a rate of 5 kHz

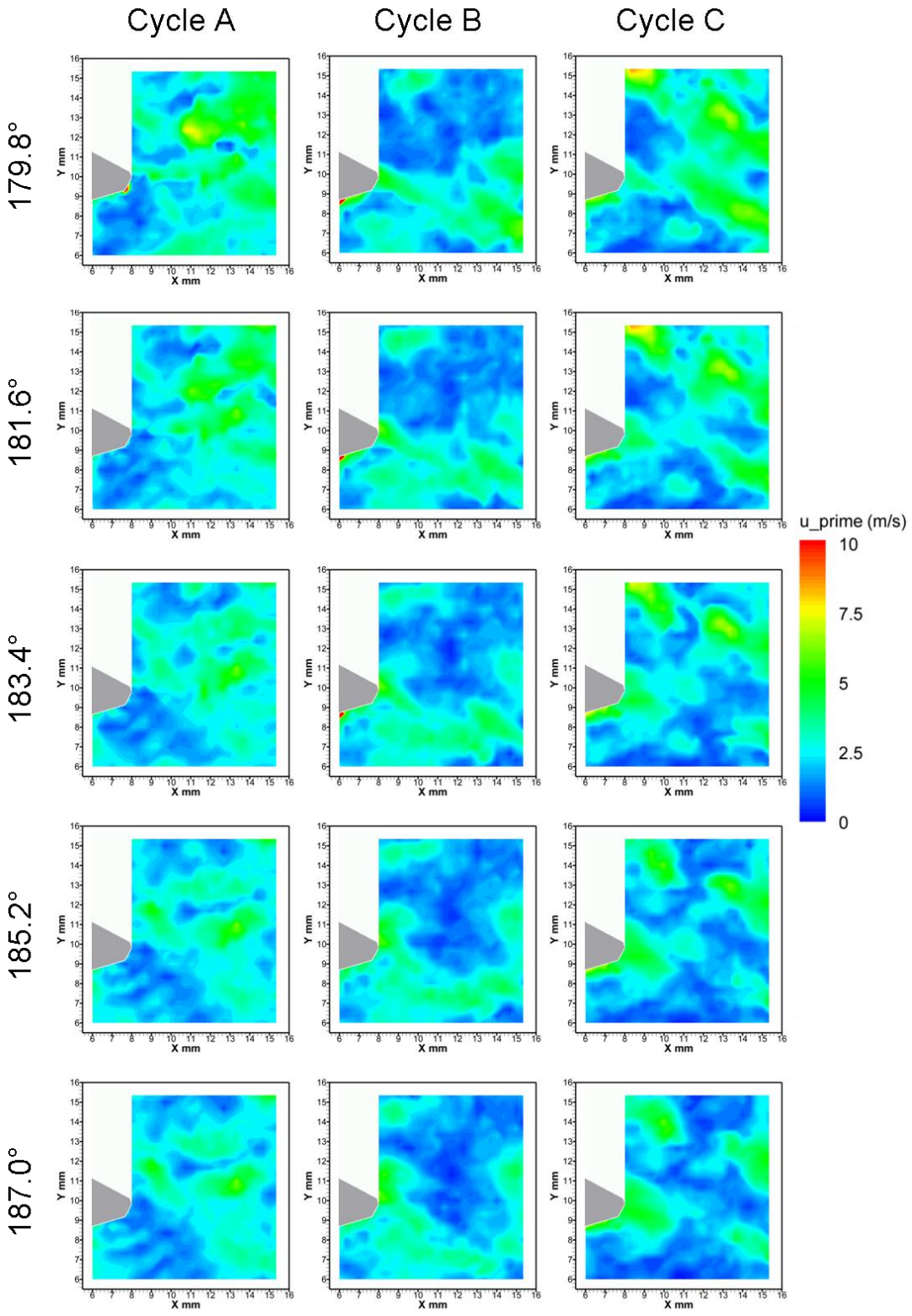

Figure 6.41 - Contour plot of u' on a plane through the intake valve jet for three individual cycles from 179.8° to 187° CA ATDC captured with HSDPIV at a rate of 5 kHz

6.3.2.2 With tumble flap

A modification of the standard flow profile entering the ports was achieved through the use of a tumble flap (see Chapter 3). Altering the port flow in this manner provides a subtle change to the flow and allows the cyclic variation characteristics of this alternative 'geometry' to be compared to the standard case. The measurement conditions were as presented in Section 6.3.1.

Raw velocity fields for valve jet flow over a range from 91.6° to 98.8° CA ATDC gas exchange are presented for three arbitrary selected cycles in Figure 6.42. At 91.6° CA the flow field for cycle A shows a jet which is only visible at the top of the frame, and has a region of entraining flow underneath. Its velocity is also something to note as it is > 50 ms^{-1}. This high velocity is shown consistently across the three cycles and is higher than experienced in the flow fields presented in Figure 6.17, which show flow fields at the same crank angle but without the tumble flap fitted. Throughout the range of CA presented in Figure 6.42, the jet remains high in the frame whilst its velocity is starting to decay. At 91.6 ° CA, the valve jet shown for cycle C starts with a wider jet than that shown in cycle A, with a clear vortex underneath which appears to be leaving the frame on the next image shown. The range 142° to 149.2° CA has been presented in Figure 6.43. This has been plotted to the same scale as Figure 6.19 to enable a direct comparison to be made, although, due to the higher velocities observed with the presence of the tumble flap, much of the flow within the jet are saturated and are therefore >20 ms^{-1}. Across all three cycles presented the raw velocity is higher with the tumble flap, leading to a broader jet flow, confirming that a greater proportion of the flow enters the cylinder. The higher velocity remains as the cycle progresses, see Figure 6.44 for the range 179.8° to 187.0° CA ATDC. When the tumble flap is fitted there is an obvious change in the flow characteristics when compared to those data without the tumble flap (see Figure 6.18 to Figure 6.20). As desired, the presence of the tumble flap has driven flow to be redistributed around the valve's annulus which should subsequently positively affect tumble within the cylinder. This has been further investigated in Chapter 7.

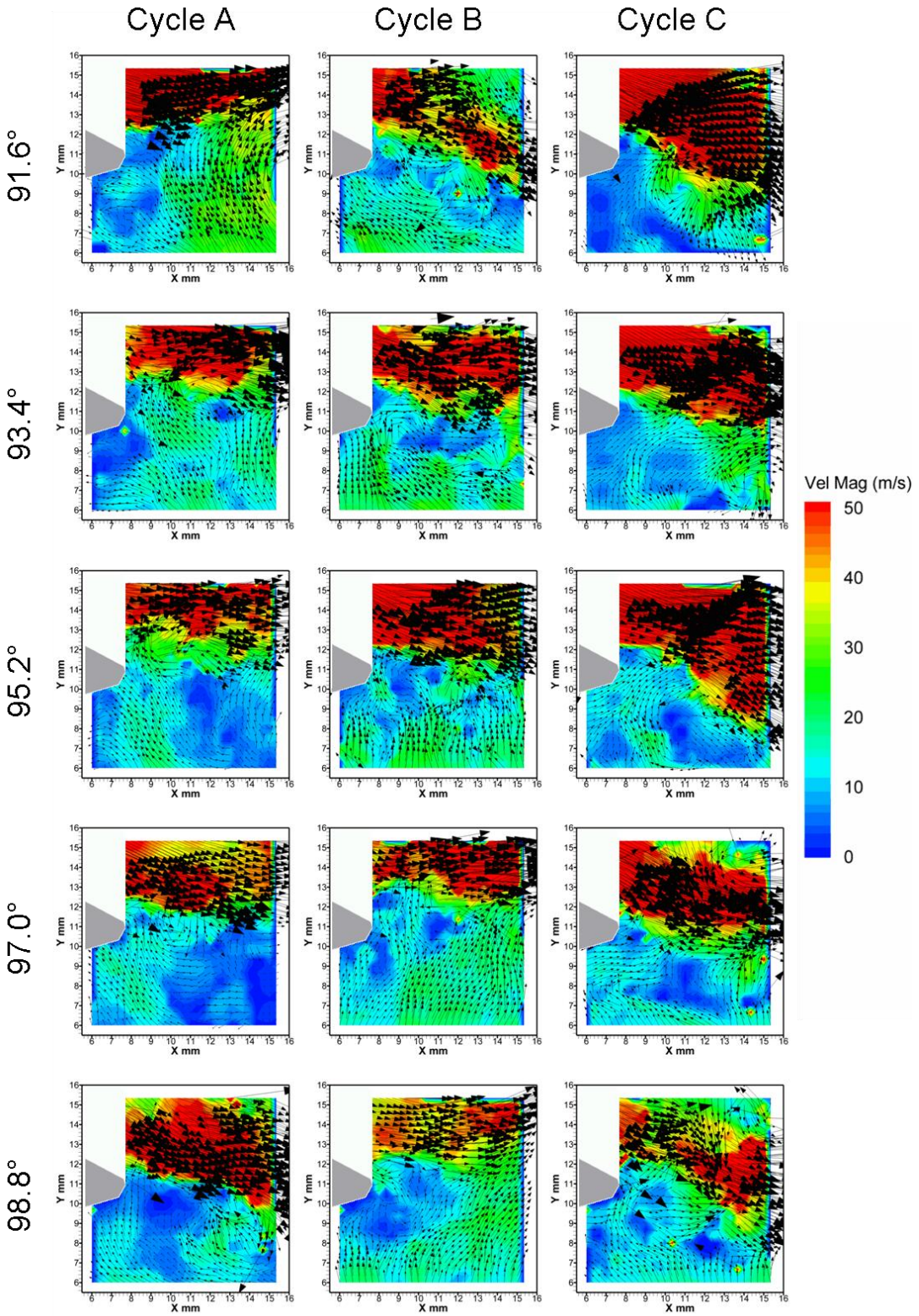

Figure 6.42 - Raw flow fields of a plane through the intake valve jet, with the tumble flap fitted, for three individual cycles from 91.6° to 98.8° CA ATDC captured with HSDPIV at a rate of 5 kHz

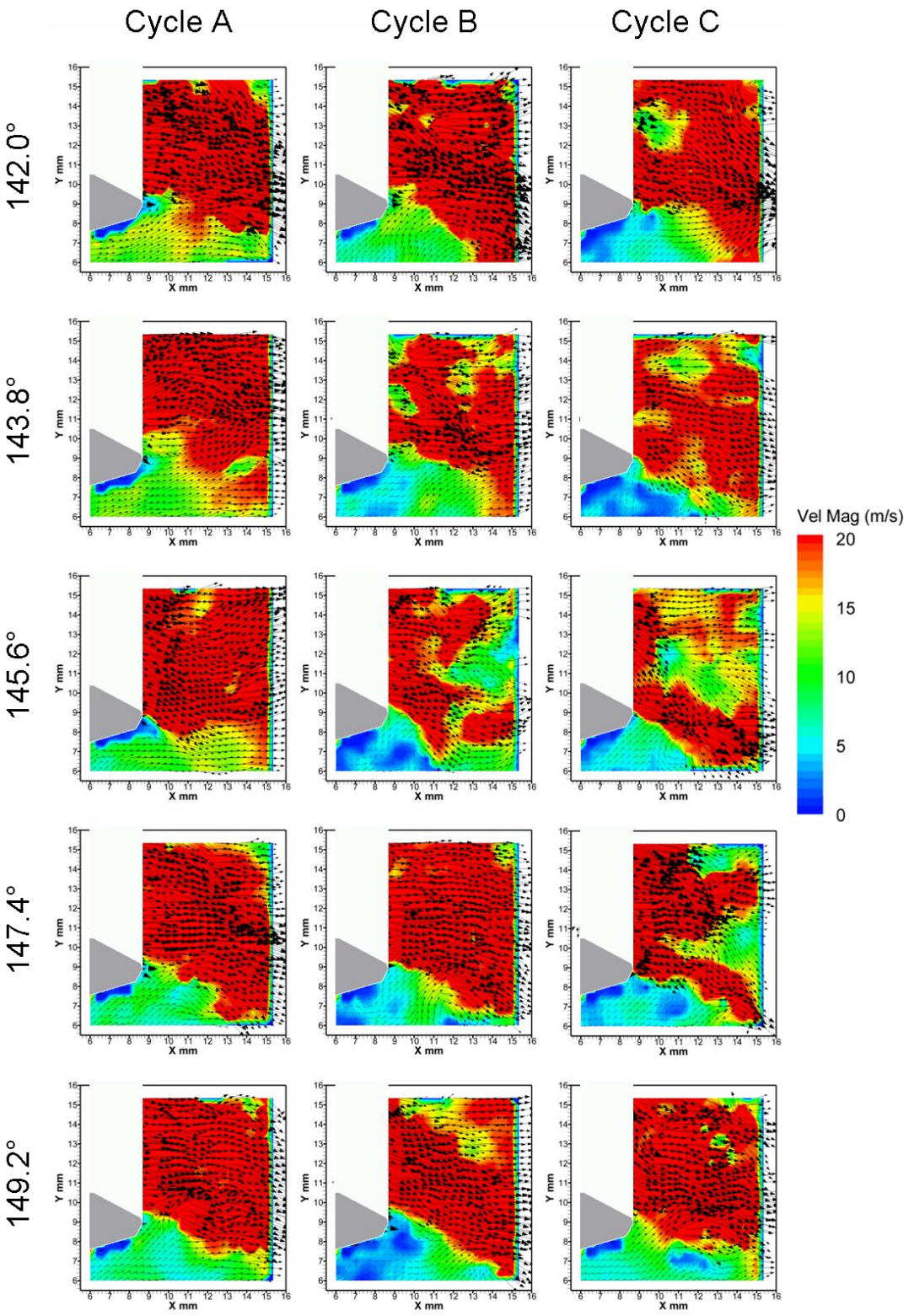

Figure 6.43 - Raw flow fields of a plane through the intake valve jet, with the tumble flap fitted, for three individual cycles from 142° to 149.2° CA ATDC captured with HSDPIV at a rate of 5 kHz

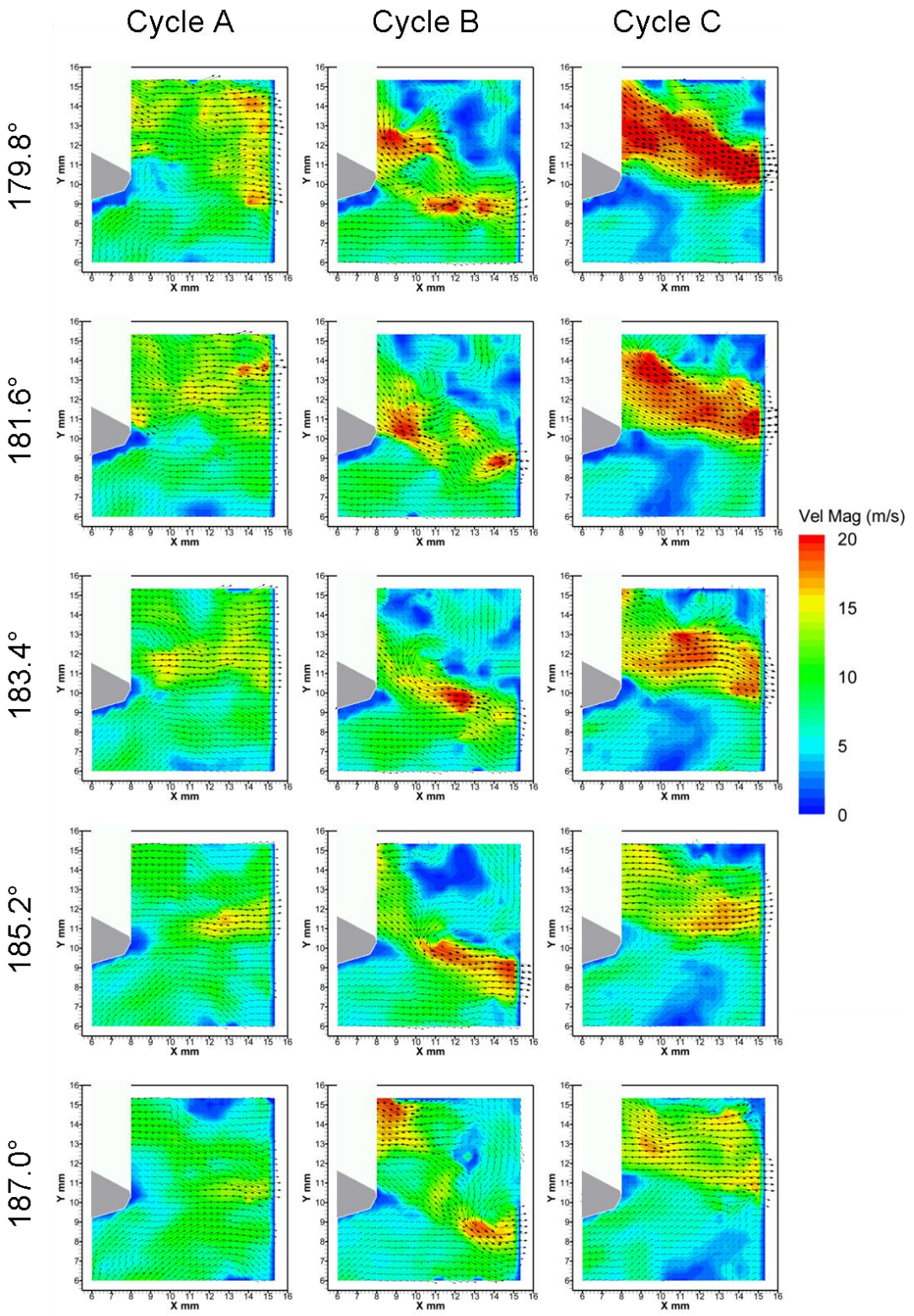

Figure 6.44 - Raw flow fields of a plane through the intake valve jet, with the tumble flap fitted, for three individual cycles from 179.8° to 187° CA ATDC captured with HSDPIV at a rate of 5 kHz

The mean low frequency flow fields have been shown in Figure 6.45 for the range 91.6° to 100.6° CA ATDC and can be directly compared to the data presented without the presence of the tumble flap in Figure 6.27. This confirms the change in characteristics caused by the tumble flap, most notably the higher velocity flow fields and the change in exit angle.

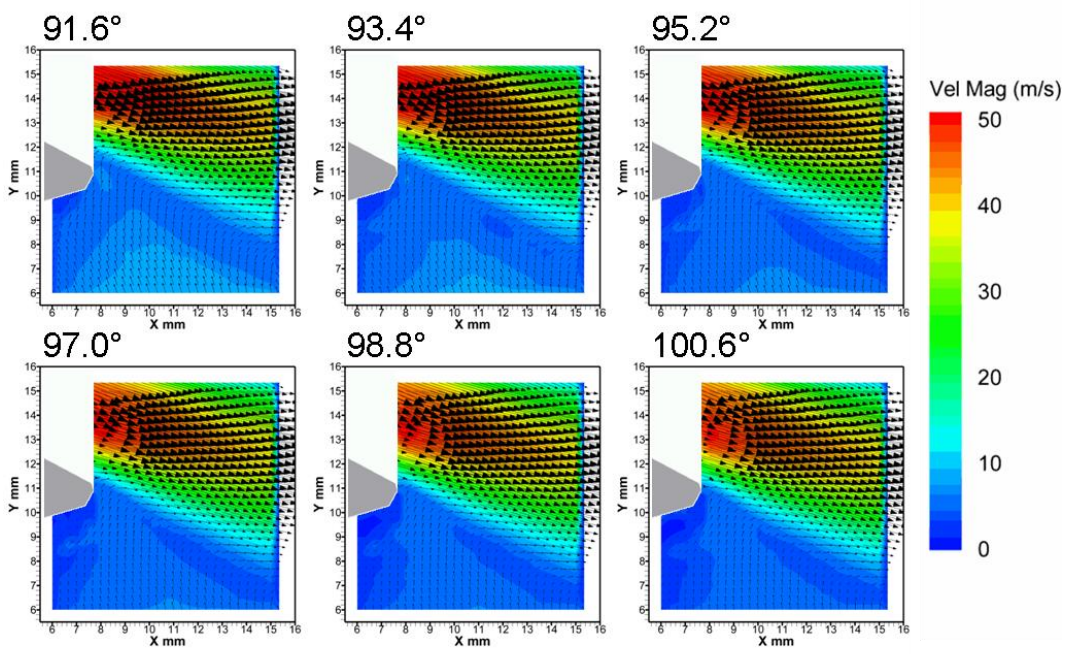

Figure 6.45 – Mean low frequency flow fields of a plane through the intake valve jet from 91.6° to 100.6° CA ATDC captured with HSDPIV at a rate of 5 kHz

The *rms* low frequency cyclic variation flow fields for 100 captured cycles, with the tumble flap fitted, have been shown in Figure 6.46 to Figure 6.48. These figures are comparable to those presented in Figure 6.33 to Figure 6.35 which describe the standard case. For the range 91.6° to 100.6° CA ATDC, presented in Figure 6.46 and Figure 6.33, the variable zone in the jet shear layer is clear, however, when the tumble flap is fitted the velocity variation is lower, at *circa* 6m.s^{-1}, compared to over 10ms^{-1}, even though the velocity is higher. The cyclic variability has also dropped within the jet core to *circa* 2 to 3 m.s^{-1}, which is approximately 6% of the mean flow velocity. In Figure 6.34 there is a clear core region still present across the range 142.0° to 151.0° CA ATDC, however, with the tumble flap fitted in Figure 6.47, this is not the case and a

more homogeneous cyclic variation across the intake flow is present with a region of higher variability above the jet. Additionally the region beneath the valve displays lower *rms* cyclic variation when the tumble flap is present. In the range 179.8° to 188.8° CA ATDC continued decay is present for both cases, with (Figure 6.48) and without (Figure 6.35) the tumble flap.

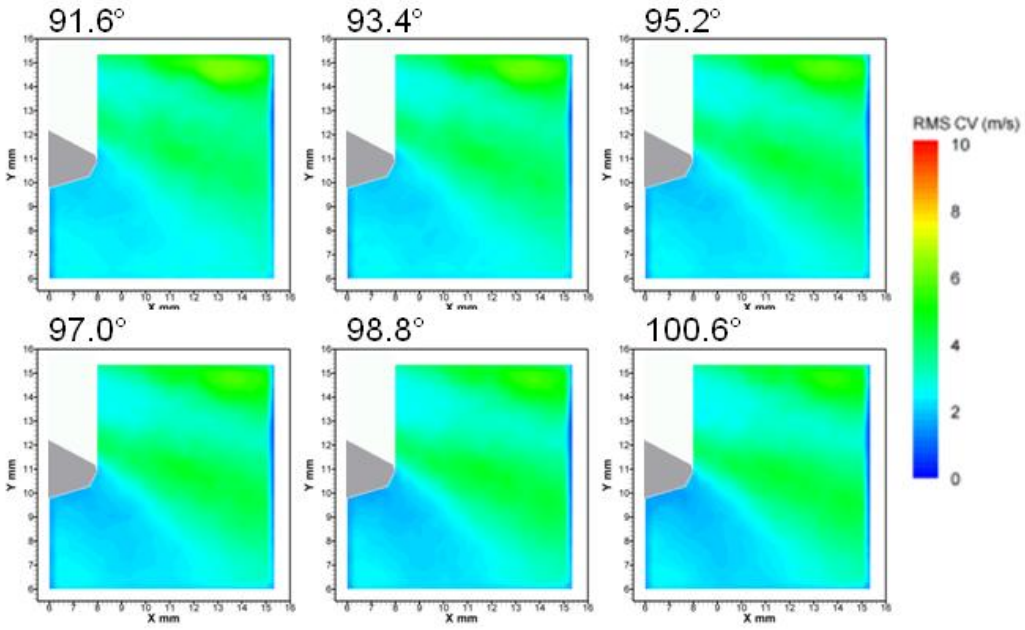

Figure 6.46 -*rms* of 100 low frequency cyclic variation flow fields of the intake valve jet from 91.6° to 100.6° CA ATDC with the tumble flap captured with HSDPIV at a rate of 5 kHz

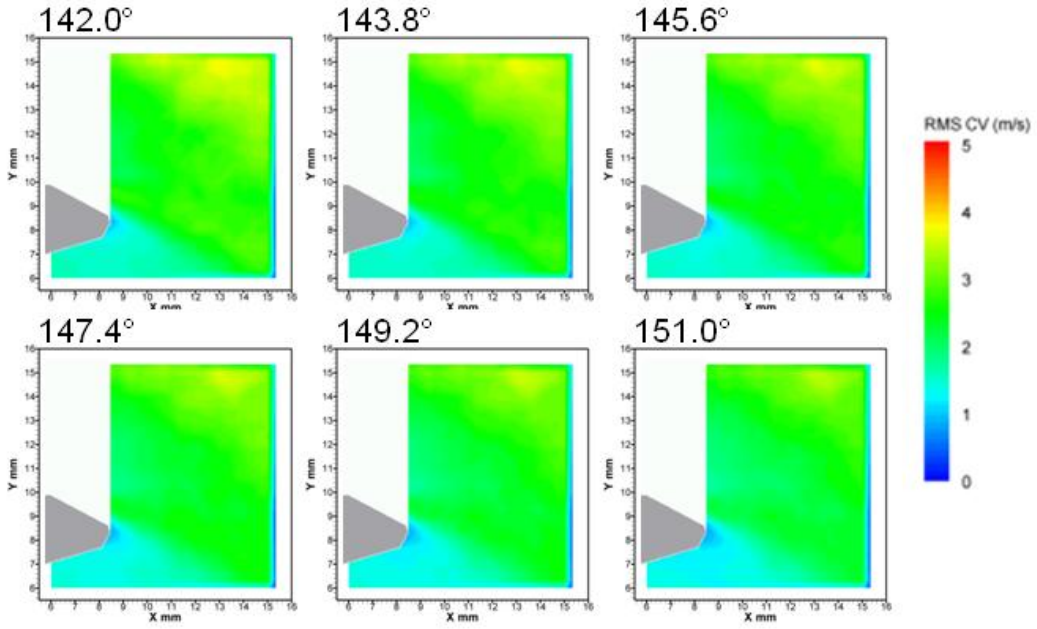

Figure 6.47 - *rms* of 100 low frequency cyclic variation flow fields of the intake valve jet from 142.0° to 151.0° CA ATDC with the tumble flap captured with HSDPIV at a rate of 5 kHz

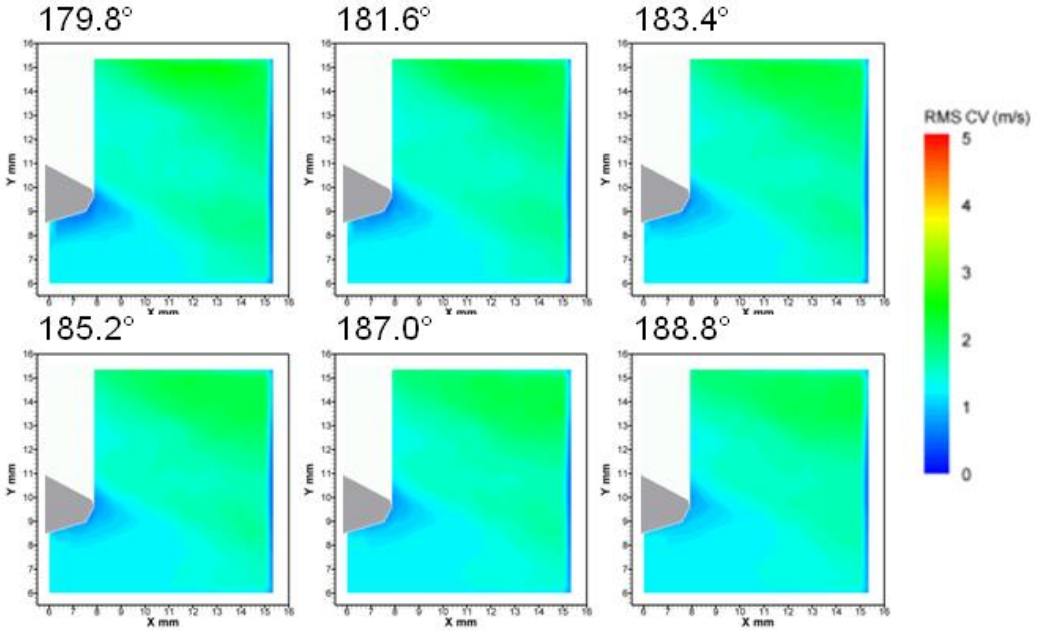

Figure 6.48 - *rms* of 100 low frequency cyclic variation flow fields of the intake valve jet from 179.8° to 188.8° CA ATDC with the tumble flap captured with HSDPIV at a rate of 5 kHz

6.4 Summary

The intake valve jet flow occurring in the imaged plane has been shown to exhibit significant cyclic variation in both bulk motion and turbulence characteristics. This study has only focused on one of the two intake valves, therefore, it is reasonable to assume the other valve suffers from similar variations in flow over the course of a statistically representative sample of cycles. As these vary from one cycle to the next so will the in-cylinder flow field since it is the intake flow along with the cylinder geometry which establishes the characteristics of this flow.

The intake flow has been shown to exhibit fluctuations in the flow towards the cylinder; these fluctuations, however, are surpassed by the fluctuations shown in the flow exiting the intake valve. Therefore, the data shown in this chapter suggest that the in-cylinder flow fields are more strongly influenced by instabilities introduced to the intake flow as it passes through the intake valve than by instabilities which exist within the flow as it is in the intake runner. Knowledge of this is of significant benefit to engine designers, since the intake system may be optimised for best breathing, noise/sound, packaging and cost rather than minimising cyclic variability.

Chapter 5 examined cyclic variations which occur within the pent roof flow fields preceding the combustion event and the characteristics of the flame during its development process. How flow field variation could be attributed to variation within the combustion event was also discussed in Chapter 5. In the current chapter cyclic variation characteristics displayed by both flows within the intake runner and within the intake valve exit flows are discussed. These showed that the intake valve jet displays both high and low frequency spatial and temporal variations which enter into the cylinder thereby affecting the characteristics of this flow. In Chapter 7 a discussion of the characterisation of the in-cylinder flow field as it develops during the course of the cycle has been presented.

Chapter 7 Cyclic variability of in-cylinder flows

7.1 Introduction

In this chapter, flow field behaviour within the cylinder during both the intake and compression strokes is discussed. The initial in-cylinder flow field, produced by the intake valve exit flow, have been investigated to demonstrate how low and high frequency fluctuations within the intake valve jet generate cyclic variations within the early in-cylinder flow fields. This led to an investigation of the in-cylinder flow field development, leading up to the combustion event, in both tumble and swirl flow planes during both the intake and into the compression stroke. Studying the progression of the in-cylinder flow fields during the course of cycle shows the formation of influential flow fields which affect both mixture preparation and combustion. By generating a better understanding of the mechanisms which lead to cyclic variations in the in-cylinder flow field, specifically near the combustion event, the flow field variations which affect cycle performance will be better understood.

7.2 Tumble plane

7.2.1 Bore centre line

7.2.1.1 Measurement conditions

The data presented within this section investigate the characteristics of the flow field and its cyclic variation on the bore centreline, in the tumble plane, during the intake and compression strokes. The schematics shown in Figure 7.1 and Figure 7.2 highlight the

imaged area used to capture the HSDPIV images presented within this section. The engine was motored at 1500 rpm with an intake plenum pressure of 525 mbar.

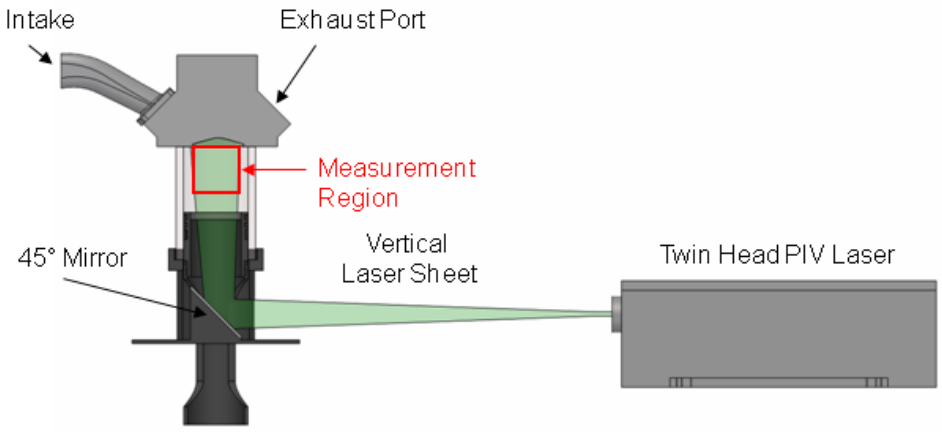

Figure 7.1 - Schematic to show the measurement location used to investigate large scale flows in the tumble plane on the bore centreline

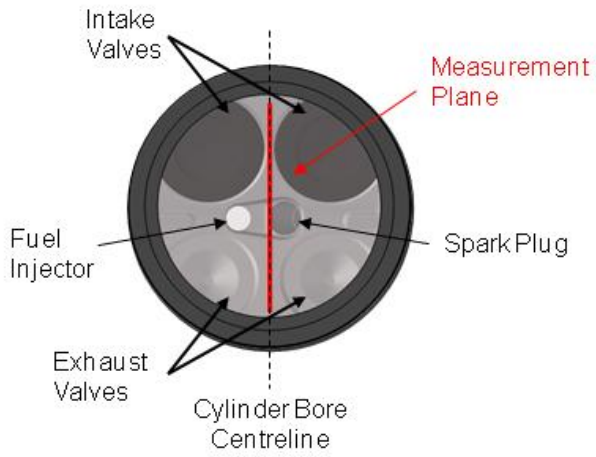

Figure 7.2 - Schematic to show the measurement plane created by the laser sheet when investigating large scale flows in the tumble plane on the bore centreline (as viewed via the 45° mirror under the piston)

The configuration of the HSDPIV system to capture these measurements is shown in Figure 7.3. The output from the Nd:YLF laser was formed into a thin vertical sheet and introduced into the combustion chamber via the 45° mirror mounted under the piston and the flat topped optical piston crown. To achieve the correct laser sheet height and width in the image region, a -25 mm cylindrical lens was used in conjunction with a 1000 mm spherical lens. These lenses also allowed the laser to be positioned in a convenient location.

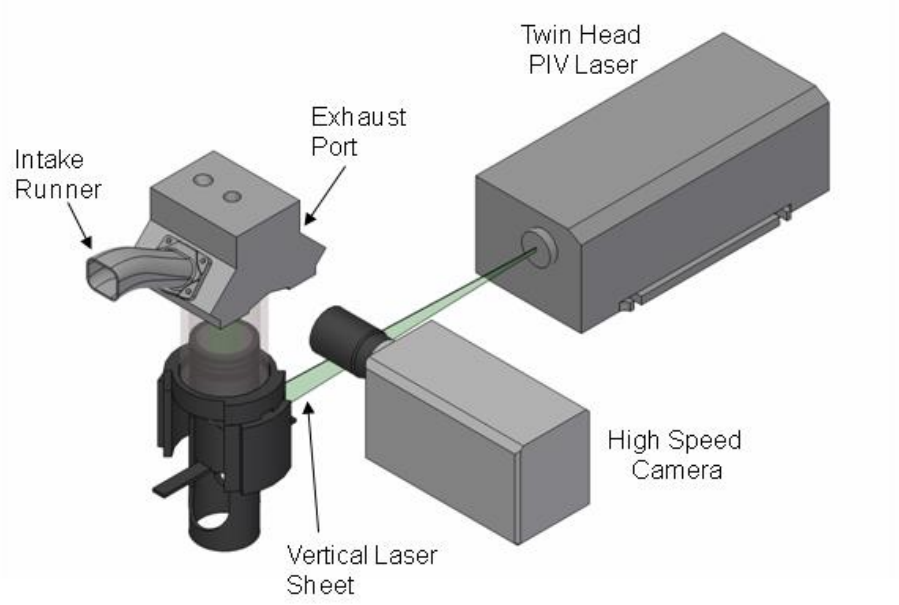

Figure 7.3 - Schematic to show the configuration of the HSDPIV system to achieve measurements to investigate large scale flows in the tumble plane on the bore centreline

At this measurement location the larger scale bulk flow motion development is of primary interest; however, the energy cascade of this bulk flow and the existing turbulent flow is also something to consider. The camera was operated with its full resolution of 1024 by 1024 pixels which allowed a frame rate of 3 kHz and therefore the capture of two frame cross correlation images to provide flow fields at 1.5 kHz. With the engine being motored at 1500 rpm the temporal resolution of the HSDPIV system for these measurements equated to 6° CA of revolution between captured flow fields.

A 105 mm AF Micro Nikkor lens was used to image a region 60 mm by 60 mm onto the active array of 1024 by 1024 pixels. Analysis of the captured PIV image pairs was performed with the TSI Insight 3G software. Velocity vectors were evaluated from the image pairs on a Nyquist grid with 32 by 32 pixel interrogation regions, equating to an area approximately 1.88 mm by 1.88 mm within the flow. The interrogation regions were positioned to overlap neighbouring regions by 50 % leading to a vector spacing in the resulting velocity vector field of 0.94 mm. This allows the investigation of the bulk motion flow field characteristics of the in-cylinder flow and gives an adequate spatial resolution to study the variations which influence these bulk motion characteristics. Also, this spatial resolution will be adequate to capture smaller scale structures which exist within this bulk flow and have enough energy to contribute to the bulk cycle development.

To control the imaged diffraction limited spot size the laser was operated at full power and the largest $f^{\#}$ which gave adequate contrast in the particle images was used. Ideally the $f^{\#}$ for the measurements presented within this Section would need to be >16 to give a calculated diffraction limited spot size greater than 2 pixels in diameter. The HSDPIV system, limited by laser power and camera sensitivity, required that the $f^{\#}$ = 8. This gives a calculated diffraction limited spot size of 0.8 pixels (therefore more susceptible to sub pixel displacement errors). However, the calculated spot size is for an ideally focussed system, therefore by taking the image slightly out of focus the actual measured imaged particle size on the camera array could be controlled to be greater than 2 pixels.

Two groups of HSDPIV data were recorded for this measurement location. The first covered the time period from 62° to 128° CA ATDC, and the second from 100° to 316° CA ATDC. The two overlapping sequences allowed the HSDPIV capture settings to be optimised. Firstly this was to allow the density of seed to be increased for the early capture sequence to ensure that sufficient particles were present within each interrogation region. This also allowed the dynamic range of the PIV to be configured to minimise error in the low velocity flows whist capturing the highest velocities present.

For the HSDPIV captured over the period 62° to 128° CA ATDC gas exchange the time separation, Δt, between the two laser pulses controlling the exposure of the image pair was set to 30 μs. This Δt allows the flow to travel with a velocity of *circa* 31.3 $m.s^{-1}$ before the particles will move beyond 16 pixels (half of the interrogation region). For the flow field under investigation this Δt was considered to be adequate to minimise out of plane flow motion whilst allowing enough movement in the particles to control errors in sub pixel displacement for the slower flows of interest within the region. One pixel movement between frames is equivalent to 1.95 $m.s^{-1}$. The capture sequence, triggered at 62° CA, was for 12 image pairs and therefore allowed 87 cycles to be captured before the 2 Gb on-board memory available on the camera was full. Performing two capture sequences gave an adequate sample of cycles to calculate a statistically significant mean flow.

For the second time period covering the range 100° to 316° CA ATDC gas exchange the peak velocity within the imaged area has reduced. This allows the Δt between the two laser pulses to be increased to 35 μs leading to reduced errors in the lower velocities measured towards the end of the cycle. This Δt allows the flow to travel with a velocity of up to *circa* 26.8 $m.s^{-1}$ before the particles will move beyond 16 pixels (half of the interrogation region). One pixel movement at this Δt is equivalent to 1.67 $m.s^{-1}$. The 37 image pairs in the capture sequence allowed 28 cycles to be captured before the 2 Gb available on-board memory was filled. Performing four capture sequences gave an adequate sample of cycles to calculate a statistically significant mean flow.

7.2.1.2 Measured velocity fields

7.2.1.2.1 Measurements from 62° to 128° CA ATDC gas exchange

Those data presented within this section are for HSDPIV taken in the tumble plane on the bore centreline. The HSDPIV was captured over the range 62° to 128° CA ATDC gas exchange. Figure 7.4 shows a large scale plot of an example flow field at 92.0° CA ATDC. Image sequences from three cycles are presented in Figure 7.5 and show the development of the in-cylinder flow field in the tumble plane and on the bore centreline

from 68.0° to 92.0° CA ATDC, at every 6.0° CA interval where a flow field measurement was recorded.

Over the sequence of crank angle degrees presented a jet is seen to travel down cylinder on the left hand side of the imaged area. This is the result of the flow exiting the segment of the intake valve annuli closest to this side of the cylinder. At 68.0° CA this flow is seen in all three presented cycles to impact onto the piston surface as a result it is shown to have been turned right towards the centre line of the cylinder. This flow is met head on with an opposing flow generated by the valve jet flow which exits through the top of the intake valve as per those data presented in section 6.3. As a result, these opposing flows are deflected upwards, ultimately creating both a clockwise and counter clockwise rotation. During cycle B at 86.0° CA these two rotating motions appear to be of similar size in the image, with the collision of the flows occurring close to X = 30 mm. In contrast, cycle C displays a clockwise rotation which is larger than the counter clockwise rotation, the collision between the jets is seen in this case to be closer to X = 20 mm. This appears to be due to the left hand jet having a lower velocity magnitude and hence momentum. One further observation is that the left hand (counter clockwise) rotation, underneath the intake valve, occurs lower within the cylinder than the right hand (clockwise) rotation.

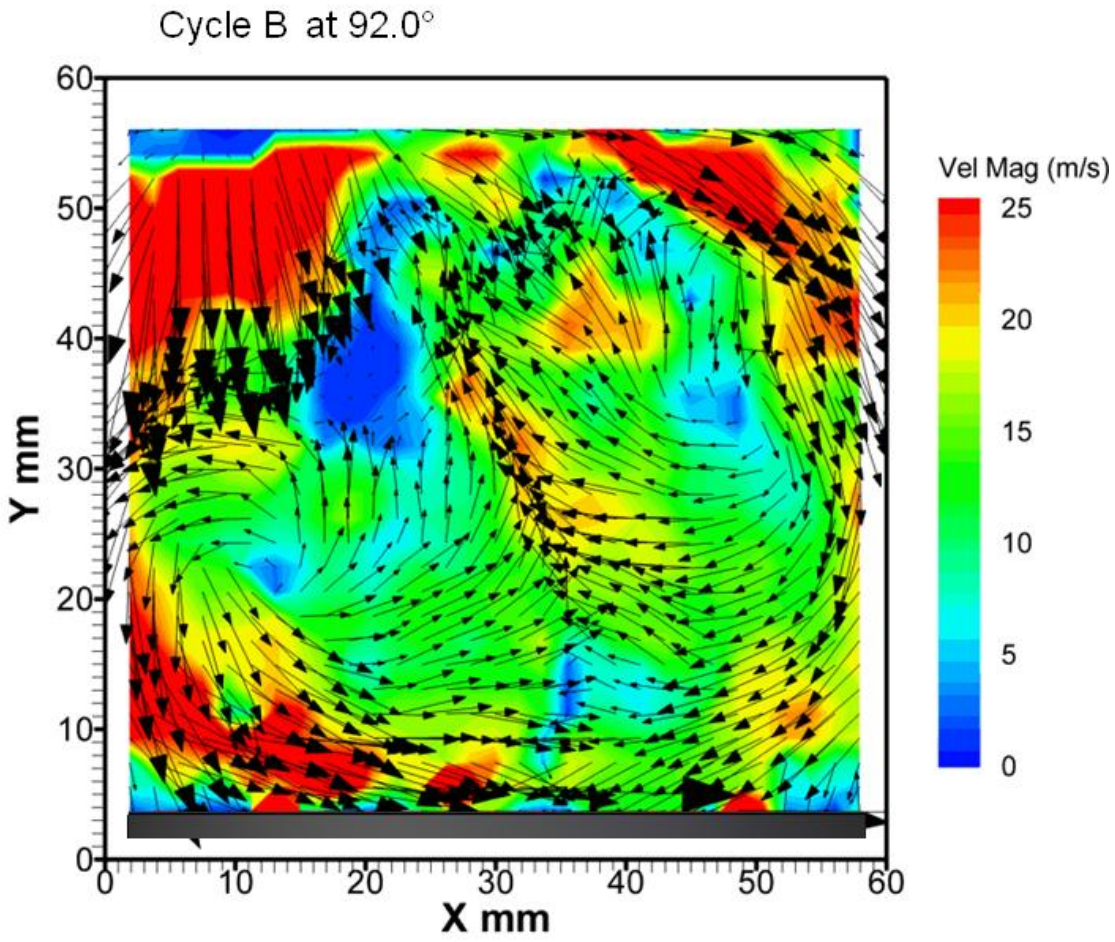

Figure 7.4 - Large scale image to show a raw flow fields on the bore centreline at 92.0° CA ATDC captured with HSDPIV at a rate of 1.5 kHz

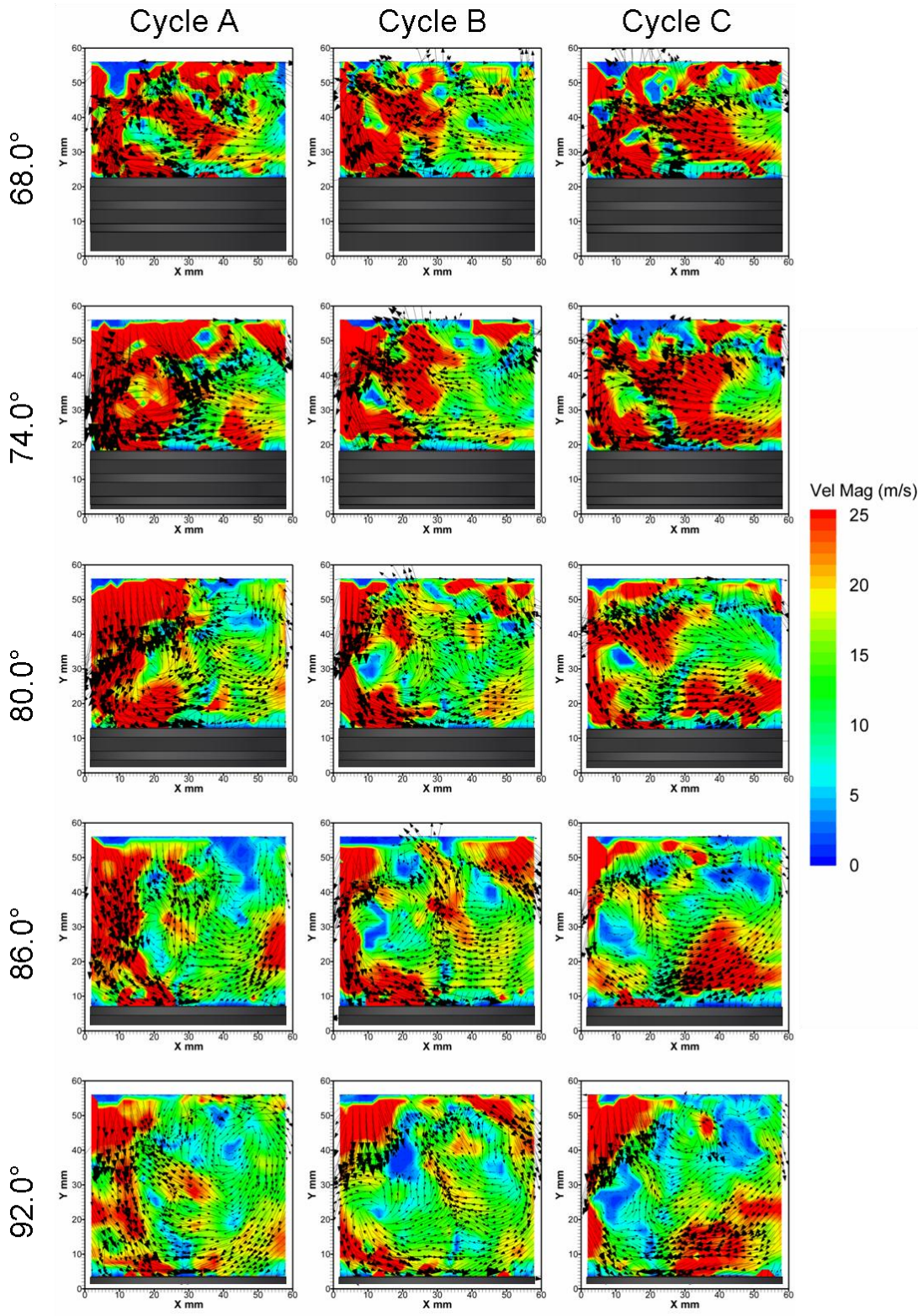

Figure 7.5 - Raw flow fields on the bore centreline for three individual cycles from 68.0° to 92.0° CA ATDC captured with HSDPIV at a rate of 1.5 kHz

Using the same technique as previously presented in Chapter 5 and Chapter 6 the raw velocity fields were filtered into their high and low frequency components using a cut-off frequency of 280 Hz. The resulting low frequency fields for cycles A to C, over the range 62° to 128° CA ATDC, as previously presented, are shown in Figure 7.6. The low pass frequency filtering has allowed the large scale bulk flow features to become more obvious when compared to the raw flow fields of Figure 7.5. This includes the downward motion on the left hand side of the image, along with the turning of it as it approaches the piston surface. The point of interaction between this flow and its opposing flow, which moves across the piston surface from right to left, can be identified by a stagnation point. The flow behaviour around this point is different on each of the presented cycles. For cycle A, at 80.0° CA, the left hand flow pushes the top of the stagnation region further towards the right of the cylinder. This allows a larger recirculating region to form on the left hand side for this cycle in comparison to the two other cycles presented. This is shown by the centre of the rotation being further towards the centreline of the cylinder at *circa* X = 20 mm compared to the centre of rotation being closer to X = 10 mm for cycles B and C. By 92.0° CA cycle C does not exhibit a strong clockwise recirculation as in the other two cycles, the author is left to assume a greater 3-dimentional flow is present in this cycle.

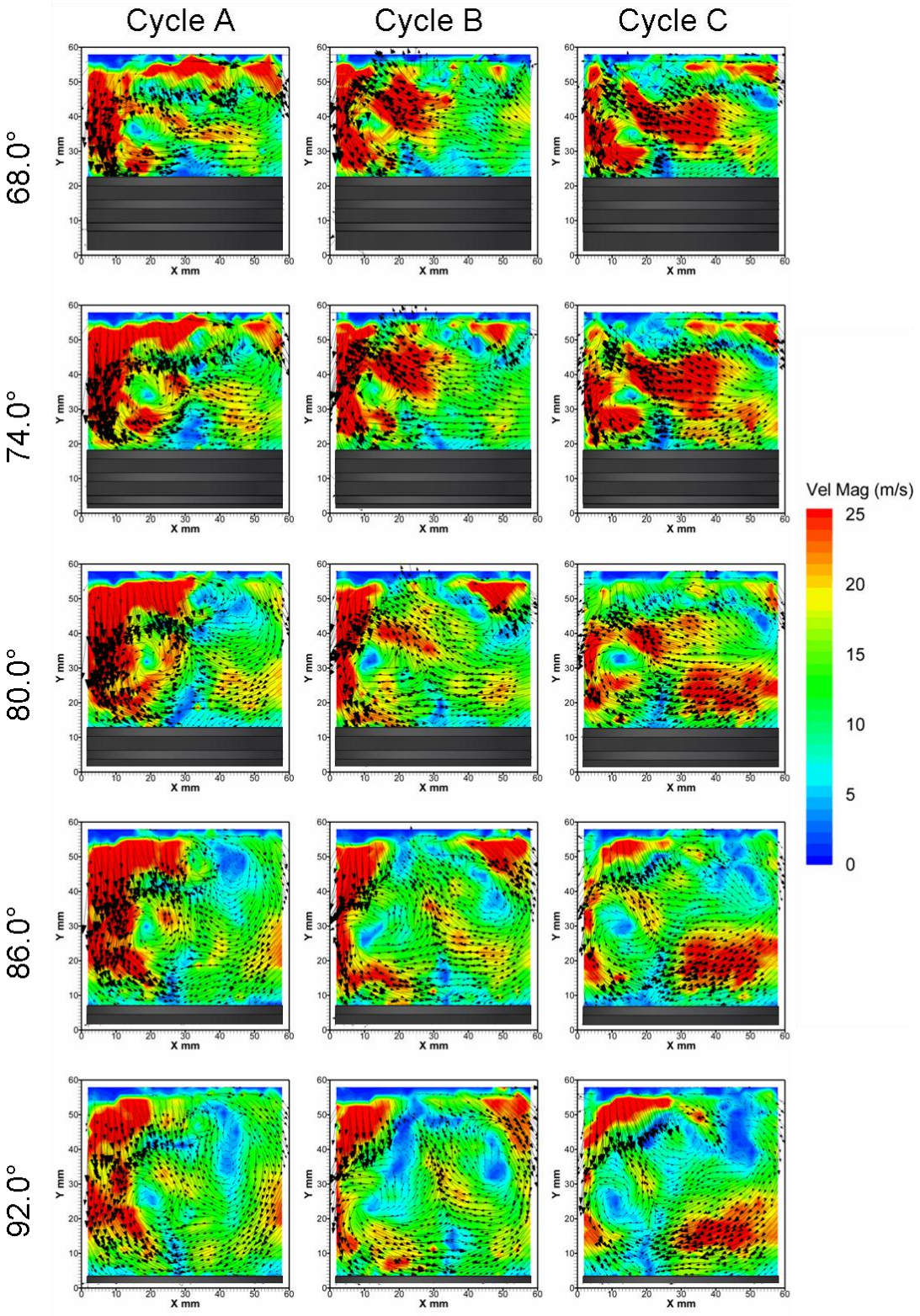

Figure 7.6 – Low frequency flow fields on the bore centreline for three individual cycles from 68.0° to 92.0° CA ATDC captured with HSDPIV at a rate of 1.5 kHz

The mean (ensemble average) low frequency flow field for those recorded from 62.0° to 110.0° CA ATDC are shown in Figure 7.7. This illustrates the clockwise and counter clockwise rotations previously discussed, along with the interaction point of the opposing flows crossing the piston surface. The clockwise rotation (upper right hand corner of the image) is shown to move into the field of view from the right towards the cylinder centreline during the period 62.0° to 74.0° CA ATDC. This rotating structure continues to move left over the remaining images. The motion of this clockwise rotation is attributed to the behaviour of the counter clockwise rotation which is seen to drop down the cylinder in line with the motion of the piston (Stansfield *et al.* (2007)). The speed at which the counter clockwise vortex drops is not however the same as the piston speed. At 62.0° CA the centre of rotation is circa 10 mm above the piston surface, by 92.0° CA it is closer to 20 mm above the piston.

The magnitude of the low frequency cyclic variations are presented in Figure 7.8 for the three cycles previously presented. The images have been plotted with the low frequency velocity vectors overlaid so that the images highlight areas of high variation and show the structure of the cycle's bulk flow at this point. These plots show how the individual cycle's low frequency flow fields presented in Figure 7.6 differ from the mean low frequency flow fields presented in Figure 7.7. It can be seen that there is a larger magnitude of variation in the upper left hand portion of the image for the early images shown. This corresponds to variation in the flow resulting from the collision of the two flow streams and the generation of the counter clockwise rotation. Over the sequence of images presented, the cyclic variation of bulk flow in cycle A remains largely contained within the left hand side of the image, decaying in magnitude as the cycle progresses. In cycle B, however, the region of highest variation in bulk flow moves from the top left of the image into the central region where this cycle displays continuing impingement of flow from the left and right of the cylinder. In cycle C, although starting similarly to cycle B, a large region of variation magnitude emerges in the lower right region of the image, this supports the assumption of greater 3-dimentional flow behaviour.

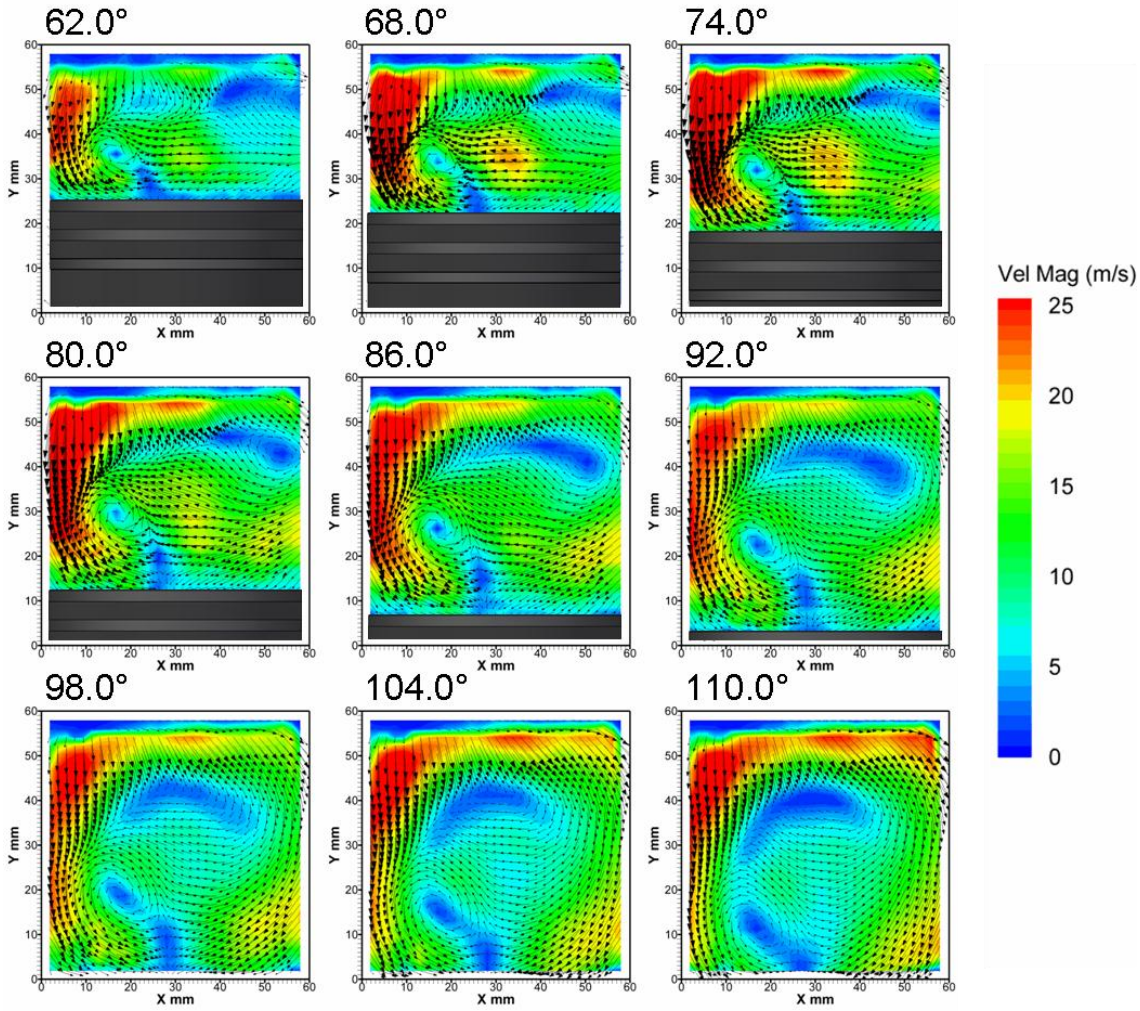

Figure 7.7 – Mean low frequency flow fields on the bore centreline from 62.0° to 110.0° CA ATDC captured with HSDPIV at a rate of 1.5 kHz

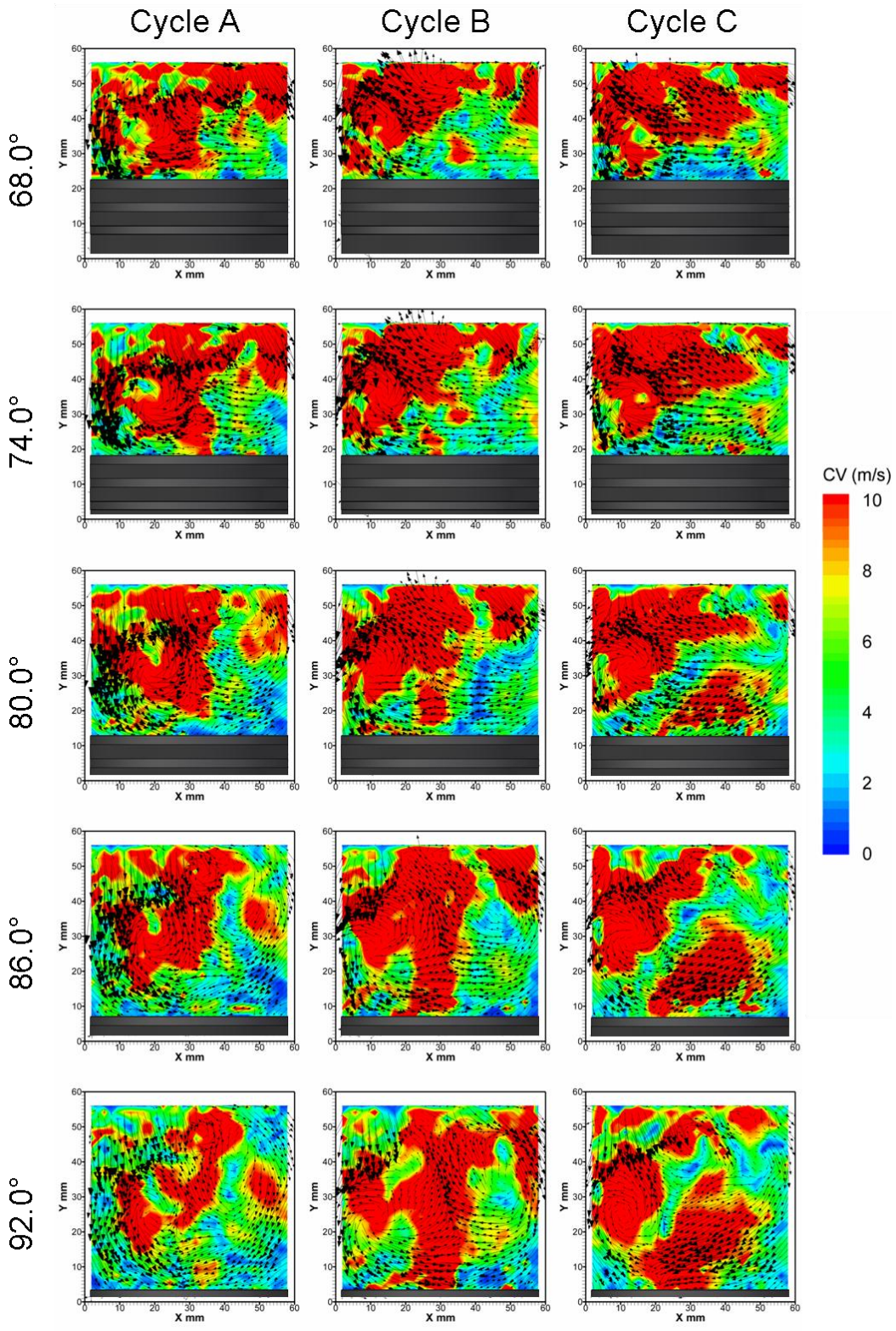

Figure 7.8 – Low frequency cyclic variation flow fields on the bore centreline for three individual cycles from 68.0° to 92.0° CA ATDC captured with HSDPIV at a rate of 1.5 kHz

To allow comparison of cyclic variation in the low frequency component of the flow field, between different engine geometries and operating conditions, the root-mean-square (*rms*) of the low frequency cyclic variation can be calculated as follows

$$U_{rmsCVLF(\theta,x,y)} = \sqrt{\frac{1}{n}\sum_{i=1}^{n}\left(U_{CVLF(\theta,i,x,y)}{}^{2}\right)}. \qquad \text{Equation 7.1}$$

The normalisation of the *rms* low frequency cyclic variation by the mean low frequency cycle highlights spatial and temporal variations in cyclic variation relative to the mean low frequency flow. The normalisation is performed as follows

$$\frac{U_{rmsCVLF(\theta,x,y)}}{\left|\overline{U_{LF(\theta,x,y)}}\right|}. \qquad \text{Equation 7.2}$$

The magnitude of the *rms* of the low frequency cyclic variation is presented in Figure 7.9. This plot is overlaid with the mean low frequency flow fields to show the mean flow structure and how this relates to the areas displaying high *rms* of variation. Initially, at 62.0° CA the areas of high variation are shown to occur across the top of the image and around the counter clockwise rotation on the left hand side. As the cycle progresses to 74.0° CA this high variation is seen expand to include the clockwise rotation in the top right hand of the image. The high variation region in the centre of the image is seen to result from the flow coming from the right interacting with the flow from the left and the resulting rotations. At 80.0° CA the variation which is seen to occur within the flow on the left hand side of the image has reduced indicating that the intake valve flow in this region has become more stable as its velocity reduces. At this crank angle and up to the last image presented at 110.0° CA, the areas of high variation become centralised within the imaged region. Therefore, the variations in the opposing flows which travel across the piston leading to changes in the location and character of the interaction, is shown to be an area where substantial variations in the bulk in-cylinder flow field can be intensified.

Figure 7.10 shows the *rms* of the low frequency cyclic variation normalised by the mean low frequency flow. This highlights areas of high variation relative to the local mean velocity. It results in drawing out the regions where velocity in the mean flow field is low, indicated by the red 'hot spots' in the image. It does, however, further indicate the level of variation occurring within the central region of the image which, later in the sequence, can be seen to be in the order of 1.5 times the local mean flow velocity.

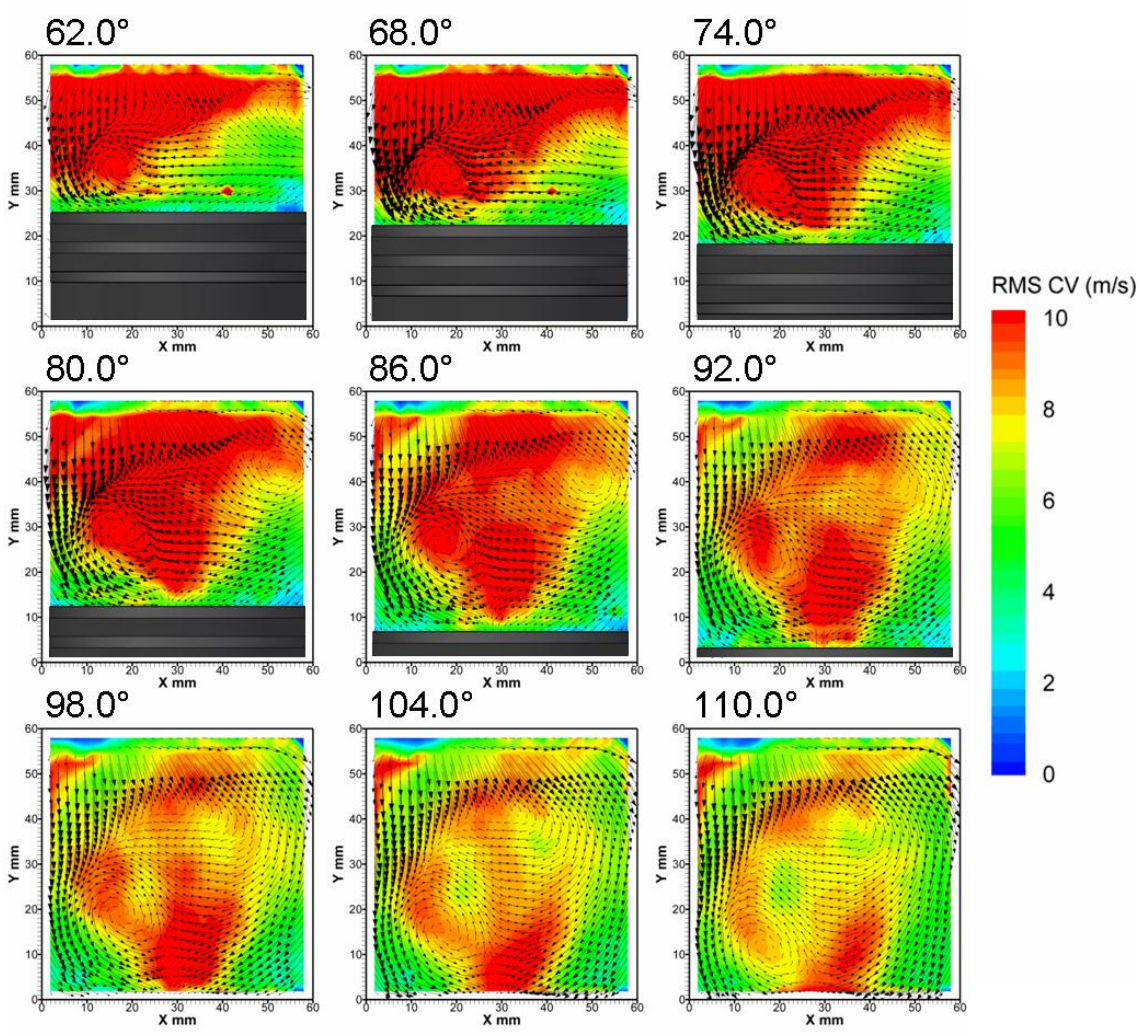

Figure 7.9 – *rms* of 100 low frequency cyclic variation flow fields on the bore centreline from 62.0° to 110.0° CA ATDC captured with HSDPIV at a rate of 1.5 kHz

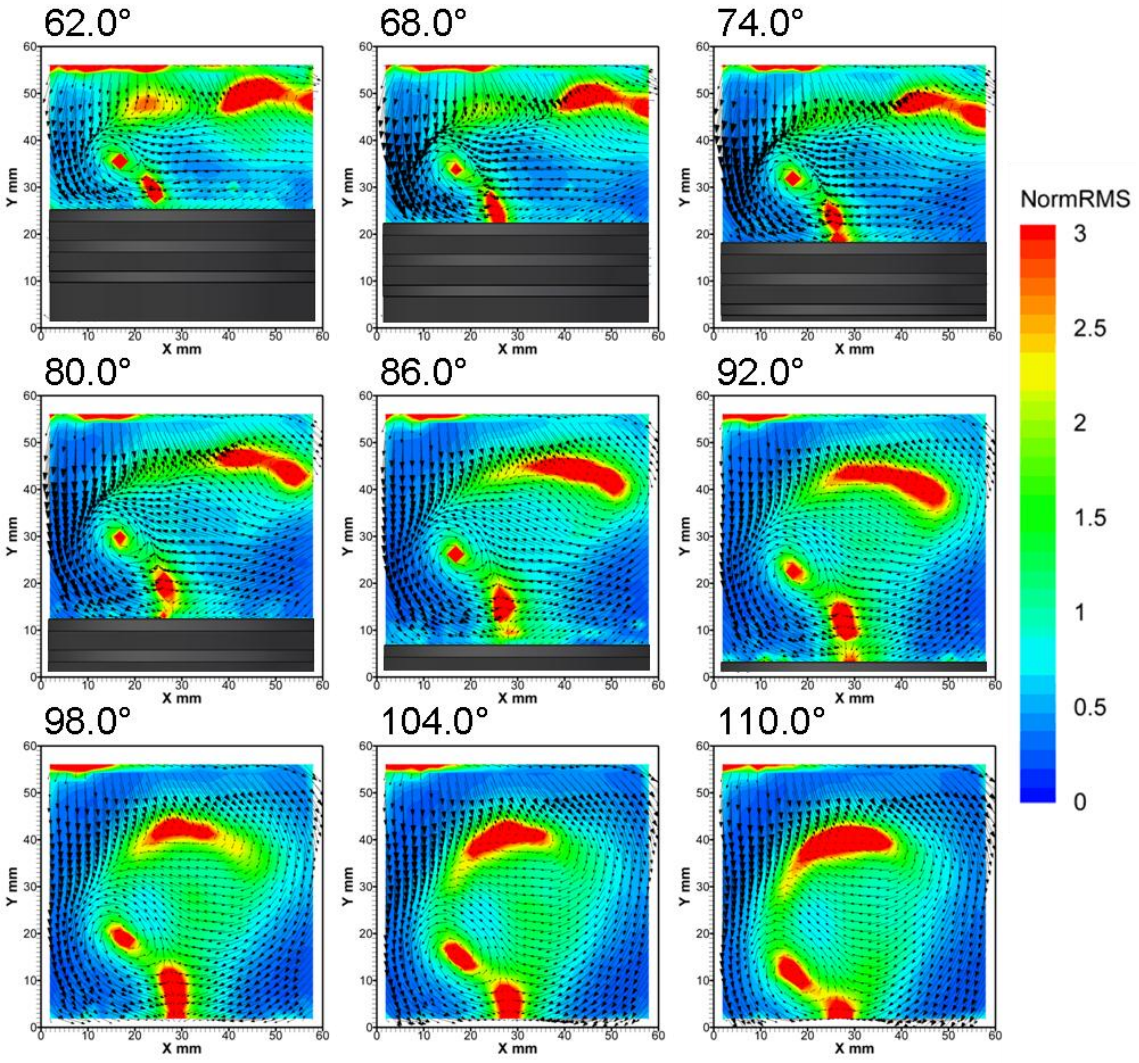

Figure 7.10 –*rms* of 100 low frequency cyclic variation flow fields on the bore centreline normalised by the mean low frequency flow, plotted for 62.0° to 110.0° CA ATDC and captured with HSDPIV at a rate of 1.5 kHz

7.2.1.2.2 Measurements from 100° to 316° CA ATDC

Those data presented in the previous section have shown flow variations to be established within the bulk in-cylinder flow motion. The benefit of the spatial and temporal flow field development, captured with the HSDPIV measurement system, has allowed the sequence of events feeding these flow variations to be studied. The data presented within this section are taken on the same image location and captured over the range 100° to 316° CA ATDC. Therefore, these data cover the latter stages of the intake

stroke and into the compression stroke, past the point of intake valve closure and towards the point of ignition.

Data presented in Figure 7.11 show the in-cylinder raw velocity flow fields for three arbitrary cycles within the tumble plane and on the bore centreline over the range 100.0° to 124.0° CA ATDC. The velocity scale for the presented data ranges from 0 to 25 $m.s^{-1}$ and shows the relatively high velocity jets due to the intake flow, and the interaction of the left and right jets as they collide above the piston as shown previously. In line with earlier findings, variation in the visible downward flow on either side of the image can be seen. For example, at 100.0° CA the width of visible downward flow on the left of the image in cycle A is substantially broader than that shown in cycle B. Also visible are the differing structures which were seen to occur within the central portion of the image. As the cycle progresses these differences are seen to lead to different flow field characteristics. The counter clockwise rotation in cycle A, visible early in the sequence has, by 124.0° CA, dropped out of the bottom of the imaged region. However, at this point in cycle C this feature is still visible at *circa* Y = 15 mm. In all cases decay in the overall velocity magnitude can be seen to occur over the duration of this sequence.

The progression of the three cycles is presented in Figure 7.12 for the range 160.0° to 184.0° CA ATDC. This sequence, therefore, covers the end of the intake stroke. As the velocity magnitude in the previous sequence was decaying, these images have been plotted with a velocity scale of 0 to 10 ms^{-1}. This highlights that the flow on the right hand side of the cylinder is now dominant in velocity magnitude of that of the left. It appears from these images that structures, which were previously clear, are now more difficult to distinguish. This suggests that as the intake valve jet flow slows and becomes less dominant towards the end of the intake stroke, the already established in-cylinder flow motions are left to interact with each other. There is relatively little additional energy released into the flow at this stage compared to the earlier stages of the intake stroke. The removal of the influence of the flows through the intake valve results in the interactions between the existing structures being ever more influential.

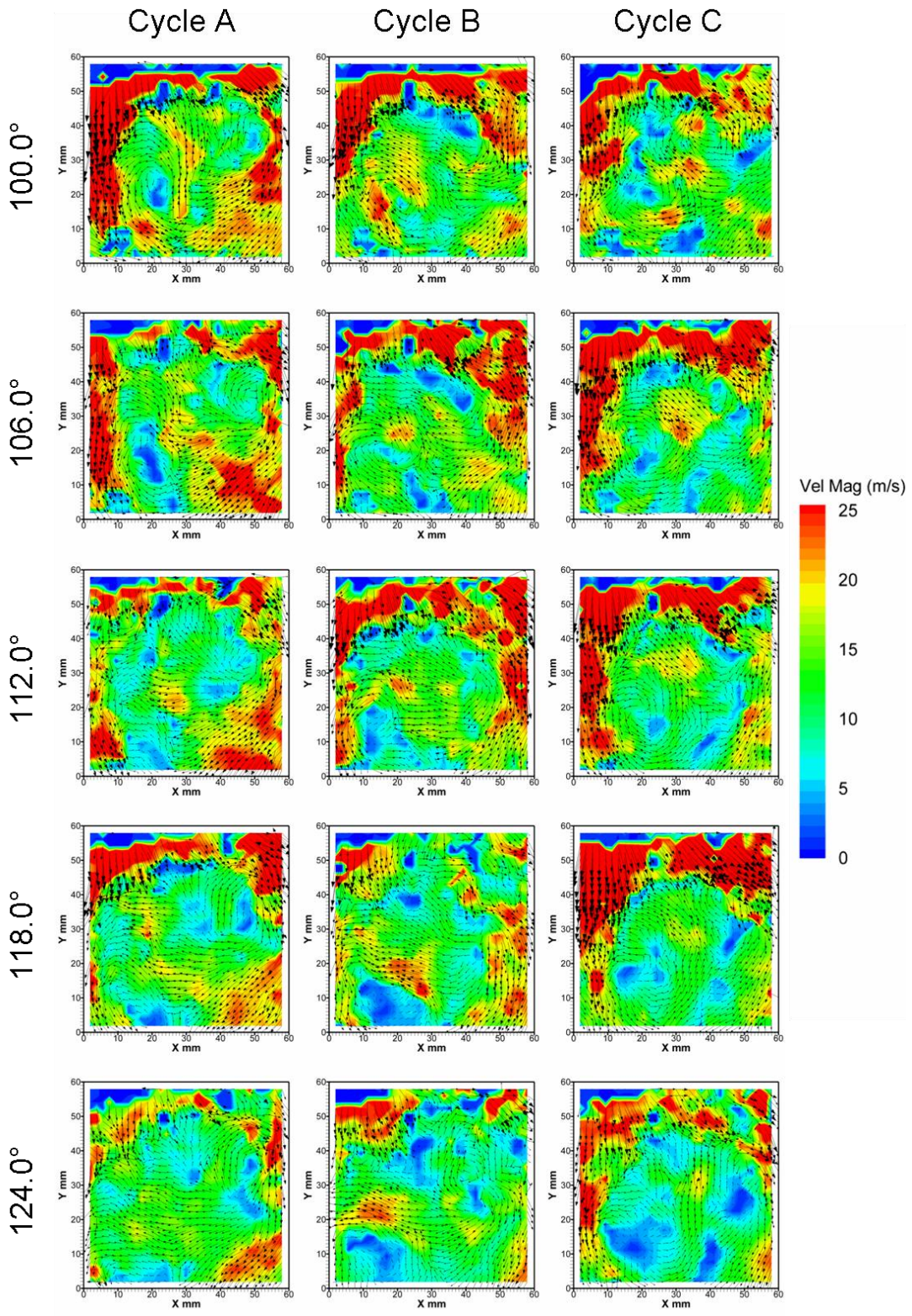

Figure 7.11 - Raw flow fields on the bore centreline for three individual cycles from 100.0° to 124.0° CA ATDC captured with HSDPIV at a rate of 1.5 kHz

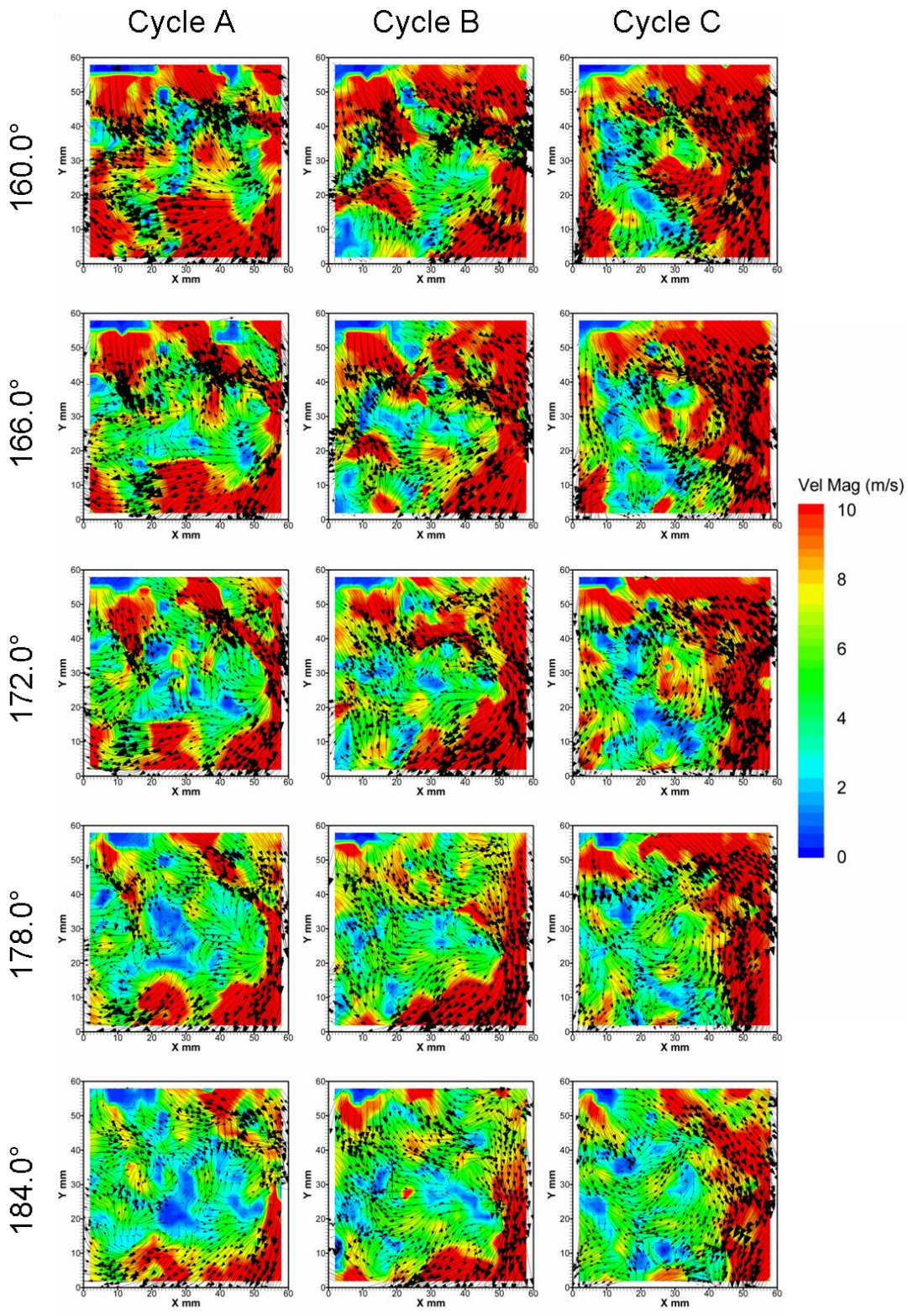

Figure 7.12 - Raw flow fields on the bore centreline for three individual cycles from 160.0° to 184.0° CA ATDC captured with HSDPIV at a rate of 1.5 kHz

Figure 7.13 and Figure 7.14 present the further development of these three cycles for the ranges 214.0° to 238.0° CA and 268.0° to 292.0° CA ATDC respectively. These show further decay in the energy contained within the flow field along with increasingly random flows which appear to be heavily influenced by 3-dimensional motions. For example, at 214.0° CA ATDC cycle B shows a source of flow, at *circa* X = 40 mm and Y = 20 mm, entering the measurement plane. Cycle A shows the most organised flow, and by 238.0° CA exhibits a clockwise recirculation in the lower left quadrant of the image. In Figure 7.14 the piston is rising through the measurement region. The flow in the top of the images can be seen to have decayed further; however, some level of bulk clockwise recirculation is visible in each of the three cycles presented.

In Figure 7.15 to Figure 7.18, the low frequency bulk motion flow fields, filtered using a low pass frequency of 280 Hz, are shown for the same three cycles and four image sequences presented above. The flow over the range 100.0° to 124.0° CA ATDC is shown in Figure 7.15, where the application of the low frequency filter, results in providing an indication of bulk flow motion. At 100.0° CA, the flow in the bottom right hand quadrant of cycle A shows a much larger magnitude than is shown within the same region of either cycle B or C. This high relative velocity magnitude is still evident at the end of the image sequence presented. As a result of this higher velocity flow, the counter clockwise rotation which is visible in the bottom left quadrant appears to be forced into a different shape in cycle A than that shown in cycle C. This rotation in cycle C is seen to be more circular and exist higher in the cylinder, giving the appearance that the clockwise rotation (primary tumble motion) is less dominant than in either cycles A and B. By 124.0° CA significant decay in the intake flows, shown on both sides of the measurement region, has occurred.

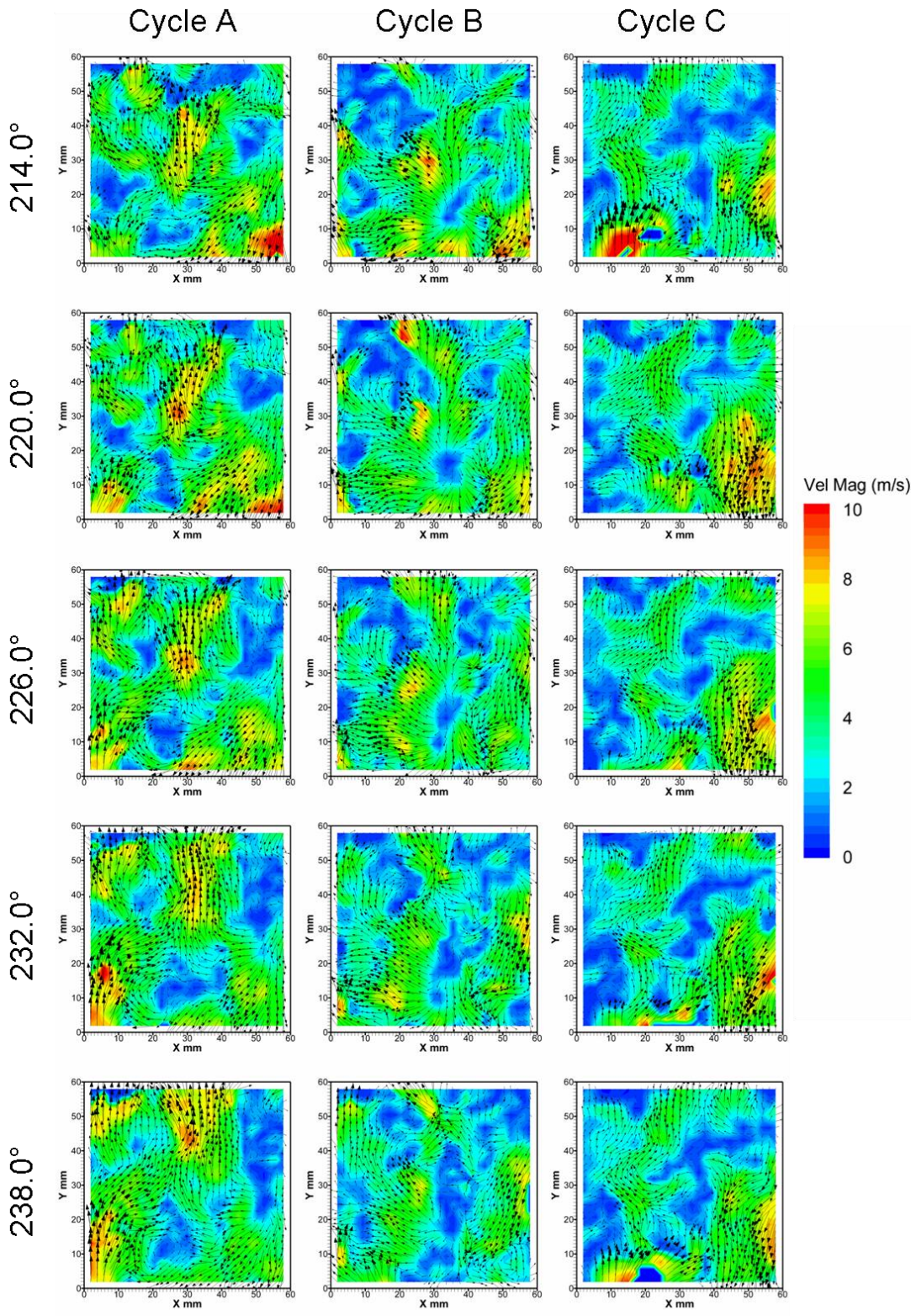

Figure 7.13 - Raw flow fields on the bore centreline for three individual cycles from 214.0° to 238.0° CA ATDC captured with HSDPIV at a rate of 1.5 kHz

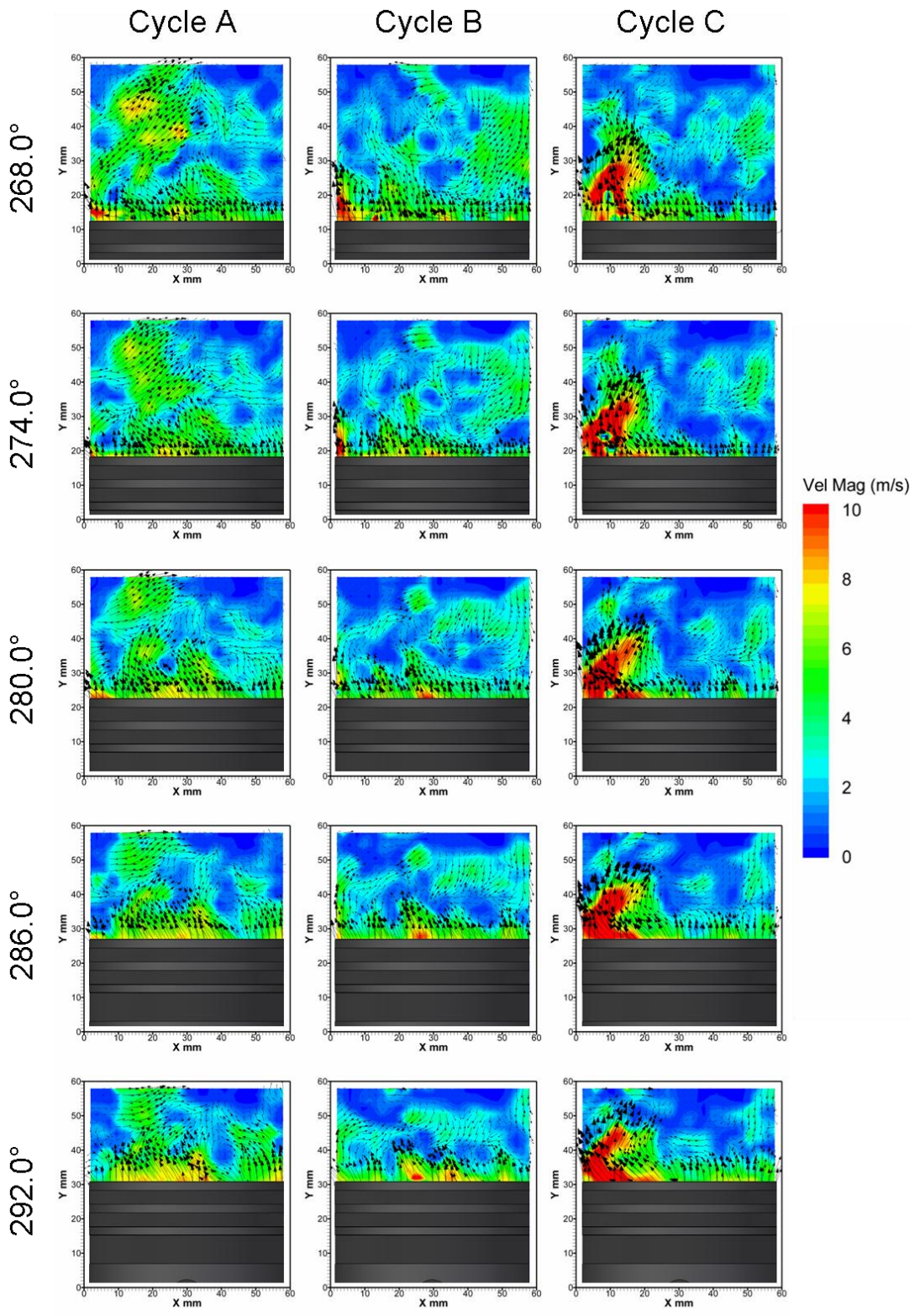

Figure 7.14 - Raw flow fields on the bore centreline for three individual cycles from 268.0° to 292.0° CA ATDC captured with HSDPIV at a rate of 1.5 kHz

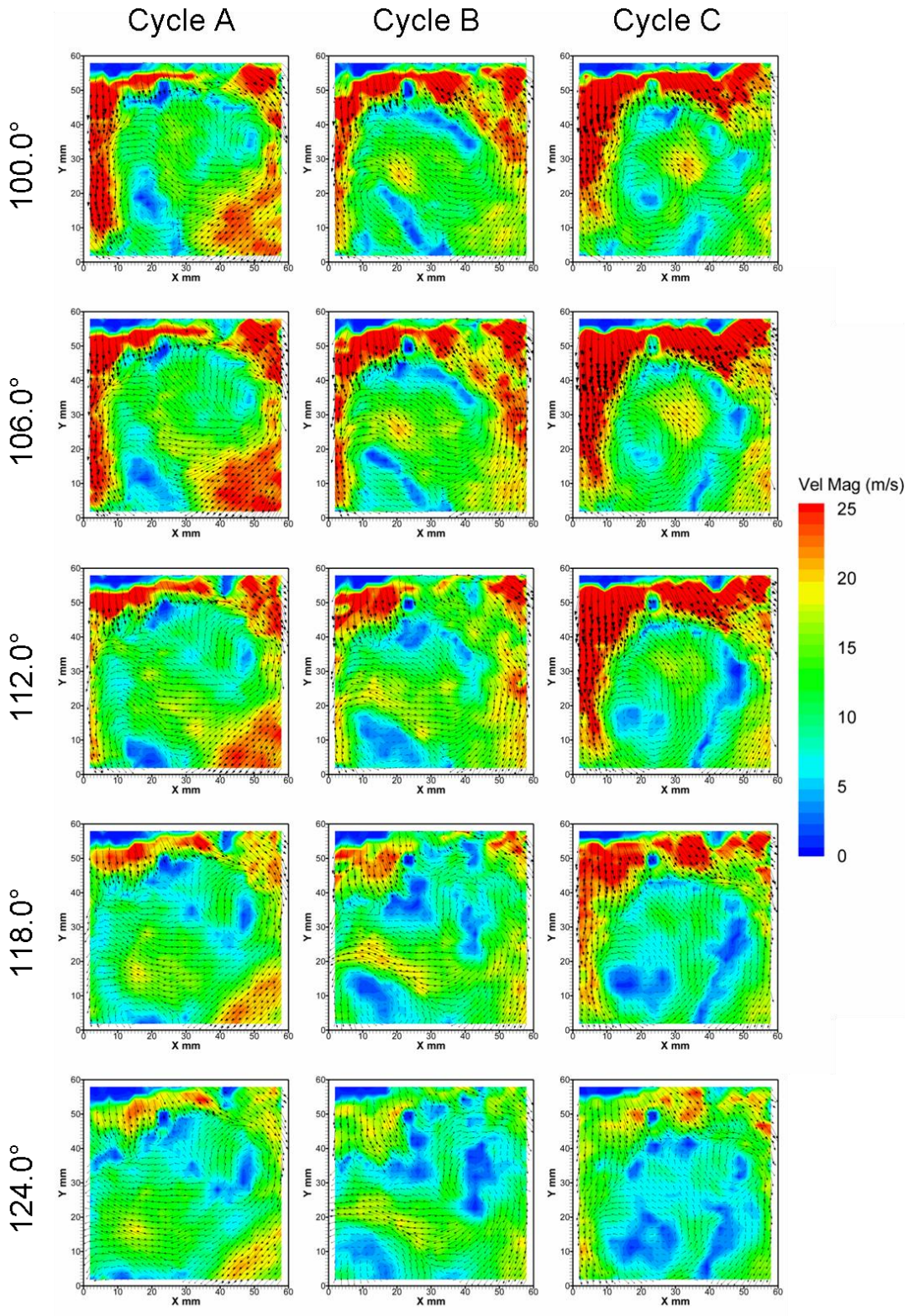

Figure 7.15 – Low frequency flow fields on the bore centreline for three individual cycles from 100.0° to 124.0° CA ATDC captured with HSDPIV at a rate of 1.5 kHz

Figure 7.16 presents the low frequency bulk flow for the range 160° to 180.0° CA. These low frequency flow fields, when compared to the raw data shown in Figure 7.12, appear smoothed both spatially and temporally. As discussed previously, a strong flow on the right hand side of the region is visible, with a clockwise rotation in the upper right hand quadrant of the images at 160.0° CA. Relative to the raw flow field images, the low frequency fields presented here display slightly clearer structures within the flow.

Figure 7.17 and Figure 7.18 present the low frequency bulk flow for the ranges 214.0° to 238.0° CA ATDC and 268.0° to 292.0° CA ATDC respectively. In these images the same trends, as per the raw velocity fields, can be seen to be smoothed both temporally and spatially. These low frequency fields help to draw out existing structures within the bulk flow motions. For example, at 220.0° CA, across all three cycles presented, bulk clockwise tumble motion can be seen, due to downward motion on the right of the images and upwards on the left. At 268.0° CA, in Figure 7.18, both cycle B and C display eddies contained within the bulk flow, with diameters of *circa* 10 mm. For cycle B one instance occurs between X = 20 to 30 mm and Y = 30 to 40 mm.

It is questionable whether the existence of these small eddies suggests that a lower frequency filter should have been applied. However, as the eddies appear to remain in a similar position across a number of CA, and the filtering is applied temporally at one spatial location, this helps these structures pass into the low frequency filtered data. The low frequency raw data presented previously uses the same low frequency cut-off value from the valve jet through to flows in the pent roof leading up to combustion. In these cases this frequency has shown to adequately draw out the bulk motion flows within the images. As discussed in Chapter 2, the selection of the cut-off frequency to apply is not trivial as there is no discrete transition between the high and low frequency flows.

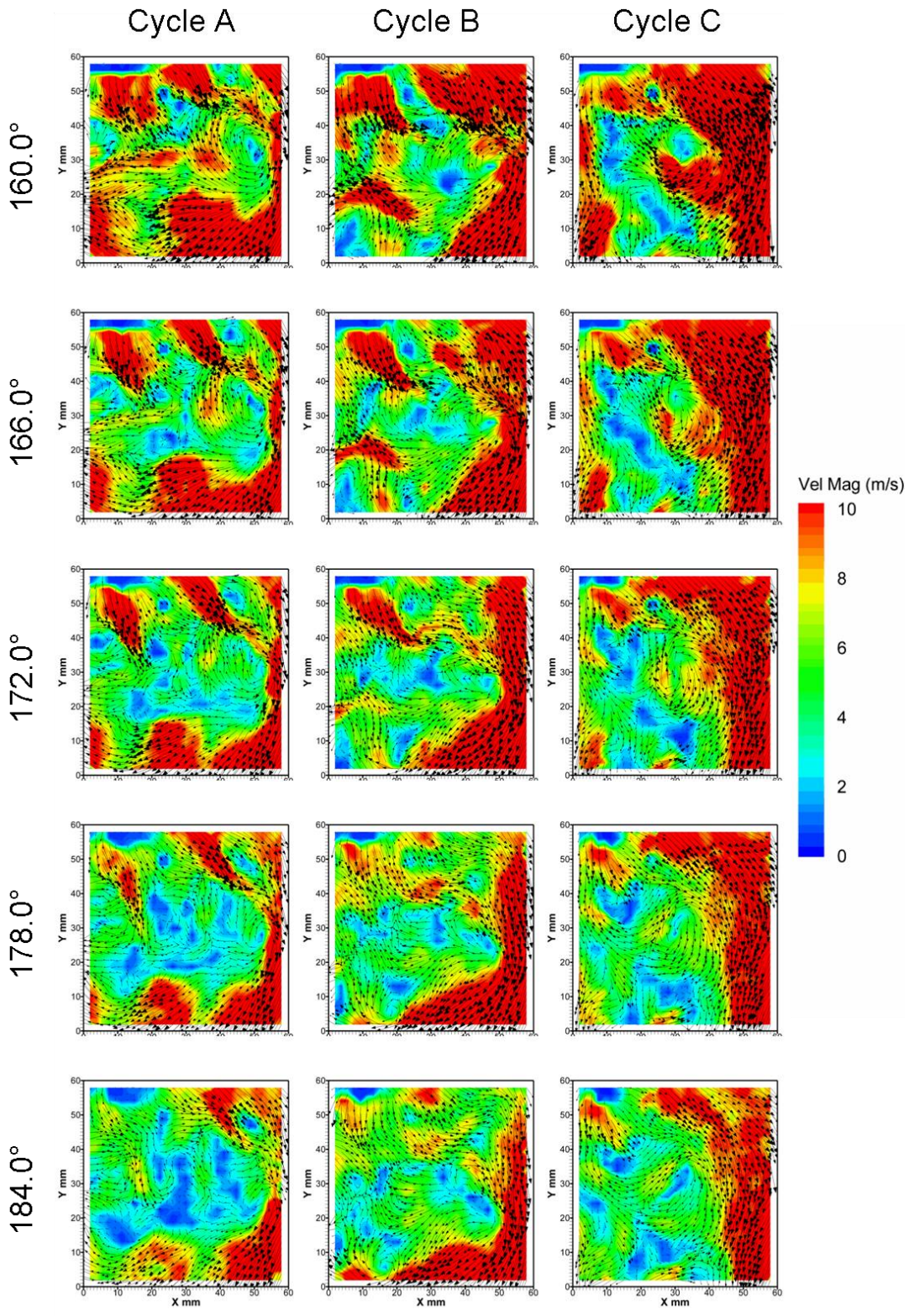

Figure 7.16 – Low frequency flow fields on the bore centreline for three individual cycles from 160.0° to 184.0° CA ATDC captured with HSDPIV at a rate of 1.5 kHz

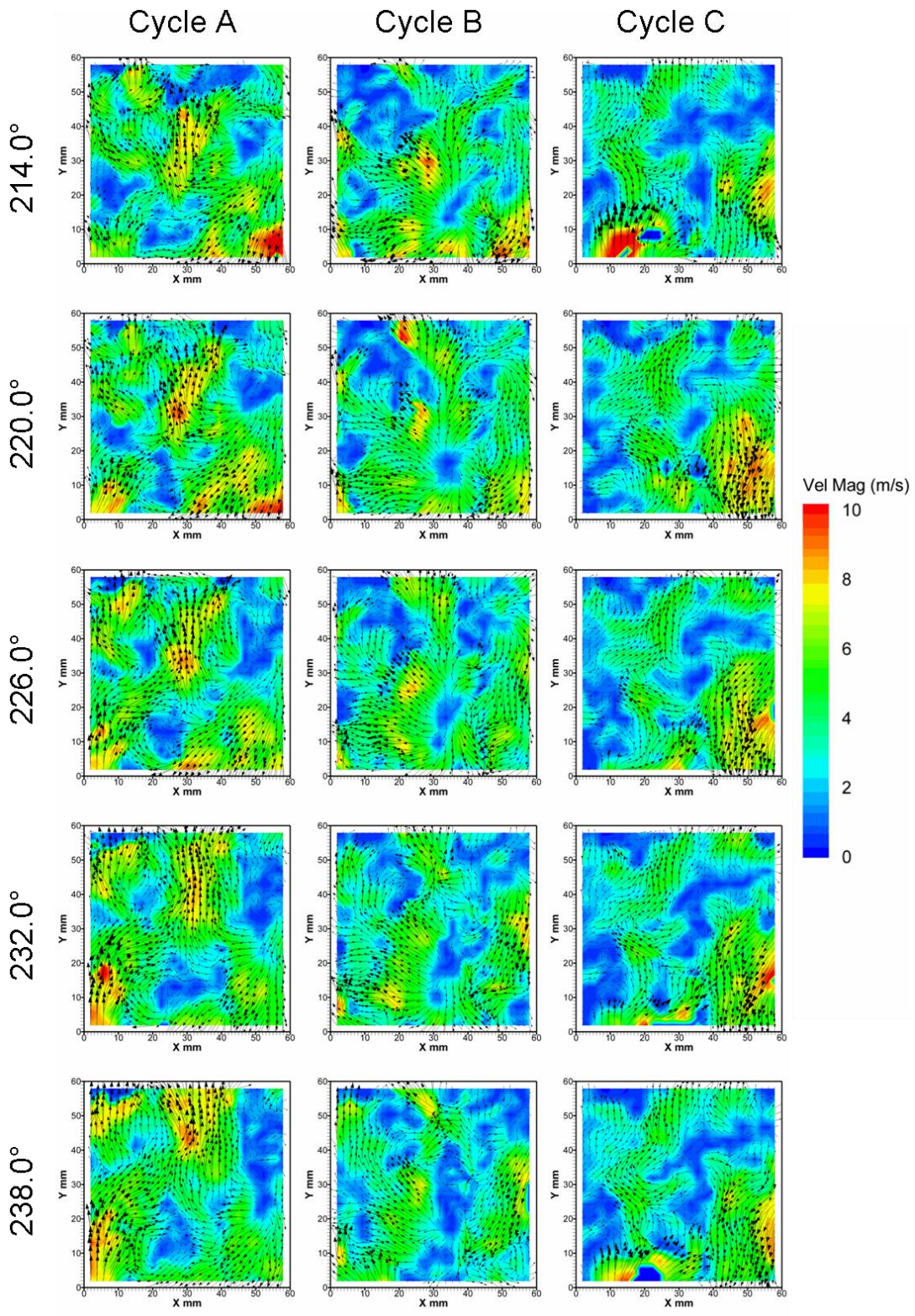

Figure 7.17 – Low frequency flow fields on the bore centreline for three individual cycles from 214.0° to 238.0° CA ATDC captured with HSDPIV at a rate of 1.5 kHz

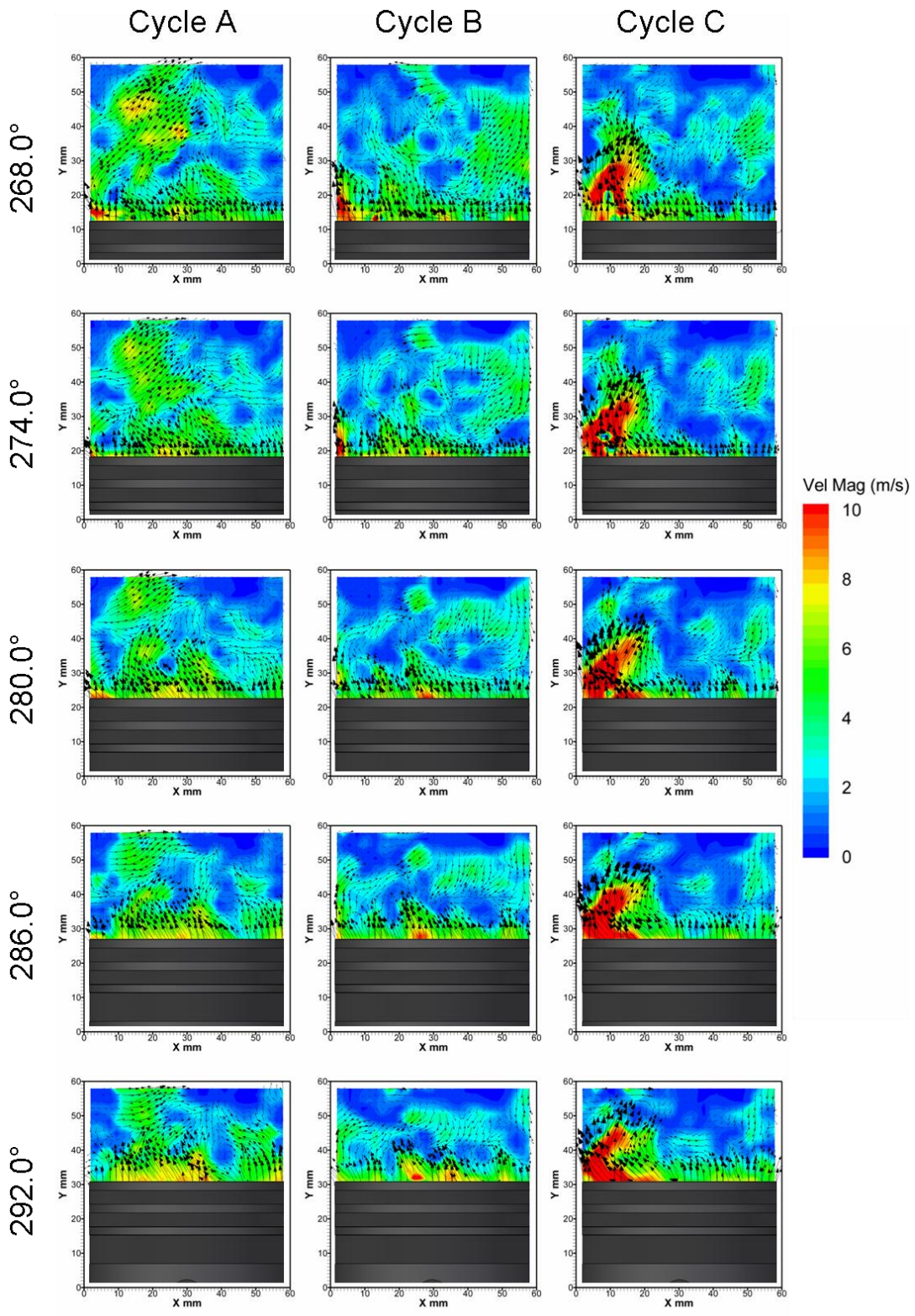

Figure 7.18 – Low frequency flow fields on the bore centreline for three individual cycles from 268.0° to 292.0° CA ATDC captured with HSDPIV at a rate of 1.5 kHz

In Figure 7.19 and Figure 7.20, the mean low-frequency flow fields on the bore centreline have been presented for the ranges 100.0° to 184.0° CA and 232.0° to 316.0° CA ATDC respectively. This sequence shows the progression of mean low frequency flow fields relative to those presented in Figure 7.7. Initially, when compared with the previous figure, distinct similarities are shown, as would be expected. However, as the mean low frequency fields are derived from a different sample set of 100 cycles, these minor differences suggest that the sample size used is not quite large enough. For the purpose of this thesis, where the focus of the novel research is based upon spatial and temporal cyclic variations, the sample size was, however, still considered to be adequate.

Figure 7.19 shows the continuing development of bulk tumble motion within the mean flows as the clockwise rotation remains relatively stable in location between 100.0° CA and 148.0° CA. Beyond this it drops by approximately 5 to 10 mm, remaining firmly within the field of view. The counter-clockwise rotation visible at 100.0° CA, at *circa* X = 15 mm and Y = 15 mm, drops consistently throughout the frame and by 130.0° CA its centre is outside the field of view. In Figure 7.20 the bulk tumble motion is still evident with a stagnating region in the centre of the image at approximately X = 30 mm. As the piston moves up the base of the stagnating region is raised through the image.

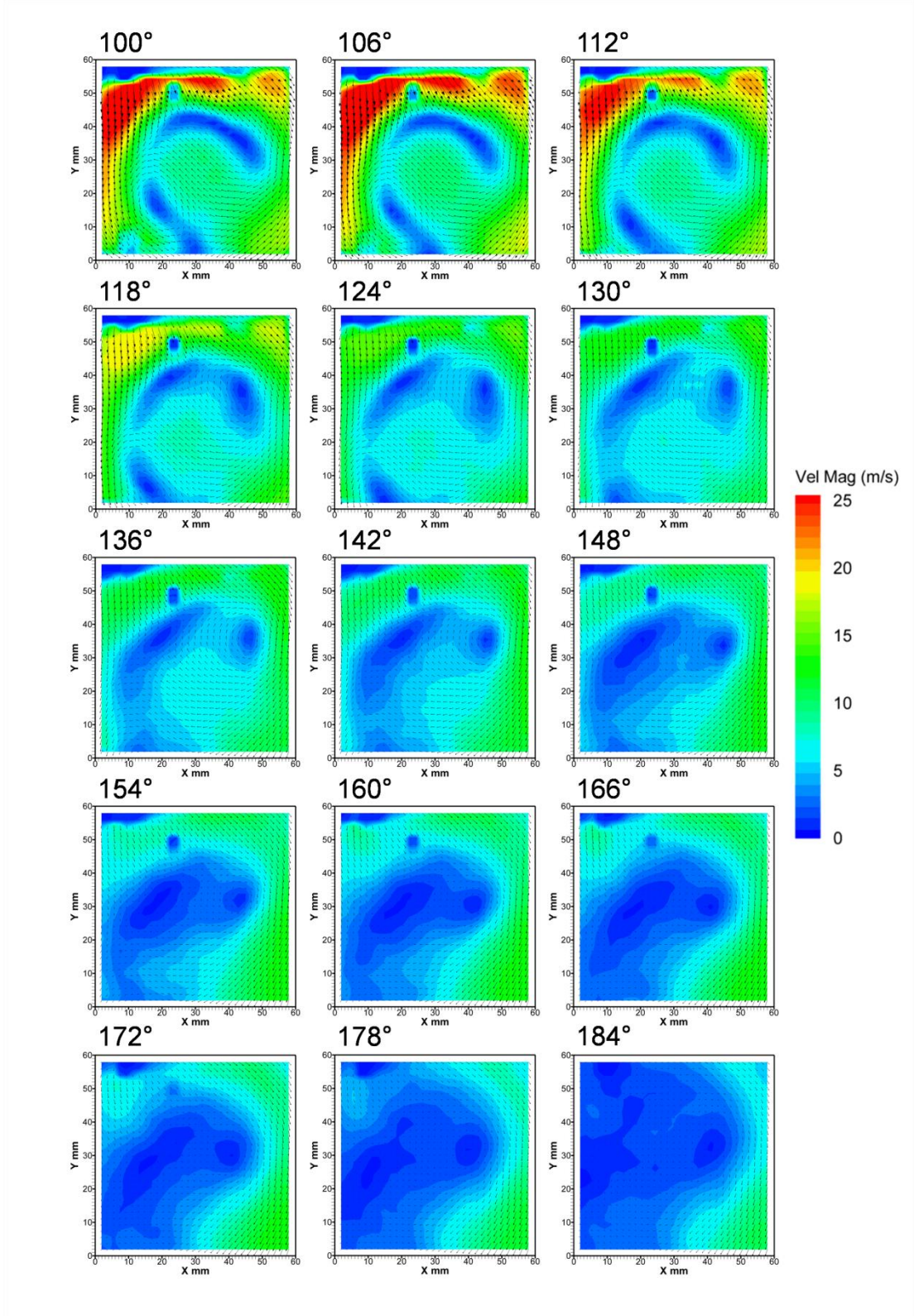

Figure 7.19 - Mean low frequency flow fields on the bore centreline from 100.0° to 184.0° CA ATDC captured with HSDPIV at a rate of 1.5 kHz

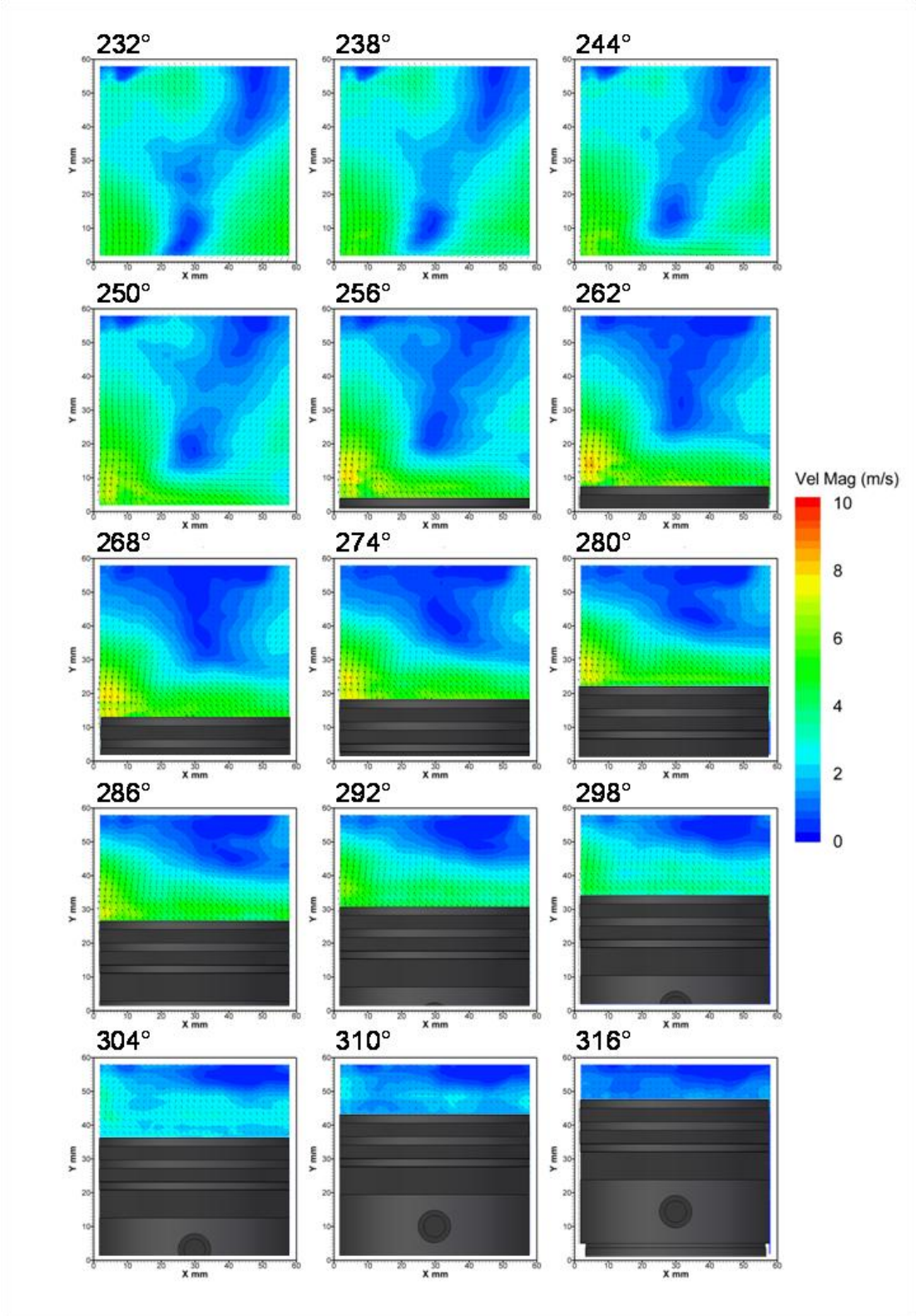

Figure 7.20 – Mean low frequency flow fields on the bore centreline from 232.0° to 316.0° CA ATDC captured with HSDPIV at a rate of 1.5 kHz

Figure 7.21 to Figure 7.24 present the low frequency cyclic variations relative to the mean low frequency flow field presented previously. As discussed, these low frequency cyclic variations show how the cycle's bulk flow motion varied from the mean flow. The images show magnitude of cyclic variation with overlaid low frequency flow field vectors. Figure 7.21, across the range 100.0° to 124.0° CA ATDC, shows differing regions of high variation in magnitude across the three cycles presented. At 112.0° CA this is evident in cycles A and B which both display a region of high variation in the bulk flow motion on the right hand side of the image, as a result of the high velocity downward flows previously discussed. Conversely, in cycle C, which exhibited greater balance between the clockwise and counter clockwise rotations previously, the variation is seen to result from a more significant flow from the left hand side of the image, contributing to the counter clockwise rotation evident in this cycle.

Figure 7.22 shows the range 160.0° to 184.0° CA ATDC and the range of cyclic variation magnitude presented has been reduced to 0 to 5 $m.s^{-1}$. Even though many regions of the image display a variation greater than 5 $m.s^{-1}$, and therefore appear saturated, this range has been chosen to lead into the subsequent figures (Figure 7.23 and Figure 7.24) to track characteristics over time more easily. In Figure 7.22 the regions of variation have become more fragmented. This follows into Figure 7.23 and correlates with previous observations made where out of plane motions become more evident. Over time the magnitude of the variations decay as the bulk velocities also decay.

In Figure 7.24 cycle A exhibits a lower magnitude of cyclic variation than cycles B and C, which show a similar magnitude to that of the raw flow velocities. This therefore, demonstrates the high level of variation occurring, especially when considering the velocity of the bilk motion. This has been further investigated in Figure 7.25 to Figure 7.28 where the magnitude of the cyclic variation relative to the local bulk motion velocity is shown. This has been done by normalising the cyclic variation using the local bulk flow velocity. In these figures the contour plot is of the normalised cyclic variation and the vectors superimposed are the low frequency flow fields.

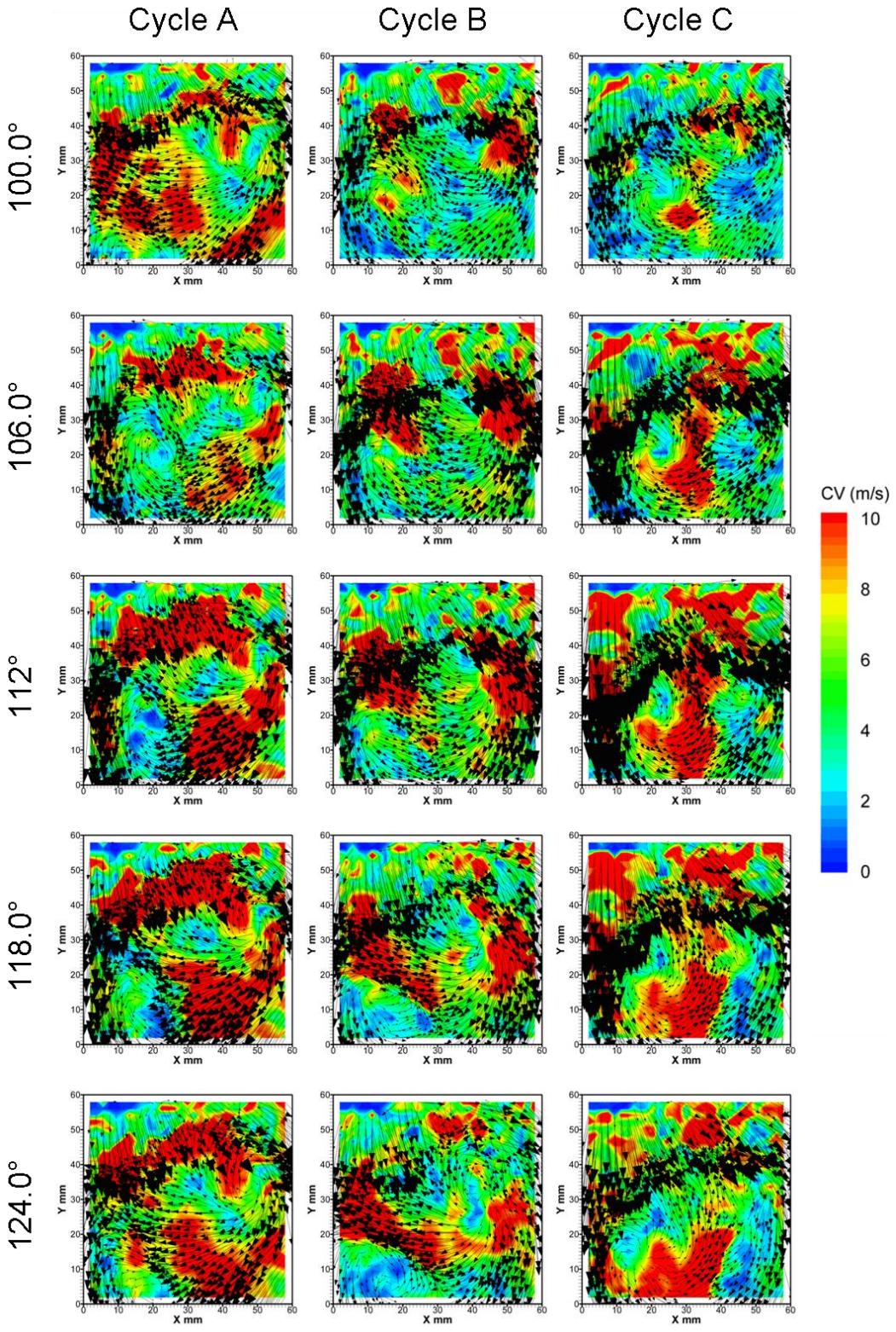

Figure 7.21 - Low frequency cyclic variation flow fields on the bore centreline from 100.0° to 124.0° CA ATDC captured with HSDPIV at a rate of 1.5 kHz

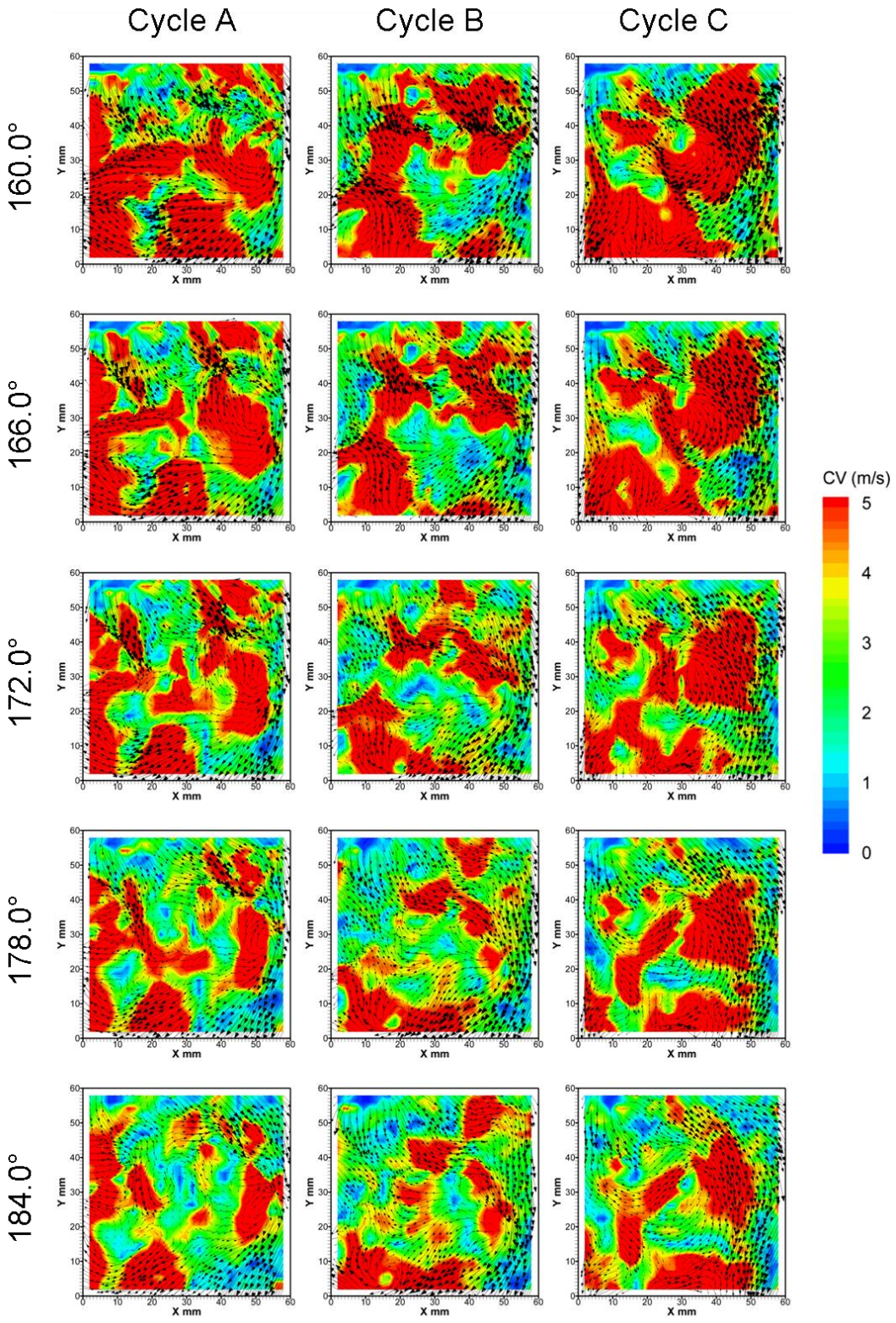

Figure 7.22 - Low frequency cyclic variation flow fields on the bore centreline from 160.0° to 184.0° CA ATDC captured with HSDPIV at a rate of 1.5 kHz

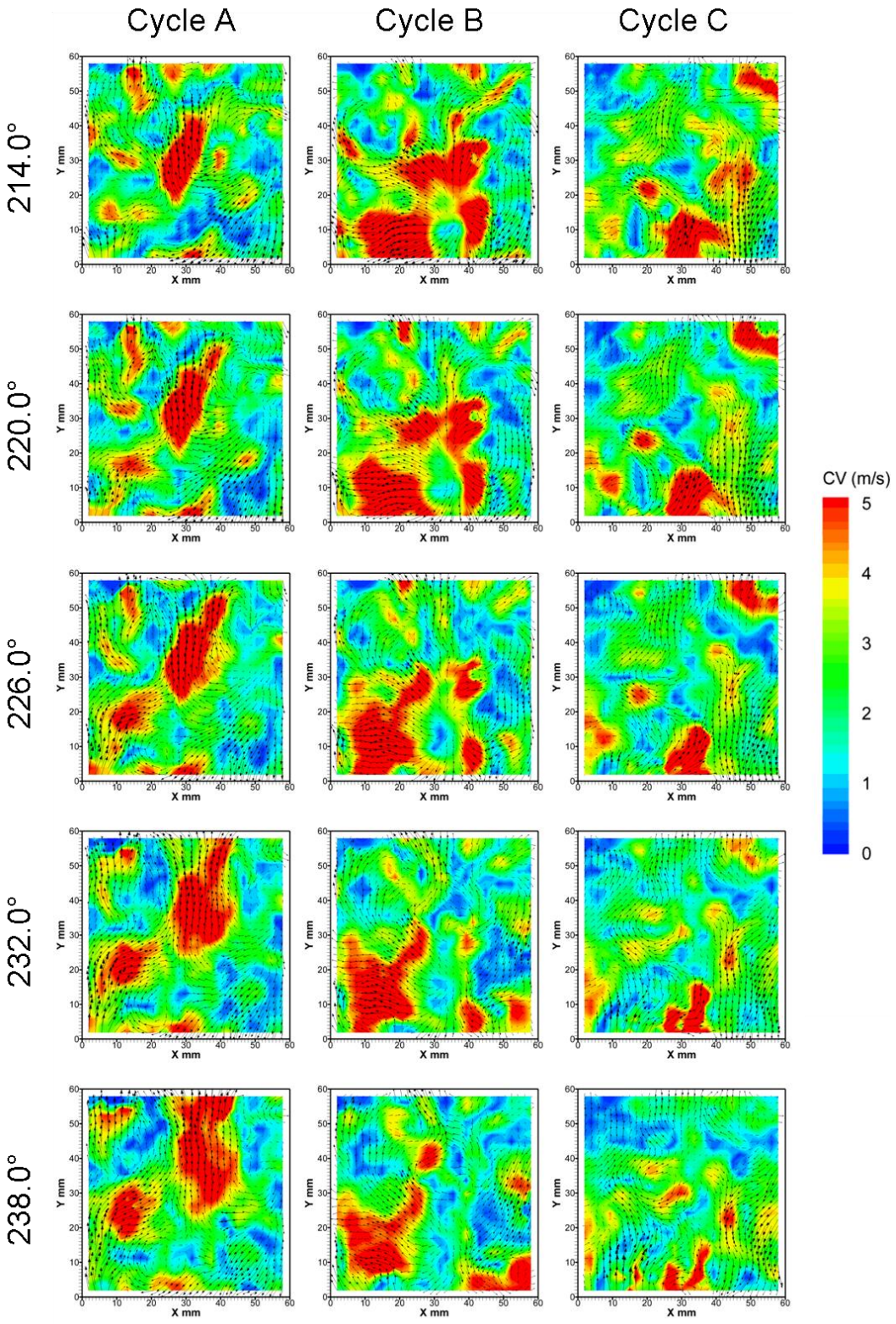

Figure 7.23 - Low frequency cyclic variation flow fields on the bore centreline from 214.0° to 238.0° CA ATDC captured with HSDPIV at a rate of 1.5 kHz

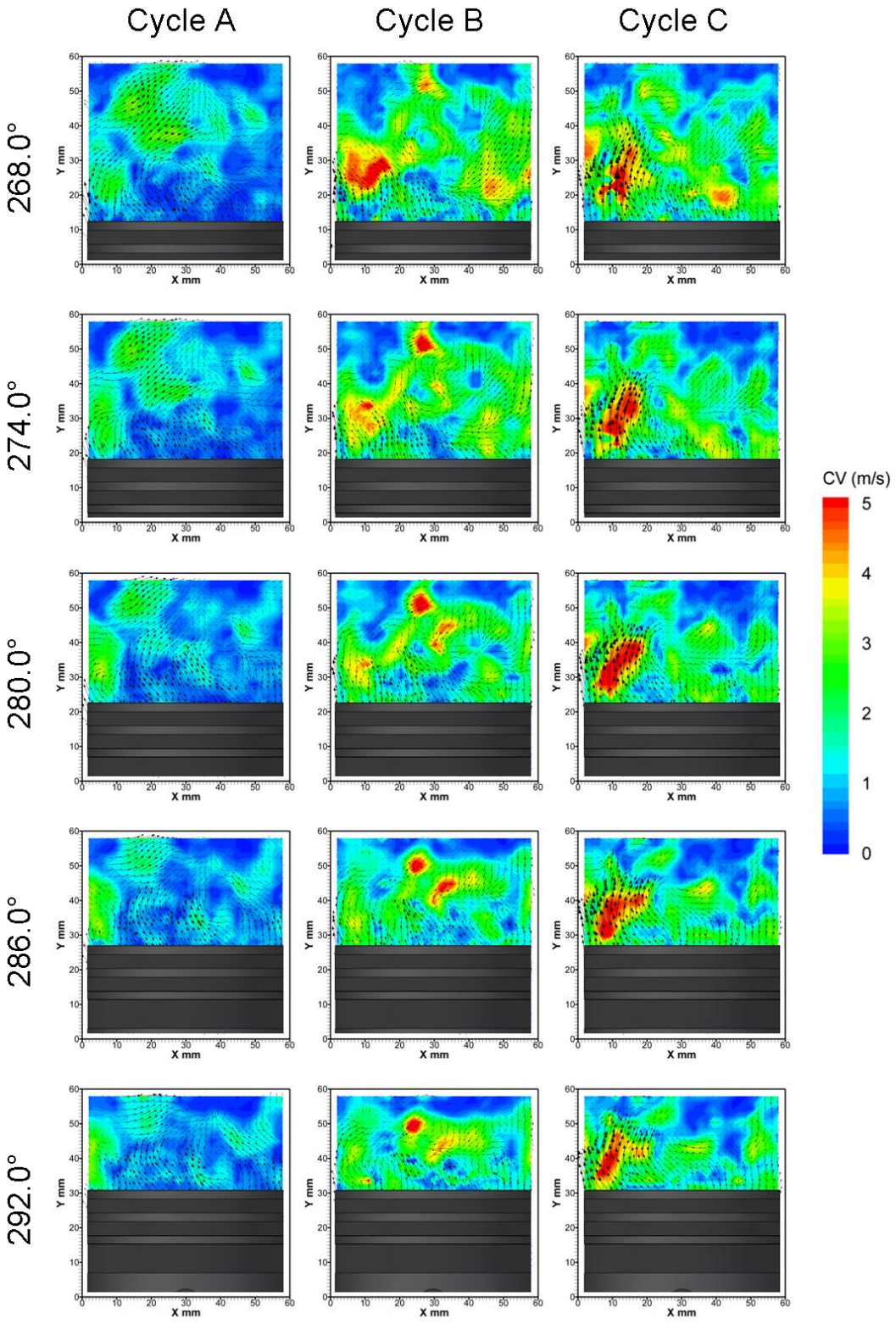

Figure 7.24 - Low frequency cyclic variation flow fields on the bore centreline from 268.0° to 292.0° CA ATDC captured with HSDPIV at a rate of 1.5 kHz

In Figure 7.25 the low velocity regions are highlighted due to the nature of the data being presented. In each case the clockwise and counter clockwise rotation centres are emphasized along with the interaction of the jets colliding above the piston.

In Figure 7.26 and Figure 7.27 the focus remains largely on the low velocities occurring within the central region of the images. By Figure 7.28 this region is located in the upper central portion of the image for all three cycles, throughout the range 268.0° to 292.0° CA ATDC. This region is being compressed and pushed up towards the top of the image by the piston rising. If this remains the case leading up to ignition this area of high relative cyclic variation is located around the spark plug, leading to the variations observed within Section 5.3. It is clear from Figure 7.28 that the regions of high relative variability show differences in the size and fragmentation across all three cycles.

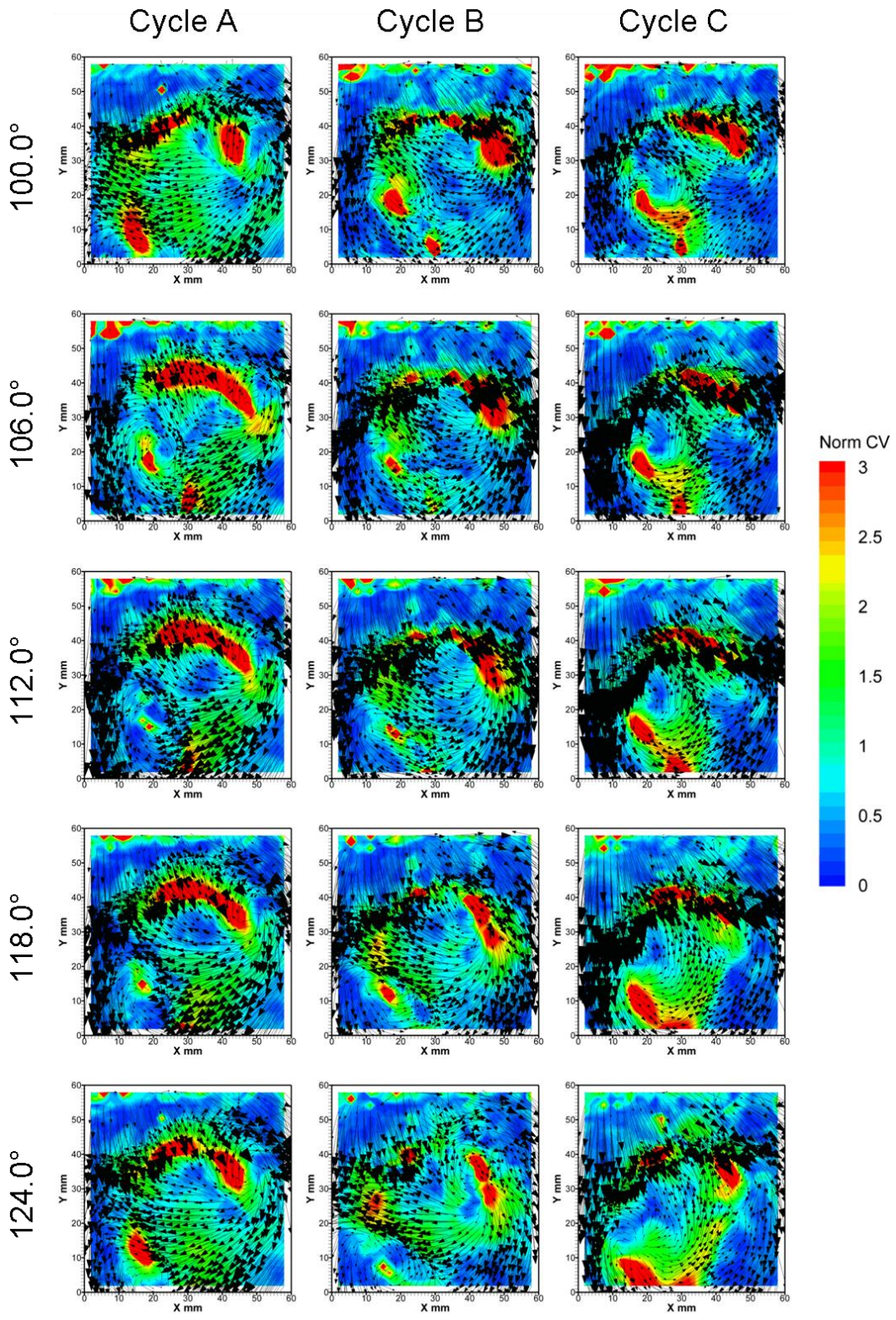

Figure 7.25 – Low frequency cyclic variation normalised by the mean low frequency flow field for the range 100.0° to 124.0° CA ATDC

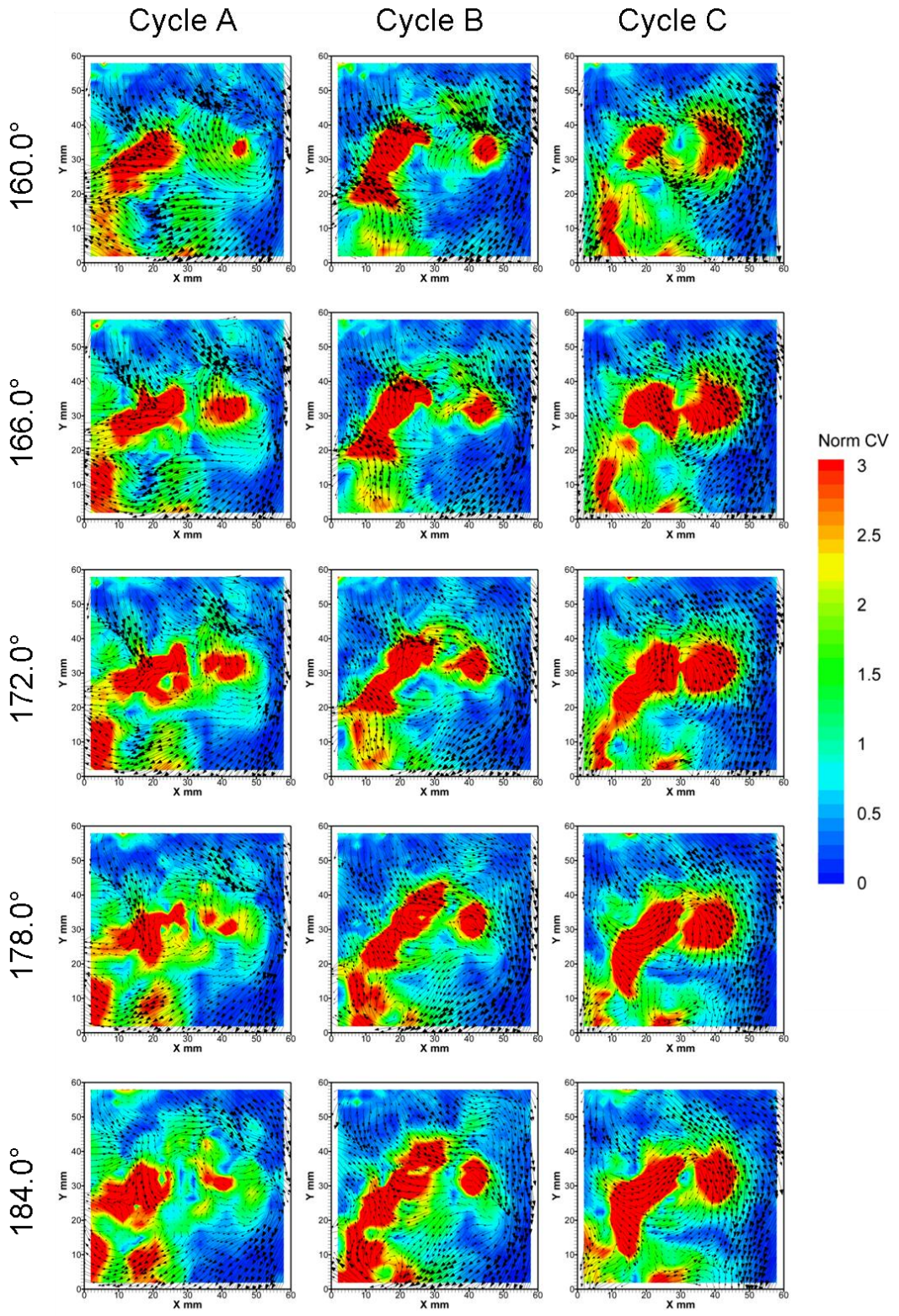

Figure 7.26 - Low frequency cyclic variation normalised by the mean low frequency flow field for the range 160.0° to 184.0° CA ATDC

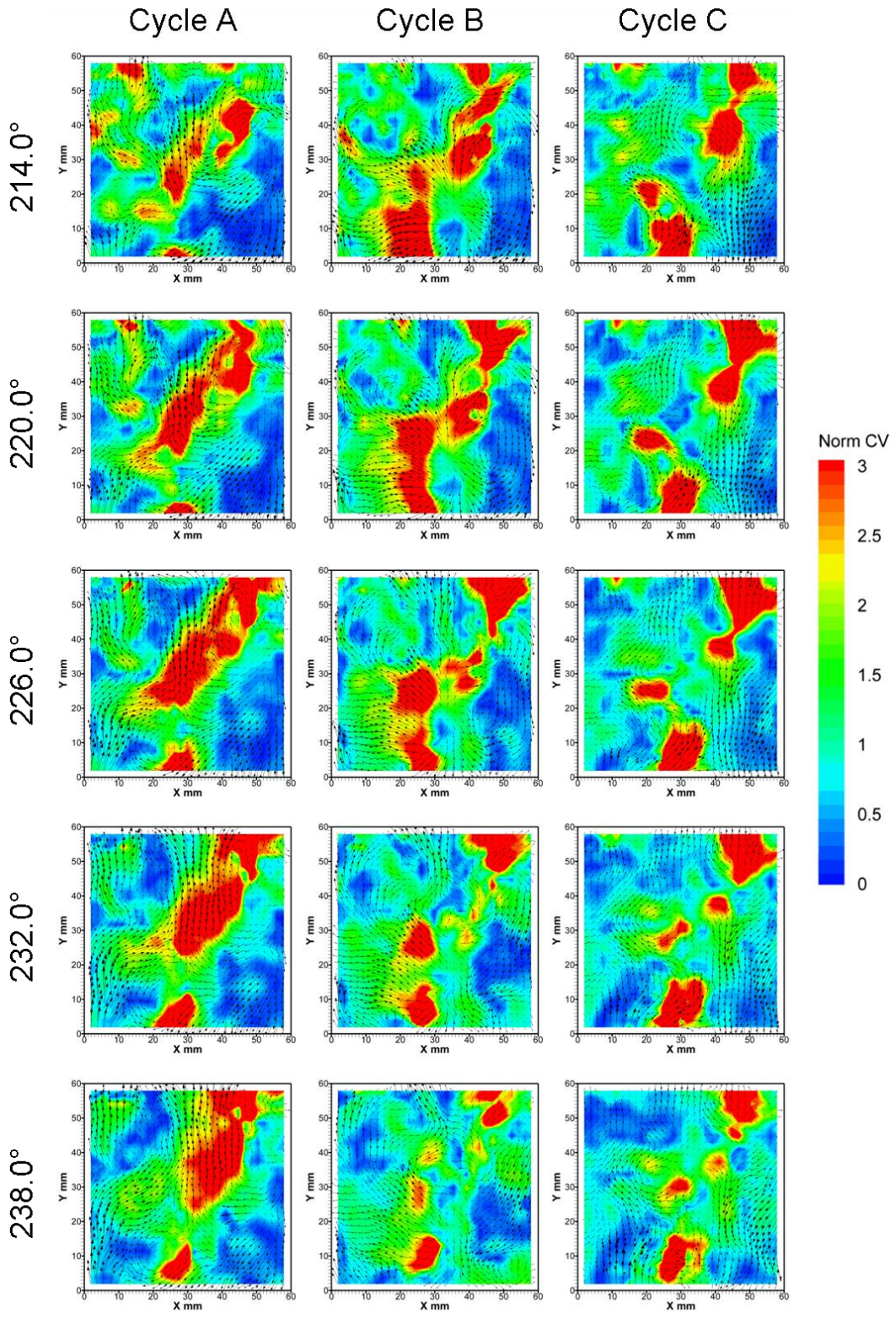

Figure 7.27 - Low frequency cyclic variation normalised by the mean low frequency flow field for the range 214.0° to 238.0° CA ATDC

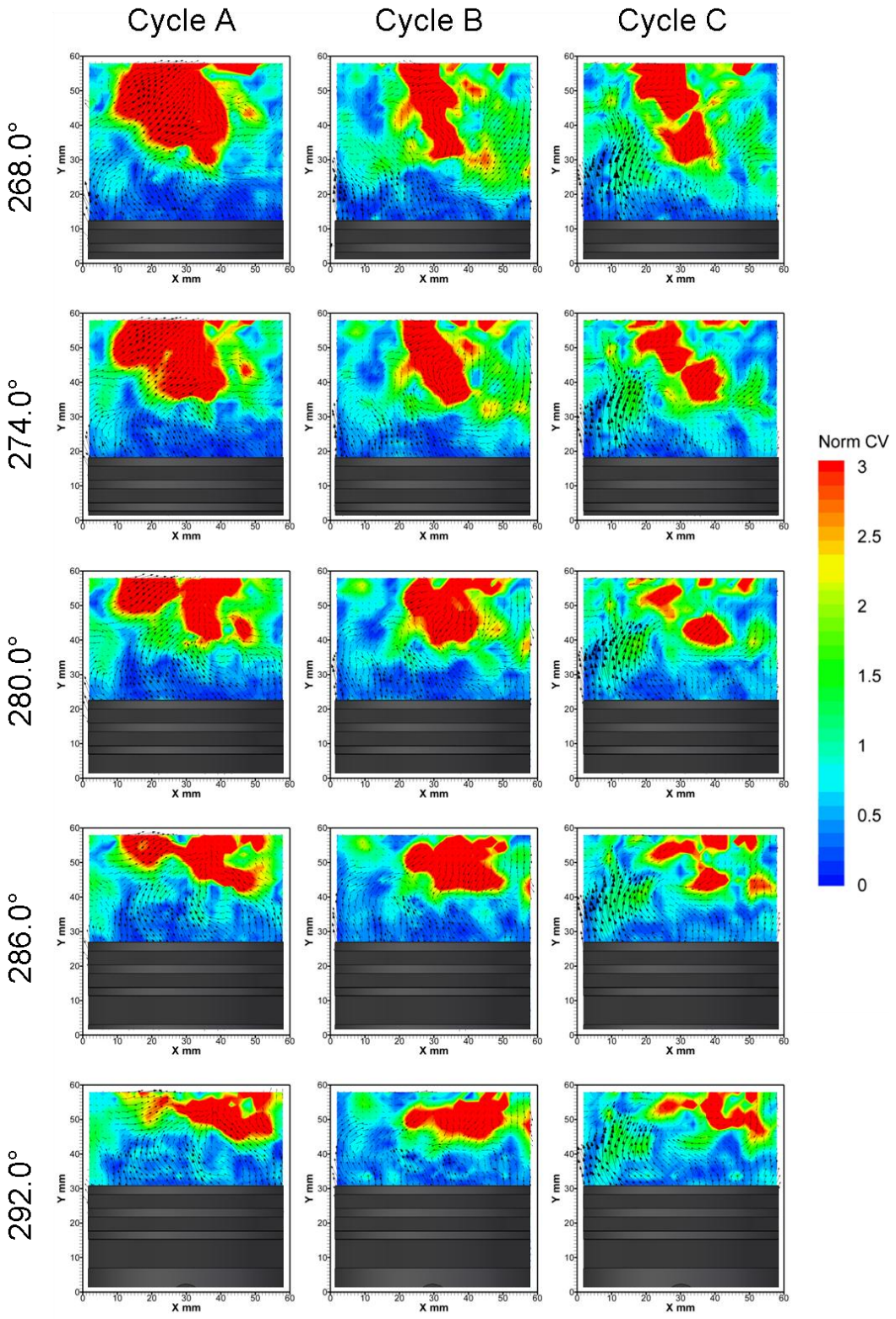

Figure 7.28 - Low frequency cyclic variation normalised by the mean low frequency flow field for the range 268.0° to 292.0° CA ATDC

Figure 7.29 presents the magnitude of the *rms* of the low frequency cyclic variation calculated over 100 cycles for the range 100.0° to 184.0° CA ATDC. In this case the overlaid vectors are for the low frequency mean flow. This time sequence therefore follows on from that presented in Figure 7.9. It can be seen that the region of high variation caused by the mixing of the intake flows within the centre of the imaged region decays in magnitude and, over the course of the sequence, against the range of the scale (0 to 10 $m.s^{-1}$), appears to become more homogeneous. In Figure 7.30 the time sequence is continued for the range 232.0° to 316.0° CA ATDC, note this sequence has a revised scale of 0 to 5 $m.s^{-1}$. This shows a region of larger variation in the lower left quadrant, where the mean flow passing horizontally across the image (from right to left) then turns upwards, the highest variation occurs where the change in direction has the tightest radius.

The temporally derived u', as calculated in Section 6.3, has been shown in Figure 7.31 to Figure 7.34 for the three cycles and for the four CA ranges previously presented. These data are based on the high frequency fluctuations remaining from the frequency filtering of the raw data. In Figure 7.31 all cycles display a region of high u' in the top right hand quadrant which can be correlated to the intake valve jet (see Section 6.3 and particularly Figure 6.39). The remainder of the imaged region shows spatial variations in u' with the mean magnitude appearing to decay over time, as expected.

This decay continues in Figure 7.32. At 160.0° CA, all three cycles exhibit spatial variations in u' in the right hand side of the image, this is more prominent in cycle C which has consistently shown different characteristics to the other two cycles within this region. Further decay is evident throughout the CA ranges considered within Figure 7.33 and Figure 7.34. The u' range observed within the data presented in Figure 7.34 is of a similar magnitude to that shown within the pent roof region later in the cycle, as presented in Section 5.3. In line with those data, significant spatial variations are seen to exist.

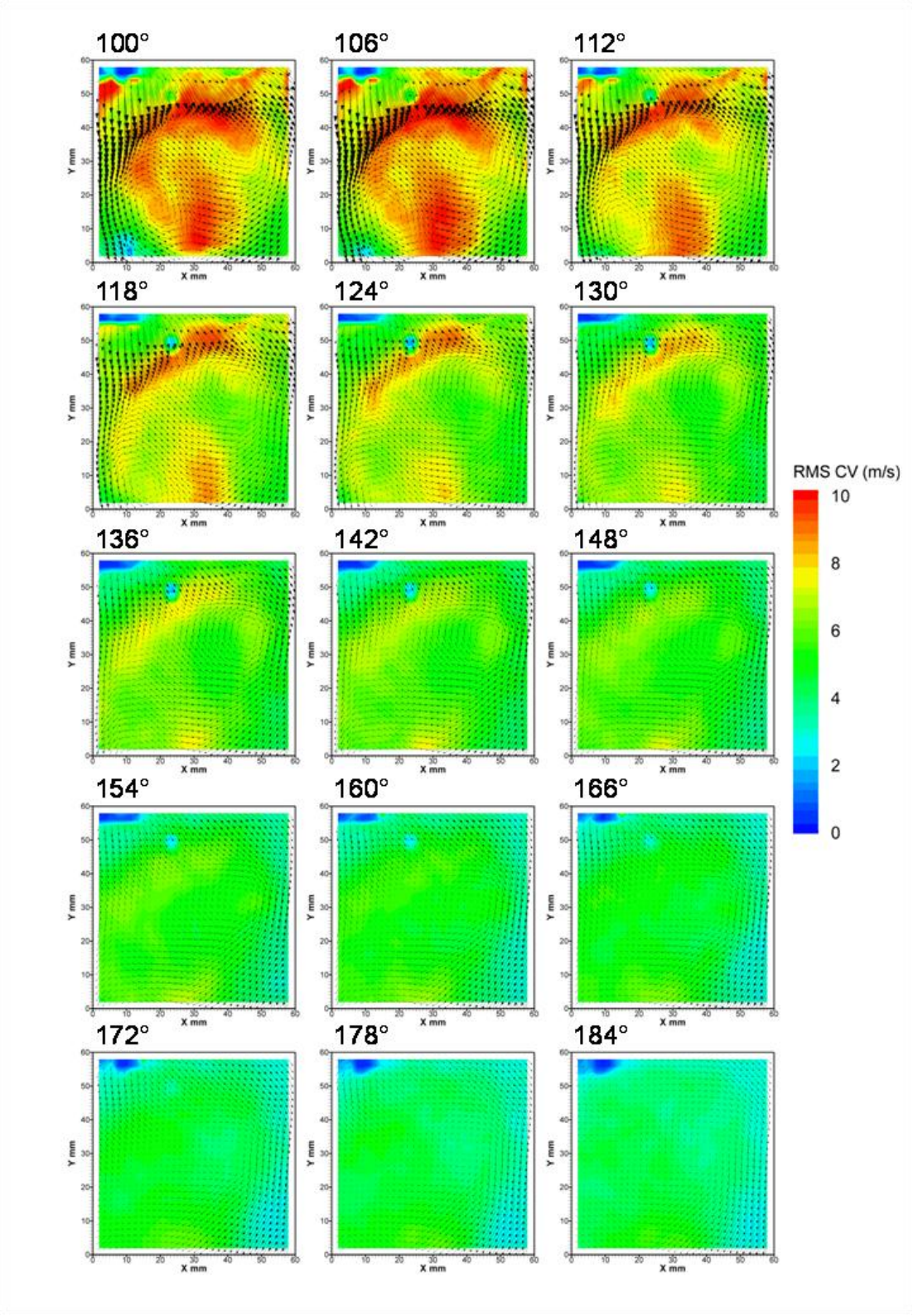

Figure 7.29- *rms* of 100 low frequency cyclic variation flow fields on the bore centreline for 100.0° to 184.0° CA ATDC captured with HSDPIV at a rate of 1.5 kHz

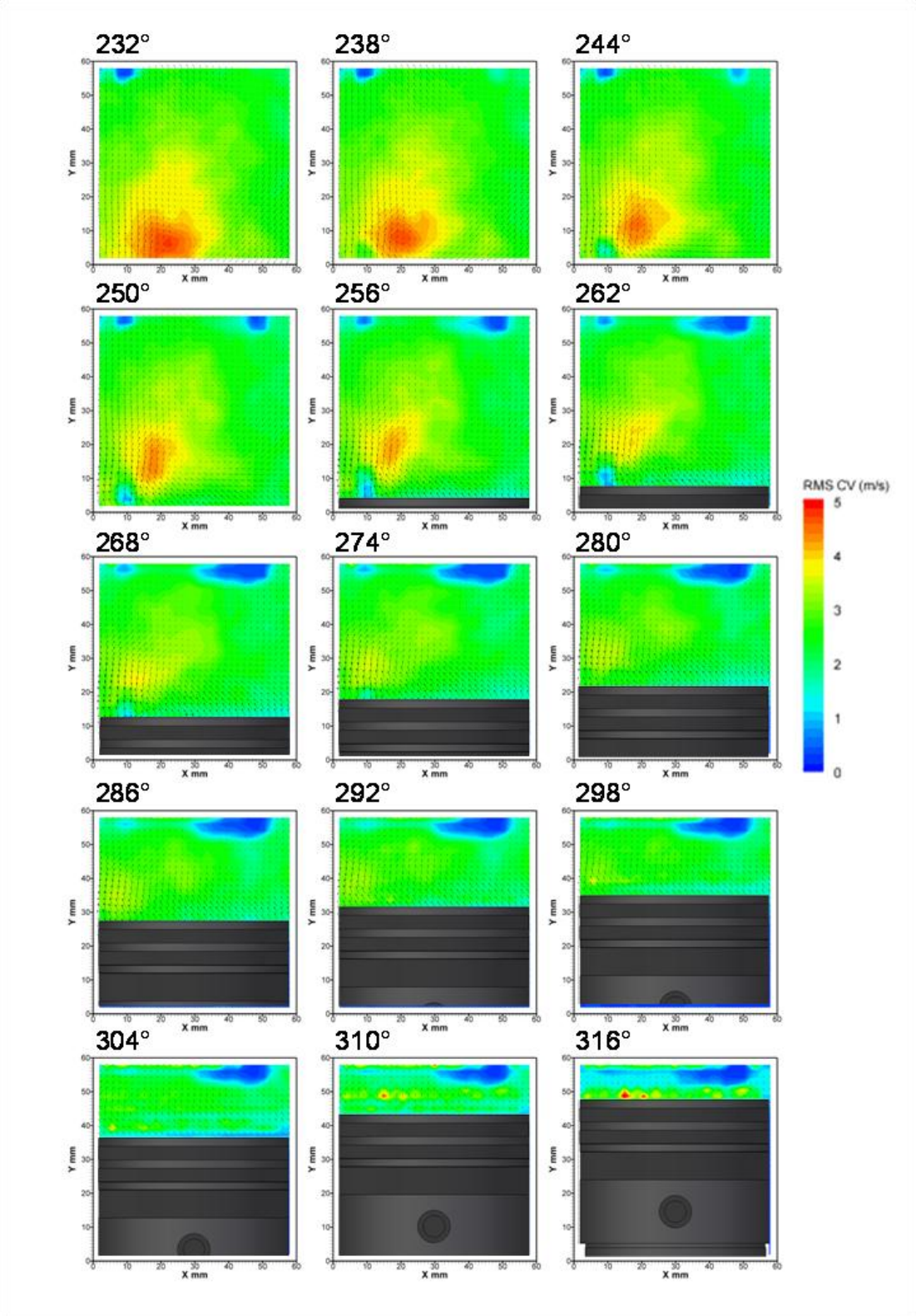

Figure 7.30 - *rms* of 100 low frequency cyclic variation flow fields on the bore centreline for 232.0° to 316.0° CA ATDC captured with HSDPIV at a rate of 1.5 kHz

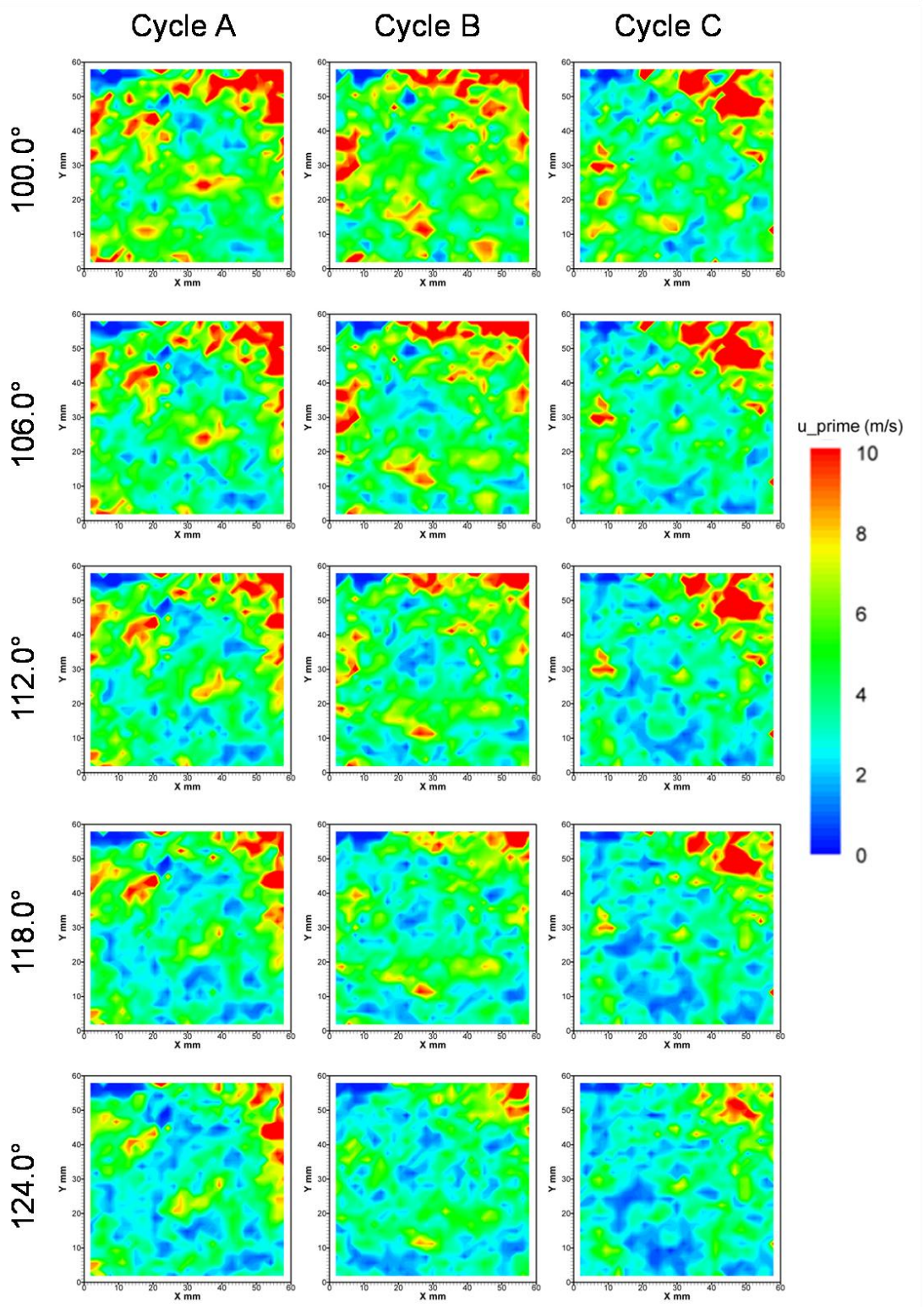

Figure 7.31 - Contour plot of u' for three individual cycles from 100.0° to 124.0° CA ATDC captured with HSDPIV at a rate of 1.5 kHz

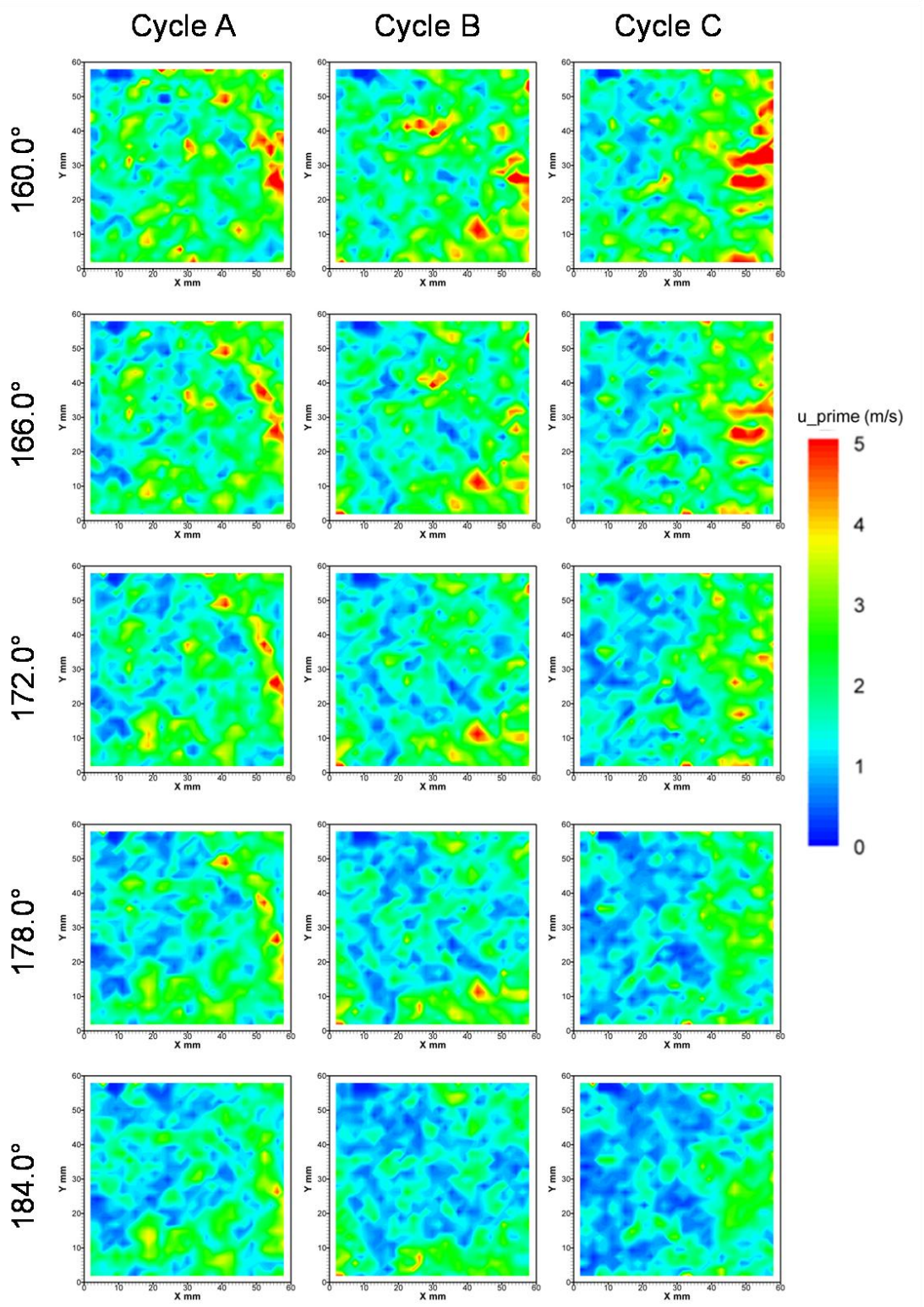

Figure 7.32 - Contour plot of u' for three individual cycles from 160.0° to 184.0° CA ATDC captured with HSDPIV at a rate of 1.5 kHz

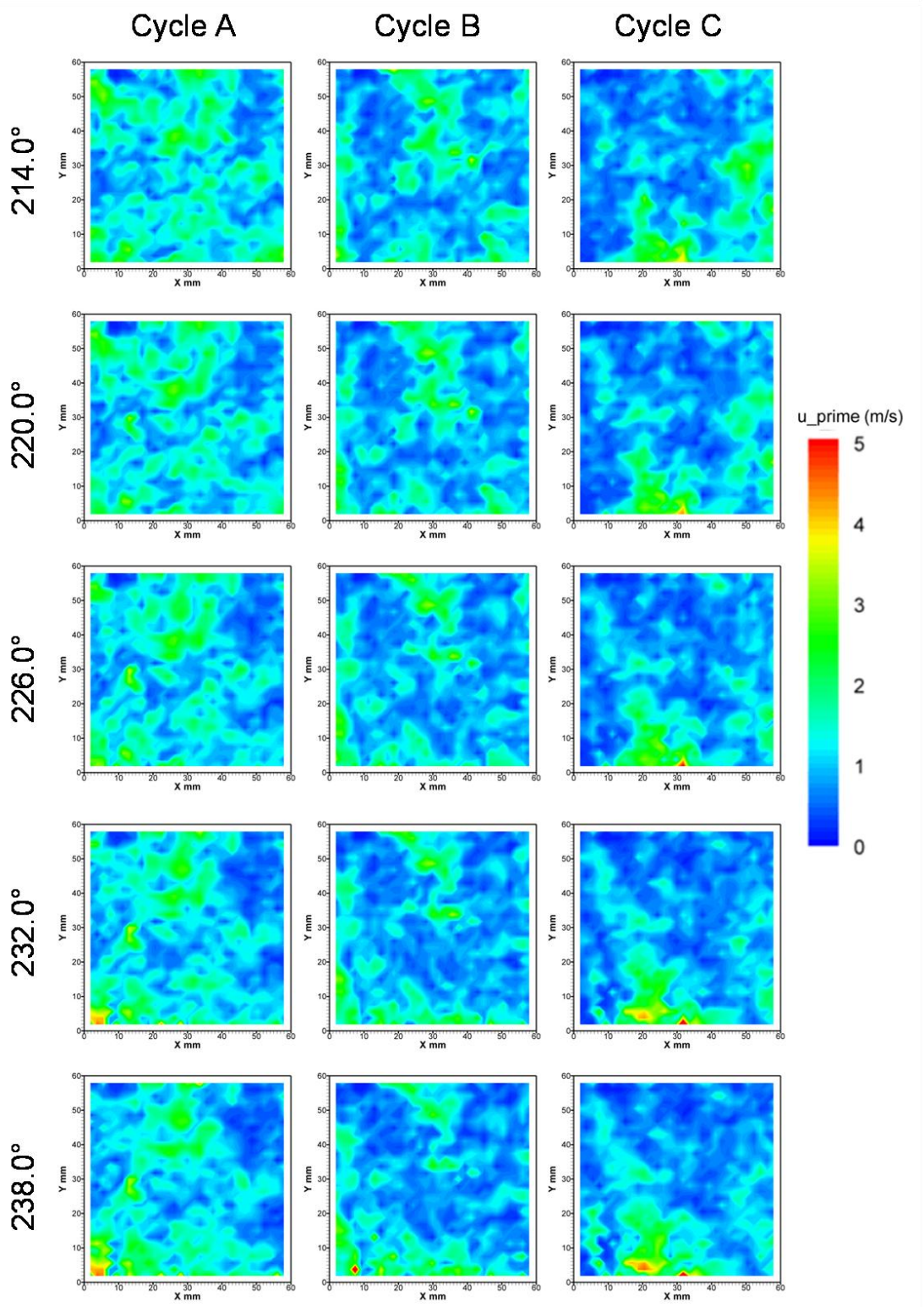

Figure 7.33 - Contour plot of u' for three individual cycles from 214.0° to 238.0° CA ATDC captured with HSDPIV at a rate of 1.5 kHz

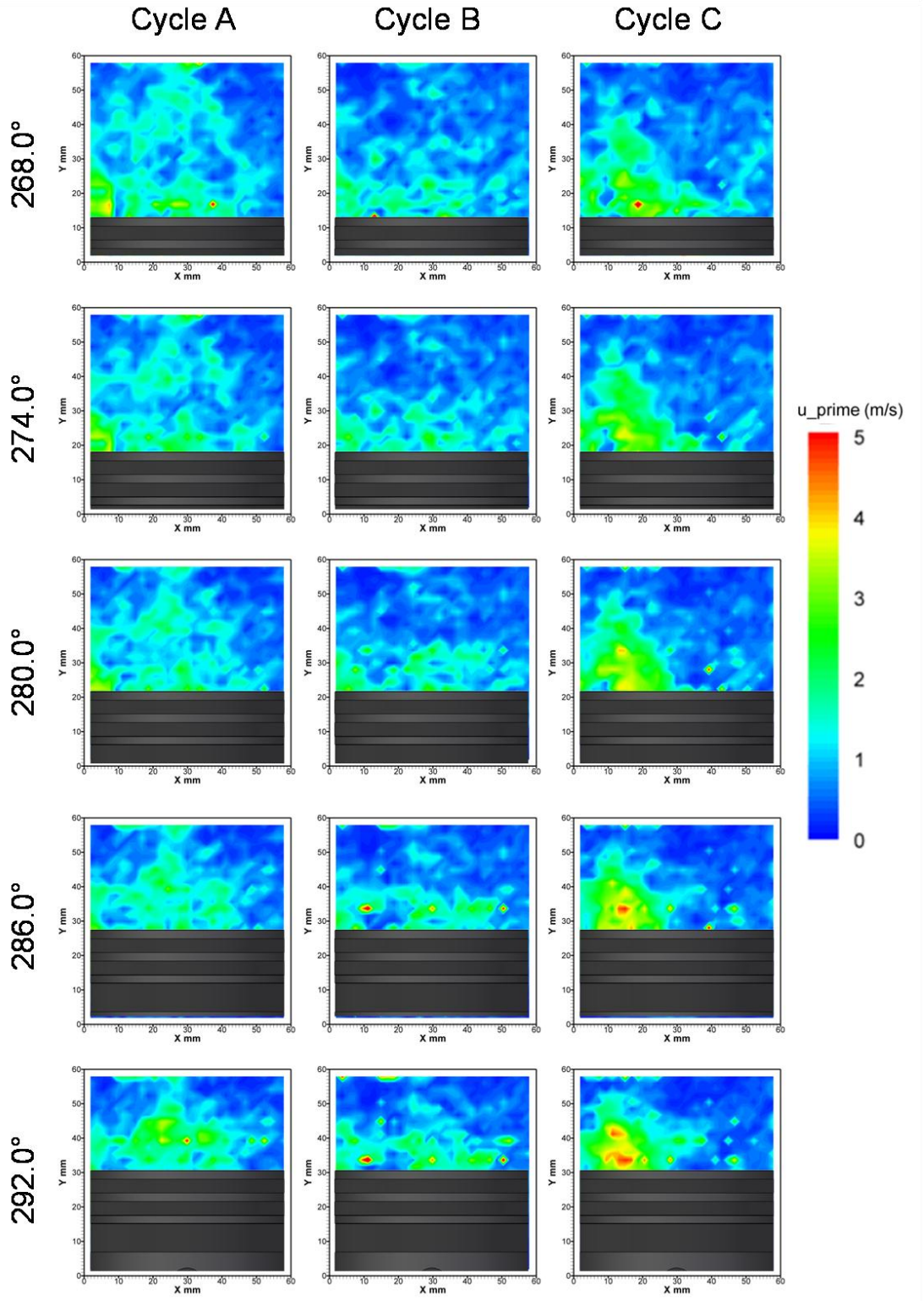

Figure 7.34 - Contour plot of u' for three individual cycles from 268.0° to 292.0° CA ATDC captured with HSDPIV at a rate of 1.5 kHz

7.2.1.2.3 With tumble flap

Similar flow fields as those presented in the previous section have also been captured using the tumble flap introduced in Chapter 4. The set-up of the measurement system and the engine operating conditions were as per Section 7.2.1.1. The work presented here follows on from that of Section 6.3, which also used this tumble flap configuration when considering intake valve jet flows.

Three example cycles are presented in Figure 7.35 to Figure 7.38 for the raw flow fields. When compared to the flow fields generated without the tumble flap (see previous section), the flow has similar main features. The intake flow, which generates downward flow on the right of the image, is the one which is most affected by the presence of the tumble flap. This has resulted in this motion being pushed out of the right hand side of the image; however, it is now a more dominant flow which can be seen by the region of interaction above the piston having moved further to the left of the image. As the cycle progress it can be seen in Figure 7.38, which is concerned with the range 268.0° to 292.0° CA ATDC, that the dominance of this flow has promoted bulk tumble, resulting in higher velocity and greater structure at this point in the cycle.

Figure 7.39 to Figure 7.42 present the low frequency flow fields for the cycles whose raw data are presented in Figure 7.35 to Figure 7.38. At 100.0° CA the counter clockwise rotation in the lower left quadrant of the images is visible for all three cycles. As the cycles progress this structure is visibly distorted by the flow from the right hand side of the image, supporting the intended purpose of the tumble flap and leading to a greater dominance to the clockwise tumble flow. This is also apparent when the cycle reaches the range 268.0° CA, shown in Figure 7.42, and continues through this sequence of images.

Figure 7.43 and Figure 7.44 show the mean low frequency flow fields for this engine configuration for the ranges 100.0° to 184.0° CA ATDC and 232.0° to 316.0° CA ATDC respectively. The bulk structures contained within this mean flow highlight the

observations made above, when compared back to the mean flow fields for the case without the tumble flap in the previous section (Figure 7.19 and Figure 7.20). Initially the flow fields for both cases are similar, but develop differences which are most prominent in the central region of the image from approximately 118.0° CA. In this area variations in the shape of the clockwise rotation appear due to the direction of the flow in the lower right hand quadrant. This results in a larger region of low velocity flow which is linked to the centre of the rotation. By 268.0° CA it appears that there is more clockwise bulk tumble motion evident.

Further comparison of these flow fields is provided in Figure 7.45 and Figure 7.46, where the magnitude of *rms* of low frequency cyclic variation is presented. Initially, although the flows are similar, the dominance of the flows occurring on the right hand side of the image is highlighted. At 100.0° CA the central region of high *rms* of cyclic variation, in the lower half of the image, is seen to be constrained further to the left of the image at approximately X = 30 mm, whereas for the same CA position without the tumble flap (Figure 7.29), the area of high *rms* of cyclic variation extends to approximately X = 40 mm. At 118.0° CA the rotation of the remaining area, where the *rms* > 7, appears around the counter clockwise rotation (X < 20 mm) whereas for the case without the tumble flap this occurs around the mean interaction point of the two opposing flows (X ≈ 30 mm). As the cycle progresses to 232.0° CA, the effect of the tumble flap appears to have a reducing affect on the *rms* of cyclic variation. The position of the region of high variation is similar both with and without the tumble flap (see Figure 7.46 and Figure 7.30 respectively); however, for the case with the tumble flap this region remains visible further into the cycle, for instance, remnants are still visible at 292.0° CA.

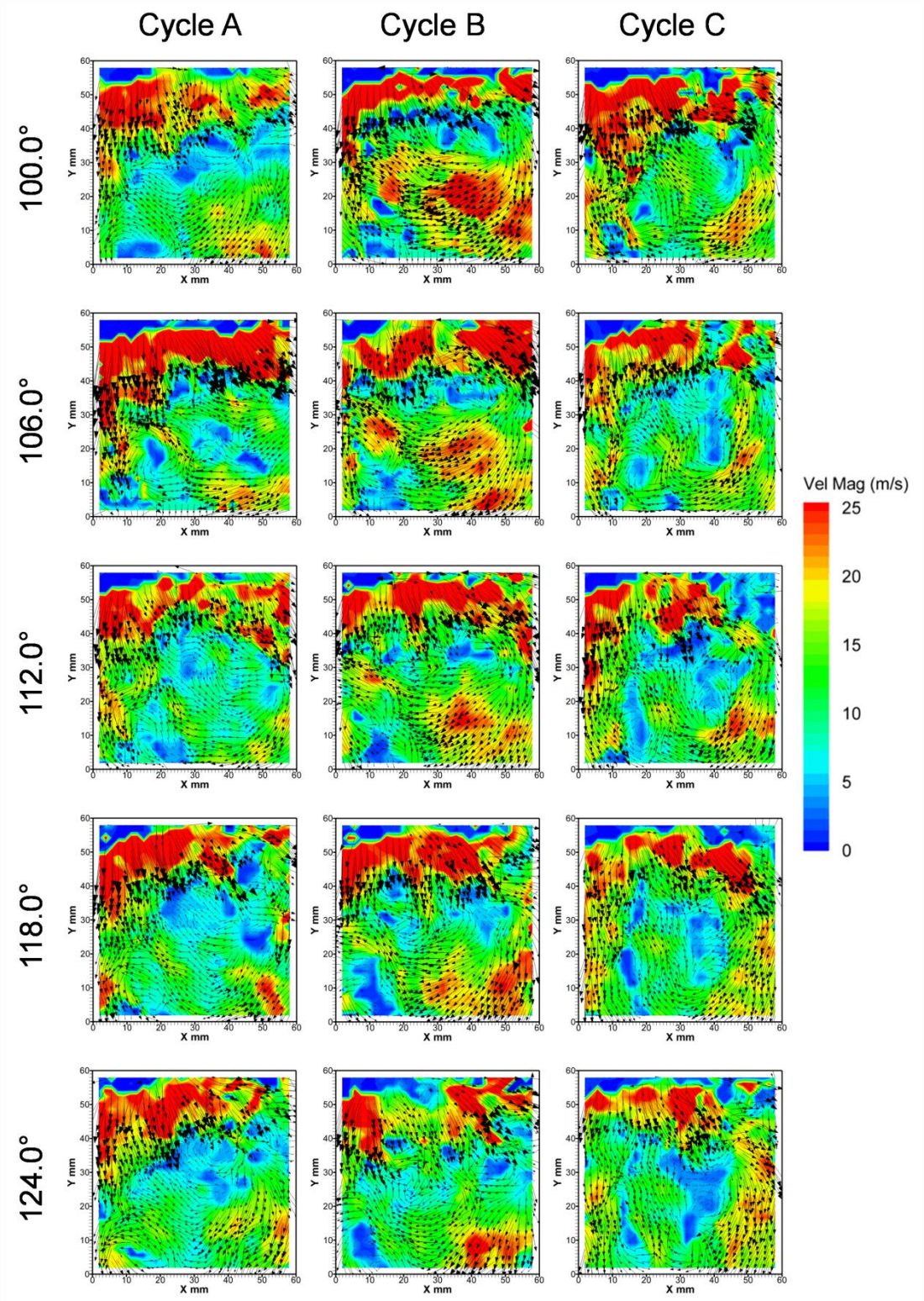

Figure 7.35 – Raw flow fields on the bore centreline, generated with the tumble flap fitted, for three individual cycles from 100.0° to 124.0° CA ATDC captured with HSDPIV at a rate of 1.5 kHz

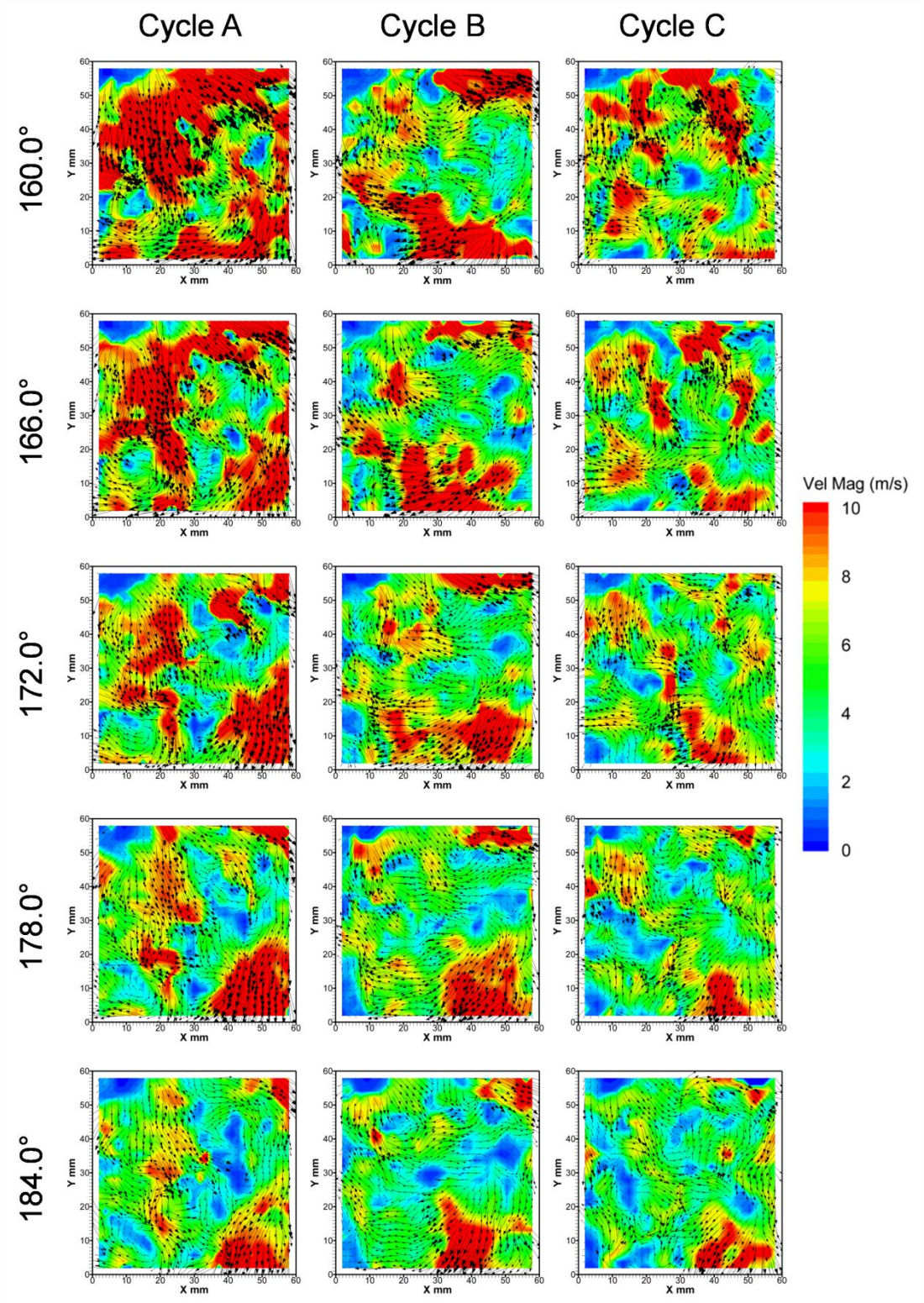

Figure 7.36 - Raw flow fields on the bore centreline, generated with the tumble flap fitted, for three individual cycles from 160.0° to 184.0° CA ATDC captured with HSDPIV at a rate of 1.5 kHz

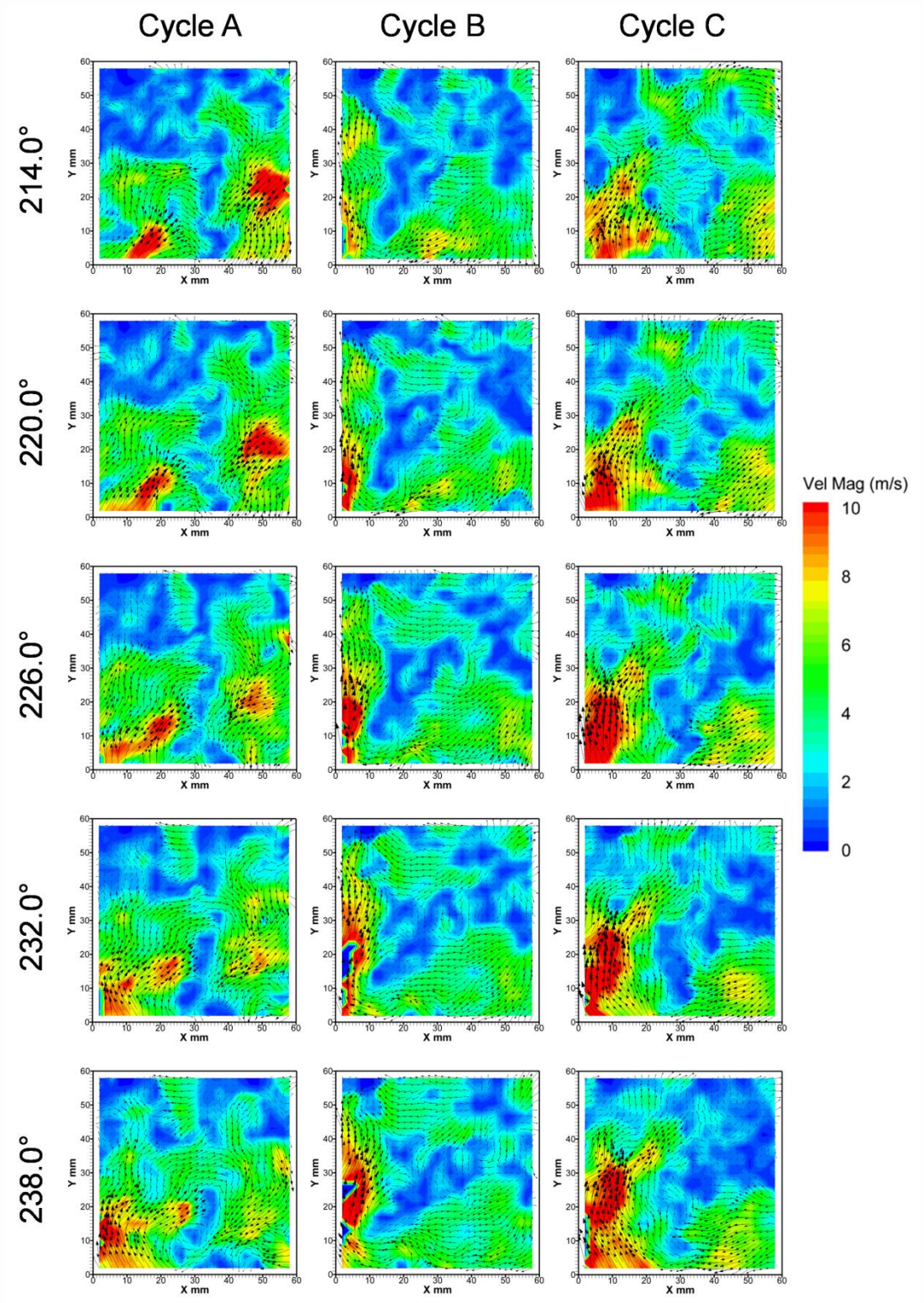

Figure 7.37 – Raw flow fields on the bore centreline, generated with the tumble flap fitted, for three individual cycles from 214.0° to 238.0° CA ATDC captured with HSDPIV at a rate of 1.5 kHz

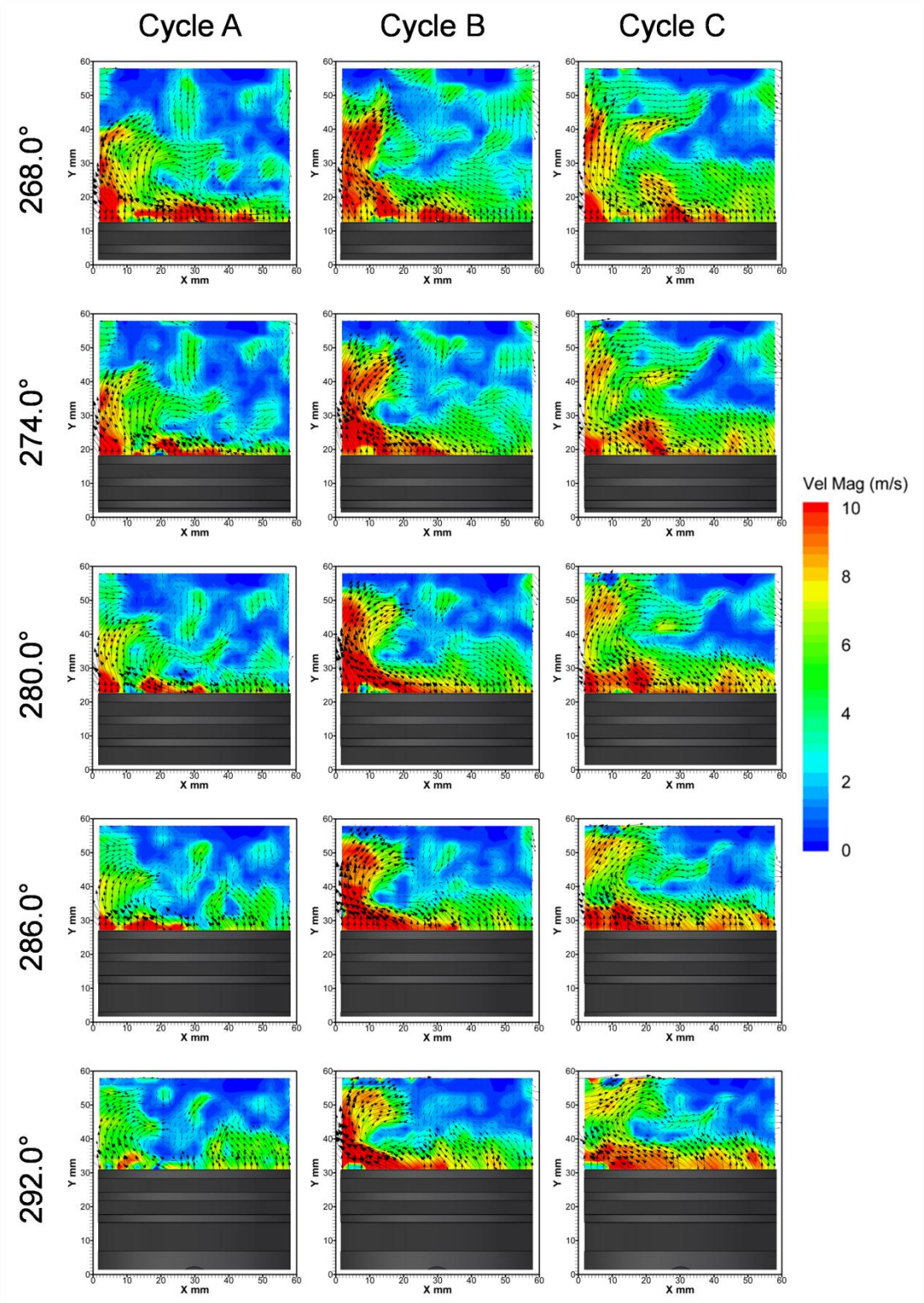

Figure 7.38 – Raw flow fields on the bore centreline, generated with the tumble flap fitted, for three individual cycles from 268.0° to 292.0° CA ATDC captured with HSDPIV at a rate of 1.5 kHz

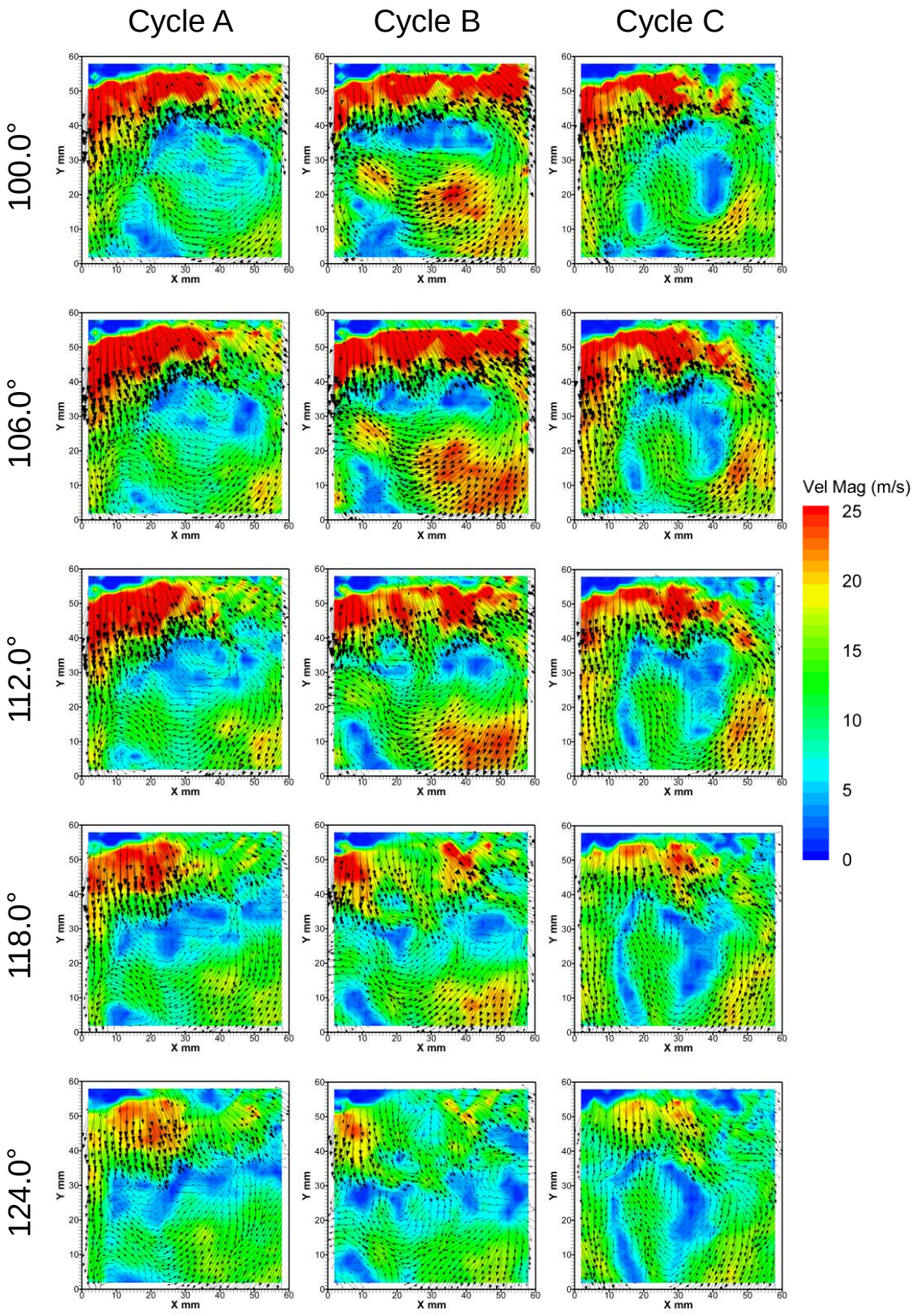

Figure 7.39 – Low frequency flow fields on the bore centreline, generated with the tumble flap fitted, for three individual cycles from 100.0° to 124.0° CA ATDC captured with HSDPIV at a rate of 1.5 kHz

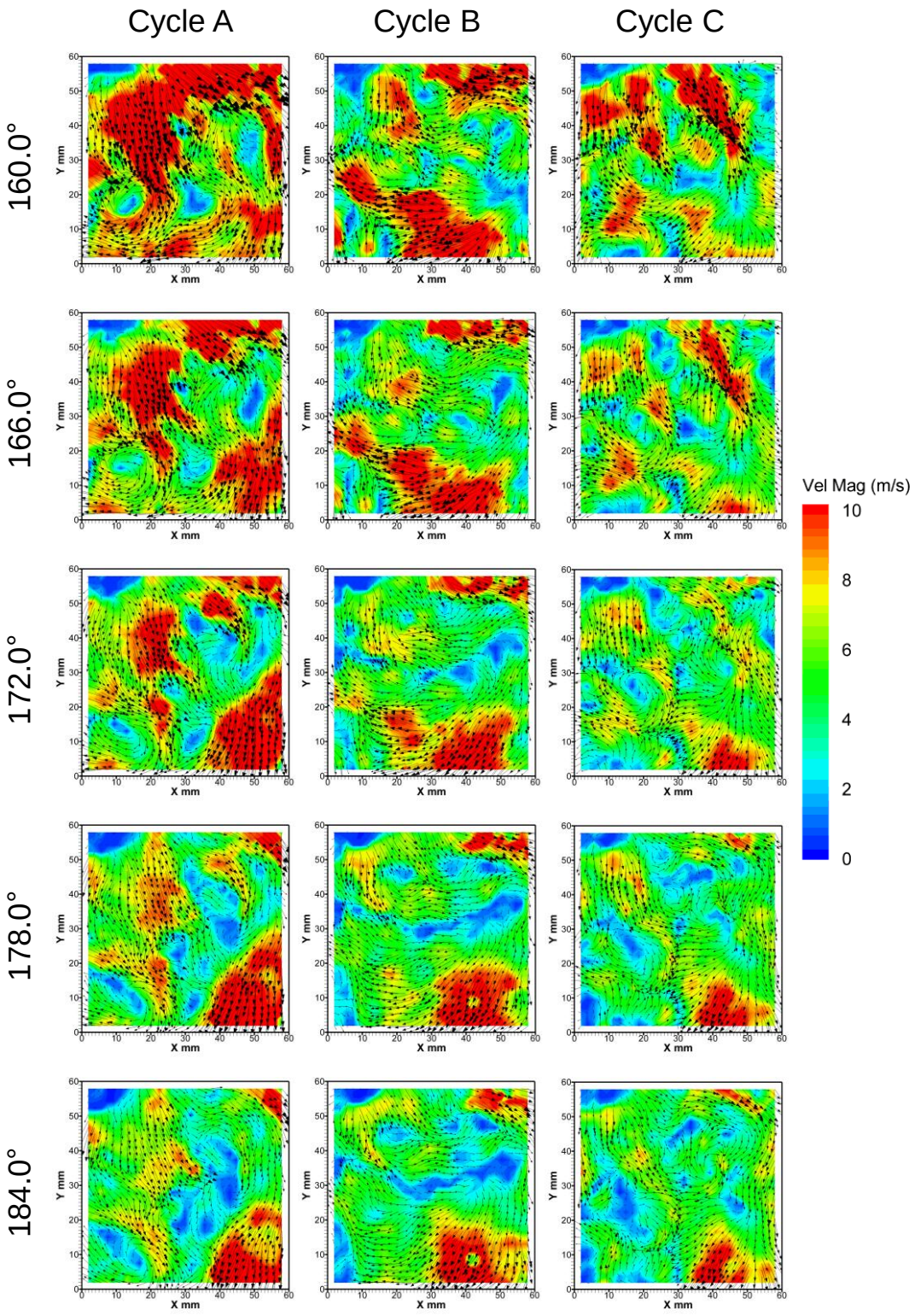

Figure 7.40 - Low frequency flow fields on the bore centreline, generated with the tumble flap fitted, for three individual cycles from 160.0° to 184.0° CA ATDC captured with HSDPIV at a rate of 1.5 kHz

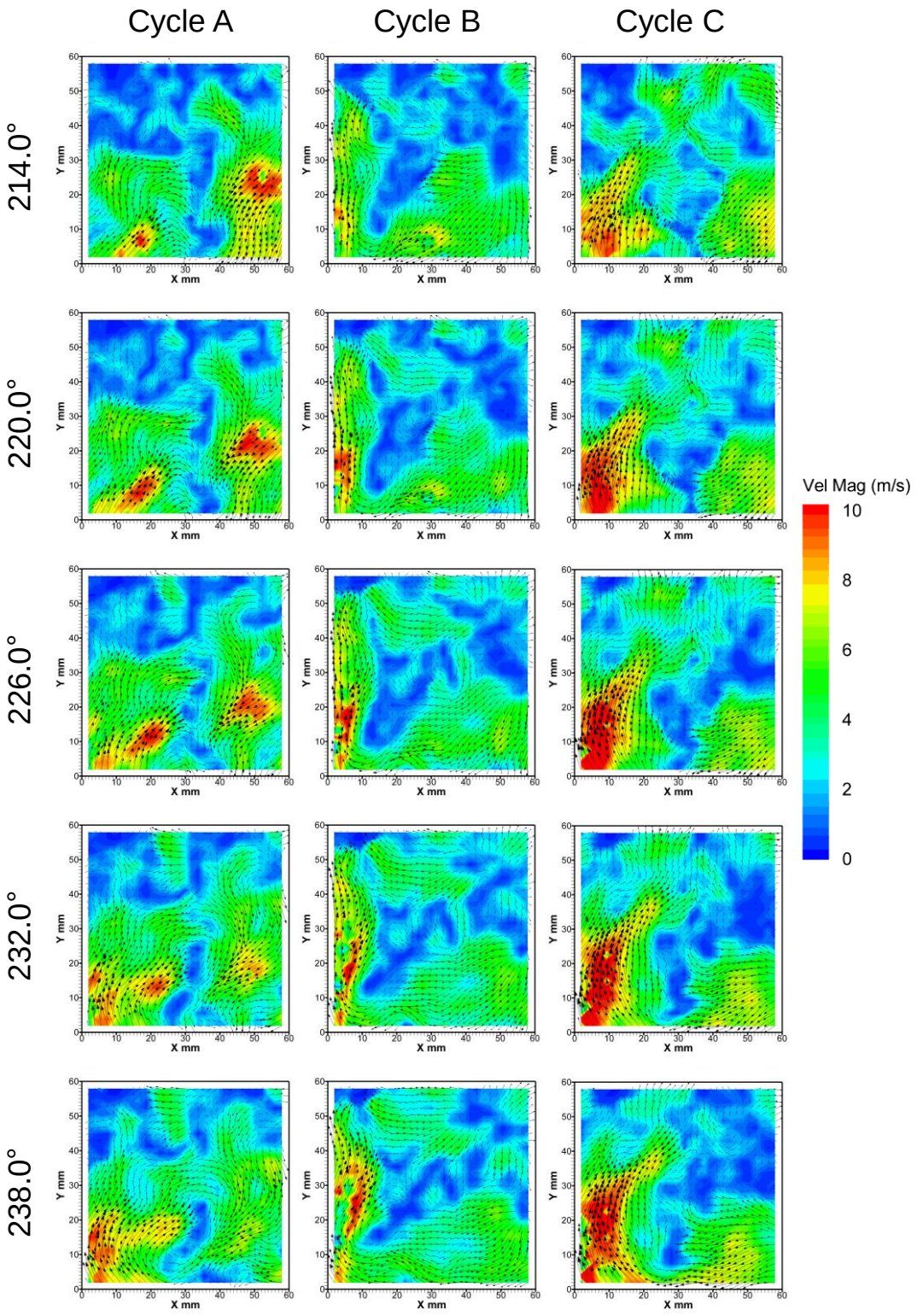

Figure 7.41 - Low frequency flow fields on the bore centreline, generated with the tumble flap fitted, for three individual cycles from 214.0° to 238.0° CA ATDC captured with HSDPIV at a rate of 1.5 kHz

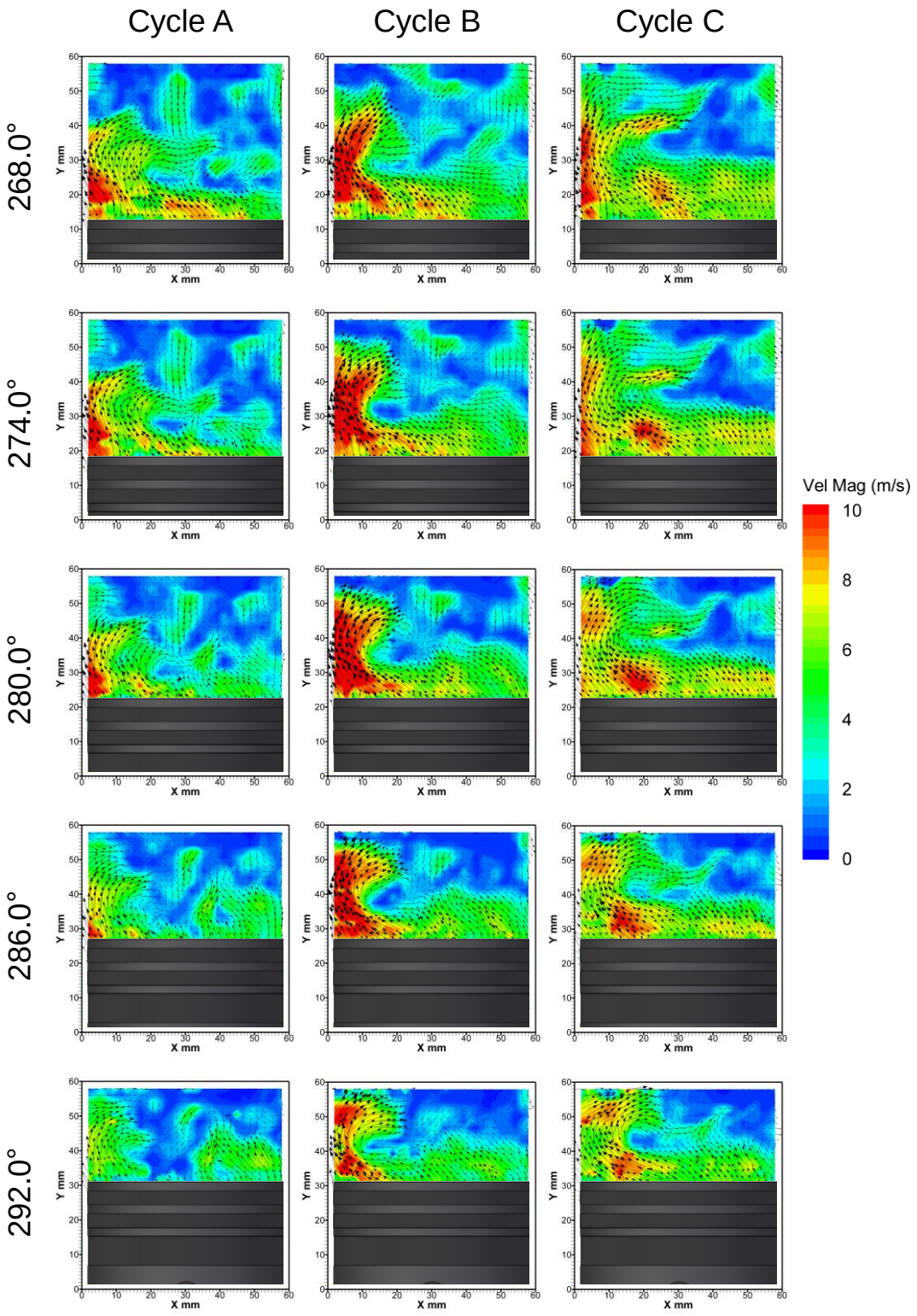

Figure 7.42 - Low frequency flow fields on the bore centreline, generated with the tumble flap fitted, for three individual cycles from 268.0° to 292.0° CA ATDC captured with HSDPIV at a rate of 1.5 kHz

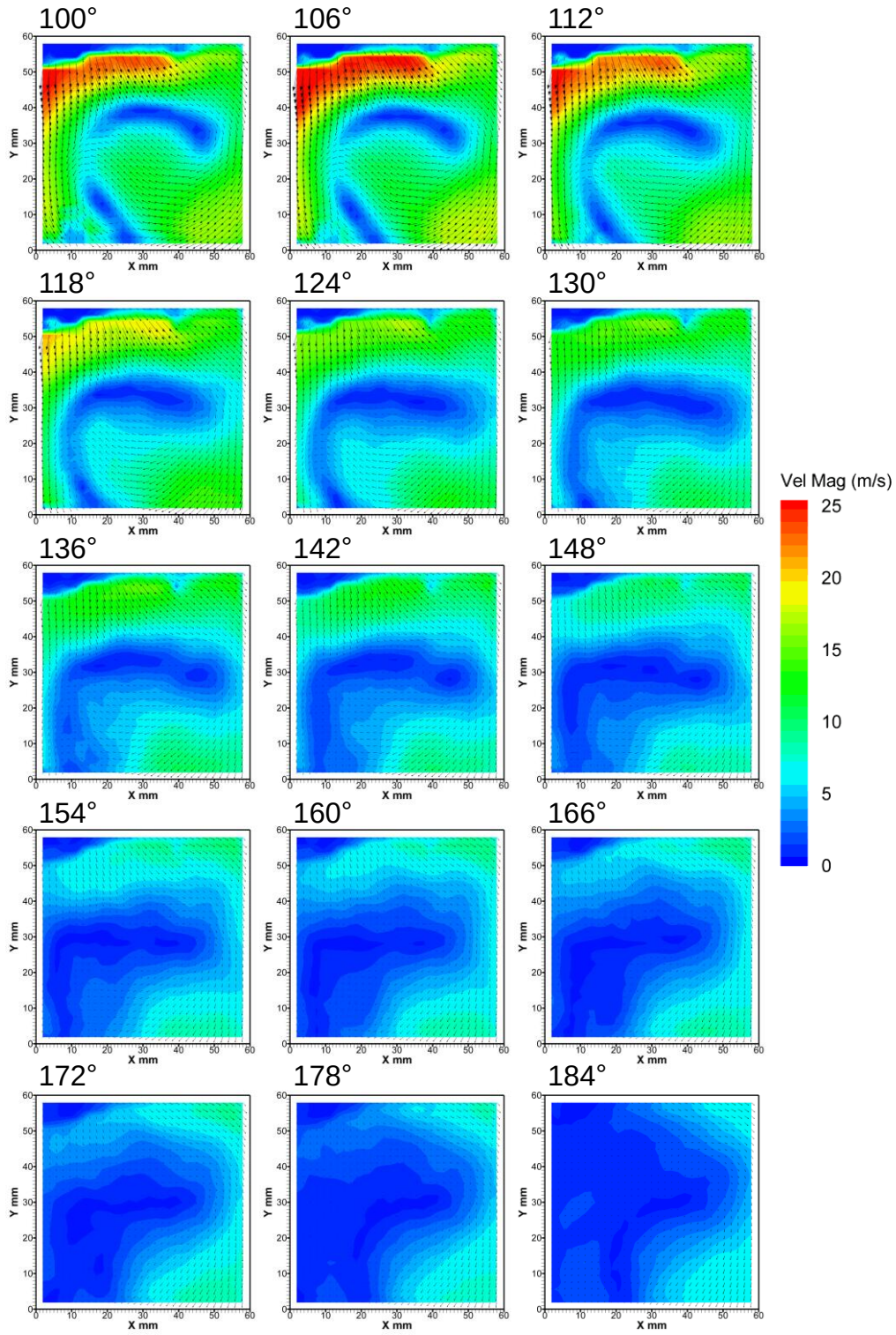

Figure 7.43 – Mean low frequency flow fields on the bore centreline, generated with the tumble flap fitted, from 100.0° to 184° CA ATDC captured with HSDPIV at a rate of 1.5 kHz

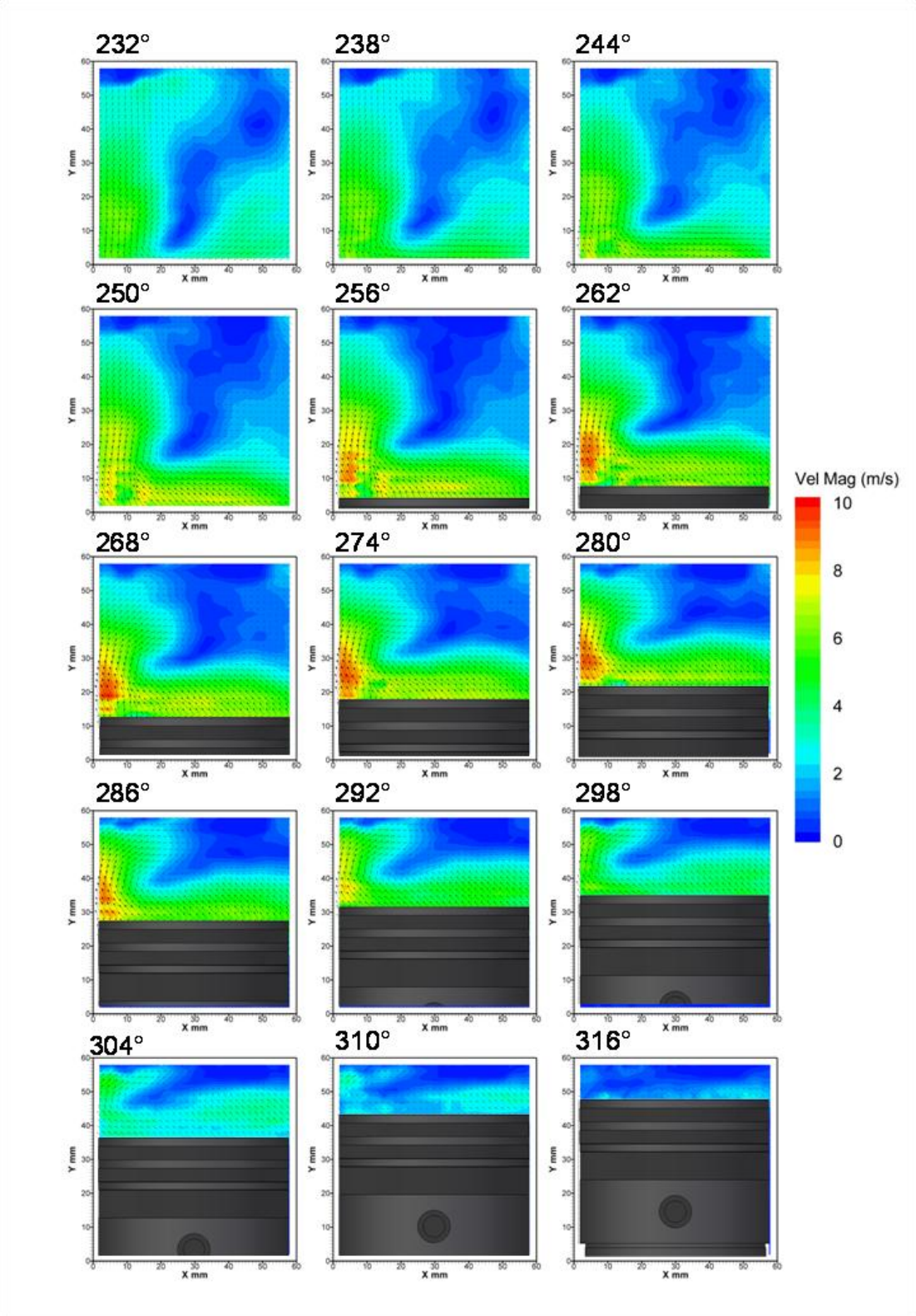

Figure 7.44 - Mean low frequency flow fields on the bore centreline, generated with the tumble flap fitted, from 100.0° to 184° CA ATDC captured with HSDPIV at a rate of 1.5 kHz

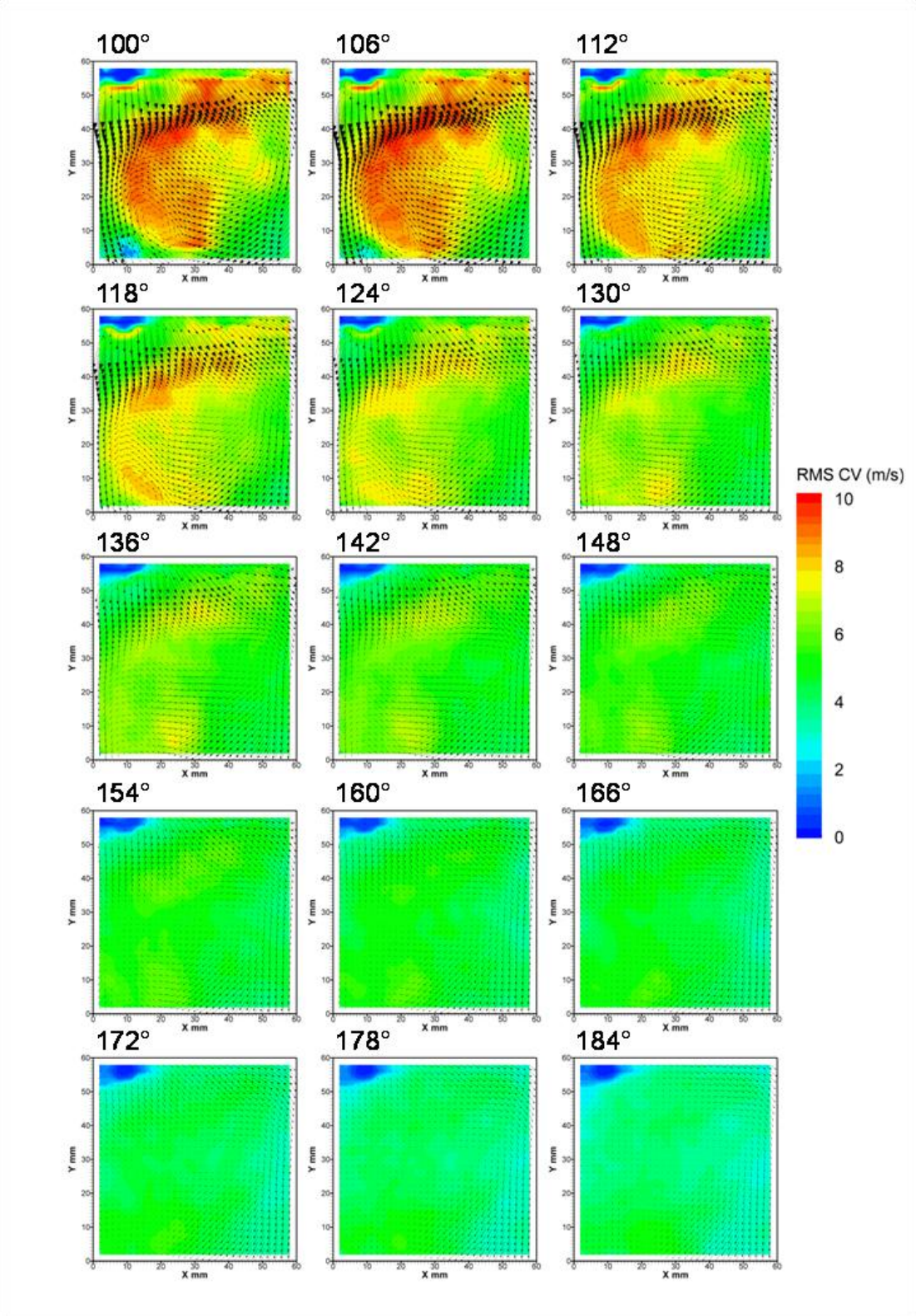

Figure 7.45 - *rms* of 100 low frequency cyclic variation flow fields on the bore centreline, generated with the tumble flap fitted, from 100.0° to 184.0° ATDC captured with HSDPIV at a rate of 1.5 kHz

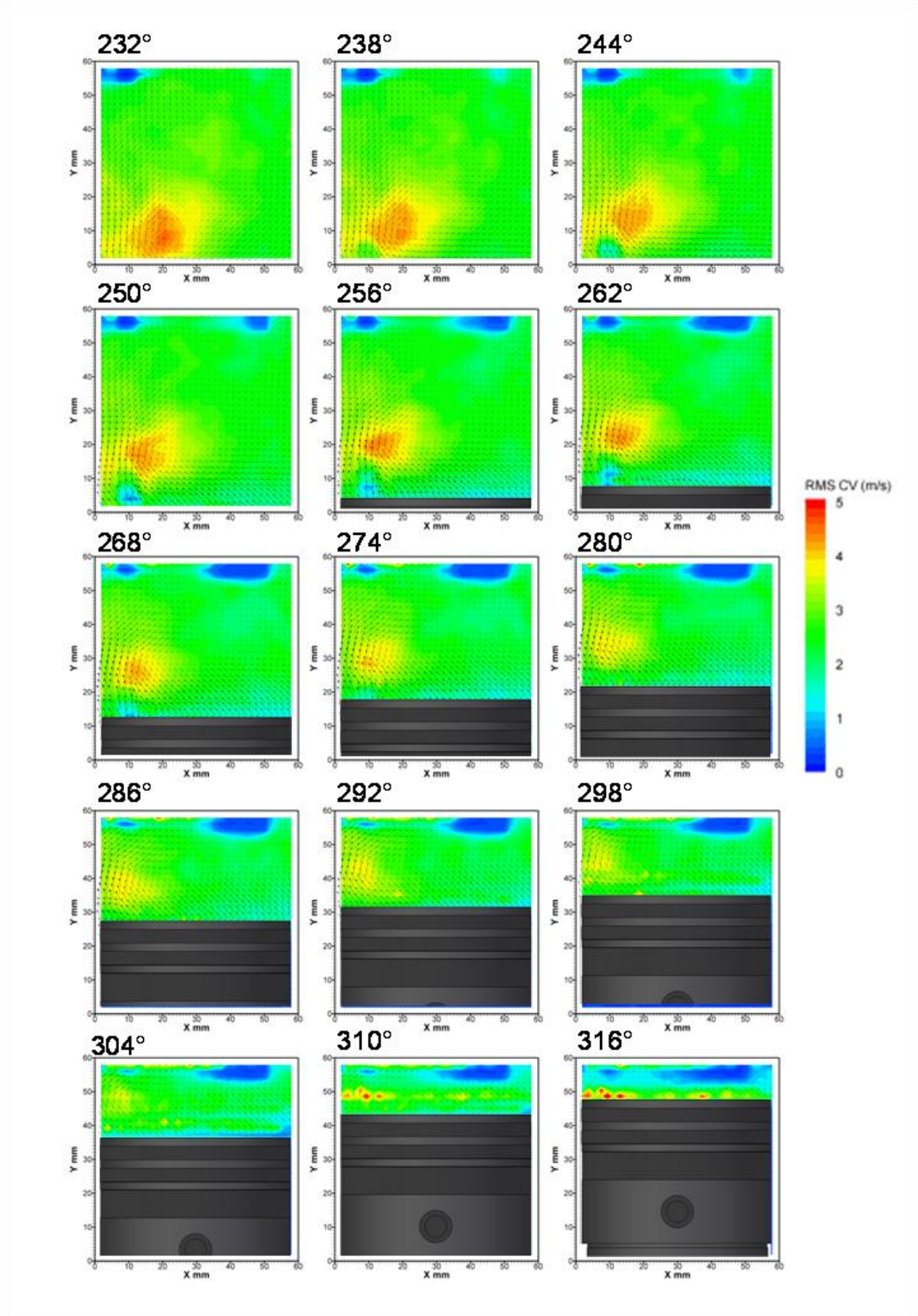

Figure 7.46 - *rms* of 100 low frequency cyclic variation flow fields on the bore centreline, generated with the tumble flap fitted, from 232.0° to 316.0° ATDC captured with HSDPIV at a rate of 1.5 kHz

In Figure 7.47 to Figure 7.50 contour plots of the turbulence intensity, u', have been presented for the range 100.0° to 292.0° CA ATDC for the three cycles under consideration with the tumble flap fitted. These plots are directly comparable to the case without the tumble flap, presented in Figure 7.31 to Figure 7.34. Throughout the measurement range the data show visually similar u' values, however they appear less spatially fragmented for the case where the tumble flap is fitted. Across all three cycles presented in Figure 7.47, for the range 100.0° to 124.0° CA ATDC, there is a region of low u', at Y = 10 to 30 mm and X = 20 to 40 mm. This is where there are low velocity regions, as shown in Figure 7.39. As the cycle progresses into Figure 7.48 and Figure 7.49 (ranges 160.0° to 184.0° CA and 214.0° to 238.0° CA ATDC respectively), the turbulence intensity continues to decay becoming more similar to the case without the tumble flap in position. In Figure 7.50 a region of high u' is visible where the region of higher velocity tumble flow is visible in Figure 7.42.

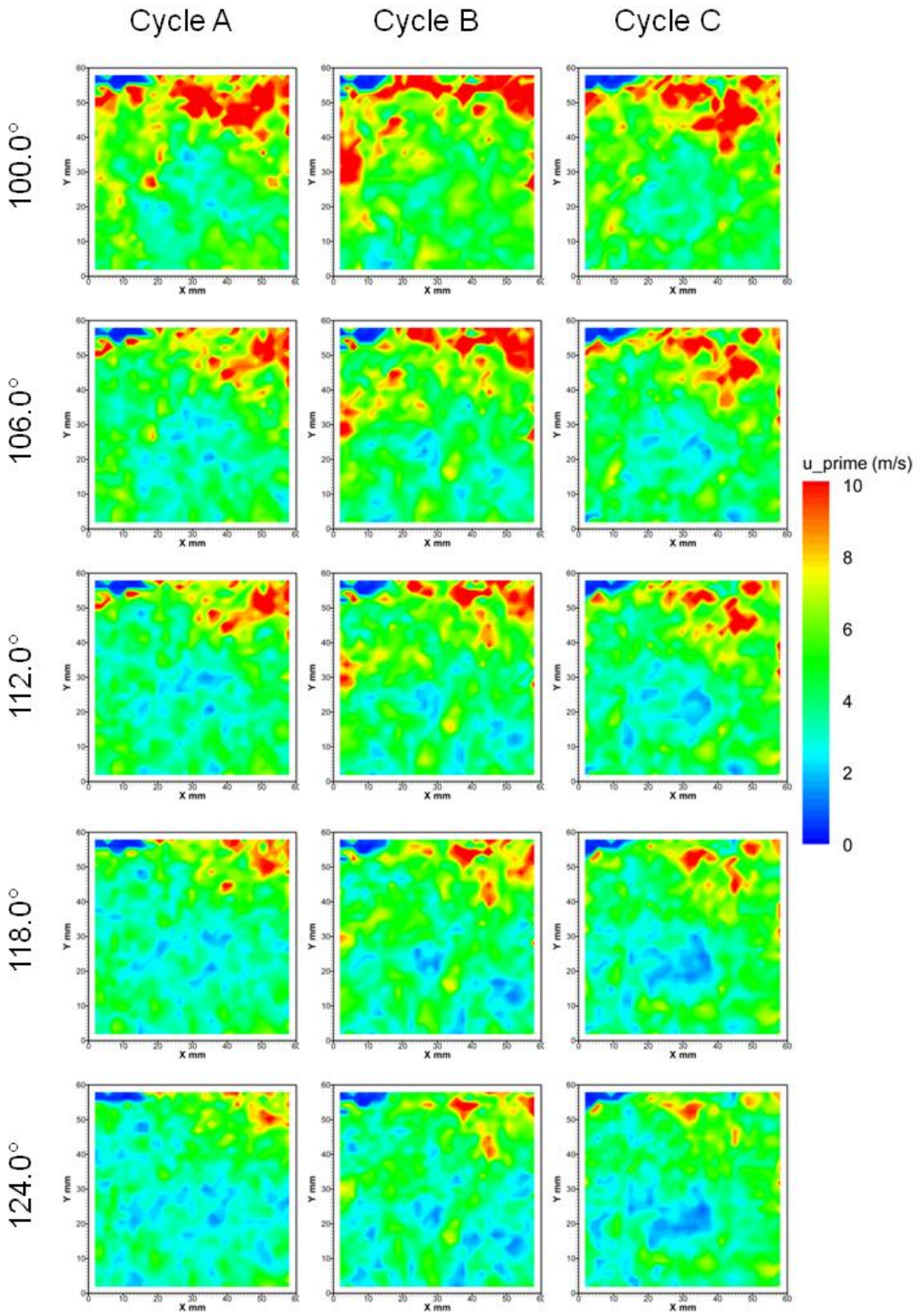

Figure 7.47 - Contour plot of u' for three individual cycles, generated with the tumble flap fitted, from 100.0° to 124.0° CA ATDC captured with HSDPIV at a rate of 1.5 kHz

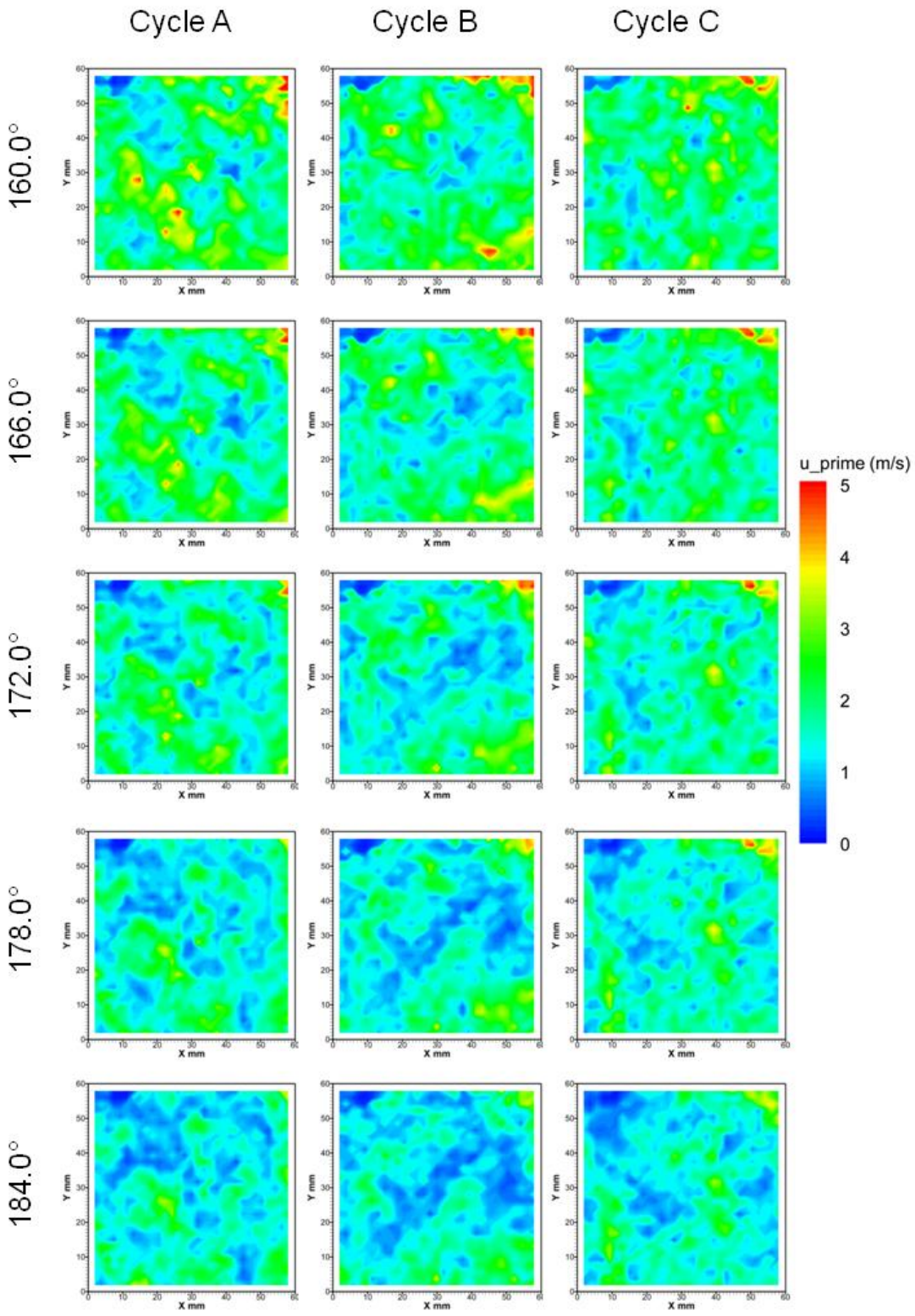

Figure 7.48 - Contour plot of u' for three individual cycles, generated with the tumble flap fitted, from 160.0° to 184.0° CA ATDC captured with HSDPIV at a rate of 1.5 kHz

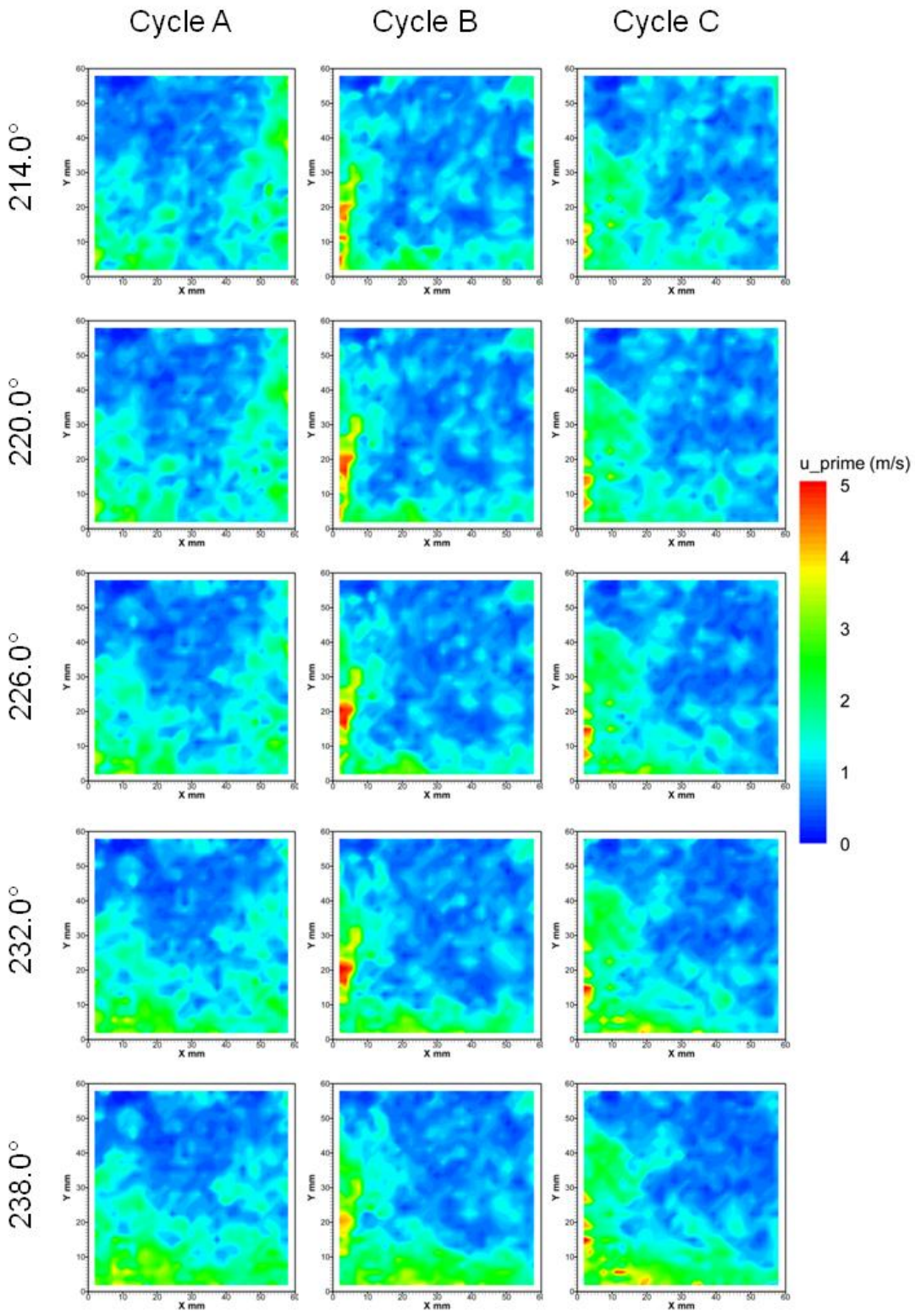

Figure 7.49 -Contour plot of u' for three individual cycles, generated with the tumble flap fitted, from 214.0° to 238.0° CA ATDC captured with HSDPIV at a rate of 1.5 kHz

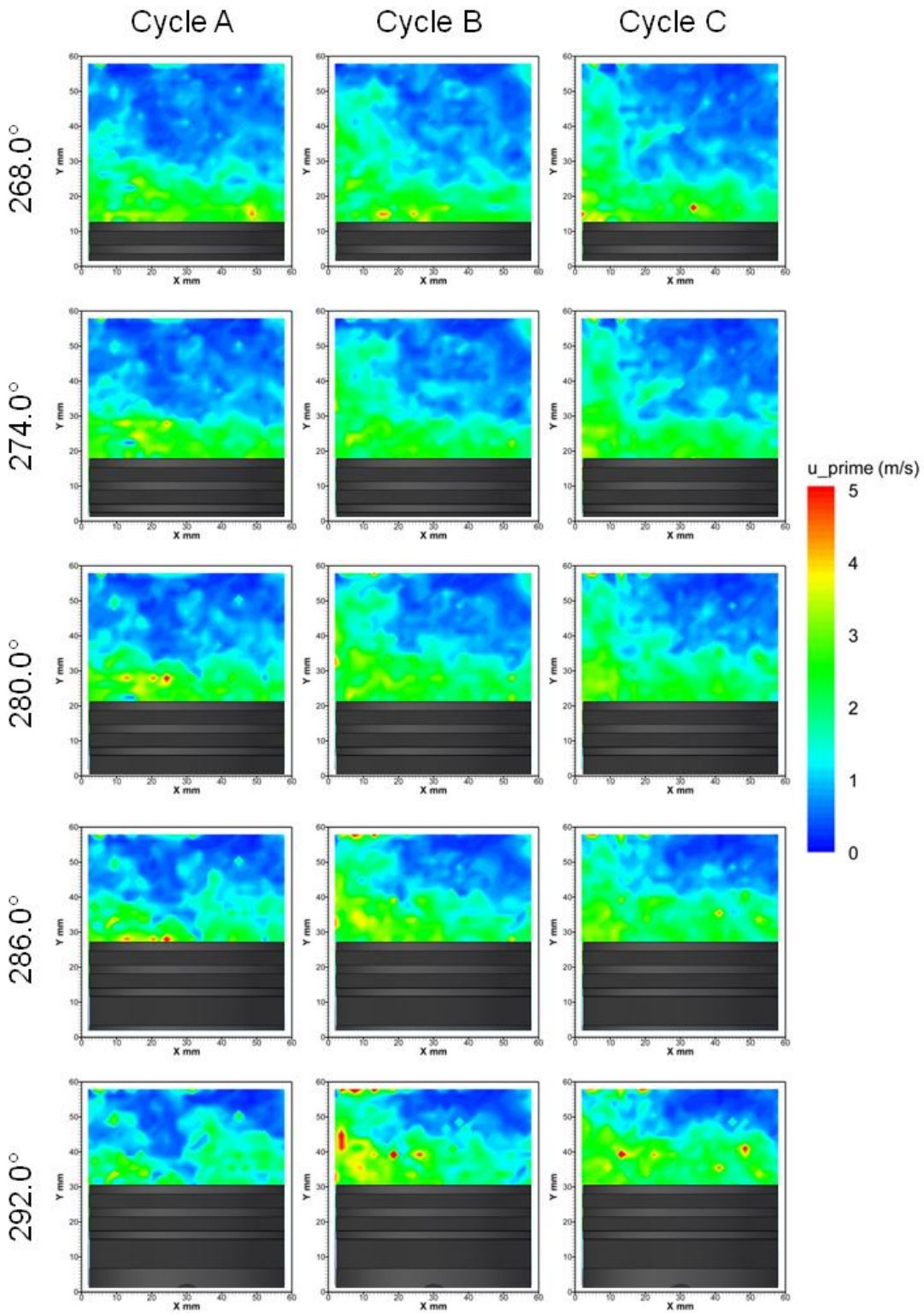

Figure 7.50 - Contour plot of u' for three individual cycles, generated with the tumble flap fitted, from 268.0° to 292.0° CA ATDC captured with HSDPIV at a rate of 1.5 kHz

7.3 Swirl plane

7.3.1 Measurement conditions

The data presented in this section have been used to investigate the characteristics of flows contained within the swirl plane during the intake and compression stroke. The measured fields were captured on the swirl plane 10 mm below the piston surface at TDC. The schematic shown in Figure 7.51 highlights the image area used to capture the HSDPIV images presented within this section. The engine was motored at 1500 rpm with an intake plenum pressure of 525 mbar.

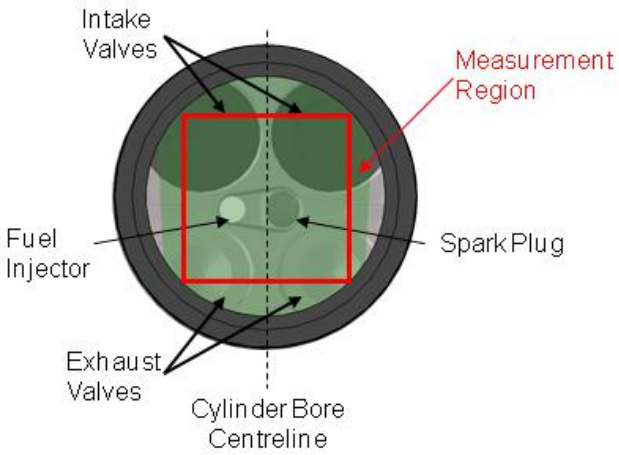

Figure 7.51 - Schematic to show the measurement location used to investigate large scale flows in the swirl plane 10 mm below the peak height of the piston

The configuration of the HSDPIV system to capture these measurements is shown in Figure 7.52. The output from the Nd:YLF laser was formed into a thin horizontal sheet and introduced into the combustion chamber through the wall of the optical cylinder. To achieve the correct laser sheet height and width in the image region, a -25 mm cylindrical lens was used in conjunction with a 500 mm spherical lens. These lenses also allowed the laser to be positioned in a convenient location.

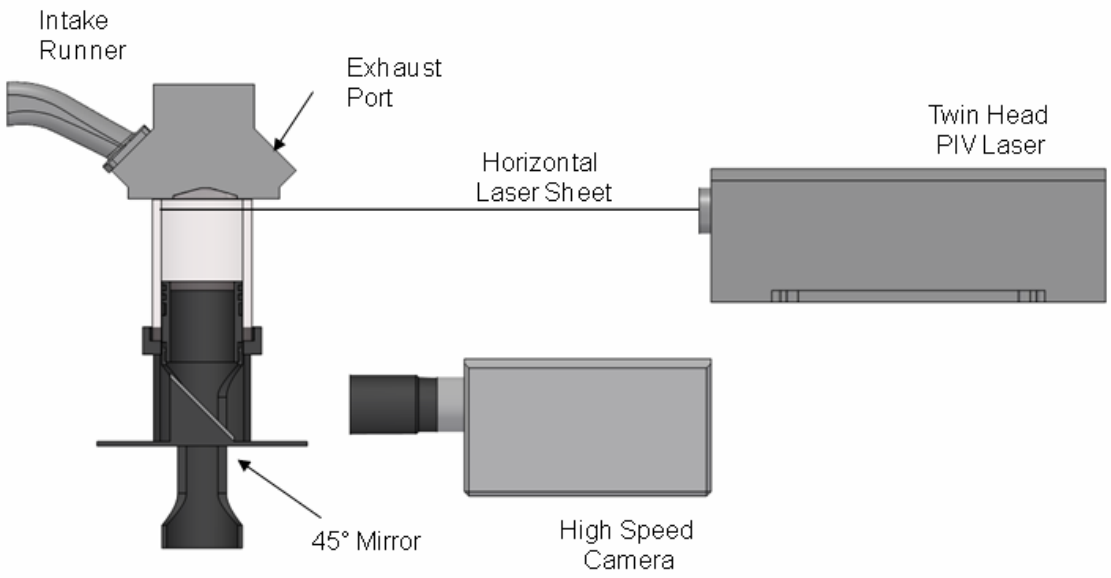

Figure 7.52 - Schematic to show the configuration of the HSDPIV system to achieve measurements to investigate large scale flows in the swirl plane 10 mm below the peak height of the piston

At this measurement location the larger scale bulk flow motion development is of primary interest; however, the energy cascade of it and existing turbulent flow is also something to consider. The camera was operated with its full resolution of 1024 by 1024 pixels which allowed a frame rate of 3 kHz and therefore the capture of two frame cross correlation images to provide flow fields at 1.5 kHz. With the engine being motored at 1500 rpm, the temporal resolution of the HSDPIV system for these measurements equated to 6 crank angle degrees of revolution between captured flow fields.

A 105 mm AF Micro Nikkor lens was used to image a region 55 mm by 55 mm onto the active array of 1024 by 1024 pixels. Analysis of the captured PIV image pairs was performed with the TSI Insight 3G software. Velocity vectors were evaluated from the image pairs on a Nyquist grid with 32 by 32 pixel interrogation regions, equating to an area approximately 1.72 mm by 1.72 mm within the flow. The interrogation regions were positioned to overlap neighbouring regions by 50% leading to a vector spacing in resulting velocity vector field of 0.86 mm. This allows the investigation of the bulk motion flow filed characteristics of the in-cylinder flow and gives an adequate spatial

resolution to study the variations which influence these bulk motion characteristics. Also, this spatial resolution will be adequate to capture smaller scale structures which exist within this bulk flow and have enough energy to contribute to the bulk cycle development.

To control the imaged diffraction limited spot size the laser was operated at full power and the largest $f^{\#}$ which gave adequate contrast in the particle images was used. Ideally the $f^{\#}$ for the measurements presented within this Section would need to be >16 to give a calculated diffraction limited spot size greater than 2 pixels in diameter. The HSDPIV system, limited by laser power and camera sensitivity, required that the $f^{\#} = 8$. This gives a calculated diffraction limited spot size of 0.8 pixels (therefore more susceptible to sub pixel displacement errors). However, the calculated spot size is for an ideally focussed system, therefore by taking the image slightly out of focus the actual measured imaged particle size on the camera array could be controlled to be greater than 2 pixels.

The time separation, Δt, between the two laser pulses controlling the exposure of the image pair was set to 10 μs. This Δt helps minimise the loss of particle image pairs out of the 2-dimensional measurement plane. However because one pixel movement equates to a velocity of 5.4 ms^{-1}, the data is subject to larger sub-pixel displacement errors. The nature of the flow field being characterised in this case means this is unavoidable. The HSDPIV system was triggered at 100° CA ATDC. From this external trigger, the PIV system was programmed to capture 37 image pairs at 1.5 kHz, therefore, at 6° CA increments until 316.0° CA ATDC was reached. This allowed 28 cycles to be captured before the 2 Gb on-board memory available on the camera was full. Performing 4 capture sequences gave an adequate sample of cycles to calculate a statistically significant mean flow.

7.3.2 Measured velocity fields

7.3.2.1 Standard intake geometry

The data presented within this section are for HSDPIV taken in the swirl plane 10 mm below the piston surface when it is at TDC. The HSDPIV was captured over the range 100.0° to 316.0° CA ATDC. Figure 7.53 shows a large scale plot of an example flow field at 100.0° CA ATDC. Image sequences from three cycles are presented in Figure 7.54 for the range 100.0° to 124.0° CA ATDC, where the intake valves are at the top of the image and the exhaust valves at the bottom. In the initial flow fields, for each cycle, a downwards flow (from the intake side to the exhaust side of the cylinder) is apparent in the central region at $X \approx 30$ mm and $Y < 30$ mm. Opposing flows can be seen on either side of the bore's centreline, therefore leading to clockwise and counter clockwise rotations being present. By design the engine has symmetric intake ports which are not designed to lead to bulk swirl motion; the presence of the opposing rotating structures is evidence of this. In cycles B and C there is a bias apparent at 112.0° CA where the upper portion of the image has a left to right flow motion, however this bias fades through the cycle and the flow becomes more symmetric, especially in cycle B, by 124.0° CA. Apart from these bulk features there is little in common between the three cycles presented. Across the range 160.0° to 184.0° CA ATDC, see Figure 7.55, the flows appear to lose equivalent structures, becoming increasingly disorganised. This trend continues through Figure 7.56 and Figure 7.57 across the ranges 214.0° to 238.0° CA and 268.0° to 292.0° CA ATDC respectively.

The low frequency filtered bulk flow fields calculated with a 280 Hz cut-off frequency are shown in Figure 7.58 to Figure 7.61. Within Figure 7.58, for the range 100.0° to 124.0° CA ATDC, the downwards flow in the lower central region is apparent for all three cycles at all CA presented. Cycle A displays the greatest symmetry about this centreline with the two rotations clearly identifiable on the left and right hand sides of the images. Conversely, cycle B, does not show this level of symmetry and by 124.0° CA the original symmetry visible in cycle A has also decayed. The less structured motion, observed for the case of the raw data is also apparent throughout the

remaining CA of interest for this low frequency filtered data, as presented in Figure 7.59 to Figure 7.61.

The mean low frequency flows across the range 100.0° to 184.0° CA ATDC are presented in Figure 7.62. At 112.0° CA the intended symmetry of the flow field can be seen; with the strong downwards flow in the centre and these flows parting to the left and right, returning upwards through the frame and rejoining the downward motion. This generates balanced clockwise and counter clockwise rotations which have been termed ‘wing vortices’, see Section 2.3.2. As the cycle progresses the rotations remain broadly in place underneath the intake valves but are seen to separate slightly by 148.0° CA. Additionally the magnitude of the velocity decays with time. The progression of flow within this plane, for the range 232.0° to 316.0° CA ATDC can be seen in Figure 7.63. In this case there does not appear to be any additional decay in energy of the flow. The area of higher velocity shown underneath the intake valves at around 292.0° CA correlates with the flow fields shown when considering the bulk tumble flows, as this had a bulk clockwise rotation which was therefore flowing from the intake to the exhaust in a similar position in the cylinder. At the end of the presented range of CA the flow field again appears predominantly symmetric, but with a slight bias to higher velocities on the left hand side of the image.

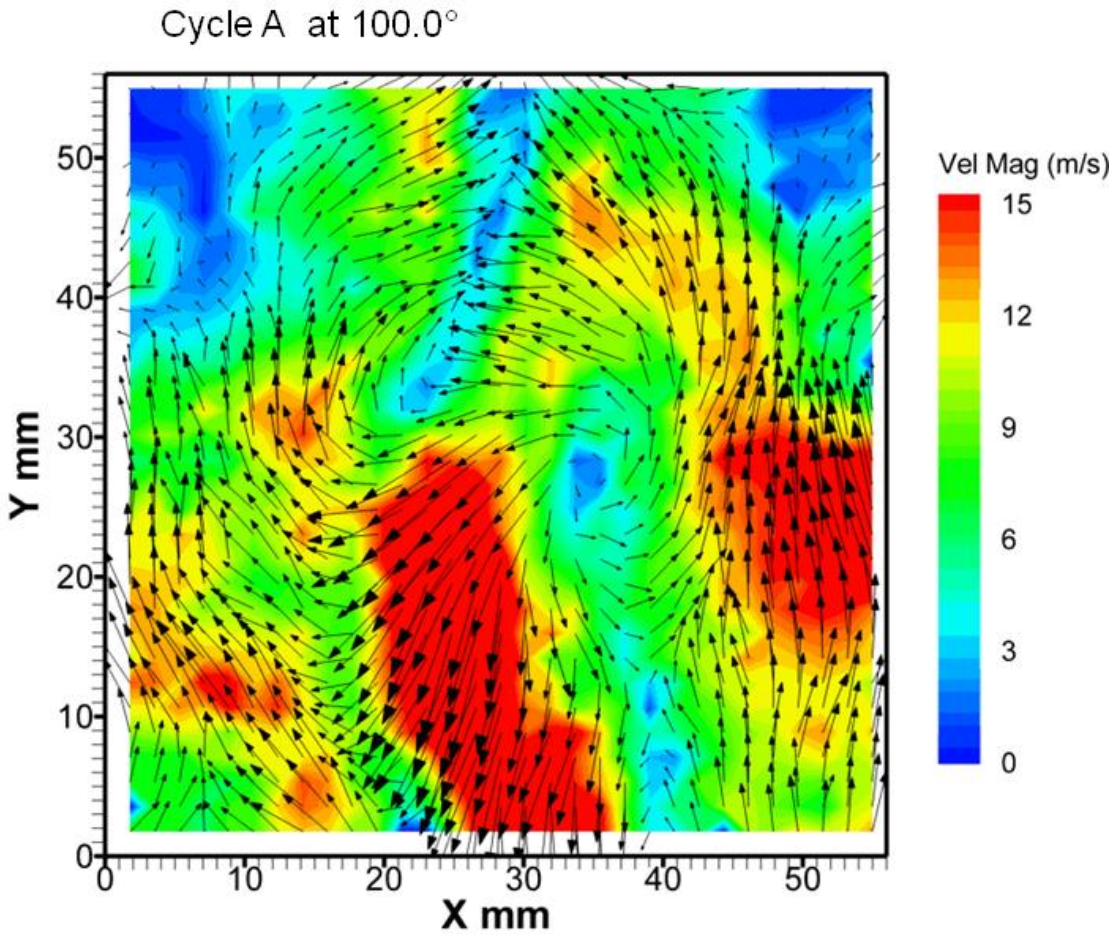

Figure 7.53 - Large scale image to show a raw flow fields on the swirl plane 10 mm below the peak height of the piston at 100.0° CA ATDC captured with HSDPIV at a rate of 1.5 kHz

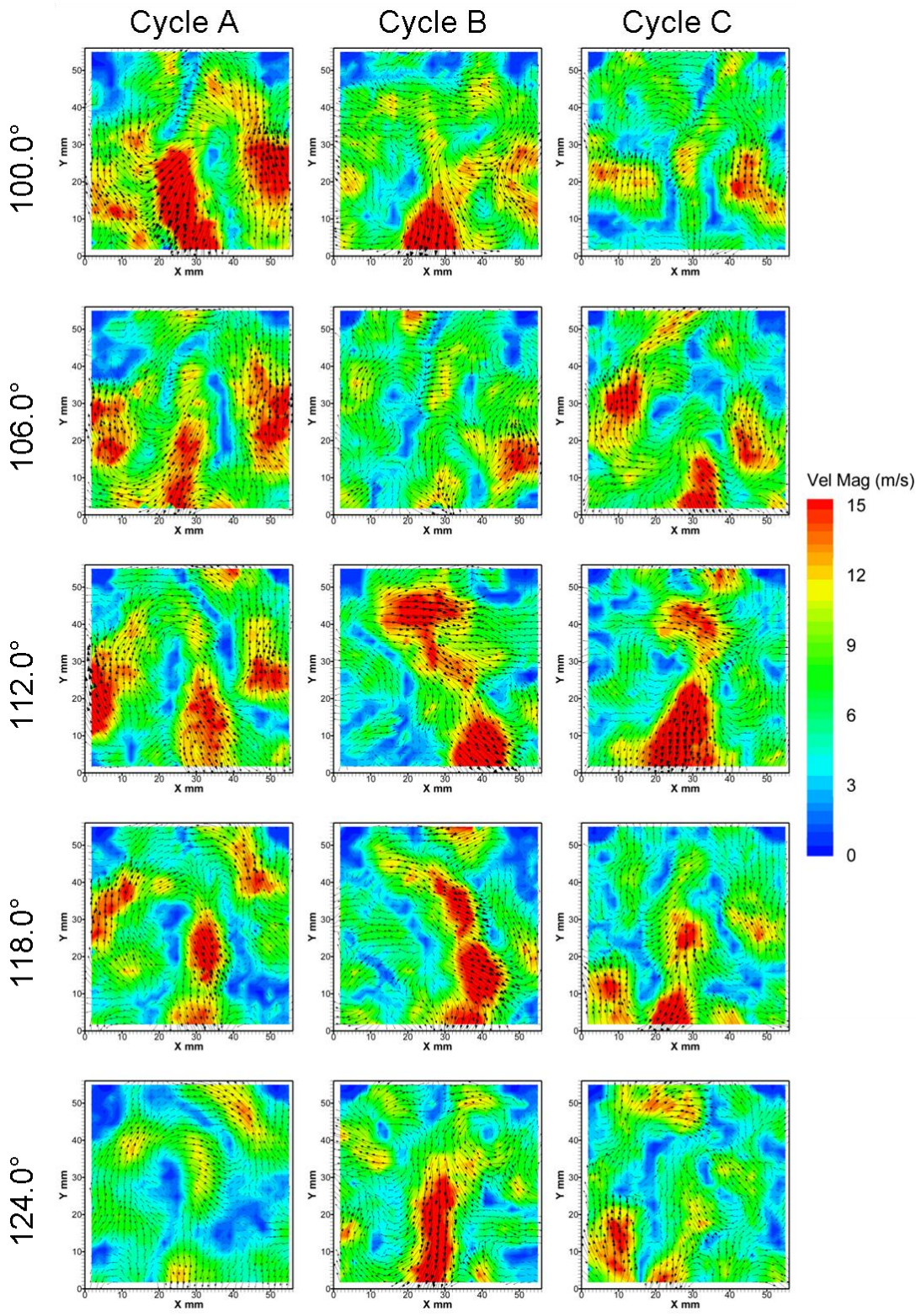

Figure 7.54 - Raw flow fields on the the swirl plane 10 mm below the peak height of the piston for three individual cycles from 100.0° to 124.0° CA ATDC captured with HSDPIV at a rate of 1.5 kHz

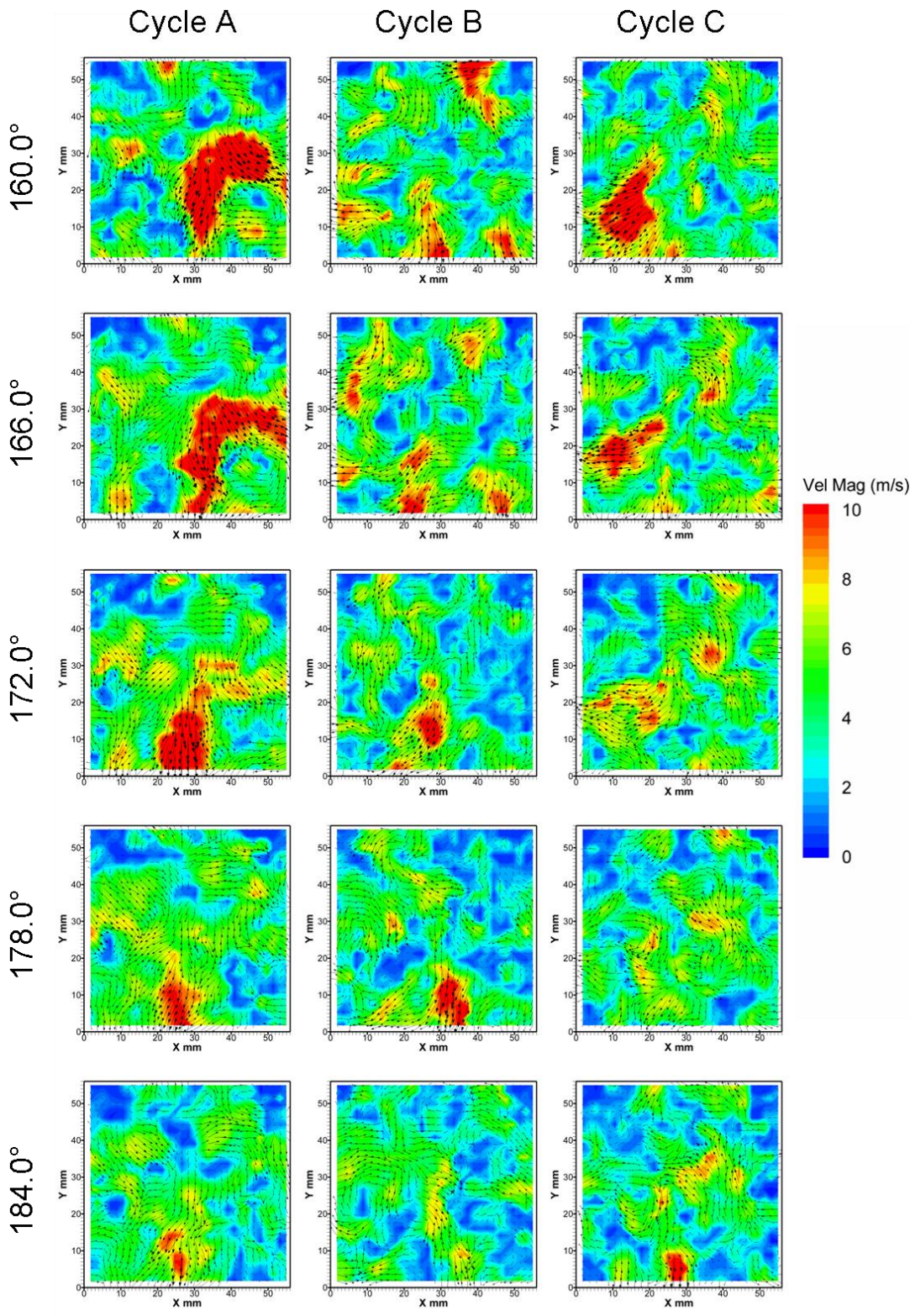

Figure 7.55 - Raw flow fields on the the swirl plane 10 mm below the peak height of the piston for three individual cycles from 160.0° to 184.0° CA ATDC captured with HSDPIV at a rate of 1.5 kHz

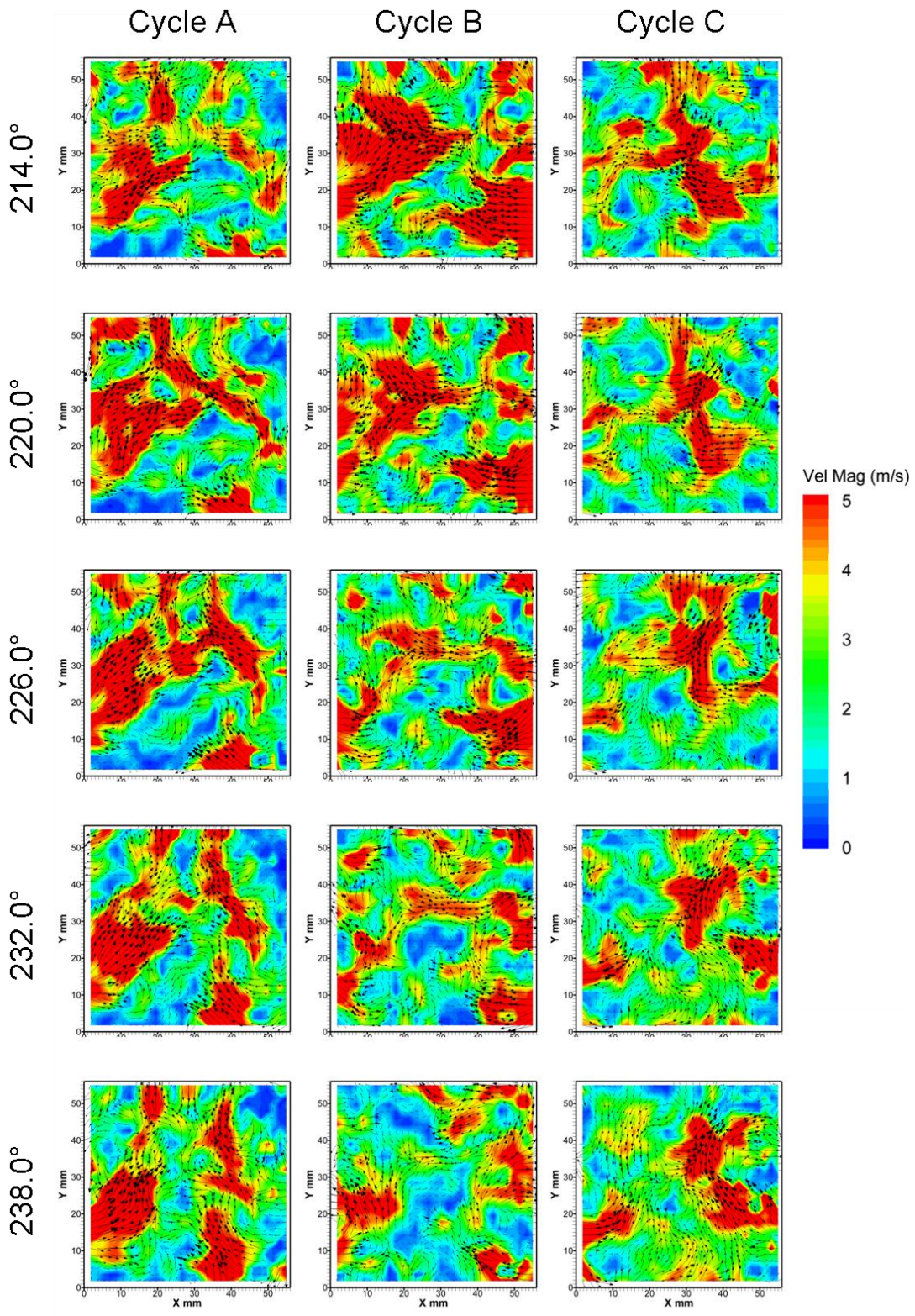

Figure 7.56 - Raw flow fields on the the swirl plane 10 mm below the peak height of the piston for three individual cycles from 214.0° to 238.0° CA ATDC captured with HSDPIV at a rate of 1.5 kHz

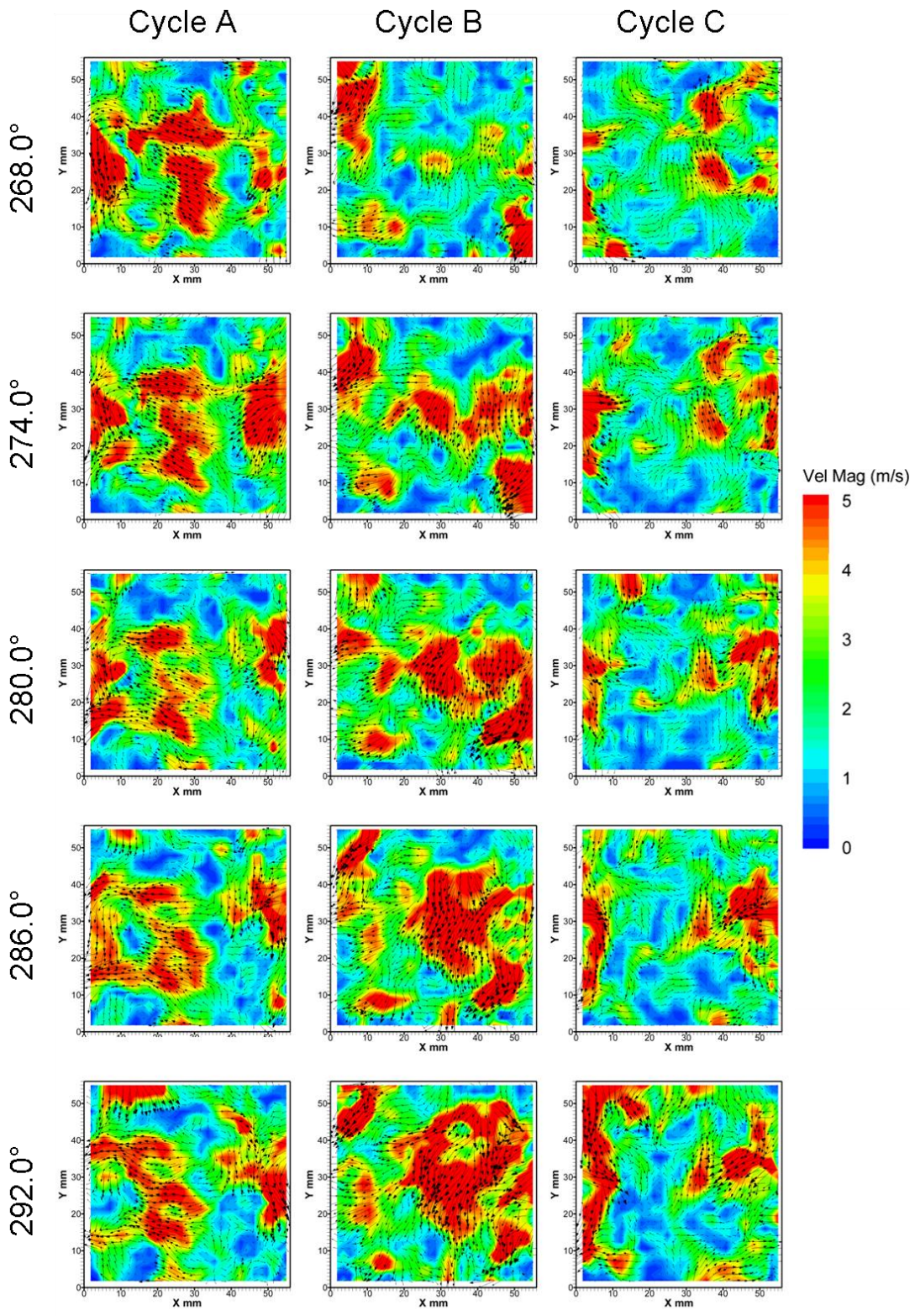

Figure 7.57 - Raw flow fields on the the swirl plane 10 mm below the peak height of the piston for three individual cycles from 268.0° to 292.0° CA ATDC captured with HSDPIV at a rate of 1.5 kHz

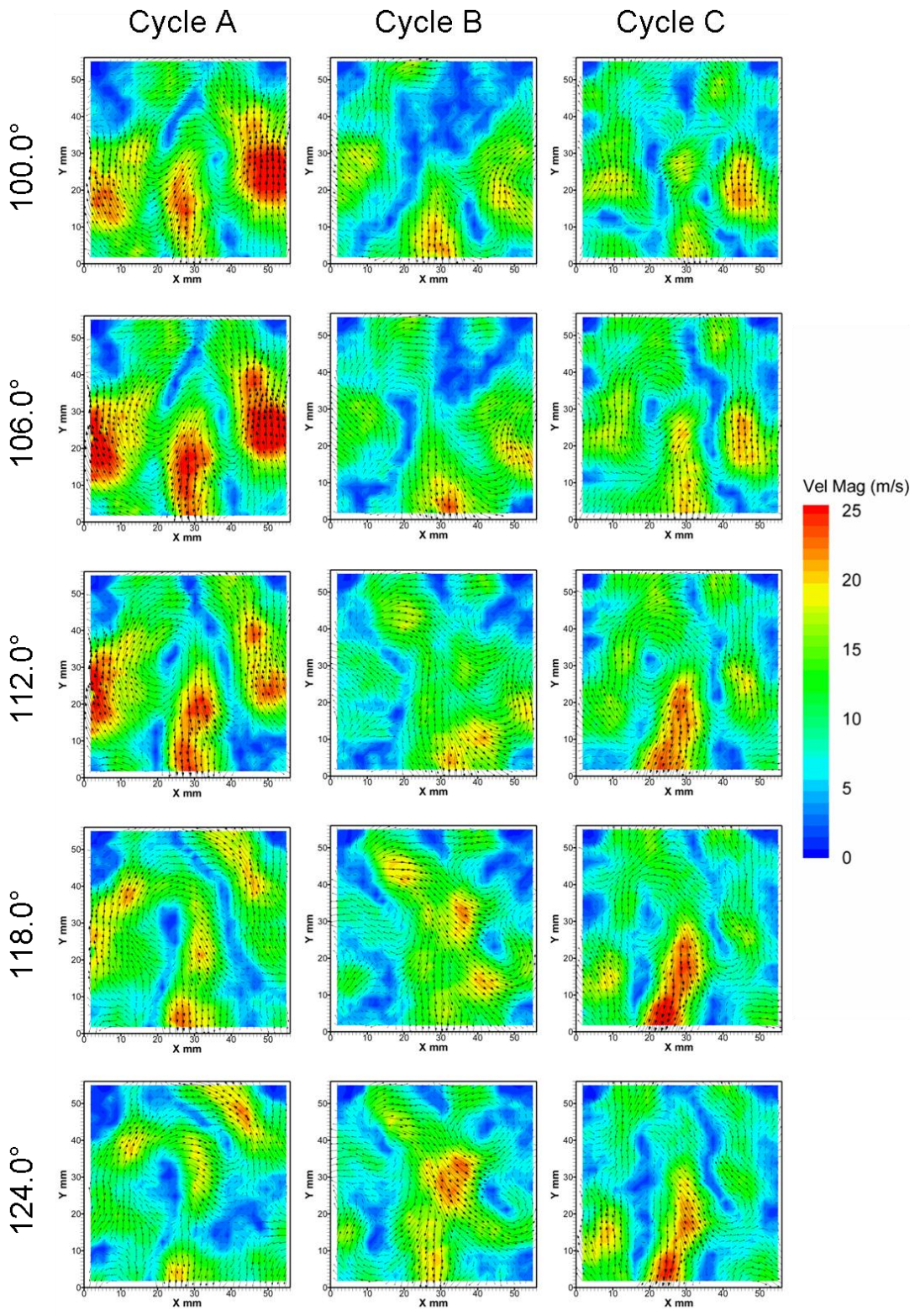

Figure 7.58 – Low frequency flow fields on the the swirl plane 10 mm below the peak height of the piston for three cycles from 100.0° to 124.0° CA ATDC captured with HSDPIV at a rate of 1.5 kHz

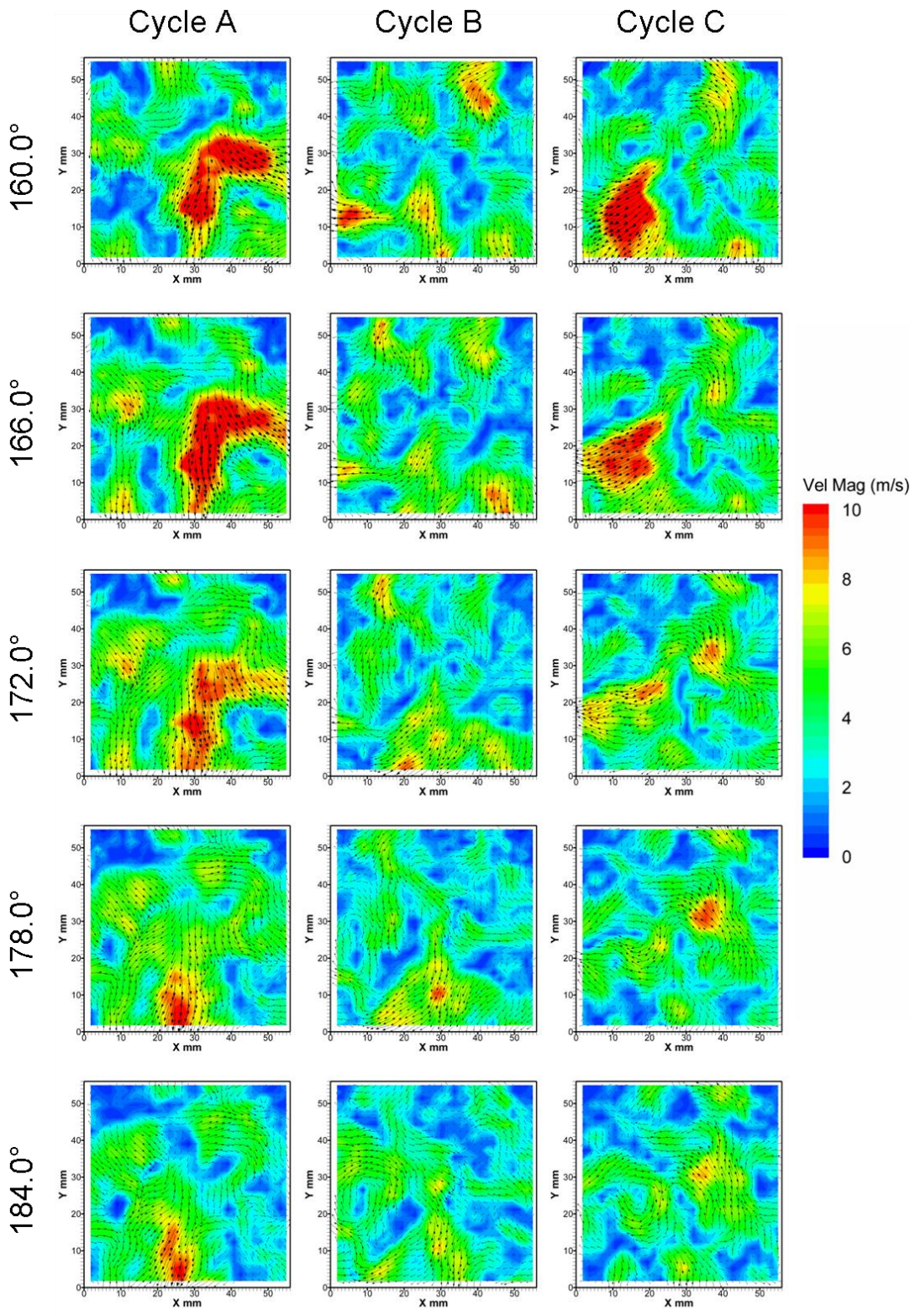

Figure 7.59 - Low frequency flow fields on the the swirl plane 10 mm below the peak height of the piston for three cycles from 160.0° to 184.0° CA ATDC captured with HSDPIV at a rate of 1.5 kHz

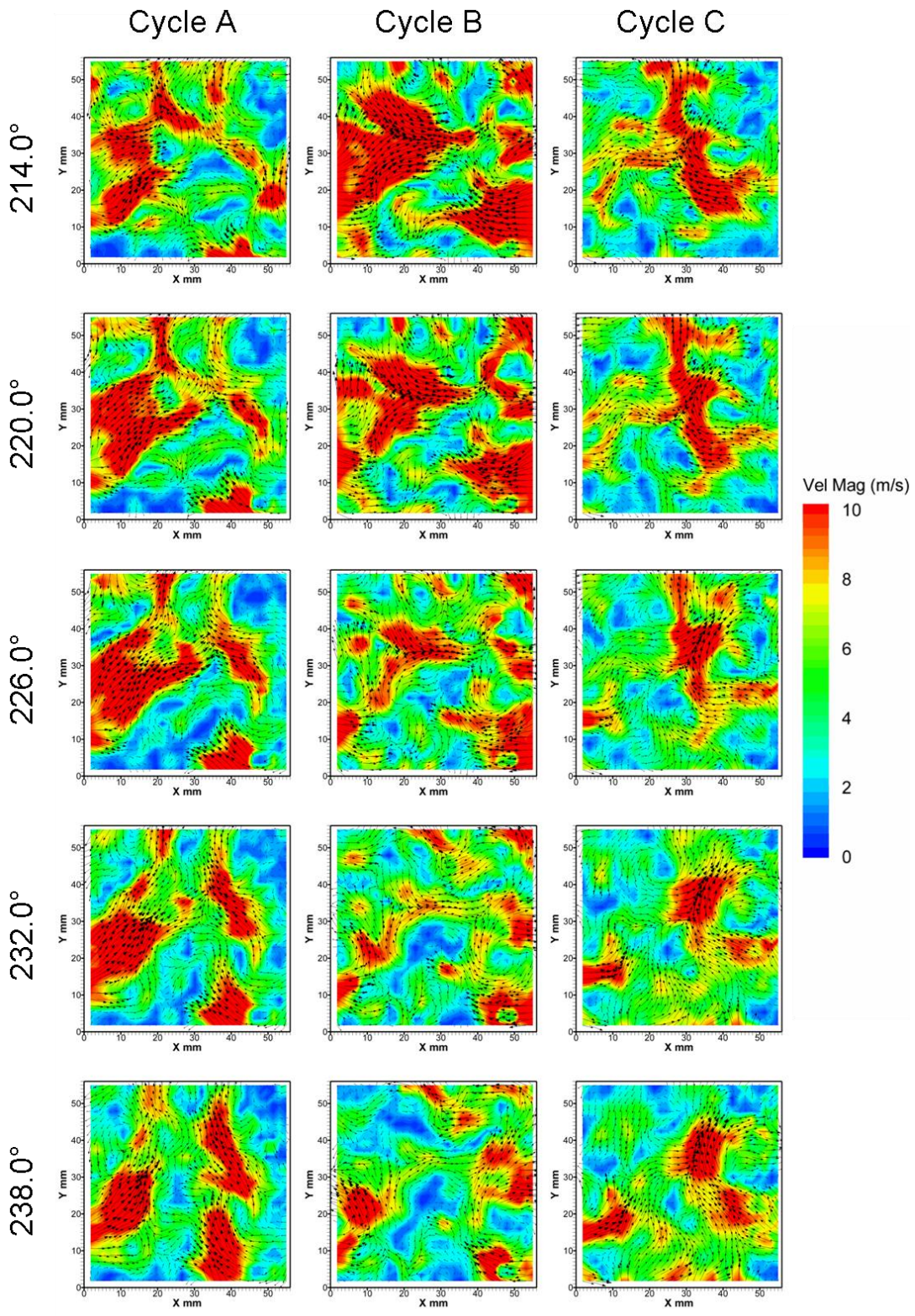

Figure 7.60 - Low frequency flow fields on the the swirl plane 10 mm below the peak height of the piston for three cycles from 214.0° to 238.0° CA ATDC captured with HSDPIV at a rate of 1.5 kHz

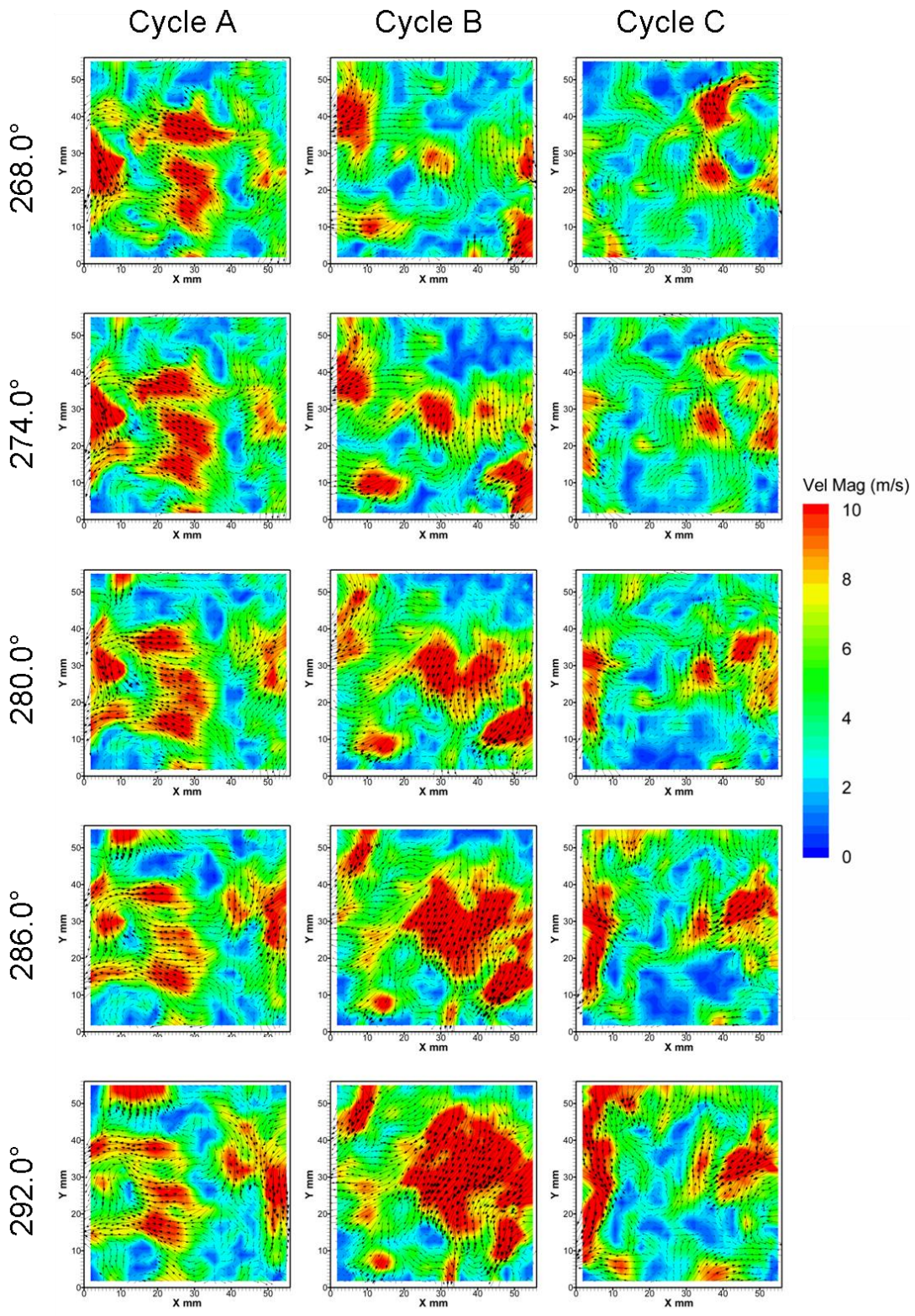

Figure 7.61 - Low frequency flow fields on the the swirl plane 10 mm below the peak height of the piston for three cycles from 268.0° to 292.0° CA ATDC captured with HSDPIV at a rate of 1.5 kHz

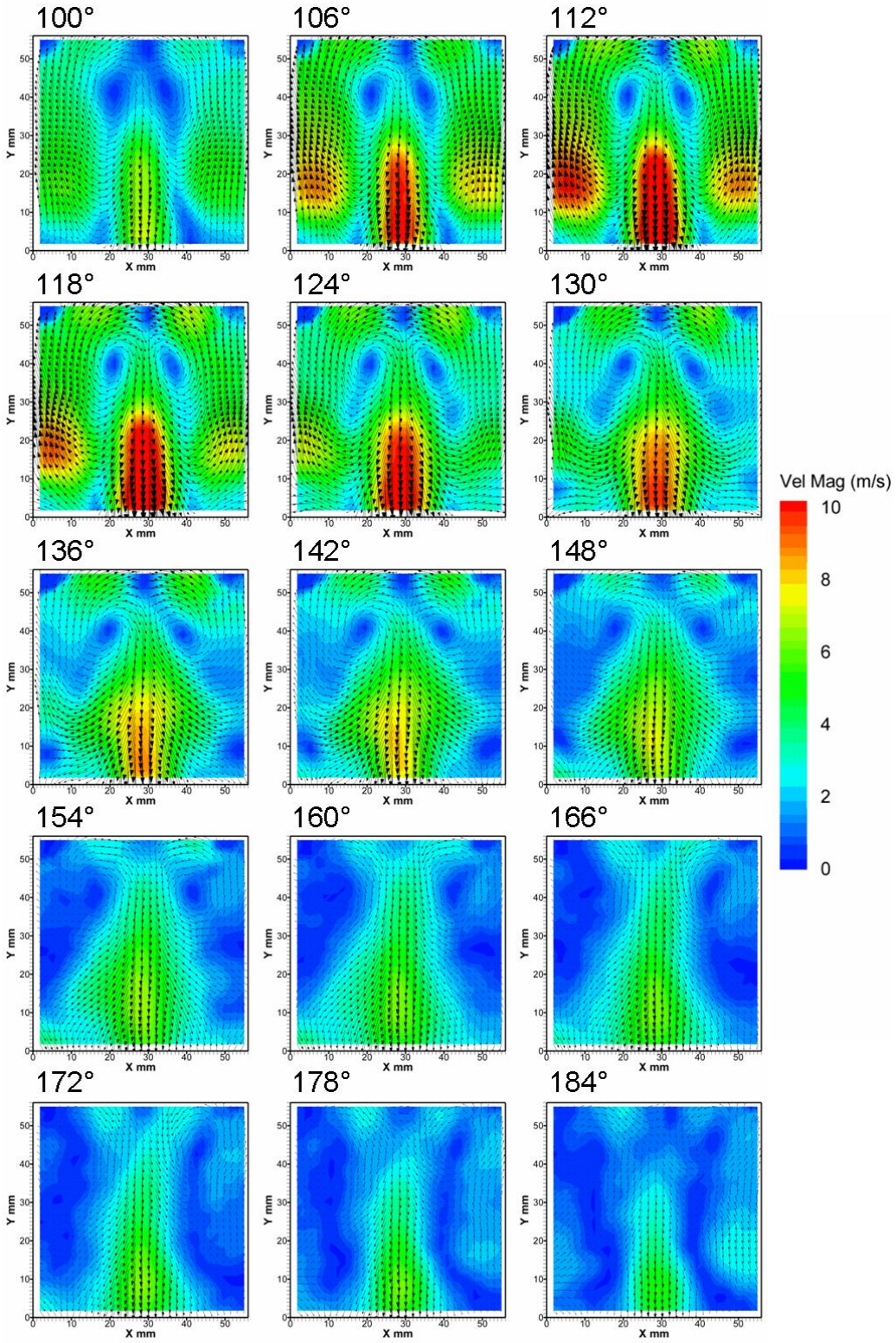

Figure 7.62 – Mean low frequency flow fields on the the swirl plane 10 mm below the peak height of the piston from 100.0° to 184.0° CA ATDC captured with HSDPIV at a rate of 1.5 kHz

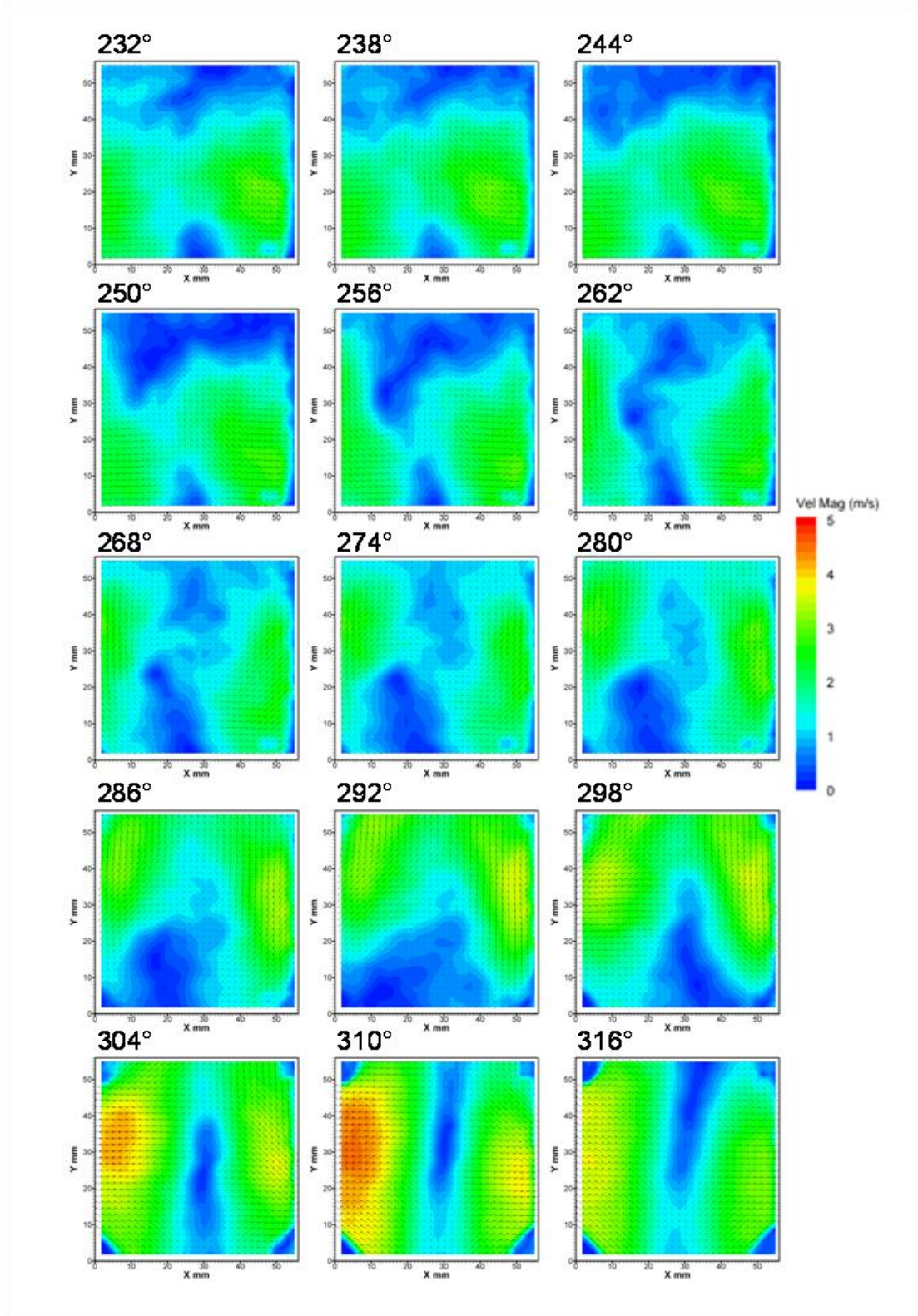

Figure 7.63 – Mean low frequency flow fields on the the swirl plane 10 mm below the peak height of the piston from 232.0° to 316.0° CA ATDC captured with HSDPIV at a rate of 1.5 kHz

Figure 7.64 to Figure 7.67 show velocity magnitude contours of low frequency cyclic variation for the three cycles previously discussed within this section. These images have been plotted with the low frequency velocity vectors overlaid so they highlight areas of variation whilst showing the structure of the cycles' bulk flow. Figure 7.64 shows images from the range 100.0° to 124.0° CA ATDC. At 100.0° CA cycle A, which appeared most symmetric previously when considering the low frequency flow, displays a region of higher variation on the right hand side in the flow towards the intake valves when compared to that similar flow on the left. The region of variation suggests an imbalance relative to the mean flow, but over the course of the CA range presented in this figure, the cyclic variation in this specific region decays only for other high variation regions to appear in the image. The peaks in velocity of low frequency cyclic variation across all cycles are in the same order of magnitude as the peaks in mean low frequency velocity at the same CA, shown previously.

In Figure 7.65 the cycles (specifically B and C) show randomly distributed regions of high cyclic variation about the centre line of the cylinder. Comparing back to the mean low frequency flow fields presented in Figure 7.62, these regions show very low velocity. Therefore, it is reasonable to assume that the *circa* 5 $m.s^{-1}$ velocity variations occur evenly in all directions, which results in the low mean flow observed. Interestingly, comparing the magnitude and fragmented nature of the cyclic variations occurring within these figures for the swirl plane and the tumble plane (shown in Figure 7.21 to Figure 7.24) similar trends are shown. This being the case for these two orthogonal planes in the cylinder suggests that the spatial variations are globally similar within the combustion chamber as a whole.

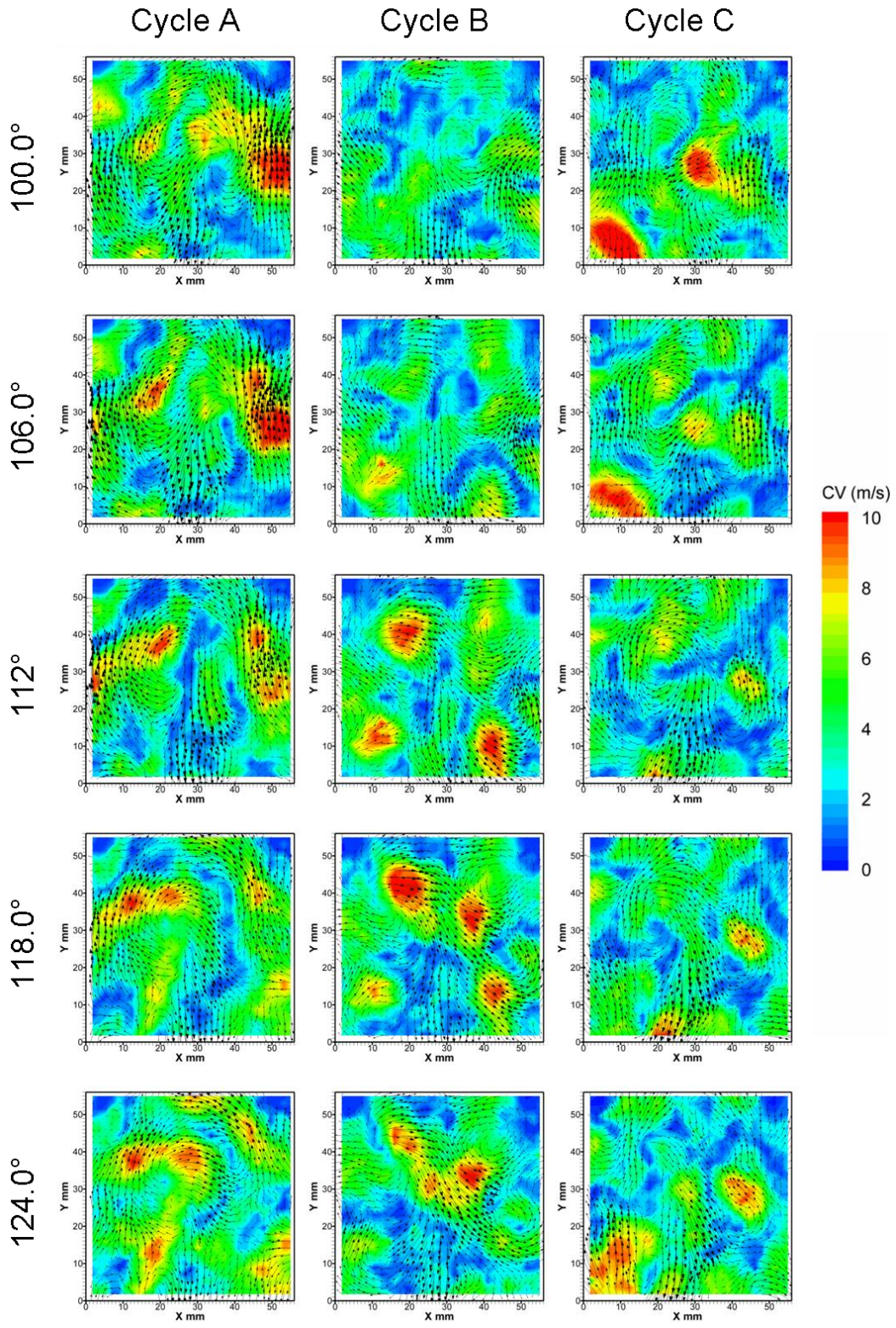

Figure 7.64 - Low frequency cyclic variation flow fields on the the swirl plane 10 mm below the peak height of the piston for three cycles from 100.0° to 124.0° CA ATDC captured with HSDPIV at a rate of 1.5 kHz

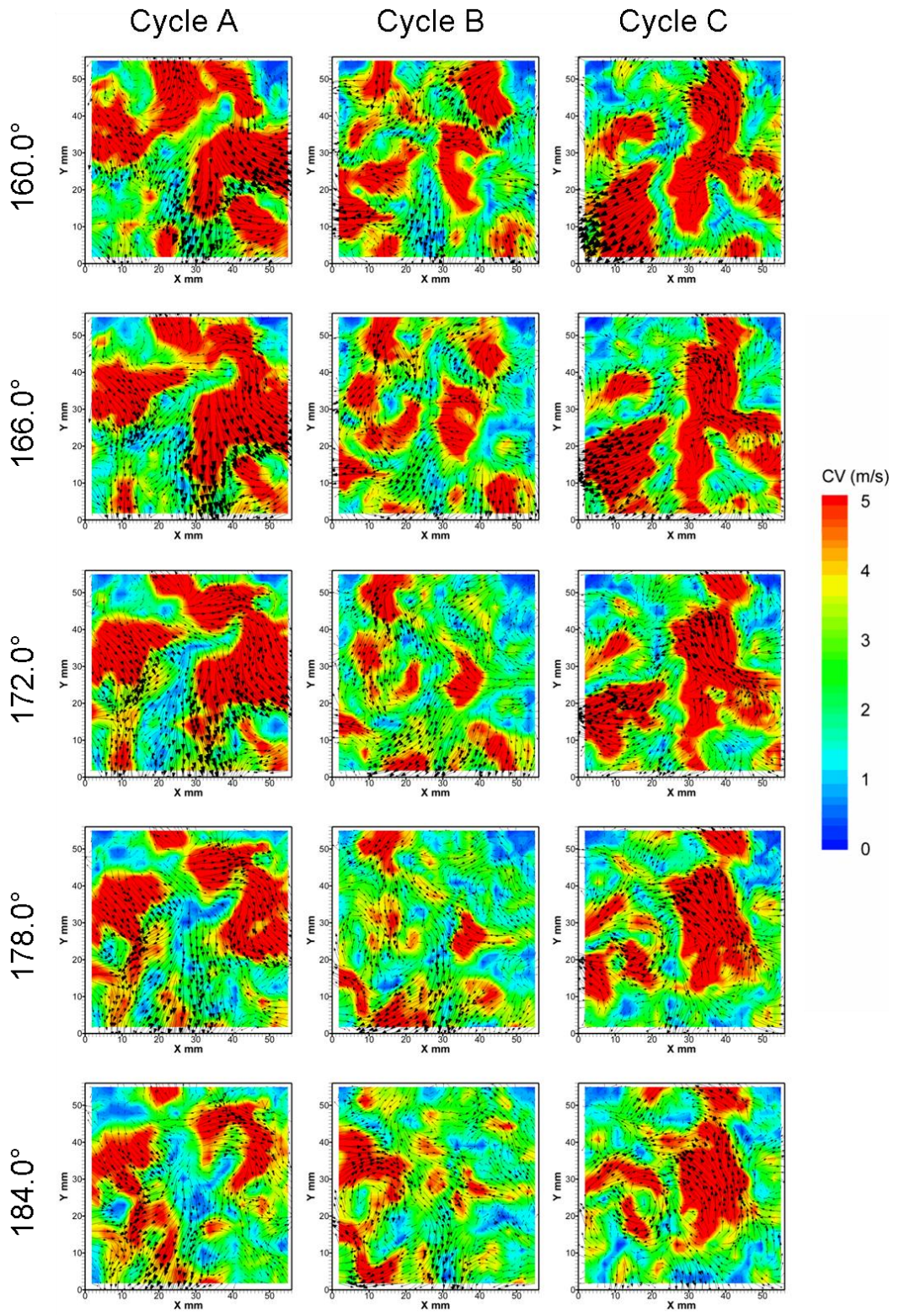

Figure 7.65 - Low frequency cyclic variation flow fields on the the swirl plane 10 mm below the peak height of the piston for three cycles from 160.0° to 184.0° CA ATDC captured with HSDPIV at a rate of 1.5 kHz

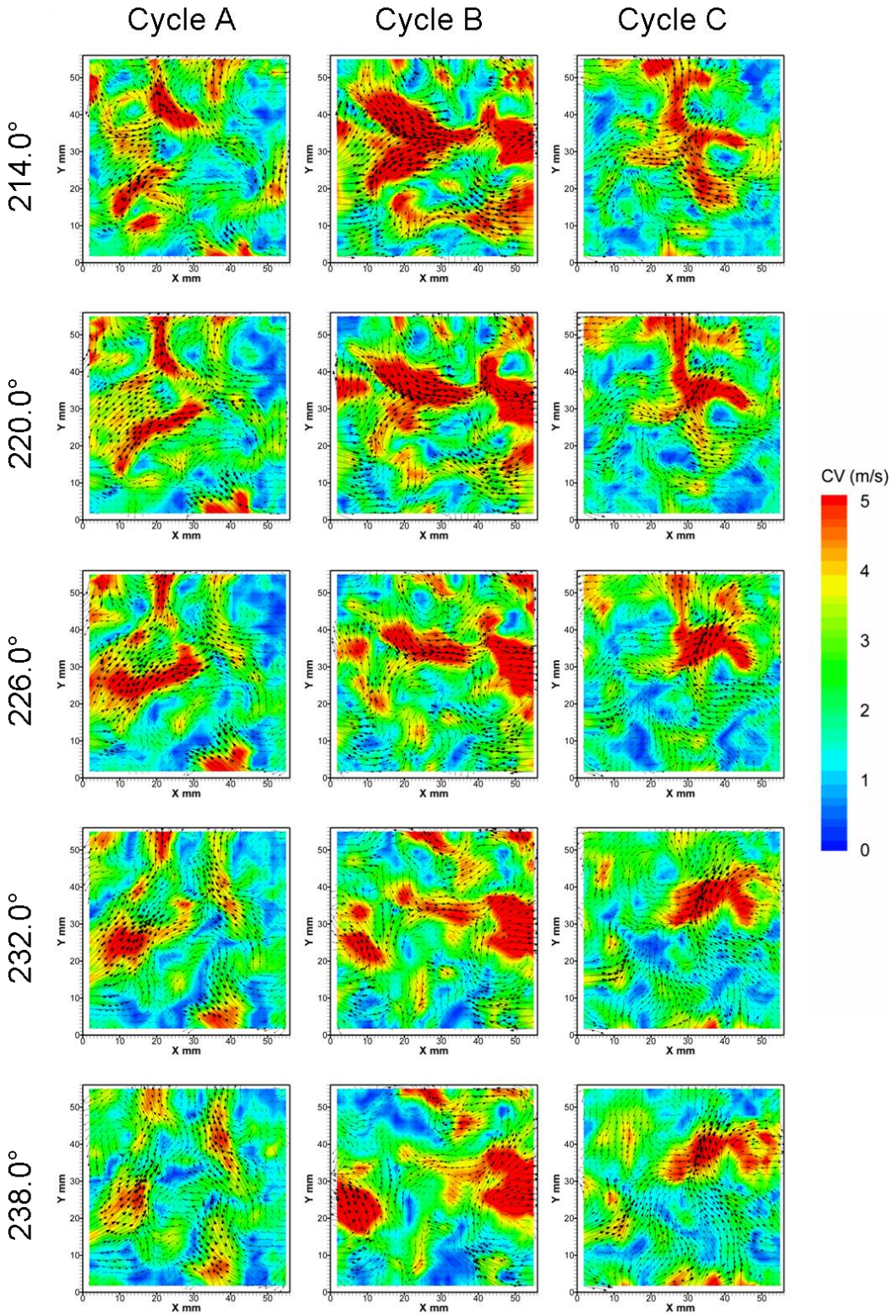

Figure 7.66 – Low frequency cyclic variation flow fields on the the swirl plane 10 mm below the peak height of the piston for three cycles from 214.0° to 238.0° CA ATDC captured with HSDPIV at a rate of 1.5 kHz

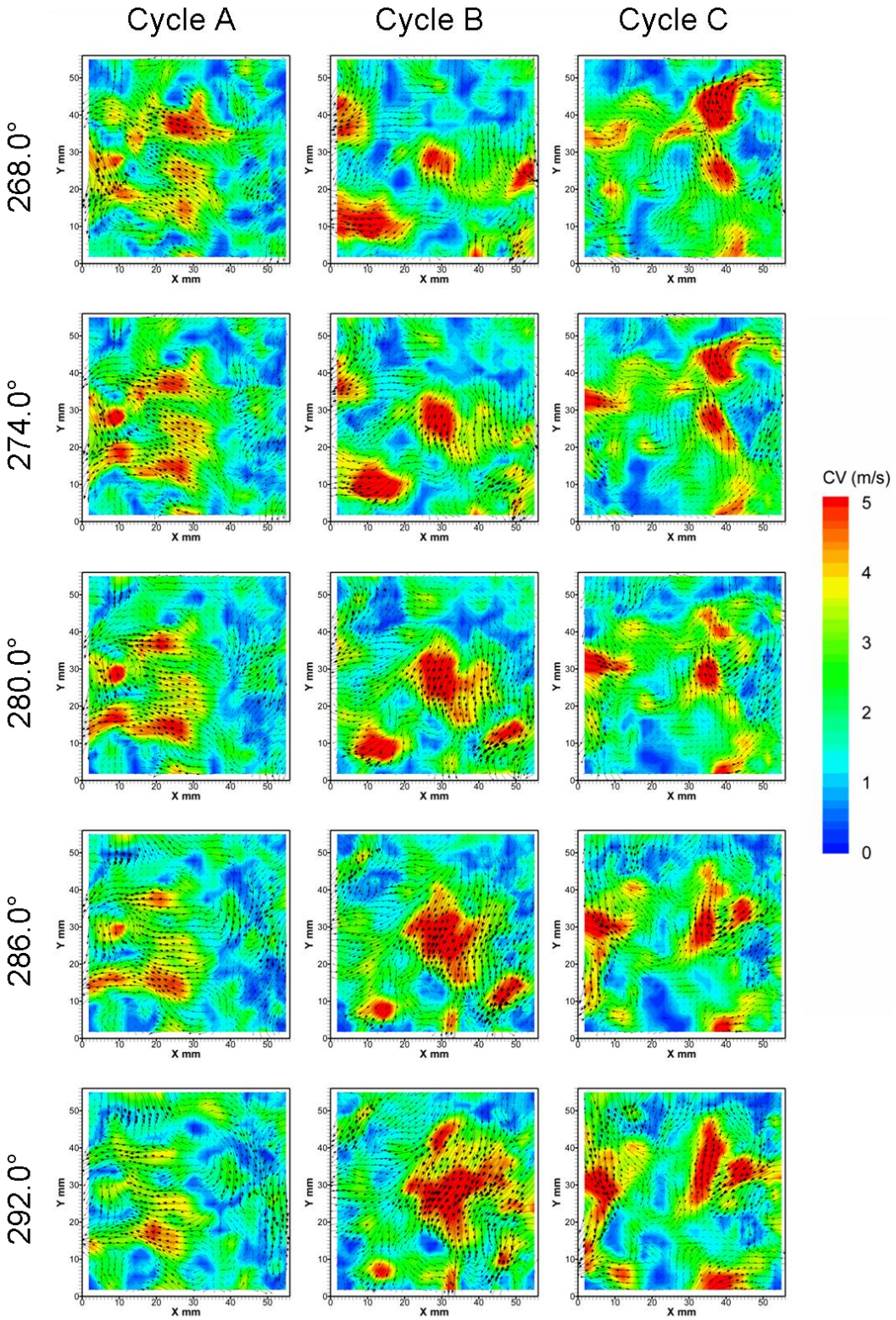

Figure 7.67 – Low frequency cyclic variation flow fields on the the swirl plane 10 mm below the peak height of the piston for three cycles from 268.0° to 292.0° CA ATDC captured with HSDPIV at a rate of 1.5 kHz

The *rms* of the low frequency cyclic variations are shown in Figure 7.68 and Figure 7.69 for the ranges 100.0° to 184.0° CA ATDC and 232.0° to 316.0° CA ATDC respectively. Initially there is a high *rms* of cyclic variation in the low velocity region which correlates with the recirculation centres for the clockwise and counter clockwise motions previously discussed. These are seen to decay up to 142.0° CA where they become lost into the background *rms* of variation displayed within the images. As the cycle further progresses homogeneity within this parameter remains, suggesting that the cyclic variations in the flow fields on this plane are largely random. Drawing a comparison between the *rms* of low frequency cyclic variation in the swirl plane and the tumble plane (see Figure 7.29 and Figure 7.30), where both show a similar magnitude throughout the cycle, confirms the observations made above which suggested that the variations are largely independent of mean flow structure.

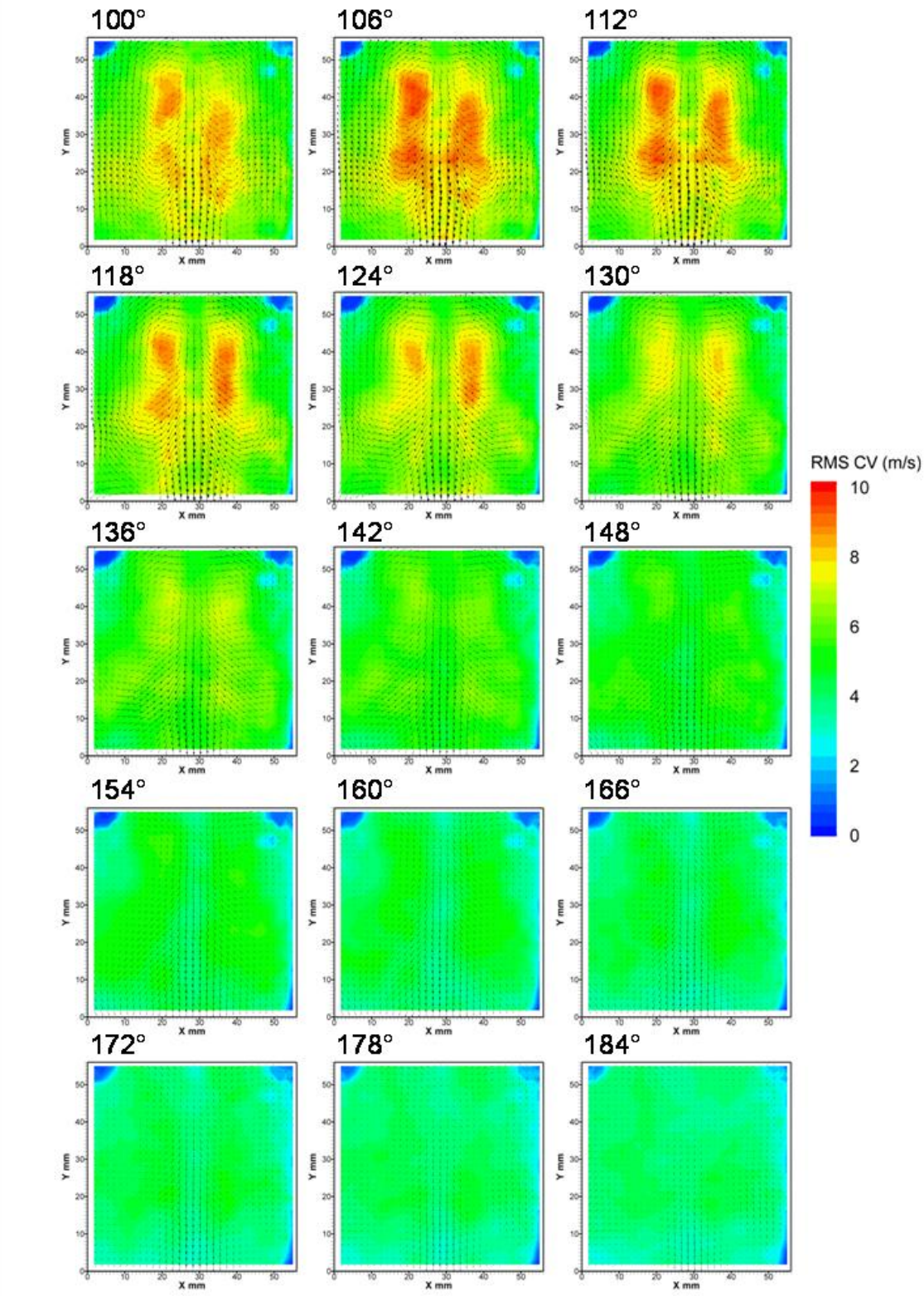

Figure 7.68 – *rms* of 100 low frequency cyclic variation flow fields on the swirl plane 10 mm below the peak height of the piston from 100.0° to 184.0° CA ATDC captured with HSDPIV at a rate of 1.5 kHz

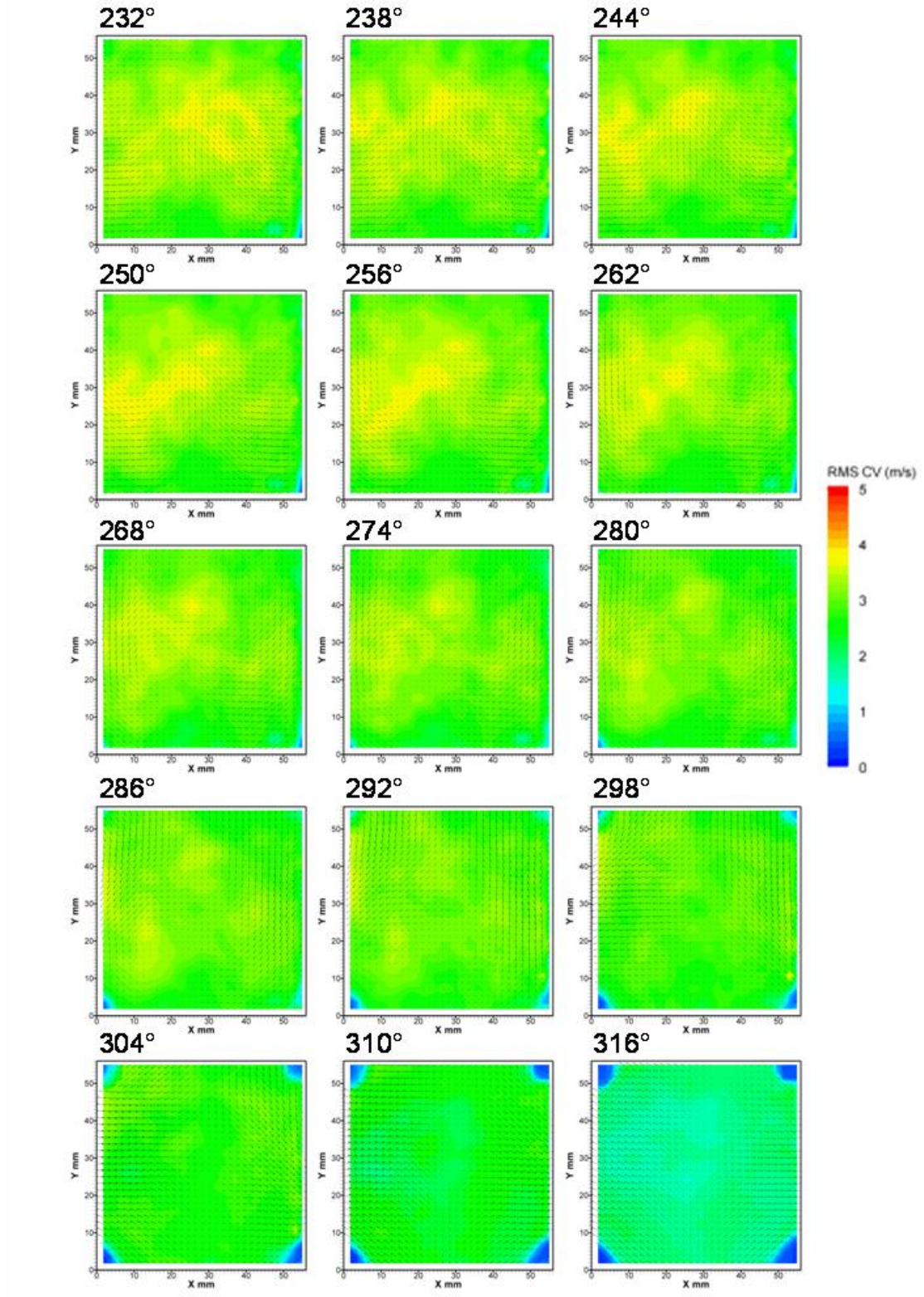

Figure 7.69 - *rms* of 100 low frequency cyclic variation flow fields on the swirl plane 10 mm below the peak height of the piston from 232.0° to 316.0° CA ATDC captured with HSDPIV at a rate of 1.5 kHz

7.3.2.2 With tumble flap

Similar flow fields as those presented in the previous section have also been captured using the tumble flap introduced in Chapter 4. The set-up of the measurement system and the engine operating conditions were as per Section 7.3.1. This tumble flap has been employed to introduce a change to the bulk flow structure entering the cylinder through the intake valve and therefore examine its effect on the cyclic variation experienced by the flow. Data in this case has only been presented for the mean low frequency flow fields over the range 100.0° to 184.0° CA and 232.0° to 316° CA in Figure 7.70 and Figure 7.71 respectively and for the *rms* of the low frequency cyclic variation for the same CA ranges in Figure 7.72 and Figure 7.73.

Figure 7.70 shows that the tumble flap has increased the velocity within the central region flowing towards the exhaust side of the cylinder and reduces the flow returning towards the intake valves. Additionally, and a likely result of these flow changes, the two opposing rotations are less obvious. The velocity in this central region remains high for longer into the cycle than for that observed without the tumble flap (see Figure 7.62). This increased tumble (see Section 7.2) is evident later in the cycle, see Figure 7.71, as can be seen by the higher velocity flow appearing at the top of the images from *circa* 268° to 298° CA. Considering the *rms* of cyclic variations in Figure 7.72 and Figure 7.73 shows that initially the region of high variation, although similar in magnitude, has moved slightly towards the exhaust side of the cylinder. However, by 184.0° CA the two configurations are indistinguishable. In the latter stages of the cycle, from 280.0° CA onwards, the stronger tumble motion is again apparent as the higher velocity (see Figure 7.71) brings with it greater *rms* of cyclic variation. In general, the strength of bulk motions caused by the tumble flap can affect where regions of high relative cyclic variation occur.

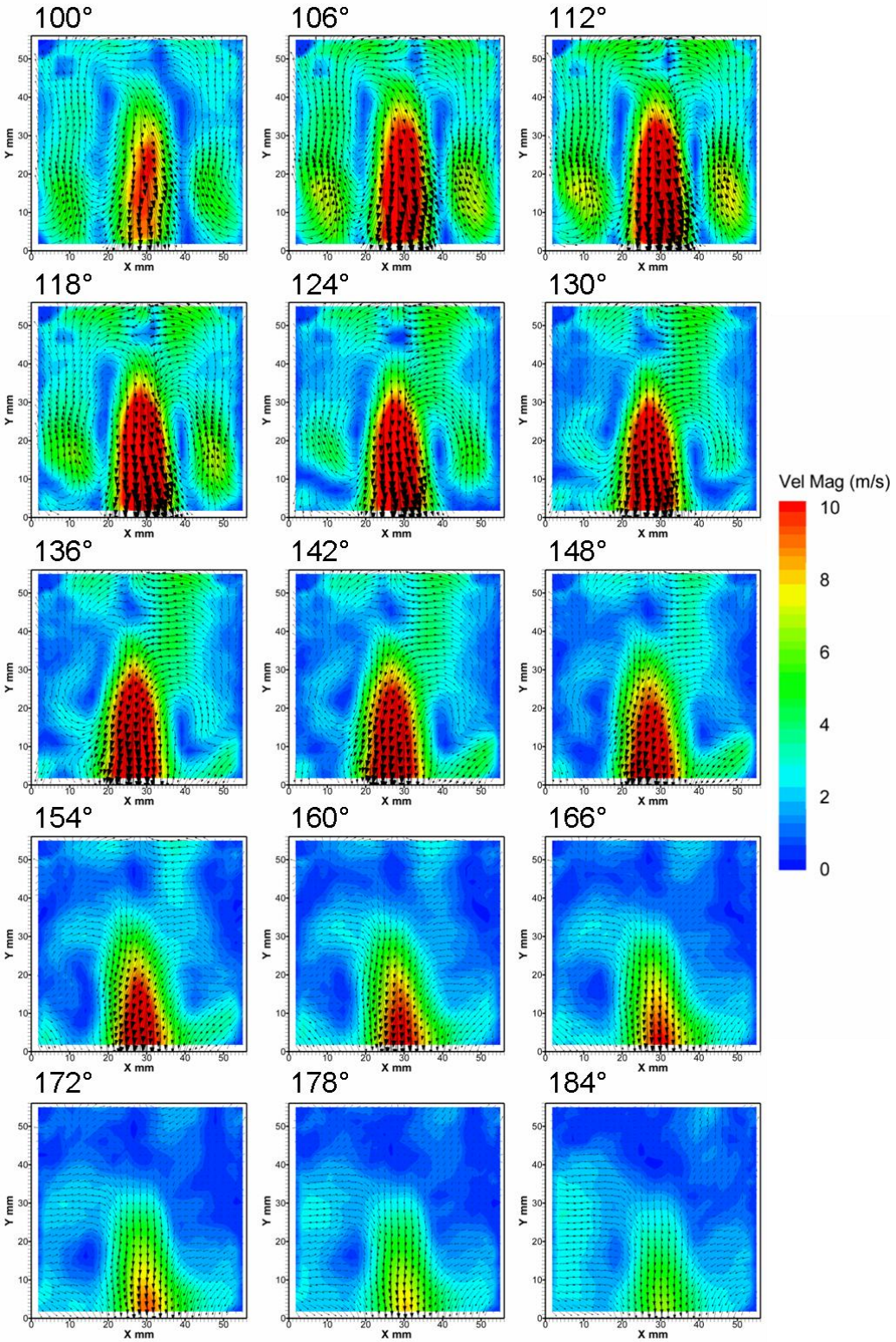

Figure 7.70 – Mean low frequency flow fields on the the swirl plane 10 mm below the peak height of the piston, generated with the tumble flap fitted, from 100.0° to 184.0° CA ATDC captured with HSDPIV at a rate of 1.5 kHz

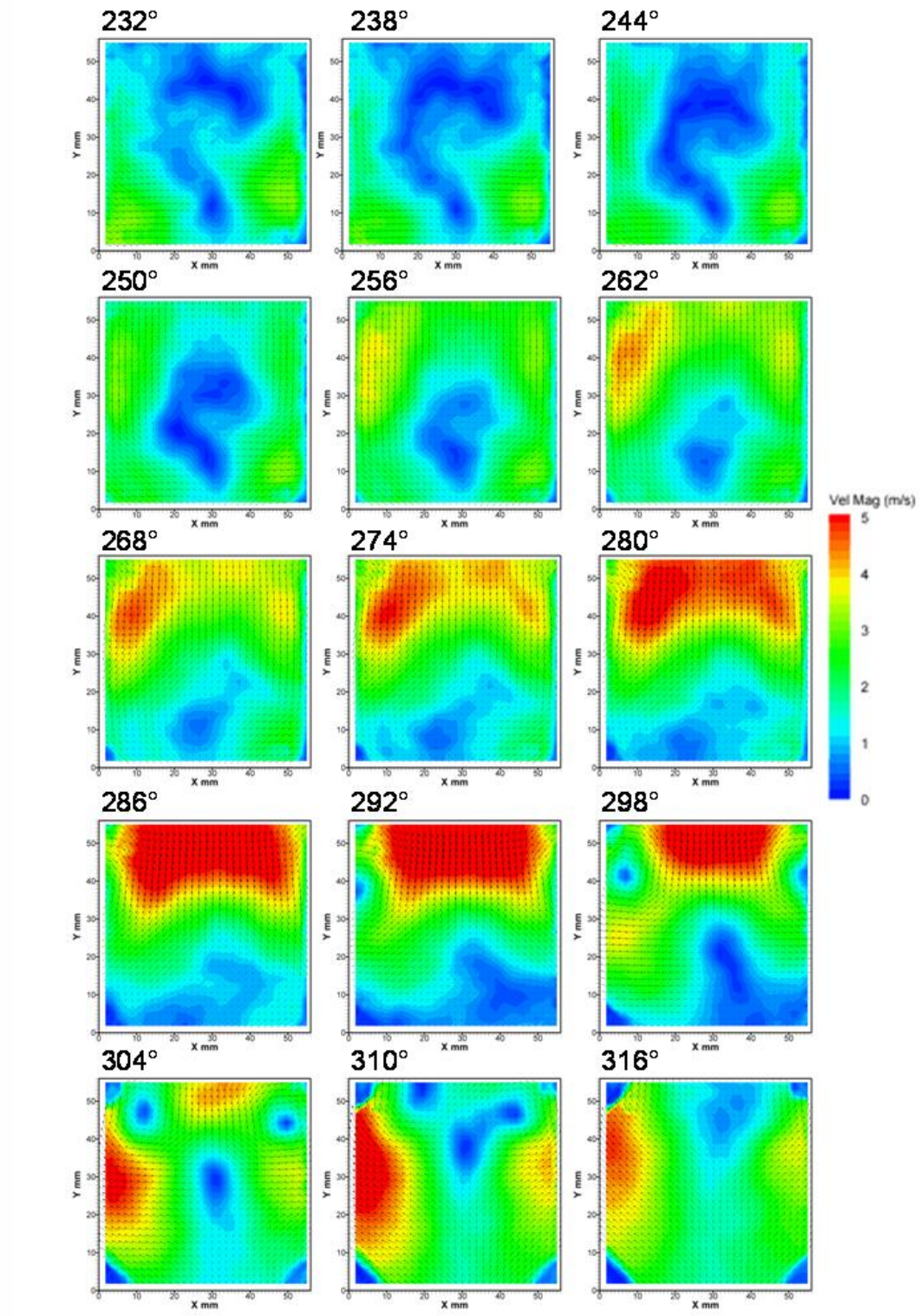

Figure 7.71 - Mean low frequency flow fields on the the swirl plane 10 mm below the peak height of the piston, generated with the tumble flap fitted, from 232.0° to 316.0° CA ATDC captured with HSDPIV at a rate of 1.5 kHz

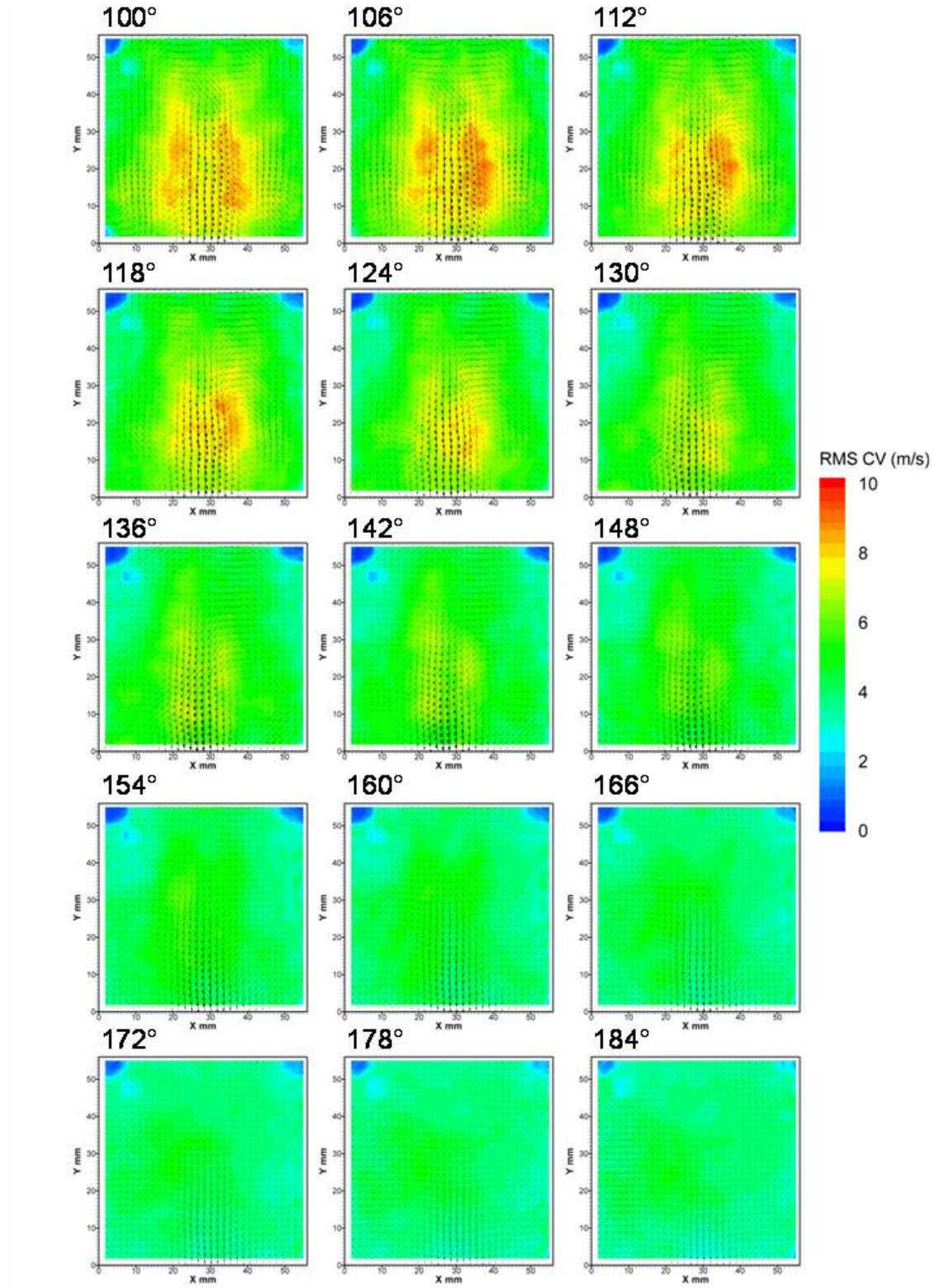

Figure 7.72 - *rms* of 100 low frequency cyclic variation flow fields on the swirl plane 10 mm below the peak height of the piston, generated with the tumble flap fitted, from 100.0° to 184.0° CA ATDC captured with HSDPIV at a rate of 1.5 kHz

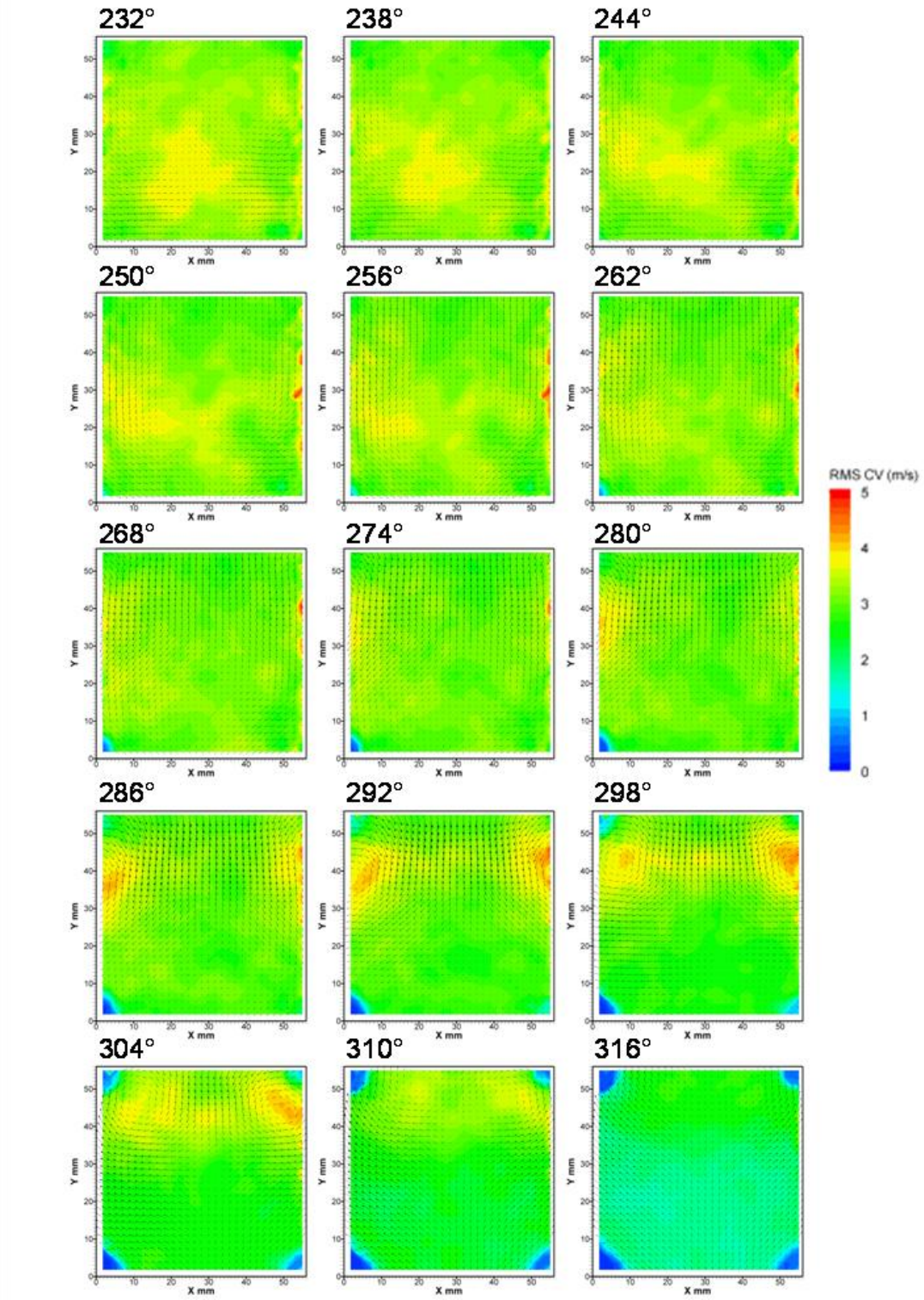

Figure 7.73 - *rms* of 100 low frequency cyclic variation flow fields on the swirl plane 10 mm below the peak height of the piston, generated with the tumble flap fitted, from 232.0° to 316.0° AC ATDC captured with HSDPIV at a rate of 1.5 kHz

7.4 In Cylinder u' Spatial Averaging

Chapter 5 demonstrated a link between u' and cycle pressure data, therefore, the development of u' over the course of the cycle is an important factor to consider. This will, by association, affect the combustion event and hence lead to variations in measurable cycle output. The current chapter has investigated the spatial variations in turbulence intensity, u', for flow fields both with and without the tumble flap in position. Within the tumble plane these plots can be seen in Figure 7.31 to Figure 7.34 and Figure 7.47 to Figure 7.50 respectively. The purpose of the tumble flap was to apply a physical change to the flow field characteristics, allowing an investigation into the effect this had on the variability of the bulk flow motion within the cylinder along with the decay of the flow and, therefore, the resulting u'. In order to compare the spatial and temporal data gathered, and presented previously within this chapter, calculation of spatial mean u' values, as per Chapter 5, has been carried out. This is shown over the CA range captured for the bore centreline in the tumble plane in Figure 7.74, and swirl plane (10 mm below the peak height of the piston) in Figure 7.75 for the case without the tumble flap. The hump observed in the data (from 230° CA) presented for the tumble plane corresponds to the piston entering the view and therefore affecting the calculation. There is also, however, the recirculating flow re-entering the frame ahead of the piston which may also act to increase the average turbulence intensity of the field of view. The piston entering the view is obviously not an issue in the swirl plane. It can be seen that in both cases there is a larger variation in spatial mean u' early in the sequence which diminishes as the energy of the flow decays.

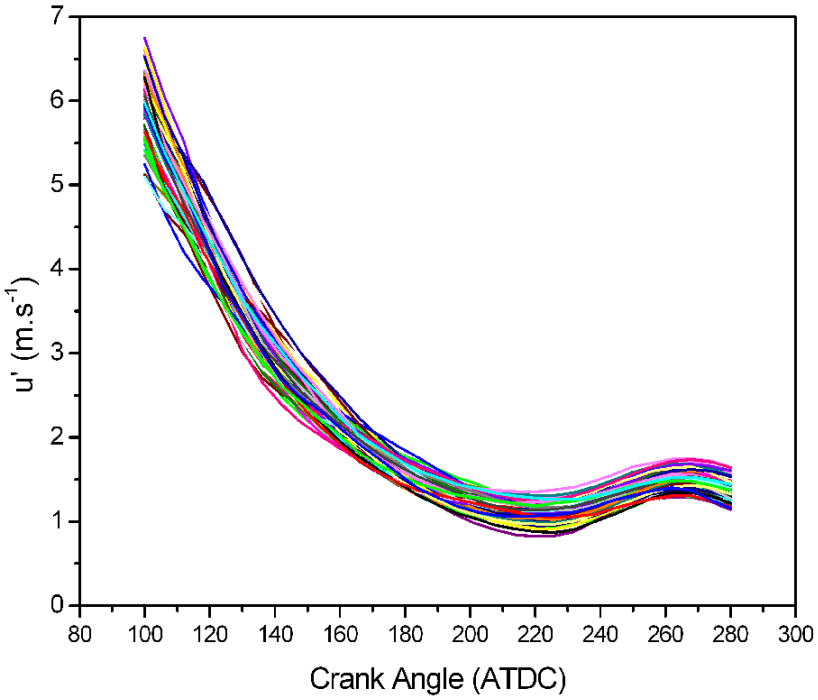

Figure 7.74 - The development of the spatial averaged u', on the bore centreline in the tumble plane, for 100 cycles for the standard geometry example

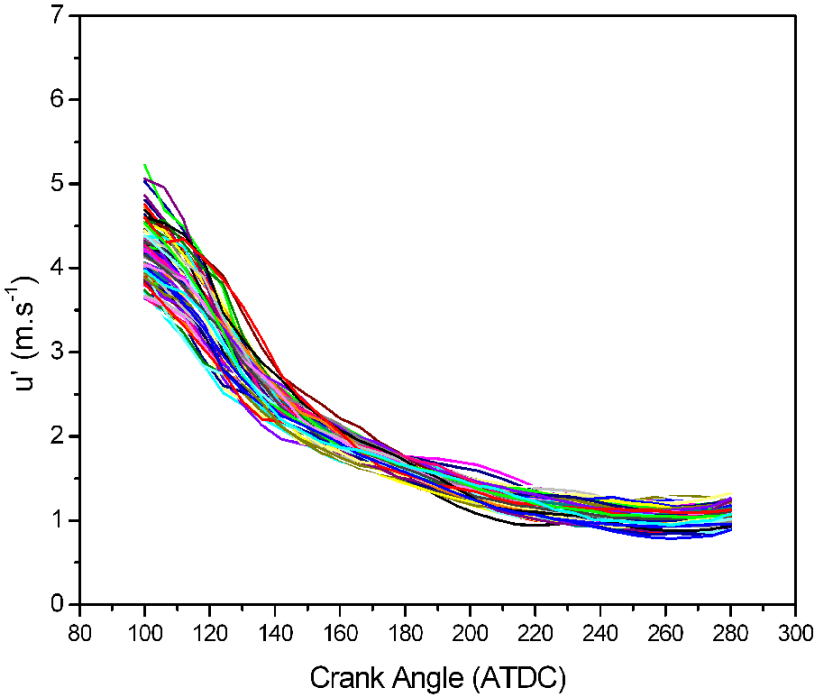

Figure 7.75 - The development of the spatial averaged u', on the swirl plane 10 mm below the peak height of the piston, for 100 cycles for the standard geometry example

To compare whether the tumble flap has affected the decay of u' and variations within it, Figure 7.76 and Figure 7.77 show the mean and standard deviation in u' for both the standard and tumble flap geometry over the range of data available, for the tumble and swirl planes respectively. It can be seen that even though the tumble plane exhibits similar decay in u' for both cases over the course of the cycle, at circa 280° CA the tumble flap case ends with a higher mean, and a lower standard deviation in u'. The swirl plane flow fields display a slightly different story in which the tumble flap case, which was shown to exhibit higher peak velocity, also has a higher spatial mean u' which remains higher throughout the range of the cycle shown. However, even though the mean u' for the two cases differ, the standard deviation of u' in the swirl plane is similar ending on virtually identical values. The standard deviation in u' for the standard geometry case, in both the tumble and swirl planes, starts higher and decays more quickly. By 180° CA it has fallen below that of the tumble flap case but then levels out. The decay for the tumble flap case continues and by the end of the presented range the standard deviation in u' is lower.

The change to the valve jet flow characteristics and subsequent modification to the in-cylinder flow field as a result of the tumble flap has been shown to the affect both high and low frequency characteristics of the cycle. This suggests that the design of the intake port and fundamental concept of the flow behaviour can affect cyclic variation as has been previously discussed by many researchers (for example Church and Farrell (1998); Lee and Lee (2003)).

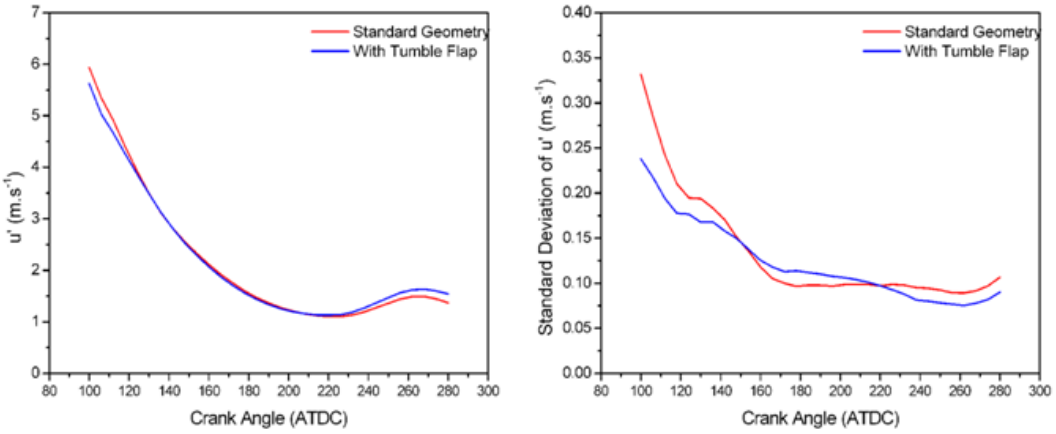

Figure 7.76 - The mean and standard deviation of u', on the bore centreline in the tumble plane, for 100 cycles in both the standard and tumble flap geometry examples

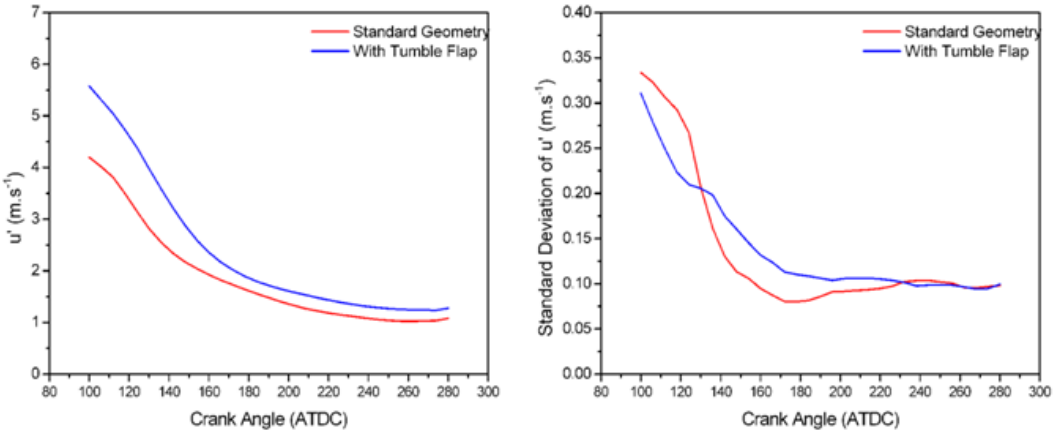

Figure 7.77 - The mean and standard deviation of u', 10mm below the peak height of the piston in the swirl plane, for 100 cycles in both the standard and tumble flap geometry examples

Not only does the change in geometry affect the high and low frequency characteristics of the cycle but also the behaviour of the cyclic variation in u'. By performing a linear correlation between the calculated temporal u' at the end of the captured range with those throughout it, it was possible to investigate the extent to which the u' field at the end of the cycle was affected by earlier events within the field of view. This is presented in Figure 7.78 for both the tumble and swirl planes and for the standard and tumble flap

geometries. Initially there is little correlation in all four experimental conditions presented, however, from approximately 180° CA the correlation is seen to increase, first for the standard geometry and later for the tumble flap case. It is important to note that due to the temporal averaging performed in the calculation of u', the u' from 256° CA includes an increasing number of values also used in the derivation of the final u' data point. As such, one would expect an increasing correlation from this point; however, this does not explain the increased correlation clearly visible earlier in the cycle.

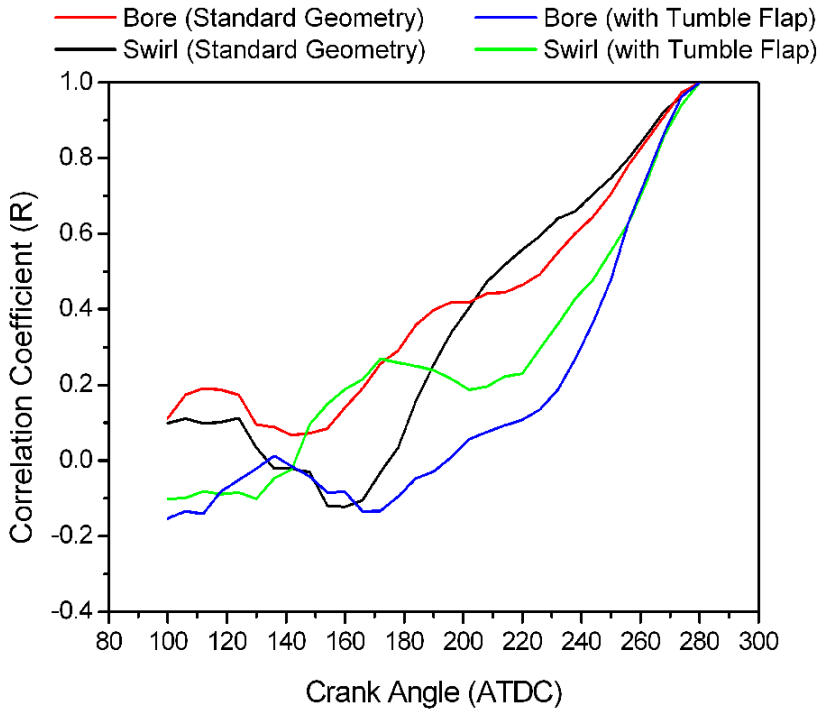

Figure 7.78 - Correlation coefficient for a linear fit of u'

Chapter 5 investigated the link between u' within the pent roof of the combustion chamber leading up to ignition and the resulting pressure related cycle performance parameters. Throughout Chapters 6 and 7 the development of in cylinder flow fields and cyclic variations occurring have been presented. It has been shown that introducing a geometry change to influence the flow field behaviour can change the characteristics in the turbulent structures and resulting energy cascade. This can be seen in-cylinder

through a change in the mean and standard deviation of u' over the course of the cycle as presented above. These changes in u' and its cyclic variation throughout the development of the cycle are likely to lead to differing conditions within the flow field at the point of ignition. As a result the optimisation of intake and combustion chamber geometry to produce favourable u' characteristics which lead to a reduction in overall engine cyclic variation should be possible.

7.5 Summary

In-cylinder flow field characteristics have been considered both in the tumble and swirl planes. It has been shown that the individual bulk flow characteristics are not well represented by the ensemble mean of the low frequency flow fields. From this, the importance of considering the bulk low frequency flow characteristics alongside higher frequency fluctuations has been further emphasized. Characteristics which drive high variation in the low frequency bulk motions, such as the opposing flows across the piston, have been highlighted and comparative *rms* of cyclic variation plots have been presented.

Comparison studies with and without the tumble flap in the tumble and swirl planes, have shown that the nature of the cyclic variation in the flow field can be altered by affecting the flow entering into the cylinder and therefore the bulk motion characteristics. It has also been shown that the intake flow characteristics affect the in-cylinder flow structure.

The presence of the tumble flap has been shown to alter the characteristics of u' over the course of a cycle. This change was shown to occur in both the development of the mean u' and its standard deviation. These results can be linked back to the findings from Chapter 5 which showed that variations in u' correlated with variations in pressure related performance parameters. From the study of in-cylinder flows within this chapter, the implied link between engine geometry and cyclic variation in cycle output has been strengthened.

Chapter 8 Conclusions and further work

8.1 Conclusions

The work presented in this thesis has addressed two major objectives (as introduced in Section 1.2), namely:

1. The development of an optical engine research facility at Loughborough University as well as a robust set of experiment tools for the routine application of temporally resolved HSDPIV;
2. Investigation of spatial and temporal behaviours of flow field cyclic variations.

These research objectives have been met and presented within this thesis. During the course of this work a world class experimental facility comprising of an optical direct injection gasoline engine, capable of operating under fired engine conditions was developed. This facility included systems to control the triggering of diagnostic measurement equipment and the development of data acquisition systems to monitor the engine and record operating conditions, see Chapter 4. Additionally, this thesis has presented a detailed investigation of in cylinder flow field spatial and temporal development using a novel high speed digital particle image velocimetry (HSDPIV) system. This has allowed high spatial resolution measurements of the flow to be made whilst capturing these flow fields with sufficient temporal resolution to follow the development of flow field structures within an individual engine cycle.

The HSDPIV system allowed data to be captured at temporally resolved rates up to 5 kHz, which resulted in large amounts of data being collected at a number of different

measurement locations. The effect of the flow variability has been studied within the intake runner, the valve jet, in the cylinder and in the pent roof using the optical engine facility. The in-cylinder flow fields have been studied in both the tumble and swirl planes. It has only been possible to present a small selection of the data collected within this thesis.

Temporally filtering the data gathered into high and low frequency components has allowed the study of low frequency bulk flow motions through the cycle. By investigating where the major differences occur within these bulk flow characteristics from cycle to cycle it is possible to investigate where instabilities in the flow fields are generated and follow their progression throughout the cycle. It has been shown in this work that the remaining high frequency characteristics of the flow are influential during the combustion event. Therefore, an initial understanding of the nature of the decay of these high frequency fluctuations has been investigated, but requires further analysis using the tools developed as part of this research to understand how different frequency components behave over time.

In Chapter 5 the flame growth and flow fields leading up to the time where the flame is growing has been presented. The flame growth shows that the flame appears to be affected by both bulk convective flow and small scale turbulent structures. This led to an investigation of flow field around the spark plug leading up to ignition. This highlighted a correlation of u' to engine cycle parameters such as imep and 0 to 10% mass fraction burn time. From this, and previous studies in this area, we know that u' is an important parameter in the control of cycle output. Therefore flow fields throughout the cycle have been investigated to identify instigators of cyclic variation in flow field characteristics.

In Chapter 6 cyclic variation within an optical intake runner and a plane through the valve jet were studied. Spatial variations in the flow within the intake have been observed. These have shown variations up to 2.5 $m.s^{-1}$, during the main inlet phase. Cycle by cycle variations have also been seen of up to 3 $m.s^{-1}$ in the flow towards the intake valve. These flow variations have been surpassed by the flow occurring within

the intake valve jet, where variations of approximately 5 to 10 $m.s^{-1}$ depending on the region of interest have been observed. It is not clear whether these variations are a magnification of those variations seen within the intake runner or whether they are instigated by variations in the valve jet, as it is only possible to look at a single 2-dimensional plane through one of the two valve annuli.

In Chapter 7 variations in flow fields that develop within the cylinder have been investigated in both a tumble and swirl plane. This has shown that fluctuations in the high velocity flows entering the cylinder affect how resulting interactions occur and therefore how zones of higher cyclic variability are created. The decay of the high frequency fluctuations within the cylinder have been presented along with the turbulence intensity, u', and have shown that the flow field characteristics beyond 180° CA affect the nature of u' later in the cycle.

8.2 Future work

During the course of this work an experimental facility has been developed to allow a DISI optical engine to be operated under fired conditions. This facility allows the routine capture of synchronised HSDPIV and cylinder pressure data. Future work should use this world class facility and HSDPIV capability to study the characterisation of the flow leading up to and during the combustion process. Using the spatial and temporal resolution of the HSDPIV, and the work presented in this thesis, the flow field can be decomposed into its bulk flow and higher frequency turbulent fluctuations. These should be used to investigate correlations between the turbulent flows and the propagation of the flame into the unburned charge. This will allow the progression of fundamental turbulent combustion studies into an in-cylinder environment therefore investigating the effects of cyclic variation in flow fields characterised within this thesis to be further understood. The frequency used within the decomposition should be investigated to gauge which scales of fluctuations are most influential on burn rate. The use of stereoscopic high speed digital PIV to gain insight into third component motions would be useful, however, the current architecture of the optical engine would require

amending to allow adequate optical access around the engine head support pillars. By introducing some information about the third component of motion improved correlation may be found.

A simplification to the true engine geometry, to facilitate the optical piston crown window, was used in this facility to give the piston it a flat surface. Since bulk motion variation in the in-cylinder flow field appears to be exacerbated by the interaction of the opposing flows discussed in this work, studies incorporating tumble ramps on the piston surface should be made to investigate whether features such as these act to stabilise this flow and help reduce variation in bulk motion decay.

Some experimentation by the author, during the work contributing to this thesis, has highlighted the use of dual plane PIV, using the polarization of the laser to separate the two planes and therefore ensure the cameras only image one plane. Further work in this area will allow investigation into the shear between two close measurement planes, and would be of significant interest in the pent roof of the combustion chamber as the combustion event is initiated. This does, however, require two PIV systems and as such requires significant investment in capital equipment, especially if employing HSDPIV in the study.

The investigation of how the timing of fuel introduction into the cylinder affects the flow field and its decay into combustion affecting turbulence should be studied. The tools presented in this work allow important flow characteristics to be extracted. These should be monitored as variations in fuel timing are made to assess the impact of these changes to fuel timing or the introduction of split injection events on the conditions seen in the flow around the time of ignition and subsequent combustion event.

The use of alternative decomposition techniques such as Proper Orthogonal Decomposition (POD) and Wavelets should be considered. However, at the time of writing, the use of POD on HSDPIV data with high spatial and temporal resolution with a sufficient number of cycles represented required computing resource far greater than

that routinely available to the author. The use of Wavelets to allow decomposition of the three dimensional data being captured is an emerging field which is currently the reserve of mathematicians, but promises to be a useful tool replacing the use of the FFT used in this study.

References

Abdi Aghdam, E., Burluka, A. A., Hattrell, T., Liu, K., Sheppard, C. G. W., Neumeister, J. and Crundwell, N. (2007). "Study of cyclic variation in an SI engine using quasi-dimensional combustion model." SAE Paper **2007-01-0939**.

Adrian, R. J. (1984). "Scattering Particle Characteristics and Their Effect on Pulsed Laser Measurements of Fluid Flow: Speckle Velocimetry v/s Particle Image Velocimetry." Applied Optics **Vol. 23**(No. 11): pp. 1690-1691.

Adrian, R. J. (1997). "Dynamic Ranges of Velocity and Spatial Resolution of Particle Image Velocimetry." Measurement Science and Technology **Vol. 8**: pp. 1393-1398.

Adrian, R. J. (1986). "An Image Shifting Technique to Resolve Directional Ambiguity in Double Pulsed Velocimetry." Applied Optics **Vol. 25**: pp. 3855-3858.

Adrian, R. J. (1991). "Particle Imaging Techniques for Experimental Fluid Mechanics." Annual Review of Fluid Mechanics **Vol. 23**: pp. 261-304.

Annand, W. J. D. and Roe, G. E. (1974). Gas flow in the internal combustion engine, Foulis. Yeovil.

Arcoumanis, C. and Bae, C. S. (1993). "Visualization of Flow / Flame Interaction in a Consant Volume Combustion Chamber." SAE Paper **930868**.

Arcoumanis, C., Hu, Z., Vafidis, C. and Whitelaw, J. H. (1990). "Tumbling Motion a Mechanism for Turbulence Enhancement in Spark Ignition Engines." SAE Paper **900060**.

Ball, J. K. (1998). Cycle by Cycle Variation in Spark Ignition Internal Combustion Engines, University of Oxford. **PhD Thesis**.

Barnard, J. A. and Bradley, J. N. (1985). Flame and Combustion, Chapman and Hall. London.

Baumgarten, C. (2006). Mixture formation in internal combustion engines, Springer-Verlag. Berlin.

Bernard, P. S. and Wallace, J. M. (2002). Turbulent Flow, Analysis, Measurement and Prediction, John Wiley and Sons, inc. New Jersey.

Bradley, D. (1992). How Fast Can We Burn? Twenty Fourth Symposium (Internationa) on Combustion / The Combustion Institute.

Bradley, D. , Lawes, M., Kexin Liu, Verhelst, S. and Woolley, R. (2007). "Laminar Burning Velocities of Lean Hydrogen-Air Mixtures at Pressures up to 1.0 MPa." Combustion and Flame **Vol. 149**: pp. 162 - 172.

Bradley, D. and Sheppard, C. G. (1988). "Limitations to Turbulence Enhanced Burning Rates in Lean Burn Engines." Proceedings - Institution of Mechanical Engineers Part C Journal of Mechanical Engineering Science **C46/88**.

Bray, K. N. C. (1985). "Laminar Flamelet Modelling of Turbulent Combustion." Lecture Notes in Physics **Vol. 241**: 1 - 19.

Bray, K. N. C. (1996). The Challenge of Turbulent Combustion. 26th Symposium on Combustion, The Combustion Institute.

Brown, A. G., Stone, R. and Beckwith, P. (1996). "Cycle-by-cycle variations in spark ignition engine combustion - Part 1: Flame Speed and Combustion Measurements and a Simplified Turbulent Combustion Model." SAE Paper **960612**.

Brunt, M. F. J. and Emtage, A. L. (1997). "Evaluation of Burn Rate Routines and Analysis Errors." SAE Paper **970037**.

Burch, J. M. and Taokarski, J. M. J. (1968). "Production of Multiple Beam Fringes From Photographic Scatters." Optica Acta **Vol. 15**(No. 2): pp. 101-111.

Calendini, P. O., Duverger, T., Lecerf, A. and Trinite, M. (2000). "In-Cylinder Velocity Measurements with Stereoscopic Particle Image Velocimetry in a SI Engine." SAE Paper **2000-01-1798**.

Church, W. and Farrell, P. V. (1998). "Effects of Intake Port Geometry on Large Scale In-Cylinder Flows." SAE Paper **980484**.

Davidson, P. A. (2004). Turbulence: An Introduction for Scientists and Engineers, Oxford University Press. Oxford.

Drain, L. E. (1980). The Laser Doppler Technique, J Wiley and sons. Chichester.

Dring, R. P. (1982). "Sizing criteria for laser anemonetry particles." Transactions ASME, Journal of Fluids Engineering **104**: 15-17.

Dudderar, T. D. and Simpkins, P. G. (1977). "Laser Speckle Photography." Nature **Vol. 270**: pp 45-47.

Durst, F., Melling, A. and Whitelaw, J. H. (1981). Principles and Practice of Laser-Dopple Anemometry, Academic. London

Fansler, T. D. and French, D. T. (1988). "Cycle Resolved Laser Velocimetry Measurements in a Re-entrant Bowl in Piston Engine." SAE Paper **880377**.

Ferguson, C. R. (2001). Internal Combustion Engines, Applied Thermoscience, John Wiley & Sons.0471356174.

Fischer, J., Velji, A. and Spicher, U. (2004). "Investigation of cycle-by-cycle variation of in-cylinder processes in gasoline direct injection engines operating with variable tumble systems." SAE Paper **2004-01-0044**.

Fraser, R. A., and Bracco, F. V., (1989). "Cycle Resolved LDV Integral Length Scale Measurements Investigating Clearance Height Scaling, Isotropy, and Homogeneity in an IC Engine." SAE Paper **890615**.

Ghandhi, J. B., Herold, R. E., Shakal, J. S. and Strand, T. E. (2005). "Time Resolved Particle Image Velocimetry Measurements in an Internal Combustion Engine." SAE Paper **2005-01-3868**.

Gillespie, L. , Lawes, M., Sheppard, C. G. W. and Woolley, R. (2000). "Aspects of Laminar and Turbulent Burning Velocity Relevant to SI Engines." SAE Paper **2000-01-0192**.

Gindele, J., Kech, J. M., Scholl, D. M. and Spicher, U. (1997). "Time Resolved Investigation of Unsteady Flow Inside Inlet Manifolds and Characterisation of Inlet Flow Behaviour." SAE Paper **972828**.

Grant, I. (1997). "Particle Image Velocimetry: A Review." Proceedings - Institution of Mechanical Engineers Part C Journal of Mechanical Engineering Science **Vol. 211**: pp. 55-76.

Hadded, O. and Denbratt, I. (1992). "Turbulence Characteristics of Tumbleing Air Motion in Four Valve SI Engines and their Correlation with Combustion Parameters." SAE Paper **920478**.

Heywood, J. B. (1988). Internal Combustion Engine Fundamentals, McGraw-Hill. New York.

Hu, Z., Vafidis, C., Whitelaw, J. H., Chapman, J. and Head, R. A. (1992). "Correlation Between In-Cylinder Flow, Performance and Emissions Characteristics of a Rover Pentroof Four-Valve Engine." Proceedings - Institution of Mechanical Engineers Part C Journal of Mechanical Engineering Science **C448/026**.

Huang, H., Dabiri, D. and Gharib, M. (1997). "On Errors of Digital Particle Image Velocimetry." Measurement Science and Technology **Vol. 8**: pp. 1427-1440.

Internal Combustion Engine Group, Department of Engineering Science University of Oxford (2004). CoBRA User Manual, Combustion Burn Rate Analysis and Data Processing.

Jarvis, S., Justham, T., Garner, C. P., Hargrave, G. K., Clarke, A. and Richardson, D. (2006). "Motored SI IC Engine In-Cylinder Flow Field Measurment Using Time Resolved Digital PIV for Characterisation of Cyclic Variation." SAE Paper **2006 -01-1044**.

Jarvis, S. (2003). Premixed Flame Propagation and Interaction with Turbulent Flow Structures in a Semi-Confined Combustion Chamber. Ph.D Thesis, Loughborough University.

Jeon, C.-H., Chang, Y.-J., Cho, K.-B. and Kang, K.-Y. (1998). "Effects of Intake Ports on In-Cylinder Flow and Lean Combustion in a 4-Valve Engine." SAE Paper **981048**.

Joo, S. H., Srinivasan, K. K., Lee, K. C. and Bell, S. R. (2004). "The Behaviour of Small and Large Scale Variations of In-Cylinder Flow During Intake and Compression Strokes in a Motored Four Valve Spark Ignition Engine." International Journal of Engine Research (IMechE) **Vol. 5**(No. 4): pp. 317-328.

Justham, T., Jarvis, S., Garner, C. P., Hargrave, G. K., Clarke, A. and Richardson, D. (2006). "Single Cylinder Motored SI IC Engine Intake Runner Flow Measurement Using Time Resolved Digital Particle Image Velocimetry " SAE Paper **2006-01-1043**.

Kang, K. Y. and Baek, J. H. (1998). "Turbulence Characteristics of Tumble Flow in a Four Valve Engine." Experimental Thermal and Fluid Science **Vol. 18**: pp. 231-243.

Keane, R. D. and Adrian, R. J. (1992). "Theory of cross-correlation analysis of PIV images." Applied Scientific Research **Vol. 49**: pp. 189-190.

Kim, M., Park, J., Lee, N. and Choi, K.-H. (1999). Analysis of In-Cylinder Flow in a Spark Ignited Direct Injection Engine Using PIV and CFD. Proc. of the 15th International Internal Combustion Engine Symposium, Seoul, Korea.

Kiyota, Y., Akishino, K. and Ando, H. (1992). "Concept of Lean Combustion by Barrel Stratification." SAE Paper **920678**.

Kuwahara, K., Watanabe, T., Takemura, J., Omori, S., Kume, T. and Ando, H. (1994). "Optimisation of in-cylinder flow and mixing for a centre-spark four vlave engine employing the concept of barrel stratification." SAE Paper **940986**.

Lawson, N. J. (1995). The Application of Particle Image Velocimetry to High Speed Flows, Loughborough University of Technology.

Le Coz, J.-F., Henriot, S. and Pinchon, P. (1990). "An Experimental and Computational Analysis of the Flow Field in a Four-Valve Spark Ignition Engine - Focus on Cycle Resolved Turbulence." SAE Paper **900056**.

Lee, J. and Farrell, P. V. (1993). "Intake Valve Flow Measurements of an IC Engine Using Particle Image Velocimetry." SAE Paper **930480**.

Lee, K. H. and Lee, C. S. (2003). "Effects of Tumble and Swirl Flows on Turbulence Scale Near Top Dead Centre in a Four-Valve Spark Ignition Engine." Proceedings - Institution of Mechanical Engineers Part D Journal of Automobile Engineering **Vol. 217**(D04502): pp. 607-615.

Li, Y., Zhao, H. and Ladommatos, N. (2002). "Analysis of Large-Scale Flow Characteristics in a Four-Valve Spark Ignition Engine." Proceedings - Institution of

Mechanical Engineers Part C Journal of Mechanical Engineering Science **216**: pp. 923 - 938.

Li, Y., Zhao, H., Peng, Z. and Ladommatos, N. (2001). "Analysis of Tumble and Swirl Motions in a Four Valve SI Engine." SAE Paper **2001-01-3555**.

Li, Y., Zhao, H., Peng, Z. and Ladommatos, N. (2002). "Tumbling flow analysis in a four-valve spark ignition engine using particle image velocimetry." International Journal of Engine Research (IMechE) **Vol. 3**(No. 3): pp. 139-155.

Lourenco, L. and Krothapalli, A. (1986). "The role of photographic parameters in laser speckle or particle image velocimetry." Experements in Fluids **5**: 29-32.

Melling, A. (1997). "Tracer Particles and Seeding for Particle Image Velocimetry." Measurement Science and Technology **Vol. 8**: pp. 1406-1416.

Mueller, C. J., Driscoll, J. F., Reuss, D. L. and Drake, M. C. (1996). Effects of unsteady stretch on the strength of a freely-propagating flame wrinkled by a vortex. Twenty sixth symposium (international) on Combustion

Munson, B. R., Young, D. F. and Okiishi, T. H. (1998). Fundamentals of Fluid Mechanics, John Wiley & Son's. New York.

Nadarajah, S., Balabani, S., Tindal, M. J. and Yianneskis, M. (1998). "The turbulence structure of the annular non-swirling flow past an axisymmetric poppet valve." Proceedings - Institution of Mechanical Engineers Part C Journal of Mechanical Engineering Science **Vol. 212**(C01597).

Namazian, M., Hansen, S. P., Lyford-Pike, E. J., Sanchez-Barsse, J., Heywood, J. B. and Rife, J. (1980). "Schlieren visualisation of the flow and density fields in the cylinder of a spark ignition engine." SAE Paper **800044**.

NewWave Research (2004). Pegasus-PIV A High-Speed Laser for Particle Image Velocimetry (Product Data Sheet Doc. No. PV-SEL-DSa4-0311).

Omori, S., Iwachido, K., Motomochi, M. and Hirako, O. (1991). "Effect of Intake Port Flow Pattern on the In-Cylinder Tumbling Air Flow in Multi-Valve SI Engines." SAE Paper **910477**.

Ozdor, N., Dulger, M. and Sher, E. (1994). "Cyclic Variability in Spark Ignition Engines - A Literature Survey." SAE Paper **940987**.

Patel, S. N. D. H. and Ibrahim, S. S. (2002). "Calculations of Burning Velocity of Turbulent Premixed Flames Using a Flame Surface Density Model." JSME International Journal Series B **Vol. 45**(No. 3): pp. 725-735.

Pickering, C. J. D. and Halliwell, N. A. (1984). "Laser Speckle Photography and Particle Image Velocimetry: Photographic Film Noise." Applied Optics **Vol. 23**(No. 17): pp. 2961-2969.

Pischinger, S. and Heywood, J. B. (1990). "How heat losses to the spark plug electrodes affect flame kernel development in an SI Engine." SAE Paper **900021**.

Pitcher, G., Turner, J., Wigley, G. and Chen, R. (2003). "A Comparison of the Flow Fields Generated for Spark and Controlled Auto Ignition." SAE Paper **2003-01-1798**.

Pope, S. B. (1987). "Turbulent Premixed Flames." Annual Review of Fluid Mechanics **Vol. 19**: pp.237-270.

Pope, S. B. (2000). Turbulent Flows, Cambridge University Press.

Raffel, M., Willert, C. and Kompenhans, J. (1998). Particle Image Velocimetry - A Practical Guide, Springer-Verlag. Berlin.

Rassweiler, G. M. and Withrow, L. (1980). "Motion of Engine Flames Correlated with Pressure Cards." SAE Paper **800131**.

Reeves, M., Garner, C. P., Dent, J. C. and Halliwell, N. A. (1996). "Particle image velocimetry measurements of in-cylinder flow in a multi-valve internal combustion engine." Proceedings - Institution of Mechanical Engineers Part D Journal of Automobile Engineering **210**(1): 63-70.

Reeves, M., Haste, M. J., Garner, C. P. and Halliwell, N. A. (1999). "Barrel Swirl Brake Down in Spark-Ignition Engines: Insights from Particle Image Velocimetry Measurements." Proceedings - Institution of Mechanical Engineers Part D **Vol. 213**(6): pp. 595-608.

Reeves, M. (1995). Particle Image Velocimetry Applied to Internal Combustion Engine In-Cylinder FLows. Ph.D Thesis, Loughborough University.

Reuss, D. L. (2000). "Cyclic Variability of Large Scale Turbulent Structures in Directed and Undirected IC Engine Flows." SAE Paper **2000-01-0246**.

Reuss, D. L., Adrian, R. J. and Landreth, C. C. (1989). "Two-Dimensional Velocity Measurements in a Laminar Flame Using Particle Image Velocimetry." Combustion Science and Technology **Vol. 67**: pp. 73-83.

Rimmer, J. E. T., Long, E. J., Garner, C. P., Hargrave, G. K., Richardson, D. and Wallace, S. (2009). "The Influence of Single and Multiple Injection Strategies on In-Cylinder Flow and Combustion within a DISI Engine." SAE Paper **2009-01-0660**.

Song, Y. S., Hong, J. W. and Lee, J. T. (2001). "The Turbulence Measurement During the Intake and Compression Process for High Turbulence Generation Around Spark Timing." Proceedings - Institution of Mechanical Engineers Part D Journal of Automobile Engineering **Vol. 215**(D03500): pp. 493-501.

St. Hill, N., Asadamongkon, P. and Lee, K. C. (2000). A study of turbulence and cyclic variation levels in internal combustion engine cylinders. Proceedings of the 10th International Symposium on Applications of Laser Techniques to Fluid Mechanics, Lisbon, Portugal.

Stansfield, P., Wigley, G., Justham, T. and Catto, J. (2007). "PIV Analysis of In-Cylinder Flow Structures Over a Range of Realistic Engine Speeds." Experiments in Fluids **43**(1): 135-146.

Stone, C. R. and Green-Armytage, D. L. (1987). "Comparison of Methods for the calculation of Mass Fraction Burned from Engine Pressure Time Diagrams." Proceedings - Institution of Mechanical Engineers Part D Journal of Automobile Engineering **201**: pp. 61 - 67.

Stone, R. (1999). An Introduction to Internal Combustion Engines, PALGRAVE. Basingstoke Hampshire.

Stone, R., Brown, A. G. and Beckwith, P. (1992). A Turbulent Combustion Model Used to Give Insight Into Cycle by Cycle Variation In Spark Ignition Engine Combustion. Proceedings of the Institute of Mechanical Engineers, Combustion in Engines, International Confrence, IMechE.

Sullivan, P., Ancimer, J. and Wallace, J. (1999). "Turbulence Averaging within Spark Ignition Engines." Experiments in Fluids **Vol. 27**: pp. 92-101.

Towers, D. P. and Towers, C. E. (2001). Cyclic Variability Measurement in I.C. Engine In-Cylinder Flows Using High Speed PIV. 4th International Symposium on Particle Image Velocimetry, Göttingen, Germany.

TSI Incorporated (1992). Model 9306 Six Jet Atomizer, Instruction Manual, Revison D, TSI Incorporated.

TSI Incorporated (2000). TSI Insight Version 3.03 Operation Manual, TSI Incorporated. USA.

Tsuchiya, K. and Nagashima, K. (2003). "A Calculation Method for Indicated Mean Effective Pressure Based on Harmonic Analysis of Pressure Waveform." International Journal of Engine Research **Vol. 4**(2): pp. 87 - 101.

Turns, S. R. (2000). An Introduction to Combustion: Concepts and Applications, McGraw-Hill. Singapore.

Wassenberg, H. and Adomeit, G. (1996). Experimental and Numerical Investigations of the Structure of Flames Under Engine Conditions. 26th Symposium on Combustion, The Combustion Institute.

Williams, F. A. (1985). Combustion Theory: The fundamental theory of chemically reacting flow systems, The Benjamin/Cummings Publishing Company.

Wilson, N. D., Watkins, A. J. and Dopson, C. (1993). "Asymmetric Valve Strategies and Their Effect on Combustion." SAE Paper **930821**.

Winterbone, D. E. and Pearson, R. J. (1999). Design Techniques for Engine Manifolds, Professional Engineering Publishing Bury St. Edmunds.1 86058 179 X.

Witze, P. O. (1982). "The effect of spark location on combustion in a variable-swirl engine." SAE Paper **820044**.

Yianneskis, M., Lee, K. C., Easson, W. J., McCluskey, D. R. and Hind, A. K. (1993). "Investigation of Flow Variations in Inlet Ports With Particle Image Velocimetry Techniques." Proceedings - Institution of Mechanical Engineers Part C Journal of Mechanical Engineering Science **C465/033/93**.

Appendix A Combustion calculations

The combustion analysis of cylinder pressure data from the engine was performed by a program written within Matlab™. The input was taken directly from a data file saved by the data acquisition system, and the output data was given as a tabulation against cycle number. The analysis calculated:

- Peak pressure and the crank angle at which peak pressure occurs ($p_{\max}$, $\theta_{p_{\max}}$)
- Rate of pressure rise ($dp/d\theta$)
- Net and Gross imep
- Mass fraction burned (mfb)

The code was designed to work with data recorded at 3600 samples per second as recorded by the data acquisition system described in Chapter 4. The once per revolution signal from the crank encoder was used as a datum for TDC and the once per 0.1 degree signal which was the basis of the acquisition sample clock was then used to calculate the revolution from this. In order to analyse the in-cylinder pressure signal recorded from the piezo capacitive pressure transducer, it is necessary to reference it to a known datum pressure to know its absolute level. This is required because of the effect of thermal drift on the piezo capacitive pressure transducer and the integration of the transducer signal by the charge amplifier. The datum can be provided by assuming that the in-cylinder pressure is equal to atmospheric pressure at either exhaust TDC or inlet BDC. Alternatively, to avoid this approximation, a piezo resistive pressure transducer located in the barrel can be used to provide the required datum pressure. This was located in such a position that it measures in-cylinder pressure when the piston is near BDC but is not exposed to the in-cylinder pressure as the piston rings move past it towards TDC. This cyclic redatuming of the in-cylinder pressure measured by the

piezo-capacitive transducer is performed by setting the in-cylinder pressure equal to the datum pressure at each intake BDC.

The knowledge of the crank rotation at each data point (given by the encoder) allowed the combustion chamber volume to be calculated (Heywood (1988)). Extracting max pressure ($p_{\max}$), the location of max pressure ($\theta_{p_{\max}}$), rate of pressure rise ($dp/d\theta$) and imep is academic once the pressure measurement has been conditioned as stated above.

The calculation of mass fraction burned however still remains. The technique which was used is that first developed by G.M. Rassweiler and L. Withrow in 1938 (Rassweiler and Withrow (1980)).Guidance was provided by the Internal Combustion Engine Group, Department of Engineering Science, University of Oxford as they have a well developed routine named 'CoBRA' (Combustion Burn Rate Analysis and Data Post Processing). The following text is taken from their user manual and describes the process used to perform this calculation which was implemented in the analysis routines employed within the work presented in this thesis.

Extract from Combustion Burn Rate Analysis and Data Post Processing User Manual (Internal Combustion Engine Group (2004))

> The combustion process was approximated by considering a series of small crank angle intervals ($\Delta\theta$), during each of which the change in pressure (Δp) is the sum of two parts:
>
> 1. The pressure rise due to piston motion (Δp_v)
> 2. The pressure rise due to combustion (Δp_c)
>
> The concept is shown graphically in Figure A.1; the charge is compressed polytropically by the piston, then a small amount of charge burns causing a pressure rise. In the next crank angle interval, the pressure again changes polytropically and another bit of charge burns, and this continues throughout the combustion period. Rassweiler and Withrow illustrated the method by

using a ‘spread sheet’ calculation procedure as an example, but this was not expounded mathematically.

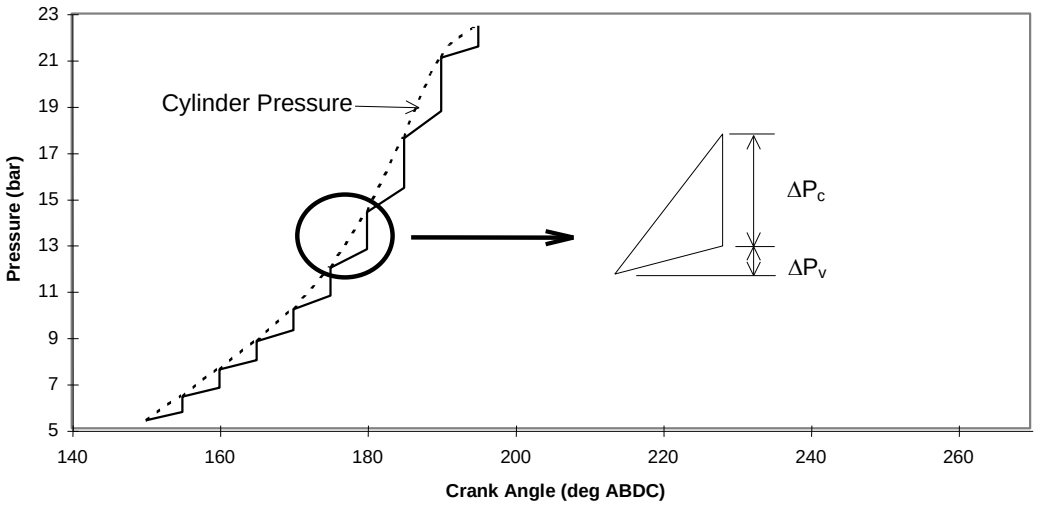

Figure A.1 – Measured pressure change as a sum of piston motion and combustion

A number of texts, *e.g.* Stone (1999), give a mathematical derivation of the method which will henceforth be referred to as the ‘standard’ method. Since the total pressure rise over one crank interval is the sum of the pressure rise due to piston motion (Δp_{v}) and the pressure rise due to combustion (Δp_{c}),

$$\Delta p = \Delta p_{\mathrm{c}} + \Delta p_{\mathrm{v}} \tag{1}$$

As the crank angle θ_i increments to θ_{i+1}, the volume changes from V_i to V_{i+1} and the pressure from p_i to p_{i+1}. It is assumed that the pressure change due to piston motion at time step i, $\Delta p_{\mathrm{v},i}$, is approximated by a polytropic process with an index n, hence:

$$p_i V_i^n = (p_i + \Delta p_{\mathrm{v},i}) V_{i+1}^n \tag{2}$$

$$\Rightarrow \Delta p_{\mathrm{v},i} = p_i \left[\left(\frac{V_i}{V_{i+1}} \right)^n - 1 \right]. \tag{3}$$

Substituting (3) into (1) produces

$$p_{i+1} - p_i = \Delta p_{c,i} + p_i \left[\left(\frac{V_i}{V_{i+1}} \right)^n - 1 \right], \tag{4}$$

from which the pressure rise due to combustion can be calculated

$$\Delta p_{c,i} = p_{i+1} - p_i \left(\frac{V_i}{V_{i+1}} \right)^n \tag{5}$$

Since combustion is not taking place at constant volume, equation (5) must be normalised to some reference volume, so that the resulting parameter is proportional to the heat released by the charge burnt during each time step. This reference volume is arbitrary (Rassweiler and Withrow used the volume at ignition); here the cylinder volume at TDC was used. This normalised pressure change is denoted by Δp_c^*

$$\Delta p_c^* = \Delta p_{c,i} \left(\frac{V_i}{V_{TDC}} \right) \tag{6}$$

The point at which Δp_c^* is no longer positive indicates the end-of-combustion (EOC), because then no more heat is being released by charge burn. Assuming that the cumulative normalised pressure rise due to combustion is proportional to the mass fraction burned (x), then for N total increments

$$x = \frac{\sum_0^i \Delta p_c^*}{\sum_0^N \Delta p_c^*} \text{ (standard method)} \tag{7}$$

The total normalised pressure change due to combustion is known as

$$\psi = \sum_{0}^{N} \Delta p_c^* \ .$$

Several key observations were pointed out in the original work regarding this method:

1. Since the piston motion and combustion are considered to progress in a stepwise fashion, small step sizes should be used to minimise errors.
2. The effects of heat transfer are accounted for only in the choice of the polytropic index *n*. The accuracy of the index thus influences the accuracy of the calculations.
3. Blowby will affect the results, by making the compression and expansion process deviate from polytropic.
4. In order to normalise the pressure rises due to combustion, it was assumed that pressure rise was inversely proportional to total volume.
5. In order to calculate the pressure rise due to combustion, the polytropic indices for the burned and unburned regions were assumed to be equal.

Further assumptions are also inherent in this method (Heywood (1988); Stone (1999)):

1. it assumes that the referenced pressure rise is proportional to the mass of fuel burned rather than the amount of chemical energy released, and
2. there is no allowance for heat transfer, dissociation, or change in composition beyond the fact that the polytropic index differs from the ratio of specific heats

Despite these limitations, comparisons of mass fraction burned calculated using the Rassweiler and Withrow method with the results of other more complex thermodynamic models show remarkably close agreement (Stone and Green-Armytage (1987); Brunt and Emtage (1997)).

As mentioned above, the sensitivity of the method to the calculation and selection of the polytropic index is very important. If the compression index is used throughout the calculation, it results in a characteristic fall in the mass fraction burned curve after the end of combustion. This is due to heat transfer and the presence of combustion products resulting in a different polytropic index after the combustion event than before it. An accurate index would produce a curve that rose to 1.0 and remain there through to the end of the cycle. Rassweiler and Withrow evaluated the index during compression and expansion, and used an appropriately averaged value during combustion. Other researchers, detailed by Ball (1998), propose switching from one index to the other at TDC, and also various methods for determining EOC for the purposes of calculating the expansion index.

Calculation of the compression index must also be done with care since the pressure rise at the beginning of the stroke is small and discretisation errors (ADC steps) from the data acquisition system are more significant (Stone (1999)). This can be avoided by ignoring the initial part of compression, for example, by calculating the index from halfway between IVC and ignition to ignition.

With regard to the concerns about the calculation and selection of polytropic index, the calculation procedure adopts the following definitions and methods:

1. The compression index is evaluated from halfway between IVC and ignition to ignition.
2. EOC is defined as the point at which the cumulative sum of normalised pressure changes due to combustion is a maximum.
3. The compression index is applied throughout the calculation. The MFB results after EOC do not remain at unity as they should, because of heat transfer and leakage.

References for Appendix A

Ball, J. K. (1998). Cycle by Cycle Variation in Spark Ignition Internal Combustion Engines, University of Oxford. PhD Thesis.

Brunt, M. F. J. and Emtage, A. L. (1997). "Evaluation of Burn Rate Routines and Analysis Errors." SAE Paper 970037.

Heywood, J. B. (1988). Internal Combustion Engine Fundamentals, McGraw-Hill. New York.

Internal Combustion Engine Group, Department of Engineering Science University of Oxford (2004). CoBRA User Manual, Combustion Burn Rate Analysis and Data Processing.

Stone, C. R. and Green-Armytage, D. L. (1987). "Comparison of Methods for the calculation of Mass Fraction Burned from Engine Pressure Time Diagrams." Proceedings - Institution of Mechanical Engineers Part D Journal of Automobile Engineering 201: pp. 61 - 67.

Stone, R. (1999). An Introduction to Internal Combustion Engines, PALGRAVE. Basingstoke Hampshire.